

Lecture Notes in Electrical Engineering 538

Zainah Md Zain

Hamzah Ahmad

Dwi Pebrianti

Mahfuzah Mustafa

Nor Rul Hasma Abdullah

Rosdiyana Samad

Maziyah Mat Noh *Editors*

Proceedings of the 10th National Technical Seminar on Underwater System Technology 2018

NUSYS'18

Lecture Notes in Electrical Engineering

Volume 538

Board of Series editors

Leopoldo Angrisani, Napoli, Italy
Marco Arteaga, Coyoacán, México
Bijaya Ketan Panigrahi, New Delhi, India
Samarjit Chakraborty, München, Germany
Jiming Chen, Hangzhou, P.R. China
Shanben Chen, Shanghai, China
Tan Kay Chen, Singapore, Singapore
Ruediger Dillmann, Karlsruhe, Germany
Haibin Duan, Beijing, China
Gianluigi Ferrari, Parma, Italy
Manuel Ferre, Madrid, Spain
Sandra Hirche, München, Germany
Faryar Jabbari, Irvine, USA
Limin Jia, Beijing, China
Janusz Kacprzyk, Warsaw, Poland
Alaa Khamis, New Cairo City, Egypt
Torsten Kroeger, Stanford, USA
Qilian Liang, Arlington, USA
Tan Cher Ming, Singapore, Singapore
Wolfgang Minker, Ulm, Germany
Pradeep Misra, Dayton, USA
Sebastian Möller, Berlin, Germany
Subhas Mukhopadhyay, Palmerston North, New Zealand
Cun-Zheng Ning, Tempe, USA
Toyoaki Nishida, Kyoto, Japan
Federica Pascucci, Roma, Italy
Yong Qin, Beijing, China
Gan Woon Seng, Singapore, Singapore
Germano Veiga, Porto, Portugal
Haitao Wu, Beijing, China
Junjie James Zhang, Charlotte, USA

Lecture Notes in Electrical Engineering (LNEE) is a book series which reports the latest research and developments in Electrical Engineering, namely:

- Communication, Networks, and Information Theory
- Computer Engineering
- Signal, Image, Speech and Information Processing
- Circuits and Systems
- Bioengineering
- Engineering

The audience for the books in LNEE consists of advanced level students, researchers, and industry professionals working at the forefront of their fields. Much like Springer's other Lecture Notes series, LNEE will be distributed through Springer's print and electronic publishing channels.

More information about this series at <http://www.springer.com/series/7818>

Zainah Md Zain · Hamzah Ahmad
Dwi Pebrianti · Mahfuzah Mustafa
Nor Rul Hasma Abdullah
Rosdiyana Samad · Maziyah Mat Noh
Editors

Proceedings of the 10th National Technical Seminar on Underwater System Technology 2018

NUSYS'18

 Springer

Editors

Zainah Md Zain
Faculty of Electrical
and Electronics Engineering
Universiti Malaysia Pahang
Pekan, Pahang, Malaysia

Nor Rul Hasma Abdullah
Faculty of Electrical
and Electronics Engineering
Universiti Malaysia Pahang
Pekan, Pahang, Malaysia

Hamzah Ahmad
Faculty of Electrical
and Electronics Engineering
Universiti Malaysia Pahang
Pekan, Pahang, Malaysia

Rosdiyana Samad
Faculty of Electrical
and Electronics Engineering
Universiti Malaysia Pahang
Pekan, Pahang, Malaysia

Dwi Pebrianti
Faculty of Electrical
and Electronics Engineering
Universiti Malaysia Pahang
Pekan, Pahang, Malaysia

Maziyah Mat Noh
Faculty of Electrical
and Electronics Engineering
Universiti Malaysia Pahang
Pekan, Pahang, Malaysia

Mahfuzah Mustafa
Faculty of Electrical
and Electronics Engineering
Universiti Malaysia Pahang
Pekan, Pahang, Malaysia

ISSN 1876-1100 ISSN 1876-1119 (electronic)
Lecture Notes in Electrical Engineering
ISBN 978-981-13-3707-9 ISBN 978-981-13-3708-6 (eBook)
<https://doi.org/10.1007/978-981-13-3708-6>

Library of Congress Control Number: 2018963994

© Springer Nature Singapore Pte Ltd. 2019

This work is subject to copyright. All rights are reserved by the Publisher, whether the whole or part of the material is concerned, specifically the rights of translation, reprinting, reuse of illustrations, recitation, broadcasting, reproduction on microfilms or in any other physical way, and transmission or information storage and retrieval, electronic adaptation, computer software, or by similar or dissimilar methodology now known or hereafter developed.

The use of general descriptive names, registered names, trademarks, service marks, etc. in this publication does not imply, even in the absence of a specific statement, that such names are exempt from the relevant protective laws and regulations and therefore free for general use.

The publisher, the authors and the editors are safe to assume that the advice and information in this book are believed to be true and accurate at the date of publication. Neither the publisher nor the authors or the editors give a warranty, express or implied, with respect to the material contained herein or for any errors or omissions that may have been made. The publisher remains neutral with regard to jurisdictional claims in published maps and institutional affiliations.

This Springer imprint is published by the registered company Springer Nature Singapore Pte Ltd. The registered company address is: 152 Beach Road, #21-01/04 Gateway East, Singapore 189721, Singapore

Preface

NUSYS'18 is the 10th National Technical Seminar on Underwater System Technology organized by Faculty of Electrical and Electronics Engineering, Universiti Malaysia Pahang (UMP) on the September 26–27, 2018 at the UMP Pekan Campus, Pahang, Malaysia with a conference theme “Deeper Discoveries”. NUSYS'18 was jointly organized by the IEEE Oceanic Engineering Society (IEEE OES) Malaysia Chapter, Malaysian Society for Automatic Control Engineers (MACE) IFAC NMO and Institute of Engineer Malaysia (IEM) Marine Engineering and Naval Architecture Technical Division (MNATD).

Despite focusing on a rather specialized area of research concerning underwater technology and marine and electrical and electronics engineering technology, NUSYS'18 has successfully attracted 57 papers locally from 7 universities. This volume of proceedings from the conference provides an opportunity for readers to engage with a selection of refereed papers that were presented during the NUSYS'18 conference. Divided into four parts, the papers had been classified into the following four categories; Underwater Technology and Marine, Applied Electronics and Computer Engineering, Control, Instrumentations and Artificial Intelligent Systems and Sustainable Energy and Power Electronics.

Part I presents the research and development related to underwater system. The main contributions to this part are the design and development of underwater vehicle platforms and controller algorithms. Several autonomous underwater vehicles (AUVs) are presented in this part, such as TUAH and PANTHER AUVs. Most of the AUVs are developed for underwater data collection purposes and other applications such as surface cleaning. A water strider-like is an autonomous surface vehicle (ASV) also developed for underwater data collection. Control algorithm is very important to ensure the underwater vehicles are able to carry out the task. In this part, several control algorithms are proposed such as PID where the controller parameters are optimized using particle swarm optimization (PSO), single-input fuzzy logic controller where the PSO is used to optimize the controller parameters and robust controller algorithm based on integration of back-stepping and integral

sliding mode control strategies. Part II describes the possible control techniques and optimization algorithm approaches for consideration in underwater control system such as interval type-2 fuzzy logic, adaptive fuzzy PID controller, and optimization algorithms such as memory-based SPSA, Barnacles mating optimization, extended bat algorithm (EBA), bat algorithm (BA), and simulated Kalman filter.

The development of an AUV's integrates various engineering disciplines. In Part III, various applied electronics and computer engineering area such as image processing, signal processing, embedded technology, antenna, IoT, and artificial intelligence that can be implemented for underwater imaging system and communication system are presented. Last but not least, the most vital part of the AUV is its power distribution unit (PDU) which provides, coordinates, and distributes energy to the entire onboard electrical system devices. Therefore, in Part IV several papers are identified to be useful in managing the AUV power system. Looking at the aspect of AUV efficiency and stability, a number of papers have provided an overview of the factors to be considered such as the current and voltage analysis. These are among the important parameters in guaranteeing long-lasting battery operation. It is expected that by the information obtained in this book, researchers as well as any interested readers would find the relevant information on research and development of the AUV, which covers a wide range of aspects; technologies, control system and instrumentation, electronics design and application, and power system analysis.

We wish to take the opportunity to thank all individuals and organizations, who have contributed in some way in making NUSYS'18 a success and a memorable gathering. Also, we wish to extend my gratitude to the members of the IEEE OES Malaysia Chapter Committee and Organizing Committee for their tireless effort. Finally, we would like to thank Mr. Ramesh for his support and encouragement in undertaking this publication.

Pekan, Malaysia

Zainah Md Zain
Hamzah Ahmad
Dwi Pebrianti
Mahfuzah Mustafa
Nor Rul Hasma Abdullah
Rosdiyana Samad
Maziyah Mat Noh

Contents

Part I Underwater Technology and Marine

PSO Fine-Tuned Model-Free PID Controller with Derivative Filter for Depth Control of Hovering Autonomous Underwater Vehicle	3
Mohd Zaidi Mohd Tumari, Amar Faiz Zainal Abidin, Mohamed Saiful Firdaus Hussin, Ahmad Muzaffar Abd Kadir, Mohd Shahrieel Mohd Aras and Mohd Ashraf Ahmad	
Optimization of Single Input Fuzzy Logic Controller Using PSO for Unmanned Underwater Vehicle	15
Mohd Shahrieel Mohd Aras, Shahrums Shah Abdullah, Hazriq Izuan Jaafar, Ahmad Anas Yusof, Mohd Zaidi Mohd Tumari and Ho Gui Yan	
UTeM Autonomous Underwater Vehicle Competition Initiatives: Project TUAH and PANTHER	27
Ahmad Anas Yusof, Mohd Khairi Mohamed Nor, Shamsul Anuar Shamsudin, Mohd Rizal Alkahari, Mohd Shahrieel Mohd Aras, Mohamad Riduwan Md. Nawawi, Mohd Zaidi Mohd Tumari and Mohammad Afif Kasno	
Deep Underwater Image Enhancement Through Integration of Red Color Correction Based on Blue Color Channel and Global Contrast Stretching	35
Kamil Zakwan Mohd Azmi, Ahmad Shahrizan Abdul Ghani, Zulkifli Md Yusof and Zuwairie Ibrahim	
Development of Surface Cleaning Robot for Shallow Water	45
Muhamad Qayyum Dahlan, Herdawatie Abdul Kadir, Khalid Isa, Radzi Ambar, Mohd Rizal Arshad and Maziyah Mat Noh	

Design and Development of an Autonomous Underwater Vehicle for Underwater Target Navigation Mission Module	55
Muhammad Muzakkir Ahmad Roslan, Herdawatie Abdul Kadir, Khalid Isa, Radzi Ambar, Mohd Rizal Arshad, Maziyah Mat Noh and Mohd Helmy Wahab	
Development of an Autonomous Underwater Vehicle for Target Acquisition	65
Leong Wai Lunn Alexander, Khalid Isa, Herdawatie Abdul Kadir and Radzi Ambar	
Robust Controller Design for Autonomous Underwater Glider Using Backstepping Super Twisting Sliding Mode Control Algorithm	79
Maziyah Mat Noh, M. R. Arshad, Rosmiwati Mohd-Mokhtar, Zainah Md Zain, Quadrat Khan and Herdawati Abdul Kadir	
PSpHT-II: A Water Strider-Like Robot with Cylindrical Footpad	99
Vi Vi Gan, Addie Irawan, Niirmel Ranjanendran and Siti Noor Zuliana	
An Accurate Characterization of Different Water Properties Using Resonant Method for Underwater Communication Activity	113
Salwa Awang Akbar, Ahmad Syahiman Mohd Shah, Airul Sharizli Abdullah, Nurhafizah Abu Talip Yusof, Sabira Khatun, Syamimi Mardiah Shaharum and Mohamad Shaiful Abdul Karim	
Statistical Relationship Between Multibeam Backscatter, Sediment Grain Size and Bottom Currents	121
Mohd Azhafiz Abdullah, Razak Zakariya and Rozaimi Che Hasan	
Part II Control, Instrumentation and Artificial Intelligent Systems	
Stabilization of Two-wheeled Wheelchair with Movable Payload Based Interval Type-2 Fuzzy Logic Controller	137
N. F. Jamin, N. M. A. Ghani, Z. Ibrahim, M. F. Masrom and N. A. A. Razali	
Stabilization Control of a Two-Wheeled Triple Link Inverted Pendulum System with Disturbance Rejection	151
M. F. Masrom, N. M. Ghani, N. F. Jamin and N. A. A. Razali	
Integration of PI-Anti-windup and Fuzzy Logic Control with External Derivative Solution for Leg's Robot Angular Joint Precision	161
Wan Mohd Nafis Wan Lezaini, Addie Irawan and Ahmad Nor Kasruddin Nasir	

Backstepping Control of Nonholonomic Car-like Mobile Robot in Chained Form 173
 Norsuryani Zainal Abidin, Nurul Ain Mohamed, Zainah Md. Zain, Maziyah Mat Noh, Norhafizah Md. Zain and Dwi Pebrianti

Analysis of Mobile Robot Path Planning with Artificial Potential Fields 181
 Hamzah Ahmad, Ahmad Nuur Fakhruallah Mohamad Pajeri, Nur Aqilah Othman, Mohd Mawardi Saari and Mohd Syakirin Ramli

Data-Driven PID Tuning for Liquid Slosh-Free Motion Using Memory-Based SPSA Algorithm 197
 Nik Mohd Zaitul Akmal Mustapha, Mohd Zaidi Mohd Tumari, Mohd Helmi Suid, Raja Mohd Taufika Raja Ismail and Mohd Ashraf Ahmad

Barnacles Mating Optimizer Algorithm for Optimization 211
 Mohd Herwan Sulaiman, Zuriani Mustaffa, Mohd Mawardi Saari, Hamdan Daniyal, Ahmad Johari Mohamad, Mohd Rizal Othman and Mohd Ruslim Mohamed

Random Search in Energy Management Strategy (EMS) for Hybrid Electric Vehicles 219
 Muhammad Syahmi Ghazali and Muhammad Ikram Mohd Rashid

Extended Bat Algorithm (EBA) as an Improved Searching Optimization Algorithm 229
 Dwi Pebrianti, Nurnajmin Qasrina Ann, Luhur Bayuaji, N. R. Hasma Abdullah, Zainah Md. Zain and Indra Riyanto

Performance Comparison of Perturbation Signals for Time-Varying Water Temperature Modeling Using NARX-Based BPSO 239
 Najidah Hambali, Mohd Nasir Taib, Ahmad Ihsan Mohd Yassin and Mohd Hezri Fazalul Rahiman

Adaptive Fuzzy-PID Controller for Quad-Rotor MAV with Mass Changes 257
 Goh Ming Qian, Dwi Pebrianti, Luhur Bayuaji, Rosdiyana Samad, Mahfuzah Mustafa and Mohammad Syafrullah

Investigating State Covariance Properties During Finite Escape Time in H_∞ Filter SLAM 271
 Hamzah Ahmad, Nur Aqilah Othman, Mawardi Saari and Mohd Syakirin Ramli

Diagonalization of Covariance Matrix in Simultaneous Localization and Mapping of Mobile Robot 285
 Maziatun Mohamad Mazlan, Nur Aqilah Othman and Hamzah Ahmad

Development and Control of Biped Walking Robot Using PI Control	299
K. H. Tan, N. S. M. Nor and M. Z. Md Zain	
Improved Generalized Cross Correlation Phase Transform Algorithm for Time Difference of Arrival Estimation	315
Chee Sheng Tan, Rosmiwati Mohd-Mokhtar and Mohd Rizal Arshad	
Performance Evaluation of PID Controller Parameters Gain Optimization for Wheel Mobile Robot Based on Bat Algorithm and Particle Swarm Optimization	323
Nur Aisyah Syafinaz Suarin, Dwi Pebrianti, Nurnajmin Qasrina Ann, Luhur Bayuaji, Muhammad Syafrullah and Indra Riyanto	
Restoration of Kids Leg Function Using Exoskeleton Robotic Leg (ExRoLEG) Device	335
Mohd Azrul Hisham Mohd Adib, Szeto Yang Han, Prashant Raj Ramani, Low Jian You, Law Ming Yan, Idris Mat Sahat and Nur Hazreen Mohd Hasni	
Simulated Kalman Filter Algorithm with Improved Accuracy	343
Mohd Falfazli Mat Jusof, Ahmad Azwan Abd Razak, Shuhairie Mohammad, Ahmad Nor Kasruddin Nasir, Mohd Helmi Suid, Mohd Ashraf Ahmad and Zuwairie Ibrahim	
Initial Study of Multiple Excitation Source for Electrical Resistance Tomography in Steel Pipe Application	353
Yasmin Abdul Wahab, Syazwani Amanina Syakyeen, Zainah Md. Zain, Normaniha Abd Ghani and Maziyah Mat Noh	
Simultaneous Perturbation Stochastic Approximation Optimization for Energy Management Strategy of HEV	361
Muhammad Fadhlan Afif Nazri and Muhammad Ikram Mohd Rashid	
Part III Applied Electronics and Computer Engineering	
Image Processing-Based Flood Detection	371
Angga Ariawan, Dwi Pebrianti, Ronny, Yudha Maulana Akbar, Lestari Margatama and Luhur Bayuaji	
Enhancement on Stain Detection for Automatic Handwashing Audit Vision System	381
Faradila Naim, Muhammad Aizat Romaino and Rosyati Hamid	
Classification of Transient Facial Wrinkle	391
Rosdiyana Samad, Mohammad Zarif Rosli, Nor Rul Hasma Abdullah, Mahfuzah Mustafa, Dwi Pebrianti and Nurul Hazlina Noordin	

Electromyograph (EMG) Signal Analysis to Predict Muscle Fatigue During Driving 405
 Muhammad Amzar Syazani Mohd Azli, Mahfuzah Mustafa, Rafiuddin Abdubrani, Amran Abdul Hadi, Syarifah Nor Aqida Syed Ahmad and Zarith Liyana Zahari

Time-Frequency Analysis from Earthing Application 421
 Jun Hou Ting, Mahfuzah Mustafa, Zarith Liyana Zahari, Dwi Pebrianti, Zainah Md Zain, Nurul Hazlina Noordin and Rafiuddin Abdubrani

Energy Spectral Density Analysis of Muscle Fatigue 437
 Noor Aisyah Ab Rahman, Mahfuzah Mustafa, Rosdiyana Samad, Nor Rul Hasma Abdullah and Norizam Sulaiman

Modelling Automatic IoT Home Light System (SmartLi) by NODEMCU ESP8266 447
 Muhammad Muttaqin A. Rahim, Nor Shazwanie Ramli, Najwa Raihana Abdul Wahab and Rohana Abdul Karim

Development of Automated Gate Using Automatic License Plate Recognition System 459
 Luai Taha Ahmed Al-Mahbashi, Nurhafizah Abu Talip Yusof, Syamimi Shaharum, Mohamad Shaiful Abdul Karim and Ahmad Afif Mohd Faudzi

Design of T-Shaped UWB Antenna with Dual Band Rejection Using Inverted U- and C-Shaped Slots 467
 Salwa Awang Akbar, Ahmad Syahiman Mohd Shah, Ahmad Afif Mohd Faudzi, Sabira Khatun, Syamimi Mardiah Shaharum, Nurhafizah Abu Talip @ Yusof and Mohamad Shaiful Abdul Karim

Inter Vehicle Communication System for Collision Avoidance 475
 Nurul H. Noordin, Althea C. Y. Hui, Nurulfadzilah Hassan and Rosdiyana Samad

IOT—Eye Drowsiness Detection System by Using Intel Edison with GPS Navigation 485
 Auni Syahirah Abu Bakar, Goh Khai Shan, Gan Lai Ta and Rohana Abdul Karim

Automatic Detection of Diabetic Retinopathy Retinal Images Using Artificial Neural Network 495
 Syamimi Mardiah Shaharum, Nurul Hajar Hashim, Nurhafizah Abu Talip @ Yusof, Mohamad Shaiful Abdul Karim and Ahmad Afif Mohd Faudzi

Regional Assessment of Facial Nerve Paralysis Using Optical Flow Method 505
 Wan Syahirah W. Samsudin, Rosdiyana Samad, Kenneth Sundaraj, Mohd Zaki Ahmad and Dwi Pebrianti

Design of Ultra-Wideband (UWB) Horn Antenna for Non-destructive Fruit Quality Monitoring 515
 Nurhafizah Abu Talip @ Yusof, Syamimi Mardiah Shaharum, Ahmad Afif Mohd Faudzi, Sabira Khatun, Mohamad Shaiful Abdul Karim and Siti Fatimah Hazali

Ionospheric Modeling and Precision Positioning Global Navigation Satellite System 523
 Nurul Fazira Abd Rahman, Sabira Khatun, Kamarul Hawari Ghazali, Md. Moslemuddin Fakir, Mamunur Rashid and Bifta Sama Bari

Enhancing the Integrated Vaccine System (IVS) Using MyKidVAX Mobile Application 531
 Mohd Azrul Hisham Mohd Adib, Nur Hazreen Mohd Hasni, Nor Fazlin Zabudin and Muhammad Shahminan Lukman

Microwave-Assisted Synthesis for Environmentally ZnO Nanoparticle Synthesis 541
 Norlin Pauzi, Norashikin Mat Zain and Nurul Amira Ahmad Yusof

Part IV Power Systems and Sustainable Energy

Micro-Hydro Energy Estimation for Hydrokinetic Energy Harnessing at Sungai Lembing 549
 W. I. Ibrahim, R. M. T. R. Ismail and M. R. Mohamed

Investigation of Binary Search Algorithm as Maximum Power Point Tracking Technique in Solar PV System 563
 Meng Chung Tiong, Hamdan Daniyal, Mohd Herwan Sulaiman and Mohd Shafie Bakar

Filter Design for a Nine Level Voltage Source Inverter for Renewable Energy Applications 571
 Ibrahim Haruna Shanono, Nor Rul Hasma Abdullah and Aisha Muhammad

Effects of Transformer’s Turn Ratio Mismatch Towards the Performance of Dual Active Bridge Converter 587
 Suliana Ab Ghani, Hamdan Daniyal, Nur Huda Ramlan and Meng Chung Tiong

Impact of Overcurrent Protection Coordination on the Location of the Distributed Generation Sources 595
 Noor Zaihah Jamal, Mohd Herwan Sulaiman and Omar Aliman

Investigation of Power Transfer in QAB Converter Via Phase Shift Modulation 603
Suliana Ab Ghani, Hamdan Daniyal, Nur Huda Ramlan and Meng Chung Tiong

Current Measurement of Engine Oils Under Various Voltage Application 611
Benedick Conolius, Norlin Pauzi, Mohd Herwan Sulaiman, Mohd Razali Daud, Kadowaki Kazunori and Amir Izzani Mohamed

Parameter (Voltage, Current) Study of Thermoelectric Cooler (TEC) for Automobile Air-Conditioner 617
Siti Nor Aisyah Burhanudin, Mohd Shawal Jadin and Amir Izzani Mohamed

Optimal Placement of TCSC for Reactive Power Planning Using Grasshopper Optimization Algorithm Considering Line Outage (N-M) 623
Muhamad Amirul Asyraf Juhari, Nor Rul Hasma Abdullah, Ibrahim Haruna Shanono, Mahfuzah Mustafa, Rosdiyana Samad and Dwi Pebrianti

Part I
Underwater Technology and Marine

PSO Fine-Tuned Model-Free PID Controller with Derivative Filter for Depth Control of Hovering Autonomous Underwater Vehicle



Mohd Zaidi Mohd Tumari, Amar Faiz Zainal Abidin,
Mohamed Saiful Firdaus Hussin, Ahmad Muzaffar Abd Kadir,
Mohd Shahrieel Mohd Aras and Mohd Ashraf Ahmad

Abstract The tuning of PID controller by classical technique is a monotonous job and may results in inaccurate system response. This paper proposes investigations into the development of a model-free PID controller with derivative filter (PIDF) parameter tuning method by using Particle Swarm Optimization (PSO) for depth control of Hovering Autonomous Underwater Vehicle (HAUV). PIDF controller is developed to control the speed of thrusters where 4 PIDF parameters are fine-tuned using PSO algorithms and Sum Absolute Error (SAE) and Sum Square Error (SSE) are chosen as it fitness functions. In order to confirm the design of control scheme, one degree of freedom nonlinear equation of the HAUV system in heave direction is considered. Supremacy of the proposed approach is shown by comparing the results with PID Tuner in Simulink/MATLAB. The performances of the control schemes are accessed in terms of time response specifications of depth tracking capability with the absences of added mass, hydrodynamic drag force, buoyancy force, model nonlinearities, and external disturbances on the HAUV system. Finally, it is seen from the simulation results that the proposed control technique guarantees a fast depth tracking capability.

M. Z. Mohd Tumari (✉) · A. F. Zainal Abidin · A. M. Abd Kadir
Fakulti Teknologi Kejuruteraan Elektrik & Elektronik, Centre for Robotics and Industrial Automation, Universiti Teknikal Malaysia Melaka, Hang Tuah Jaya, 76100 Durian Tunggal, Melaka, Malaysia
e-mail: mohdzaidi.tumari@utem.edu.my

M. S. F. Hussin
Fakulti Teknologi Kejuruteraan Mekanikal & Pembuatan, Centre for Advanced Research on Energy, Universiti Teknikal Malaysia Melaka, Hang Tuah Jaya, 76100 Durian Tunggal, Melaka, Malaysia

M. S. Mohd Aras
Fakulti Kejuruteraan Elektrik, Universiti Teknikal Malaysia Melaka, Hang Tuah Jaya, 76100 Durian Tunggal, Melaka, Malaysia

M. A. Ahmad
Faculty of Electrical and Electronics, Universiti Malaysia Pahang, 26600 Pekan, Pahang, Malaysia

© Springer Nature Singapore Pte Ltd. 2019
Z. Md Zain et al. (eds.), *Proceedings of the 10th National Technical Seminar on Underwater System Technology 2018*, Lecture Notes in Electrical Engineering 538, https://doi.org/10.1007/978-981-13-3708-6_1

Keywords Particle swarm optimization · PID controller
Hovering autonomous underwater vehicle (HAUV)

1 Introduction

Commonly, the control of Hovering Autonomous Underwater Vehicle (HAUV) in heave direction still faces plentiful degrees of difficulties that need to be considered due to external disturbances in the underwater environment such as waves (wind generated), ocean currents and wind [1]. These external disturbances can affect the HAUV system performance especially during hovering in certain depth. Furthermore, an accurate HAUV model is difficult to derive due to the existence of added mass and hydrodynamic damping force that acting on an underwater vehicle [2].

The control concern of the HAUV is to design the controller so that it can reach a desired depth accurately. The target of heave-axis motion is to maintain its stationary and stabilize point or also called as “station keeping”. In order to achieve these objectives, several studies in the literature reporting on HAUV depth control. For instance, fuzzy self-adaptive PID controller which fuzzy logic controller adjusts the PID controller parameters (K_p , K_i , K_d) according to the system response [3], LQR control algorithm with Genetic Algorithm (GA) to choose the weighting matrices of LQR [4], nonlinear PID depth controller with adaptive compensation [5], Active Disturbance Rejection Controller (ADRC) [6], extended state observer-based backstepping control [7], optional internal model control (OIMC) [8] and fuzzy logic controller [9].

Most of the open literatures on the HAUV depth control were focused mainly on the model-based control schemes. Regrettably, it has conclusively been shown that the model-based control schemes are difficult to apply in practice and do not precisely consider the existence of added mass and hydrodynamic damping force that acting on an underwater vehicle. Thus, a model-free approach will be more attractive. On the other hand, a model-free PID controller would provide us a promising approach for the HAUV depth control. PID has been proven to be robust and tremendously beneficial in many linear and non-linear applications such as [10–12]. Even though PID control methods are very promising for solving those system control problems, they require substantial a large amount of design effort to tune the PID parameters. However, it is possible to take full benefits of PID for HAUV system if the tuning time of PID parameters is decreased.

The main concerns addressed in this paper is a fine-tuned PID controller with derivative filter (PIDF) for nonlinear HAUV model. Since there are 4 parameters to be tuned, a Particle Swarm Optimization is chosen to amend control parameters; K_p , K_i , K_d and N to the best optimal values for the preferred control response. There have been several studies in the literature reporting on PSO fine-tuned PID in various applications such as [13, 14]. The objective of the design is to maintain its stationary and stabilize at prescribed depth. To prove the efficacy of the proposed control scheme, a one degree of freedom nonlinear equation of the HAUV system

in [15] in heave direction is considered. Then, the performance of the proposed method is assessed in term of time response specifications of depth tracking capability with the absences of added mass, hydrodynamic drag force, buoyancy force, model nonlinearities, and external disturbances on the HAUV system. Supremacy of the PSO tuning is shown by comparing the results with PID Tuner in Simulink/MATLAB [16]. Finally, it is concluded that the proposed PSO tuned PIDF control scheme is yielding superior performance for HAUV system.

The brief outline of this paper is as follows. In Sect. 2, the HAUV model is described. In Sect. 3, the PSO tuned PIDF method is explained. Simulation results and discussion are presented in Sect. 4. Finally, some concluding remarks are given in Sect. 5.

2 Modelling of HAUV

This section provides a brief description on the modelling of HAUV as a basis of a simulation environment for the development and assessment of the PSO tuned PIDF technique. A HAUV model in [15] that performing vertical motion as shown in Fig. 1 is considered. The one degree of freedom nonlinear dynamic equation of the HAUV system in heave direction is given by (1) where z , M_{RB} , M_A , D_L , D_Q , g , τ and w represents depth of the HAUV, rigid-body mass, added mass, linear hydrodynamic damping coefficient, quadratic hydrodynamic damping coefficient, net buoyancy force, thruster force and external disturbances, respectively.

$$(M_{RB} + M_A)\ddot{z} + (D_L + D_Q|\dot{z}|)\dot{z} + g = \tau + w \quad (1)$$

Wave currents reacted as an external disturbance in this simulation. The model of the wave disturbance is derived in (2) [17]. The wave disturbance is defined as a sinusoidal force acting on the HAUV system in downward direction with 0.1 Hz frequency and 2 N amplitude.

$$w = 2 \sin(0.2\pi t)N \quad (2)$$

Parameters of an open frame box-shaped HAUV developed by Underwater, Control, and Robotics Group (UCRG) Universiti Sains Malaysia (USM) are used for simulation purpose [2]. The pictures of the HAUV developed by UCRG are shown in Fig. 1. The dimension of the HAUV are 79-cm-long, 61-cm-wide and 58 cm high. The HAUV used passive buoyancy element and is set to be slightly positive buoyant. Two vertical thrusters are used to control the HAUV in downward direction. The values of its parameters are shown in Table 1. Only parameters in downward direction are used.

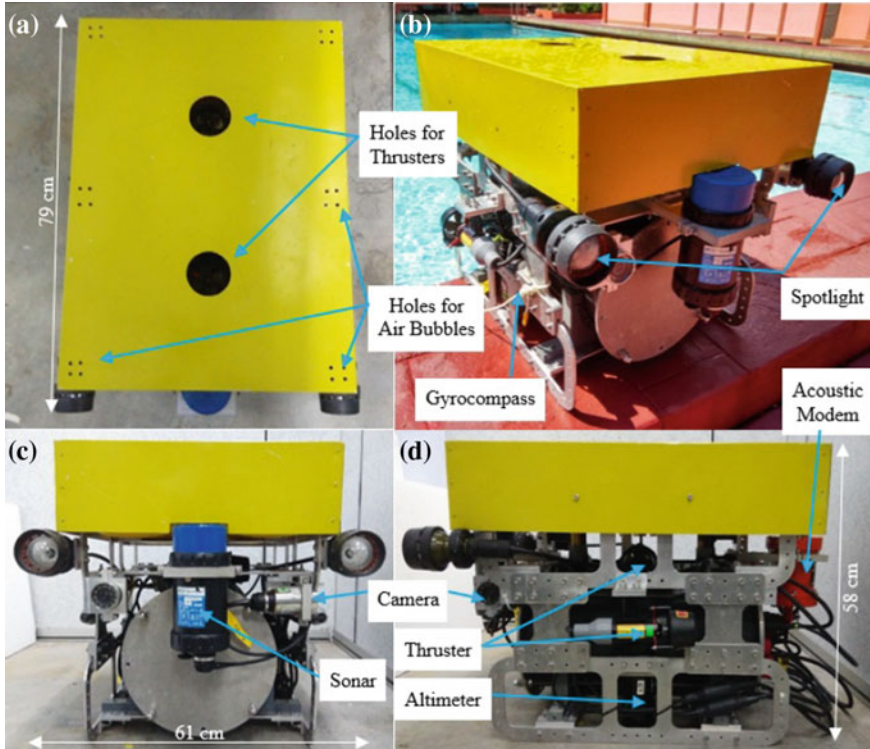


Fig. 1 Photo of HAUV developed by UCRG; **a** top view; **b** isometric view; **c** front view; **d** left view [2]

Table 1 Parameters of HAUV developed by UCRG [2]

Parameters	Values
M_{RB}	63.50 kg
M_A	44.59 kg
D_L	0 kg s^{-1}
D_Q	185.47 kg m^{-1}
g	1.96 N

3 Controller Design

3.1 PIDF Controller

Consider the PIDF control system for HAUV system in Fig. 2, where $z_d(t)$, $e(t)$, $u(t)$, $w(t)$ and $z(t)$ are reference, error, the control input, wave disturbance and the measurement of depth, respectively. Noise is typically produced by the

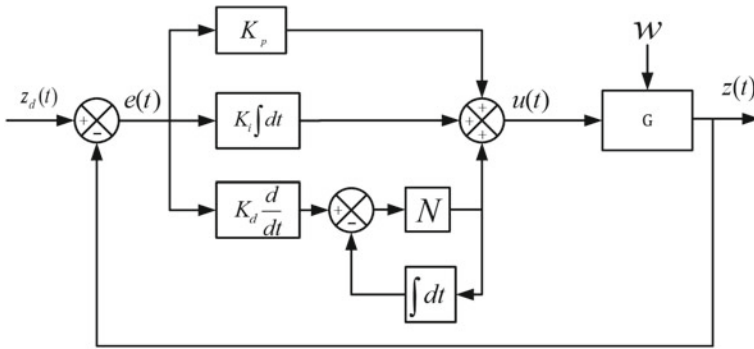


Fig. 2 PIDF control system for HAUV system

sensors and this is usually of higher frequency representing higher values of derivative of that noise. Since derivative block is effected by noise, a filter is employed in derivative block. The plant is the HAUV system, G . Transfer function of PIDF controller is given by (3).

$$TF_{PID} = K_p + \frac{K_i}{s} + K_d \times \frac{Ns}{N + s} \tag{3}$$

where

- K_p = proportional gain
- K_i = integral gain
- K_d = derivative gain
- N = filter coefficient

The model-free PIDF problem can be described as follows:

For the feedback control system in Fig. 2, a PIDF controller is determined, which minimizes the Sum Absolute Error (SAE) and Sum Square Error (SSE) with respect to K_p , K_i , K_d , and N based on the measurement data ($z(t)$).

3.2 Particle Swarm Optimization (PSO)

PSO is one of the evolutionary computation approaches to deal with optimization problems. The technique can be applied to non-linear optimization problem that includes constraints without the graduate of the objective function. In PSO algorithm, particles will move randomly in any possible direction towards it global best and current best location using its present velocity which later then being updated randomly. Therefore, the used of real-number randomness and global communication between particles will increase efficiency in swarm.

Let x_i and v_i is the position vector and velocity vector for particle i , respectively. There are 4 PIDF parameters to be tuned, therefore the design parameter is defined in (4):

$$x_i = \left[K_p \quad K_i \quad K_d \quad N \right] \quad (4)$$

For this simulation, the swarm particles, x_i and particles velocity, v_i are initially set randomly using (5) and (6), respectively, where l_b is a lower boundary and u_b is an upper boundary is limitation space or regions set for the particles, while r_1 and r_2 is random real-number between [0 1].

$$x_i = l_b + (u_b - l_b) \times r_1 \quad (5)$$

$$v_i = r_2 \quad (6)$$

In this problem, an improved PSO algorithm using a priority-based fitness method is proposed for tuning the PIDF parameters [18]. In this research, sum square error (SSE) of depth, z is set as highest priority, followed by sum absolute error (SAE) of depth. The objective is to find minimum error of those fitness functions which are as shown in (7) and (8).

$$f_1(x) = Fitness_1 = SSE = \sum e^2(t)dt \quad (7)$$

$$f_2(x) = Fitness_2 = SAE = \sum |e|(t)dt \quad (8)$$

The personal best agent is updated based on the mathematical statement in (9) as

$$x_{i+1}^* = \begin{cases} x_i^i, & f_1(x_i^i) < f_1(x_i^*) \text{ AND } f_2(x_i^i) < f_2(x_i^*) \\ x_i^*, & \text{otherwise} \end{cases} \quad (9)$$

While the global best is updated based on the mathematical statement in (10) as

$$g_{i+1}^* = \begin{cases} x_i^i, & f_1(x_i^i) < f_1(g_i^*) \text{ AND } f_2(x_i^i) < f_2(g_i^*) \\ g_i^*, & \text{otherwise} \end{cases} \quad (10)$$

The new velocity vector for this PSO is determined by (11)

$$v_i^{t+1} = w_i \times v_i + \alpha \times r_3 \times (g^* - x_i^t) + \beta \times r_4 \times (x^* - x_i^t) \quad (11)$$

where, an inertia function, w_i as (12) is used to update the velocity, v_i^{t+1} in every new iteration ($t + 1$) per (13) [19], r_3 and r_4 is random real-number between [0 1], the parameters α and β are the social coefficient and personal coefficient which is constant and typically set as 2.

$$w_i = 0.4 + 0.5 \times \frac{N_i - i}{N_i} \tag{12}$$

The new position then is updated by

$$x_i^{t+1} = x_i + v_i^{t+1} \tag{13}$$

The stopping criteria used in this research is maximum iteration where, once the iteration reached the maximum value set, the simulation will stop and the best result obtained is present.

4 Results and Discussion

In this section, the proposed control scheme is implemented and tested within simulation environment of the HAUV system and the corresponding results are presented. The performances of the control schemes are assessed in terms of input tracking capability with the presence of wave disturbance. Zero initial conditions were considered with a step input of 1 m.

The proposed controller needs to submerge the HAUV from water surface to the desired depth of 1 m in the presence of wave disturbance which is described by (2). The simulation results are considered as the system response under HAUV depth

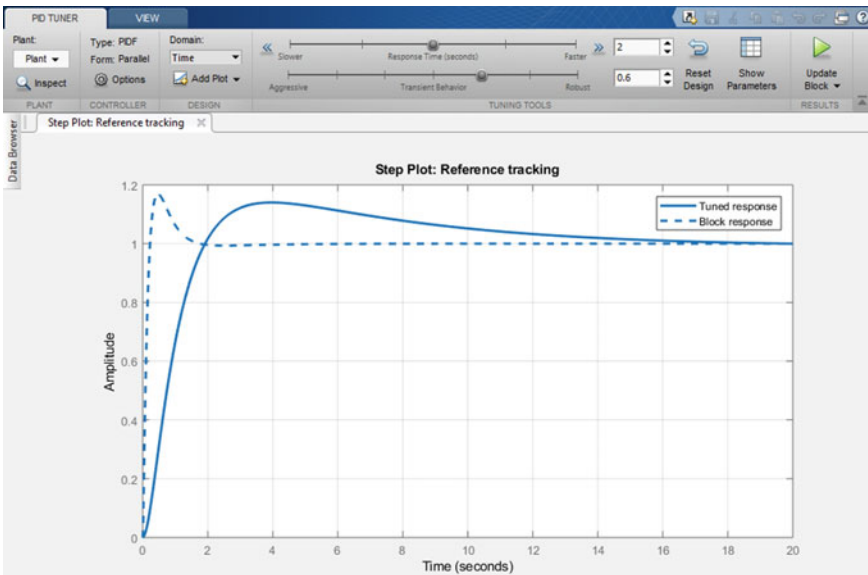


Fig. 3 PID tuner application in simulink

Table 2 PIDF parameters based on PSO tuning and PID tuner simulink

PIDF gain	PSO tuning	PID tuner simulink
K_P	19,898.52	1878.92
K_i	9897.56	819.187
K_d	1497.65	864.435
N	45.58	87.249

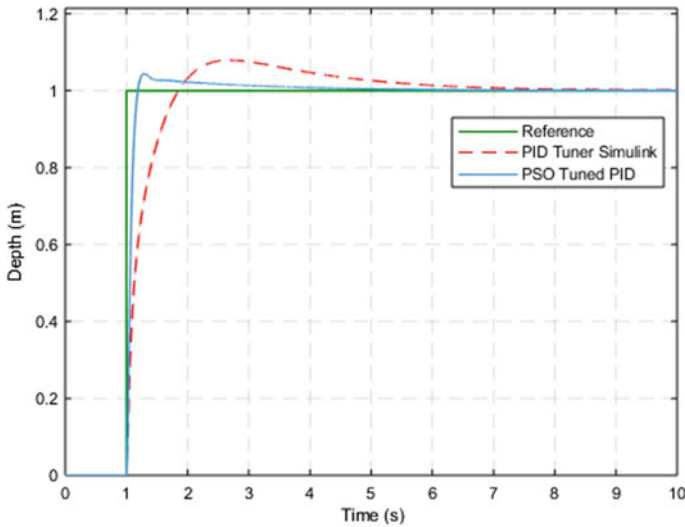


Fig. 4 Depth response of HAUV system

control and will be used to evaluate the performance of the proposed control scheme. Simulation exercises are conducted with Intel Core i7-6700 Processor, 3.41 GHz, 8 GB RAM, Microsoft Window 10 and MATLAB 2017b as a simulation platform. The HAUV system with nonlinear dynamic equations in (1) is designed via Simulink.

The proposed PSO algorithm is used to tune and find 4 optimal parameters of PIDF controller. The simulation times is set from 0 to 10 s and updates every 0.01 s. Number of iteration is set fixed at 3. The initial value of inertia function, w is set to 0.9 and updated for each iteration by (16). The fitness function or so-called objective functions is set using a priority-based fitness approach as presented in (7)–(8) to have better performance of HAUV system. Number of particle is set to 10 and the upper and lower boundary for each design parameters in (4) is set as follow:

$$\begin{aligned}
 \text{lower boundary} &= l_b = [10000 \quad 9000 \quad 1000 \quad 0] \\
 \text{upper boundary} &= u_b = [20000 \quad 10000 \quad 2000 \quad 50]
 \end{aligned}$$

Supremacy of the PSO tuning is shown by comparing the results with PID Tuner in Simulink/MATLAB [16]. The PIDF parameters are obtained with PID Tuner Appli-

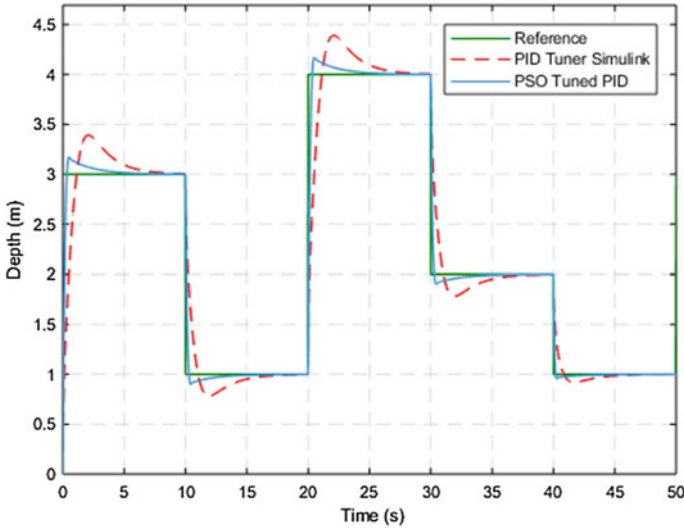


Fig. 5 Different depth response of HAUV system

Table 3 Time response specifications of HAUV system

PIDF tuning method	Settling time, Ts (s)	Rise time, Tr (s)	Percentage overshoot, %OS (%)	Steady state error
PID tuner simulink	4.5	0.55	7.9	0.0
PSO	1.5	0.12	4.4	0.0

cation by adjusting the slider of response time and transient behavior as shown in Fig. 3. Table 2 shows the optimal PIDF parameters obtained using the PSO algorithm and PID Tuner in Simulink/MATLAB.

Figure 4 shows the depth response of the PID controller tuned by PSO algorithm and PID Tuner Simulink. It is clearly shows that both tuning method satisfied the station keeping performance. It is noted in Fig. 4 that with PSO algorithm, the HAUV can track the desired trajectory input with zero steady state error and settles to the desired depth (1 m) in about 1.5 s. But, there is small overshoot occurred about 4.4%. While, by using PID Tuner, it also does not have steady state error, but the HAUV has much bigger overshoot about 7.9% and required longer time to settle at the desired depth that’s about 4.5 s. As we can see, the HAUV depth response with PSO tuning is fast with the rise time is 0.12 s while with PID Tuner the rise time is 0.55 s.

Figure 5 shows the response of HAUV with different depth; 3, 1, 4, 2 and 1 m. For each depth, the simulation run for 10 s. It is clearly shows that, for each depth, PSO tuned PID has a better response compared to PID Tuner with less overshoot, faster settling and rise time and no steady state error. Hence, we can confirm that the PSO tuning for PIDF parameters has a good potential in controlling the depth of HAUV system. The time response specifications of HAUV system is summarize in Table 3.

5 Conclusion

In this study, the development of PSO fine-tuned model-free PID controller with derivative filter (PIDF) for HAUV system has been presented. The proposed method has been tested to HAUV model in [15]. Optimal gains of the proposed controller are obtained using the PSO algorithm using a priority-based fitness approach. It is noted that significant improvements are obtained with PSO tuning compared to PID Tuner in Simulink. The simulation results demonstrate that the proposed control approach yields a good transient response with no steady state error. From above analysis and discussion, it is assured that the proposed control technique may become a suitable controller for solving the HAUV depth control problem in aforementioned industries. Nevertheless, the implementation of PSO tuning for highly nonlinear application requires a high-end computer to simulate the higher number of particles and iterations to avoid any error during simulation. Furthermore, the higher the number of particles, the longer algorithm takes to complete it iteration but the result sometimes is not even better from the previous run. Further investigation and experimentation for an online model-free technique might be investigate using a HAUV experimental rig.

Acknowledgements This work was supported by Faculty of Engineering Technology, Universiti Teknikal Malaysia Melaka, especially Robotic, Industrial and Automation (RIA) Research Group under research grant PJP/2018/FTK(10B)/S01610.

References

1. Aras, M.S.M., Abdullah, S.S., Shah, H.N.M., Rashid, M.Z.A., Aziz, M.A.A.: Robust control of adaptive single input fuzzy logic controller for unmanned underwater vehicle. *J. Theor. Appl. Inf. Tech.* **57**(3), 372–379 (2013)
2. Song, Y.S., Arshad, M.R.: (2017) Robust optimal depth control of Hovering Autonomous Underwater Vehicle. In: 2017 IEEE 2nd International Conference on Automatic Control and Intelligent Systems (I2CACIS 2017), pp. 191–195. Kota Kinabalu, Sabah, Malaysia, 21 Oct 2017
3. Hu, B., Tian, H., Qian, J., Xie, G., Mo, L., Zhang, S.: A fuzzy-PID method to improve the depth control of AUV. In: Proceeding of 2013 IEEE International Conference on Mechatronics and Automation, pp. 1528–1533, 4–7 August 2013. Takamatu, Japan
4. Syahroni, N., Seo, Y.B., Choi, J.W.: Depth control of autonomous underwater vehicle based on open control platform. In: Proceedings of the 17th World Congress, International Federation of Automatic Control, pp. 3707–3712. Seoul, Korea, 6–11 July 2008
5. Zhang, G., Du, C., Huang, H., Wu, H.: Nonlinear depth control in under-actuated AUV. In: Proceeding of 2016 IEEE International Conference on Mechatronics and Automation, pp. 2482–2486. Harbin, China, 7–10 Aug 2016
6. Tao, C., Wei, Z., Jiajia, Z., Haomiao, Y., Xiaofu, L., Yue, H.: Depth control of AUV using active disturbance rejection controller. In: Proceedings of the 33rd Chinese Control Conference, pp. 7948–7952. Nanjing, China, 28–30 July 2014
7. Gharesi, N., Ebrahimim Z., Forouzandeh, A., Arefi, M.M.: Extended state observer-based backstepping control for depth tracking of the underactuated AUV. In: 2017 5th International Conference on Control, Instrumentation, and Automation (ICCIA), pp. 354–358. Shiraz, Iran, 21–23 Nov 2017

8. Gao, D., Cheng, J., Yang, Q.: Depth control for underactuated AUV in vertical plane using optimal internal model controller. In: 2016 28th Chinese Control and Decision Conference (CCDC), pp. 5292–5296. Yinchuan, China, 28–30 May 2016
9. Aras, M.S.M., Abdullah, S.S., Othman, S.Y., Sulaiman, M., Basar, M.F., Zambri, M.K.M., Kamarudin, M.N.: Fuzzy logic controller for depth control of underwater remotely operated vehicle. *J. Theor. Appl. Inf. Tech.* **91**(2), 275–288 (2016)
10. Tumari, M.Z.M., Ahmad, M.A., Saealal, M.S., Zawawi, M.A., Mohamed, Z., Yusop, N.M.: The direct strain feedback with PID control approach for a flexible manipulator: experimental results. In: 11th International Conference on Control, Automation and Systems (ICCAS), pp. 7–12. South Korea, 26–29 Oct 2011
11. Tumari, M.Z.M., Nasir, M.A., Saealal, M.S., Aziz, A.W.A., Saat, S., Suid, M.H., Ghazali, M.R.: The control scheme of vehicle steer by wire system by using PD-PID controller. In: Proceedings of Mechanical Engineering Research Day, pp. 13–14. UTeM, Melaka, 30 Mar 2017
12. Tumari, M.Z.M., Saealal, M.S., Rashid, W.N.A., Saat, S., Nasir, M.A.: The vehicle steer by wire control system by implementing PID Controller. *J. Telecomm. Electron. Comput. Eng. (JTEC)* **9**(3–2), 43–47 (2017)
13. Noordin, A., Basri, M.A.M., Mohamed, Z., Abidin, A.F.Z.: Modelling and PSO fine-tuned PID control of quadrotor UAV. *Int. J. Adv. Sci. Eng. Inf. Technol.* **7**(4), 1367–1373 (2017)
14. Girirajkumar, S.M., Jayaraj, D., Kishan, A.R.: PSO based tuning of a PID controller for a high performance drilling machine. *Int. J. Comput. Appl.* **1**(19), 12–18 (2010)
15. Fossen, T.I.: Nonlinear modeling and control of underwater vehicles. Ph.D. thesis, Department of Engineering Cybernetics, Norwegian University of Science and Technology, Trondheim, 1991
16. MathWorks Homepage. <https://www.mathworks.com/help/slcontrol/gs/automated-tuning-of-simulink-pid-controller-block.html>. Last accessed 26 June 2018
17. Kim, J., Joe, H., Yu, S.C., Lee, J.S., Kim, M.: Time-delay controller design for position control of autonomous underwater vehicle under disturbances. *IEEE Trans. Industr. Electron.* **63**(2), 1052–1061 (2016)
18. Jaafar, H.I., Mohamed, Z., Zainal Abidin, A.F., Ab Ghani, Z.: PSO-tuned PID controller for a nonlinear gantry crane system. In: 2012 IEEE International Conference on Control System, Computing and Engineering, pp. 515–519. Penang, Malaysia, 23–25 Nov 2012
19. Adam, A., Zainal Abidin, A. F., Ibrahim, Z., Husain, A. R., Yusof, Z.M., Ibrahim, I.: A particle swarm optimization approach to robotic drill route optimization. In: Fourth Asia International Conference on Mathematical/Analytical Model and Computer Simulation, pp. 60–64. Kota Kinabalu, Sabah, 26–28 May 2010

Optimization of Single Input Fuzzy Logic Controller Using PSO for Unmanned Underwater Vehicle



Mohd Shahrieel Mohd Aras, Shahrum Shah Abdullah, Hazriq Izuan Jaafar, Ahmad Anas Yusof, Mohd Zaidi Mohd Tumari and Ho Gui Yan

Abstract This paper describes the optimization technique using Particle Swarm Optimization (PSO) are applied to tune parameter of Single Input Fuzzy Logic Controller (SIFLC) for depth control of the Unmanned Underwater Vehicle (UUV). Two parameter SIFLC will be considered to tune the parameter based on off-line results for PSO algorithm to give a best system response in terms of overshoot and rise time. The parameter after look-up table will be fixed because the gain obtained by using the PSO algorithm is almost the same. This paper also investigated the parameter of look-up table for five input rules. Simulation is conducted within MATLAB/Simulink environment to verify the performance of the controller. It is demonstrated that the controller is effective to move the UUV as fast as possible to the desired depth with the best response system in terms of zero overshoot and 5 s rise time performances.

Keywords Particle swarm optimization, single input fuzzy logic controller Unmanned underwater vehicle

M. S. Mohd Aras (✉) · H. I. Jaafar · H. G. Yan
Fakulti Kejuruteraan Elektrik, Universiti Teknikal Malaysia Melaka, Hang Tuah Jaya, 76100 Durian Tunggal, Melaka, Malaysia
e-mail: shahrieel@utem.edu.my

S. S. Abdullah
Department of Electric and Electronics, Malaysia-Japan International Institute of Technology, Universiti Teknologi Malaysia, International Campus Jalan Semarak, 54100 Kuala Lumpur, Malaysia

A. A. Yusof
Fakulti Kejuruteraan Mekanikal, Universiti Teknikal Malaysia Melaka, Hang Tuah Jaya, 76100 Durian Tunggal, Melaka, Malaysia

M. Z. Mohd Tumari
Fakulti Teknologi Kejuruteraan Elektrik dan Elektronik, Universiti Teknikal Malaysia Melaka, Hang Tuah Jaya, 76100 Durian Tunggal, Melaka, Malaysia

1 Introduction

Control performances of Fuzzy Logic Controller (FLC) are significantly influenced by the number of rules [1]. In common, the more rules being applied to an FLC, the accuracy of the control performances is better. On the other hand, large set of rules requires more execution time. Consequently, FLC implementation demands for fast and high performance processors [1]. To ease the problem, a simple yet efficient FLC is proposed in this work. It is a Single Input FLC (SIFLC) controller, where its single input is derived from a technique known as the Signed Distance method. The main benefit of the Signed Distance method is the considerable reduction in the number of rules, which in turn minimizes the computation and execution time required. Another advantage is the ability to reduce the control surface from three to two-dimension, which allows for a linear or piecewise linear approximation to take place. By having an input and output that relates to each other in this linear approach, numerous processes such as fuzzification, rules inferences and defuzzification are detached.

The following section will cover the explanation of Single Input FLC and the Signed Distance method explained in detail can be referred to [2–5]. The application of the method to a conventional FLC results in a Single Input FLC (SIFLC). Based on [2–5] the application of SIFLC is different in terms of manipulator robot and boost converter. Only [1, 6] reported using SIFLC in underwater robot called Deep Submergence Rescue Vehicle (DSRV). The input to SIFLC is a distance, d , and its control surface can be conveniently represented as a linear or piecewise linear interpolation. First of all, an analysis is carried out to ensure that the linear approximation will not dispossess SIFLC from the non-linear properties of conventional FLC. Effects of tuning parameter conditions such as membership functions arrangement for generating a linear control surface are studied in [8]. Once the appropriate conditions are obtained, a generalized output equation is derived. It can be shown by the output equation that the linear or piecewise linear control surface can be obtained by changing the peak locations of the membership functions.

The main advantage of SIFLC is the significant reduction of the rules that needs to be inferred. In conventional FLC, two inputs are fuzzified and depending on the level of fuzzification p , the number of rules to be inferred is p^2 , while the distinguishing features of SIFLC is that, it requires only p rules. The reduction in the number of rules results in faster calculation in SIFLC. This is the most encouraging contribution of signed-distance method. In addition to the new method SIFLC, there are two parameters to be tuned namely the break point and slope for the piecewise linear or slope for the linear approximation. **Unfortunately, in [6] and [7], the parameters still need to be tuned manually.** A considerable design time is required to determine the optimum combinations of these two parameter values. Therefore, Particle Swarm Optimization (PSO) can be used to assist the tuning process. The main contribution of this paper focus more on tuning parameter SIFLC using the PSO algorithm for Underwater Unmanned Vehicle (UUV) which has no reported literature. The mod-

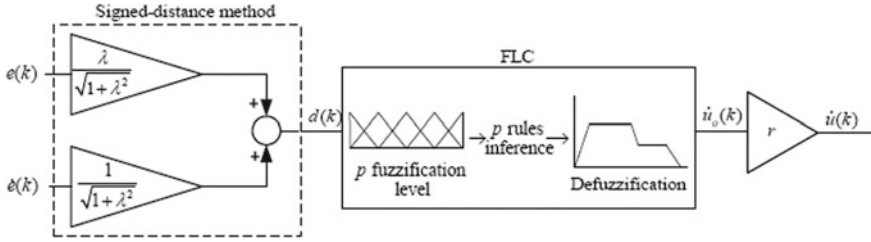


Fig. 1 Single input FLC structure

Table 1 The proposed reduced rule table (5 rules) using the signed distance method

d	L_{NL}	L_{NS}	L_Z	L_{PS}	L_{PL}
\dot{u}_o	N_L	N_S	Z	P_S	P_L

Table 2 The SISO rule table (7 rules) proposed by [1]

d	L_{NL}	L_{NM}	L_{NS}	L_Z	L_{PS}	L_{PM}	L_{PL}
	-0.7	-0.466	-0.233	0	0.233	0.466	0.7
\dot{u}_o	N_L	N_M	N_S	Z	P_S	P_M	P_L
	-0.99	-0.66	-0.33	0	0.33	0.66	0.99

elling of UUV can be referred to [9–13]. This UUV was developed by the Underwater Technology Research Group (UTeRG) from Universiti Teknikal Malaysia Melaka.

This paper is organized as follows. In Sect. 2, the brief description the Single Input Fuzzy Logic Controller (SIFLC) will be simplified. Next, Sect. 3 will be brief description on PSO and how PSO tune the Single Input Fuzzy Logic Controller while Sect. 4 will describe the simulation testing results. Finally, the final remarks are elucidated in Sect. 5.

2 Single Input Fuzzy Logic Controller (SIFLC)

This proposed technique derives from [1, 6]. Figure 1 shows the structure of Single Input FLC for ROV system based on signed-distance method. The Single Input FLC in MATLAB Simulink is shown in Fig. 2. The two circles in Fig. 2 show the parameter that will be tuned by PSO. Slope of zero diagonal line λ is equal to “1”, as both membership functions for input in Table 1 are the same. The matrix rules used in [1] are 7×7 and will be simplified into a single input as shown in Table 2. The seven input rules will be simplified into five input rules. **Based on derivation from [7], the Look-up Table using Eq. (1) can be computed.** By using Eq. (1), five input values for corresponding seven diagonal lines in Table 3 are calculated where d is the distance variable, $\dot{u}_o(k)$ is the final output of this SIFLC, w and Z_e is a scaling factor. λ represents the slope of diagonal line L_Z .

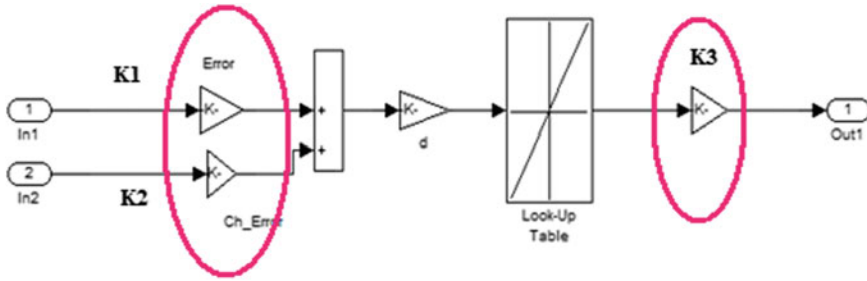


Fig. 2 Simplified single input FLC in simulink

Table 3 The proposed reduced SISO rule table (5 rules)

d	L_{NL} -0.7	L_{NS} -0.353	L_Z 0	L_{PS} 0.353	L_{PL} 0.7
\dot{u}_o	N_L -0.99	N_S -0.5	Z 0	P_S 0.5	P_L 0.99

Table 4 Look up table parameter

Row	d	\dot{u}_o
1	-0.707	-1
2	-0.707	-0.99
3	-0.353	-0.5
4	0	0
5	0.353	0.5
6	0.707	0.99
7	0.707	1

$$d = \frac{w + Ze\lambda}{\sqrt{1 + \lambda^2}} \tag{1}$$

- For diagonal line L_Z , the d is equal to “zero”.
- For diagonal line L_{NS} , the d is equal to “-0.353”.
- For diagonal line L_{NL} , the d is equal to “-0.7”.
- For diagonal line L_{PS} , the d is equal to “0.353”.
- For diagonal line L_{PL} , the d is equal to “0.7”.

The derived SISO table is given in Tables 1 and 3.

Based on Look-up table in Fig. 3, another method for piecewise linear approximation is by using a linear equation. The linear equation is based on look-up table parameter which can also be obtained from experiment for open loop test for depth. The results are almost the same. The linear equation is simpler to implement in real life application. In MATLAB Simulink, the linear equation can be represented as shown in Fig. 4 (Table 4).

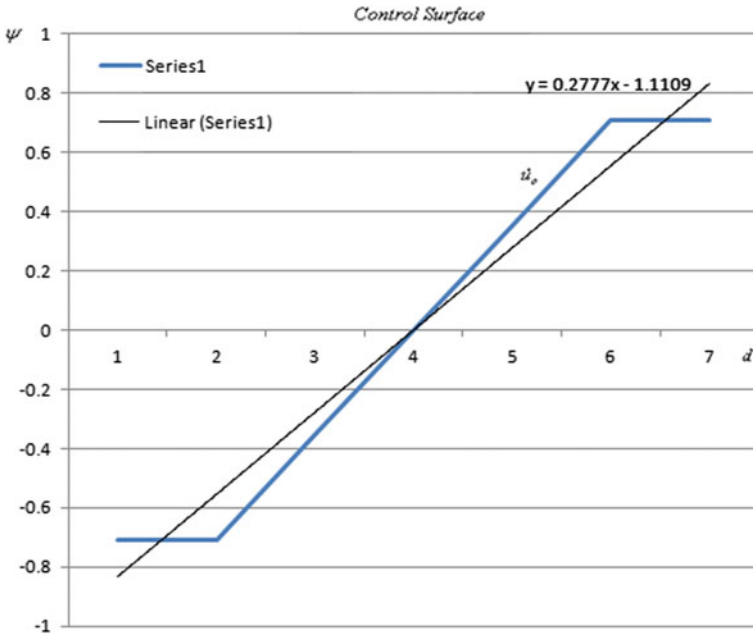
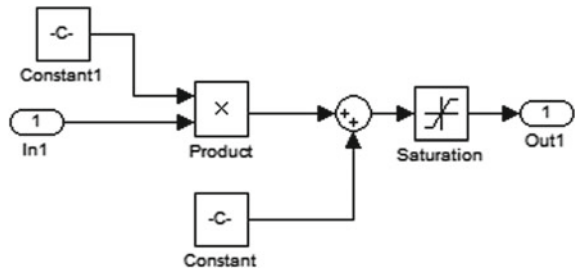


Fig. 3 Plotted graph using look-up table for control surface

Fig. 4 Linear equation in MATLAB/Simulink



At the first stage, three parameters SIFLC will be obtained for tuning using PSO based on offline results as shown in Fig. 5. Based on 20 times of experiments by PSO, two parameters for SIFLC will be considered. The parameter after look-up table will be fixed because the gain obtained by using the PSO algorithm is almost the same. Simulation is conducted within MATLAB Simulink environment to verify the performance of the controller.

Fig. 5 Linear equation for SIFLC

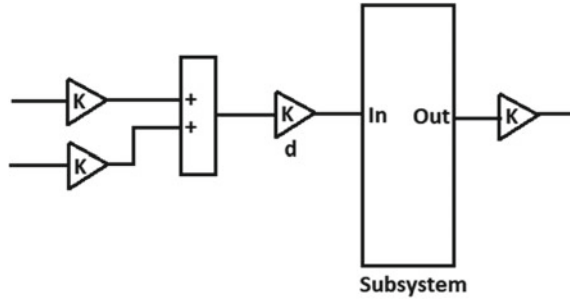


Fig. 6 Particle swarm optimization algorithm

```

Initialize Swarm
forAll particles
  calculate fitness f
endfor
Repeat
forAll particles
 $v_{t+1} = \omega v_t + c_1 r_1 (P_{BEST} - x_i) + c_2 r_2 (G_{BEST} - x_i)$ 
 $x_{t+1} = x_t + v_{t+1}$ 
endfor
forAll particles
  calculate fitness f
endfor
until Stopping criteria
    
```

3 Particle Swarm Optimization (PSO)

PSO is one of the artificial intelligence families that were proposed by Kennedy and Eberhart in 1995 [14]. The fundamental PSO is developed based on behaviors of fish schooling and bird flocking in order to search and move to the foodstuff at a certain speed and position. An analogy is established between a particle and a swarm element [15]. The particle movement is characterized by two factors, its current position x and velocity v , respectively. It has been applied successfully to a wide variety of optimization problems [16–19].

The basic PSO algorithm begins by initializing the swarm randomly in the search space as shown in Fig. 6, where t and $t+1$ represent two consecutive iterations. The position x of each particle is changed during the iterations by adding a new velocity v , respectively. This velocity is evaluated by summing an increment to the previous velocity value. The increment is a function of two components representing the cognitive and the social knowledge.

The cognitive knowledge of each particle is included by evaluating the difference between the current position x and its best position so far P_{BEST} . The social knowledge

of each particle is incorporated through the difference between its current position x and the best swarm global position achieved so far G_{BEST} . The cognitive and social knowledge factors are multiplied by randomly uniformly generated terms ϕ_1 and ϕ_2 , respectively [19].

Due to this, it could be implemented and applied easily to solve various function optimization problems especially for nonlinear models. For this problem, the particle position in PSO can be modelled as Eq. 2 for three parameters and Eq. 3 for two parameters.

$$Xi = [K_1, K_2, K_3] \quad (2)$$

$$Xi = [K_1, K_2] \quad (3)$$

where x is the particle position, K_1, K_2, K_3 are the parameter values of Single Input Fuzzy Logic Controller proposed by [1] which the SIFLC controller controls the position in terms of depth of the ROV. It is initialized and started with a number of random particles. Initialization of particles is performed using Eq. 4.

$$Xi = x_{min} + rand(x_{max} - x_{min}) \quad (4)$$

where x_{max} and x_{min} are the maximum and minimum values in the search space boundary. Then, the particles find for the local best, P_{BEST} and subsequently global best, G_{BEST} in every iteration in order to search for optimal solutions [14]. Each particle is assessed by the fitness function. Thus, all particles try to replicate their historical success and at the same time try to follow the success of the best agent. It means that the P_{BEST} and G_{BEST} are updated if the particle has a minimum fitness value compared to the current P_{BEST} and G_{BEST} value. Nevertheless, only particles that are within the range of the system's constraint are accepted. The new velocity and new position can be calculated and as in Eqs. 5 and 6.

$$v_{i+1} = \omega v_i + c_1 r_1 (P_{BEST} - x_i) + c_2 r_2 (G_{BEST} - x_i) \quad (5)$$

$$x_{i+1} = x_i + v_i + 1 \quad (6)$$

where r_1 and r_2 represent random function values [0, 1] while c_1 is the cognitive component and c_2 is the social component. The function of ω parameter is to balance between local and global search capabilities [14]. In this research, an improved PSO algorithm using a priority-based fitness approach is proposed for tuning of SIFLC parameters. In this work, overshoot, OS is set as highest priority, followed by settling time, T_s . Figure 7 shows MATLAB Simulink of the proposed PSO algorithm for tuning of SIFLC parameters. In this study, 20 particles are considered with 100 iterations. The initial particles are bounded between 0 and 200. As default values, c_1 and c_2 are set as 2. The initial value of ω is 0.9 and linearly decreased to 0.4 at a certain stage in the iteration.

System identification will take place once the platform is ready to be tested to get input-output signals. The MATLAB System Identification Toolbox will be used

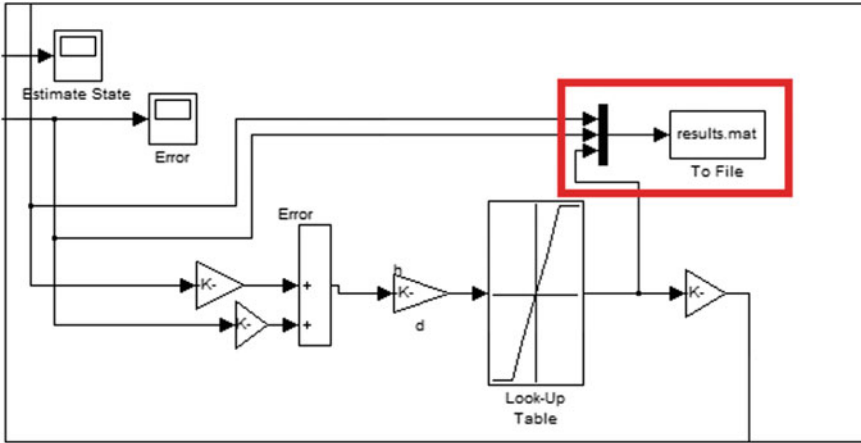


Fig. 7 PSO block diagram

to infer a model. Some theory for System Identification must be cleared so that the model obtained is acceptable, that is best fit must be more than 80%. Then the model obtained from System Identification will be verified using a simple controller such as conventional PID controller, Pole placement and etc. Transfer function state space technique yields:

$$TF = \frac{0.4871s^2 + 1.37s + 67.31}{s^3 + 4.911s^2 + 8.309s + 76.09} \tag{7}$$

4 Results and Discussion

Figure 8 shows the system response for the both models. Mathematical model is better than the system identification model but the system identification model is more suitable for real time application which includes environmental disturbance even in lab tank test or in the swimming pool. The assumptions and assertions on dynamics and uncertainties parameter needed for mathematical modeling can be referred to [13]. Figure 9 proposed five input rules. The parameter of single input is the same before tuning by PSO. The proposed five input rules give better system performances as shown in Fig. 10. Using five input rules are easier and less complex to be implemented for real time application. Once SIFLC simplified into five input rules, unfortunately the parameters still need to be tuned manually. By using PSO algorithm, parameters for SIFLC can be optimized as shown in Tables 5 and 6. At the first stage, three parameters will be optimized and be referred to Fig. 2. The MATLAB/Simulink for substitution of PSO algorithm is shown in Fig. 7. The Table

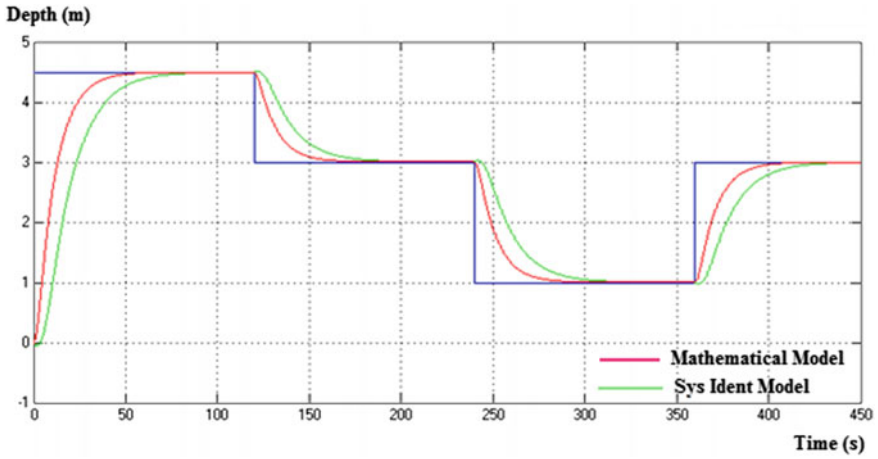


Fig. 8 Comparison between mathematical model with system identification model

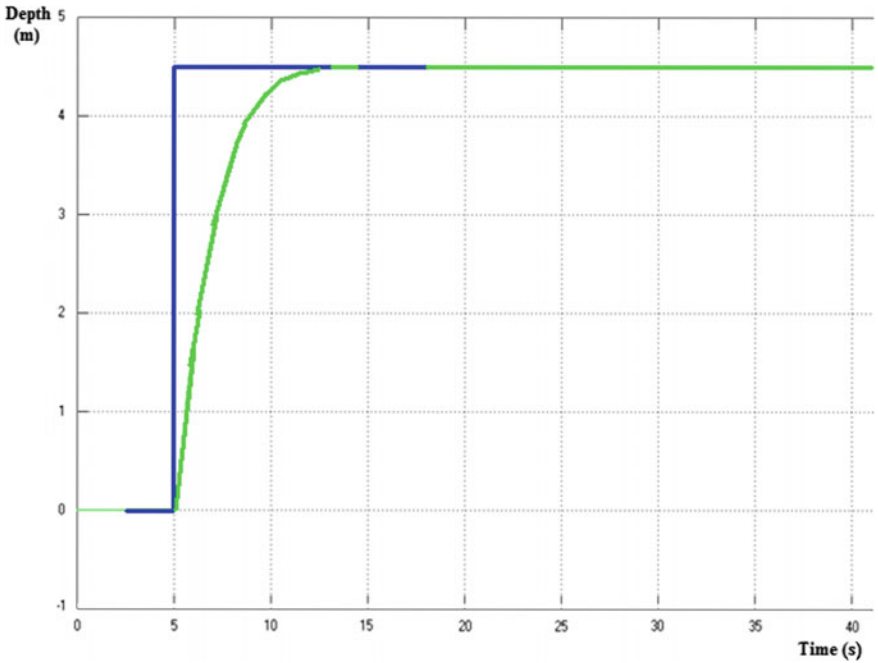


Fig. 9 The proposed five input rules SIFLC system response

shows the values of third gain is very small and negligible. The simplified PSO will be reduced to two parameters and will be optimized. The result is shown in Tables 5 and 6.

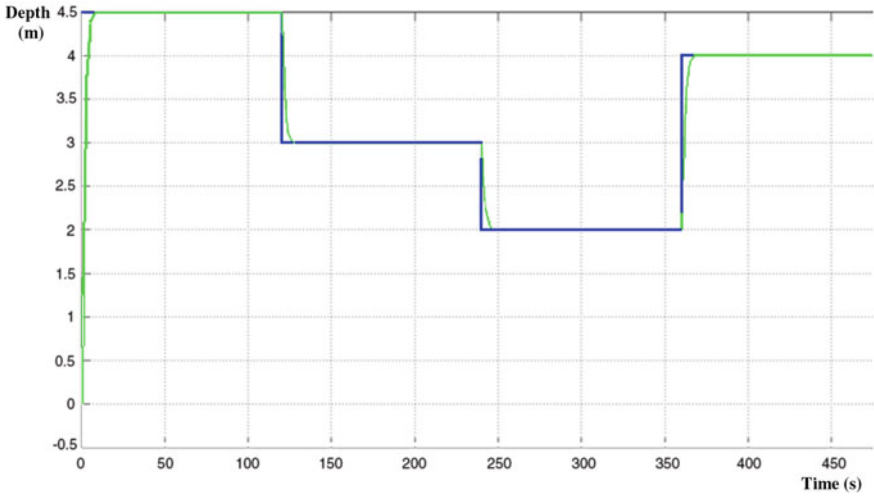


Fig. 10 PSO-tuning single input fuzzy logic controller

Table 5 Three parameter for SIFLC tuning using PSO

Parameter	Gain1	Gain2	Gain3
Test 1	24.5891883722	27.2224858454	0.07686487686

Table 6 Two parameter for SIFLC tuning using PSO

Parameter	Gain1	Gain2
Test 1	4.3859645616	35.8419001582

Table 7 System performances of SIFLC

Item	SIFLC tune by PSO
Peak time, T_p (s)	10
Rise time, T_r (s)	5
Settling time, T_s (s)	10
Overshoot percentage (%)	0
Steady state error, ess	0

Figure 10 shows the set point set up as different depth so that the UUV system can follow the set point. System performances of the controller are tabulated in Table 7. It shows that the PSO algorithm techniques give more satisfying results in terms of steady state performances with zero overshoot and fastest rise time.

5 Conclusion

The Particle Swarm optimization PSO applied to tune parameter of single input Fuzzy Logic Controller for depth control of the Remotely Operated Underwater Vehicle are successfully designed. An improved PSO algorithm is implemented for finding optimal SIFLC parameters. It is demonstrated that the controller is effective to move the ROV as fast as possible to the desired depth with the best response system in terms of overshoot and rise time performances. In this research, an improved PSO algorithm using a priority-based fitness approach is used for tuning of SIFLC parameters. In this work, overshoot, OS is set as highest priority, followed by settling time, Ts. The proposed five input rules give better system performances even though almost same results are obtained but five input rules are easier and less complex to implement in real time application.

Acknowledgements Special appreciation and gratitude to the honorable University (Universiti Teknikal Malaysia Melaka, UTeM and Universiti Teknologi Malaysia, UTM) especially to the both Faculties of Electrical Engineering for providing the financial as well as moral support to complete this project successfully.

References

1. Ishaque, K., Abdullah, S.S., Ayob, S.M., Salam, Z.: Single input fuzzy logic controller for unmanned underwater vehicle. *J. Intell. Robot Syst.* **59**, 87–100 (2010)
2. A, A.F., Sallam, E.A., Elawady, W.M.: Quasi sliding mode-based single input fuzzy self-tuning decoupled fuzzy PI control for robot manipulators with uncertainty. *Int. J. Robust Nonlinear Control* **22**(18), 2026–2054 (2012). <https://doi.org/10.1002/rnc.1805>
3. Lee, Shih-Chih, Shih, Ching-Long: Optimal single input PID-type fuzzy logic controller. *J. Chin. Inst. Eng.* **35**(4), 413–420 (2012). <https://doi.org/10.1080/02533839.2012.655902>
4. Lee, S.C., Shih, C.L.: Enhancement of a single-input fuzzy logic control system using a novel method. *J. Chin. Inst. Eng.* **35**(2), 151–163 (2012). <https://doi.org/10.1080/02533839.2012.638511>
5. Taeed, Fazel, Salam, Zainal, Ayob, Shahrin M.: FPGA implementation of a single-input fuzzy logic controller for boost converter with the absence of an external analog-to-digital converter. *IEEE Trans. Ind. Electron.* **59**(2), 1208–1217 (2012). <https://doi.org/10.1109/TIE.2011.2161250>
6. Ishaque, K., Abdullah, S.S., Ayob, S.M., Salam, Z.: A simplified approach to design fuzzy logic controller for an underwater vehicle. *Ocean Eng.* **38**, 1–14 (2010)
7. Ishaque, K.: Intelligent control of diving system of an underwater vehicle. Master Thesis. Universiti Teknologi, Malaysia (2009)
8. Aras, M.S.M., Azis, F.A., Syed Abdul Hamid, S.M.S., Ali, F.A., Abdullah, S.S.: Study of the effect in the output membership function when tuning a fuzzy logic controller. In: 2011 IEEE International Conference on Control System, Computing and Engineering (ICCSCE 2011)
9. Azis, F.A., Aras, M.S.M., Abdullah, S.S., Rashid, M.Z.A., Othman, M.N.: Problem identification for underwater remotely operated vehicle (ROV): a case study. *Procedia Eng.* **41**, 554–560 (2012)
10. Aras, M.S., Abdullah, S.S., Rahman, A.A., Aziz, M.A.: Thruster modelling for underwater vehicle using system identification method. *Int. J. Adv. Robot. Syst.* **10**, 1–12 (2013)

11. Aras, M.S., Azis, F.A., Othman, M.N., Abdullah, S.S.: A low cost 4 DOF remotely operated underwater vehicle integrated with IMU and pressure sensor. In: 4th International Conference on Underwater System Technology: Theory and Applications 2012 (USYS'12), pp 18–23. Malaysia (2012)
12. Aras, M.S.M., Abdullah, S.S., Rashid, M.Z.A., Rahman, A.A., Aziz, M.A.A.: Development and modeling of underwater remotely operated vehicle using system identification for depth control. *J. Theor. Appl. Inf. Technol.* **56**, 1 (2013)
13. Aras, M.A.M.: Adaptive simplified fuzzy logic controller for depth control of underwater remotely operated vehicle, Thesis (2015)
14. Jaafar, H.I., Mohamed, Z., Abidin, A.F.Z., Ghan, Z.A.: PSO-tuned PID controller for a nonlinear gantry, crane system. In: IEEE International Conference on Control System, Computing and Engineering, pp. 1–5, 23–25 Nov 2012
15. Kennedy, J., Eberhart, R.: Particle swarm optimization. In: Proceedings of the 1995 IEEE International Conference on Neural Networks, pp. 1942–1948 (1995)
16. Pires, E.S., Machado, J.T., de Moura Oliveira, P.B.: Particle swarm optimization: dynamical analysis through fractional calculus, Chapter 24, InTech Publisher (2009)
17. Kim, Tae-Hyoung, Maruta, Ichiro, Sugie, Toshiharu: Robust PID controller tuning based on constrained particle swarm optimization. *Automatica* **44**(4), 1104–1110 (2008)
18. Solihin, M.I., Kamal, M.A.S., Legowo, A.: Optimal PID controller tuning of automatic gantry crane using PSO algorithm. In: Proceeding of the 5th International Symposium on Mechatronics and its Applications (ISMA08), pp. 1–5. Amman, Jordan, 27–29 May 2008
19. Clerc, M.: Kennedy J (2002) The particle swarm—explosion, stability, and convergence in a multidimensional complex space. *IEEE Trans. Evol. Comput.* **6**(1), 58–73 (2002)

UTeM Autonomous Underwater Vehicle Competition Initiatives: Project TUAH and PANTHER



Ahmad Anas Yusof, Mohd Khairi Mohamed Nor,
Shamsul Anuar Shamsudin, Mohd Rizal Alkahari,
Mohd Shahrieel Mohd Aras, Mohamad Riduwan Md. Nawawi,
Mohd Zaidi Mohd Tumari and Mohammad Afif Kasno

Abstract This paper describes the development and lesson learned from the participation of PANTHER and TUAH AUV teams in the autonomous underwater vehicle competitions. The international competitions provide the participants with the opportunity to experience the engineering challenges during the development of the Autonomous Underwater Vehicle (AUV) systems, and by demonstrating their working and engineered AUVs at swimming pool. A team with enthusiasts in underwater robotics was assembled in 2017, to venture into the competitions in 2017 and 2018. Till now, 4 teams have participated in the competition held in Malaysia and Singapore, and up to 4 prototypes of AUVs, called TUAH 1.0, TUAH 2.0, PANTHER and PANTHER-J, have been developed by the engineering lecturers and students in Universiti Teknikal Melaka. The teams use 3–6 thrusters that are configured for AUV control and the Inertial Measurement Unit (IMU) interfaced with control unit and powered by commercial LiPo battery packs. In general, various lessons in AUV's navigation, localization, object recognition and manipulation had been learned from all competitions.

Keywords Autonomous underwater vehicle · Underwater vehicle competition

A. A. Yusof (✉) · M. K. Mohamed Nor · S. A. Shamsudin · M. R. Alkahari
Faculty of Mechanical Engineering, Universiti Teknikal Malaysia Melaka, 76100 Hang Tuah
Jaya, Durian Tunggal, Melaka, Malaysia
e-mail: anas@utem.edu.my

M. S. Mohd Aras · M. R. Md. Nawawi
Faculty of Electrical Engineering, Universiti Teknikal Malaysia Melaka, 76100 Hang Tuah
Jaya, Durian Tunggal, Melaka, Malaysia

M. Z. Mohd Tumari · M. A. Kasno
Faculty of Engineering Technology, Universiti Teknikal Malaysia Melaka, 76100 Hang Tuah
Jaya, Durian Tunggal, Melaka, Malaysia

1 Introduction

In 2017, a team from Universiti Teknikal Malaysia Melaka's responded to a call for participation in an autonomous underwater vehicles competition held in Singapore. The Singapore Autonomous Underwater Vehicle Challenge, dubbed as SAUVC, is an effort by the IEEE Oceanic Engineering Society (OES) to engage and expose the students to the arduous challenges of AUV's design. The international competition gives participants the opportunity to experience the engineering trials and develop skills in AUV technology. The competition was held in March 2017, at the Singapore Polytechnic [1]. From thereafter, the team continues to participate in other autonomous underwater vehicle challenges in Kuala Lumpur, Malaysia during MAUVC-USYS 2017 and the next Singapore's SAUVC in 2018 [2].

2 TUAH AUV Development

2.1 TUAH 1.0

The design for the TUAH 1.0 AUV is inspired by three main ideas, the SAUVC 2017 competition requirements, the onboard power specifications of the electronics and available fund. It is designed for independent autonomous navigation using a programming that is written and downloaded into microcontroller Arduino MEGA, which is responsible for both relaying motor commands to individual thrusters. The sensors are equipped with depth sensor for vertical movement control and Pixy (CMUcam5) camera for target recognition. Powered by a 12 V battery, the thrusters are used for forward, reverse, upward and downward movement. The electrical components need to be inside of a waterproof container, but still be able to communicate with the thrusters. The AUV hull is designed by using polyvinyl chloride tube, while acrylic is used in the frame, for weight reduction and corrosion resistance. Four skid rods are used in between the frames to improve stiffness. The Pixy camera is mounted in front of the AUV to provide a forward and downward view for navigation and object recognition [3]. Figure 1 shows both TUAH 1.0 and 2.0 in action. Table 1 shows the technical specifications of TUAH 1.0 AUV.

2.2 TUAH 2.0

The TUAH 2.0 AUV is a new AUV designed for MAUVC 2017 and SAUVC 2018. The design is based from the BlueROV platform [4]. The platform is an unassembled ROV kit with frame, watertight enclosure, thrusters, and speed controllers, from Blue Robotics©. In TUAH 2.0, the AUV uses four T200 thrusters to provide four degree-of-freedom, designed so that it can navigate independently of participants'

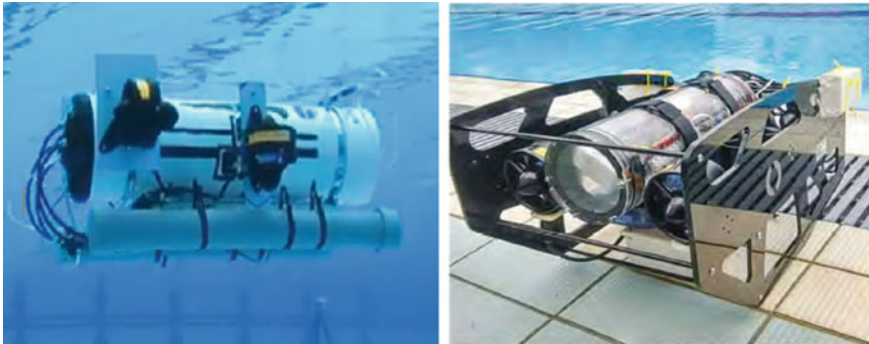


Fig. 1 AUV TUAH 1.0 (Left) and TUAH 2.0 (Right)

Table 1 TUAH 1.0 AUV technical specifications

Name	TUAH 1.0
Dimension	70cm × 50cm × 30cm
Weight	18 kg
Speed	0.4 m/s (25% of full speed)
Depth	3 m (Limitation of swimming pool depth)
Electro-mechanicals Components	Acrylic frame, PVC hull, Waterproof box, Blue Robotics Thruster T-200, Iron steel weight, Battery, Arduino MEGA, 10 DOF IMU, MPX5700AP, Afro ESC 30A

intervention. The Arduino microcontroller is used in the system communication with the Pixy camera for target recognition. The camera uses open source software that can be acquired easily from the internet and it is compatible with Arduino through SPI, USB, I2C, UART or analog/digital output interfaces. For the autonomous movement of the AUV, a coding that communicates with the camera, sensors and thrusters has been developed for instructions to complete the task.

3 PANTHER AUV Development

The PANTHER AUV team comes out with two AUV designs, namely PANTHER AUV team, which is based on the senior design project team that focuses on building an AUV from BlueROV2 platform, and PANTHER-J, which uses an OpenROV platform. The AUV team competed in both the Malaysian and Singapore Autonomous Underwater Vehicle Challenge in December 20th, 2017 and March, 9th, 2018 respectively [5]. Figure 2 shows both PANTHER and PANTHER-J AUV.

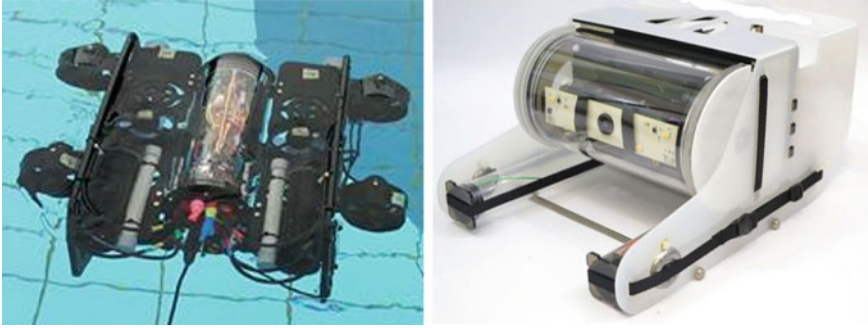


Fig. 2 PANTHER AUV (Left) and PANTHER-J (Right)

3.1 PANTHER-J AUV

PANTHER-J AUV (J for Junior) is a derivative from the remotely operated vehicle called OpenROV 2.8 [6]. The AUV weighs around 2.5 kg with dimensions of 15 cm × 20 cm × 30 cm. Powered by Li-Ion batteries, the PANTHER Junior AUV uses Arduino UNO microcontroller, instead of the original Beagle Bone Black single board computer. Other than that, the AUV retains the original ROV design, with acrylic tube and a tri-thruster configuration. Thrusters are used for forward, upward and downward movement.

3.2 PANTHER AUV

The PANTHER AUV is designed using the BlueROV2 platform [7]. The BlueROV2 standard electronic packages comprised of Pixhawk and Raspberry Pi single-board computers has been replaced by Arduino UNO microcontroller, as a standard operating procedure. The idea is to have all teams using the same programming platforms for AUV navigations and controls. The depth sensor is used for surrounding measurements, while Pixy camera is used for target detection. The vehicle is powered by 14.8 V lithium-ion batteries. There are 6 thrusters used for forward, reverse, upward and downward movement. The inertia measurement unit is used for measuring the AUV roll, pitch and yaw rate. It has a single-axis rate gyro to measure the yaw rate and a two-axis accelerometer to measure the roll and the pitch. Analog signals from these sensors and from the depth sensor and the battery monitor are converted into digital form by a 16-bit A/D converter.

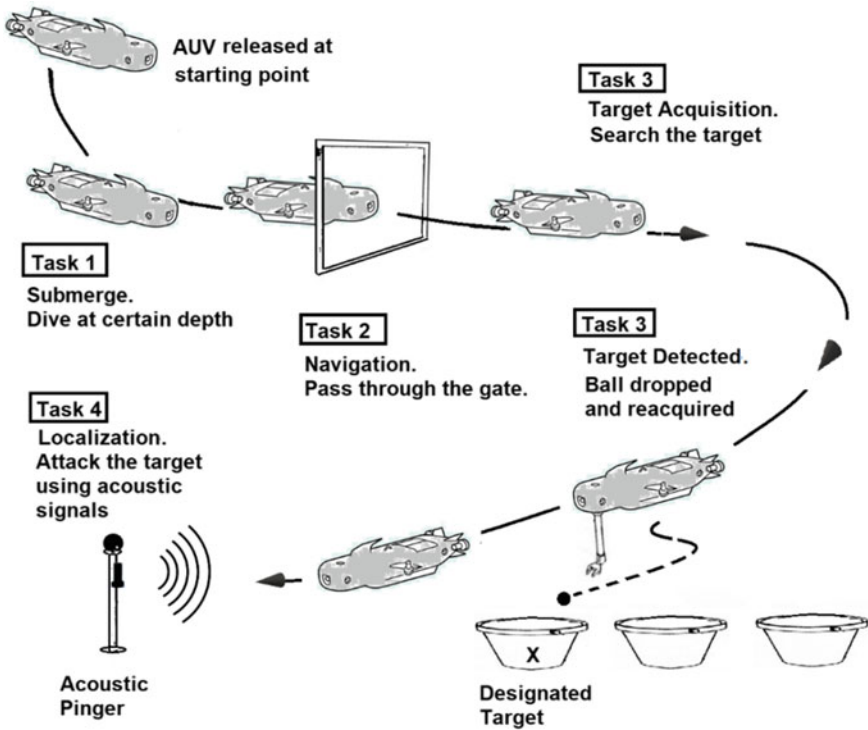


Fig. 3 Typical underwater competition tasks [5]

4 Lesson Learned

Underwater vehicle competitions usually focus on the autonomous operations in a swimming pool, with certain numbers of tasks to be completed. Hence, the AUVs are required to perform challenges such as navigation and planning, localization, object recognition and manipulation, as shown in Fig. 3.

4.1 Navigation and Planning

Navigation and planning of the AUV requires in-depth analysis of the competition requirements. Not all location of the targets is made known to the participants, hence creating difficulty by relying on a fixed navigational strategy. Task in navigation will involve sensory perception and avoiding obstacles while attempting to reach some destination [8]. Path-planning becomes crucial in these situations. Even low-budget AUVs with limited computational power can perform basic path-planning with the help of IMU which measures and reports a body's specific force and angular rate, by

using a combination of accelerometers and gyroscopes. However, limited computational power might reduce chances of success, since the participants sometimes had to choose among three tasks which are navigation, localization and object recognition that require lots of computing power. Arduino microcontroller used in the competition provides low cost navigational and planning, with limited capability and chances to win the competition.

4.2 Localization

It is important for the AUVs to maintain a sense of where it is within the world. The most common form of localization is known as dead reckoning [9]. This approach is adequate for the competitions. However, when the dynamics of the game require AUVs to cover much of the pool in completing the tasks, the unavoidable internal error to dead reckoning quickly amasses. Underwater communications are unreliable without access to the Global Positioning System (GPS). In the competition, an acoustic pinger is placed at the randomized target. Thus, success in localization will not be achieved, without the use of hydrophones sensors. Currently, the high cost of the acoustic sensors hinders the development of the teams' AUV localization capability.

4.3 Object Recognition and Manipulation

In most autonomous underwater competition, the AUVs will be given a series of tasks to complete. These tasks often include the manipulation of objects within the pool and moving them from one place to another. If the locations of these objects are given, there is no need for a search within the pool. Likewise, if their positions were not specified, but rather placed randomly throughout the field of play, then participants would be encouraged to utilize sensory capabilities to locate and approach the objects. The participants have to rely on the best strategy to achieve the task with optimum winning points. Until now, the teams still failed to provide a proper recognition and manipulation technique for the AUVs. Adequate strategy is important to preserve power consumption and energy during the operation of the robotic manipulator [10].

5 Conclusion

A group of passionate students and lecturers team up in the development of an Autonomous Underwater Vehicle (AUV) for a competition that gives them the opportunity to experience the engineering challenges and develop skills in underwater technology. Four prototypes of AUVs, called TUAH 1.0, TUAH 2.0, PANTHER and

PANTHER-J, have been developed by the engineering lecturers and students in Universiti Teknikal Melaka, Malaysia. In general, various lessons in AUV's navigation, localization, object recognition and manipulation have been learned from all competitions. The high cost of the acoustic sensors hinders the development of the teams' AUV localization capability. The teams also currently rely on using less-advanced Arduino microcontroller for AUVs' navigation and planning, thus resulting in an ineffective recognition and manipulation technique for the AUVs.

Acknowledgement The authors wish to thank Ministry of Higher Education (MOHE) and Universiti Teknikal Malaysia Melaka for their support. This publication was funded by the Fundamental Research Grant Scheme. **FRGS/1/2016/TK03/FKM-CARE-F00317.**

References

1. Singapore autonomous underwater vehicle challenge 2017. <https://sauvc.org/>. Last accessed 2017/12/10
2. Malaysia autonomous underwater vehicle challenge 2018. <http://oes.ieeemy.org/>. Last accessed 2017/12/10
3. Yusof A.A., Nor M.K.M., Shamsudin S.A., Alkahari M.R., Mohd Aras M.S., Nawawi M.R.M.: Facing the autonomous underwater vehicle competition challenge: the TUAH AUV experience. In: Hassan, M. (eds.) *Intelligent Manufacturing & Mechatronics. Lecture Notes in Mechanical Engineering*. Springer, Singapore (2018)
4. BlueROV (Retired). <https://www.bluerobotics.com/store/retired/bluerov-r1/>. Last accessed 2018/7/5
5. Yusof, A.A., Nor, M.K.M., Shamsudin, S.A., Alkahari, M.R., Musa, M.: The development of PANTHER AUV for Autonomous Underwater vehicle competition challenge 2017/2018. In: Hassan, M. (eds.) *Intelligent Manufacturing & Mechatronics. Lecture Notes in Mechanical Engineering*. Springer, Singapore (2018)
6. OpenROV 2.8. <https://www.openrov.com/products/openrov28/>. Last accessed 2018/7/5
7. BlueROV2. <https://www.bluerobotics.com/store/rov/bluerov2/>. Last accessed 2018/7/5
8. Yusof, A., Kawamura, T., Yamada, H.: Evaluation of construction robot telegrasping force perception using visual, auditory and force feedback integration. *J. Robot. Mechatron.* **24**(6), 949–957 (2012)
9. Bonin-Font, F., Oliver, G., Wirth, S., Massot, M., Negre, P.L., Beltran, J.-P.: Visual sensing for autonomous underwater exploration and intervention tasks. *Ocean Eng.* **93**, 25–44 (2015)
10. Hassan, S.N.H., Yusof, A.A., Tuan, T.B., Saadun, M.N.A., Ibrahim, M.Q. and Wan, N.W. M.N. Underwater manipulator's kinematic analysis for sustainable and energy efficient water hydraulics system. *AIP Conference Proceedings* 1660, 070112 (2015)

Deep Underwater Image Enhancement Through Integration of Red Color Correction Based on Blue Color Channel and Global Contrast Stretching



Kamil Zakwan Mohd Azmi, Ahmad Shahrizan Abdul Ghani,
Zulkifli Md Yusof and Zuwairie Ibrahim

Abstract Deep underwater images experience some complicated problems, such as low contrast and blue-green illumination effect due to light attenuation in water medium. These problems reduce the extraction rate of valuable information from the image. This paper proposes a new method of enhancing underwater image. The proposed method consists of two major steps. The first step is explicitly designed to minimize the effect of blue-green illumination. This technique operates by correcting the red color channel by taking into account the differences between the red color with blue color in term of total pixel value. The more significant the difference of total pixel value between these colors, the higher the pixel value will be added to improve the red color and vice versa. Then, the overall image contrast is improved through global contrast stretching technique that is applied to all color channels. Qualitative and quantitative evaluations prove the effectiveness of the proposed method.

Keywords Image processing · Red color correction · Contrast stretching

1 Introduction

Deep underwater images usually have high concentrations of blue-green illumination that cause difficulty in viewing and analyzing objects on the seafloor. This phenomenon occurs because of the light spectrum moving in the water medium is absorbed. This absorption depends on the wavelength where the red color is absorbed earlier than blue and green colors [1]. This causes the underwater image looks bluish and greenish. In addition, the backward scattering is a phenomenon where the portion of light has been reflected by the particles found in the water towards the camera [2].

K. Z. Mohd Azmi (✉) · A. S. Abdul Ghani · Z. Md Yusof · Z. Ibrahim
Faculty of Manufacturing Engineering, Universiti Malaysia Pahang,
26600 Pekan, Malaysia
e-mail: kamilzakwan@gmail.com

© Springer Nature Singapore Pte Ltd. 2019
Z. Md Zain et al. (eds.), *Proceedings of the 10th National Technical Seminar on Underwater System Technology 2018*, Lecture Notes in Electrical Engineering 538,
https://doi.org/10.1007/978-981-13-3708-6_4

This incident reduces the image contrast which deteriorates the quality of underwater image.

This paper explains a proposed method that enhances the visibility of deep underwater images. It integrates two main steps, which are red color correction based on blue color channel (RCCB) and global contrast stretching (GCS). Therefore, this proposed method is termed as RCCB-GCS. Qualitative and quantitative evaluations prove the effectiveness of the proposed RCCB-GCS method.

2 Related Works

The gray world (GW) assumption is a well-known approach, proposed by Buchsbaum [3]. This method assumes that the average of the captured image should be gray (achromatic). However, this method tends to make the output image reddish, especially for deep underwater images.

Histogram equalization (HE) is one of the most widely used methods in image enhancement techniques. HE works by flattening the histogram and stretching the dynamic range of the intensity levels by using the probability distribution function (PDF) and cumulative density function (CDF) [4]. However, since the image histogram is stretched and flattened, low-intensity values will become lower and high-intensity values will become higher. This problem will produce under- and over-saturated areas in output images.

Two famous methods commonly used to compare the capabilities of a technique are integrated color model (ICM) [5], and unsupervised color correction method (UCM) [6]. ICM is able to increase the image contrast, however, it tends to produce dark and very bright areas. On the other hand, the UCM method sometimes produces a greenish image which seems unnatural to human visual system.

Pixel distribution shifting color correction (PDSCC) was proposed by Mohd Naim and Mat Isa [7]. This method corrects the white reference point of the image and ensures that the white reference point is achromatic. However, this method fails to reduce the impact of blue-green illumination significantly.

Meanwhile, Hitam et al. (2013) proposed a technique named CLAHE-Mix [1]. In this technique, CLAHE is applied to underwater images in RGB and HSV color models. During the process, the distribution of pixel is set according to Rayleigh distribution in both color models. These processes will produce two output images which are CLAHE-RGB and CLAHE-HSV images. Both images are then combined by using Euclidean norm. However, in some cases, this method tends to produce greenish output images.

Abdul Ghani and Mat Isa (2015) proposed a method called integrated color model with Rayleigh distribution (ICM-RD) [8]. The ICM-RD is an extension and modification technique of ICM and UCM. The proposed technique applies the histogram modification in RGB and HSV color models. In the RGB color model, the image histograms are stretched within certain limits to reduce the effect of under- and over-saturation. The pixel distribution is shaped to follow the Rayleigh distribution. The

same technique is applied to image histograms in the HSV color model, in which limited stretching is implemented to the S and V components. Visual inspection indicates that this method is able to improve the image contrast. However, the effect of blue-green illumination is not significantly reduced in the resultant image.

In other report, Abdul Ghani and Mat Isa (2016) proposed the integrated-intensity stretched-Rayleigh histograms method (IISR) [9]. To solve the color imbalance problem, each color channel is multiplied by a gain factor which has been modified based on Von Kries hypothesis. Based on visual observation, the image contrast can be improved through this method. However, the effect of blue-green illumination remains in the image.

3 Motivation

To minimize the effect of blue-green illumination, some previous researchers have used the Von Kries hypothesis. For example, in UCM method [6], the authors have used this hypothesis to correct the two lowest color channels. However, in some cases, this method produces a large gain factor, which causes the red color to be extremely enhanced. The *coral stone* image in Fig. 1a is used to show the resultant image produced by this method. The original image is completely covered by the blue-green illumination effect that causes the object cannot be seen clearly. This effect can be seen in Fig. 1b where the color of the object turns reddish.

In another report, Abdul Ghani and Mat Isa suggested another variation of Von Kries hypothesis [9]. The gain factor is chosen as median value of the ratio of the maximum color channel to the respective color channels of the image. However, in some cases, the gain factor acquired through this method is very small. Therefore, no significant improvement can be observed because the colors are not correctly balanced as shown in Fig. 1c.

In conclusion, if the calculated gain factor value is too large, excessive color enhancement will occur and this should be avoided. On the other hand, if the value is too small, the change is very minimal, thus the color improvement is considered to be unsuccessful. Based on this discovery, it is important to introduce a technique that can balance the color channel correctly, for example, taking into account the difference between the lowest color channel (red color) and the dominant color channel (blue color) in terms of total pixel value.

4 Methodology

In this section, two major steps to enhance the underwater image are explained in detail. Figure 2 shows the overall process of the proposed method.

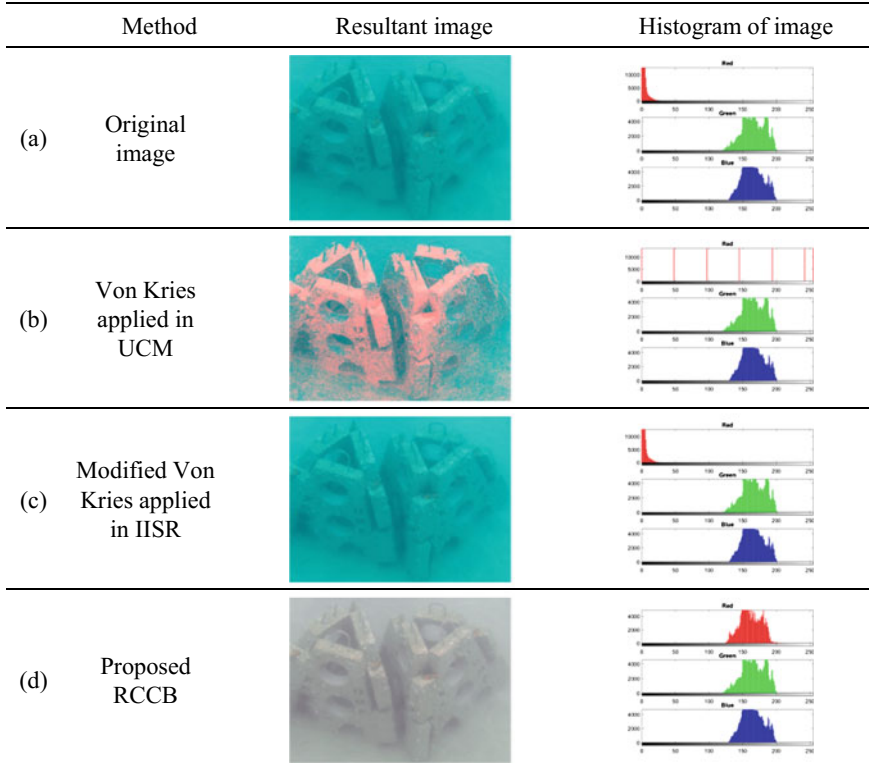


Fig. 1 Resultant images and image histograms of existing methods and the proposed RCCB

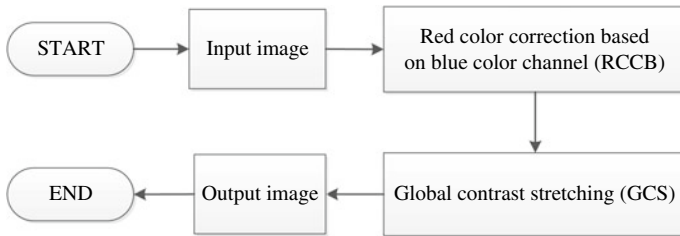


Fig. 2 Overall process of the proposed method

4.1 Red Color Correction Based on Blue Color Channel (RCCB)

Firstly, the image in RGB color model is decomposed into the red, green, and blue channels. Then, the total pixel value from red color channel, R_{sum} and blue color

channel, B_{sum} are computed. The blue color is chosen as the reference for the red color enhancement, as this color is usually dominant and less affected by light absorption [1]. A gain factor, Z is obtained using Eq. (1).

$$Z = \left| \frac{B_{sum} - R_{sum}}{B_{sum} + R_{sum}} \right| \quad (1)$$

The gain factor of Z carries information regarding the difference of the total pixel value between the blue color channel and red color channel. This information is critical to control the appropriate amount of pixel value that should be added to the red color in order to weaken the effect of blue-green illumination. Then, the red color is improved through Eq. (2). The blue color channel is multiplied by the gain factor of Z . The result of this multiplication produces the appropriate pixel value for the red color enhancement. The more significant the difference of the total pixel value between the red color channel and the blue color channel, the higher amount of the pixel will be added to enhance the red color and vice versa. As shown in Fig. 1d, the proposed RCCB is able to enhance the red color channel properly. The histograms of all color channels are well-balanced thus reduce the effect of blue-green illumination significantly.

$$P_{red} = P_{red} + (Z \times P_{blue}) \quad (2)$$

where P_{red} and P_{blue} are the pixel values of red and blue color channels, respectively.

4.2 Global Contrast Stretching

Next, global contrast stretching technique is applied to all color channels to improve overall image contrast. Equation (3) is used for the contrast stretching. P_{in} and P_{out} are the input and output pixels, respectively. i_{min} and i_{max} denote the minimum and maximum intensity level values for the input image, respectively.

$$P_{out} = 255 \left(\frac{P_{in} - i_{min}}{i_{max} - i_{min}} \right) \quad (3)$$

Thus, the green and blue color channels are stretched according to Eqs. (4) and (5), respectively. For the red color channel, Eq. (2) is integrated with Eq. (3) to form Eq. (6).

$$P_{green} = 255 \left(\frac{P_{green} - i_{min}}{i_{max} - i_{min}} \right) \quad (4)$$

$$P_{blue} = 255 \left(\frac{P_{blue} - i_{min}}{i_{max} - i_{min}} \right) \quad (5)$$

$$P_{red} = 255 \left(\frac{P_{red} + (Z \times P_{blue}) - i_{min}}{i_{max} - i_{min}} \right) \tag{6}$$

5 Results and Discussion

To evaluate the performance of the proposed RCCB-GCS technique, three deep underwater images are used in the experiment, namely *artificial coral reef*, *coral stone*, and *table coral*. Figure 3 shows the resultant images and image histograms of each step of the proposed RCCB-GCS.

The proposed technique is compared with GW [3], UCM [6], PDSCC [7], and IISR [9]. Besides visual observation, the comparison is also performed on three quantitative evaluation metrics, which are entropy [10], average gradient [11], and natural image quality evaluator (NIQE) [12].

The resultant images produced by all methods are shown in Figs. 4, 5 and 6. Based on these figures, the output images produced by GW appear reddish. There is no significant improvement can be seen from the output images processed by PDSCC, as the objects in the images look blurry and unclear. UCM has successfully enhanced the contrast of the original images, but the images become greenish especially at the background areas. For IISR, the method enhances the image contrast to some extent. However, this method fails to reduce the effect of blue-green illumination

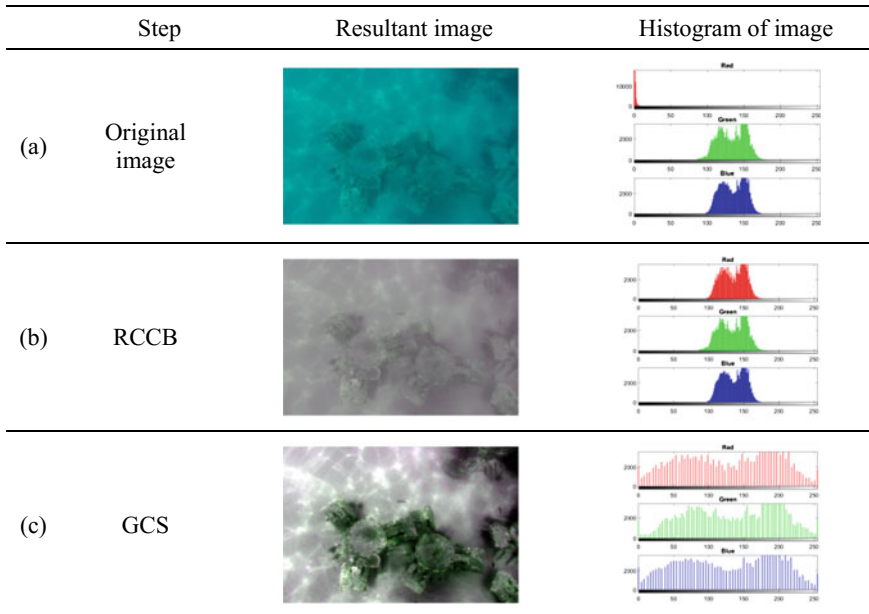


Fig. 3 Resultant images and image histograms of each step of the proposed RCCB-GCS

Table 1 Quantitative results in terms of entropy, average gradient, and NIQE

Image	Method	Quantitative analysis		
		Entropy	Average gradient	NIQE
<i>Artificial coral reef</i>	Original	5.421	0.700	5.653
	GW	4.961	15.157	19.439
	UCM	6.459	23.489	25.365
	PDSCC	6.355	8.544	20.889
	IISR	6.723	7.887	9.464
	RCCB-GCS	7.029	3.689	4.775
<i>Coral stone</i>	Original	6.025	0.794	6.375
	GW	5.401	6.224	4.946
	UCM	7.157	11.276	5.615
	PDSCC	6.330	4.029	6.446
	IISR	7.215	4.732	5.099
	RCCB-GCS	6.630	3.938	4.927
<i>Table coral</i>	Original	6.089	1.107	6.092
	GW	5.554	12.789	10.415
	UCM	6.861	18.647	13.422
	PDSCC	6.709	8.617	10.901
	IISR	7.212	7.874	5.454
	RCCB-GCS	7.232	4.284	4.025

Note The values in bold typeface represent the best result obtained in the comparison

significantly. On the other hand, the proposed RCCB-GCS method has reduced the problem of blue-green illumination effect significantly. The image contrast is also improved as the objects in the images become clear and easily distinguished from the background.

This superior performance is also verified by the quantitative analysis reported in Table 1. The proposed method is the best compared to the other methods in terms of entropy and NIQE for images *artificial coral reef* and *table coral*. A high entropy value denotes that the proposed method can produce image which has more information, while a low NIQE value suggests that the proposed method can produce higher quality of image as compared to the other methods. On the other hand, UCM gets the highest score in the average gradient evaluation for all sample images. A high average gradient value indicates that the image has a higher intensity level and thus a better contrast. However, based on visual observation, UCM produces a greenish background that does not seem appropriate to the human visual system. On the contrary, the image contrast produced by the proposed RCCB-GCS method has improved significantly despite the low score in the average gradient evaluation. In addition, the problem of blue-green illumination effect is also well-addressed as shown in the output images.

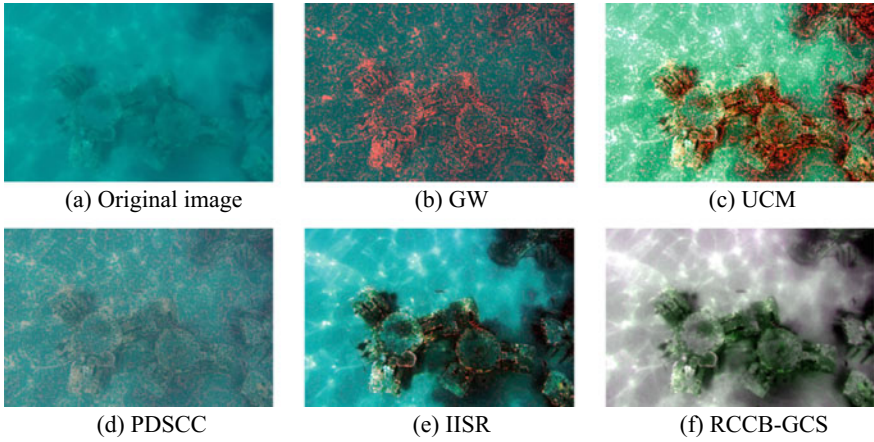


Fig. 4 Processed images of *artificial coral reef* based on different methods

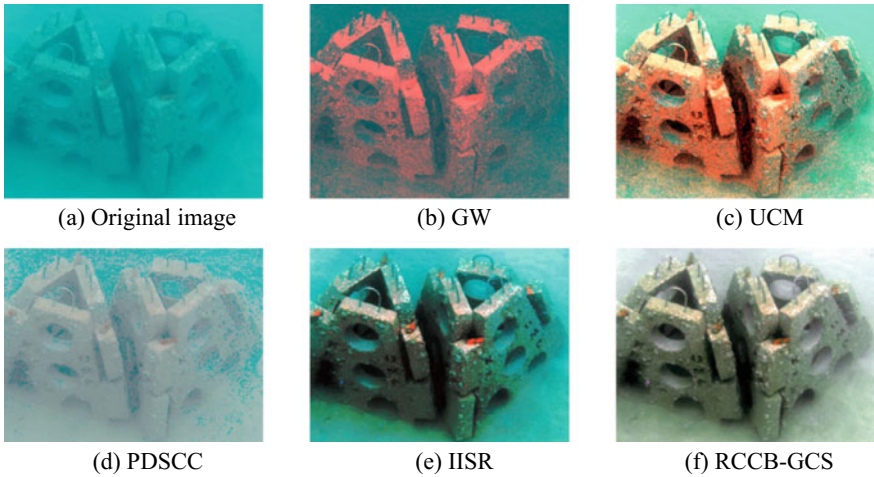


Fig. 5 Processed images of *coral stone* based on different methods

6 Conclusion

The RCCB-GCS method is proposed to solve underwater image problems, especially the image contrast and blue-green illumination effect. The method considers the difference between the blue color and red color in terms of total pixel value in order to control the red color enhancement appropriately. The effectiveness and capability of the proposed method are verified by the qualitative and quantitative evaluation results.

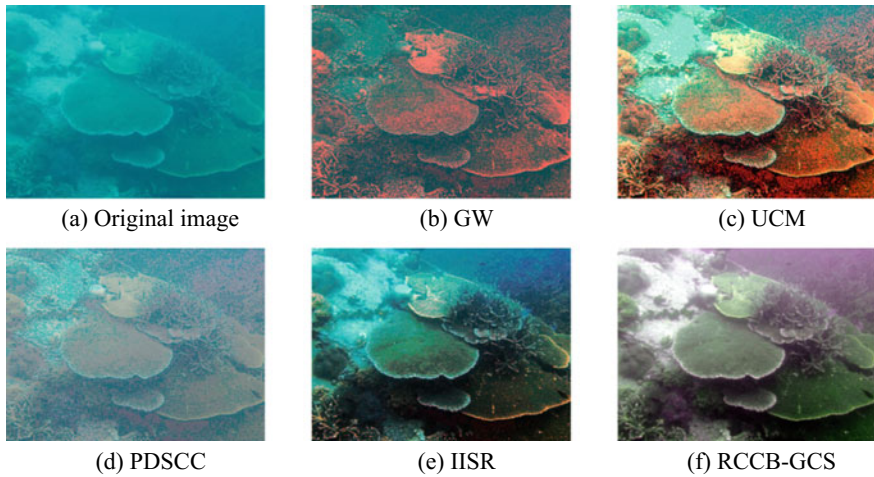


Fig. 6 Processed images of *table coral* based on different methods

Acknowledgements This work is partially supported by Universiti Malaysia Pahang research grant, RDU170392 entitled “Dual Image Fusion Technique for Enhancement of Underwater Image Contrast.”

References

1. Hitam, M.S., Awalludin, E.A., Wan Yussof, W.N.J., Bachok, Z.: Mixture contrast limited adaptive histogram equalization for underwater image enhancement. In: Proceeding of the IEEE International Conference on Computer Applications Technology (ICCAT), pp. 1–5 (2013)
2. Schettini, R., Corchs, S.: Underwater image processing: state of the art of restoration and image enhancement methods. EURASIP J. Adv. Signal Process. 1–14 (2010)
3. Buchsbaum, G.: A spatial processor model for object colour perception. J. Franklin Inst. **310**(1), 1–26 (1980)
4. Senthilkumaran, N., Thimmiaraja, J.: Histogram equalization for image enhancement using MRI brain images. In: 2014 World Congress on Computing and Communication Technologies, pp. 80–83 (2014)
5. Iqbal, K., Salam, R.A., Osman, A., Talib, A.Z.: Underwater image enhancement using an integrated color model. Int. J. Comput. Sci. **34**(2), 239–244 (2007)
6. Iqbal, K., Odetayo, M., James, A., Salam, R.A., Talib, A.Z.H.: Enhancing the low quality images using unsupervised colour correction method. In: Proceedings of the IEEE International Conference on Systems, Man and Cybernetics, pp. 1703–1709 (2010)
7. Mohd Naim, M.J.N., Mat Isa, N.A.: Pixel distribution shifting color correction for digital color images. Appl. Soft Comput. **12**(9), 2948–2962 (2012)
8. Abdul Ghani, A.S., Mat Isa, N.A.: Underwater image quality enhancement through integrated color model with Rayleigh distribution. Appl. Soft Comput. **27**, 219–230 (2015)
9. Abdul Ghani, A.S., Raja Aris, R.S.N.A., Muhd Zain, M.L.: Unsupervised contrast correction for underwater image quality enhancement through integrated-intensity stretched-Rayleigh histograms. J. Telecommun. Electron. Comput. Eng. **8**(3), 1–7 (2016)

10. Ye, Z.: Objective assessment of nonlinear segmentation approaches to gray level underwater images. *ICGST J. Graph. Vis. Image Process.* **9**(II), 39–46 (2009)
11. Wu, J., Huang, H., Qiu, Y., Wu, H., Tian, J., Liu, J.: Remote sensing image fusion based on average gradient of wavelet transform. In: *IEEE International Conference on Mechatronics and Automation*, pp. 1817–1822 (2005)
12. Mittal, A., Soundararajan, R., Bovik, A.C.: Making a ‘completely blind’ image quality analyzer. *IEEE Signal Process. Lett.* **20**(3), 209–212 (2013)

Development of Surface Cleaning Robot for Shallow Water



Muhamad Qayyum Dahlan, Herdawatie Abdul Kadir, Khalid Isa, Radzi Ambar, Mohd Rizal Arshad and Maziyah Mat Noh

Abstract Aqua pollutant (river, sea, lake, etc.) is one of the major problem that occurs around the world including Malaysia. One of the major cause of the pollution come from rubbish and illegal toxic waste dumping. This cause the destruction to the aquatic species and ecosystem. River cleaning is usually done when river pollution is in critical condition. This is due to the labor cost of each cleaning project, scheduling problems and shallow water environment. Therefore, the river cleaning system is crucial to ensure that rivers are clean and free from pollution. This project aims to design and develop river cleaning robot to enable real-time monitoring of water cleanliness. Inspired by Indian lake cleaning project, the Waste Hunter Surface Robot is smaller in size and portable. The Waste Hunter Surface Robot is tele-operated robot with two main functions, which are surface cleaning and water quality monitoring. It has a flexible design to clean the various impurities on the surface and below the river's surface and trench. By implementing an automation system, the system enables in monitoring 24/7 the cleanliness of the water. This project is expected to reduce labor costs and save a large number of states or districts of money.

Keywords Surface cleaning robot · Shallow water · Water quality monitoring

M. Q. Dahlan · H. Abdul Kadir (✉) · K. Isa · R. Ambar
Faculty of Electrical and Electronic, Universiti Tun Hussein Onn Malaysia,
Parit Raja, Malaysia
e-mail: watie@uthm.edu.my

M. R. Arshad
UCRG, School of Electrical and Electronic Engineering, Universiti Sains Malaysia,
Engineering Campus, Nibong Tebal, Malaysia

M. Mat Noh
Robotics and Unmanned Research Group (RUS), Instrument & Control Engineering (ICE)
Cluster, Universiti Malaysia Pahang, Pekan, Malaysia

© Springer Nature Singapore Pte Ltd. 2019
Z. Md Zain et al. (eds.), *Proceedings of the 10th National Technical Seminar on Underwater System Technology 2018*, Lecture Notes in Electrical Engineering 538,
https://doi.org/10.1007/978-981-13-3708-6_5

1 Introduction

Malaysia and many develop country may be assume that most the local community are not care of rivers compare with the developed country such as Netherland. For the sake of the river that mainly used for drinking and daily household work, the government have taken a lot of initiative to maintain the cleanliness of the water. One of the initiative is the river of life program and one river one state program. Due to costing in order to maintain the cleanliness of the river, an automation system or robot is seen to be the best option for maintaining the river cleanliness compare with human workforce. According to the Malaysia Nature Society (MNS) vice-president Vincent Chow, pollution have made the river to become low-oxygen environment. This cause the destruction to the aquatic species and ecosystem [1–3]. A lot of initiative has been taken by the government and non-government agencies (NGO) to clean the river. According to the Star Online article on Monday 7 April 2014, over RM25 million were spent by the federal government and the number keeps increasing from year to years [4]. This is due to the labor cost, In order to reduce the cost, many initiatives taken, including usage of autonomous machine that are more efficient compared to traditional ways [5–7].

2 Surface Cleaning Robot

2.1 Concept

The river cleaning robot or Waste Hunter Surface Robot is a semi-automatic robot with three different main functions, which are surface cleaning, purification process and water quality monitoring. In this section, there will be an explanation on the working process of the robot and all input output (I/O) used. The robot is semi-automatic control robot where the robot will be turned on and off, makes a movement form the input gain from the user. Wireless based controller were used with WI-FI based communication protocol to communicate between the user and the robot. The remote control used is the smart phone apps called (Blynk) virtual button keypad as shown in Fig. 1. The Nodemcu microcontroller module is use to interface unit between the user and robot.

The wireless based controller was used in WI-FI based communication protocol to communicate between the user and the robot. The remote control used is the smart phone apps called (Blynk) virtual button keypad. The Nodemcu microcontroller module is used to interface unit between the user and the robot. There will be several functions on the mobile apps, virtual keypad to control the robot, when the robot is connected to the WI-FI module, first button, the propeller control (virtual joystick) for the movement of the robot. One widget for monitoring the internet data connection (ping) between Blynk cloud and user interface, digital switch to turn on or off the motor pump and one virtual gauge for data quality monitoring (PH value). The block diagram of the overall system is shown in Fig. 2.

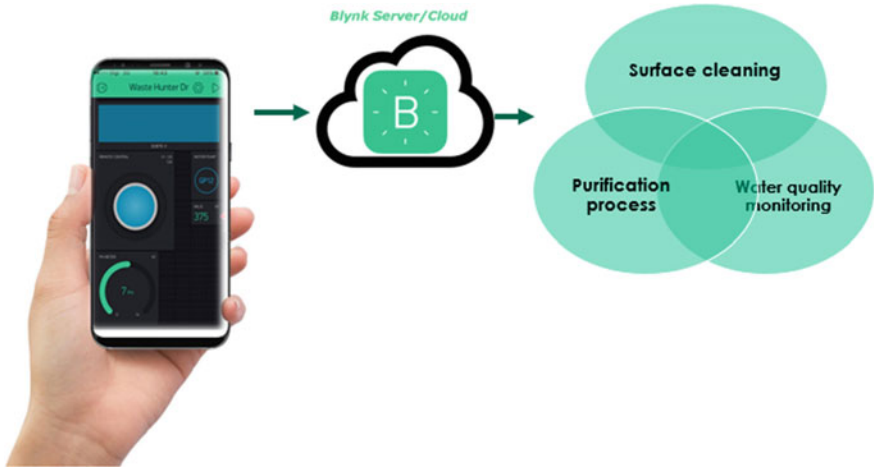


Fig. 1 Waste Hunter concept

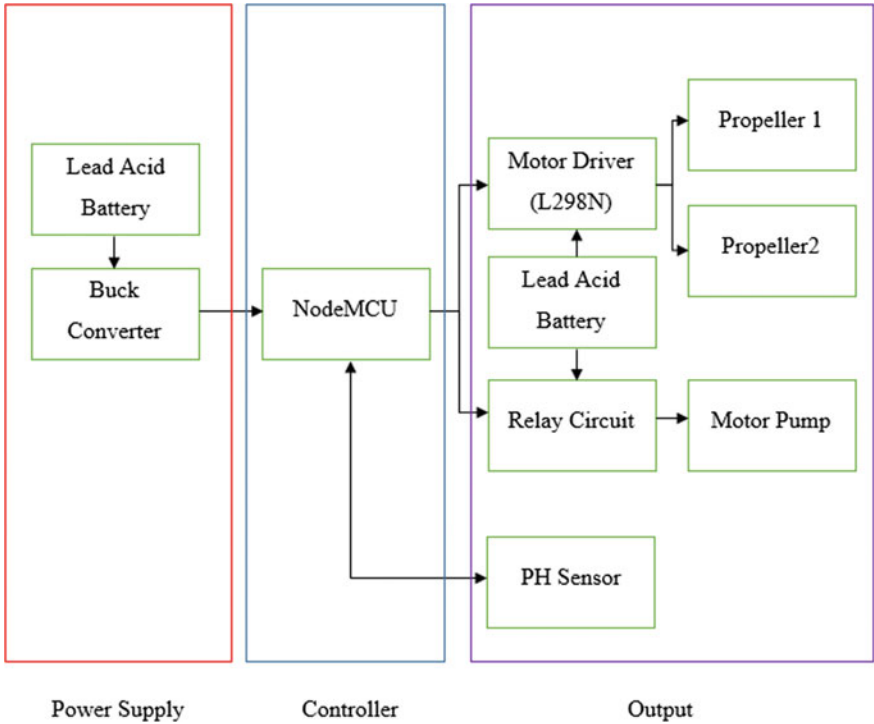


Fig. 2 Waste Hunter Surface Robot system architecture

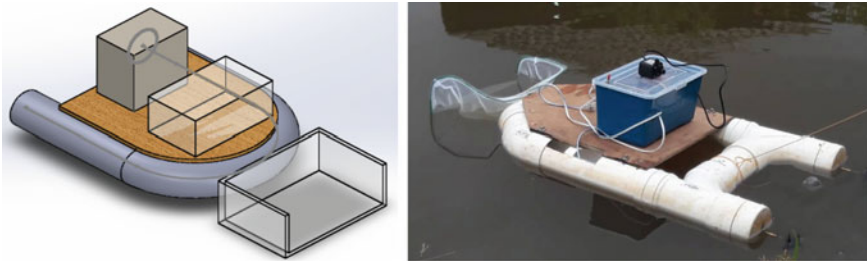


Fig. 3 Waste Hunter Robot

2.2 Design

The cleaning mechanism is inspired from the Ro-Boat where the cleaning system is surface cleaning. The concept is the robot will capture the waste on the surface and trap it. This robot features are not advancing mode where it does not have any intelligent visionary in order to detect and differentiate between waste or not waste on the water surface. The system is tele-operated, where the user need to control it and clean up the waste by controlling the robot and trap it to the trapping unit.

The robot is added on with some additional function, water purification system. The systematic use two stage filtering unit, at the first stage there will be sediment filter, the sediment filter will filter the con-termination that can be seen by the naked eyes. At the second stage the use of carbon filter will help remove the heavy iron that contains inside the water in order to increase the quality and stabilize the water PH. Figures 3 and 4 shows the design of the Waste Hunter Robot and the Virtual Joystick.

3 Result and Discussion

Initially, the trapping unit is used to trap the solid waste on the surface of the water. The trapper was installed at the front of the robot and it submerged a meter below the water surface in order to trap waste that submerge below the surface of water. The trapper is made up from the nylon net. If the net is broken or torn out, it is easy to replace and cheap in price. The nylon net is chosen due to the material strength is tough, water resist, and free from oxides compared to metal net that can easily rust and get broken.



Fig. 4 Virtual Joystick (V1)

3.1 Surface Cleaning

Since the robot is only surface cleaning, it only can trap and catch only waste that a on the surface of water only. Figure 5 show the robot taking waste on the water surface, first waste is plastic bottle and second waste is plastic bag. It is easy to trap plastic bag since half of its body are trap below the water and the movement is minimum compared with plastic bottle.



Fig. 5 Waste Hunter surface cleaning

Fig. 6 Two stage filter unit



Fig. 7 Filter water before and after



3.2 Purification Process

Figure 6 shows the filtering unit that will be used with the robot. The filtering unit is a combination between two different types of filter material. At the present time the material used for the filter is from readymade material. For the carbon filter, the target material is active carbon. However, for time being it will use charcoal and for the sediment filter the material will change to filter mate.

The result for the filtering unit is as shown in Fig. 7. Due to the filter is still on the prototype stage, so the filtering efficiency is not to excellent as predicted. However the filter capable to reduce contamination in the water and improve the colour of water and smell.

3.3 Real Data Monitoring

One of the main objective for this work is to measure and view the water quality on real time. The data measure is the water PH values. The PH value is the easy way to decide either the water is suitable or not for aquatic live to live inside the water. All the data collected will be sent to the user in real time monitoring by using Blynk apps as shown in Fig. 8.

The sensor data were send to the microcontroller and user can read the value in the gauge meter as shown above and the data will be update and auto refresh for every two second since the push notification algorithm is used. Standard value for

Fig. 8 PH monitoring indicator in real time



the PH will be display from 0 to 14; (0–6) for acid, (7) neutral, (8–14) for alkali. The sensor read the voltage changes in mV at the pin A0 and the microcontroller convert it to the standard PH value reading ranging from 0 until 14.

3.4 Maximum Range and Operating Time

The maximum range can be achieve by this robot is depend on the internet strength connectivity. At the first stage of testing the internet connection use is the personal hotspot from mobile phone. The limitation of this method is the short range of the connection which is only 20 m. The personal hotspot introduce problem in term of connection since the connection is unstable when disturbance exist. In order to increase the maximum range, portable Wi-Fi hotspot is used which extend the control range to 150 m.

In term of operating time, the maximum operating time using one lead acid battery is 7 A per hours as shown below

$$\text{Battery rating} = 7 \text{ A/h}$$

$$2 \times \text{Motor current usage (with load)} = 0.6 \text{ A} \times 2 = 1.2 \text{ A}$$



Fig. 9 Location 1 (Taman Bistari Indah trench)

Motor Pump (maximum volt) = $0.4167 \text{ A} \times 1 = 0.4167 \text{ A}$

NodeMcu (Wi-Fi module) = $0.5 \text{ A} \times 1 = 0.5 \text{ A}$

Operating Hour (full load) = $7 \text{ AH} / (1.2 \text{ A} + 0.1467 \text{ A} + 0.5 \text{ A}) = 3.8 \text{ h}$.

4 Operational Test

The operational testing were carried out in three shallow water environment. During the test, the surface cleaning robot is examined with four movement condition which are forward, backward, left and right movement. These test is important to investigate the surface cleaning robot motion behavior. The tests were performed near Batu Pahat area as shown in Fig. 9 until Fig. 11.

As shown in Fig. 9, the length of the testing point is only 5 m length. The flow rate sensor indicate almost zero flowrate reading. Second testing location is at the Lake at UTHM as shown in Fig. 10. The flow of water in this location is range of 0.3 m/s to 1.3 m/s due to light wind breeze.

Third testing location is near Taman University trench as shown in the Fig. 11. The trench is width is about 2 m. From the observation, the surface vehicle encounter difficulty to perform left and right rotation. Several adjustment are made to get the desired output for the motion. Each data were tested five times. Table 1 shows the summary of the movement performance.

The result shows that surface cleaning robot were able to reach the desired location under minimum wind condition. However, the surface cleaning robot is hard to move in open environment with strong water compare clam water environment. This may due to the open environment which allow higher wind resistance.

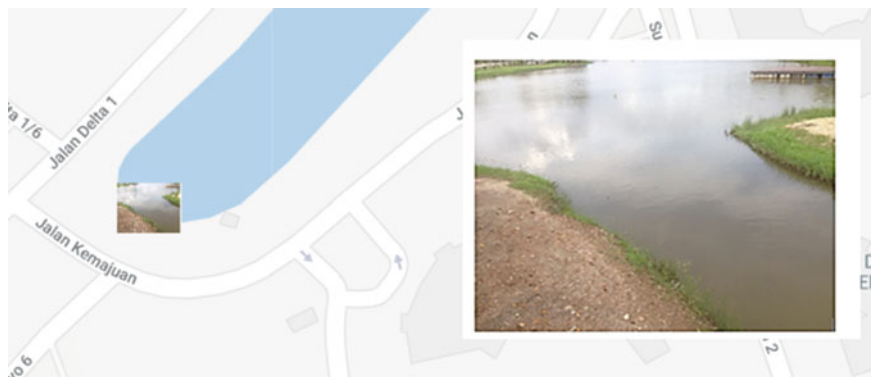


Fig. 10 Location 2 (UTHM Lake)



Fig. 11 Location 3 (Taman Universiti)

Table 1 Summary of different environment and movement

Location	Distance (m)	Time (s)	Movement			Speed (knots)	Connectivity
			Forward	Backward	Right/left		
UTHM Lake	15	105	✓	✓	360°	0.3	✓
Taman Universiti	7	47	✓	✓	360°	0.26	✓
Taman Bistari Indah	5	23	✓	✓	360°	0.25	✓

5 Conclusion

This project aim to design and develop river cleaning robot to enable in real-time monitoring for cleanliness of water. By implementing automation system, the system enable in monitoring 24/7 the cleanliness of water and can trap the physical waste that flow on the water.

Acknowledgements The authors are grateful for the financial support from Universiti Tun Hussein Onn Malaysia's TIER 1 Grant Scheme (U853).

References

1. Cline, B., Henry, M., Justice, C.: KPMG Rise of the Robot (2016)
2. Sinha, A., Bhardwaj, P., Vaibhav, B., Mohommad, N.: Research and development of Ro-boat: an autonomous river cleaning robot. In: Proceedings of SPIE 9025, Intelligent Robots and Computer Vision XXXI: Algorithms and Techniques, 90250Q (2014)
3. Garbage kills almost all life in Johor River. <http://www.todayonline.com/world/asia/garbage-kills-almost-all-life-malaysian-river>. Last accessed 11 Apr 2017
4. Over 25Mil spent on cleaning River in three years. <http://www.thestar.com.my/news/nation/2014/04/07/over-rm25mil-spent-on-cleaning-rivers-in-three-years/>. Last accessed 07 Apr 2014
5. Fornai, F., Ferri, G., Manzi, A., Ciuchi, F., Bartaloni, F., Laschi, C.: An autonomous water monitoring and sampling system for small-sized ASVs. *IEEE J. Oceanic Eng.* **42**(1), 5–12 (2017)
6. Ferri, G., Manzi, A., Fornai, F., Ciuchi, F., Laschi, C.: The hydronet asv, a small-sized autonomous catamaran for real-time monitoring of water quality: from design to missions at sea. *IEEE J. Oceanic Eng.* **40**(3), 710–726 (2015)
7. Bella, S., Belbachir, A., Belalem, G.: A centralized autonomous system of cooperation for UAVs-monitoring and USVs-cleaning. *Int. J. Softw. Innov. (IJSI)* **6**(2), 50–76 (2018)

Design and Development of an Autonomous Underwater Vehicle for Underwater Target Navigation Mission Module



**Muhammad Muzakkir Ahmad Roslan, Herdawatie Abdul Kadir,
Khalid Isa, Radzi Ambar, Mohd Rizal Arshad, Maziyah Mat Noh
and Mohd Helmy Wahab**

Abstract The Autonomous Underwater Vehicles (AUV) industry is growing dramatically with the increase in the reliability and technical abilities of these vehicles. The vehicles require autonomous guidance and control system in order to perform underwater tasks. The Target Navigation Mission Module (TNMM) permits the vehicle to follow preprogrammed trajectories wherever and whenever required. Without this module, the vehicle will not be able to achieve the desired mission. In this work, the Mission module were able to identify the task, detect the target, coordinate the state of AUV (attain desired height and yaw angle) and makes decision on path based on mission time elapsed. The Target Navigation Mission Module used the Kalman Filter algorithm to estimates the state of a system during the navigation. The results shows a reliable reading obtain by the AUV. Therefore, better decision on motion direction were achieved. The AUV was able to navigate underwater and track underwater object without the need of operator assistance.

Keywords Autonomous Underwater Vehicles · Navigation · Kalman Filter

1 Introduction

AUVs exhibit an interestingly difficult navigational issue since they work autonomously in a highly unstructured condition where satellite-based navigation

M. M. Ahmad Roslan · H. Abdul Kadir (✉) · K. Isa · R. Ambar · M. H. Wahab
Faculty of Electrical and Electronic, Universiti Tun Hussein Onn Malaysia, Parit Raja, Malaysia
e-mail: watie@uthm.edu.my

M. R. Arshad
UCRG, School of Electrical and Electronic Engineering, Universiti Sains Malaysia, Engineering
Campus, Nibong Tebal, Malaysia

M. Mat Noh
Robotics and Unmanned Research Group (RUS), Instrument & Control Engineering (ICE)
Cluster, Universiti Malaysia Pahang, Gambang, Malaysia

© Springer Nature Singapore Pte Ltd. 2019

Z. Md Zain et al. (eds.), *Proceedings of the 10th National Technical Seminar
on Underwater System Technology 2018*, Lecture Notes in Electrical Engineering 538,
https://doi.org/10.1007/978-981-13-3708-6_6

is not specifically accessible. Dissimilar to autonomous aerial vehicles, AUVs must explore utilizing different techniques when submerged. For an AUV to effectively total a typical survey mission, it must take after a way determined by the operator as nearly as could be allowed and arrive at a precise location for gathering by a surface vessel. If the last position of the AUV is not accurate, the AUV might be unrecoverable. If the AUV does not follow the path accurately during the mission, basic highlight may not be recorded and the situation of any highlight recorded amid the mission will be questionable. The accuracy of the navigation system can specifically influence the nature of the recorded information if image processing techniques are utilized to improved zones which were observed multiple times during the mission and these areas are misaligned because of navigational errors [1, 2].

The essential test in AUV navigation is keeping up the precision of an AUV's position through the span of long mission. An initially precise position can rapidly wind up indeterminate through varieties in the AUV's movement. This impact can be reduced by utilizing precise using accurate heading, velocity sensors and accelerations but these sensors cannot be made self-assertively. With long missions, these errors wind up noteworthy. Solid streams and other underwater phenomena which influence the motion of the AUV yet cannot be precisely modelled lead to greater inaccuracies [3–8]. If the AUV position are not remotely, the position are accurate will definitely corrupt throughout the mission. The lack of an effortlessly discernible, external reference will makes AUV navigation exceptionally troublesome. The system of AUV navigation will gives accuracy with long missions that are utilize an external reference. Different techniques for giving some reference are reviewed in this paper. In prohibitive situations, a portion of these strategies will not be usable. By considering the problem of giving precise navigation in these more prohibitive situations, procedure which prompt navigation which more powerful and more effective for all AUV missions. In order to increase the autonomy, of the vehicle and avoid costly pre-deployment of underwater transponders, the navigation mission module is a favorable alternative.

2 AUV Navigation System

The navigation of an AUV can be found in the core navigation system is based on the output from IMU as shown in Fig. 1. The measured angular velocity from the gyroscopes and specific force from the accelerometers are integrated using the navigation algorithm to obtain the vehicle velocity, attitude, depth and horizontal position. The output from the navigation equations are integrated with the different aiding sensors using an error state Kalman Filter (KF). Additionally, the basic aiding sensors are an optional magnetic compass and a pressure sensor. The KF estimates the state of a system from a succession of unverifiable perceptions utilizing using a predict-update cycle. Initial, a predictive estimate of the following state and its vulnerability is made utilizing a current physical model and a measurable model which portrays any uncertain factors for example process noise. This prediction

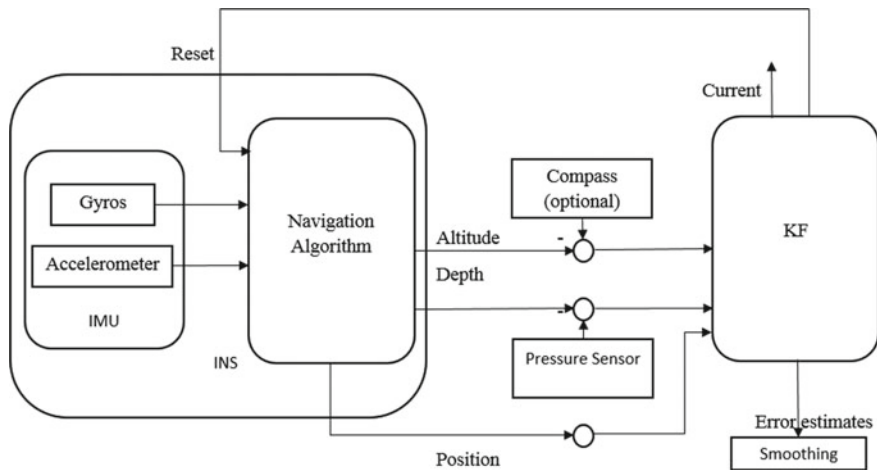


Fig. 1 AUV navigation system

is then updated utilizing an observation of the process relying upon the distinction between the prediction and the observation and their uncertainties. When this updated estimate has been calculate, another predictive estimate can be made.

Generally, a system described by the state vector \mathbf{X}_{k-1} and covariance vector \mathbf{P}_{k-1} at time $k-1$, the next state of the system is defined as $\mathbf{x}_k = \mathbf{F}_{k-1}\mathbf{x}_{k-1} + \mathbf{v}_{k-1}$ where \mathbf{F}_{k-1} describes the physical model and \mathbf{V}_{k-1} describes the Gaussian uncertainty. Similarly, the observation vector is defined as $\mathbf{z}_k = \mathbf{H}_k\mathbf{x}_k + \mathbf{w}_k$ where \mathbf{H}_k describes the physical model of the observation process and \mathbf{w}_k describes the uncertainty. Both vectors \mathbf{V}_{k-1} and \mathbf{w}_k are defined as being generated by zero-mean Gaussian distributions with covariance's \mathbf{Q}_{k-1} and \mathbf{R}_k respectively. The predictive and updated estimates of the state vector are computed by the equations:

$$\hat{\mathbf{x}}_{k|k-1} = \mathbf{F}_{k-1}\hat{\mathbf{x}}_{k-1} \tag{1}$$

$$\mathbf{P}_{k|k-1} = \mathbf{Q}_{k-1} + \mathbf{F}_{k-1}\mathbf{P}_{k-1}\mathbf{F}_{k-1}^T \tag{2}$$

$$\hat{\mathbf{x}}_k = \hat{\mathbf{x}}_{k|k-1} + \mathbf{K}_k(\mathbf{z}_k - \mathbf{H}_k\hat{\mathbf{x}}_{k|k-1}) \tag{3}$$

$$\mathbf{P}_k = \mathbf{P}_{k|k-1} - \mathbf{K}_k\mathbf{S}_k\mathbf{K}_k^T \tag{4}$$

where $\hat{\mathbf{x}}_{k|k-1}$ and $\mathbf{P}_{k|k-1}$ are the predictive estimates of the state and covariance vectors, $\hat{\mathbf{x}}_k$ and \mathbf{P}_k are the updated estimates and:

$$\mathbf{K}_k = \mathbf{P}_{k|k-1}\mathbf{H}_k^T\mathbf{S}_k^{-1} \tag{5}$$

$$\mathbf{S}_k = \mathbf{H}_k\mathbf{P}_{k|k-1}\mathbf{H}_k^T + \mathbf{R}_k \tag{6}$$

where \mathbf{K}_k is the Kalman gain and \mathbf{S}_k is the covariance of the $(\mathbf{z}_k - \mathbf{H}_k\hat{\mathbf{x}}_{k|k-1})$ term. It can be seen that the updated estimate $\hat{\mathbf{x}}_k$ differs from the predictive estimate $\hat{\mathbf{x}}_{k|k-1}$

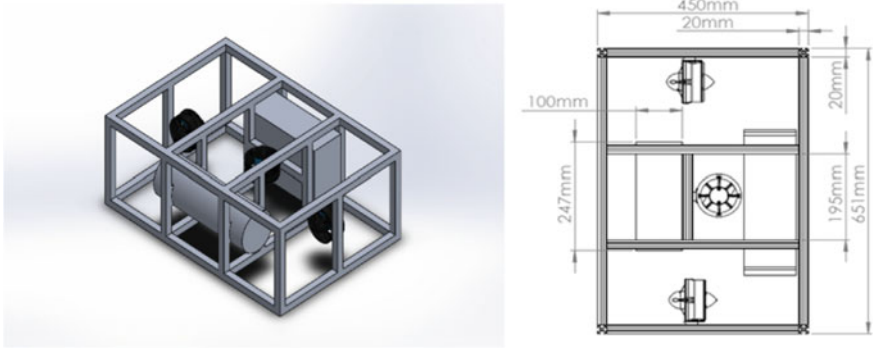


Fig. 2 AUV mechanical structure

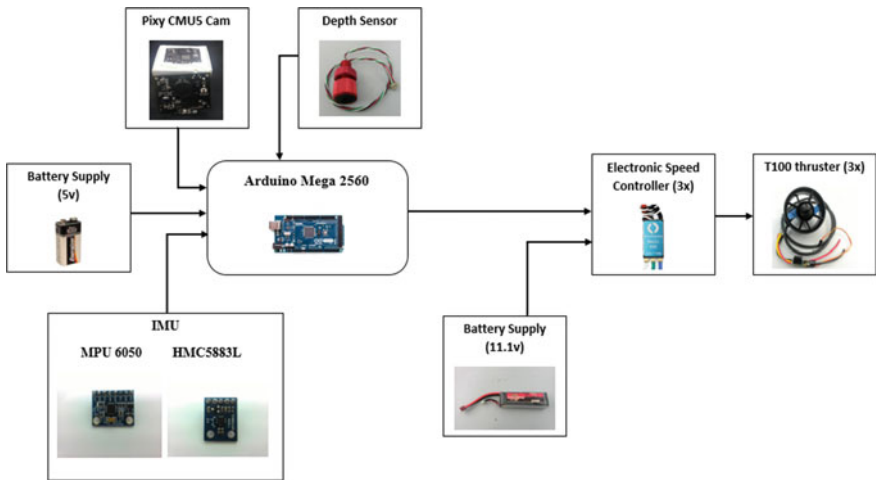


Fig. 3 Electrical and electronic module

depending on the difference between the observation z_k and the predicted observation $H_k \hat{x}_{k|k-1}$. The effect of this difference is dependent on the Kalman gain which is large when the variance of the prediction $P_{k|k-1}$ is larger than the variance of the observation R_k . In this way, predictive estimates are updated by the Kalman filter by a larger amount when the observations are more certain.

Figure 2 shows the design of an AUV drawn using SolidWork software according to the real size, dimensions and component used.

For electrical and electronic module, Fig. 3 shows the overall component used for the AUV. In this system, all electrical and electronic components used are connected to an Arduino microcontroller.

3 Result and Discussion

3.1 AUV Waterproof and Buoyancy

The waterproof test is important to ensure that the electronic module were free of water during submerge. The AUV will be tested for several hours to test the sealing capability. The test were performed in both static water using a tank and moving mode at pool. As the results, there are some bubble occur at the water tight compartment which indicate leakage inside the electronic circuit module. The compartment were identified leaking at the valve for wire section. Therefore, more sealant were added. The test were repeated again until satisfied. After several testing, it is found that the AUV pass the waterproof test. Figure 4 show the submerging testing performed using tank and pool.

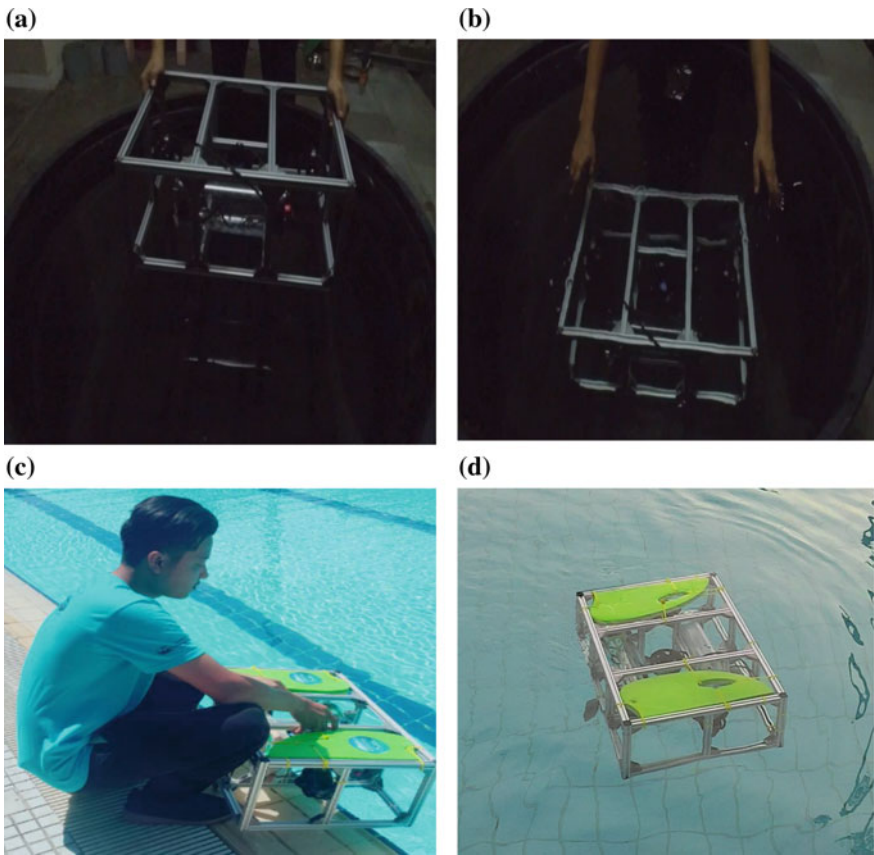


Fig. 4 Result of submerging testing of the AUV Tank: **a** before **b** after; Swimming pool: **c** before **d** after

Table 1 Analysis of AUV sensor reading

Standard deviation				
	Accelerometer X (roll)	Gyroscope X (angle)	Compass X (angle)	Kalman X (angle)
Center	0.154258081	0.496746	0.017795	0.011005
Right	0.141750955	0.490488	0.022632	0.012649
Left	0.117893549	0.500401	0.009944	0.006992
Variance				
Center	0.023796	0.246757	0.000317	0.000121
Right	0.020093	0.240579	0.000512	0.00016
Left	0.013899	0.250401	9.89E-05	4.89E-05
Average				
Center	2.218	103.407	4.345	2.151
Right	1.864	70.757	4.077	1.924
Left	1.781	144.103	3.949	1.754

The buoyancy test were performed to ensure that the AUV had the desired buoyancy or floating capability during deployment. The buoyancy level for each water will differ depending on type of water depending density. This testing need to be performed as it affect the submerged performance in different environment. It is expected, to acquire slightly negative buoyancy which means the AUV will float below the water surface with slight 95%. In the first trail, the AUV sinks in the static water due to open design which less air composition inside the body. Therefore, modification were made by adding a floating material on the structure. As the results, the AUV were able to float after some calibration made based on desired submerged percentage.

3.2 Navigation Test

The navigation module testing were performed on the AUV. Table 1 show the analysis of IMU data based on standard deviation, variance and average value which is recorded 10 times. The testing were important to ensure the AUV give correct sensors reading which will decide the performance of navigation task. The sensors reading is very crucial in order to control the AUV heading due to the existence of water turbulence during the navigation cause by thruster and underwater current movement. If the AUV were unable to correct itself, the mission may fail due to incorrect position and orientation reading and the AUV may get lost.

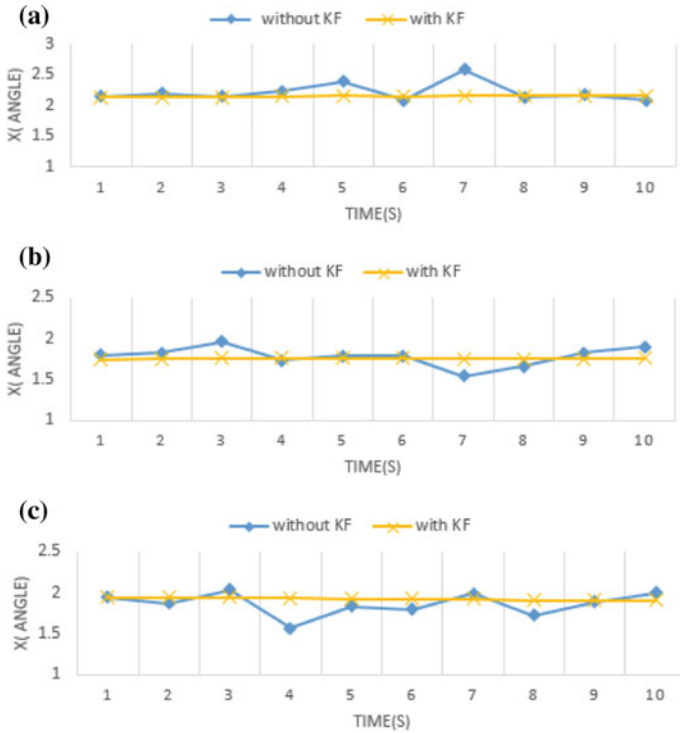


Fig. 5 Samples of reading without and with Kalman Filter

For the consistency, reading were taken 10 times. As the results, the value shows reliable reading with a low standard deviation means that recorded value are very close to the average. Thus indicate good measurement data. Figure 5 shows samples of reading for angles without and with KF, the results shows consistent reading produce by KF compared without KF.

Next, the depth sensor which cover Temperature, Pressure, Depth and Altitude were recorded as shown in Fig. 6. The depth sensor reading will be used for the AUV to surfaced, diving and submerged during navigation.

4 Conclusion

In this work, several test on AUV have been conducted. It can be concluded that the AUV able to perform the desired mission well without intervention with the operator or controller. The AUV were equip with several components such as inertial measurement unit, pressure sensor, pixy cam, and thruster that entirely controlled by the controller. The AUV will start to navigate when it is completely submerged under-

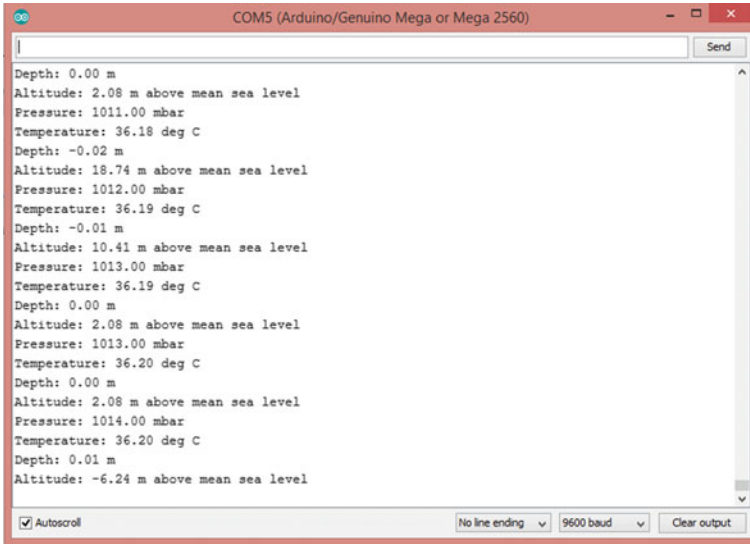


Fig. 6 Depth sensor reading based on depth (data samples)

water. Then Target Navigation Mission Module (TNMM) will assist the navigation while the depth sensor will assist the AUV to remain stay submerged underwater. Pixy cam also plays an important role to detect target underwater. When desired target are detected, the AUV will track and move toward the desired target. However, during testing, there are some problems encountered such as leakage at the main compartment. This causes the AUV to become unstable during submerged underwater. The leakage problems were solved by applying silicon adhesive to every opening place to prevent water from passing through. Several initiatives were also undertaken to prevent leakage as well as the addition of hot glue and plasticine. Other than that, the power supply is an important issue where supply of each component and equipment are sometimes insufficient. This can be solved by the addition of power supply and port for charging to facilitate power supply against the AUV to be carried out properly. In conclusion, the objective of the AUV project is well-accomplished that is to design an Autonomous Underwater Vehicle (AUV) which perform underwater and prescribed the task at given time. For the final objective, the mission of the navigation modules was successfully conducted on the AUV. The AUV was able to navigate underwater and track underwater target without the need of operator assistance.

Acknowledgements The authors are grateful for the financial support from Universiti Tun Hussein Onn Malaysia's TIER 1 Grant Scheme (U853).

References

1. Gonzalez, L.A.: Design, modelling and control of an autonomous underwater vehicle. In: Bachelor of Engineering Honours Thesis (2004)
2. Drtil, M.: Electronic and Sensor Design of an Autonomous Underwater Vehicle. Department of Electrical Engineering and Information Technology of University of Applied Science Koblenz Thesis (2006)
3. Stutters, L., Liu, H., Tiltman, C., Brown, D.J.: Navigation Technologies for Autonomous Underwater Vehicles. *IEEE Trans. Syst., Man Cybernetics—Part C: Appl. Rev.*, 581–589 (2008)
4. Hegrenæs, Ø.: Autonomous navigation for underwater vehicles. Ph.D. Dissertation, Norwegian University of Science and Technology (2010)
5. Von Alt, C.: Autonomous underwater vehicles. In: Woods Hole Oceanographic Institution in Autonomous Underwater Lagrangian Platforms and Sensors Workshop (2003)
6. Blidberg, D.R.: The Development of Autonomous Underwater Vehicle (AUV). Autonomous Undersea System Institute, Lee, NH (2001)
7. Aras, M.S.M., Kasdirin, H.A., Jamaluddin, M.H., Basar, M.F.: Design and Development of an Autonomous Underwater Vehicle (AUV-FKEUTeM). *Fakulti Kejuruteraan Elektrik, UTEM* (2009)
8. Burkardt, M., et al.: Cornell University Autonomous Underwater Vehicle: Design and Implementation of the Ragnarok AUV. *Cornell University Autonomous Underwater Vehicle* (2013)

Development of an Autonomous Underwater Vehicle for Target Acquisition



Leong Wai Lunn Alexander, Khalid Isa, Herdawatie Abdul Kadir and Radzi Ambar

Abstract Autonomous Underwater Vehicle (AUVs) are unmanned, self-propelled vehicles that are typically deployed from a surface vessel and can operate independently of that vessel for periods of a few hours to several days. This project discusses the development of an autonomous underwater vehicle (AUV) to detect an object underwater through a vision sensor. In this project, the horizontal motion of the AUV is controlled by two thrusters which are placed at the side of the AUV with the guidance of a digital magnetic compass to control the direction of the AUV. The vertical motion of the AUV is controlled by a thruster located in the middle of the AUV with the assistance of a depth sensor to ensure the AUV stays submerged underwater. A Pixy CMU cam5 is used as the vision sensor of the AUV with the function of detecting an object underwater through its specific colour code. When the sensor detects an object, the AUV automatically moves towards to the object without requiring any operator. The AUV is tested in a swimming pool to test its ability to stay submerged underwater as well as its functionality to navigate and detect object underwater. The simulation and experimental results show that the AUV able to operate and acquire targets successfully.

Keywords Autonomous underwater vehicle · Target acquisition · Vision sensor

1 Introduction

1.1 Project Background

Underwater exploration aims to discover the aspects of the sea floor for research and commercialised pursuits. Deep-sea exploration is slowly gaining attention among geophysicists in recent years compared to other fields of geophysical studies.

L. W. L. Alexander · K. Isa (✉) · H. A. Kadir · R. Ambar
Faculty of Electrical and Electronic Engineering, Universiti Tun Hussein Onn Malaysia, 86400
Parit Raja, Batu Pahat, Johor, Malaysia
e-mail: halid@uthm.edu.my

© Springer Nature Singapore Pte Ltd. 2019
Z. Md Zain et al. (eds.), *Proceedings of the 10th National Technical Seminar on Underwater System Technology 2018*, Lecture Notes in Electrical Engineering 538,
https://doi.org/10.1007/978-981-13-3708-6_7

Presently, only approximately 5% of the ocean has been discovered which opens up a gateway for further explorations.

Due to technology advancement, the equipment for deep-sea exploration has also increased such as high-resolution waterproof cameras, thermometers, depth sensors, and seismographs. These equipments are either lowered to the seabed through long cables or by attaching it directly to submersible buoys. The ocean currents can be studied by equipping ultrasonic sensors on floats to track their location from afar. Research vessels are equipped with cutting-edge navigational systems such as satellite navigation systems and global positioning systems, GPS which enables them to provide real-time data and location to the researchers [1].

Autonomous Underwater Vehicles (AUV), also known as unmanned underwater vehicles are fully automated robotic devices that navigate underwater without any interference from an operator. AUVs are used to carry out numerous underwater missions such as ocean floor mapping, underwater research, wreckage investigations and military applications. After completing its mission, the AUV automatically returns to its pre-programmed location with the data or samples it obtained for further analysis. There were more than 46 AUV models in 1999 [2, 3], and today there are approximately 200 operational AUVs, most of which are experimental [4] such as CETUS AUV [5], Xanthos AUV [6], Festo's AquaJelly AUV [7] and Evologics' Bionic Manta AUV [8].

Regarding the vision sensor, it utilises images captured by a camera to determine presence, orientation, and accuracy of parts. The principle of the vision sensor is called a colour model. The light receiving element is a colour type. Unlike the monochrome type, which identifies an intensity range between the extremes of white and black, the received light information is separated into three colours (RGB). Then, the intensity range of each of these colours is identified, which makes it possible to distinguish between targets even when their colours have minimal intensity differences [9].

Hence, the objective of this project is to develop an autonomous underwater vehicle that has a target acquisition function. The AUV has a cylindrical hull with an open body structure, three thrusters for manoeuvrability, microcontroller, compass, accelerometer for and Pixy CMU Cam5 as the vision sensors.

2 Methodology

2.1 Project Design

In order to design an AUV, the project process is classified into a few phases. The main stage focuses on the design concept of the AUV which covers mechanical and electrical design. The later stages can be described in two sections; the first section is the development of the mechanical. Thus, computer-aided software such as the SolidWorks and SketchUp software is used to draw and animate the AUV

that is proposed and expected. Another section is the development of the internal and external electrical design of the AUV. The last stage is closed with its testing, examination and a minor change of the task.

2.2 Hull Design

The AUV must contain a pressure hull to store its components in a dry and watertight environment. The hull should allow components to be easily accessible and maintainable, as well as allowing for modularity for future changes or additions. The hull should be light, strong and also be corrosive resistant due to the contact of the harsh saltwater environment. Spherical hulls offer the greatest structural integrity. However, the shape inhibits the efficient use of space available as most components and systems are rectangular. Cylindrical hulls are one of the best alternatives, comprising with high structural integrity and shape conducive to the housing of electronic components.

2.3 Submerging

The volume of a submersible vehicle is constant, and in order to dive deeper, the downward force acting upon it must be increased to counteract the buoyant force. This can be accomplished by increasing its mass using ballast tanks or by utilising external thrusters. Ballasting is the most common approach for submerging. This method is mostly mechanical in nature and involves using pumps and compressed air to take in and remove water. The usage of thrusters that point downwards is another alternative, although this system is much simpler, it is inefficient in terms of power consumption and not suitable for greater depths. AUVs are usually designed to have residual buoyancy where the weight of the vehicle is made to be more or less equal to the buoyant force.

2.4 Propulsion

Propulsion is required on all AUVs and is usually one of the main sources of power consumption. Most AUVs use motors for propulsion due to the scarcity and cost of alternative systems. The location of the motors affects which degree of freedom can be controlled and also affects the noise interference with on-board electronic components, as well as propeller-to-hull and propeller-to-propeller interactions. These interactions can have unwanted effects on the dynamics of an AUV. When travelling at a constant speed, the thrust produced by the motors is equal to the friction or drag of the vehicle, that is

$$\text{Thrust} = \text{Drag} = 0.5\rho s^2ACD \quad (1)$$

where ρ is the water density, s is the speed, A is the effective surface area, and CD is the drag coefficient. Power consumption for the propulsion system increases dramatically as the speed of the vehicle increases. This is due to the thrust power is equal to the product of the thrust and the speed, meaning that the thrust power is a function of speed cubed.

$$\text{Thrust Power} = \text{Thrust} \times s = 0.5 \rho s^2ACD \quad (2)$$

Therefore, an AUV has limited energy supply so it must travel at a speed that does not draw out too much power but at the same time does not take too long to complete its mission thus obtaining the ideal speed becomes an optimisation problem.

2.5 *Electrical Power*

Electric power is usually provided via sealed batteries. The ideal arrangement of batteries is to have them connected in parallel with diodes between each one to allow even discharge and to prevent current flow between batteries. Fuses or other protective devices should also be used to prevent excessive current flow in case of short circuits occurring or components malfunctioning. The restrictive nature of power on AUVs influences the types of components and equipment that can be utilized. Components and equipment should be chosen to draw as little power as possible to allow the batteries to provide more than enough time for the vehicle to complete its mission.

2.6 *System Design*

The AUV is made up of numerous numbers of electronic components, and the key components are the sensors, actuators and the control system. This section presents the general architecture of the AUV system. Figure 1 shows the general architecture diagram of the complete AUV system.

The sensors allow the AUV to perceive its surrounding environment. It plays a crucial role in providing accurate and detail information of the environment to the AUV. The sensors include an accelerometer, a compass, a pixy cam and a depth sensor. The accelerometer is used to measure proper acceleration, which is the acceleration it experiences relative to free fall and is the acceleration felt by people and objects. The compass is used to provide the direction for the AUV so that it can navigate underwater at a fixed angle. Pixy cam is a fast vision sensor which is widely used for DIY robotics. It is capable of tracking hundreds of objects simultaneously and only provides the data that we need. The depth sensor is used to provide information about the depth of the water to the AUV by detecting the pressure underwater.

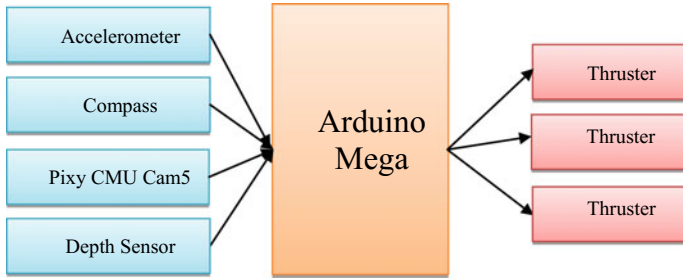


Fig. 1 The general architecture of the AUV system



Fig. 2 T100 thruster

2.7 Hardware Requirements

The actuators used for the AUV are the T100 thrusters from BlueRobotics as shown in Fig. 2. This thruster is a patent-pending underwater thruster designed specifically for marine robotics. It's high performing with over 5 lb of thrust and durable for usage in Open Ocean at great depths. The T100 is made of high-strength, UV resistant polycarbonate injection moulded plastic. The core of the motor is sealed and protected with an epoxy coating, and it uses high-performance plastic bearings in place of steel bearings that rust in salt water. Everything that isn't plastic is either aluminium or high-quality stainless steel that doesn't corrode.

The specially designed propeller and nozzle provide efficient, powerful thrust while active water-cooling helps cool the motor. Unlike other thrusters, this design doesn't have any air- or oil-filled cavities. Water flows freely through all parts of the motor while it's running and can handle extreme pressures. The thruster is easy to use and compatible with numerous embedded platforms. It also has a variety of mounting options, simple control, low price tag and a clockwise and counter-clockwise propeller to counter torque, making it a perfect choice as the actuator system for the AUV.

The control system that is utilised by the AUV is an Arduino Mega 2560 micro-controller. This microcontroller has 54 digital input/output pins, 16 analogue inputs,

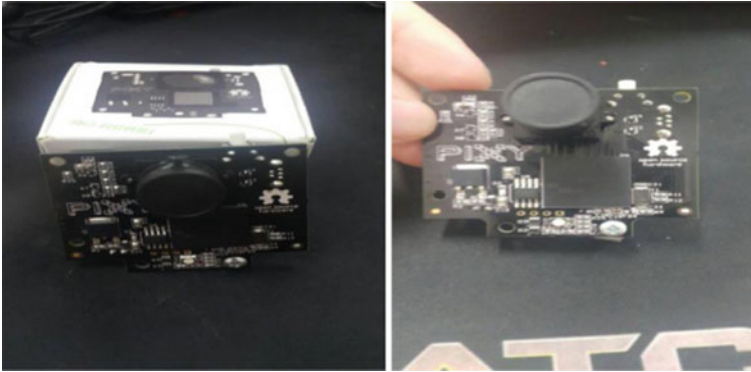


Fig. 3 Pixy CMUcam5

4 UARTs (hardware serial ports), a 16 MHz crystal oscillator, a USB connection, a power jack, an ICSP header, and a reset button. This microcontroller is easy to use and compatible with numerous electric components. The main purpose of this microcontroller is to control the thrusters, digital magnetic compass, accelerometer, depth sensor, echo sounder and Pixy CMUcam5.

The vision sensor that is used by the AUV is a Pixy CMUcam5. Pixy cam uses a hue-based colour filtering algorithm to detect objects. This Pixy calculates the hue and saturation of each RGB pixel from the image sensor and uses these as the primary filtering parameters. The hue of an object remains largely unchanged with changes in lighting and exposure. The changes in lighting and exposure can have a frustrating effect on colour filtering algorithms. Pixy addresses these problems by pairing a powerful dedicated processor with the image sensor. Pixy processes images from the image sensor and only sends the useful information to the microcontroller. The pixy is unique because it can be physically taught to sense anything that we want and very easy to use making it a perfect choice as the vision sensor for the AUV. Figure 3 shows the Pixy CMUcam5.

The AUV works on the principle of accelerometer ADXL335 which records the AUV movements and sends the data to the comparator which assigns proper voltage levels to the recorded movements. This accelerometer has a three-axis analogue accelerometer IC, which reads off the X, Y and Z acceleration as analogue voltages. By measuring the amount of acceleration due to gravity, the accelerometer can figure out the angle it is tilted at with respect to the earth. By sensing the amount of dynamic acceleration, the accelerometer can find out how fast and in what direction the device is moving. This accelerometer needs a 3–6 V dc supply voltage and can be interfaced with 3.3 V or 5 V microcontroller which works very well with the AUV's microcontroller.

The HMC6532 digital magnetic compass module is used to provide yaw or heading feedback. This small module delivers high accuracy and has low power consumption, interfacing with the Arduino Mega 2560 microcontroller via a dig-

ital input port. HMC6352 is a fully integrated compass module that combines 2-axis magneto-resistive sensors with the required analogue and digital support circuits, microprocessor and algorithms for heading computation. By combining the sensor elements, processing electronics, and firmware into a 6.5 mm by 6.5 mm by 1.5 mm LCC package. This digital magnetic compass only need low voltage operation (2.7–5.2 V).

3 Results and Analysis

3.1 AUV Prototype

The AUV is a box-shaped design which is designed according to the features needed for a passive stabilisation system. The mechanical system of the AUV is designed in a way that the centre of buoyancy (COB) is above the centre of gravity (COG). The body structure of the AUV is fully constructed with aluminium alloy strut. This metal is strong, light-weight, anti-rusting, corrosive resistant, and easily interchangeable elements in a variety of profile types. This metal can also be easily assembled and dissembled making it very convenient to modify in order to fit every component into the AUV. The metals are cut into 70 cm × 50 cm × 50 cm in length before assembling into its box-shaped design. The length of the metal should be precise as it affects the balance of the vehicle especially underwater.

After the body structure is completed, the underwater compartment is tested by submerging it in a bathtub for an hour in order to be assured that no leakage is present in the underwater compartment so that the electronic components always be in a dry condition when submerged underwater. As the leakage test was successful, all the thrusters and sensors are calibrated and tested for its functionality before installing them onto the AUV.

The thrusters are powered up by an external 11 V power supply and are connected to the AUV's control system in order to control the thrusters speed and direction. The thrusters are precisely mounted in the middle of the vehicle to prevent the AUV from being imbalance when submerged underwater. In order to give instructions to the AUV to submerge or float underwater, a depth sensor is used to fulfil this task. The depth sensor detects the depth of the water through its pressure sensor and sends the data to the control system. The control system gives instructions to the thrusters whether to submerge deeper or rise depending on the preset value.

The navigation system of the AUV is using an HMC6532 digital magnetic compass. The compass provides directional data to the microcontroller, and the AUV moves into the pre-set direction. An accelerometer is also tested in order to record the AUV movements and sends the data to the comparator which assigns proper voltage levels to the recorded movements. As for target acquisition, a pixy cmucam5 is utilised as the AUV's vision sensor while an echo sounder is used as the AUV's acoustic sensor. The pixy cam can detect an object-specific which makes it very

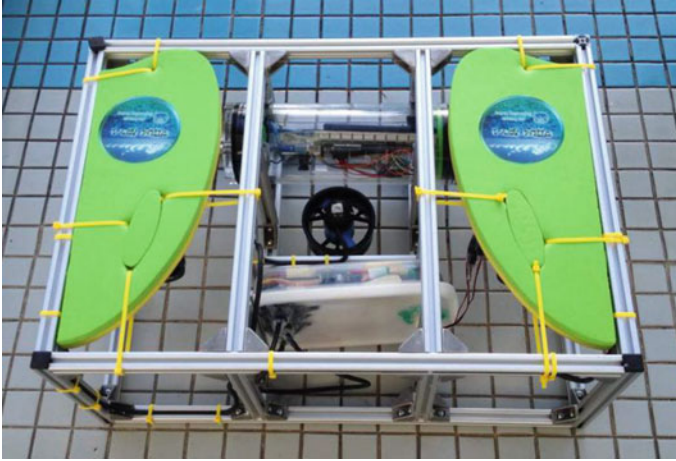


Fig. 4 The AUV prototype

suitable for underwater target acquisition. An echo sounder is an alternate method by sending pulses and hearing the echo from the pulse to detect the distance between an object with the AUV.

After all the calibration and testing is complete, the sensor instructions are compiled together and are uploaded into the microcontroller. All the electric components are to be placed into the underwater compartment, and the thrusters are mounted onto the AUV in order to test its overall functionality. Figure 4 shows the AUV prototype.

3.2 *Weight Distributions of the AUV*

Buoyancy also called as buoyancy force, is the force exerted on an object that is wholly or partially immersed in a fluid. Buoyancy is caused due to the differences in pressure acting on opposite sides of an object immersed in a static fluid. Archimedes' principle states that an upward buoyant force is exerted on a body immersed in a fluid, whether fully or partly submerged, is equal to the weight of the fluid that the body displaces and acts in the upward direction at the centre of mass of the displaced fluid. Table 1 shows the weight distribution of the AUV.

In order to calculate the buoyancy force, the following equations are used.

$$F_b = \rho V g \quad (3)$$

$$F_b = 1000 \text{ kg/m}^3 \times 112 \text{ m}^3 \times 9.81 \text{ N/kg} \quad (4)$$

$$F_b = 1,098,720 \text{ N} \quad (5)$$

Table 1 Weight distribution list of the AUV

List of items	Unit	Weight per unit (g)	Total weight (g)
Thruster	3	344	1032
Float	2	104	208
Underwater compartment	2	795	1590
Body of AUV	1	6600	6600
Total weight (g)			9430

The density of the AUV which is 2700 kg/m^3 is greater than the density of water which is only 1000 kg/m^3 while the buoyancy force, F_b that is obtained is a total of $1,098,720 \text{ N}$. In conclusion, the apparent weight of the AUV must be greater than the buoyancy force in order for the AUV to stay submerged underwater.

3.3 AUV Submerging and Leaking Test

After the AUV is completely assembled, a submerging test was carried out at the pond located in UTHM to test whether the AUV can stay fully submerged underwater for a period of time. The floats are added to the sides of the AUV in order to act as a floating mechanism for the AUV to reduce the buoyant force acted upon the AUV. Extra weights are also added to the AUV to act as sinking mechanism for the AUV to prevent the AUV from surfacing back to the water surface. Both mechanisms work together so that the AUV can stay afloat underwater.

The underwater compartments of the AUV play an important role as it is used to store the control system of the AUV. Since the control system of the AUV is not waterproof, thus it is very crucial to ensure that the control system of the AUV does not come in contact with the water. A leakage test is also carried out at the same time to ensure that no water can enter into the AUV's underwater compartments. Figure 5 shows how the submerging test was carried out.

3.4 Underwater Target Acquisition Test

Before implementing the vision sensor into the AUV, an underwater target acquisition test was carried out to ensure that the Pixy CMUcam5 was able to detect objects that are fully submerged underwater. Pixy cam uses a hue-based colour filtering algorithm to detect objects. The object needs to have a distinct hue for the pixy cam to detect it. Pixy cam can learn up to seven different types of colour signatures which include red, orange, yellow, green, cyan, blue and violet. By utilising a computer software

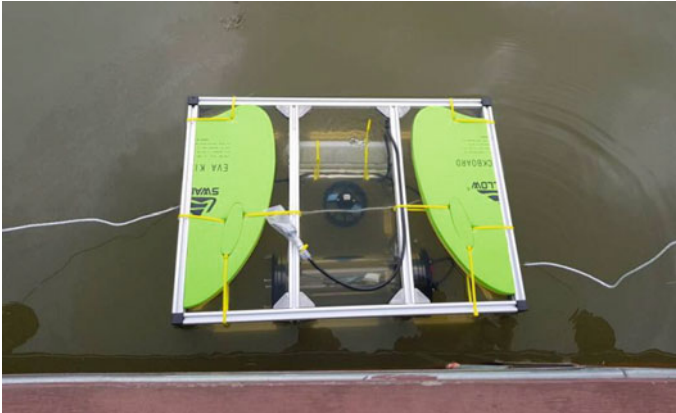


Fig. 5 Submerging and leaking test

called ‘Pixymon’, it is very easy and simple to teach the Pixy cam to detect an object and easier to control which pixel to choose for teaching.

Since the Pixy cam uses a hue-based colour filtering algorithm to detect objects, a green colour object is chosen to carry out this testing due to its distinct hue. Black, white and grey objects are considered as bad objects to be detected by the Pixy cam because those colours have no hue, or the hue is not distinct. Based on the results shown in Fig. 6, it is clearly shown that the Pixy cam is still able to successfully detect the green object, even though it has been fully submerged underwater.

3.5 Experimental Results

Figure 7 shows that the AUV was experimentally tested in a swimming pool. The AUV consist of three thrusters, two thrusters are used for horizontal motion, and one thruster is utilised for vertical motion. The AUV has two compartments which are used to store all its electronic components to prevent them from getting wet. The front compartment is utilised to store all the sensors of the AUV such as an accelerometer, digital magnetic compass, depth sensor, Pixy cam, and echo-sounder while the back compartment is used to store the speed controllers and power supply for the thrusters. The floats and weights were used to provide enough buoyancy force for the AUV so that it can stay afloat while being fully submerged underwater. The underwater compartments of the AUV are reinforced with Teflon tape and epoxy to ensure that no water can go into the compartment to avoid the components from coming into contact with water which cause a short circuit to the whole circuitry. Plasticine was also used to seal off all the openings of the compartment as an added reinforcement.

When the power supply is switched on, the depth sensor and the compass start to gather data and send the data back to the Arduino. If the data obtained from the

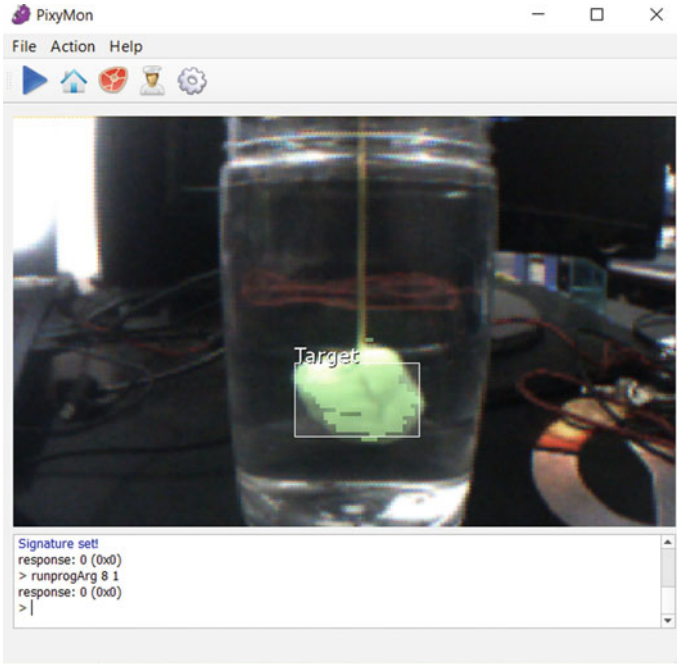


Fig. 6 Pixy CMU Cam5 target acquisition

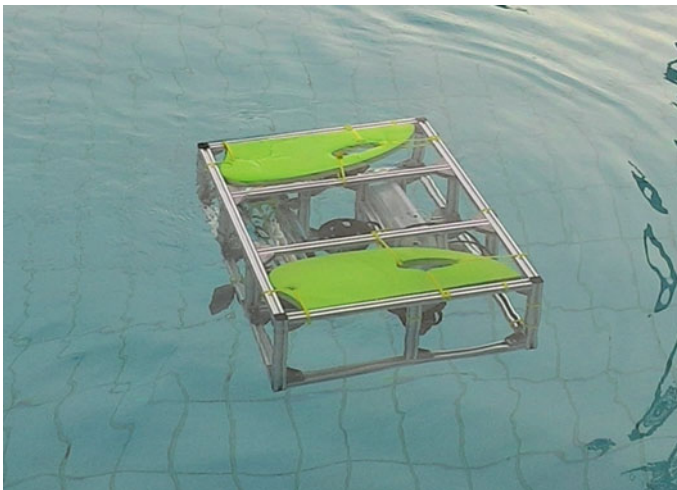


Fig. 7 An experimental test in a swimming pool

compass is higher than the value that was pre-programmed into the Arduino, the right thruster will be switched on for 0.5 s. If the data obtained from the compass is lower

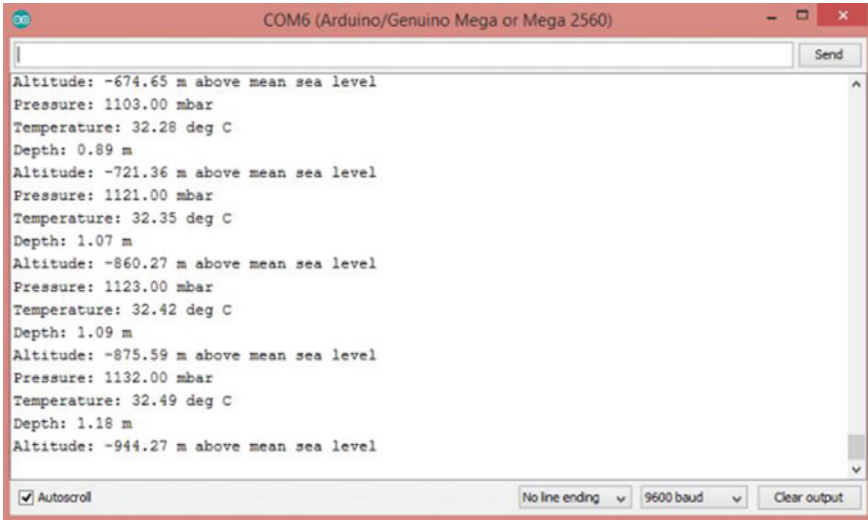


Fig. 8 Depth sensor data

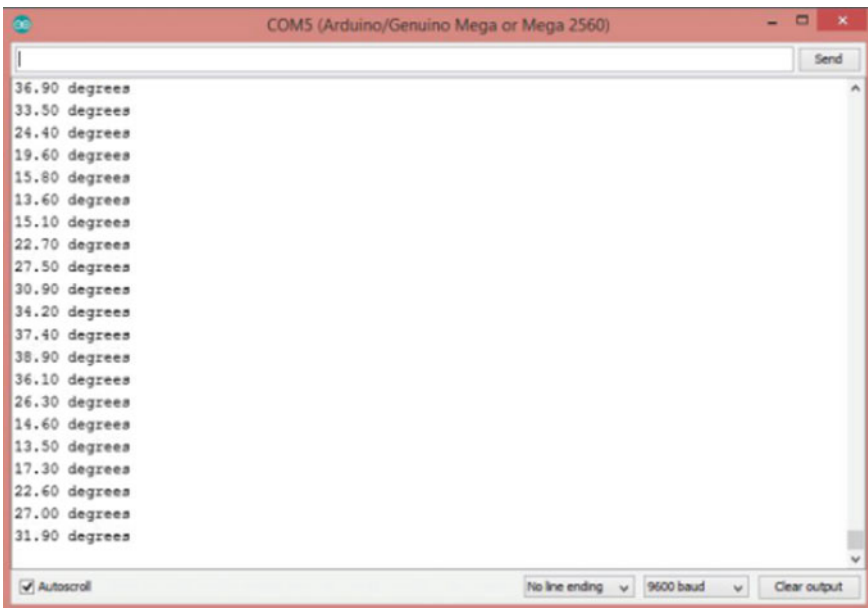


Fig. 9 Digital magnetic compass data

than the pre-programmed value, the left thruster of the AUV will be switched on for 0.5 s. When the data obtained from the compass is equal to the pre-programmed value, both of the thrusters remain stationary. By implementing this navigation system, the

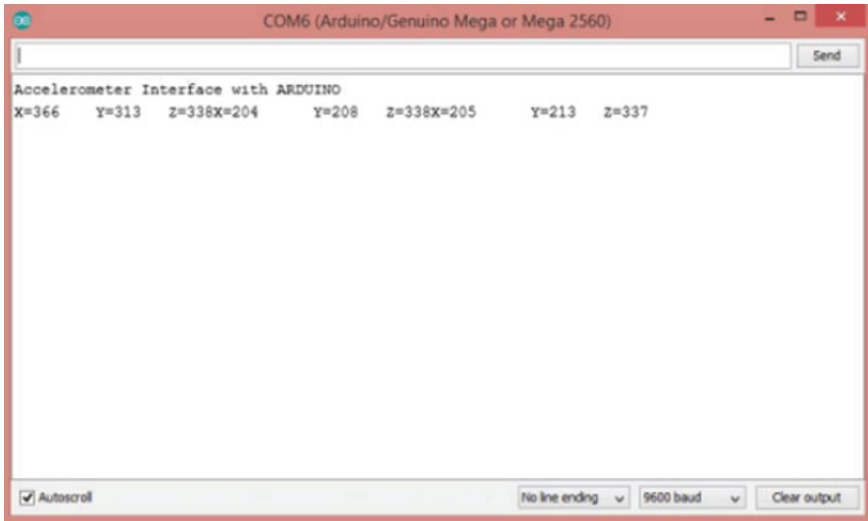


Fig. 10 Accelerometer data

direction of the AUV can be controlled automatically as the horizontal thrusters readjust the AUV to return to its instructed direction.

The depth sensor works similarly to the compass. If the data obtained from the depth sensor is higher than the pre-programmed value, the middle thruster rotates anti-clockwise for 1 s which thrusts the AUV to go deeper underwater. If the data obtained from the depth sensor is lower than the pre-programmed value, the middle thruster rotates clockwise for 1 s which provides an upward force for the AUV to be nearer to the water surface. When the data obtained from the depth sensor is equal to the pre-programmed value, the middle thruster remains stationary. By implementing this system, the AUV constantly stay afloat underwater while be prevented from surfacing on the surface and also from hitting the bottom of the pool.

The target acquisition of the AUV is separated into two different methods which are through vision and acoustic. For the acoustic part, an echo-sounder is placed in front of the AUV. The echo-sounder is used to detect the distance between an object with the AUV by emitting a pulse and hearing it back after being reflected by the object. For the vision part, a Pixy CMU cam5 places in front of the AUV to detect an object through its specific colour code. When both sensors manage to detect an object underwater, the AUV move towards to the object.

Figure 8 shows the data that were obtained from the depth sensor. The depth sensor not only can detect the depth of the water, but also can detect the temperature of the water and the altitude above sea level. The most important data is the depth detected by the sensor because the instruction for the AUV to submerge or rise is based on the depth of the water. Figure 9 shows the data from the digital magnetic compass. The digital magnetic compass provides us with directional data which is used to navigate the AUV in a certain direction while the accelerometer is used to

measure acceleration forces in order to sense movement or vibrations of the AUV. Figure 10 shows the data from the accelerometer.

4 Conclusion

After testing out the AUV in a swimming pool, it can be summarized that the AUV is able to carry out its given task without requiring the interference of an operator. As the pixy cam detects an object underwater, the AUV head towards the object as instructed beforehand. In conclusion, the objective of the project is to design and develop a functional autonomous underwater vehicle, which performs the task given at a prescribed time, is achieved and the experimental results are satisfactory.

References

1. Funk & Wagnails, Deep-sea Exploration. [https://web.archive.org/web/20090501194025, http://www.history.com/](https://web.archive.org/web/20090501194025/http://www.history.com/). Last accessed 2017/11/1
2. Budiyo, A.: Advances in unmanned underwater vehicles technologies: modeling, control and guidance perspective. *Indian J. Geo-Mar. Sci.* **38**(3), 282–295 (2009)
3. Yuh, J.: Design and control of autonomous underwater robots: a survey. *Auton. Robots* **8**(1), 7–24 (2000)
4. Antonelli, G., Fossen, T., Yoerger, D.: Underwater robotics. In: Siciliano, B., Khatib, O. (eds.). *In: Springer Handbook of Robotics SE*, vol. 44, pp. 987–1008. Springer, Heidelberg (2008)
5. MIT Sea Grant College Program: AUV Laboratory at MIT Sea Grant: CETUS. <http://auvlab.mit.edu/vehicles/vehiclespecCETUS.html> (2007)
6. MIT Sea Grant College Program: AUV Laboratory at MIT Sea Grant: CETUS. <http://auvlab.mit.edu/vehicles/vehiclespec2x.html> (2007)
7. Festo: AquaJellies 2.0. Retrieved on 2 Nov 2017 at <https://www.festo.com/group/en/cms/10227.htm> (2014)
8. Evologics: BOSS Project-Manta Ray AUV with Fin Ray Effect. <https://www.evologics.de/en/products> (2013). Last accessed 2017/11/3
9. Keyence: What is Vision Sensors? <https://www.keyence.com/ss/products/sensor>. Last accessed 2017/11/11

Robust Controller Design for Autonomous Underwater Glider Using Backstepping Super Twisting Sliding Mode Control Algorithm



Maziyah Mat Noh, M. R. Arshad, Rosmiwati Mohd-Mokhtar,
Zainah Md Zain, Qudrat Khan and Herdawati Abdul Kadir

Abstract This paper proposes the design methodology of the backstepping super twisting sliding mode control algorithm. The proposed controller algorithm is designed to improve the tracking performance of the original super twisting sliding mode. The controller is designed for trajectory tracking problem in existence of external disturbance and parameter variations. The controller is designed for the gliding path from 25° downward to 25° upward. The performance of the proposed controller is compared to original super-twisting algorithm. The simulation results have shown that the proposed controller has improved the performance and the undesired chattering in control input and sliding surface has been reduced.

Keywords Autonomous underwater glider (AUG) · Backstepping
Super twisting sliding mode control · Chattering reduction

M. Mat Noh (✉) · Z. Md Zain

Instrumentation and Control Engineering (ICE) Cluster, Faculty of Electrical and Electronics Engineering, Universiti Malaysia Pahang, 26600 Pekan, Pahang, Malaysia
e-mail: maziyah@ump.edu.my

M. Mat Noh · M. R. Arshad · R. Mohd-Mokhtar

Underwater, Control Robotics Research Group (UCRG), School of Electrical and Electronic Engineering, Engineering Campus, Universiti Sains Malaysia, 14300 Nibong Tebal, Pulau Pinang, Malaysia

Q. Khan

Center for Advanced Studies in Telecommunications, CIIT, Park Road, Chak Shahzad, Islamabad 44000, Pakistan

H. Abdul Kadir

Faculty of Electrical and Electronic Engineering, Universiti Tun Hussein Onn Malaysia, 84600 Parit Raja, Batu Pahat, Johor, Malaysia

© Springer Nature Singapore Pte Ltd. 2019

Z. Md Zain et al. (eds.), *Proceedings of the 10th National Technical Seminar*

Underwater System Technology 2018, Lecture Notes in Electrical Engineering 538,

https://doi.org/10.1007/978-981-13-3708-6_8

1 Introduction

Ocean covers almost 70% of earth surface and therefore has a great effect on the future existence of all human beings, beside the land and aerospace and also offers great research opportunities. Underwater vehicle is divided into three main categories that are manned submersible, remotely operated vehicles (ROVs) and autonomous underwater vehicles (AUVs). Autonomous underwater glider (AUG) is considered as a special class of AUVs.

The AUG was inspired by Stommel in 1989 [1]. The Henry's idea was realized after more than a decade later when Slocum [2], Spray [3] and Seaglider [4] gliders were successfully designed, developed and tested in 2001. These three gliders are known as legacy gliders and being used by many agencies and research centers for oceanography data collection [5, 6]. The laboratory scale gliders also being developed by many research centers for research purposes such as robotic gliding fish (Michigan State University) [7], USM glider [8] (University of Science, Malaysia), FOLAGA [9] (IMEDEA, ISME and University of Genova, Italy) ALEX [10] (Osaka Prefecture University) and ROGUE [11] (University of Princeton).

The glider dives through the water column using its internal masses and pumping of the ballast. The internal masses are moved translational or/and cylindrical depending on the design track which is located inside the glider's hull.

The glider is categorized as multi-input-multi-output nonlinear system. Many issues related to AUG such as AUG is underactuated system, is highly nonlinear, time-varying dynamic behaviour in nature, uncertainties in hydrodynamic coefficients, and also disturbances by ocean currents [12]. Some control methods were proposed for the motion control of the AUG. Ullah et al. in [13] reviewed the control methods used for AUG. The review covers the control methods ranging from proportional-integral-derivative (PID), linear quadratic regulator (LQR) up to neural network and fuzzy logic. The PID controller was proposed in [14, 15]. The PID is the most popular used due to its simple architecture and less tuning parameters. The LQR was proposed in [11, 16–18]. The LQR use simple architecture where only two tuning parameters need to be varied to achieve the desired performance. Both PID and LQR provide good performance. Nonetheless, since the model is linearized about the equilibrium point, therefore the performance of the controller only effective in a small neighbourhood of the equilibrium.

The model predictive control (MPC) was proposed in [19, 20]. In [19] the MPC was designed to control the attitude of Slocum glider. The control architecture was divided into higher-level and lower-level controllers for controlling the internal configurations of the glider and was made the actuator to execute actions for maintaining the imposed internal configurations. The MPC was used in [21] in conjunction with the path-following technique for online tuning of the desired vehicle velocity along with the trajectory and thus validated the 3D motion dynamics of the Slocum glider. Shan and Zheng in [20] designed the MPC using one-layer recurrent neural network to improve the computational problem in MPC to control the longitudinal of AUG.

The sliding mode control (SMC) is another technique used in [22, 23]. The boundary layer SMC was proposed in [22] and [24] for 1 degree of freedom (DOF) and 2 DOF internal movable sliding mass respectively. The Taylor's series expansion method is used in obtaining the linearized model of AUG. Yang and Ma in [25] and [26] proposed the SMC for nonlinear system of longitudinal plane of AUG. The reaching law is designed based on rapid-smooth reaching law. In [26] the performance of [25] is improved using inverse system method where the output equations are differentiated repeatedly until the input are appeared in the equations, then the control laws are designed based on that equations. Mat-Noh et al. in [23] proposed SMC to control the pitching and the net buoyancy of the longitudinal plane system. The control law is designed based on super twisting sliding mode control (STSMC). The standard STSMC composed only discontinuous part, however in [23] the control law consists of equivalent and discontinuous parts. The intelligent technique was proposed in [27]. The neural network is used to control the horizontal and vertical plane of the AUG. The controller was designed based on the linearized model.

The aim of this paper is to propose the nonlinear robust controller with integration of backstepping and super twisting sliding mode control strategies which will be applied to AUG system. The new control strategy is hoped to improve the performance of the tested system. The integration of these two control strategies is considered new with regards to controlling the longitudinal plane of AUG system application and that will be the contribution for this paper. Furthermore, the performance of the proposed controller will be compared to the performance of super twisting SMC (STSMC) strategy only.

This paper is organised as follows. In dynamic model section discusses the mathematical model of the longitudinal plane of the AUG. The detail derivation of control for the proposed controller and STSMC is discussed in Section controller design. The results are discussed in Section results and discussion. Finally the paper is summarised in Section conclusion.

2 AUG Dynamic System

This section presents the dynamic of the AUG system. The dynamic model of the glider is adopted from Graver's work. The detail derivation can be found in [11] and [5]. The model is obtained for longitudinal plane. The internal movable mass is moved along x-axis and the ballast is pumped back and forth to control the motion of the glider. The rudder is fixed to stabilize the straight longitudinal plane of the glider. Table 1 gives the parameter of glider used in this paper.

The desired path, ξ_d and desired speed V_d are used to specify the glide path.

$$\xi = \theta - \alpha \quad (1)$$

where θ = pitching angle, α = angle of attack.

Table 1 Glider parameter definition

Parameter	Definition
θ	Pitching angle
ω_2	Pitching rate
v_1	Surge velocity
v_3	Heave velocity
r_{p1}	Internal movable mass position in x-axis
\dot{r}_{p1}	Internal movable mass velocity
m_b	Ballast mass

$$V = \sqrt{v_1^2 + v_3^2} \quad (2)$$

(x', z') are the initial coordinates where x' is positioned along the desired path and is defined as

$$\begin{pmatrix} x' \\ z' \end{pmatrix} = \begin{pmatrix} \cos\xi_d & -\sin\xi_d \\ \sin\xi_d & \cos\xi_d \end{pmatrix} \begin{pmatrix} x \\ z \end{pmatrix} \quad (3)$$

z' measures the position of the vehicle in the direction perpendicular to the desired path. The dynamics of the z' is given in Eq. (4)

$$\dot{z}' = \sin\xi_d \dot{x} + \cos\xi_d \dot{z} \quad (4)$$

In this paper the internal movable mass only moves along the x-axis. Thus the original dynamic equations in [11] are rewritten with r_{p3} is fixed at one position. The motion equations are rewritten in Eqs. (5)–(11)

$$\dot{\theta} = \omega_2 \quad (5)$$

$$\begin{aligned} \dot{\omega}_2 = \frac{1}{a} \{ & (m_p + m_1)(m_p + m_3)Y - \} m_p m_3 (m_p + m_1) r_{p1} \dot{r}_{p1} \omega_2 \\ & - m_p (m_p + m_3) r_{p3} X_1 + m_p (m_p + m_1) r_{p1} X_3 \\ & - m_p m_1 (m_p + m_3) r_{p3} u_1 \} \end{aligned} \quad (6)$$

$$\begin{aligned} \dot{v}_1 = \frac{1}{a} \{ & -m_p (m_p + m_3) r_{p3} Y - m_p^2 m_3 r_{p1} r_{p3} \dot{r}_{p1} \omega_2 + m_p [J_2 (m_p + m_3) \\ & + m_p m_3 r_{p1}^2 + m_p (m_p + m_3) r_{p3}^2] X_1 - m_p^2 r_{p1} r_{p3} X_3 \\ & - m_p [J_2 (m_p + m_3) + m_p m_3 r_{p1}^2] u_1 \} \end{aligned} \quad (7)$$

$$\begin{aligned} \dot{v}_3 = & \frac{1}{a} \{ m_p [J_2(m_p + m_1) + m_p m_1 r_{p3}^2] r_{p1} \omega_2 - m_p^2 r_{p1} r_{p3} X_1 \\ & + [J_2(m_p + m_1) r_{p1}^2 + m_p m_1 r_{p3}^2] X_3 \\ & - m_p^2 r_{p1} r_{p3} X_3 - m_p^2 m_1 r_{p1} r_{p3} u_1 \} \end{aligned} \quad (8)$$

$$\dot{r}_{p1} = \dot{r}_{p1} \quad (9)$$

$$\ddot{r}_{p1} = u_1 \quad (10)$$

$$\dot{m}_b = u_b \quad (11)$$

where

$$a = J_2(m_p + m_1)(m_p + m_3) + m_p m_3(m_p + m_1) r_{p1}^2 + m_p m_1(m_p + m_3) r_{p3} \quad (12)$$

$$X_1 = -m_3 v_3 \omega_2 - P_{p3} \omega_2 - m_{em} g \sin \theta + L \sin \alpha - D \cos \alpha \quad (13)$$

$$X_3 = m_1 v_1 \omega_2 + P_{p1} \omega_2 + m_{em} g \cos \theta - L \cos \alpha - D \sin \alpha \quad (14)$$

$$\begin{aligned} Y = & (m_{f3} - m_{f1}) v_1 v_3 - [r_{p1} P_{p1} + r_{p3} m_p (v_3 - r_{p1} \omega_2) \omega_2] \\ & - m_p g (r_{p1} \cos \theta + r_{p3} \sin \theta) + M_{DL2} \end{aligned} \quad (15)$$

$$P_{p1} = m_p (v_3 - r_{p3} \omega_2) \quad (16)$$

$$P_{p3} = m_p (v_3 - r_{p1} \omega_2) \quad (17)$$

where m_{em} is the net buoyancy, m_{f1} , and m_{f3} are the added masses, D , L , and M_{DL2} represent the drag, lift and viscous moment of the hydrodynamic force and moment as defined in [11] as

$$m_{em} = m_h + m_p + m_b - m_{df} \quad (18)$$

$$L = (K_{LO} + K_L \alpha) (v_1^2 + v_3^2) \quad (19)$$

$$D = (K_{DO} + K_L \alpha^2) (v_1^2 + v_3^2) \quad (20)$$

$$M_{DL2} = (K_{MO} + K_M \alpha) (v_1^2 + v_3^2) + K_{\omega_1} \omega_2 + K_{\omega_2} \omega_2^2 \quad (21)$$

where m_h , m_p , and m_{df} are the hull mass, internal movable mass, and displaced fluid mass. α is the angle of attack. K_L , K_{LO} , K_D , K_{DO} , K_M , and K_{MO} are the hydrodynamics lift, drag and pitching moment coefficients. K_{ω_1} , and K_{ω_2} are the linear and quadratic damping constant coefficients. The state and input vectors are written in Eqs. (22) and (23) respectively.

$$\begin{aligned} x = & [x_1 \ x_2 \ x_3 \ x_4 \ x_5 \ x_6 \ x_7]^T \\ = & [\theta \ \omega_2 \ v_1 \ v_3 \ r_{p1} \ \dot{r}_{p1} \ m_b]^T \end{aligned} \quad (22)$$

$$u = [u_1 \ u_b]^T \quad (23)$$

Since the AUG system is under-actuated system, therefore in this study only two parameters are considered that are pitching angle, θ and net buoyancy, m_{em} as written in Eqs. (24)–(25). The net buoyancy is indirectly obtained through the ballast mass, m_b .

$$y_1 = x_1 = \theta \quad (24)$$

$$y_2 = m_{em} = m_h + m_p + m_b - m_{df} \quad (25)$$

3 Controller Design

This section presents design methodology of the controller. The proposed controller is designed based on backstepping and super twisting SMC (STSMC) control strategies. Two controllers are designed and simulated that are the proposed controller and STSMC for the gliding path from 25° downward to 25° upward. The motion equations in Eqs. (5)–(11) are rewritten in the general form of nonlinear equation as given in Eqs. (26) and (27):

$$\dot{x} = f(x, t) + g(x, t)u + \delta(x, t) \quad (26)$$

$$y = b(x, t) \quad (27)$$

where, $x \in R^n$, $u \in R^m$ and $b \in R^p$ be the state, and input vectors, $\delta(x, t)$ represents the bounded matched perturbations and $\delta(x, t)$ is bounded with a known norm upper bound.

$$|\delta(x, t)| \leq |\rho(x, t)| \quad (28)$$

For simplicity, following assumptions are made:

Assumption 1 Consider the system in Eq. (26) is rewritten in n-th order system and in the form that is suitable for controller algorithms as written in Eq. (29)

$$\dot{x}_1 = x_2$$

$$\dot{x}_2 = x_3$$

$$\vdots$$

$$\begin{aligned} \dot{x}_k &= \varphi_k(x, t) + g_k(x, t)u_i + \delta_k(x, t) \\ &= \chi_k(x, u_i, t) + u_i + \delta_k(x, t) \end{aligned} \quad (29)$$

where $\chi_k(x, u_i, t) = f_k(x, t) + (g_k(x, t) - 1)u_i$, $k = 1, 2, 3, \dots, n$, and $i = 1, 2, 3, \dots, p$. Equation (29) is known as General Global Controller Canonical Form

(GGCCF) as explained in [28]. The nominal system or the system without perturbation is defined when $\delta_k(x, t) = 0$.

Assumption 2 The system in Eq. (29) is minimum phase when zero dynamic $\chi_k(0, u_i, t) = 0$ is uniformly asymptotically stable.

The design of the controller is divided into two subsystems that are pitching control subsystem and net buoyancy subsystem as written in Eqs. (30) and (31) respectively.

$$\dot{x}_1 = x_2$$

$$\dot{x}_2 = f_2(x, t) - g_2(x, t)u_1 - g_2(x, t)\delta_2(x, t) \quad (30)$$

$$\dot{x}_7 = u_2 + \delta_7(x, t) \quad (31)$$

The controllers are designed for the tracking problems. The errors of outputs are defined in Eqs. (32) and (33).

$$e_1 = x_1 - x_{1d} \quad (32)$$

$$e_2 = x_7 - x_{7d} \quad (33)$$

3.1 Design of Super Twisting Algorithm (STSMC)

The super twisting sliding mode control (STSMC) is considered as second order sliding mode control (SOSMC). The STSMC was proposed by A. Levant in 1993 [29]. The STSMC is a good alternative for the researchers to avoid chattering phenomena in conventional SMC. The typical STSMC trajectory is shown in Fig. 1.

The control law of STSMC only contain the discontinuous part and is free from plant parameter therefore it is called model free sliding mode control. However in this paper the STSMC is designed based on conventional SMC where equivalent is derived from and the STSMC is employed in discontinuous control. The control law for tracking the pitching angle and the net buoyancy are written in Eqs. (34) and (35), respectively.

$$u_1 = u_{1eq} + u_{1STSMC} \quad (34)$$

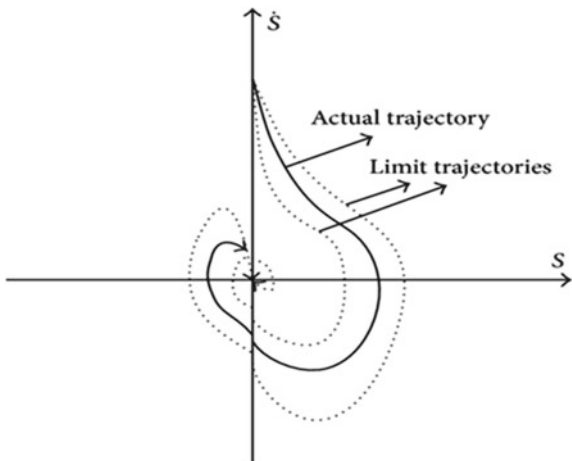
$$u_2 = u_{2eq} + u_{2STSMC} \quad (35)$$

The sliding surfaces and their derivatives for tracking pitching angle, and the net buoyancy are defined in Eqs. (36)–(39) respectively.

$$s_1 = c_1 e_1 + \dot{e}_1 \quad (36)$$

$$s_2 = e_2 \quad (37)$$

Fig. 1 The trajectory of super-twisting algorithm on phase plane



and

$$\dot{s}_1 = c_1 \dot{e}_1 + \ddot{e}_1 \quad (38)$$

$$\dot{s}_2 = \dot{e}_2 \quad (39)$$

The equivalent control laws are defined as $\dot{s}_1 = 0$, and $\dot{s}_2 = 0$

$$u_{1eq} = \frac{1}{g_2} \{ f_2 + g_2 \delta_2(x, t) + c_1 \dot{e}_1 - \ddot{x}_{1d} \} \quad (40)$$

$$u_{2eq} = -\delta_7(x, t) \quad (41)$$

The reachability conditions are chosen as super-twisting SMC given as

$$u_{1dis} = -\beta_{11} |s_1|^p \text{sign}(s_1) - \beta_{12} \int_0^t \text{sign}(s_1) dt \quad (42)$$

$$u_{2dis} = -\beta_{21} |s_2|^p \text{sign}(s_2) - \beta_{22} \int_0^t \text{sign}(s_2) dt \quad (43)$$

Finally the control laws are written as in Eqs. (44) and (45).

$$u_1 = \frac{1}{g_2} \{ f_2 + g_2 \delta_2 + c_1 \dot{e}_1 - \ddot{x}_{1d} \} - \beta_{11} |s_1|^p \text{sign}(s_1) - \beta_{12} \int_0^t \text{sign}(s_1) dt \quad (44)$$

$$u_2 = -\delta_7(x, t) - \beta_{21}|s_2|^p \text{sign}(s_2) - \beta_{22} \int_0^t \text{sign}(s_2) dt \quad (45)$$

where $u_1 = u_{1eq} + u_{1dis}$ and $u_2 = u_{2eq} + u_{2dis}$.

3.2 Design of Backstepping Super Twisting Sliding Mode Control (BSTSMC)

This section presents the design formulation of the proposed controller. The backstepping super twisting sliding mode control (BSTSMC) is designed based on integration of backstepping and super twisting sliding mode control (STSMC). The algorithm employed the backstepping control strategy to design the sliding surface and super twisting is used for reachability condition. The design procedure is shown in the following steps.

Step 1: Define the tracking error of x_1 and its time derivative

$$e_1 = x_1 - x_{1d} \quad (46)$$

$$\dot{e}_1 = \dot{x}_1 - \dot{x}_{1d} = x_2 - \dot{x}_{1d} \quad (47)$$

Define the Lyapunov function and its time derivative as

$$V_1(e_1) = \frac{1}{2}e_1^2 \quad (48)$$

$$\dot{V}_1(e_1) = e_1 = e_1(x_2 - \dot{x}_{1d}) \quad (49)$$

x_2 is viewed as a virtual control. The desired virtual control known as stabilizing function then is defined as

$$\alpha_1 = -K_{11}e_1 + \dot{x}_{1d} \quad (50)$$

where K_{11} is a positive constant. Thus Eq. (49) become

$$\dot{V}_1 = e_1(-K_{11}e_1 + \dot{x}_{1d} - \dot{x}_{1d}) = -K_{11}e_1^2 < 0 \quad (51)$$

Step 2: Sliding surface is defined as second error variable as in Eq. (52)

$$s_1 = x_2 - \alpha_1 \quad (52)$$

Rearrange Eq. (52)

$$x_2 = s_1 + \alpha_1 \quad (53)$$

and the dynamic of the sliding surface is written as in Eq. (54) along with Eq. (30).

$$\dot{s}_1 = \dot{x}_2 - \dot{\alpha}_1 = f_2(x, t) - g_2(x, t)u_1 + g_2(x, t)\delta_2(x, t) + K_{11}\dot{e}_1 - \ddot{x}_{1d} \quad (54)$$

The Lyapunov function and its time derivative are now defined as

$$V(e_1, s_1) = \frac{1}{2}(e_1^2 + s_1^2) \quad (55)$$

and

$$\begin{aligned} \dot{V}(e_1, s_1) &= e_1\dot{e}_1 + s_1\dot{s}_1 \\ \dot{V}(e_1, s_1) &= e_1(s_1 - K_{11}e_1 + \dot{x}_{1d} - \dot{x}_{1d}) \\ &\quad + s_1\{f_2(x, t) - g_2(x, t)u_1 + g_2(x, t)\delta_2(x, t) + K_{11}\dot{e}_1 - \ddot{x}_{1d}\} \\ \dot{V}(e_1, s_1) &= -K_{11}e_1^2 + s_1\{f_2(x, t) - g_2(x, t)u_1 + g_2(x, t)\delta_2(x, t) + e_1 + K_{11}\dot{e}_1 - \ddot{x}_{1d}\} \end{aligned}$$

The equivalent control is determined when $\dot{s}_1 = 0$ as given in Eq. (56)

$$u_{1eq} = \frac{1}{g_2}\{f_2(x, t) + g_2(x, t)\delta_2(x, t) + e_1 + K_{11}\dot{e}_1 + K_{12}s_1 - \ddot{x}_{1d}\} \quad (56)$$

Step 3: The sliding surface for subsystem in Eq. (31) is designed based on error as define in Eq. (57).

$$s_2 = e_2 = x_7 - x_{7d} \quad (57)$$

The time derivative of sliding surface is written as

$$\dot{s}_2 = \dot{e}_2 = \dot{x}_7 - \dot{x}_{7d} = u_2 - \dot{x}_{7d} + \delta_7(x, t) \quad (58)$$

The Lyapunov function and its time derivative are defined as

$$V(s_2) = \frac{1}{2}s_2^2 \quad (59)$$

and

$$\dot{V}(s_2) = s_2\dot{s}_2 = s_2(u_2 - \dot{x}_{7d} + \delta_7(x, t)) \quad (60)$$

The equivalent control is determined when $\dot{s}_2 = 0$ as given in Eq. (61)

$$u_{2eq} = -(K_{21}s_2 + \delta_7(x, t) - \dot{x}_{7d}) \quad (61)$$

Step 4: The reachability conditions of BSTSMC are defined based on super twisting SMC are written in Eqs. (62) and (63).

$$u_{1dis} = -\beta_{11}|s_1|^p \text{sign}(s_1) - \beta_{12} \int_0^t \text{sign}(s_1) dt \quad (62)$$

$$u_{2dis} = -\beta_{21}|s_2|^p \text{sign}(s_2) - \beta_{22} \int_0^t \text{sign}(s_2) dt \quad (63)$$

Finally the control laws of BSTSMC are written as Eqs. (64) and (65).

$$\begin{aligned} u_{1BSTSMC} &= u_{1eq} + u_{1dis} \\ u_{1BSTSMC} &= \frac{1}{g_2} \{ f_2(x, t) + g_2(x, t) \delta_2(x, t) + e_1 + K_{11} \dot{e}_1 + K_{12} s_1 - \ddot{x}_{1d} \} \\ &\quad - \beta_{11}|s_1|^p \text{sign}(s_1) - \beta_{12} \int_0^t \text{sign}(s_1) dt \end{aligned} \quad (64)$$

$$\begin{aligned} u_{2BSTSMC} &= u_{2eq} + u_{2dis} \\ u_{2BSTSMC} &= -(K_{21} s_2 + \delta_7(x, t) - \dot{x}_{7d}) - \beta_{21}|s_2|^p \text{sign}(s_2) - \beta_{22} \int_0^t \text{sign}(s_2) dt \end{aligned} \quad (65)$$

3.3 Stability Analysis

The stability analysis is important to ensure the convergence of the controlled parameters of the plant stabilize at the desired. This is ensured when the sliding mode is ensured. In this paper Lyapunov stability theorem is used for stability analysis as explained in the following.

Theorem Consider the nonlinear systems in Eqs. (30) and (31) subjected to bounded uncertainty in Eq. (28) with assumptions 1 and 2. If the sliding manifolds (s_1, s_2) as written in Eqs. (52) and (57), and the discontinuous controls (u_{1dis}, u_{2dis}) as written in Eqs. (62) and (63), then the convergence conditions are satisfied.

Proof Consider the Lyapunov functions in Eqs. (66), and (67)

$$V_1(e_1, s_1) = \frac{1}{2}(e_1^2 + s_1^2) \quad (66)$$

$$V_2(s_2) = \frac{1}{2}s_2^2 \quad (67)$$

The time derivative of the Lyapunov functions along with Eqs. (47), (54), and (58), yields

$$\begin{aligned}\dot{V}_1(e_1, s_1) &= e_1 \dot{e}_1 + s_1 \dot{s}_1 \\ &= e_1(x_2 - \dot{x}_{1d}) + s_1\{f_2(x, t) - g_2(x, t)u_1 + g_2(x, t)\delta_2(x, t) + K_{11}\dot{e}_1 - \ddot{x}_{1d}\} \\ &= e_1(s_1 - K_{11}e_1) + s_1\{f_2(x, t) - g_2(x, t)u_1 + g_2(x, t)\delta_2(x, t) + K_{11}\dot{e}_1 - \ddot{x}_{1d}\}\end{aligned}\quad (68)$$

$$\begin{aligned}\dot{V}_2(s_2) &= s_2 \dot{s}_2 \\ \dot{V}_2(s_2) &= u_2 - \dot{x}_{7d} + \delta_7(x, t)\end{aligned}\quad (69)$$

Substitute Eq. (64) into Eq. (68), and Eq. (65) into Eq. (69). For stability

$$\begin{aligned}\dot{V}_1(e_1, s_1) &\leq e_1(-K_{11}e_1) \\ &+ s_1 \left(-K_{12}s_1 - \beta_{11}|s_1|^\rho \text{sign}(s_1) - \beta_{12} \int_0^t \text{sign}(s_1) \right) < 0\end{aligned}\quad (70)$$

$$\dot{V}_2(s_2) \leq s_2 \left(-K_{21}s_2 - \beta_{21}|s_2|^\rho \text{sign}(s_2) - \beta_{22} \int_0^t \text{sign}(s_2) \right) < 0\quad (71)$$

where $-K_{11}e_1^2 < 0$ for K_{11} , $-K_{12}s_1^2 < 0$ for K_{12} and $-K_{21}s_2^2 < 0$ for K_{21} are positive constants. The following sufficient conditions for finite time convergence must be satisfied [30, 31].

$$\begin{aligned}\beta_{i1}^2 &\geq \frac{4C_0 K_M (\beta_{i2} + C_0)}{K_m^2 K_m (\beta_{i2} - C_0)} \\ \beta_{i2} &> \frac{C_0}{K_m} \\ 0 &< p \leq 0.5\end{aligned}$$

4 Result and Discussion

This section presents the results and discusses the performance of the controllers designed in previous section. Table 2 shows the value of the glider parameters used in the simulations. All the parameters are adopted from [5]. All the controllers were simulated for the system without perturbation, system with disturbance and system with parameter variations.

The simulation results for the system without perturbation are shown in Figs. 2, 3 and 4. From the figures, both controllers are able to converge to desired values. The proposed controller (BSTSMC) gives faster convergence time than super twisting SMC where it is stabilized at vicinity of 25° within 5 s for pitching angle and stabilized

Table 2 Glider's parameter

Parameter	Value	Unit
Hull mass, m_h	40	kg
Internal sliding mass, m_p	9	kg
Displaced fluid mass, m_{df}	50	kg
Added mass, m_{f1}, m_{f2}, m_{f3}	50, 60, 70	kgm ²
Inertia, J_1, J_2, J_3	4, 12, 11	–
Lift coefficient, K_{LO}, K_L	0, 132.5	–
Drag coefficient, K_{DO}, K_D	2.15, 25	–

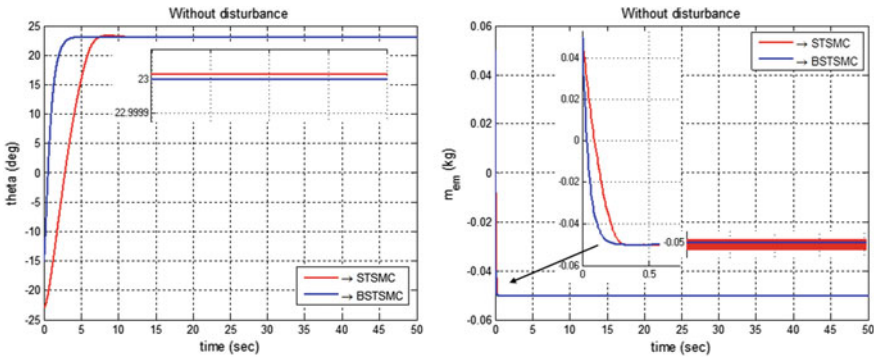


Fig. 2 Pitching angle θ and net buoyancy m_{em} (without disturbance)

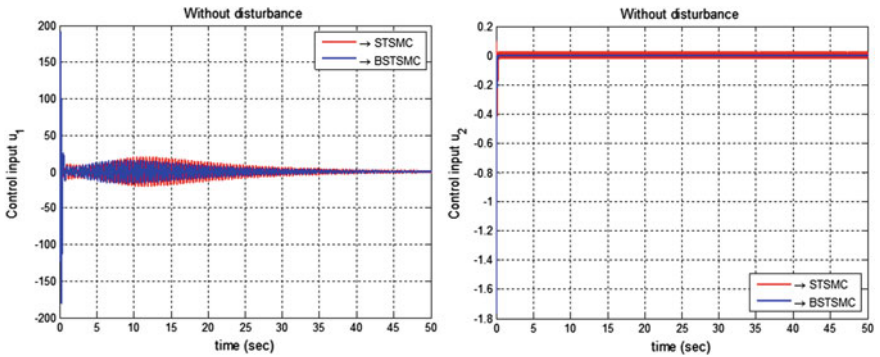


Fig. 3 Control input u_1 and u_2 (without disturbance)

at -0.05 within less than 0.25 s. The BSTSMC also provide lower control effort and smaller chattering.

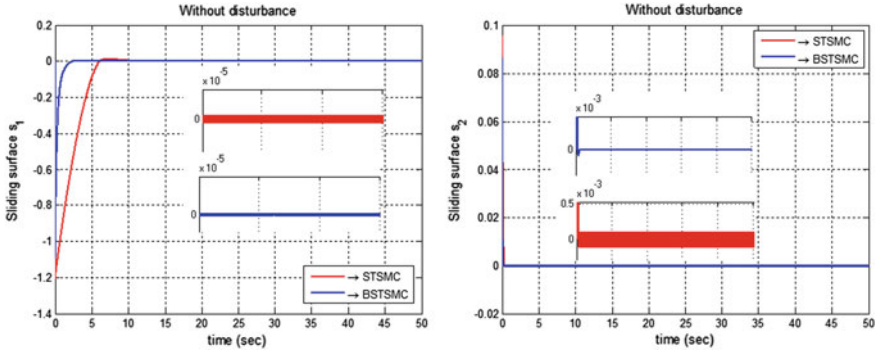


Fig. 4 Sliding surface s_1 and s_2 (without disturbance)

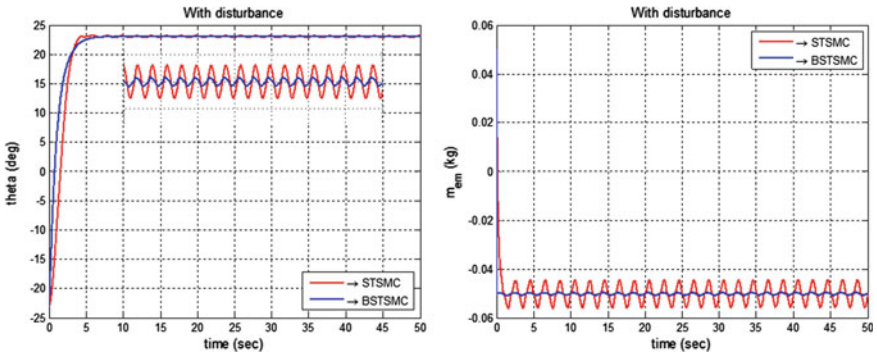


Fig. 5 Pitching angle θ and net buoyancy m_{em} (with disturbance)

The results for system with disturbance are shown in Figs. 5, 6 and 7. The BSTSMC provides with better disturbance rejection as compared to STSMC with all the observed outputs are converged within the desired values with smaller errors. The smaller control effort and chattering are also can be seen in control inputs and sliding surfaces.

Figures 8, 9 and 10 show the results for the system with parameter variations. The selected parameters are increased by 30% as shown in Table 3. All the selected parameters only appear in equation for pitching angle, therefore the effect of the changes only can be seen for the results related to pitching angle and the results for net buoyancy just remain unchanged as per the system without perturbation. From Fig. 8, the proposed controller shows no effect on its performance when the increment is applied time $t=30$ s. Smaller control effort and smaller chattering are also seen in control input and sliding surface. However STSMC shows small deviation from the desired value, higher control effort and larger chattering are seen in control input and sliding surface. All the controller parameters are depicted in Table 4.

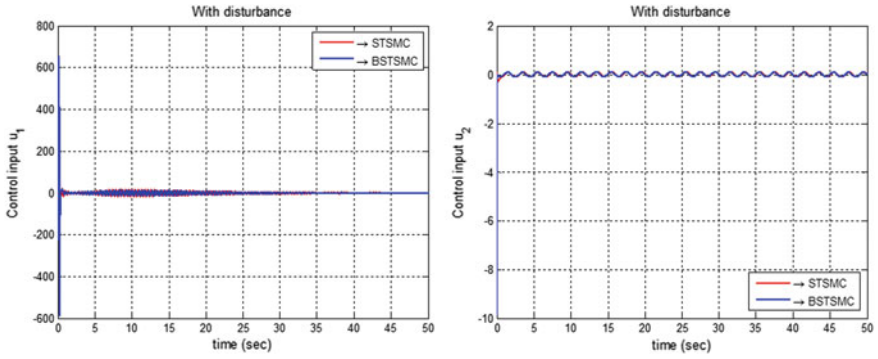


Fig. 6 Control input u_1 and u_2 (with disturbance)

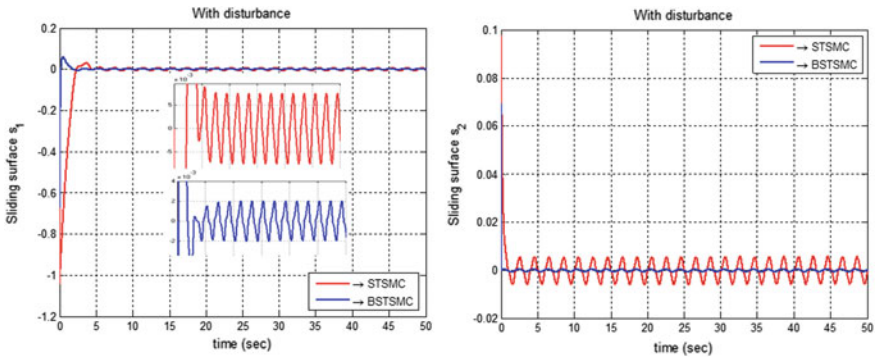


Fig. 7 Sliding surface s_1 and s_2 (with disturbance)

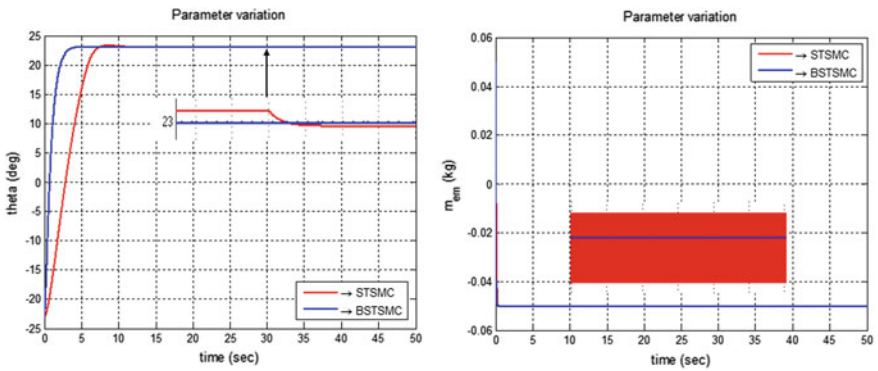


Fig. 8 Pitching angle θ and net buoyancy m_{em} (parameter variation)

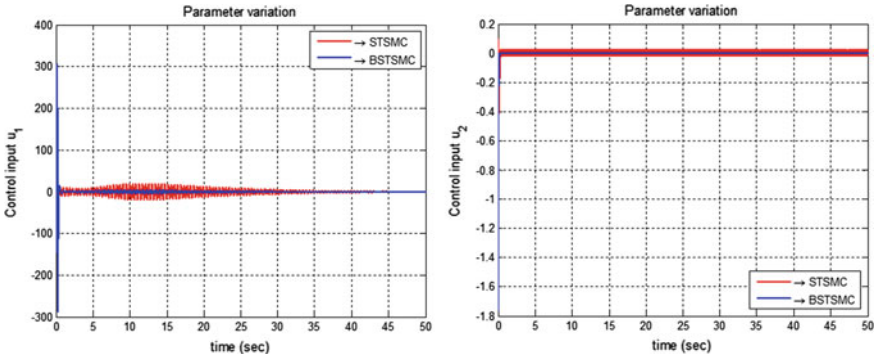


Fig. 9 Control input u_1 and u_2 (parameter variation)

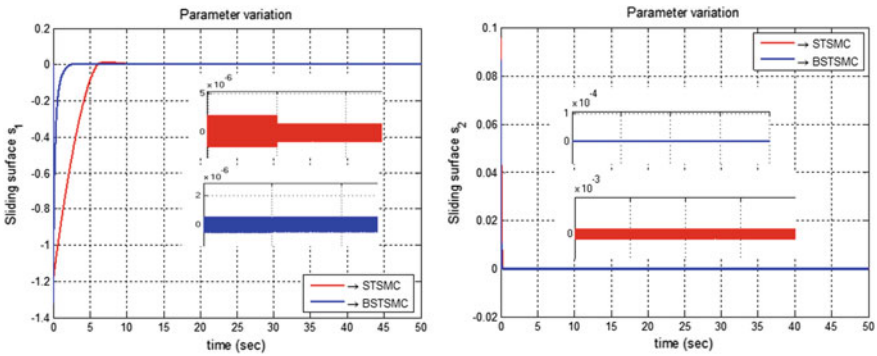


Fig. 10 Sliding surface s_1 and s_2 (parameter variation)

Table 3 Parameter increment (30%)

Parameter	Nominal	After increment
m_{f1}	5	6.50
m_{f3}	70	91
J_2	12	15.60
K_{LO}	0	0.30
K_L	132.5	172.25
K_{DO}	2.15	2.80
K_D	25	32.50
K_{MO}	0	0.30
K_M	-100	-130
$K_{\omega_2^1}, K_{\omega_2^2}$	50, 50	65, 65

Table 4 Controller parameter value

STSMC	Nominal	Disturbance	Parameter variation
c_1	1.5	1.3	1.5
β_{11}	9	20	9
β_{12}	0.2	2	0.2
β_{21}	2	1.2	2
β_{22}	0.005	0.005	0.005
P	0.5	0.5	0.5
BSTSMC	Nominal	Disturbance	Parameter variation
K_{11}	1.68	0.90	1.68
K_{12}	2.98	9.50	2.98
K_{21}	20	140	20
β_{11}	5	10	5
β_{12}	0.5	4	0.5
β_{21}	0.1	0.7	0.1
β_{22}	0.01	0.05	0.01
p	0.5	0.5	0.5

5 Conclusion

A robust nonlinear backstepping super twisting sliding mode control has been proposed and applied for autonomous underwater glider. With the numerical simulation results show in previous section, a conclusion can be made that the proposed controller provide a significant improvement in reducing the chattering phenomenon in control input and sliding surface and improve transient performance in existence of external disturbance and uncertainties in hydrodynamics and glider parameters as compared to STSMC.

Acknowledgements This research is supported by Universiti Malaysia Pahang (UMP) research grant Vot: RDU1703134, Development of Controller for an Underactuated Autonomous Underwater Vehicle (AUV).

References

1. Stommel, H.: The Slocum mission. *Oceanography* **2**, 22–25 (1989)
2. Webb, D.C., Simonetti, P.J., Jones, C.P.: SLOCUM: an underwater glider propelled by environmental energy. *IEEE J. Ocean. Eng.* **26**(4), 447–452 (2001)
3. Sherman, J., Davis, R.E., Owens, W.B., Valdes, J.: The autonomous underwater glider ‘Spray’. *IEEE J. Ocean. Eng.* **26**(4), 437–446 (2001)
4. Eriksen, C.C., Osse, T.J., Light, R.D., Wen, T., Lehman, T.W., Sabin, P.L., Ballard, J.W., Chiodi, A.M.: Seaglider: a long-range autonomous underwater vehicle for oceanographic research.

- IEEE J. Ocean. Eng. **26**(4), 424–436 (2001)
5. Graver, J.G.: Underwater gliders: dynamics, control and design. PhD thesis, Princeton University, USA (2005)
 6. Rudnick, D.L., Davis, R.E., Eriksen, C.C., Fratantoni, D.M., Perry, M.J.: Underwater gliders for ocean research. *Mar. Technol. Soc. J.* **38**(2), 73–84 (2004)
 7. Zhang, F., Zhang, F., Tan, X.: Steady spiraling motion of gliding robotic fish. In: IEEE International Conference on Intelligent Robots and Systems, pp. 1754–1759. Vilamoura, Portugal (2012)
 8. Isa, K., Arshad, M.R.: Experimental analysis of homeostatic-inspired motion controller for a hybrid-driven autonomous underwater glider. *J. Teknologi* **74**(9), 51–63 (2015)
 9. Alvarez, A., Caffaz, A., Caiti, A., Casalino, G., Gualdesi, L., Turetta, A., Viviani, R.: Fòlaga: a low-cost autonomous underwater vehicle combining glider and AUV capabilities. *Ocean Eng.* **36**(1), 24–38 (2009)
 10. Arima, M., Ichihashi, N., Miwa, Y.: Modelling and motion simulation of an underwater glider with independently controllable main wings. In: Oceans 2009-Europe, pp. 1–6. Bremen, Germany (2009)
 11. Leonard, N.E., Graver, J.: Model-based feedback control of autonomous underwater gliders. *IEEE J. Ocean. Eng.* **26**(4), 633–645 (2001)
 12. Yuh, J.: Design and control of autonomous underwater robots: a survey. *Auton. Robots*, Kluwer Academic Publishers, **8**(1), 7–24 (2000)
 13. Ullah, B., Ovinis, M., Baharom, M.B., Javaid, M.Y., Izhar, S.S.: Underwater gliders control strategies: a review. In: 2015 10th Asian Control Conference: Emerging Control Techniques for a Sustainable World (ASCC 2015), pp. 1–6. Kota Kinabalu, Malaysia (2015)
 14. Bender, A., Steinberg, D.M., Friedman, A.L., Williams, S.B.: Analysis of an autonomous underwater glider. In: Proceedings of ACRA 2008, pp. 1–10. Canberra, Australia (2008)
 15. Mahmoudian, N., Woolsey, C.: Underwater glider motion control. In: 2008 47th IEEE Conference on Decision and Control, pp. 552–557. Cancun, Mexico (2008)
 16. Mat-Noh, M., Arshad, M.R., Mokhtar, R.M.: Depth and pitch control of USM underwater glider: performance comparison PID vs. LQR. *Indian J. Geo-Marine Sci.* **40**(2), 200–206 (2011)
 17. Kan, L., Zhang, Y., Fan, H., Yang, W., Chen, Z.: MATLAB-based simulation of buoyancy-driven underwater glider motion. *J. Ocean Univ. China* **7**(1), 113–118 (2008)
 18. Isa, K., Arshad, M.R.: Modeling and motion control of a hybrid-driven underwater glider. *Indian J. Geo-Marine Sci.* **42**(8), 971–979 (2013)
 19. Tatone, F., Vaccarini, M., Longhi, S.: Modeling and attitude control of an autonomous underwater glider. In: 8th IFAC International Conference on Manoeuvring and Control of Marine Craft, pp. 217–222. Guarujá, Brazil (2009)
 20. Shan, Y., Yan, Z.: Model predictive control of underwater gliders based on a one-layer recurrent neural network. In: 2013 Sixth International Conference on Advanced Computational Intelligence, pp. 328–333. Hangzhou, China (2013)
 21. Abraham, I., Yi, J.: Model predictive control of buoyancy propelled autonomous underwater glider. In: 2015 American Control Conference, pp. 1181–1186. Chicago, USA (2015)
 22. Mat-Noh, M., Arshad, M. R., Mokhtar, R.M.: Control of 1 DoF USM underwater glider (USMUG). In: 4th International Conference on Underwater System Technology: Theory and Applications 2012, pp. 1–6. Shah Alam, Malaysia (2012)
 23. Mat-Noh, M., Arshad, M.R., Mokhtar, R.M.: Nonlinear control of autonomous underwater glider based on super-twisting sliding mode control (STSMC). In: 2017 7th IEEE International Conference on System Engineering and Technology (ICSET 2017), pp. 71–76. Shah Alam, Malaysia (2017)
 24. Mat-Noh, M., Arshad, M.R., Mokhtar, R.M.: The evaluation of controller tracking performance based on Taylor's series expansion model. *J. Teknologi* **74**(9), 175–181 (2015)
 25. Yang, H., Ma, J.: Sliding mode tracking control of autonomous underwater glider. In: 2010 International Conference on Computer Application and System Modeling (ICCASM2010), pp. 555–558. Taiyuan, China (2010)

26. Yang, H., Ma, J.: Nonlinear control for autonomous underwater glider motion based on inverse system method. *J. Shanghai Jiaotong Univ.* **15**(6), 713–718 (2010)
27. Isa, K., Arshad, M.R.: Neural networks control of hybrid-driven underwater glider. In: 2012 Oceans—Yeosu, pp. 2–8. Yeosu, South Korea (2011)
28. Fliess, M.: Generalized controller canonical forms for linear and nonlinear dynamics. *IEEE Trans. Autom. Control* **35**(9), 994–1001 (1990)
29. Levant, A.: Sliding order and sliding accuracy in sliding mode control. *Int. J. Control* **58**(6), 1247–1263 (1993)
30. Bartolini, G., Ferrara, A., Levant, A., Usai, E.: On second order sliding mode controllers. In: Young, K.D., Ozgiine, U. (eds.) *Variable Structure Systems Sliding Mode Nonlinear Control*, vol. 247, pp. 329–350. Springer, London, Great Britain (1999)
31. Levant, A., Pridor, A.: Aircraft pitch control via second order sliding technique. *AIAA J. Guidance Control Dyn.* **23**(4), 586–594 (2000)

PSpHT-II: A Water Strider-Like Robot with Cylindrical Footpad



Vi Vi Gan, Addie Irawan, Niirmel Ranjanendran and Siti Noor Zuliana

Abstract Water strider or Gerridae is very lightweight insect and has a long leg that able to stand and even jump on the surface of water surface tension. Mimicking this creature become one of the favorable areas in the bioinspired robotics field. A Portable Striding pH Tester (PSpHT) is one of the robotics systems that mimicking water strider with quadruped mechanism. The first PSpHT design had successfully operated with real-time pH monitoring, and long-haul remotely control. However, weakness in its footpad still existed when the rapid spatial motions were not making PSpHT faster enough on the water surface. Therefore this paper presents the improvement progress on PSpHT and introducing its second version named PSpHT-II. In this progress, a new footpad with light cylindrical shape is proposed by considering the water surface tension. The polypropylene-based footpad hold with light aluminum alloy as a link of the spatial leg and the flat plate was added as the paddler on each side of the footpad as water surface breaker. The leg design is recalculating and fabricated regarding the Archimedes principle and surface tension theory by considering the balance forces between the air and water. According to the calculations and buoyed test, the proposed cylindrical footpad is less submerged compares to the previous footpads designed. On the other hand, the proposed spatial motion was simulated for verification. As for validation, PSpHT-II was validated by running the system on the lakeside of Universiti Malaysia Pahang, Pekan, Pahang Campus. The experiment shows the additional paddlers help PSpHT-II striding faster and stable although with a mild and windy situation.

Keywords Water strider · Cylindrical footpad · Spatial striding gait pattern

V. V. Gan · A. Irawan (✉) · N. Ranjanendran · S. N. Zuliana
Robotics and Unmanned System (RUS) Group, Faculty of Electrical & Electronics Engineering,
Universiti Malaysia Pahang, 26600 Pekan, Pahang, Malaysia
e-mail: addieirawan@ump.edu.my

© Springer Nature Singapore Pte Ltd. 2019
Z. Md Zain et al. (eds.), *Proceedings of the 10th National Technical Seminar on Underwater System Technology 2018*, Lecture Notes in Electrical Engineering 538,
https://doi.org/10.1007/978-981-13-3708-6_9

1 Introduction

Water strider characteristics have gained more attention and attracted among robots especially for those who focus on bio-inspired arthropods robot, to develop a bionic water strider systems or at least mimicking its biological behaviors [1–4]. Water Strider, or *Gerridae*, is an insect that able to stand, walk and even jump on the surface of water such as rivers, ponds and open seawater with weight 10 dynes and length at about 1 cm [5]. With these advantages, water strider robot and water strider-like system had applied in many areas such as water quality monitoring, aquatic searching, and rescues [6, 7]. A few approaches have been made in realizing *on water surface striding* elements in some research and development works which mainly focused on the leg, foot, and other extra propeller design. The water strider exploits the principles of water tension to stay on the surface using its long splayed legs with hydrophobic micro-hair to repel the water and prevent water droplets from weighing down on its body, which helps it to float. According to the Gao and Jiang, this tiny insect can move on the surface of the water at speed 1.5 m/s without breaking the surface.

Moreover, the insect could maintain the force of surface tension around its legs that are covered with several layers of tiny hairs (about 3 mm in diameter) that consist of several nano-grooves and ability to trap air bubbles [8]. On top of that, waxy secretion on the hairs resists osmosis keeping the hair in place, in which used its legs like oars. The sweeping motion of its legs create vortices behind the water strider that propels it forward [9]. Several water-strider robots research and development works which are published such as Water Dancer IIa [10], Water Walking Robot [11] and STRIDER II [12] generally emphasized on giving stable striding and locomotion operations on the surface of the water.

Water Dancer II-A [10], a water strider robot was designed by Minzu University of China with collaboration Beihang University and University of Cassino, Italy, equipped with the capability of turning, speed-regulation, tele-controlled using infrared signals and features with lightweight structure design and low power consumption. With 0.2 mm diameter stainless steel thread leg with a hydrophobic agent, this water strider robot able to 120° contact with the surface of the water and eliminates any rotational imbalance during striding operation with its cross-shaped design. The same floating approach has been made in [6] in which can-link mechanism is proposed to gear up the leg striding in locomotion.

The different had presented by Harbin Institute of Technology, China in their Water-walking robot [3, 13], configured with the decoupled parallel mechanism. Two micro-electromagnets were used to achieve the forward, or backward motion of the driving mechanism and one micro-electromagnet used for uplifting motion. Moreover, this water-walking robot the selected material for a single leg is much smaller than the output force of the electromagnet. This scenario makes the friction of the slider, revolute joint, a moment of inertia and the inertial force need to be calculated.

Circular footpad innovated for STRIDER II [14] also present the difference in realizing *Gerridae* biological structure and behaviors. This footpad was designed for high lift, stability, payload capability and elliptical leg rotation mechanism to increase the efficiency of water surface propulsion. The same idea proposed by Zhang et al. [15] in which lightweight nickel foam sheets with superhydrophobicity and high carrying capacity footpad was designed. Moreover, the spring-based actuating mechanism was equipped that can release and swing backward, generating a large instance driving force in its locomotion. More lightweight water-strider robot design was proposed in the recent design such as in [3, 4, 16], in which case the robot uses light and compact structure and features low power consumption to realizing jumping behaviors. This mechanism, structure design, and weight are mimicking water strider biological characteristic but limited regarding applications primarily in the rage of its payload.

Therefore this research has taken the initiative to involve in developing a strider-like system, named Portable Striding pH Tester (PSpHT) [17], that able to stride on the surface of the water and acting as a moving beacon to send the information about the water quality status with a more bigger payload. This proposed strider robot system is focusing on providing striding behavior on the surface of water by understanding the Archimedes principle of the floating object on the liquid instead of designing the hydrophobic agent that currently consider unable to stand with the high payload. This article presents the improved design of the PSpHT system, named as PSpHT-II, that equipped with improved footpad.

2 Water Strider Mechanical Framework

2.1 PSpHT Mechanical Structure Design and Mechanism

Similar to other water strider robot research and development PSpHT is developed for mimicking biological *Gerridae* creature that able to stride on the water surfaces. The different PSpHT with other existed water strider robot is on the payload and sizes. This water strider robot design is not only focused on mimicking *Gerridae* but also applicable to assist human in giving information about the water. The first attempt was with polystyrene foam-based footpad as shown in Fig. 1a, which is only successful for floating on the water surface and short striding [18]. The design were improved in developing Portable Striding pH Tester (PSpHT) with bigger sizes and with cone footpad as shown in Fig. 1b. This version had successfully used for long distance water monitoring system as its name imply [7]. Concerning the PSpHT performances, this research had moved to another step by improving its foot-pad design with a cylindrical shape for efficient striding operation as shown in Fig. 1c. In enhancing PSpHT footpads, the main frame of the revised with new actuator unit to support new footpad design an end effector for each robot's leg. Moreover, PSpHT-

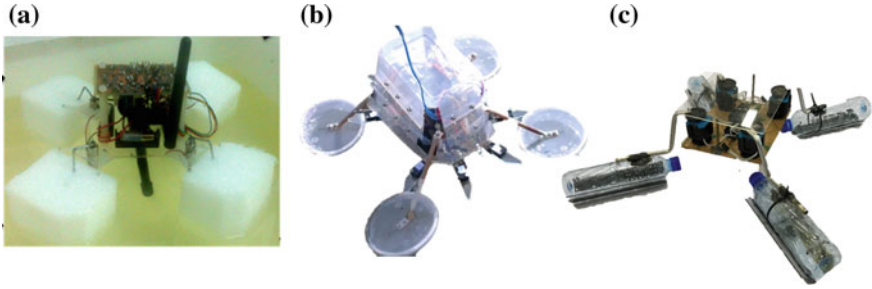
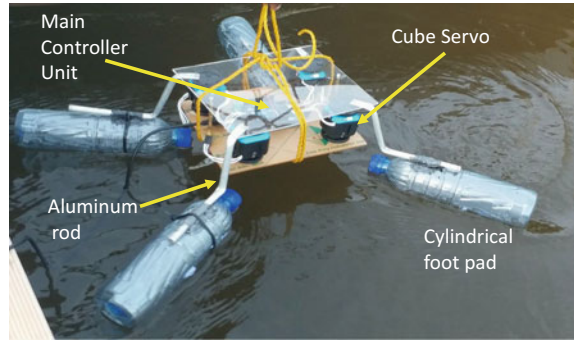


Fig. 1 Generation of PSpHT system **a** Water strider robot with polystyrene foam-based footpad, **b** Portable Striding pH Tester (PSpHT) and **c** PSpHT-II with cylindrical footpad

Fig. 2 Proposed PSpHT-II system structure overview



II equipped with cube servo motor as its spatial actuator with the ability to support moving both aluminum rod link and cylindrical footpad as shown in Fig. 2.

The body design of PSpHT-II retains symmetry with all components installed at the center of the body (CoB) to ensure all legs are spatially symmetric. The factor of balance striding is the motor/actuator that drives the leg; it must move almost similarly in time [8]. As shown in Fig. 3 and with reference to Archimedes' Principle, PSpHT-II body can be considered as an object that needs to be denser than water to ensure it is buoyed to the surface with the buoyant force (F_b). However, this force is insufficient to the force of gravity (W) with a different vector as shown in Fig. 3. Therefore, it is crucial that to place all payload at the center of the robot body to centralize all W to the CoB and the changes of Center of Gravity (CoG) started from CoB of the robot.

2.2 Improved Footpad Design

The design of the PSpHT was improved by changing its footpad with the cylindrical shape as shown in Fig. 4. Footpad design is a vital aspect to realize *striding behavior* in water strider robot design. The cylindrical shape is chosen because it is

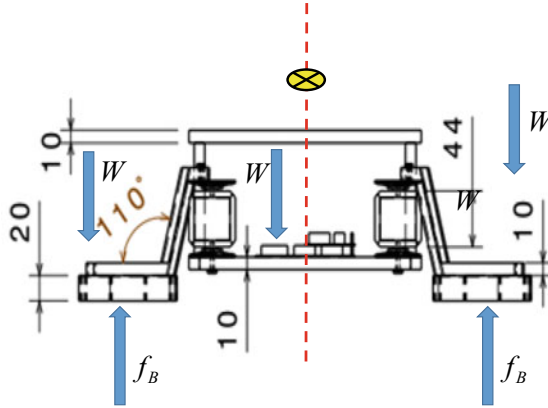


Fig. 3 Overall force vectors on PSpHT-II unit (scale in mm)

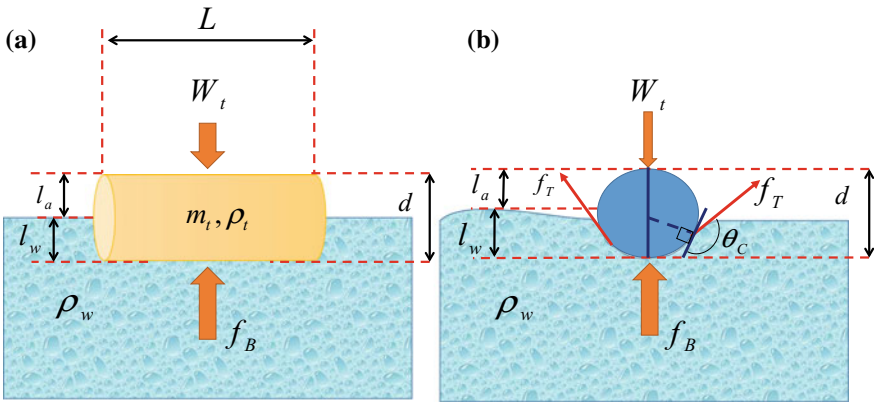


Fig. 4 Archimedes Principle Relation for a cylindrical object floating on water **a** Side view, **b** End view with surface tension

round shape that intense to achieve $l_a \gg l_w$ as shown in Fig. 4a and compensate with water surface tension is explained in Fig. 4b for each end cylinder face. According to Archimedes Principles [19], the weight of a submerged object is equal to the weight of the water being displaced by the object.

Therefore the mass of the robot (m_r) is assumed to be evenly distributed to each tip; hence, the mass at each footpad is equal to $4m_t = m_r$. The volume of the footpad that buoyed on the surface of the water (V_B) can be calculated using Eq. 1:

$$V_t = \pi \frac{d^2}{4} l_a \tag{1}$$

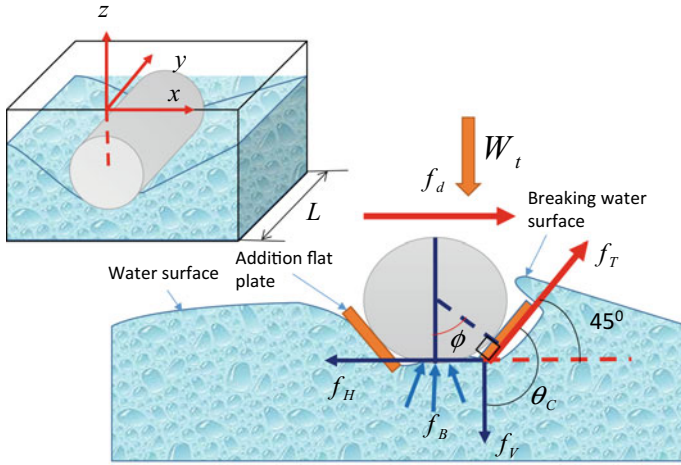


Fig. 5 2-D dynamic model of the problem with depth of footpad with dimension L into y -axis

where d is the diameter of the cylinder. Moreover, another element need to emphasize to ensure the PSpHT-II robot has a stable float on the surface of the water is the density of the robot (ρ_R) in which can be assumed to be calculated as Eq. 2 as follows;

$$\rho_R = \sum_{n=1}^4 \rho_{t_n} + \rho_b \quad (2)$$

where robot body density (ρ_b) is included condition between robot density and water density (ρ_w) must be $\rho_R \ll \rho_w$.

In terms of dynamics point of view, each leg will suffer from gravitational forces and leg-water interaction forces if air resistance is neglected. Concerning contact angle (θ_C), rigid round shape of cylindrical footpad contribute arbitrary cancellation on f_T that almost zero cancellation at almost all time. This can be explained in Fig. 4b, where the horizontal force (f_H) is an adhesive force that needs to be canceled to achieve the balance forces at the contact point as expressed in Eq. 3 as follows;

$$f_H = f_T \sin \theta_C \quad (3)$$

Thus, 45° plates were added on each side of each footpad of PSpHT-II as shown in Fig. 5 to ensure the force cancellation is happening during striding and drag force (f_d) at the condition f_d in realizing striding locomotion. Moreover an additional flat plate able to break the water surface as well that makes $f_B \gg W_t$ and $l_w \rightarrow 0$ during striding as shown in Fig. 5. The typical value for each physical parameter defined in Table 1.

Table 1 Physical parameter definitions used in framework design

Parameters	Symbol	Typical value
Contact angle	θ_C	$0^\circ - 90^\circ$
Submerge angle	ϕ	$0^\circ - 180^\circ$
Footpad weight	W_t	2 mg
The total mass of the robot	m_r	1.6 kg
Buoyancy force	f_B	N/A
Vertical force (from footpad)	f_V	
Horizontal force (from footpad)	f_H	
Drag force	f_d	
Robot density	ρ_R	
Water density	ρ_w	

3 Striding Gait Pattern Design System

A leg of PSpHT-II was equipped with a servo motor that allows this system to perform the spatial motion. Figure 5 shows the quadruped PSpHT-II coordination system with spatial motion limited to 90° for adjacent legs collision avoidance. The angular motion for each leg can be expressed in Eq. 4 in which z-axis is zero as follows;

$$\theta_n = \arctan\left(\frac{x_n}{y_n}\right) \quad (4)$$

where $n = 1, 2, \dots, 4$ is the number of PSpHT-II leg. The basic trajectory generation is designed which is include latitudinal with forwarding and backward directions, and longitudinal with left and right directions. With reference to Figs. 6 and 7a, the front legs will spatially move at first followed by rear legs after front legs are stopped moving to perform forward direction move, and vice versa for backward direction move. It is different leg sequences for right direction moving as shown in Fig. 7b, where right legs moved at first followed by left legs when right legs are stopped, and vice versa for left direction moves.

The sequences of gait pattern are represented in a finite state diagram as shown in Fig. 8. As shown in Fig. 7, the spatial motion is different poles for a different leg for each direction of movement. Table 2 shows the spatial sequences for θ_n for different direction of movement. For the motions of latitudinal movements, both sets of couple legs; Set A: Leg 1 and 2 and Set B: Leg 3 and 4; are programed to be spatially moved in different poles from initial value (θ_{n_o}) .

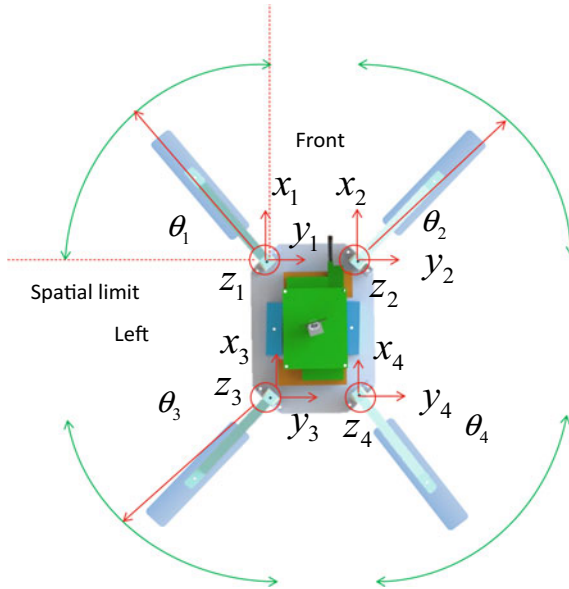


Fig. 6 PSpHT-II system coordination

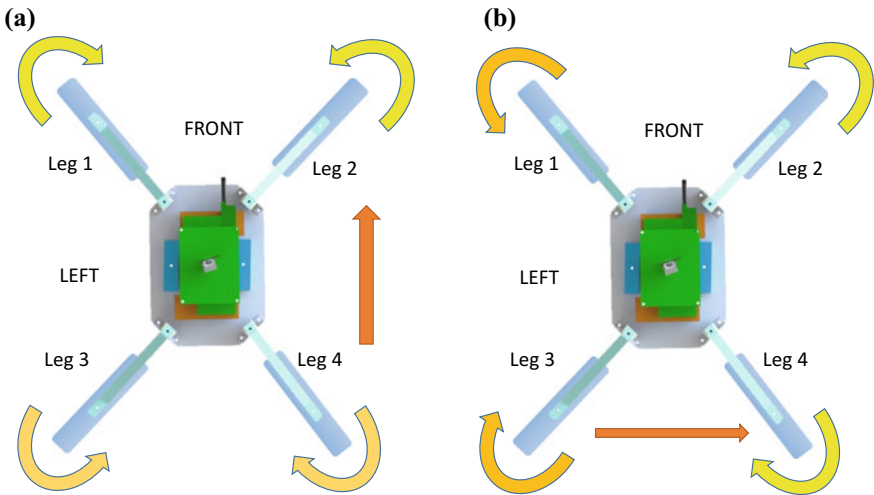


Fig. 7 Graphical representation for PSpHT-II gait pattern **a** Latitudinal motion: an example of front direction, **b** Longitudinal motion: example of the right direction

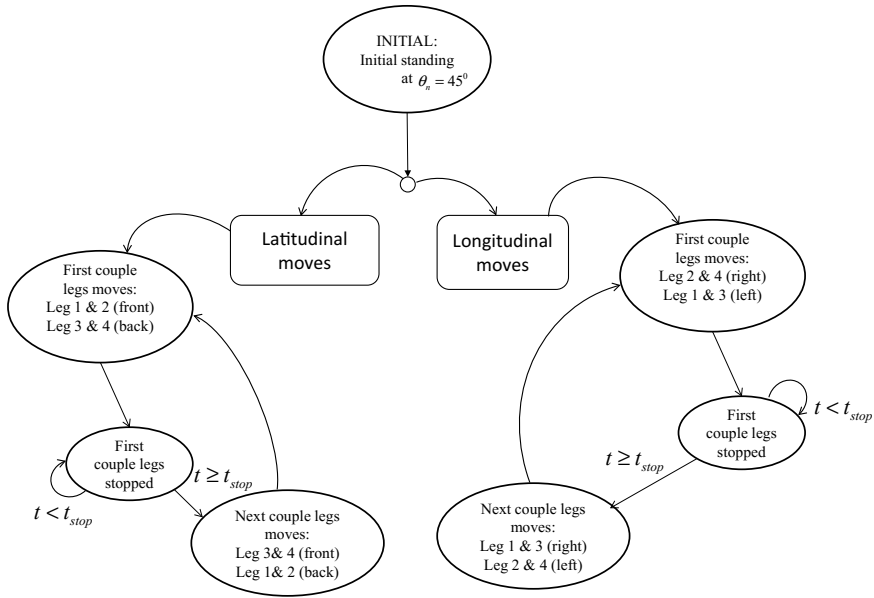


Fig. 8 The finite state diagram for PSpHT-II trajectory input

Table 2 Spatial angular motion for each leg by direction

Direction	Set A	Set B
Front	$\theta_{1_o} \rightarrow -\theta_1$	$\theta_{3_o} \rightarrow +\theta_3$
	$\theta_{2_o} \rightarrow +\theta_2$	$\theta_{3_o} \rightarrow -\theta_4$
Back	$\theta_{1_o} \rightarrow +\theta_1$	$\theta_{3_o} \rightarrow -\theta_3$
	$\theta_{2_o} \rightarrow -\theta_2$	$\theta_{3_o} \rightarrow +\theta_4$
Right	$\theta_{1_o} \rightarrow +\theta_1$	$\theta_{3_o} \rightarrow -\theta_3$
	$\theta_{2_o} \rightarrow +\theta_2$	$\theta_{3_o} \rightarrow -\theta_4$
Left	$\theta_{1_o} \rightarrow -\theta_1$	$\theta_{3_o} \rightarrow +\theta_3$
	$\theta_{2_o} \rightarrow -\theta_2$	$\theta_{3_o} \rightarrow +\theta_4$

It is different for the spatial motions of longitudinal directions where both Set A and Set B of the legs are programmed to be moved at the same poles from θ_{n_o} . All sets of leg moved spatially with exchange activation each other after holding time (t_{stop}) as shown in Fig. 8.

4 Experimental and Results

As for the system validation, several experiments have been done for the proposed PSpHT-II platform. In the case of frameworks, the footpad design also being calculated for comparative study with previous footpads. As shown in Fig. 12, the $l_a \gg l_w$ conditions are more promising for PSpHT-II with cylindrical footpad compares to the previous designed PSpHT, which had designed with the cube, sphere, small-cone, and large-cone (Fig. 9).

The test is further on leg motion designed as discussed in Sect. 3. The spatial motion on each leg is designed with a range of $80^\circ \geq l_w > 9^\circ$ from the initial position, 45° as shown in Fig. 10a. As shown in Fig. 10a, the 2D plot between the x-axis and y-axis Cartesian of motion for a leg of PSpHT-II was performing quarter-circle motions with the radius at about 9 cm according to the designed leg. This quarter motion will be move according to the pool sequences of PSpHT-II direction of movement as discussed in Sect. 3. For thoroughly experimental and validation, PSpHT-II is run on the water with a bit windy situation at Universiti Malaysia Pahang Lake, Pekan, Pahang. The experiment was done in two situations; without and without the designed flat plate considered as a paddler. As shown in Fig. 11, PSpHT-II showed successfully stride from the initial setup position as shown in Fig. 11a and start moving forward, backward, right and left and back to the initial position as snapshots as shown from Fig. 11b–e respectively.

The experiment has been furthered by adding a couple of paddlers on each footpad as discussed in Sect. 2. The same operation has been done as the first experiment

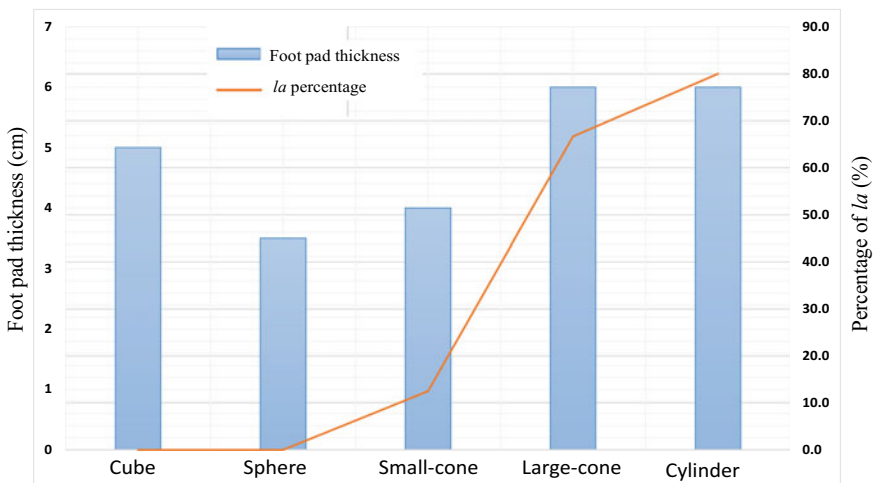


Fig. 9 l_a percentage versus footpad thickness between all footpad shapes previously and currently designed for PSpHT system

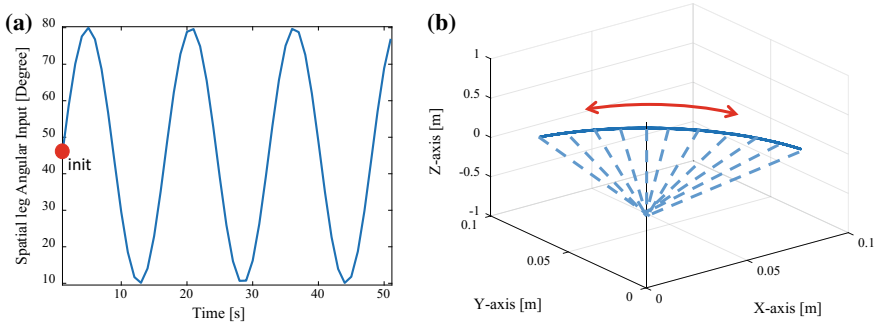


Fig. 10 A sample of simulation results for spatial motion and trajectory input, **a** angular input sequences for a leg, **b** Cartesian motion for a leg

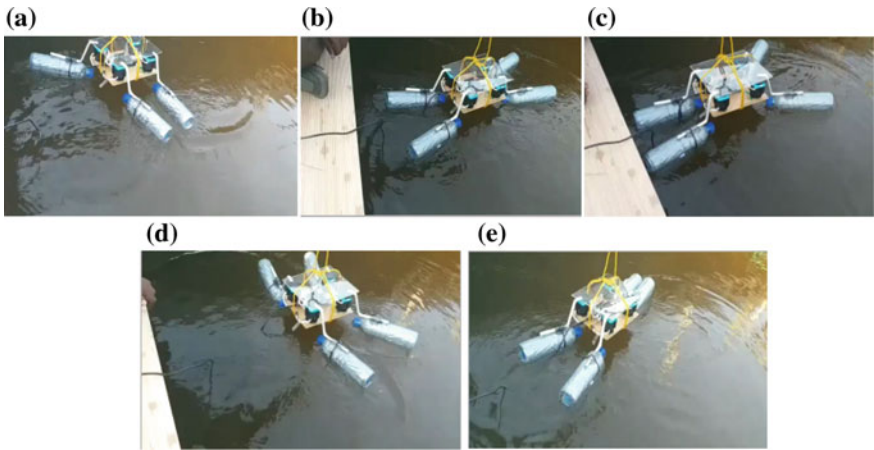


Fig. 11 Snapshots of the PSpHT-II striding test without paddler; **a** forward, **b** backward, **c** right, **d** left and then back to **e** initial position on water

as shown in Fig. 12. According to the experimental time record PSpHT-II with proposed paddlers on each footpad stride a bit faster than without paddlers which is about 200 ms according to digital timer recorder for about 90–100 cm distances. As shown in Fig. 13, the water ripple during PSpHT-II with paddler’s locomotion is more evident and radical than without attached paddlers. This scenario shows that the water surface has been pulled hardly or break during strider locomotion by the paddlers that are explained and calculated in Sect. 2.

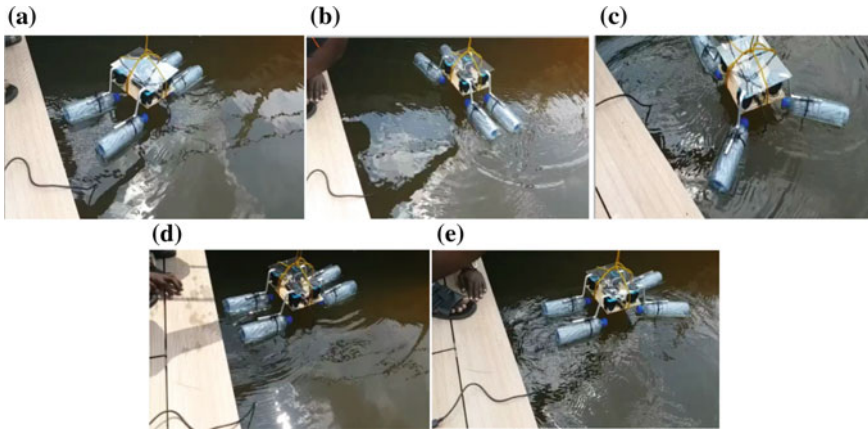


Fig. 12 Snapshots of the PSpHT-II striding test with paddler; **a** forward, **b** backward, **c** right, **d** left and then back to **e** initial position on water

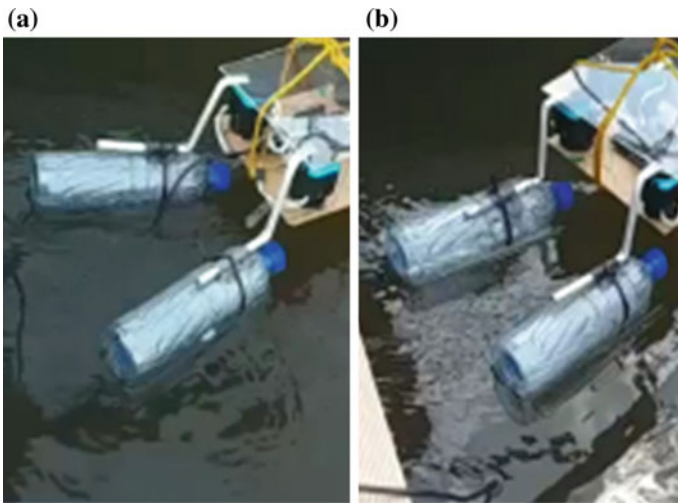


Fig. 13 Snapshots of water ripple for PSpHT-II on the water surface **a** without paddlers on footpad **b** with paddlers on footpad

5 Conclusion

The framework for the improved development of PSpHT-II was presented. The proposed modified footpad with a cylindrical shape and small change on leg link have been validated able to float the overall robot system on the water surface. This results also had proven the submerged theory of the footpads with cylindrical shape has less drowning in the water is compared to the cube, sphere, small-cone and large-

cone footpads. Moreover, the capability of performing locomotion with the designed striding gait pattern makes the proposed cylindrical footpad reliable to mimicking water-striding locomotion. In addition, additional paddlers on each PSPHT-II footpad able to increase striding speed with small water surface breaking on each spatial motion. With reference to the overall experimental results, the improvement in speed has potentially become the future works on PSPHT-II system other than complete this system with remote control system and data acquisition unit.

Acknowledgements This research and development are supported by the Faculty of Electrical & Electronics Engineering, Universiti Malaysia Pahang (UMP) under the Integrated Engineering Design courses. Also, partial of this research are supported by the Ministry Of Higher Education Malaysia under the Fundamental Research Grant Scheme (FRGS) (Grant No. FRGS/1/2016/TK04/UMP/02/9) and Universiti Malaysia Pahang (UMP) Research Grant (RDU160147).

References

1. Suzuki, K., Ichinose, R.W., Takano, H., Miura, H.: Development of water surface mobile robot inspired by water striders. *IET Micro Nano Lett* **12**(8), 575–579 (2017)
2. Sheng, C., Huang, L., Shen, Y., Wu, J., Zhang, C., Zhang, S., Guo, Y., Huang, H.: Stability analysis and hydrodynamic modeling of a water strider-like robot. In: *OCEANS 2017—Anchorage*, pp. 1–6. Anchorage, Alaska (2017)
3. Kai, Y., Gangfeng, L., Jihong, Y., Tao, W., Xinbin, Z., Jie, Z.: A water-walking robot mimicking the jumping abilities of water striders. *Bioinspiration Biomimetics* **11**(6), 066002 (2016)
4. Koh, J.-S., Yang, E., Jung, G.-P., Jung, S.-P., Son, J.H., Lee, S.-I., Jablonski, P.G., Wood, R.J., Kim, H.-Y., Cho, K.-J.: Jumping on water: Surface tension-dominated jumping of water striders and robotic insects. *Science* **349**(6247), 517–521 (2015)
5. Hu, D.L., Chan, B., Bush, J.W.M.: The hydrodynamics of water strider locomotion. *Nature* **424**(6949), 663–666 (2003)
6. Yan, J.H., Zhang, X.B., Zhao, J., Liu, G.F., Cai, H.G., Pan, Q.M.: A miniature surface tension-driven robot using spatially elliptical moving legs to mimic a water strider's locomotion. *Bioinspiration Biomimetics* **10**(4), 046016 (2015)
7. Irawan, A., Khim, B.K., Yin, T.: PSPHT a water strider-like robot for water inspection: framework and control architecture. In: *2014 11th international conference on ubiquitous robots and ambient intelligence (URAI)*, pp 203–440. Kuala Lumpur, Malaysia
8. Yun Seong, S., Sitti, M.: Surface-tension-driven biologically inspired water strider robots: theory and experiments. *IEEE Trans Rob* **23**(3), 578–589 (2007)
9. Gao, X., Jiang, L.: Biophysics: Water-repellent legs of water striders. *Nature*, 432, 36 (2004)
10. Wu, L., Lian, Z., Yang, G., Ceccarelli, M.: Water dancer II-a: a non-tethered telecontrollable water strider robot. *Int. J. Adv. Rob. Syst.* **8**(4), 10–17 (2011)
11. Wang, L., Gao, T., Gao, F., Dong, L., Wu, J.: Dynamic research on a water walking robot inspired by water striders. In: *Second symposium international computer science and computational technology*, pp. 439–442. Huangshan, China (2009)
12. Ozcan, O., Han, W., Taylor, J.D., Sitti, M.: Surface tension driven water strider robot using circular footpads. In: *2010 IEEE International Conference on Robotics and Automation (ICRA)*, pp. 3799–3804. Anchorage, Alaska (2010)
13. Jie, Z., Xinbin, Z., Qinmin, P.: A water walking robot inspired by water strider. In: *2012 IEEE international conference on mechatronics and automation (ICMA)*, pp. 962–967. Chengdu, China (2012)

14. Ozcan, O., Wang, H., Taylor, J.D., Sitti, M.: STRIDE II: A water strider-inspired miniature robot with circular footpads. *Int J Adv Rob Syst* **11**, 85 (2014)
15. Zhang, X., Yan, J., Zhao, J., Gangfeng, L., Hegao, C., Pan, Q.: A miniature surface tension-driven robot mimicking the water-surface locomotion of water strider. In: 2015 IEEE international conference on robotics and automation (ICRA), pp. 3172–3177 (2015)
16. Song, Y.S., Sitti, M.: Surface-tension-driven biologically inspired water strider robots: theory and experiments. *IEEE Trans Rob* **23**, 578–589 (2007)
17. Irawan, A., Khi Khim, B.: A system for water monitoring. In: Malaysia Intellectual Properties Organization (MyIPO), (2014)
18. Lim, A.C., Irawan, A.: Polystyrene foam-based leg tip strider robot. In: The 2nd international conference on electrical, vol. Control and Computer Engineering 2013 (InECCE2013), pp. 143–146 (2013)
19. Wiley. <http://www.credoreference.com/book/wileysp>. Last accessed 25 June 2018

An Accurate Characterization of Different Water Properties Using Resonant Method for Underwater Communication Activity



Salwa Awang Akbar, Ahmad Syahiman Mohd Shah,
Airul Sharizli Abdullah, Nurhafizah Abu Talip Yusof, Sabira Khatun,
Syamimi Mardiah Shaharum and Mohamad Shaiful Abdul Karim

Abstract Underwater communication has a great importance in either industrial, military or for scientific purposes. The applications of underwater communication such as pollution monitoring, underwater surveillance and collection of scientific data from the bottom of the ocean require specific development of devices. In order to design these crucial devices for such activities, an accurate characteristic of water involved should be noted. The velocity of signal propagates in underwater is different from the speed of light in free space and closely related to complex permittivity. There are few types of water bodies such as rivers, streams, pond, bays, gulfs and seas where each of them possessed different characteristics. In this paper, the main focus is to determine the water bodies' characteristics by using material characterization method. This paper provides the characterization of the different water bodies such as tap water, river water, sea water and lake water where the complex permittivity are determined by using resonant method. Estimated complex permittivity of different water are in good agreement with existing method; the error is below than 6%. The present method shows a great potential to be used in characterizing wide-variety of liquid samples.

Keywords Underwater communication · Sea water · Complex permittivity Resonant method

1 Introduction

In recent year, communication devices such as mobile phone and personal computer are very essential to keep one connected with others. It is not limited only to terrestrial and satellite systems, researchers are now focusing on underwater com-

S. Awang Akbar · A. S. Mohd Shah · A. S. Abdullah · N. Abu Talip Yusof · S. Khatun
S. M. Shaharum · M. S. Abdul Karim (✉)
Faculty of Electrical and Electronics Engineering, Universiti Malaysia Pahang, 26600 Pekan,
Pahang, Malaysia
e-mail: mshaiful@ump.edu.my

© Springer Nature Singapore Pte Ltd. 2019
Z. Md Zain et al. (eds.), *Proceedings of the 10th National Technical Seminar on Underwater System Technology 2018*, Lecture Notes in Electrical Engineering 538,
https://doi.org/10.1007/978-981-13-3708-6_10

munication systems to provide the same facility for underwater environment [1]. However, the underwater communication is much more complex than the terrestrial communication due to the degradation of wave propagation velocity. In the free space, the propagation velocity of signal/wave is equal to speed of light. In other word, the effect of the permittivity can be ignored since the relative permittivity of free space is 1 and the velocity can be defined as $v = \frac{1}{\sqrt{\epsilon_0 \mu_0}}$, where ϵ_0 and μ_0 are permittivity and permeability of free space, respectively. Meanwhile, factors such as salinity, temperature and density of water mainly affect the electrical property (permittivity) of the propagated medium [2], which leads to different transmission characteristics and signal propagation's behavior. The wave propagation velocity is strongly depends on permittivity, ϵ and permeability, μ of the propagated medium which equates as $v = \frac{1}{\sqrt{\epsilon \mu}}$. Permeability, μ of water is same as permeability of free space. Therefore, designing underwater communication devices require an accurate characteristic (complex permittivity) of the nature involved since in our nature there are a lot of types of water bodies and each of them possessed different characteristics. It is necessary to characterize the different water bodies. The main techniques to characterize material in microwave region are free space [3], transmission-line [4–7] and resonant method [8–11].

In this paper, rectangular waveguide resonator is utilized in order to afford an accurate material characterization of the water bodies. The information of known characteristics obtained from the material characterization can be used to develop devices that are working well in underwater.

2 Method of Material Characterization

2.1 Resonant Method

Resonant method can only evaluate material at certain frequency (mono frequency), but this method is proven to be more accurate [8, 9] compared to other methods. In this paper, a rectangular waveguide resonator with adjustable size of windows, W (Fig. 1) is used in order to avoid the problems of not enough Q (quality) factor [12] and too small transmission wave. A closed system possessed a very high Q factor which approaching to infinity value. However, it is impossible to design a completely closed system so small openings in the system designed can cause the Q factor to drop to a certain value. Wide window has smaller Q factor if compared to narrower windows which means high Q factor can cause lower rate of energy loss. In order to provide high accuracy measurement of high-loss sample, large transmission signals are needed as the input to the cavity and it cannot be achieved with narrower windows. This is because narrower windows may cause the amplitude of S_{21} during measurement of high-loss materials to drop and possibly drop to the noise floor. This will cause inaccuracy in measurement readings so narrow windows are only suitable in measuring low-loss materials. Complex permittivity of sample is derived from

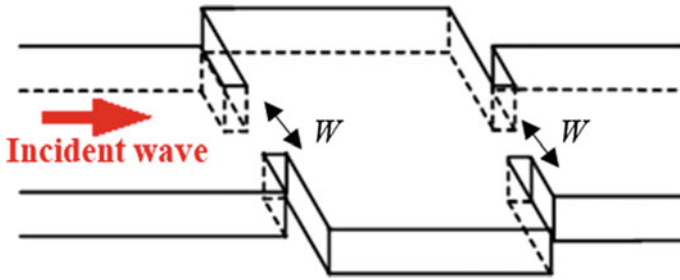


Fig. 1 Model of rectangular waveguide resonator with adjustable windows, W

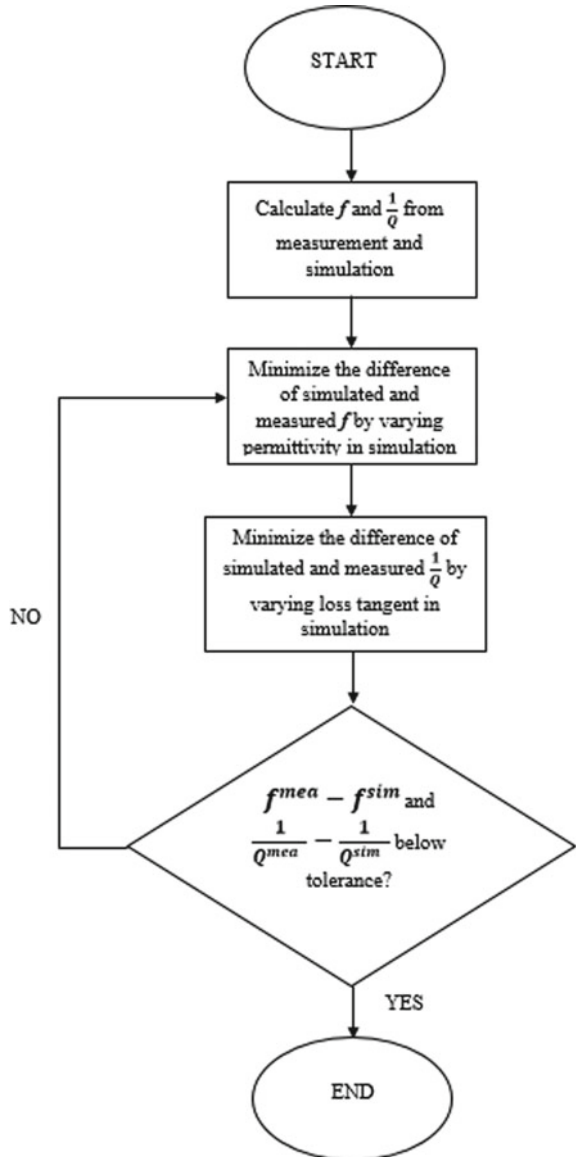
resonant frequency and Q factor based on inverse problem techniques that will be explained in the next sub-chapter. Q factor is calculated using basic resonant circuit theory i.e. using center and -3 dB points. In measurement, resonant frequency and Q factor are extracted from transmission parameters, S_{21} which affected by conductor loss and external loss. In conventional resonant method, the measurement values are simply compared to simulation values that based on resonant analysis. Resonant analysis in most simulation software neglects the factor of external Q factor and this may lead to the degradation of measurement accuracy. Therefore, in this paper, the simulation conducted based on scattering analysis [10] and then the resonant frequency and Q factor are derived from the S_{21} same as measurement.

2.2 Inverse Problem

The complex permittivity for the water bodies are obtained by using the inverse solving problem. It can be done by pre-assigning the permittivity and loss of tangent values in the simulation. The difference between the simulation and the measurement will be the factors in evaluating the characteristics of the unknown material. Figure 1 shows the rectangular resonator for characterizing the samples. Input (incident wave) is fed from one side of the adjustable window and scattering parameters S_{21} of the samples will be the output.

Figure 2 shows the inverse problem technique to derive complex permittivity and loss tangent from measured resonant frequency, f and Q factor. First, the resonant frequency and Q factor are derived from the measurement (f^{mea} , Q^{mea}) and simulation (f^{sim} , Q^{sim}) results. Then, the difference of resonant frequency between measurement and simulation results are minimized by varying the value of permittivity in simulation. When the difference is below than the tolerance, the last varied value of complex permittivity is considered as best suited value for the sample. Basically the technique is also applied when deriving the value of loss tangent. In order to derive the loss tangent values from this technique, the inverse Q factor value is used. The difference between the measurement and simulation result is calculated. Then the difference

Fig. 2 Flow chart to determine the complex permittivity of samples



between measurement and simulation result is minimized by varying the value of loss tangent in simulation. When the difference is below than the tolerance, the last varied value of loss of tangent is considered as best suited value for the sample.

3 Measurement

3.1 Sample Collection and Measurement Setup

Widely-characterized samples are used in the measurement to confirm the validity of this technique, i.e., tap water and seawater available from Universiti Malaysia Pahang neighborhood. In addition, underwater communication is not only limited to an ocean and a sea environment, therefore river water and lake water are also prepared to be characterized.

Four samples of water bodies consist of tap water, river water, seawater and lake water are collected for about 500 ml each and are placed in a room temperature. The water sample is filled inside a container with the same height as resonator, inner radius 3.41 mm and outer radius 4.81 mm.

3.2 Measurement Setup

Samples are evaluated using the resonant method where a rectangular waveguide resonator is used for the material characterization and the window size used in this measurement is 10 mm which can afford -5.16 dB of transmission wave and 2651 of Q factor. Figure 3 shows the measurement setup for rectangular waveguide resonator with WR-187 waveguide connected at each end. Samples are placed at the center of the resonator using low-loss sample container and then connected to the vector network analyzer (VNA) at operating frequency from 4 to 6 GHz.

4 Results and Discussion

The parameters such as the amplitude of S_{21} , resonant frequencies and bandwidth are obtained from the measurement. The water is kept in the room temperature around $25-27$ °C. After running the simulation, the results from the simulation are compared with the measurement results and the material characterization is performed as explained above. Figure 4 shows the results of the simulation and the measurement for empty cavity where both of them are compared. There is only small deviation of the resonant frequencies between the simulation and measurement so the results are fit in performing material characterization. From Fig. 4, the material characterization takes place at resonant frequency, 4.98 GHz where the mode is TE_{304} and the amplitude of S_{21} is -5.61 dB.

Table 1 shows the measured complex permittivity for all four types of water including the values from literature for comparison. The present method shows that the tap water has the highest permittivity followed by sea water, river water and lake water. Tap water also has the highest loss of tangent compared to the other three types

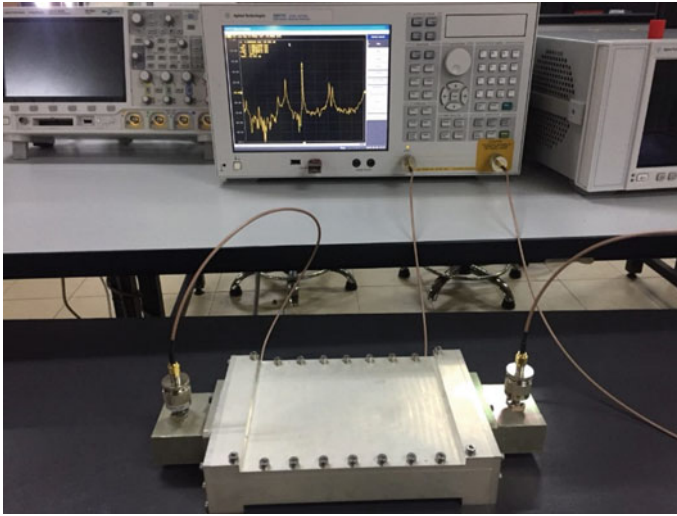


Fig. 3 Rectangular waveguide resonator with WR-187 connected to vector network analyzer

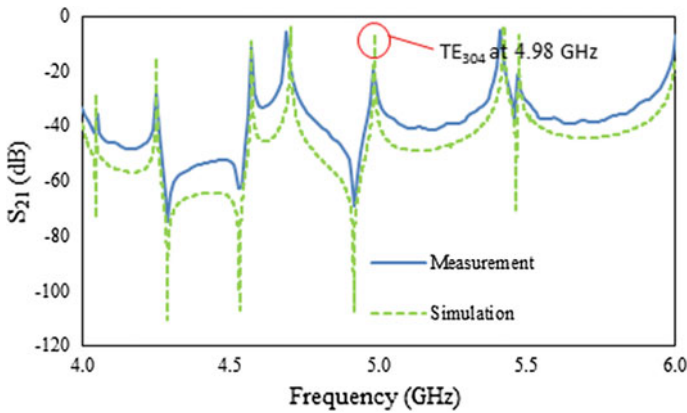


Fig. 4 Comparison between measurement and simulation result for empty cavity

of water. However, the literature value shows that the sea water has higher loss of tangent than the tap water. For tap water, the permittivity shows a good agreement with literature value [13], but not the loss tangent. This is probably because of the quality of tap water in Universiti Malaysia Pahang neighborhood is hugely affected by nearby seawater. The pH level for tap water in Universiti Malaysia Pahang neighborhood is quite higher than the normal pH level of tap water. While the permittivity and loss tangent for sea water are in the good agreement with literature [14]. The difference between permittivity and loss tangent of river water and lake water can be considered relatively small since they come from the same sources.

Table 1 Permittivity and loss of tangent for different water bodies

Sample	Present method		Literature value	
	Permittivity	Loss of tangent	Permittivity	Loss of tangent
Tap water	80.98	0.70	$\approx 77^{*1}$	$\approx 0.34^{*1}$
Sea water	73.89	0.42	$\approx 78^{*2}$	$\approx 0.45^{*2}$
River water	69.00	0.40	NA ^{*3}	NA ^{*3}
Lake water	67.02	0.30	NA ^{*3}	NA ^{*3}

*1 Measurement had been done at 25 °C at 4 GHz [13]

*2 Measurement had been done at 25 °C at 4 GHz and 25 ppt of salinity [14]

*3 Complex permittivity from literature are not available

5 Conclusion

The information of the complex permittivity is very crucial to help designer to design an efficient device for underwater activity. In this paper, high loss samples of different type of waters are characterized using rectangular waveguide resonator. The model employs scattering analysis instead of resonant analysis to provide an accurate estimation of complex permittivity of samples. Measurements at G-band are done for tap water, seawater, river water and lake water. Estimated complex permittivity of seawater by present method is in good agreement with existing method and confirms the validity of the characterization technique. While the estimation of river water and lake water show that the present method has an excellent potential in determining wide-variety of liquid or water.

Acknowledgements The work was partly supported by the Research and Innovation Department, Universiti Malaysia Pahang (grant number RDU170370).

References

1. Kaushal, H., Kaddoum, G.: Underwater optical wireless communication. *IEEE Access* **4**, 1518–1547 (2016)
2. Zhang, X., et al.: Underwater wireless communications and networks: theory and application: Part 1 [Guest Editorial]. *IEEE Commun. Mag.* **53**(11), 40–41 (2015)
3. Kim, S., et al.: A free-space measurement method for the low-loss dielectric characterization without prior need for sample thickness data. *IEEE Trans. Antennas Propag.* **64**(9), 3869–3879 (2016)
4. Karim, M.S.B.A., Konishi, Y., Kitazawa, T.: Robustness analysis of simultaneous determination method of complex permittivity and permeability. In: 2014 international conference on numerical electromagnetic modeling and optimization for RF, microwave, and terahertz applications (NEMO), pp. 1–4, Pavia (2014)
5. Karim, M.S.B.A., et al.: Determination of complex permittivities of layered materials using waveguide measurements. *IEEE Trans. Microw. Theory Tech.* **62**(9), 2140–2148 (2014)

6. Kobata, T., et al.: Determination of complex permittivity of materials in rectangular waveguides using a hybrid electromagnetic method. In: Computational electromagnetics workshop (CEM), pp. 56–57, Izmir (2013)
7. Karim, M.S.B.A., Kitazawa, T.: Determination of material parameters based on hybrid numerical methods using complementary source quantities. *IEICE Trans. Electron* **J98-C**, 356–365 (2015)
8. Baker-Jarvis, J., et al.: Dielectric characterization of low-loss materials a comparison of techniques. *IEEE Trans. Dielectr. Electr. Insul.* **5**(4), 571–577 (1998)
9. Baker-Jarvis, J. et al.: Dielectric and conductor-loss characterization and measurements on electronic packaging materials. In: Technical note (NIST TN), No. 1520 (2001)
10. Karim, M.S.B.A., Binti Abu Talip Yusof, N., Kitazawa, T.: Scattering analysis of rectangular cavity with input and output waveguides and its application to material characterization. In: *IEEE Asia Pacific Microwave Conference*, Kuala Lumpur, pp. 588–591 (2017)
11. Kinoshita, M., et al.: A method of evaluating high-permittivity and lossy materials using a cylindrical cavity based on hybrid electromagnetic theory. *Jpn. J. Appl. Phys.* vol. 9, pp. 09LF03–09LF03-5 (2012)
12. Krupka, J.: Properties of shielded cylindrical quasi-TE_{0mn}-mode dielectric resonators. *Trans. Microw. Theor. Tech.* **36**(4), 774–779 (1988)
13. Ellison, W.J.: Permittivity of tap water, at standard atmospheric pressure, over the frequency range 0–25 THz and the temperature range 0–100 °C. *J. Phys. Chem. Ref. Data* **36**(1) (2007)
14. Somaraju, R., Trumpf, J.: Frequency, temperature and salinity variation of the permittivity of seawater. *IEEE Trans. Antennas Propag.* **54**(11), 3441–3448 (2006)

Statistical Relationship Between Multibeam Backscatter, Sediment Grain Size and Bottom Currents



Mohd Azhafiz Abdullah, Razak Zakariya and Rozaimi Che Hasan

Abstract The bathymetry data and backscatter data are collected using multibeam sonar (MBES) system to recognize seafloor types was identified in the three study area coral reef, natural reef, and artificial reef. Ground truth data in using Ponar grab for collect sediment samples and ADCP in currents flow were is collected 34 stations.in the study, the relationship between backscatter, sediment grain size and bottom currents is examined using linear regression and multiple linear regressions. As a result, show that there is significant backscatter from multibeam sonar and ground truth data. In linear regression, relationship R^2 backscatter with sediment is a 0.703, sediment with bottom current (speed) is a 0.810 and multiple linear regression, relationship R^2 backscatter, sediment and currents is a 0.709. The study provided a good relationship between backscatter, sediment and currents (speed).

Keywords Backscatter · Sediment · Currents

1 Introduction

Seafloor mapping using multibeam echosounder is still being used around the world. Multibeam able to sounding with broad scope, high accuracy and can be used to determine characteristics of seabed type [1–6]. Backscatter is important for determining underwater conditions. Backscatter intensity was obtained from the signal receiver provide preliminary information on sediments type in sounding location spatially [6–13].

M. A. Abdullah (✉) · R. Zakariya
School of Marine Science and Enviroment, University Malaysia Terengganu, 21300 Kuala Nerus,
Terengganu, Malaysia
e-mail: azhafiz88@gmail.com

R. C. Hasan
UTM Razak School of Engineering and Advanced Technology, Universiti Teknologi Malaysia,
Jalan Semarak, 54100 Kuala Lumpur, Malaysia

© Springer Nature Singapore Pte Ltd. 2019
Z. Md Zain et al. (eds.), *Proceedings of the 10th National Technical Seminar
on Underwater System Technology 2018*, Lecture Notes in Electrical Engineering 538,
https://doi.org/10.1007/978-981-13-3708-6_11

Sedimentation and erosion processes are influenced by hydro-oceanography factors. Factor such as the currents that cause the sediment process is large enough to affect the occurrence of siltation. The process of silting occurs because of the sediment that moves significantly and spreads between the bottom surfaces. Sediment distribution that occurs can be classified in the form of distribution patterns based on the size and type of sediment. The dominant factor in the process of erosion and sedimentation are waves, currents, and tides as they interact directly with the coastal areas [14].

The grain size of deposited sediments depends on the velocity of the bottom currents. In high energetic environments (high speed of current), the larger material is precipitated. The speed of the current decreases the farther it moves and finer material is deposited. This process results in a correlation between distance to the continent, water depth and grain size: The farther away from the continent, the larger the water depth and the smaller the grain size.

In this study, linear regression was adopted to quantify the relationships between (a) backscatter and sediment grain size and (b) sediment grain size and bottom currents. The multiple linear regression for the relationship backscatter grain size sediment and bottom currents. The correlations investigated were measured by the R-square (coefficient of determination), representing the variation in backscatter explained by each sediment grain size and bottom currents as between 0 and 1.

2 Materials and Methods

2.1 Study Area

The Pulau Payar is located approximately 29 km off Kedah state, on the east coast of Peninsular Malaysia. This island lies between $6^{\circ} 03' 45.28''\text{N}$ and $100^{\circ} 02' 24''\text{E}$ in the strait of Malacca. Pulau Payar covers three islands comprising of Pulau Segantang, Pulau Lembu and Pulau Kaca. The Pulau Payar is rich in coral reefs and gazetted as a full marine park under the Establishment of Marine Park Malaysia in the year 1994. Pulau Payar is the biggest of the entire island in the marine protected areas (MPAs) measuring about 7 km long and 6 km wide.

The Pulau Bidong is located approximately 35 km off Terengganu state, on the east coast of Peninsular Malaysia. This island lies between $5^{\circ} 37' 16.00''\text{N}$ and $103^{\circ} 03' 39''\text{E}$ of the South China Sea, which is a well-known island with the history of Vietnamese refugees. The island also consists of well-developed coral reef ecosystems which engage a variety of coral and rocky reef-associated fishes [15]. Basically, the data of this study is based on the data collected on the south of the Pulau Bidong which is at the coral patch. Figure 1 shows the area under studies.

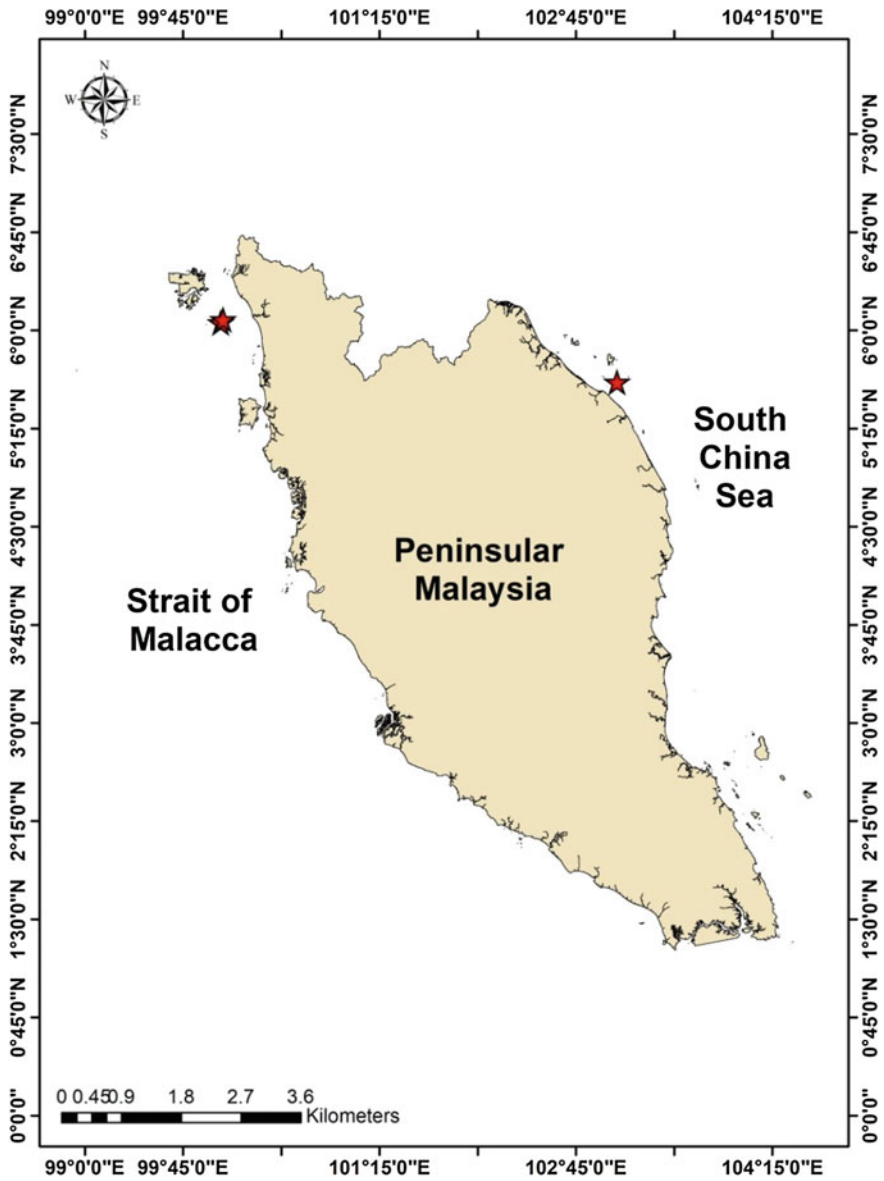


Fig. 1 Study Area Pulau Payar (Natural Reef and artificial reef) and Pulau Bidong (Coral Reef)

2.2 Currents

Nortel Acoustic Doppler Current Profiler (ADCP) is used to measure current speed at each sampling point. This ADCP probe has a frequency range of 400 kHz with a

maximum profiling range of 90 m. ADCP position during measurement is positioned down to the side of the vessel during the sampling period. ADCP has been set to profiles of 35 layers of depth 1 m each. ADCP has been set to profiles of 35 layers of depth 1 m each. ADCP profile and each layer for every two minutes with 10 s average time for each observation. The data used in the bottom surface current to the relationship in sediment sample and backscatter data.

2.3 Sediment Grain Size Information

The sediment samples were collected from 10 stations in the artificial reef area, 13 stations natural reef area and 12 station coral reef, respectively. Sampling point was selected in the area of the shipwreck in the sense of fulfilling the purpose of obtaining the sediment distribution in the study areas, a sediment sampler (Ponar grab) was used because it is compatible and easy to handle. Samples ranges from 1 to 7 cm thick were taken from the surface layer, then were placed in plastic bags, labeled and brought back to the laboratory for analysis

Sediment analyses were carried out to find the grain size of the sediments using the standard of dry and wet sieving techniques. For the coarse fraction, particles with a diameter greater than 63 μm were analyzed using dry sieving techniques. Approximately 100 g of the samples were passed through a set of sieves arranged consecutively finer downwards. Sieving time was between 15 and 20 min per sample using a sieve shaker. For silt and clay (particles with diameters lesser than 63 μm), the laser diffraction method using a Particle Size Analyzer (PSA) CILAS 1180 was employed to obtain the statistical value. The classification between coarser and finer particles was based on Went-worth's scale [16]. Based on the data obtained, statistical measures were calculated, and computation of mean size (ϕ), sorting (ϕ) and measurement of skewness was carried out using the moment method of Folk and Ward [17].

2.4 Acoustic Data Acquisition and Processing

Acoustic data acquired natural reef area, artificial reef area and coral reef. Multibeam echosounder system (MBES) R² Sonic 2020 is used in this study for collecting bathymetry image and backscatter image. The average speed for survey vessel is 5 knot. This instrument produces 256 beams equiangular arrayed over an arc of 130° and at the frequency of 400 kHz. Differential Global Position System (DGPS), Trimble 461 was used for system navigation and heading (gyrocompass). The vessel's motion was quantified using DMS10 motion sensor with 0.05° accuracy for heave, roll and pitch. Real-time speed of sound for MBES transducer is measured using Valeport Mini sound velocity sensor (SVS). Software QINSy v8.0 was used during a survey for data logging, real-time quality control, display and navigation. The sound

velocity profile (SVP) collect from cast away-CTD was used for measuring sound velocity during data acquisition to correct the effect of refraction.

The bathymetry raw data was processed using Qimera software version 1.4. Huang et al. in [18] recommended the bathymetry raw data to be processed according to the following steps: (1) Correct the sound velocity variation of the water column, (2) correct the measurement of depth of tide water, (3) correct the motion sensor information, (4) removal of spike or noise. The MBES backscatter raw data were processed in Fledermaus Geocoder Toolbox software version 7.4 (FMGT) to obtain backscatter mosaic [8]. In [19, 20], this software applied for manual FMGT processing procedure to generate backscatter mosaic. The backscatter intensity data were filtered based on beam angle, and then an anti-aliasing pass was run on the result.

2.5 *Linear Regression*

The data is analyzed in two different ways in the SPSS 22 which are constant variables (Backscatter and sediment grain sizes) and outputs are classified from software (sediment grain size and bottom currents). In terms of statistical analysis, continuous data is analyzed using linear regression. Linear regression uses the relationship between the response variable or the dependent variable and the descriptor variable or the independent variables, to minimize the remaining squared.

2.6 *Multiple Linear Regression*

Multiple linear Regressions is simply extended a form of Simple regression in which two or more variables are independent variables are used and can be expressed as:

$$Y = a + bX_1 + cX_2 \quad (1)$$

where: Y = lead dependent variable; X₁, X₂ = all independent variables including grain size sediment and bottom currents. The concentration of lead was chosen as the dependent variable chosen as dependent variable in the multiple linear regressions of backscatter intensity (dB). The interested independent variables included in the proposed multiple linear regressions were selected on grain size sediment and bottom currents. The order of independent variables could varied depending on the result of the regression analysis [21, 22].

3 Result

3.1 Backscatter Map

The backscatter mosaic is a picture of seeing the floor that storage information from seabed features such as intensity in time series or beam average. Backscatter mosaics can be used as initial information to see the distribution of intensity value sounding results. Figure 2 shows the backscatter mosaic intensity from the seabed. Backscatter intensity of natural reef range from -44 to -79 dB, artificial reef range from -41 to -70 dB and coral reef range from -36 to -63 dB. This value is obtained from the ratio between power transmitted and power received by the transceiver. Based on the distribution, higher intensity is observed in the nadir area. This is because the signal is still in aperture or known as the narrow beam.

3.2 Ground Truth Data

Based on the analyzed results, grain size sediment measurements have been taken for 35 samples in 3 different areas i.e. natural reefs (13 samples), artificial reefs (10 samples) and coral reefs (12 samples). The sediment type consists of granule very coarse sand, median sand coarse sand, very fine sand, coarse silt, medium silt. Table 1 shows the station of samples collected from 35 ground truth stations with backscatter, sediment and currents.

3.3 Relationship Between Backscatter Intensity (dB), Sediment Grain Size (Mm) and Currents ($M s^{-1}$)

The backscatter intensity data was compared with sediment grain size and bottom currents classes using linear regression. Figure 2a shows the backscatter intensity is directly correlated with sediment grain size and inversely correlated with bottom currents. Based on the result, linear regression was used for comparison of backscatter and sediment grain size. It allows detection of the true effects of coupling method when it exists. The linear regression analysis of backscatter intensity and sediment size shows the multiple R-value is 0.839 and the adjusted R^2 value is 0.703. The standard error is 2.571. The P value is computed using R^2 and degree of freedom (Df) with $P < 0.0001$ and considered to be statistically significant. The first graph generated from the backscatter data processing and grain size sediment is determined by the coefficient of determination. The result obtained has BS equation (dB) = $0.12(x) + 7.343$. The first graph shows the relationship between two relatively high variables by looking at the value of R^2 of 0.703. By increase the particle size of the

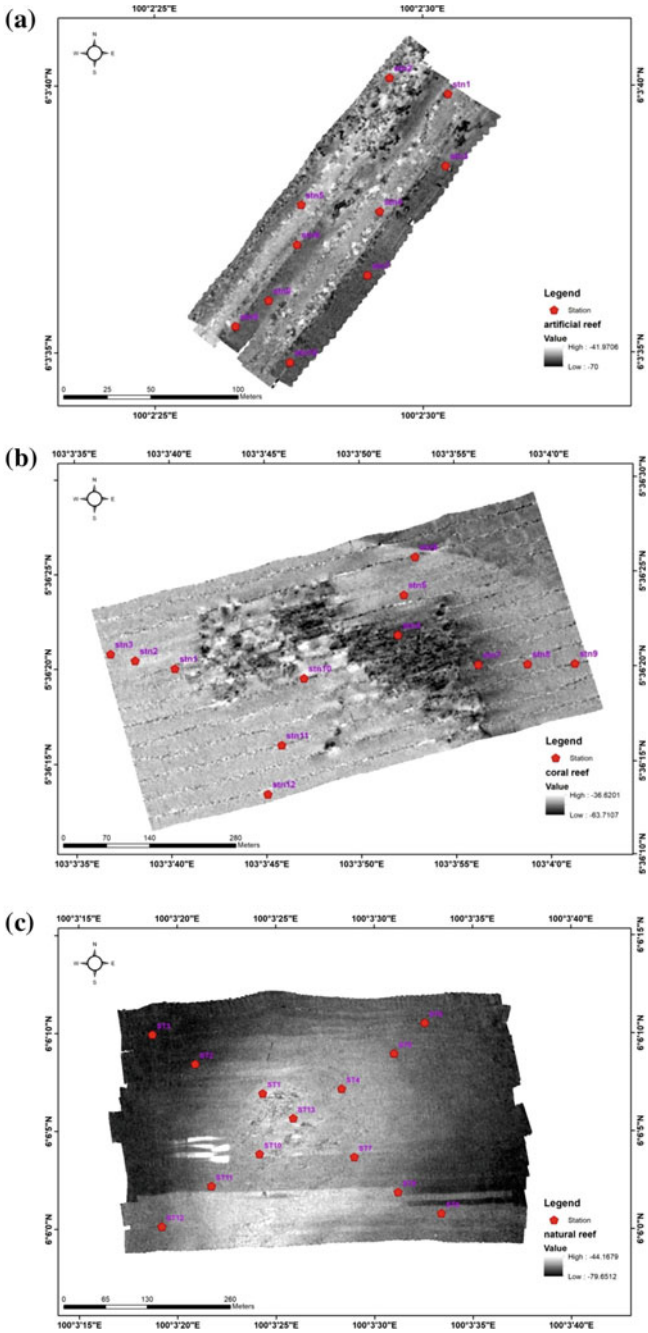


Fig. 2 Acoustic data of the study area multibeam backscatter with the positions of ground truth station in **a** artificial reef, **b** coral reef and **c** natural reef

Table 1 Station of samples collected from 35 ground-truth stations with backscatter, sediment and currents

Area	Station	Backscatter	Grain size (mm)	Sediment	Current (speed ms^{-1})
Coral reef	1	-47.331	1.137	Very coarse sand	0.169
	2	-47.961	1.362	Very coarse sand	0.162
	3	-48.271	1.808	Very coarse sand	0.253
	4	-48.271	1.653	Very coarse sand	0.224
	5	-47.641	1.595	Very coarse sand	0.217
	6	-47.011	1.678	Very coarse sand	0.331
	7	-47.961	1.851	Very coarse sand	0.258
	8	-48.591	1.638	Very coarse sand	0.26
	9	-48.901	1.594	Very coarse sand	0.228
	10	-47.011	1.279	Very coarse sand	0.163
	11	-45.4411	2.025	Granule	0.301
	12	-45.751	2.511	Granule	0.796
Artificial reef	1	-52.370	1.21	Very coarse sand	0.225
	2	-57.411	0.015	Medium silt	0.024
	3	-51.740	0.908	Coarse sand	0.08
	4	-54.261	0.497	Medium sand	0.054
	5	-47.331	1.20	Very coarse sand	0.278
	6	-53.001	1.087	Very coarse sand	0.297
	7	-52.680	0.507	Coarse sand	0.071
	8	-56.781	0.035	Coarse silt	0.0082
	9	-52.680	0.507	Coarse sand	0.073
	10	-52.370	0.774	Coarse sand	0.012
Natural reef (rock)	1	-53.430	1.25	Very coarse sand	0.204
	2	-56.351	0.63	Coarse sand	0.092
	3	-60.451	0.02	Coarse silt	0.014
	4	-54.910	1.42	Very coarse sand	0.201

(continued)

Table 1 (continued)

Area	Station	Backscatter	Grain size (mm)	Sediment	Current (speed ms ⁻¹)
	5	-55.641	0.91	Coarse sand	0.09
	6	-60.871	0.04	Coarse silt	0.011
	7	-56.261	1.01	Very coarse sand	0.163
	8	-59.750	0.04	Coarse silt	0.011
	9	-55.910	0.06	Very fine sand	0.027
	10	-55.560	1.00	Very coarse sand	0.293
	11	-56.411	0.88	Coarse sand	0.094
	12	-61.451	0.04	Coarse silt	0.0243
	13	-54.490	1.57	Very coarse sand	0.216

particle grains, will affect the value of backscatter produced. The x-axis is the grain size (mm) and the y-axis as the backscatter value (dB).

The backscatter values resulting from four types of sediments such as gravel, sand, mud and clay indicate a relation to grain size [23]. The same statement is also explained by Pujiyati [24] that the backscatter value is affected by the particle size of the particle. In addition to particle size grains, basal water backscatter values can be expected to be influenced by other factors such as porosity, organic matter content and biota present in the sediments. Additionally, the linear regression analysis (see Fig. 4b) Grain size sediment and bottom currents show the multiple R-value was 0.9004 and the adjusted R² value was 0.8107. The value of standard error was 0.2946 and based the P value was computed using R² and degree of freedom (Df) with *P* < 0.0001 and considered to be statistically significant. The second graph is the result of the relation of the value of backstroke with bottom current which has the equation (mm) = 0.15995 (x) + 0.0029245. The meaning of this statement is that the increasing value of bottom currents, it will affect the value of grain size sediment produced, between the two high variables by looking at the value of R² of 0.8107 x-axis as the grain size (mm) and the y-axis as the bottom current value (ms⁻¹). Many authors [25–29] have studied the relationship between mean grain size sediment and current speed. Many transport equations are developed for different parameters [29] (Figs. 3, 4 and 5).

Multiple linear regression was used for comparisons of backscatter from the image, grain size sediment and bottom currents. It allows detection of the true effects of coupling methods when it exists. The multiple linear regression analysis of Backscatter from image grain size sediment and bottom currents show significant at 95% confidence level (n = 35, R² = 0.709). The multiple R value was 0.842 and the adjusted R² value was 0.6904. The value of standard error was 2.588. The *P* value

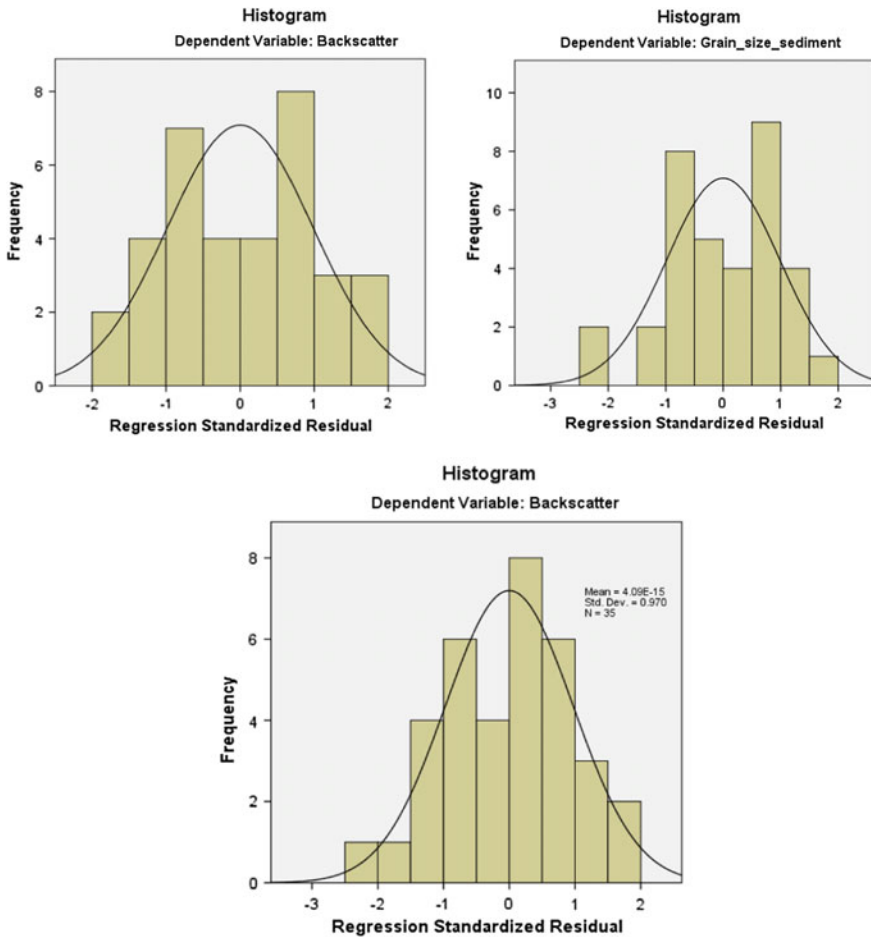


Fig. 3 Standardized residual analysis

was computed using R^2 and degree of freedom (Df) with $P < 0.0001$ and considered to be extremely statistically significant. It is considered that following Eq. 2:

$$Y = -58.649 + 6.90 X_1 - 6.53 X_2 \tag{2}$$

Based on the result, According to the general Eq. (2) for multiple linear modeling by taking the unstandardized coefficients as using the SPSS 22, which X_1 = grain size sediment, X_2 = bottom currents, while Y = lead. The proposed model (2) means that the interested predictors (grain size sediment and bottom currents) yielded a linear impact on the lead (Table 2).

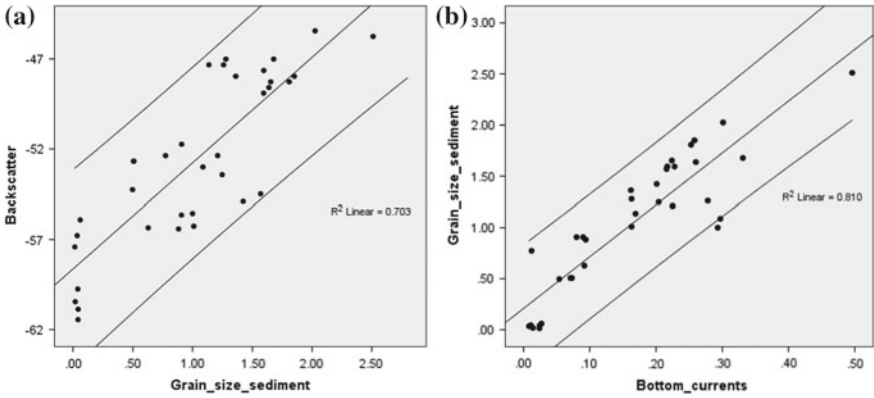


Fig. 4 Linear regression **a** backscatter intensity (dB) and Grainz size (mm) **b** Grain size (mm) and Bottom currents (ms⁻¹)

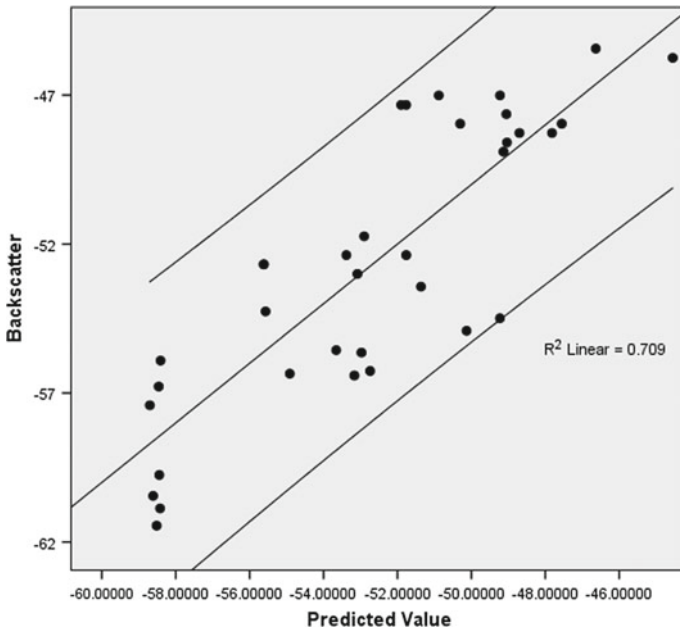


Fig. 5 Multiple linear regression backscatter intensity (dB), Grainz size (mm) and Bottom currents (ms⁻¹)

Table 2 Summary model for linear regression and multiple linear regressions

Regression	Model	Equation	R ²
Linear regression	Backscatter-grain size sediment	$Y = 0.12009x + 7.3437$	0.703
Linear regression	Grain size sediment—bottom currents	$Y = 0.15995x - 0.0029$	0.810
Multiple linear regression	Backscatter-grain size sediment—Bottom currents	$Y = -58.649 + 6.90 X_1 - 6.53 X_2$	0.709

4 Conclusion

The combination statistics for backscatter, grain size sediment and bottom sediment was investigated in the 3 study area is a coral reef, natural reef, and artificial reef using linear regression and multiple linear regressions. Backscatter intensity was much more strongly correlated with grain size sediment of R² is a 0.703 and bottom current of R² is a 0.8107 using linear regression. The Multiple linear regression analysis of Backscatter, grain size sediment and bottom current of R² is a 0.6904. This study has set out to examine the validity of relationship in a field setting, with realistic data. It is intended to give end users a realistic view of useful or reliable acoustic data could be in term of trying to predict material properties of the seafloor.

References

1. Anderson, J.T., Holliday, V., Kloser, R., Reid, D. & Simard, Y.: Acoustic seabed classification of marine physical and biological landscapes. International Council for the Exploration of the Sea, p. 198. Copenhagen, Denmark (2007)
2. Anderson, J.T., van Holliday, D., Kloser, R., Reid, D.G., Simard, Y.: Acoustic seabed classification: current practice and future directions. *J. Mar. Sci.* **65**(6), 1004–1011 (2008)
3. Fernandes, W, Chakraborty, B.: Multi-beam backscatter image data processing techniques employed to EM 1002 system. 2009 International symposium on ocean electronics (SYMPOL 2009), pp. 93–99. Cochin, India (2009)
4. Brown, C.J., Smith, S.J., Lawton, P., Anderson, J.T.: Benthic habitat mapping: a review of progress towards improved understanding of the spatial ecology of the seafloor using acoustic techniques. *Est. Coast. Shelf Sci.* **92**(3), 502–520 (2011)
5. Hasan, R.C., Ierodiaconou, D., Rattray, A., Monk, J., Laurenson, L.: Applications of multi-beam echosounder data and video observations for biological monitoring on the south east Australian continental shelf. In: International symposium and exhibition on geoinformation 2011 (ISG2011) & ISPRS 2011, pp. 1–16. Shah Alam, Malaysia (2011)
6. Manik, H.M.: Underwater acoustic detection and signal processing near the seabed. *Sonar System, N. Z. Kolev, IntechOpen*, 225–274 (2011)
7. Jackson, D., Brigs, K.: High-frequency bottom backscattering roughness versus sediment volume scattering. *J. Acoust. Soc. Am.* **92**(2), 962–977 (1992)
8. Fonseca, L., Mayer, L.: Remote estimation of surficial seafloor properties through the application angular range analysis to multibeam sonar data. *Mar. Geophysical Res.* **28**(2), 119–126 (2007)

9. Jackson, D., Richardson, M.: High-frequency seafloor acoustics. The underwater acoustics series, pp. 1–442. Springer, New York (2007)
10. Tegowski, J., Gorska, N., Kruss, A., Nowak, J., Blenski, P.: Analysis of single beam, multibeam and sidescan sonar data for benthic habitat classification in the southern Baltic Sea. In: Proceedings of the 3rd international conference and exhibition on underwater acoustic measurements: Technologies and Results, pp. 21–26, Poland (2009)
11. Ruiz-Cortés, V., Dainty, C.: Backscattering measurements from double-scale randomly rough surfaces. *J. Opt. Soc. Am. A* **29**(6), 1154–1160 (2012)
12. Huang, Z., Siwabessy, J., Nichol, S., Anderson, T., Brooke, B.: Predictive mapping of seabed cover types using angular response curves of multibeam backscatter data: Testing different feature analysis approaches. *Continental Shelf Res.* **61**, 12–22 (2013)
13. Zhi, H., Siwabessy, J., Nichol, S.L., Brooke, B.P.: Predictive mapping of seabed substrata using high-resolution multibeam sonar data: a case study from a shelf with complex geomorphology. *Mar. Geol.* **357**, 37–52 (2014)
14. Dyer, K.R.: *Coastal and Estuarine Sediment Dynamics*. Wiley Interscience, Chichester, New York, Brisbane, Toronto, Singapore (1986)
15. Matsunuma, M., Motomura, H., Matsuura, K., Shazili, N.A.M., Ambak, M.A. (eds.): *Fishes of Terengganu-East coast of Malay Peninsula, Malaysia*, National Museum of Nature and Science, Tokyo, Universiti Malaysia Terengganu, Terengganu, and Kagoshima University Museum, Kagoshima, 251 pp (2011)
16. Wentworth, C.K.: A scale of grade and class terms for clastic sediments. *Geol. J.* **30**, 377–392 (1922)
17. Folk, R.L., Ward, W.C.: Brazos river bar: a study on significance of grain size parameters. *J. Sediment. Petrol.* **31**, 514–529 (1957)
18. Huang, Z., Siwabessy, J., Nichol, S.L., Brooke, B.P.: Predictive mapping of seabed substrata using high-resolution multibeam sonar data: a case study from a shelf with complex geomorphology. *Mar. Geol.* **357**, 37–52 (2014)
19. Quas, L., Church, I., O’Brien, S. J., Wiggert, J. D. & Williamson, M.: Application of high-resolution multibeam sonar backscatter to guide oceanographic investigations in the Mississippi Bight. In: *US Hydro2017 (USHYDRO2017)*, pp. 1–15, Galveston, USA (2017)
20. QPS: *FMGeocoder Toolbox Online Manual, Fledermaus 7.7.x Documentation* (2016)
21. Chatterjee, S., Price, B.: *Regression analysis by example*, 2nd edn, Wiley, New York (1997)
22. George, D., Maller, P.: *SPSS for Windows Step by Step. A Simple Guide and Reference* 11 Update, 4th edn, Pearson Education, Inc., Boston (2003)
23. Stanic, S., Briggs, K.B., Fleischer, P., Sawyer, W.B., Ray, R.I.: High frequency acoustic backscattering from a coarse shell ocean bottom. *J. Acoust. Soc. Am.* **85**, 125–136 (1989)
24. Pujiyati S., Hartati S., Priyono, W.: Effect of size of granules, roughness, and basic hardness of waters on the returning value of hydro acoustic detection results. *E-J. Trop. Mar. Sci. Technol.* **2**(1), 59-67 (2010)
25. Shields, A.: Application of similarity principles and turbulence research to bedload movement. *Mitteilungen der Preussischen Versuchs anstalt für Wasserbau und Schiffbau, Berlin*. In: Ott, W.P., van Uchelen, J.C. (eds.) *California Institute of Technology. W. M. Kech Lab. of Hydraulics and Water Resources*, Rept. No. 167 (1936)
26. Vanoni, V.A. (ed.): *Sedimentation Engineering, Manual and Reports on Engineering Practice*. No. 54. American Society of Civil Engineers, New York (1977)
27. Gao, S., Collins, M.: Net sediment transport patterns inferred from grain- size trends, based upon definition of “transport vectors” *Sediment. Geol.* **81**(1–2), 47–60 (1992)
28. Li, M.Z., Amos, C.L.: SEDTRANS96: the upgraded and better calibrated sediment transport model for continental shelves. *Comput. Geosci.* **27**(6), 619–645 (2001)
29. Yang, C.T.: Non cohesive sediment transport. In: Yang, C.T. (ed.), *Erosion and Sedimentation Manual: U.S. Bureau of Reclamation, Technical Service Center, Denver, CO*, chapter 3, 111 p (2006)

Part II
Control, Instrumentation and Artificial
Intelligent Systems

Stabilization of Two-wheeled Wheelchair with Movable Payload Based Interval Type-2 Fuzzy Logic Controller



N. F. Jamin, N. M. A. Ghani, Z. Ibrahim, M. F. Masrom and N. A. A. Razali

Abstract In this paper, an Interval Type-2 Fuzzy Logic Control (IT2FLC) is proposed to control a stabilization of two-wheeled wheelchair system with moving payload. The two-wheeled wheelchair system is similarly with double-links inverted pendulum system but with additional of movable payload up to 0.3 m to reach a higher level of height. Thus, this two-wheeled wheelchair configuration becomes more complex, unstable and highly nonlinear system. The 300 N concentrated force is applied at the back of the wheelchair seat in two conditions; in the initial condition before the payload is lifted and in the maximum height of the payload to test the robustness of the controller. SimWise 4D (SW4D) software is used to develop a 3-Dimensional (3D) model of the two-wheeled wheelchair, which replaces a complex mathematical representation. The SW4D is used to visualize the movement of the system as it is integrated with Matlab Simulink. IT2FLC will be compared with Fuzzy Logic Control Type 1 (FLCT1) and the simulation results show that the IT2FLC give a good performance in term of angular position of both links in the upright position and maintain stable.

Keywords Two-wheeled wheelchair with movable payload
Double-link inverted pendulum · Interval Type-2 fuzzy logic control
SimWise 4D

1 Introduction

Generally, disabled and elderly people depend on the use of wheelchair as an important transportation device to perform their daily routine and mobile from one place to another independently.

N. F. Jamin (✉) · N. M. A. Ghani · M. F. Masrom · N. A. A. Razali
Department of Electrical & Electronics Engineering, Universiti Malaysia Pahang, Pekan, Malaysia
e-mail: nunfadz86@gmail.com

Z. Ibrahim
Department of Manufacturing Engineering, Universiti Malaysia Pahang, Pekan, Malaysia

© Springer Nature Singapore Pte Ltd. 2019
Z. Md Zain et al. (eds.), *Proceedings of the 10th National Technical Seminar on Underwater System Technology 2018*, Lecture Notes in Electrical Engineering 538,
https://doi.org/10.1007/978-981-13-3708-6_12

Basically, the movable two-wheeled wheelchair system uses the same concept as double-link inverted pendulum which is known as very unstable and complex system. Stabilization of inverted pendulum system is a very challenging problem and it has three important aspects need to be considered; swing-up, stabilization, motion and steering motion. There are several types of inverted pendulum system; single link inverted pendulum, double-links inverted pendulum and triple-links inverted pendulum and the mechanism varies from inverted pendulum on cart [1] inverted pendulum with rotational [2] to inverted pendulum on two-wheels [3–6].

Many control algorithms for inverted pendulum system stability has been presented by a several researches including Sliding Mode Control (SMC) [7–10], Fuzzy Logic Control (FLC) [11–14], Linear Quadratic Regulator (LQR) [15, 16], Neural Network based controller (NN) [17, 18] and Proportional Integral Derivative (PID) [19]. The IT2FLC controller also has been applied successfully to control an autonomous wheeled inverted pendulum robot [20–24] with a good result in their research. The existing researcher has been applied IT2FLC for robot navigation, to control a positioning of the wheeled robot, to control the stability of trajectory-tracking and the stability of the inverted pendulum robot. However, none of them applied IT2FLC to control a stability of double inverted pendulum system.

There are authors who applied IT2FLC to control the stability of two-wheeled wheelchair [28] and self-balancing iBot-like wheelchair [29]. The two-wheeled wheelchair uses double link inverted pendulum system by transforming from four-wheeled to two-wheeled wheelchair. However, the design of their two-wheelchair is not a movable payload. In this paper, a double inverted pendulum two-wheeled wheelchair with movable payload is implemented using IT2FLC controller. The performance of wheel displacement, angular Link1 and angular Link2 are analyzed by integrating the design in SW4D with Matlab. This paper is organized as follow. Section 1 is introduction of the study. In Sect. 2, the system model and parameters is presented. Section 3 is the IT2FLC architecture. Section 4 is the simulation results and discussion. The conclusion is explained in Sect. 5.

2 System Model and Parameters

In this research, a complex derivations and long equations of mathematical modeling is replaced with the use of SW4D software. The two-wheeled wheelchair with movable payload is modeled for motion visualization using SW4D software environment when executing the Matlab Simulink program.

The two-wheeled wheelchair with a movable payload is modeled using double-links inverted pendulum system as shown in Fig. 1. The model comprises of a bottom base that is connected to the left wheel and right wheel using motor for each, first link that is fixed to the base, followed by second link that is connected with the first link using a motor, seat is connected with the second link using linear actuator and the humanoid that was attached on top. Figure 2 shows the schematic diagram of the two-wheeled wheelchair.

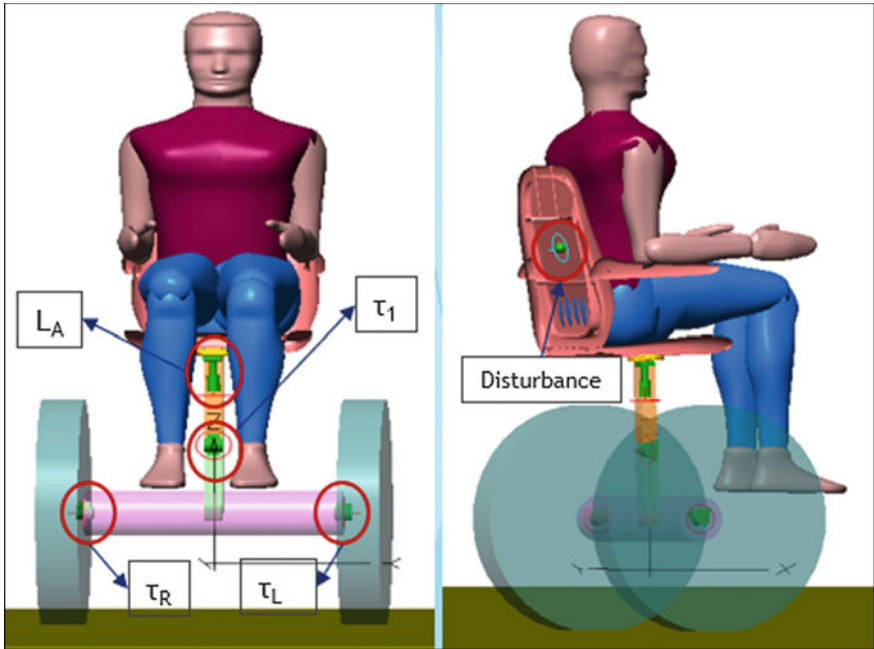
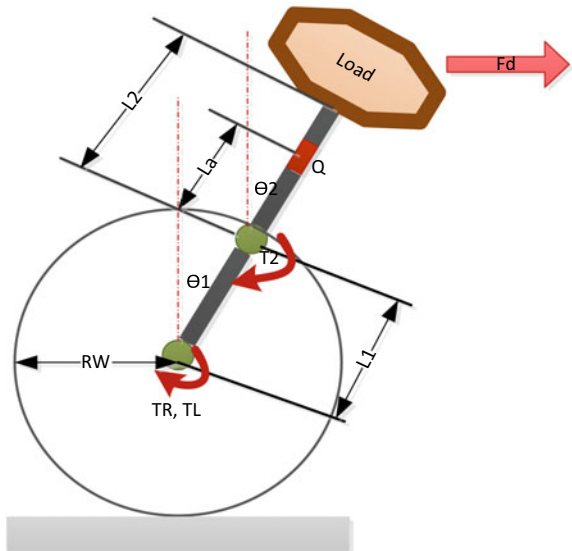


Fig. 1 Complete model of two-wheeled wheelchair with movable payload

Fig. 2 Schematic diagram of two-wheeled wheelchair



The basic wheelchair dimensions were taken from a standard wheelchair in the market by making some changes to produce a compact two-wheeled wheelchair,

Table 1 Parameters of two-wheeled wheelchair

Symbol	Description	Parameter
Θ_1, Θ_2	Angular position of Link1 and Link2	Degree
R_W	Radius of wheel	0.3 m
τ_R, τ_L, τ_2	Torque at right/left wheel and between Link1 & Link2	Nm
L_1, L_2	Length of Link1 and Link2	0.2, 0.22 m
Q	Displacement of the linear actuator	m
L_a	Length of linear actuator from the upper link	m
F_d	External disturbance force	N

Table 2 Basic dimension and specification of two-wheeled wheelchair with movable payload

Part	Size (m)	Weight (Kg)
Wheel	Radius = 0.3, Width = 0.09	1.5
Axle	Radius = 0.06, Length = 0.55	20
Link1	Width = 0.04, Length = 0.04, Height = 0.2	3
Link2	Width = 0.04, Length = 0.04, Height = 0.22	3
Chair seat	Width = 0.4, Length = 0.5, Height = 0.101	0.205
Back rest	Width = 0.04, Length = 0.04, Height = 0.22	0.3
Humanoid	Height = 1.75 m	70

lightweight and use less space to move. The torques τ_R , τ_L and τ_2 represent torque at the right wheel, torque between Link1 and Link2 respectively, while L_A represents a linear actuator to lift the seat. The entire torques are used to cater for the whole human body weight and the linear actuator is used to extend the seat to reach an optimal higher level. The dimension and specification of two-wheeled wheelchair model in SW4D is shown in Table 2 while the parameters of two-wheeled wheelchair are shown in Table 1.

3 Interval Type-2 Fuzzy Logic Controller (IT2FLC)

The purpose of using IT2FLC is to control the environmental disturbances, uncertainties and nonlinearities of the nonlinear system as two-wheeled wheelchair with movable payload. Many researches have been applied IT2FLC to control their difficult and complex system successfully [19–23, 25].

The architecture of IT2FLC consists of 5 components; fuzzifier, rule base, inference engine, type-reducer and defuzzifier as shown in Fig. 3. Basically, IT2FLC uses an Interval Type-2 Fuzzy Set (IT2FS) and the membership function of IT2FS includes upper boundary, lower boundary and footprint of uncertainty which is able to handle any nonlinearities and uncertainties as shown in Fig. 4. The flow of IT2FLC

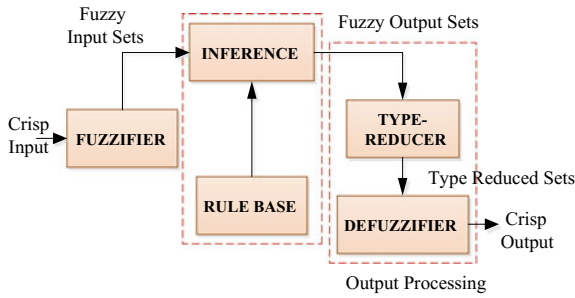


Fig. 3 Architecture of IT2FLC

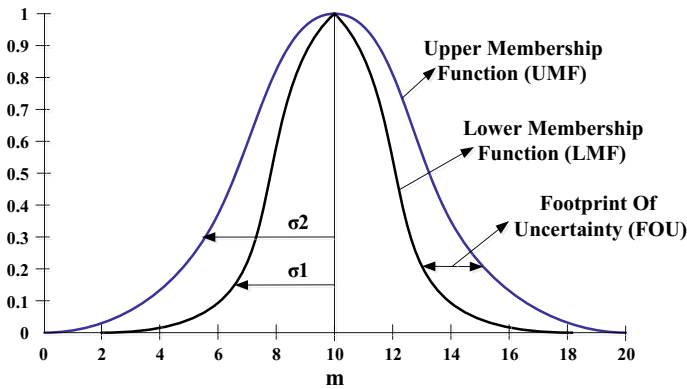


Fig. 4 Fuzzy set of IT2FLC

started with crisp input is fuzzified into IT2FS using singleton fuzzifiers then the fuzzy output will be produced when inference engine is activated by the input of IT2FS. After that, the type-reducer will convert the output of IT2FS from inference engine to Type-1 Fuzzy Set (T1FS) and lastly, the fuzzy output will convert back into crisp output in defuzzification process then sent to the actuators for control purpose [26].

A Sugeno-type fuzzy rules are adopted and two inputs to the IT2FLC are considered in this paper. The controller of IT2FLC is divided by two subsystems as there are two links considered in this work, the first subsystem IT2FLC1: the controller inputs are the change of error for angular position of Link1 ($\Delta e\theta_1$) and the error for angular position of Link1 ($e\theta_1$). The second subsystem IT2FLC2: the controller inputs are the change of error for angular position of Link2 ($\Delta e\theta_2$) and the error for angular position Link2 ($e\theta_2$). Figure 5 shows the two subsystems of IT2FLC in Matlab Simulink integrated with SW4D.

Table 3 shows 5 levels of membership functions using Gaussian resulting in 25 rules (5×5) comprises of $e\theta_1$, $\Delta e\theta_1$, $e\theta_2$, $\Delta e\theta_2$ and the output torque in IT2FLC and the IF-THEN rules is applied. In order to construct a rule base, the error of

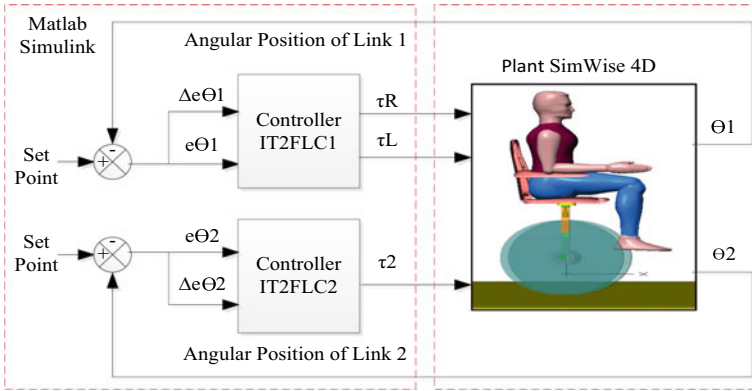


Fig. 5 Matlab Simulink integrated with SW4D

Table 3 Rules of IT2FLC for the control input of system

$E\Delta e$	NB	NS	Z	PS	PB
NB	PB	PB	PB	PS	Z
NS	PB	PB	PS	Z	NS
Z	PB	PS	Z	NS	NB
PS	PS	Z	NS	NB	NB
PB	Z	NS	NB	NB	NB

angular position, change of error of angular position and output torque are portioned into five levels of membership function.

Error of angular position, $e = \{NB \ NS \ Z \ PS \ PB\}$.

Change of error of angular position, $\Delta e = \{NB \ NS \ Z \ PS \ PB\}$.

Torque, $u = \{NB \ NS \ Z \ PS \ PB\}$.

The number of rule (nth) of the rule base for the IT2FLC, with the e , Δe and u , is given by,

R_n : IF (e is e_i), AND (Δe is Δe_j), THEN (u is u_k)

where, R_n is the nth fuzzy rule, $n = 1, 2, \dots, N_{max}$, e_i , Δe_j and u_k for $i, j, k = 1, 2, \dots, 5$ are the five levels of membership function [30]. The rules are typically fired as,

- If e is NB and Δe is NB then u is PB.
- If e is NB and Δe is NS then u is PB.
- If e is NB and Δe is Z then u is PB.
- If e is NB and Δe is PS then u is PS.
- If e is NB and Δe is PB then u is Z.

The Gaussian shape was used to represent the Sugeno-type IT2FLC algorithm because it gives smooth of output surface and steady response of the system [27] as shown in Fig. 6. The levels of membership function are negative big (NB), negative

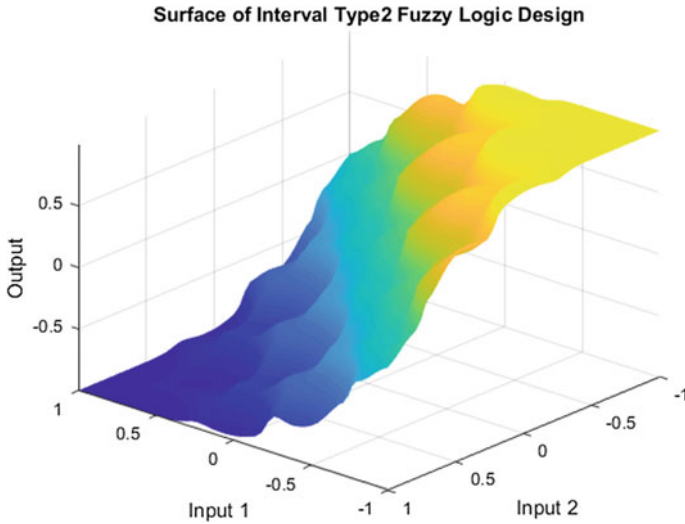


Fig. 6 Three-dimensional output surface of IT2FLC

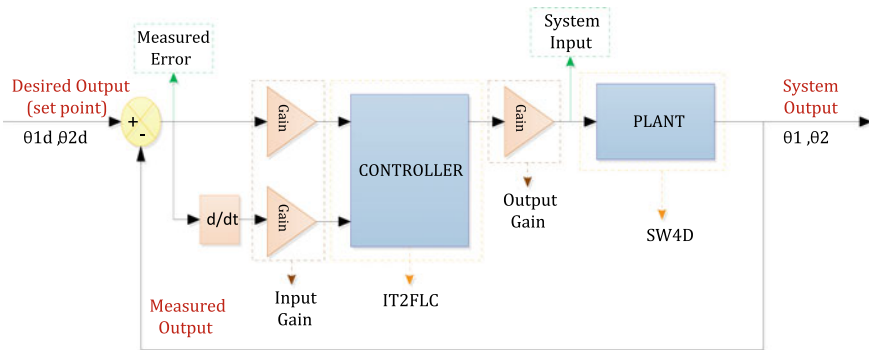


Fig. 7 General block diagram of MIMO of stabilization of two-wheeled wheelchair system

small (NS), zero (Z), positive small (PS) and Positive Big (PB) and the wheelchair system in this paper is a multi-input multi-output (MIMO) system as it consists of several inputs and need to control several outputs. Figure 7 shows the general block diagram of MIMO system of stabilization of two-wheeled wheelchair with movable payload.

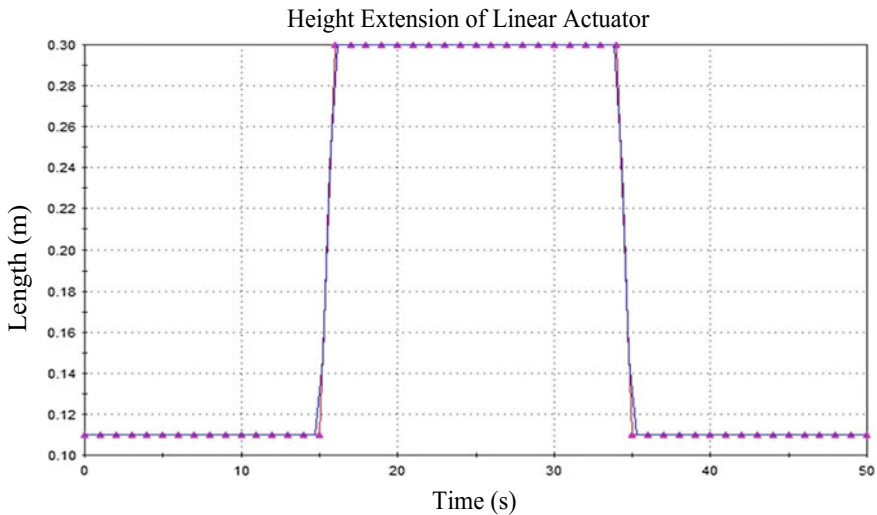


Fig. 8 Height extension of linear actuator up to 0.3 m

4 Simulation Results

In order to stabilize the two-wheeled wheelchair with movable payload, there are 8 control input gain parameters and 4 control output gain parameters need to be added in this research. The value of input gain is used as the lowest gains between 0.025–7.15 for IT2FLC and between 0.03–7.25 for FLCT1, while the value of output gain is used the highest gains between 50 and 200 for IT2FLC and between 70 and 220 for FLCT1 to ensure the two-wheeled wheelchair is stable in the upright position. It is obviously shows that the FLCT1 used a huge value of gains compared to IT2FLC.

Figures 8 and 9 show the height extension of linear actuator and external disturbances respectively. In this research, the linear actuator was extended up to 0.3 m by lifting the seat to reach a higher level of height and the maximum concentrated force was applied at the back of the wheelchair at 10 s (without height extension) and 30 s (with height extension) to test the robustness of the controller. Based on Fig. 9, FLCT1 is able to handle disturbance up to 220 N while IT2FLC is able to handle disturbance up to 300 N to stabilize at the upright position. It shows that the IT2FLC is able to handle uncertainties that FLCT1.

Figures 10, 11, 12 and Fig. 13 show the angular position of Link1 without height extension, the angular position of Link1 with height extension, the angular position of Link2 without height extension and the angular position of Link2 with height extension respectively. All the information of the system's performance for angular Link1 and angular Link2 was tabulated in Table 4 including rise time, settling time, peak overshoot at normal condition, peak undershoot at normal condition, peak overshoot at maximum height and peak undershoot at maximum height.

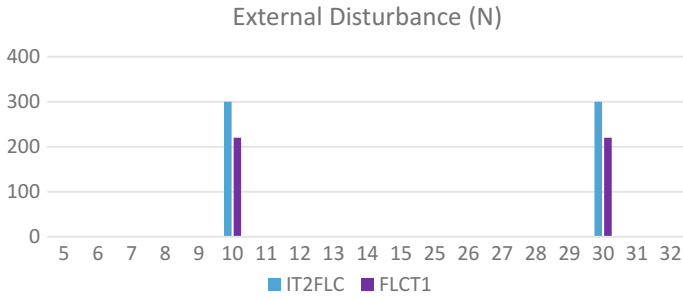


Fig. 9 External disturbance (time vs. force)

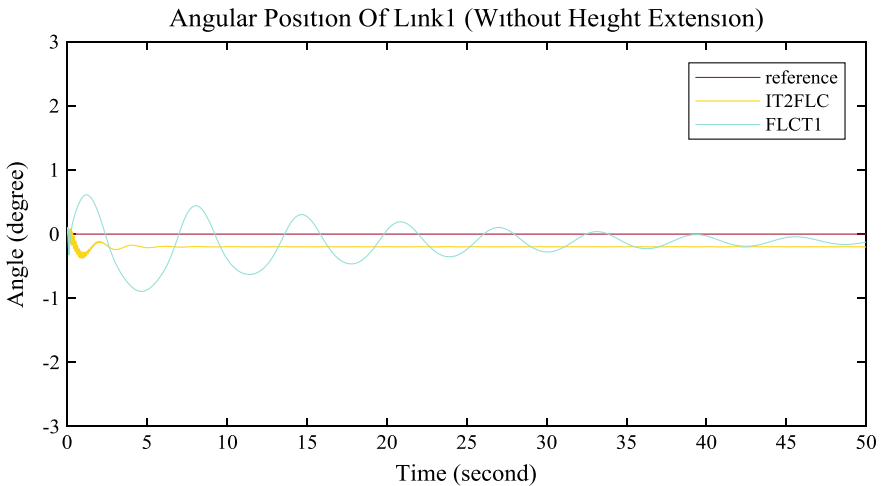


Fig. 10 Angular position of Link1 without height extension

The movement of wheel displacement shows only minimal distance range with 0.0015 m using both controllers while maintaining stability of the system at the upright position. It shows that the wheelchair does not travel far from 0 m. All the information of the system controlled by IT2FLC and FLCT1 is clearly shown in the Table 4 based on performance in Figs. 10, 11, 12 and 13 respectively after simulating the Matlab Simulink up to 50 s. The graph keeps oscillate until 50 s when the system controlled by FLCT1. While, the system is settled less than 3.3 s for both angle Link1 and Link2 using IT2FLC.

The graph shows a slightly high oscillation when the concentrated force applied with height extension of 0.3 m as compared to without height extension. This situation happens because the system tried to stabilize the angle of Link1 and Link2 at the upright position after gives disturbances 300 N for IT2FLC and 220 N for FLCT1 to avoid the humanoid falling. It caused a high value of peak overshoot and peak undershoot.

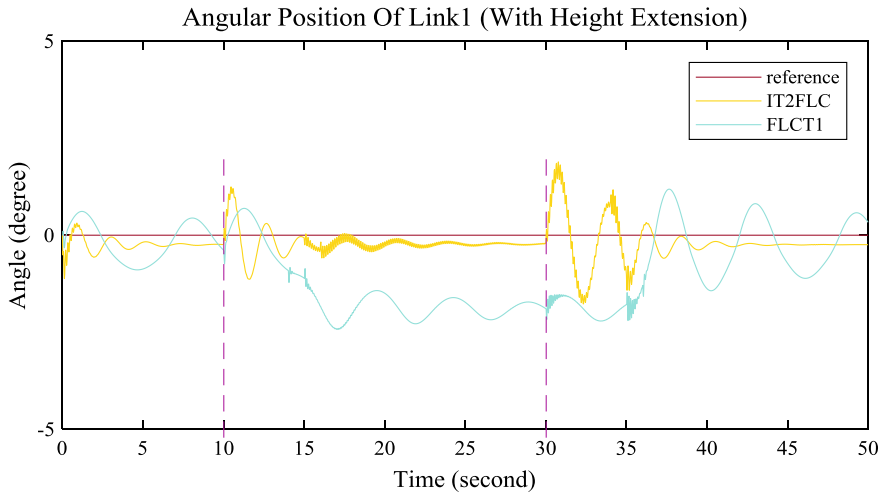


Fig. 11 Angular position of Link1 with height extension

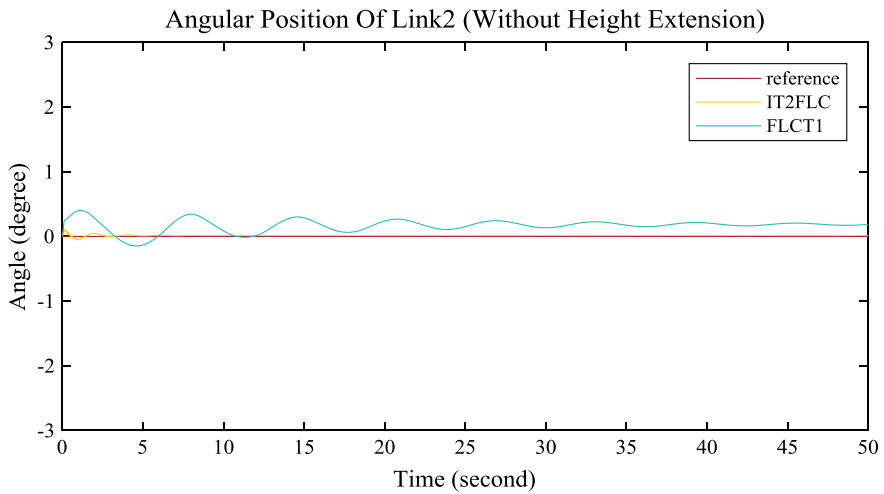


Fig. 12 Angular position of Link2 without height extension

Even though the angular position of Link1 and Link2 did not really at 0° , but the visualization movement in SW4D shows that the two-wheeled wheelchair with movable payload was maintain the stability in the upright position for both IT2FLC and FLCT1.

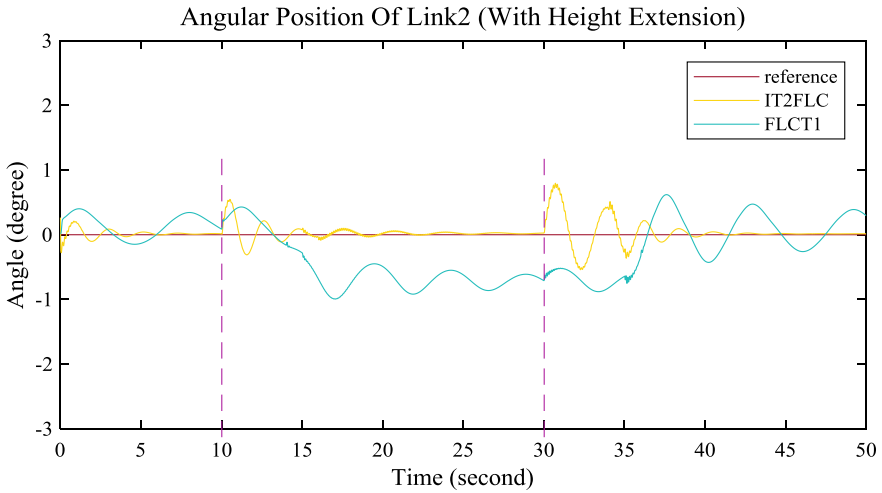


Fig. 13 Angular position of Link1 with height extension

Table 4 Information of the two-wheeled wheelchair using IT2FLC

	Angle Link1 FLCT1	Angle Link1 IT2FLC	Angle Link2 FLCT1	Angle Link2 IT2FLC
Rise time (s)	–	0.44	–	1.32
Settling time (s)	–	3.36	–	2.28
O/shoot without height extension (°)	0.6131	0.0892	0.4013	0.0847
U/shoot without height extension (°)	–0.8929	–0.3774	–0.1477	–0.0514
O/shoot with height extension (°)	1.186	1.889	0.6196	0.7971
U/shoot with height extension (°)	–2.426	–1.772	–0.9946	–0.5407

5 Conclusion

A control approach based on IT2FLC of a movable payload of a two-wheeled wheelchair has been presented in this paper. The model of two-wheeled wheelchair is designed based on a double-link inverted pendulum structure using SW4D environment. Then, the model of two-wheeled wheelchair with movable payload is integrated with Matlab Simulink to visualize the motion of the system when the program is executed. Based on the comparison result between IT2FLC and FLCT1, it is clearly shown that the IT2FLC gives good performance than FLCT1 in terms of rise time, settling time, steady state angle, overshoot and undershoot of the system. IT2FLC is able to handle uncertainties and nonlinearities with a good result and ensure the

system to able to maintain stability in the upright position. There are best 12 parameters of the system that was divided into two range for IT2FLC; lowest gains between 0.027 and 7.15 for input gain and the highest gains between 50 and 200 for output gain that were tuned heuristically. The entire parameters can be improved using an optimization algorithm to get optimal values with a less computational time for future work.

Acknowledgements The work presented in the paper has been supported by Research Grant PGRS170344 from the Research and Innovation Department, Universiti Malaysia Pahang and sponsored by Mybrain15, Ministry of Education Malaysia.

References

1. Yi, J., Yubazaki, N.: Stabilization fuzzy control of inverted pendulum systems. *Artif. Intell. Eng.* **14**, 153–163 (2000)
2. Henmi, T., Deng, M., Inoue, A., Ueki, N., Hirashima, Y.: Swing-up control of a serial double inverted pendulum. In: *Proceeding of the 2004 American Control Conference Boston, Massachusetts* (2004)
3. Adam, B., Robert, R.: Experimental verification of the dynamic model for a quarter size self-balancing wheelchair. In: *Proceeding of American Control Conference Boston, Massachusetts*, 488–492 (2004)
4. Grasser, F., D'arrigo, A., Colombi, S., Rufer, A.C. Joe.: A Mobile, Inverted Pendulum. *IEEE Trans. Ind. Electron.* **49**(1), 107–114 (2001)
5. Pathak, K., Franch, J., Agrawal, S.K.: Velocity and position control of a wheeled inverted pendulum by partial feedback linearization. *IEEE Trans. Robot* **21**(3), 505–513 (2005)
6. Seonghee, J., Takayuki, T.: Wheeled inverted pendulum type assistant robot: design concept and mobile control. *Intel. Serv. Robot.* **1**, 313–320 (2008)
7. Abeygunawardhana, P.K.W., Defoort, M., Murakami, T.: Self-sustaining control of two-wheel mobile manipulator using sliding mode control. In: *The 11th IEEE International Workshop on Advanced Motion Control* (2010)
8. Qian, D., Yi, J., Zhao, D., Hao, Y.: Hierarchical sliding mode control for series double inverted pendulums system. In: *International Conference on Intelligent Robot and Systems* (2006)
9. Lashin, M., Ramadan, A., Abbass, H.S., Ismail, A.A.: Design of an optimized sliding mode control for loaded double inverted pendulum with mismatched uncertainties. In: *International Conference on Intelligent Control and Information Processing* (2014)
10. Lashin, M., Ramadan, A.: Optimal Design of a State Feedback Sliding Mode Controller of a Loaded Double Inverted Pendulum. *Conference Paper, Elsevier* (2015)
11. Al-Hadithi, B.M., Barragan, A.J., Andujar, J.M., Jimenez, A.: Fuzzy optimal control for double inverted pendulum. In: *7th IEEE Conference on Industrial Electronics and Applications* (2012)
12. Wang, L., Zheng, S., Wang, X., Fan, L.: Fuzzy control of a double inverted pendulum based on information fusion. In: *International Conference on Intelligent Control and Information Processing* (2010)
13. Bhangal, N.S.: Design and performance of LQR and LQR based fuzzy controller for double inverted pendulum system. *J. Image Graph.* **1**(3), 143–146 (2013)
14. Jamin, N.F., Ghani, N.M.A.: Two-wheeled wheelchair stabilization control using fuzzy logic controller based particle swarm optimization. In: *IEEE International Conference on Automatic Control and Intelligent Systems (I2CACIS)* (2016)
15. He, L.Y.: Analysis on application of fusion function on fuzzy controller for double inverted pendulum. In: *Communications and information processing*, pp. 144–151. Springer, Berlin, Heidelberg (2012)

16. Wang, L., Sheng, Z.: LQR-fuzzy control for double inverted pendulum. International Conference on Digital Manufacturing and Automation (2010)
17. Bogdanov, A.: Optimal Control of a Double Inverted Pendulum on a Cart. Technical Report CSE-04-006 (2004)
18. Chen, W., Li, Q., Gu, R.: Chaos optimization neural network control for the stability of double inverted pendulum. In: 2nd International Conference on Industrial Mechatronics and Automation (2010)
19. Stilman, M., Olson, J., Gloss, W., Golem Krang.: Dynamically stable humanoid robot for mobile manipulation. In: IEEE International Conference on Robotics and Automation (2010)
20. Hagaras, H.A.: Hierarchical type-2 fuzzy logic control architecture for autonomous mobile robots. IEEE Trans. Fuzzy Syst. **12**(4) (2004)
21. Farooq, U., Gu, J., Luo, J.: An Interval Type-2 Fuzzy LQR Positioning Controller for Wheeled Mobile Robot. Proceeding of the IEEE International Conference on Robotics and Biomimetics (ROBIO) Shenzhen, China (2013)
22. Ri, M.H., Huang, J., Ri, S., Yun, H., Kim, C.S.: Design of interval type-2 fuzzy logic controller for mobile wheeled inverted pendulum. In: 12th World Congress on Intelligent Control and Automation (WCICA) Guilin, China (2016)
23. Hsiao, M.Y., Chen, C.Y.: Interval type2 adaptive fuzzy sliding-mode dynamic control design for wheeled mobile robots. Int. J. Fuzzy Syst. **10**(4) (2008)
24. Huang, J., Ri, M.H., Wu, D., Ri, S.: Interval type-2 fuzzy logic modeling and control of a mobile two-wheeled inverted pendulum. IEEE Trans. Fuzzy Syst. (2017)
25. Hsiao, M.Y., Wang, C.T.: A finite-time convergent interval type-2 fuzzy sliding-mode controller design for omnidirectional mobile robots. In: International Conference on Advanced Robotics and Intelligent Systems, Tainan, Taiwan (2013)
26. Jamin, N.F., Ghani, N.M.A., Ibrahim, Z., Masrom, M.F., Razali, N.A.A., Almeshal, A.M.: Two-wheeled wheelchair stabilization using interval type-2 fuzzy logic controller. Int. J. Simul. Syst. Sci. Technol. **19**(3) (2018). (IJSST)
27. Ahmad, S., Tokhi, M.O.: Modelling and control of a wheelchair on two wheels. In: Second Asia International Conference on Modelling & Simulation, IEEE (2008)
28. Chotikunnan, P., Panomruttanarug, B.: The application of fuzzy logic control to balance a wheelchair. CEAI **18**(3), 41–51 (2016)
29. Panomruttanarug, B., Chotikunnan, P.: Self-balancing iBOT-like wheelchair based on type-1 and interval type-2 fuzzy control. In: Proceedings of ECTI-CON, IEEE (2014)
30. Ahmad, M.A., Tumari, M.Z.M., Nasir, A.N.K.: Composite fuzzy logic control approach to a flexible joint manipulator. Int. J. Adv. Robot. Syst. **10**(58) (2013)

Stabilization Control of a Two-Wheeled Triple Link Inverted Pendulum System with Disturbance Rejection



M. F. Masrom, N. M. Ghani, N. F. Jamin and N. A. A. Razali

Abstract This paper focuses on the robust controller for triple Links inverted pendulum on two-wheeled system. The development of triple Link inverted pendulum on two-wheeled model using CAD based soft-ware, SimWise 4D is proposed. Interval Type-2 Fuzzy Logic Control (IT2FLC) is used as control algorithm for the system. This system is multi input and multi output system which means each motor in this system is controlled by one controller to achieve stability or upright position for these three links. The robustness of the controller is tested by applying disturbance to the model to observe the response from the model to handle the uncertainties. The performance of IT2FLC is compared with Type-1 Fuzzy Logic Control (T1FLC) to demonstrate best controller for the system. The experiment results concerning the angular position for each three Links and the maximum value of disturbance rejection for both controllers are obtained by using heuristic tuning for input and output gain control.

Keywords Triple links inverted pendulum on two-wheeled
Type-1 fuzzy logic control · Interval type-2 fuzzy logic control

1 Introduction

Self-balancing inverted pendulum system has evoked a lot of interest among education both in theory and application for decades. Inverted pendulum system varies from rotary, on cart, and on wheels system. Inverted pendulum system is capable to maintain its upright position even after facing disturbance or any uncertainties. There are also several works done on inverted pendulum which could maintain at any desired angle. The robustness of the inverted pendulum controllers is evaluated

M. F. Masrom (✉) · N. M. Ghani · N. F. Jamin · N. A. A. Razali
Department of Electrical and Electronics Engineering, Universiti Malaysia Pahang, 26600 Pekan,
Pahang, Malaysia
e-mail: firdausmasrom@gmail.com

© Springer Nature Singapore Pte Ltd. 2019
Z. Md Zain et al. (eds.), *Proceedings of the 10th National Technical Seminar on Underwater System Technology 2018*, Lecture Notes in Electrical Engineering 538,
https://doi.org/10.1007/978-981-13-3708-6_13

on how fast the system can achieve its stability, the closeness of the system to 0° , and the capability of the system in handling disturbance or uncertainties.

There are several works done for stabilization of inverted pendulum on two-wheeled system [1–4]. Single link mobile inverted pendulum system has been proposed using fuzzy logic based PID controller as stabilizing control to stabilize the model. In this system, 2 loops of controllers are used in order to control the angle and the position of the model independently [1].

Even though inverted pendulum on two-wheeled system have been developed in many ways and shown a promising success in term of stability, the system is not suitable to resemble a more complex and flexible system for instance walking robot [5], an air-craft landing system, and mobile robot [6]. Therefore, in this paper, triple Links inverted pendulum on two-wheeled system using IT2FLC is proposed. The robustness of IT2FLC with the capability to reject disturbances is discussed and compared with T1FLC.

2 System Modelling

In order to retain the complexity of triple Link inverted pendulum on two-wheeled system and to satisfy the real system, SimWise 4D is used to model the system. SimWise 4D is a four-dimension design software which provides designing features and allow to develop the model easily. Moreover, this software is capable to be integrated with Simulink to perform the simulation and to observe the simulation of the system and all mobility features involved in the model.

The model is designed based on the previous work done by the researchers in [7–9]. Triple links inverted pendulum on two-wheeled model consists of the bottom base as the connector for two wheels. The first link is hinged on the bottom base followed by second and third link which are connected by motor as shown in Fig. 1. Radius and mass of the wheel is presented as r_w and m_w while L_1 and m_1 resemble length and mass for first link, L_2 and m_2 resemble length and mass for second link and L_3 and m_3 resemble length and mass for third link. The parameters of the model which include length, mass and dimension are tabulated in Table 1. Figure 2 shows the model designed in SimWise 4D. It specifies the torques and the motors in the model. Each torque designed to balance its link for instance τ_R and τ_L are used to balance the first link, τ_1 and τ_2 are used to balance the second and third link respectively.

3 Stabilization Control

Stabilization control used in this system is by using T1FLC and IT2FLC in order to compare those two controllers performance. T1FLC has been proven to be working properly in inverted pendulum system. T1FLC is used to produce the output from

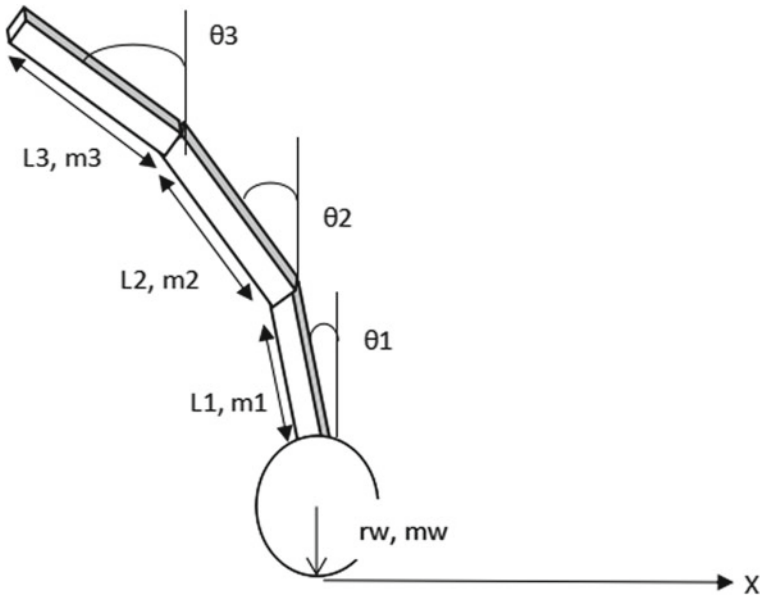


Fig. 1 Schematic diagram of triple links inverted pendulum on two-wheeled system

Table 1 Parameter for triple links inverted pendulum on two-wheeled system

Part	Material	Dimension (m)	Weight (kg)
Wheel	Rubber	Radius = 0.065 Width = 0.06	0.7
Bottom base	Aluminium	Radius = 0.03 Length = 0.3	1.5
Link 1	Aluminium	Width = 0.04 Length = 0.04	3
		Height = 0.22	
Link 2	Aluminium	Width = 0.04 Length = 0.04	3
		Height = 0.22	
Link 3	Aluminium	Width = 0.04 Length = 0.04	3
		Height = 0.22	

the input that has been given to it. T1FLC block diagram is comprised with fuzzifier, inference engine and defuzzifier. T1FLC working process starts when fuzzifier accepts the crisp output of input variable then converts it into fuzzy set by following the membership function which have to be defined first. Inference engine will then produce the fuzzy outputs based on the rule framed. Finally, defuzzifier will convert

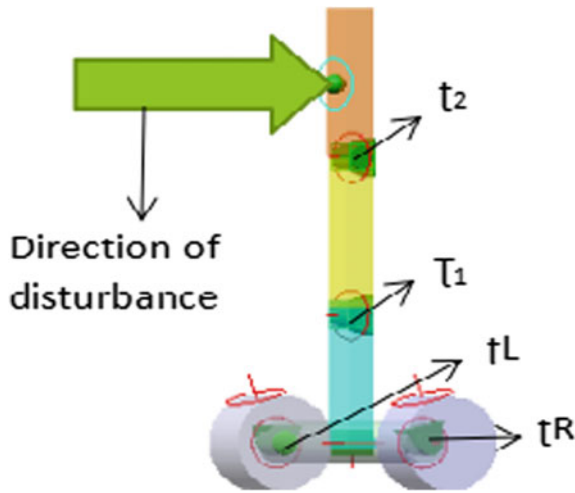


Fig. 2 Modelling of triple links inverted pendulum on two-wheeled system in Simwise 4D

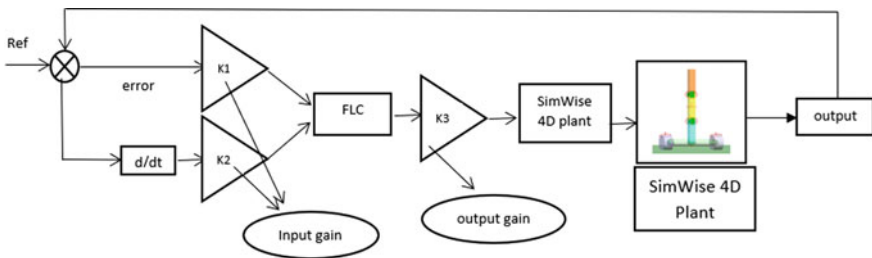


Fig. 3 Simulink block diagram for stabilization control

Table 2 Rule for fuzzy logic control [11]

E	dE				
	NB	NS	Z	PS	PB
NB	PB	PB	PB	PS	Z
NS	PB	PB	PS	Z	NS
Z	PB	PS	Z	NS	NB
PS	PS	Z	NS	NB	NB
PB	Z	NS	NB	NB	NB

back the fuzzy output into crisp value which will then be used for control purpose [10].

Due to the limitation of T1FLC, IT2FLC is introduced and proposed to overcome the issues and the limitation of T1FLC, mainly in handling the uncertainties in membership function. The main difference between those two controllers is IT2FLC has three dimensional membership function graph includes upper boundary, lower

boundary and footprint of uncertainties which offers an additional degree of freedom and able to handle the uncertainties [10]. Furthermore, IT2FLC has another additional feature which is ‘type reduction’ method to convert type-2 fuzzy sets from inference engine to type-1 fuzzy sets in order to convert into crisp value by defuzzification to be used in control purpose.

The stabilization control was designed in Simulink. Firstly, the desired output was defined. In this case the desired output was 0 degree. Stabilization control starts working when it receives an error feedback from output of the system. The error was divided into two which was error and rate of error to be used as the input variable of the controller. Controller produces an output and the output value in term of torque is used to control the motor in the model. Since the model has 4 motors, the stabilization control consists of 4 loops which control all motor independently. Figure 3 shows stabilization control designed in Simulink/Matlab.

The controller was designed using Gaussian membership function because the curve is more flexible compared to the other curve. The rule used in this system was a standard rule used in many inverted pendulum systems. There are 25 rules created by 5 membership function defined as Negative Big (NB), Negative Small (NS), Zero (Z), Positive Small (PS), and Positive Big (PB) as shown in Table 2 [11].

Table 3 Gains used in T1FLC and IT2FLC controller

Gain	T1FLC	IT2FLC
K1	0.24	0.117
K2	0.005	0.0034
K3	100	90
K4	0.7	0.4
K5	0.01	0.005
K6	86	75
K7	0.064	0.043
K8	0.0064	0.0064
K9	110	100
K10	0.3	0.2
K11	0.02	0.01
K12	90	80
K13	0.7	0.7
K14	0.004	0.004
K15	120	120
K16	0.2	0.085
K17	0.009	0.004
K18	100	85

4 Result

Triple links inverted pendulum on two-wheeled system is simulated in SimWise 4D in order to observe the performance and the response of the system when disturbance is applied. The performance for both controllers T1FLC and IT2FLC are obtained and compared to identify better controller to withstand higher disturbance given to the system while maintaining upright in stable position. Table 3 shows the value of gains used in T1FLC and IT2FLC in order for the system to work properly. Based on the table, gains used in T1FLC is bigger than IT2FLC to stabilize the model.

The robustness of the controllers is tested by applying disturbance to the model. In this paper, the disturbance is applied to third link because that is the critical link due to its top position in the model where the load is usually given. Figure 4 shows the maximum value of disturbance managed to handle for both controllers given at 5 and

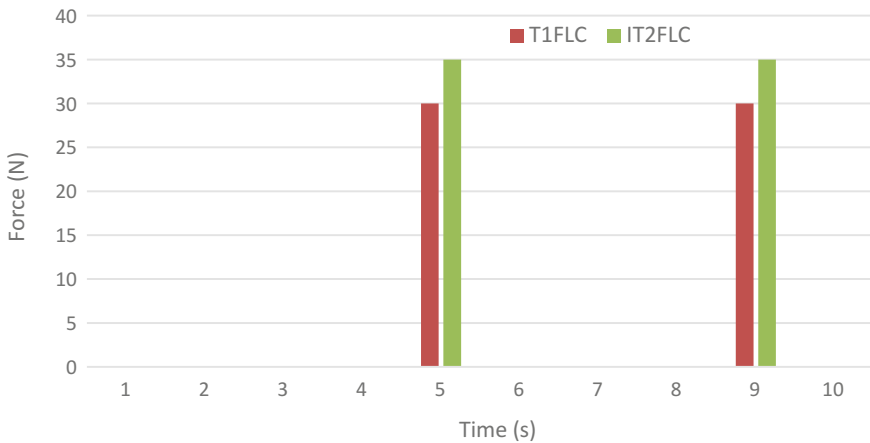


Fig. 4 Maximum value of disturbance for T1FLC and IT2FLC

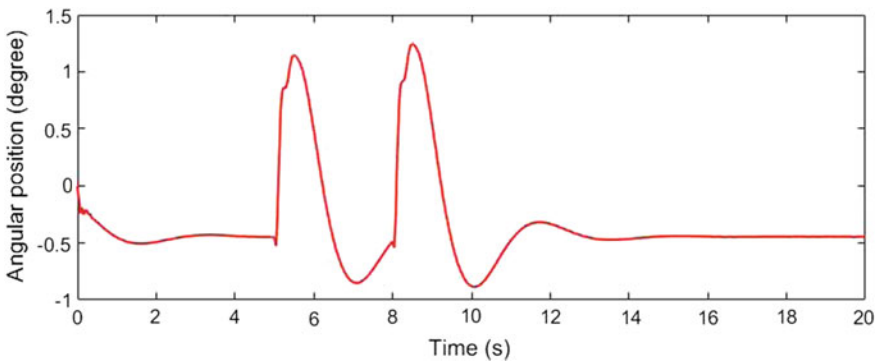


Fig. 5 Angular position of link 1 for T1FLC

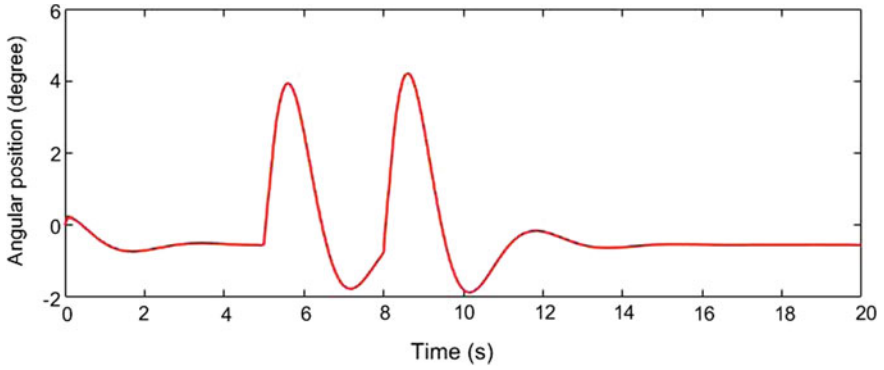


Fig. 6 Angular position of link 2 for T1FLC

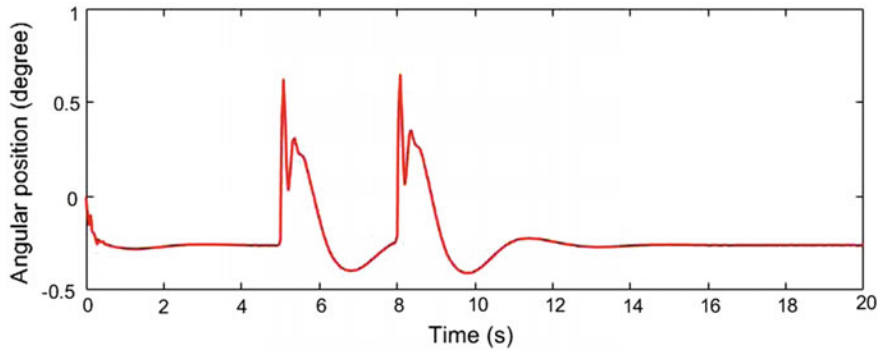


Fig. 7 Angular position of link 3 for T1FLC

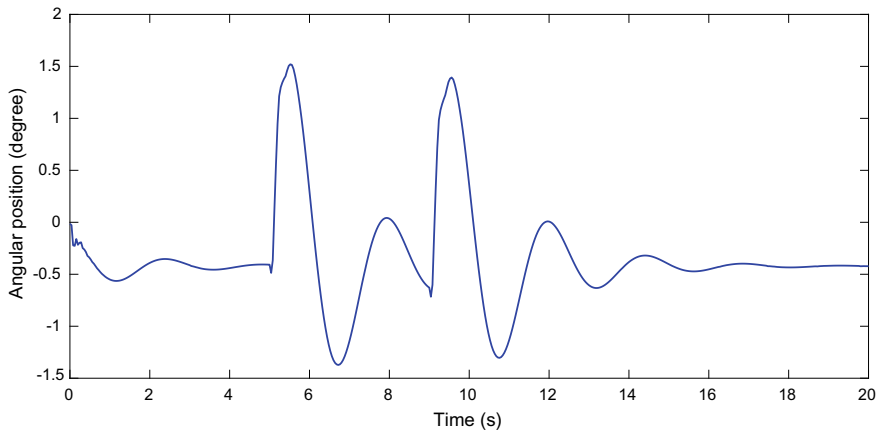


Fig. 8 Angular position of link 1 for IT2FLC

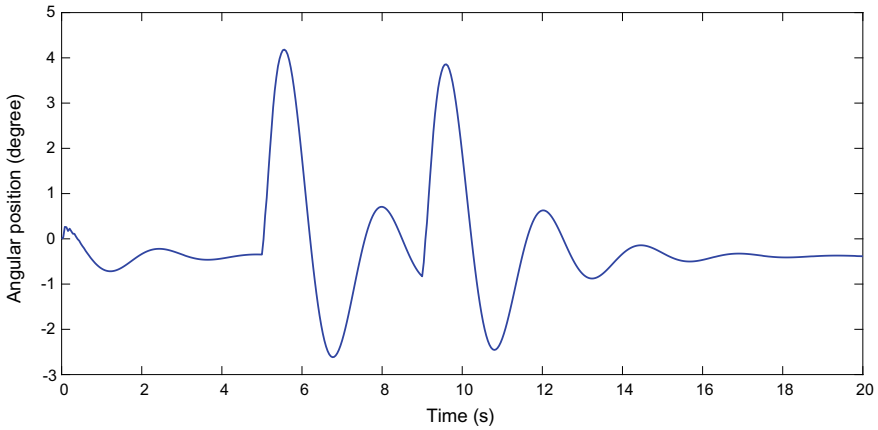


Fig. 9 Angular position of link 2 for IT2FLC

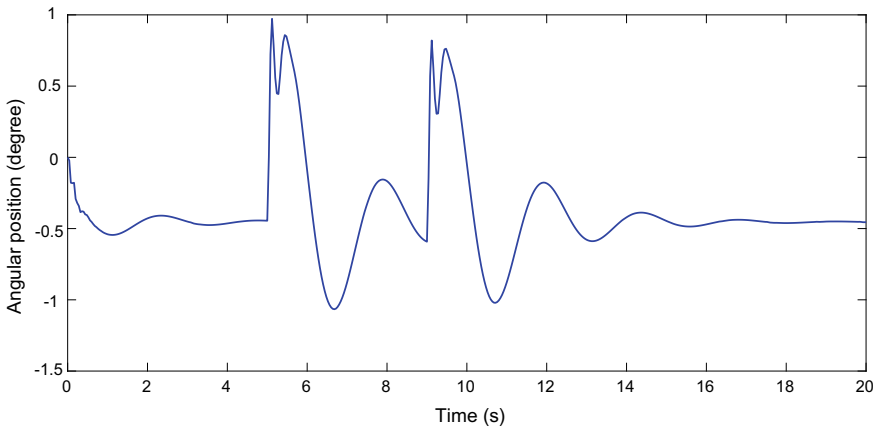


Fig. 10 Angular position of link 3 for IT2FLC

9 s. T1FLC managed to handle disturbance up to 30 N while IT2FLC successfully handled disturbance up to 35 N. Based on this result, IT2FLC is a better controller compared with T1FLC.

Figures 5, 6 and 7 show the graph of response from these three links for T1FLC while Figs. 8, 9 and 10 show the graph of response for IT2FLC obtained from all three links. From the graph, we can conclude that the model was successfully withstand the disturbance applied to the link. The most affected link between these three links was the second link because the link was off track up to 4° and this could be due to the second link is the intermediate link.

5 Conclusion

T1FLC and IT2FLC have been successfully designed as stabilizing control and implemented in triple links inverted pendulum on two-wheeled system. The model has been designed using SimWise 4D software to enable observation of the simulation. The model was then integrated with T1FLC and IT2FLC in Simulink to control these three links stabilization independently. Based on the simulation result, IT2FLC is superior than T1FLC in term of the capability to handle bigger disturbance. IT2FLC managed to withstand 16% bigger disturbance than T1FLC. In future work, optimization control could be done with this controller to get the best parameter and a better result since this work only use a heuristic tuning.

Acknowledgements The work presented in the paper has been supported by Research Grant RDU170502 from the Research and Innovation Department, Universiti Malaysia Pahang.

References

1. Paliwal, S., Chopra, V., Singla, S.K.: Stabilization of mobile inverted pendulum using fuzzy PID controller (2016)
2. Ri, M., Huang, J., Ri, S., Yun, H., Kim, C.: Design of interval type-2 fuzzy logic controller for mobile wheeled inverted pendulum, pp. 535–540 (2016)
3. Yu, C., Wu, J.: Intelligent PID control for two-wheeled inverted pendulums, pp. 2–5 (2016)
4. Jaswal, A., Chand, S., Abdullah, A., Chakraborty, R.: Design and fabrication of self balancing two Wheeler. *Int. J. Eng. Sci.* **6**(5), 5002–5005 (2016)
5. Ismail, H.A., Packianather, M.S., Grosvenor, R.I., Eldhukri, E.E.: The application of IWO in LQR controller design for the Robogymnast, vol. 2, pp. 274–279 (2015)
6. Tedeschi, F., Carbone, G.: Design of a novel leg-wheel hexapod walking robot (2017)
7. Ahmad, S., Aminnuddin, M., Shukor, M.A.S.M.: Modular hybrid control for double-link two-wheeled mobile robot. In: *International Conference on Computer and Communication Engineering*, pp. 3–5 (2012)
8. Goher, K.M., Tokhi, M.O.: A new configuration of two-wheeled inverted pendulum: a lagrangian based mathematical approach, pp. 1–5 (2010)
9. Urakubo, T., Tsuchiya, K., Tsujita, K.: Motion control of a two-wheeled mobile robot. *Adv. Robot.* **1864**, 2012 (2001)
10. Naik, K.A., Gupta, C.P.: Performance comparison of type-1 and type-2 fuzzy logic systems. In: *4th IEEE International Conference on Signal Processing, Computing and Control*, pp. 72–76 (2017)
11. Jamin, N.F., Ghani, N.M.: Two-wheeled wheelchair stabilization control using fuzzy logic controller based particle swarm optimization, pp. 78–83 (2016)

Integration of PI-Anti-windup and Fuzzy Logic Control with External Derivative Solution for Leg's Robot Angular Joint Precision



Wan Mohd Nafis Wan Lezaini, Addie Irawan
and Ahmad Nor Kasruddin Nasir

Abstract Various ideas were proposed in designing and developing the bio-inspired robot legged robot and its control system. Researchers may confront numerous challenges in designing control architecture of the legged robot, especially in controlling leg position. As the leg and joints number increases, the complexity of the multi-limbed system will increase. Thus, robust control is needed. For the case of motion precision in a legged robot, position control is essential to cater fast response of the angular motion during locomotion. Therefore, this paper presents a modification on hybrid Proportional Integral with the antiwindup algorithm and Fuzzy Logic Control (PIA-FLC) with an external derivative element named as PIA-FLC-D to improve the speed of controller response for Hexaquad robot leg's joints. The proposed PIA-FLC-D control is validated on the first leg of Hexaquad robot, and the results were analyzed and compared with the previous PIA-FLC. The results show that the proposed PIA-FLC-D control had enhanced the performance of angular joint precision with fast response and minimal delay in each leg's joint motion tracking compares to the previous PIA-FLC controller.

Keywords Legged robot · Angular precision · Anti-windup · Fuzzy logic control

1 Introduction

In enabling a manipulator or legged robot or so-called limbed robot mechanism moving around the workspace, effective actuation is required to ensure the force on end-effector focus on targeted workspace [1]. Prismatic and revolute are the types of joints that used in connecting between the two or more links of the limbed robot, depending on design and application. For the case of a limbed system with revolute joint, electric motor becoming a common device since this configuration required

W. M. N. W. Lezaini (✉) · A. Irawan · A. N. K. Nasir
Robotics and Unmanned System (RUS) Group, Faculty of Electrical and Electronics Engineering,
Universiti Malaysia Pahang, 26600 Pekan, Pahang, Malaysia
e-mail: wannafis93@gmail.com

© Springer Nature Singapore Pte Ltd. 2019

Z. Md Zain et al. (eds.), *Proceedings of the 10th National Technical Seminar*

on Underwater System Technology 2018, Lecture Notes in Electrical Engineering 538,

https://doi.org/10.1007/978-981-13-3708-6_14

the direct actuating and direction feedback measurement as well. It is different to the limbed robot with a prismatic joint that some of configured with the pneumatic and hydraulic actuator. However with the recent technology, electric motor with linear guided features becoming a favorable device for prismatic limbed robot mechanism due to the cost, precision and safety factors if compared to the pneumatics and hydraulic type.

Regarding on control point of view, the prismatic limbed robot required the specific translation in drive process since the actuating process on each joint is indirect. Also, precise control of each joint of the prismatic limbed robot is essential and crucial to ensure the effectiveness of the motion input to the system. For this case, the control objective is emphasized in handling the actual joint position ($\theta_f(t)$) track the same as the desired joint motion ($\theta_d(t)$) from trajectory input to ensure end-effector of the robot able to complete the task precisely. Fundamentally, this situation is related to the joint's actuating devices as well as for kinematics chains as a translator.

A conventional control is known as Proportional, Integral and Derivative (PID) control are commonly and practically used in industrial automation, in which the robustness only required simple fine-tuning [2]. However, the complexity increases as it confronted with the nonlinear event such as, noise and interference, a windup phenomenon as well as gravitational factors, this control method need some adaptive element or maybe need to be replaced with another more intelligent control system. The interference of sensor noise occurred especially to the system that implemented sensor with voltage leveling type. During trajectory tracking, to complete the error correction into zero error, a controller may results in a jerky movement even when the sensor used in the system have a good and stable range of feedback reading as the sensitivity of the controller toward error is high. A method to implement deadband for error proposed by [3] in the simple Proportional and Derivative (PD) position control, is used to set an acceptable range of error in controlling the cab rotation. Unfortunately, the method will reduce the accuracy of the physical driven devices placement. Another issue that needs tackle is when implementing a controller that used an integral element such as in PID is the windup phenomenon.

The windup phenomenon happens when the control signal ($u(t)$) from PID continuously accumulating and increasing due to the action of the integral term as soon as the physical variables reached the saturation point (physical limitation). This phenomenon caused overshoot response. As proposed by [4] this problem can be eliminated by immobilizing the integral term, where the windup phenomenon eliminated through anti-windup approaches. Furthermore, rather than emphasized on nonlinearity in the internal system of any types of the control system, an external factor such as the gravity effect on the moving link should be taken into account. The gravity compensation happened as any of the link moving in a robotic leg or manipulator mechanism. The scenario happened when the link's weight does not yield a significant fraction or any of torque at the actuation of the actuator [5]. This condition occurred when the force direction of the moving link is the same as the direction of the gravitational force.

Recently, the involvement of the artificial intelligent algorithm in robot dynamics becoming trendy especially in cater the positioning control encompassing indirect

control of force/torque. As for example, a reconfigurable constraint arm implemented a hybrid combination of force into position control by using the adaptive neural network (NN) [6], where Li et al. suggested to use compensator which is adaptive NN onto the targeted robot dynamic model uncertainty. Besides, NN also is adapted to underactuated robotic arm position control through forwarding learning and inverse estimating in resolving the inverse problem by the network inversion [7]. The main objective of the proposed method is to ensure the passive joint of the robotic arm capable of follows the motion reference based on the predictable trajectory. On the other hand, Fuzzy Logic Control (FLC), as stated in [8, 9], is also one of the favorable model-free control with artificial intelligence that widely deployed in industrial level. The benefits of FLC in the control practices is on its flexibility in the characterizing of linguistic term usage while escaping complex mathematical methods [2]. For instance, a two-link planar type robot with underactuated link configuration used two inputs single output FLC [10], where the active link was the only highlighted as controlled link while the position of the passive link is in consideration. The advantage of intelligent control integration into conventional mathematical-based control is to reduce the complexity of the control and to realize model-free approach that able to avoid iteration processes.

Therefore this research has taken the initiative to improve the previous works on giving better position control on each leg joints of a multi-legged robot named Hexaquad. This progress is a sequel of a hybrid of proportional and integral anti-windup with FLC (PIA-FLC) proposed in [11] for each n th-joint of bio-inspired Hexaquad robot leg [12]. The adaptive derivative (D) element in the controller is proposed to increase the precision of each dominant n th-joint better than previous PIA-FLC. The structure of this paper is arranged as follows: Sect. 2 discusses briefly on the summary of Hexaquad robot mechanism as well as its leg kinematics chain whereas Sect. 3 explained the details of the proposed PIA-FLC with D element system design and Sect. 4 discusses the experimental setup, results, and analysis. Lastly, in Sect. 5, conclusions are drawn.

2 Overview of Hexaquad Robot Mechanisms and Leg Kinematics

A bio-inspired legged robot with converting form between Hexapod and Quadruped known as Hexaquad [13], with the objective to be operated submerged on the riverbed or seabed and expected to conduct task of the pick-and-place object that weight maximum of 50 kg. Hexaquad development was inspired by the characteristics of arthropod which having a quadruped or hexapod configurations and peristaltic creatures [12] where during Quadruped mode, the center set of Hexaquad's legs can move in either of two directions as displayed in Fig. 1. Also, on each tip of the Hexaquad's leg is equipped with foot-to-gripper (FTG) transformation. The actuators specifications on each joint of Hexaquad's leg are listed Table 1 where one bipolar stepper motor is

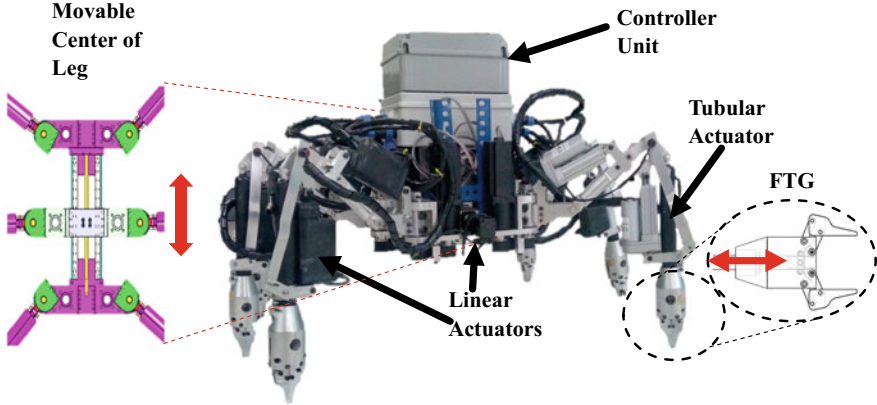


Fig. 1 Hexaquad robot system

Table 1 Actuator specification for hexaquad robot

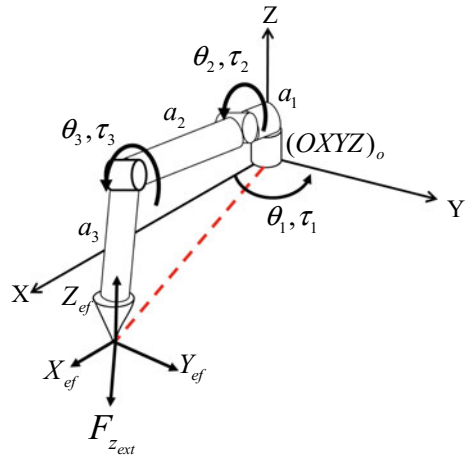
Item	Value	Remarks
Linear actuator load (N), voltage input (V), current (A)	200, 12, 2	12 units
Tubular actuator load (N), voltage input (V), current (A)	200, 12, 2	6 units
Bipolar stepper, torque (N/m), voltage input (V), current (A)	54, 4.5, 3	6 units
Bipolar stepper motor (body) torque (N/m), voltage input (V), current (A)	7.2, 24, 3	1 unit

equipped on joint 1 (θ_1) as actuating devices while joint 2 (θ_2) and joint 3 (θ_3) of Hexaquad's leg are installed with one linear actuator on each joint. Moreover, to enable the ability of FTG transformation, tubular actuator motor is equipped on each of leg's tip. The Hexaquad's legs are considered to be in underactuated configuration.

However, in designing control system, the system is considered as fully actuated with 3 degrees of freedom (DOF) formation since the movement of the linear actuator on each link is influenced by a position sensor installed directly to each joint. As shown in Fig. 2, a_1 , a_2 and a_3 denotes as the length of Link 1, Link 2 and Link 3 respectively. By using Denavit-Hartenberg (DH) conversion as in Eqs. 1 and 2, a translation between Cartesian coordinates of the tip of the Hexaquad's leg (end-effector) and Hexaquad leg's joints angular coordinates are expressed.

$$\begin{pmatrix} x_e \\ y_e \\ z_e \end{pmatrix} = \begin{pmatrix} a_1 \cos(\theta_1) + a_2 \cos(\theta_1) \cos(\theta_2) + a_3 \cos(\theta_1) \cos(\theta_{23}) \\ a_1 \sin(\theta_1) + a_2 \sin(\theta_1) \cos(\theta_2) + a_3 \sin(\theta_1) \cos(\theta_{23}) \\ a_2 \sin(\theta_2) + a_3 \sin(\theta_{23}) \end{pmatrix} \quad (1)$$

Fig. 2 Hexaquad’s leg link orientation



$$\begin{aligned}
 \theta_3 &= \cos^{-1} \frac{\left(\frac{x_e}{\cos(\theta_1)} - a_1\right)^2 + z_e^2 - a_2^2 - a_3^2}{2a_2a_3} \\
 \theta_2 &= \tan^{-1} \left(\frac{a_3 \sin(\theta_3)}{a_2 + a_3 \cos(\theta_3)} \right) \\
 &\quad + \sin^{-1} \left(\frac{z_e^2}{\sqrt{a_2^2 + a_3 \cos(\theta_3)^2 + a_3 \sin(\theta_3)^2}} \right) \\
 \theta_1 &= \tan^{-1} \left(\frac{x_e}{y_e} \right)
 \end{aligned} \tag{2}$$

3 PIA-FLC-D for a Hexaquad’s Leg Precision Motion

3.1 Inner Loop System of Hexaquad’s Leg

The same architecture of inner-loop control was designed on each Hexaquad’s leg but with different parameters values as illustrated in Fig. 3. The Hexaquad’s leg n th-joint position control was originated from [14] which is Proportional Integral with Antiwindup (PIA) control to control each joints positioning of Hexaquad robot’s legs. However a modification is made in [11], by adding gravity compensator using single input single output (SISO) Fuzzy Logic Control (FLC) into the PIA controller during walking trajectory tracking where FLC will compensate to decrease control output ($u(t)$) of PIA during Hexaquad’s leg links movement yielding with gravity force and increase $u(t)$ when against it.

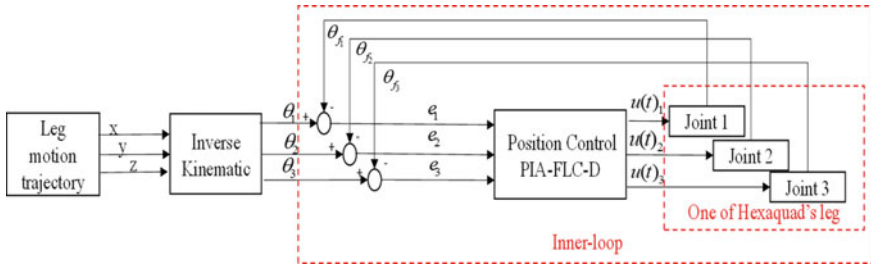


Fig. 3 Hexaquad’s leg position control architecture

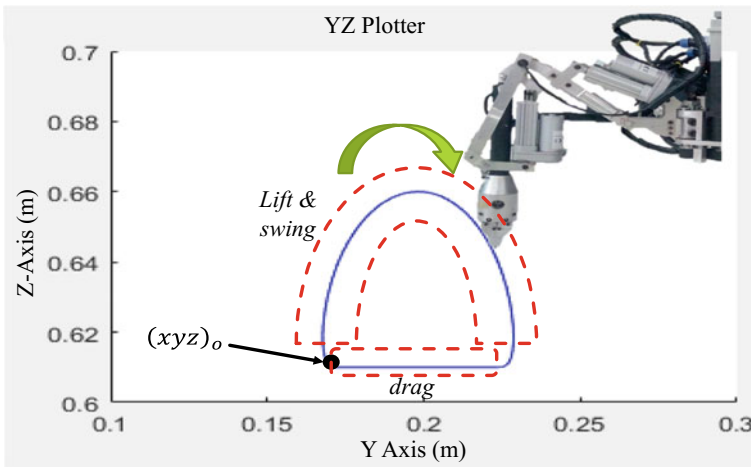


Fig. 4 Hexaquad basic leg motion according to the foot point

In order to achieve a walking pattern, there is only two basic sequences are designed which are a lift to swing sequence and drag sequence. By referring to Fig. 4, the basic sequence is portrayed where during the lift to swing sequence, the Hexaquad’s leg required to lift the leg to place the leg into new placement while at dragging sequence, the leg imparting force to the environment to move the robot’s body to a new location. The walking motion was designed with a semi-circle shaped where $(xyz)_o$ was the starting point and green arrow indicating the direction of motion of Hexaquad’s leg tip. The Cartesian coordinates of Hexaquad’s leg tip generated via the designed motion in Fig. 4 were translated using inverse kinematics, as expressed in Eq. 2, into Hexaquad leg’s joint angular coordinates and supplied to the inner-loop system in Fig. 3.

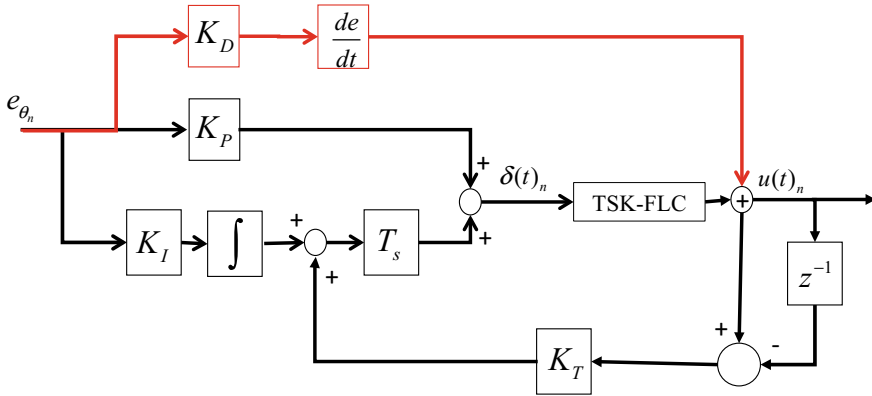


Fig. 5 The detail on proposed PIA-FLC-D control architecture

3.2 An Addition of a Derivative Element into PIA-FLC

As presented in [11], the PIA-FLC is incapable of following precisely and responding quickly toward the motion track as it lagging behind. This situation will reduce the accuracy of the joints moving and unable to give satisfactory results. The controller required to respond faster to the motion designed so that no problem arises in the future. A precise trajectory tracking is vital in order to enable physical hardware to translate the designed pattern into actual movement. As previously shown in PIA-FLC performance, the controller had delay especially during swing sequence since the motion speed during swing sequence is faster than motion speed during drag sequence. This situation happened due to no element for error speed response control toward the motion track. Hence, the addition of derivative (D) element into PIA-FLC is done. The D element is the representation of the change in error in the controller over time as expressed in (3). As shown in Fig. 5, K_P , T_s , K_T and K_I are proportional gain, sampling time, anti-windup gain and integral gain respectively for PIA unit in the proposed controller and the modification is made as illustrated by the red outline indicated the addition of D element where K_D is denote as derivative gain. The D element is expected to generate new value based on the speed of the motion. As the change in error increases, the D element generates higher output which then added to the PIA-FLC $u(t)$.

$$K_D \left(\frac{de(t)}{dt} \right) = K_D \left(\frac{e(t) - e(t-1)}{\Delta t} \right) \tag{3}$$

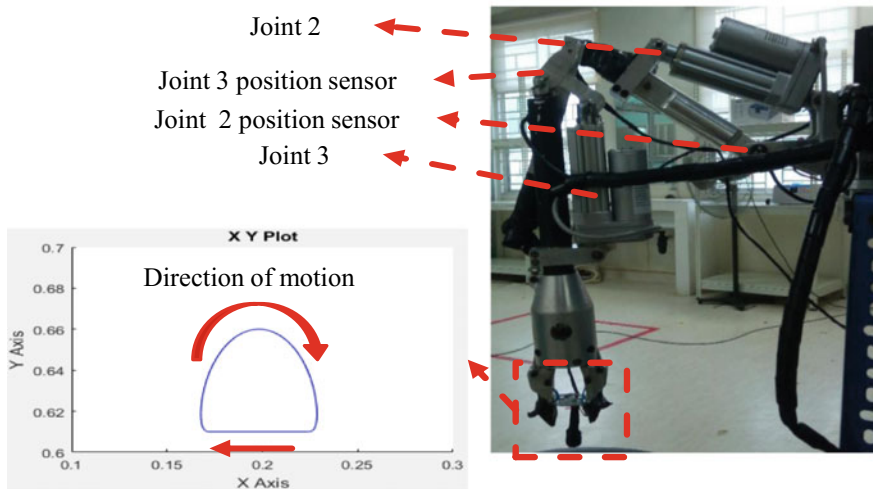


Fig. 6 Test rig setup on the 1st leg of Hexaquad

Table 2 Gain parameters for joint 2 and 3

MF	Joint 2	Joint 3
K_T	0.25	0.25
T_S	0.001	0.001
K_I	0.5	0.5
K_P	300	40

4 Results and Discussions

4.1 Experiment Setup

The modified controller, PIA-FLC-D is tested on joint 2 and joint 3 of Hexaquad's 1st leg based on designed motion in Fig. 4. In this experiments, only two dominant joints are considered for validation since joint 1 is set to static (zero). As shown in Fig. 6, the 1st leg of Hexaquad robot is left hanging, and the direction of motion is shown in the figure. A 360° rotational type potentiometer is equipped on each of Hexaquad's leg joints as a position sensor. The experiment is run in two sessions whereby the 1st session is for PIA-FLC controller and the second session is for PIA-FLC-D controller. After fine-tuning, the gain parameters for PIA-FLC were obtained as listed in Table 2 for both Hexaquad's leg joints. The gain parameters value listed in Table 2 also applied to PIA-FLC-D with derivative gain (K_D) is set to 0.0001.

4.2 Performance Comparison Between PIA-FLC and PIA-FLC-D

As shown in Figs. 7 and 8, the comparison of performance for both controller are presented for joint 2 (θ_2) and joint 3 (θ_3) respectively, whereby black, blue and red lines denote the reference, PIA-FLC, and PIA-FLC-D tracks respectively. For both figures, the swing sequence started at 15–19.5 s and continue with drag sequence

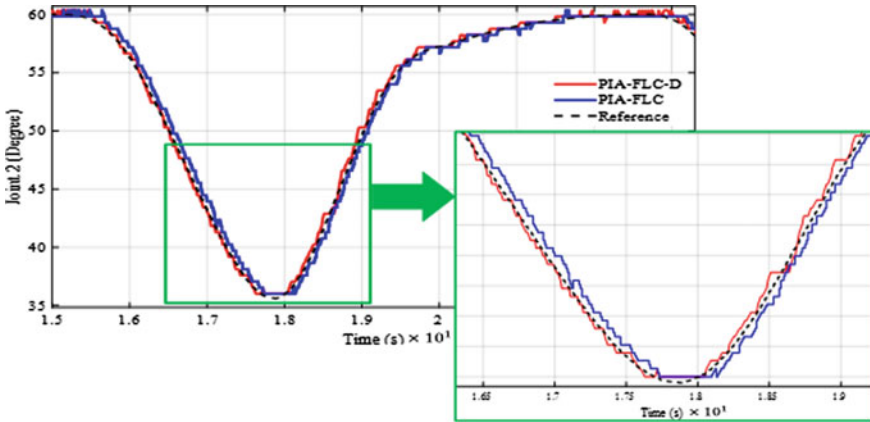


Fig. 7 Sample experiment of θ_2

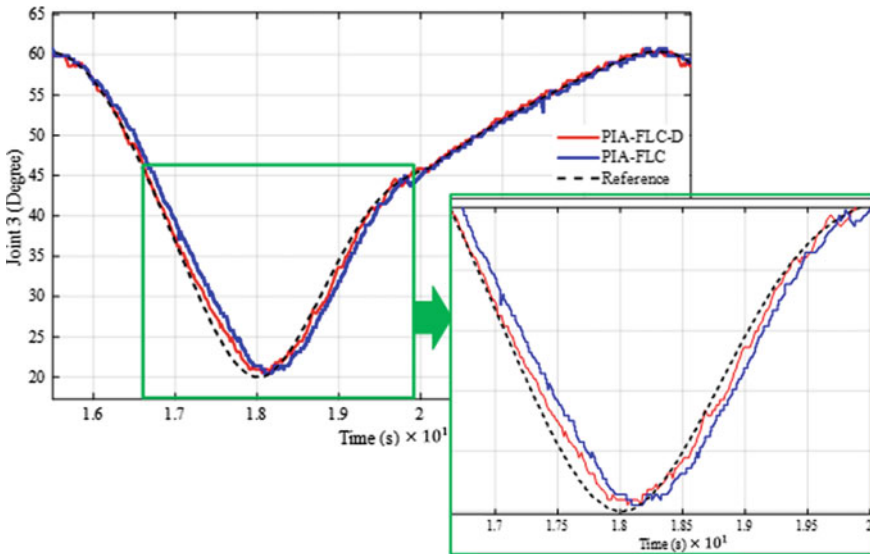


Fig. 8 Sample experiment of θ_3

at 19.5–23 s. The change in motion during swing sequence is faster than in drag sequence. Both controllers showed a good response during drag sequence without overshooting and delay. However, the performance during swing sequence showed that PIA-FLC is having a gap between its track with the reference track especially at 16.5–19 s on both joints. Also, the performance distinction between the two controllers can be seen in Fig. 8 where PIA-FLC delayed approximately 0.25 s from the reference track while PIA-FLC-D only yields with approximately 0.1 s lagging behind the track. Contrary to the PIA-FLC, the controller with the additional D parameter showed a better response toward the reference track as it is able to directly follow the reference motion on both joints.

5 Conclusion

The proposed PIA-FLC-D for joint position control was successfully applied to both joints of Hexaquad's leg. The results showed that both joints especially during swing sequence, the PIA-FLC-D responses faster to the reference track whereas the PIA-FLC has a response delay and resulting in lagging behind the track due to the change between motions is faster than during drag sequence. The result was validated that PIA-FLC-D has given precise results in following the reference input during drag and swing sequences. The additional of proposed D element helped the original PIA-FLC to increase or decrease $u(t)$ of the controller while completing the trajectory tracking. As for the future works, the improvement will be emphasized on giving a dynamic response on each Hexaquad leg in facing a soft terrain with mild unstructured terrain.

Acknowledgements This research and development are supported by the Ministry of Higher Education Malaysia under the Fundamental Research Grant Scheme (FRGS) (Grant No. FRGS/1/2016/TK04/UMP/02/9) and Universiti Malaysia Pahang (UMP) Research Grant (RDU160147).

References

1. Bekey, G.A.: *Autonomous robots: from biological inspiration to implementation and control* (intelligent robotics and autonomous agents series). MIT press, Massachusetts, USA (2005)
2. Adewuyi, P.A.: DC motor speed control: a case between PID controller and fuzzy logic controller. *Int. J. Multi. Sci. Eng.* **4**, 36–40 (2013)
3. Winck, R.C., Elton, M., Book, W.J.: A practical interface for coordinated position control of an excavator arm. *Autom. Constr.* **51**, 46–58 (2015)
4. Luo, B.Y., Li, M.C., Wang, P., Yu, T.Y.: An anti-windup algorithm for PID controller of PMSM SVPWM speed control system. In: *Proceedings of the 3rd International Conference on Mechatronics, Robotics and Automation (ICMRA 2015)*. pp. 529–534. Shenzhen, China (2015)
5. Boisclair, J., Richard, P.L., Laliberté, T., Gosselin, C.: Gravity compensation of robotic manipulators using cylindrical halbach arrays. *IEEE/ASME Trans. Mechatron.* **22**(1), 457–464 (2017)
6. Li, Y., Wang, G., Dong, B., Zhao, B.: Hybrid position–force control for constrained reconfigurable manipulators based on adaptive neural network. *Adv. Mech. Eng.* **7**(9), 1–10 (2015)

7. Hasan, A.T.: Under-actuated robot manipulator positioning control using artificial neural network inversion technique. *Adv. Artif. Intell.* **2012**, 1–6 (2012)
8. Resceanu, C.F.: Control algorithms for multi-legged robots in fault conditions using fuzzy logic. In: 15th International Conference on System Theory, Control and Computing, pp. 1–5. Sinaia, Romania (2011)
9. Ayas, M.S., Altas, I.H.: Fuzzy logic based adaptive admittance control of a redundantly actuated ankle rehabilitation robot. *Control Eng. Pract.* **59**, 44–54 (2017)
10. Jun-Qing, C., Xu-Zhi, L., Min, W.: Position control method for a planar Acrobot based on fuzzy control. In: 2015 34th Chinese Control Conference (CCC), pp. 923–927. Hangzhou, China (2015)
11. Lezaini, W., Irawan, A., Razali, A., Adom, A.: Hybrid antiwindup-fuzzy logic control for an underactuated robot leg precision motion. In: 2017 IEEE 3rd International Symposium in Robotics and Manufacturing Automation (IEEE-ROMA2017), pp. 1–6. Kuala Lumpur, Malaysia (2017)
12. Irawan, A., Razali, A.R., Wan Ishak, W.F., Arshad, M.R., Yin, T.Y.: Development of hexaquad robot: modeling and framework. *ARPN J. Eng. Appl. Sci.* **10**, 17506–17513 (2015)
13. Irawan, A., Tumari, M.Z.: Hexa-quad robot with prismatic body configuration and leg-to-arm transformation. Malaysia Patent (2014)
14. Zainol, M.A.F.: Precision control on hexaquad robot's leg using anti-windup PID control approach. Universiti Malaysia, Pahang, Malaysia (2016)

Backstepping Control of Nonholonomic Car-like Mobile Robot in Chained Form



Norsuryani Zainal Abidin, Nurul Ain Mohamed, Zainah Md. Zain, Maziyah Mat Noh, Norhafizah Md. Zain and Dwi Pebrianti

Abstract This project is attempts to stabilize an underactuated system based on the backstepping approach. The discontinuous time-invariant state feedback controller is designed for exponential stabilization of underactuated nonholonomic systems in chained form. System dynamic of the car-like robot with nonholonomic constraints were employed. The validity of the proposed approaches is tested through simulation on a car-like vehicle using Matlab software.

Keywords Backstepping control · Underactuated system · Mobile robot

1 Introduction

The motion control of nonholonomic wheeled mobile robot (WMR) has received a great attention from researchers over the last few years. Most of the researches are focused on the fact that the WMR does not meet Brockett's necessary condition for smooth feedback stabilization [1]. It is accepted that the larger the gap between the controllable and total degrees-of-freedom (DOF) of the WMR, the harder it is to control the robot [2, 3]. The WMR cannot be stabilized to a point using the familiar smooth static-state feedback control laws due to this nonholonomic constraint.

The dynamic equations of a car-like vehicle mobile robot can be written in chained form as:

N. Zainal Abidin · N. A. Mohamed · Z. Md. Zain (✉) · M. Mat Noh · D. Pebrianti
Robotics and Unmanned Research Group (RUS), Instrument and Control Engineering (ICE)
Cluster, Faculty of Electrical and Electronics Engineering, Universiti Malaysia Pahang, 26600
Pekan, Pahang, Malaysia
e-mail: zainah@ump.edu.my

N. Md. Zain
Faculty of Agro-Based Industry, University of Malaysia Kelantan, Locked Bag no. 100, 17600
Jeli, Kelantan, Malaysia

$$\begin{aligned}
\dot{x}_1 &= u_1 \\
\dot{x}_2 &= u_2 \\
\dot{x}_3 &= x_2 u_1 \\
&\vdots \\
\dot{x}_n &= x_{n-1} u_1
\end{aligned} \tag{1}$$

where $x = (x_1, x_2, \dots, x_n)^T \in IR^n$ represents the state vector and $u = (u_1, u_2)^T \in IR^2$ represents the input vector.

Such a class of nonlinear systems cannot be stabilized via continuous based time-invariant system [1], which driven the search of other stabilizing controls for this type of systems. Kolmanovsky and Mc-Clamroch [4] stated the art of existing solution for nonholonomic systems. Many authors exhibit a particular attention to the design of discontinuous controller for chained systems in [5–8].

In this paper, we propose a backstepping control approach for the design of a discontinuous time invariant controller for nonholonomic chained forms with application to nonholonomic mobile robot systems.

2 Backstepping Control Design

Our main result is stated in the following Theorem 1 in order to apply backstepping approach procedure.

Theorem 1 Consider system (1) under the following control law defined over $\Lambda = \{x \in IR^n / x_1(t) \neq 0, \forall t \in IR_+\}$

$$\begin{aligned}
u_1 &= -k_n y_n \\
u_2 &= \dot{\Psi}_{n-2} - k_{n-1} z_{n-1} + k_n y_n z_{n-2}
\end{aligned} \tag{2}$$

where $\dot{\Psi}_{n-2}$, z_{n-1} and z_{n-1} are evaluated recursively, such that

$$\begin{aligned}
\Psi_1 &= k_1 \frac{y_1}{y_n}, \\
\Psi_i &= -z_{i-1} + k_i \frac{z_i}{y_n} - \frac{\dot{\Psi}_{i-1}}{k_n y_n}, \quad 2 \leq i \leq n-2 \\
z_1 &= y_1,
\end{aligned}$$

$$z_i = y_i - \Psi_{i-1}, \quad 2 \leq i \leq n-2$$

$$y_i = x_{n-i+1} \text{ for } 1 \leq i \leq n$$

Assume that $x_1(0) \neq 0$, then

- a. the whole state of the closed-loop system (1)–(2) remains in Λ ,
- b. the closed loop system (1)–(2) is exponentially stable,
- c. the control law is bounded and well defined.

3 Mobile Robot Case

The dynamic model of the car in [9] as shown in Fig. 1 is an example of underactuated systems with 5-DOFs, two control inputs and two velocity constraints. For (x, y) , denotes the position of the center of axle between the rear wheels, θ is the orientation of the car body with respect to x-axis, ψ is the angle rotation of the each wheel and ϕ is the steering angle with respect the car body. l and r denotes as distance and radius of wheel.

The overall dynamics of the car can be written as:

$$\begin{aligned} \dot{x} &= \dot{\psi} r \cos \theta \\ \dot{y} &= \dot{\psi} r \sin \theta \\ \dot{\theta} &= \dot{\psi} \frac{r}{l} \tan \theta \\ \ddot{\psi} &= \tau_1 \\ \ddot{\phi} &= \tau_2 \end{aligned} \tag{3}$$

After normalization of the units of (x, y) by r , and taking

$$\dot{\psi} = \omega_1$$

So, it gets

$$\begin{aligned} \dot{x} &= \omega_1 r \cos \theta \\ \dot{y} &= \omega_1 r \sin \theta \\ \dot{\theta} &= \omega_1 \frac{r}{l} \tan \theta \\ \dot{\phi} &= \omega_2 \end{aligned} \tag{4}$$

where

$$\begin{aligned} \dot{\omega}_1 &= \tau_1 \\ \dot{\omega}_2 &= \tau_2 \end{aligned} \tag{5}$$

τ_1 and τ_2 denotes as thrusts of the vehicle. Applying the change of coordinates and control as

$$\begin{aligned}
 x_1 &= x \\
 x_2 &= \frac{\tan \phi}{l \cos^3 \theta} \\
 x_3 &= \tan \theta \\
 x_4 &= y \\
 u_1 &= \omega_1 \phi \cos \theta \\
 u_2 &= \frac{1 + \tan^2 \phi}{l \cos^3 \theta} \omega_2 + \frac{3 \tan \theta \tan^2 \phi}{l^2 \cos^3 \theta}
 \end{aligned} \tag{6}$$

The $x, y, \theta, \phi, \omega_1, \omega_2$ can be obtained by rearrange (6) as

$$\begin{aligned}
 x &= x_1 \\
 y &= x_4 \\
 \theta &= \tan^{-1} x_3 \\
 \phi &= \tan^{-1} [l \cos^3 \theta x_2] \\
 \omega_1 &= \frac{u_1}{\phi \cos \theta} \\
 \omega_2 &= \left[\frac{l u_2 \cos^3 \theta}{1 + \tan^2 \phi} \right] - \left[\frac{(3 \tan \theta \tan^2 \phi)(l \cos^3 \theta)}{(l^2 \cos^3 \theta)(1 + \tan^2 \phi)} \right]
 \end{aligned} \tag{7}$$

The values of $x = (x_1, x_2, x_3, x_4)$ and $u = (u_1, u_2)$ were in systems (8) and (9).

The dynamic model of a car-like mobile robot can be transformed, via coordinates and inputs transform, to the following forth order system in chained form

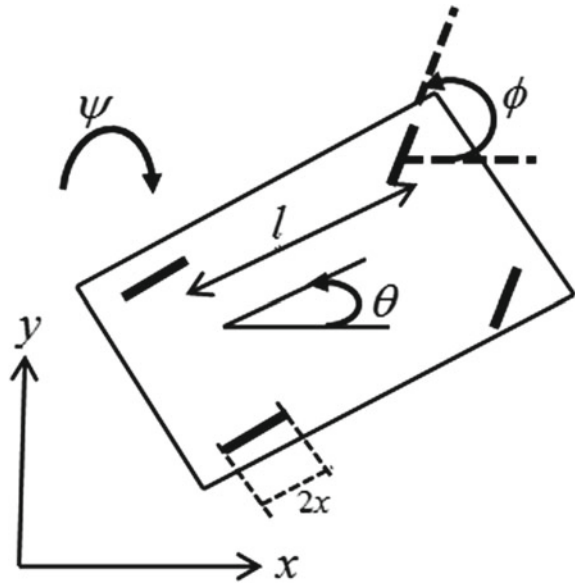
$$\begin{aligned}
 \dot{x}_1 &= u_1 \\
 \dot{x}_2 &= u_2 \\
 \dot{x}_3 &= x_2 u_1 \\
 \dot{x}_4 &= x_3 u_1
 \end{aligned} \tag{8}$$

A straight forward application of Theorem 1, leads to the following result.

Proposition 1 Consider the (8) under the control law defined over $\Lambda = \{x \in \frac{IR^n}{x_1} \neq 0, \forall t \in IR_+\}$,

$$\begin{cases} u_1 = -k_4 y_4 \\ u_2 = \dot{\psi}_2 - k_3 z_3 + k_4 y_4 z_2 \end{cases} \tag{9}$$

Fig. 1 Dynamic model of mobile robot [9]



with

$$\Psi_1 = k_1 \frac{y_1}{y_4},$$

$$\dot{\Psi}_1 = -k_1 k_4 y_2 + k_4 \Psi_1 \Psi_2 = -y_1 - k_1(1 + k_2) \frac{y_1}{y_4} + (k_1 + k_2) \frac{y_2}{y_4},$$

$$\dot{\Psi}_2 = k_4 y_2 y_4 - (k_1 + k_2) k_4 y_3 - 2k_4 k_1(1 + k_2) \frac{y_1}{y_4} + k_4(2k_1 + k_1 k_2 + k_2) \frac{y_2}{y_4}$$

$$z_2 = y_2 - \Psi_1$$

$$z_3 = y_3 - \Psi_2$$

$$y_1 = x_4$$

$$y_2 = x_3$$

$$y_3 = x_2$$

$$y_4 = x_1$$

Assume that $x_1(0) \neq 0$, then

- a. the whole state of the closed-loop system (8)–(9) remains in Λ ,
- b. the closed loop system (8)–(9) is exponentially stable,
- c. the control law is bounded and well defined.

4 Simulation Results

The method presented in this paper is tested on the system [6].

$$\begin{aligned} \dot{x} &= v \cos \theta \\ \dot{y} &= v \sin \theta \\ \dot{\theta} &= \frac{v}{l} \tan \theta \\ \dot{\phi} &= \omega \end{aligned}$$

where v is the content linear velocity of the car and l is the distance between the front and rear wheels axles. Results are depicted in Figs. 2 and 3. The initial conditions are taken as

$$x(0) = [x_{10}, x_{20}, x_{30}, x_{40}]^T = [2, 2, 2, 2]^T$$

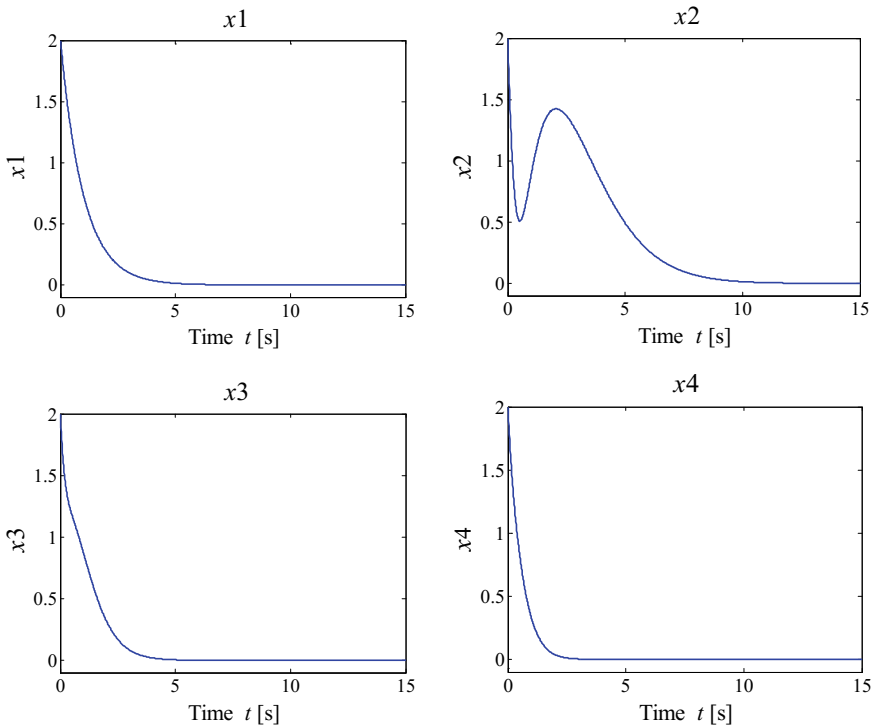


Fig. 2 Time evolution of the state variables

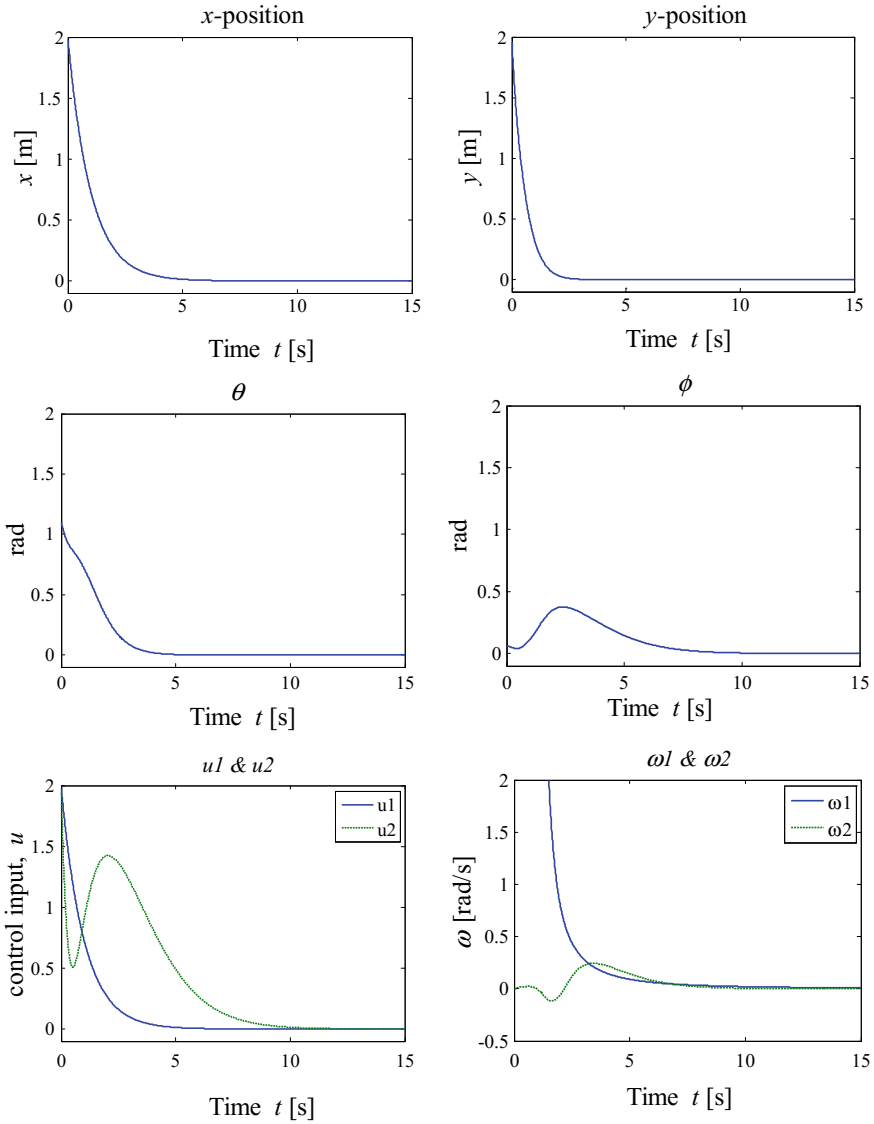


Fig. 3 Time history of the positions, angles and input variable

The mobile robot is asked to reach the origin starting from initial configuration. Figure 2 shows the convergence of the whole state of the system (8) to the origin under control law (9) with the following gains $k_1 = 3, k_2 = 2, k_3 = 1, k_4 = 1$. These gains are selected using try and error method. The time behavior of the variable x, y, θ, ϕ and input variables are shown in Fig. 3. It is clear that the discontinuous

backstepping approach presented in this paper guarantees the convergence and the exponential stabilization of all the states of the system.

5 Conclusion

The paper presents a backstepping discontinuous control approach with the application to the stabilization of a nonholonomic mobile robot. The proposed control scheme is smooth everywhere except at $x_1 = 0$. The discontinuity involved in the control is not very restrictive since it occurs just for $x_1(0) = 0$. The simulation results made on a car-like mobile robot demonstrate the effectiveness of the proposed control.

Acknowledgements The authors would like to thank for the support given to this research by Universiti Malaysia Pahang (UMP) under grant RDU170366.

References

1. Brockett, R.W.: Asymptotic stability and feedback stabilization. In: Brockett, R.W., Milman, R.S., Sussman, H.J. (eds.) *Differential Geometric Control Theory*, pp. 181–191. Birkhäuser Boston Inc, USA (1983)
2. Walsh, G., Tilbury, D., Sastry, S., Murray, R., Laumond, J.P.: Stabilization of trajectories for system with nonholonomic constraints. *IEEE Trans. Autom. Control* **39**(1), 216–222 (1994)
3. Panimadai Ramaswamy, S.A., Balakrishnan, S.N.: Formation control of car-like mobile robots: a Lyapunov function based approach. In: *2008 American Control Conference* (2008)
4. Klomanovsky, I., Mc-Clamroch, N.H.: Developments in nonholonomic control problem. *IEEE Control Syst. Mag.* **15**(6), 20–36 (1995)
5. Tayebi, A., Rachid A.: Discontinuous control design for stabilization of nonholonomic systems in chained form using backstepping approach. In *36th Proceeding of the IEEE CDC*, pp. 3089–3090 (1997)
6. Tanner, H.G., Kyriakopoulos, K.: Discontinuous backstepping for stabilization of nonholonomic mobile robot. In: *Proceedings of the IEEE ICRA*, pp. 3948–3953 (2002)
7. Dierks, T., Jagannathan, S.: Control of nonholonomic mobile robot formations: backstepping kinematics into dynamics. Thesis Dissertation, UMR (2007)
8. Francisco, V., Francisco, R., Carlos, L., Juan, I.C.: Influence of the friction coefficient on the trajectory performance for a car-like robot. In: *Mathematical Problems in Engineering*, Article ID 4562647 (2017)
9. Mnif, F.: On the reduction and control for a class of nonholonomic underactuated systems. *J. Electr. Eng.* **54**(1–2), 22–29 (2003)

Analysis of Mobile Robot Path Planning with Artificial Potential Fields



Hamzah Ahmad, Ahmad Nur Fakhruallah Mohamad Pajeri,
Nur Aqilah Othman, Mohd Mawardi Saari and Mohd Syakirin Ramli

Abstract This paper presents an analysis of a mobile robot path planning using potential field technique. The mobile robot has four wheels which can be driven and steered independently. For simplicity, this paper assumes Ackermann steering such that the vehicle can be modelled as a two-wheel system for path planning purposes. The potential field method which emphasizes on attractive potential and repulsive potential fields for path planning are proposed for analysis. For simulation settings, the mobile robot priorly does not pose any information on the environment and then moves until it reaches its goal using the calculated attractive and repulsive potential fields. The control gains which represents the attractive and repulsive force are studied to determine the effectiveness of the proposed method. Based on the simulation results, the robot is able to avoid obstacle and at the same time successfully arrived at the goal. Different cases of the potential fields and landmarks positions are also presented to determine the effectiveness of the technique.

Keywords Mobile robot · Path planning · Potential field

1 Introduction

It has been a comprehensive investigation about mobile robotics nowadays as almost every university has at least one laboratory focusing on the research. Besides, many system such as in industrial application, army and security system have applied the mobile robot as an alternative solution for various conditions. Based on the Japanese Industrial Robot Association (JIRA) [1], robots is categorized into several classes explaining about its function and level of complexity. This has makes the research becomes fascinating and challenging since a number of decades.

H. Ahmad (✉) · A. N. F. Mohamad Pajeri · N. A. Othman · M. M. Saari · M. S. Ramli
Faculty of Electrical and Electronics Engineering, University Malaysia Pahang,
Pekan, Pahang, Malaysia
e-mail: hamzah@ump.edu.my

© Springer Nature Singapore Pte Ltd. 2019
Z. Md Zain et al. (eds.), *Proceedings of the 10th National Technical Seminar on Underwater System Technology 2018*, Lecture Notes in Electrical Engineering 538,
https://doi.org/10.1007/978-981-13-3708-6_16

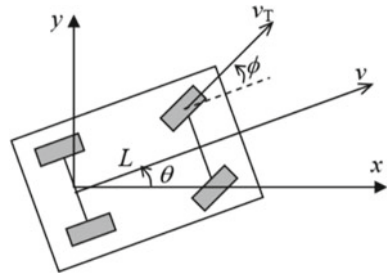
Mobile robot navigation is an important field in the research since its functionality is greatly depends on its controllability and observability features. The mobile robot must work efficiently and intelligently to pursue its objectives. Engineers, researchers and technologist are consistently explores the potential of robots in helping and managing daily chores such as house cleaning, babysitting, tour lead, shopping attendant, and many other applications. Such systems further demands exact navigation and a suitable control system to function efficiently.

When a mobile robot is designed, there are three important questions that have to be answered i.e. location of the robot, the robot motions and its goal. However to achieve the desired movements in real world environments is not a straightforward problem. One of the major concerns in designing robotics system is the cost analysis which incurs investigation and analysis to assess various mobile robot designs. In fact, to construct, model and perform a simulation platform for mobile robot system has becomes an essential practise to gain the desired results. Most of the mobile robot modelling concentrates on the design of the control systems and algorithms. Earlier study on the navigation is basically based on the wall-following method and edge detection. The system performs only for specific conditions such as working in a maze environment where no dynamic features are available. Mechanical design is also one part not to be missed. Moreover, the mechanical design may also affect the whole mobile robot performance. Therefore it is also needed to be considered to optimize the proposed control system for the mobile robot. Regardless to the mechanical issues, this paper will only focusing on the control system for analysis purposes.

The potential field approach [2, 3] is one of the popular method in mobile robotics for path planning. There are various technique available for path planning as discussed by Latombe et al. [4] and the research has currently extended to the more modern approach such as the behavioural based methods namely the particle swarm optimization and genetic algorithm [5–9]. The potential field technique is suggested in this paper as it has less complexity and require less computational cost. These advantages can be reviewed from several papers which have been analyzed the performance in different cases [10–15]. Differs to those papers, this research analyze the behavior of mobile robot movements and performance considering the time consumed with different gains.

The proposed technique is basically emulates the reflex action of a living organism. An attractive and repulsive potential fields are considered for the analysis. A fictitious attractive potential field is considered to ensure that the mobile robot arrived at the goals while repulsive potential fields acts as distance to be avoided when the mobile robot encounters any obstacle [3]. This paper mainly discussed and analyzed the effect and relationship of having different mobile robot wheel base, different repulsive, k_o and attractive force, k_g to the mobile robot path planning. The simulation results describe that the higher the attractive force, the distance travelled will be shorter but can consumed higher time. On the other hand, if the repulsive smaller, then the distanced travelled by the mobile robot becomes shorter. This is expected as the mobile robot avoids the obstacle with minimum distance with minimum time consumption to arrive at the goal.

Fig. 1 Car like robot model



2 Mathematical Modelling of the Proposed System

This research starts with a study about mobile robot model using car like vehicle as shown in Fig. 1. It is a nonholonomic framework, so it can just turn with a limited turn span. In this work, the potential field determines how the mobile robot moves whenever it encounters any obstacle in its pathway. Hence the potential field must be designed appropriately to guarantee that the mobile robot moves efficiently. In the technique, a force will be created when the mobile robot moves in the environment. The information from the calculated force derives the mobile robot motions to pursue its target and at the same time avoiding any obstacles.

Assume that the mobile robot makes a turn. This will make the car-like robot model moves in a circular path. These circular path or arc is concentrated in a point known as the Instantaneous Centre of Rotation (ICR). By using this information, the angular velocity can be determined by

$$\theta = v/R \tag{1}$$

where θ is the vehicle orientation with respect to the x -axis, and v is the forward speed of the robot (imposed by the real wheels). Note that R is the turning radius, which is defined by $R = L/\tan(\phi)$ where L is the length of the vehicle or wheel base. The steering angle, ϕ is mechanically constrained and its maximum value influences the robot motions. Remark that this important feature is to be analyzed by considering the maximum angle that the steering wheel can turn.

The velocity of the mobile robot based on the steering angle is given as follow.

$$v = v_T \cos \phi \tag{2}$$

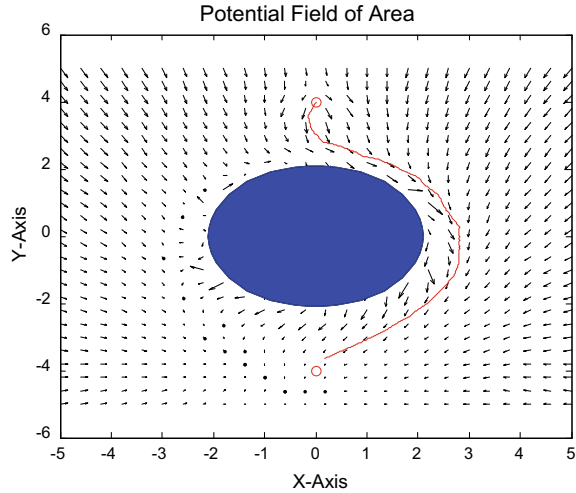
where v_T is the total velocity. Using above derived mathematical expression, the following equations presents the car-like robot kinematics.

$$x = v_T \cos \phi \cos \theta \tag{3}$$

$$y = v_T \cos \phi \sin \theta \tag{4}$$

$$\theta = v_T/L \sin \phi \tag{5}$$

Fig. 2 A sample 2-D potential field



with (x, y) defines the mobile robot x - y position in cartesian coordinates, and v_T defines the forward wheel velocity. In this model, the control input is the steering angle $\phi(t)$.

A simplified model of a vehicle is then given by

$$x = v \cos \theta \quad (6)$$

$$y = v \sin \theta \quad (7)$$

In this model, the control input is the heading angle $\theta(t)$.

3 Development of Artificial Potential Field

This paper considers an artificial potential field method for path planning. The potential is a scalar field whose negative gradient is a vector field of eternal forces vector. Consider a planar field that has some goals and some obstacles. A sample of calculated 2-D potential field is shown in Fig. 2. The targets are allocated with attractive potentials while the obstacles with repulsive potentials. The mobile robot will be attracted to the goal and at the same time avoids obstacles using the associated forces generated by the potentials.

Note that, at any Cartesian coordinates (x, y) in the x - y plane, the total sum of forces at that specific point provides a net force produced by all the goals and all the obstacles. The net force is a function of place that defines the vector force field. It represents the resultant force gained by summing the effects of the attraction force of the target and the repulsion forces of the obstacles.

In potential field motion control, it is important to keep track of forces, their components, and their directions. For mobile ground robot applications, the potential fields are usually used in a 2-D space. Consider that $\vec{r} = [x \ y]^T \in R^2$, then the force gradient are as follow

$$\vec{F}(\vec{r}) = \overrightarrow{F_{target}}(\vec{r}) + \sum_{i=1}^n \overrightarrow{F_{obs_i}}(\vec{r}) = -\nabla V(\vec{r}) \quad (8)$$

where $\overrightarrow{F_{target}}$ and $\overrightarrow{F_{obs_i}}$ describes the forces exist for the target and obstacles respectively. Consequently,

$$\nabla V(\vec{r}) = \left[\frac{\partial V}{\partial x} \ \frac{\partial V}{\partial y} \right]^T = [F_x \ F_y]^T \in R^2 \quad (9)$$

while its associated x, y components are defined by

$$F_x(x, y) = -\frac{\partial V(x, y)}{\partial x} \quad (10)$$

$$F_y(x, y) = -\frac{\partial V(x, y)}{\partial y} \quad (11)$$

The direction of movement for a mobile robot is produced persistently for any position (x, y) of the robot by following the course of the steepest drop in the potential field which simulates the bearing of movements. This can be considered as an optimization problem that searches for the point of minimum potential. Some of the generated sample potential fields and the forces will be simulated and will be referred for analysis purposes in later section.

Assume that the goal is at (x_1, y_1) and the current vehicle position is situated at $(x(t), y(t))$. A linear attractive potential is defined by

$$V(r) = k_g r \quad (12)$$

where the distance to the target is $r = [(x - x_1)^2 + (y - y_2)^2]^{-1/2}$. k_g acts as the system proportional gain. Then the gradient force for x, y components are generated as follows.

$$\begin{aligned} F_x &= -\frac{\partial V}{\partial x} = -k \frac{1}{2} [(x - x_1)^2 + (y - y_2)^2]^{-\frac{1}{2}} 2(x - x_1) \\ &= k \frac{(x_1 - x)}{r} \end{aligned} \quad (13)$$

$$\begin{aligned} F_y &= -\frac{\partial V}{\partial y} = -k \frac{1}{2} [(x - x_1)^2 + (y - y_2)^2]^{-\frac{1}{2}} 2(y - y_1) \\ &= k \frac{(y_1 - y)}{r} \end{aligned} \quad (14)$$

Above are the components of a unit vector. Remark that, the attractive force is constantly independent of the distance to the target. This means that the attractive effects of the target have an unbounded range of influence.

Suppose that a mobile robot needs to avoid an obstacle located at (x_1, y_1) and the current vehicle position is $(x(t), y(t))$. The repulsive potential is measured by

$$V(r) = \frac{k_o}{r} \quad (15)$$

where the distance to the target is $r = [(x - x_1)^2 + (y - y_2)^2]^{-1/2}$. k_o acts as the gain to the system to ensure the mobile robot avoids efficiently any obstacle. Then the gradient force generated from these information yields

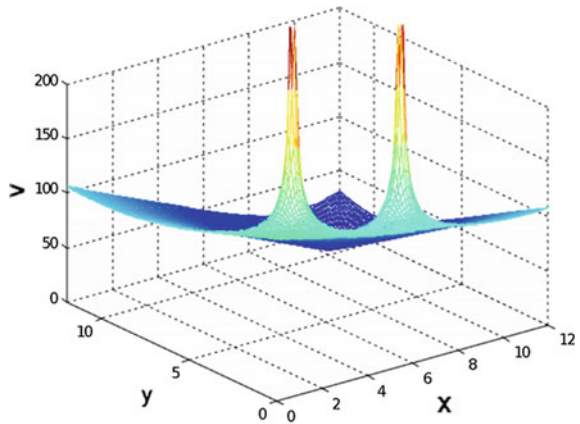
$$\begin{aligned} F_x &= -\frac{\partial V}{\partial x} \\ &= -\frac{\partial r^{-1}}{\partial x} \\ &= -k(-r^{-2})\frac{1}{2}[(x - x_1)^2 + (y - y_2)^2]^{-\frac{1}{2}}2(x - x_1) \\ &= -\frac{k}{r^2} \frac{(x_1 - x)}{r} \end{aligned} \quad (16)$$

$$\begin{aligned} F_y &= -\frac{\partial V}{\partial y} \\ &= -\frac{\partial r^{-1}}{\partial y} \\ &= -k(-r^{-2})\frac{1}{2}[(x - x_1)^2 + (y - y_2)^2]^{-\frac{1}{2}}2(y - y_1) \\ &= -\frac{k}{r^2} \frac{(y_1 - y)}{r} \end{aligned} \quad (17)$$

The above determinations are similar to the electrostatic force or gravitational force. This also means that the repulsive effects of the obstacles have a limited range of influence.

Consider an environment that has size of square $[0, 12] \times [0, 12]$ in the (x, y) plane and has a goal or target at $(x_G, y_G) = (10, 10)$ and two obstacles at $(x_1, y_1) = (3, 3)$ and $(x_2, y_2) = (7, 2)$ respectively. If those parameters are taken into account, then the resulting sample of potential fields can be shown in Fig. 3. The figure shows how the potential fields affects the mobile robot movements. As depicted, there are two positions demonstrates higher repulsive forces at the pre-defined obstacles. If k_o is bigger, then the force to move the mobile robot to the goal will be changing rapidly i.e. produces a steep curves to the surface. The results will be shown in later sections demonstrating how the mobile robot moves when a given situations are described.

Fig. 3 Sample of potential fields surface



4 Result and Discussion

This section presents the simulation outcomes which has been analyzed in MATLAB software. There are few examples with attracting controller and repulsing controller gathered in this analysis with regards to different cases.

4.1 Simulation Setup

To start the analysis, some parameters must be defined. The parameters for k_g and k_o are selected such that it provides the best results for the mobile robot movements. The attractive potential field for the target in (10, 10) is defined as

$$V_G = k_g r_G \tag{18}$$

where k_g is a design gain and r_G is the distance between the robot and the target:

$$r_G = [(x - x_1)^2 + (y - y_2)^2]^{-1/2} \tag{19}$$

Two obstacles in (3, 3) and (9, 9) have a repulsive potential field satisfying the below equation.

$$V_o = \frac{k_o}{r_o} \tag{20}$$

where k_o and r_o are the equivalents for the gain and the distance from the robot, respectively. The total potential field of the scene can be calculated by adding this three distinctive fields

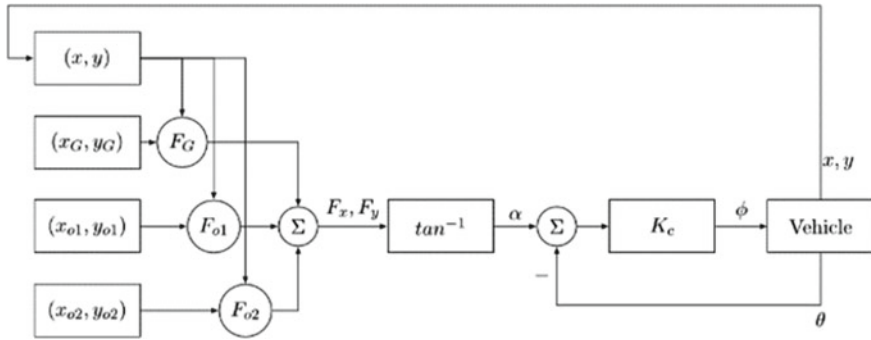


Fig. 4 The block diagram of the proposed system

$$(V = V_G + V_{O1} + V_{O2}) \quad (21)$$

Then, the attractive force component from the goal are generated as

$$F_{Gx} = -\frac{\partial V_G}{\partial x} = k_g \frac{(10 - x)}{r_G} \quad (22)$$

$$F_{Gy} = -\frac{\partial V_G}{\partial y} = k_g \frac{(10 - y)}{r_G} \quad (23)$$

whereas the repulsion force of the obstacle are computed as

$$F_{Oix} = -\frac{\partial V_{Oi}}{\partial x} = k_o \frac{(x_{oi} - x)}{r_{oi}} \quad (24)$$

$$F_{Oiy} = -\frac{\partial V_{Oj}}{\partial y} = k_o \frac{(y_{oi} - y)}{r_{oi}} \quad (25)$$

The total force components affecting the vehicle are $F_x = F_{Gx} + F_{O1x} + F_{O2x}$ and $F_y = F_{Gy} + F_{O1y} + F_{O2y}$. The desired heading angle can be computed as

$$\alpha = \tan^{-1} \left(\frac{F_y}{F_x} \right) \quad (26)$$

A proportional controller K_c is designed to make the robot arrived to target. Then the control input is

$$\phi = K_c(\alpha - \theta) \quad (27)$$

A block diagram for the mobile robot model and environments are shown as follows (Fig. 4).

For verification purposes, simulation is performed by considering first the following parameters; $k_g = 30$, $k_o = 30$, $k_c = 2$, $v = 1$ and $L = 2$. As the velocity is not

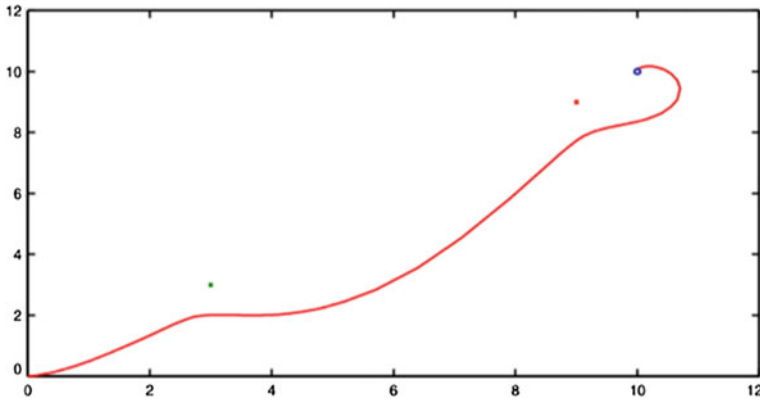


Fig. 5 Mobile robot movements with $k_g = 30$, $k_o = 30$, $k_c = 2$, $v = 1$ and $L = 2$

involved in the control law computation, some modification is made to ensure the vehicle stop when it is close enough to the goal. Initial conditions for the position and initial heading angle of the robot are all set to zero. The system response is shown in Fig. 5 which explains the mobile robot has arrived at its target.

Further analysis in 2-D environment are demonstrated that has 1 goal and 3 obstacles. The goal is located at coordinate (10, 10), while the obstacle at coordinate (4, 2), (9, 6), and (9, 9) respectively.

4.2 Robot Movements with Adjusted Control Gain of Goal, k_g

This control gain aiming to investigate elapsed time which that begin process until end process a robot from initial pose to goal. This simulation takes fix value of velocity ($v = 10$) and control gain of obstacle ($k_o = 10$). The black line refer to trajectory of the robot to the goal without any existence of obstacle, while the other colour line refer to trajectory of the robot to the goal with obstacle.

Figures 6, 7, 8, 9 and Table 1 shows the effects of having the control gain of goal from 5 until 30 and effects of various wheel base sizes from 10 until 25. The time consumed for the mobile robot to moves at its initial position until its goal are recorded to analyze any differences. It was found that the time consumption has almost a proportional relationship with k_g . Besides this from Figs. 6, 7, 8 and 9, the distance of the mobile robot to the goal becomes shorter when it has lower k_g as a result of having bigger wheel base. Thus designer must select the right wheel base to achieve an efficient path planning. For reference, Table 2 describes the trajectory without obstacle force which denotes slightly higher time consumption compared to the case of having obstacle force. This is due to the total force calculated through

Fig. 6 Wheel base, $L = 10$

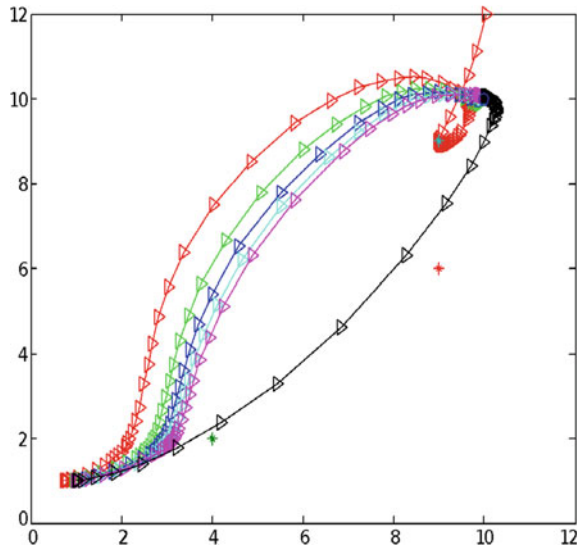
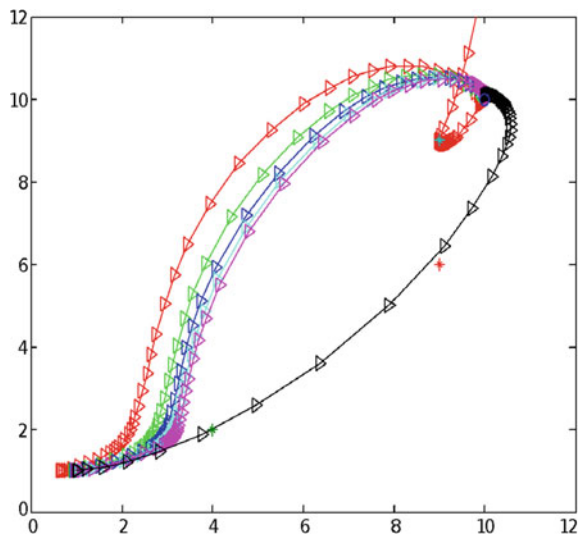


Fig. 7 Wheel base, $L = 15$



Eqs. (16)–(17) produces smaller forces compared when there are obstacles to the system.

In Figs. 6 and 7, it can be observed that the mobile robot did not moves efficiently even though has arrived at its goal. This is happened because of the mobile robot velocity moves relatively fast that it should be. This also requires velocity to be considered as part of control system in path planning technique. If the velocity is reduced to 0.8, the result has a promised outcome as demonstrated in Figs. 10 and 11.

Fig. 8 Wheel base, $L = 20$

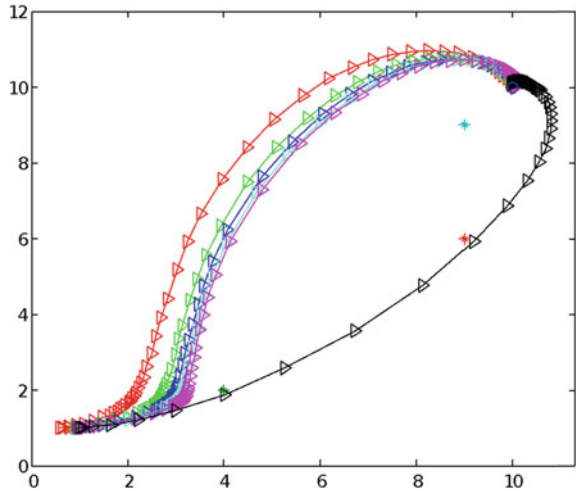
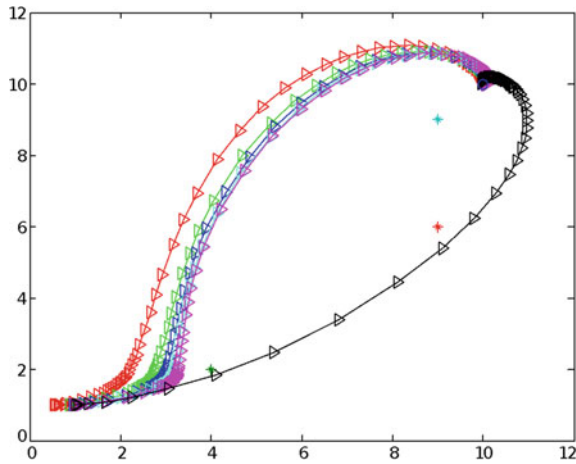


Fig. 9 Wheel base, $L = 25$



4.3 Robot Movements with Adjusted Control Gain of Obstacle, k_o

This section analyzes the effect of having different k_o to the system. This simulation is taking fix value of velocity ($v = 10$) and control gain of obstacle ($k_g = 10$). The black line refer to trajectory of the robot to the goal without obstacle while the other colour line refer to trajectory of the robot to the goal with obstacle.

Figures 12, 13, 14 and Table 3 shows the mobile robot trajectory with goal force from 10 until 50 and fixed obstacle force with respect to the increase of wheel base from 10 until 25. Table 4 on the other hand defines the trajectory without obstacle force. Based on Tables 3 and 4, it is seems that k_o have relationship with the distance

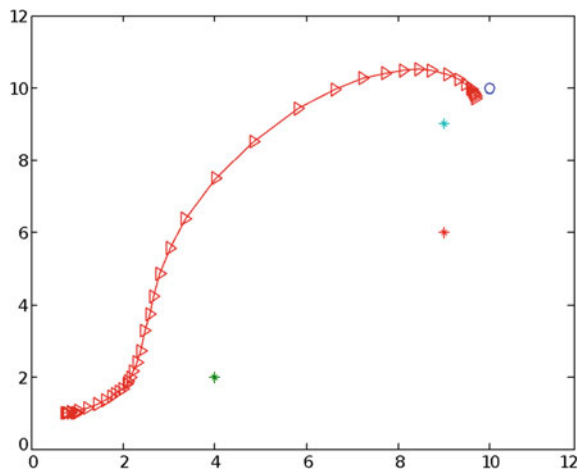
Table 1 Time consumption on different k_g (with obstacle)

Colour	k_g	Elapsed time, t(s)			
		L = 10	L = 15	L = 20	L = 25
Red	10	0.042029	0.040981	0.041487	0.039959
Green	20	0.005447	0.005348	0.005319	0.004872
Blue	30	0.005318	0.005778	0.005686	0.005380
Cyan	40	0.005743	0.005453	0.005288	0.005352
Magenta	50	0.005308	0.005521	0.005361	0.005444

Table 2 Time consumption on different k_g (no obstacle)

Colour	k_g	Elapsed time, t(s)			
		L = 10	L = 15	L = 20	L = 25
Black	50	0.005341	0.005356	0.005774	0.005596

Fig. 10 Wheel base, $L = 10$, velocity, $v = 0.8$



i.e. smaller k_0 produces shorter distance for mobile robot to arrive at the goal. As a result, the time consumed is decreasing whenever smaller is k_0 selected. Looking on the wheel base size, the bigger the size, the longer time mobile robot needs to achieve its goal.

Some problem can be viewed from Fig. 11 for the mobile robot path due to inappropriate selection of repulsive and attractive forces. So, to minimize the error, the velocity must be reduced to 0.63 to produce better result demonstrated in Fig. 15. If more errors occurred during the movement, then the mobile robot cannot arrive accurately at the final positions. As there are a lot of noises that affects the performance of mobile robot which includes the tire slippage, the motors conditions, sensors and power source, the mobile robot must be well-configured to reduce the noise consequences.

Fig. 11 Wheel base, $L = 10$

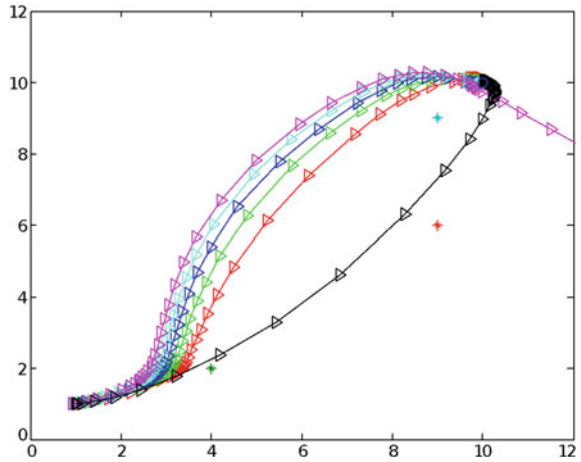


Fig. 12 Wheel base, $L = 15$

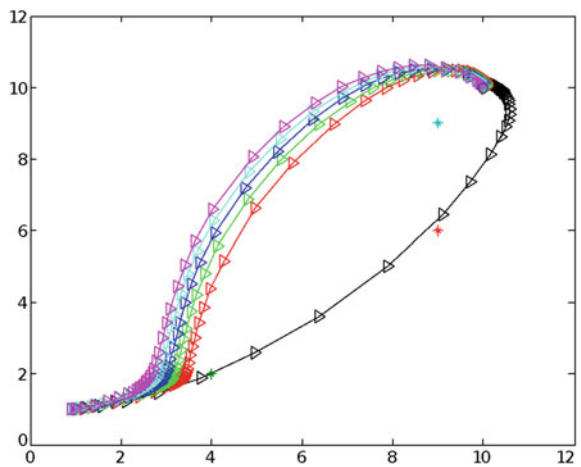


Table 3 Time consumption on different k_o (with obstacle)

Colour	k_o	Elapsed time, t(s)			
		L = 10	L = 15	L = 20	L = 25
Red	10	0.043368	0.005428	0.005503	0.005269
Green	20	0.005613	0.005812	0.005202	0.005656
Blue	30	0.006024	0.005632	0.005371	0.005770
Cyan	40	0.005671	0.005462	0.005484	0.006017
Magenta	50	0.006045	0.005460	0.005939	0.005454

Fig. 13 Wheel base, $L = 20$

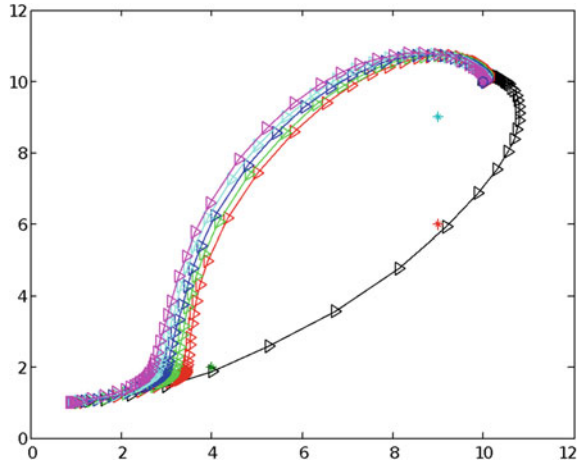


Fig. 14 Wheel base, $L = 25$

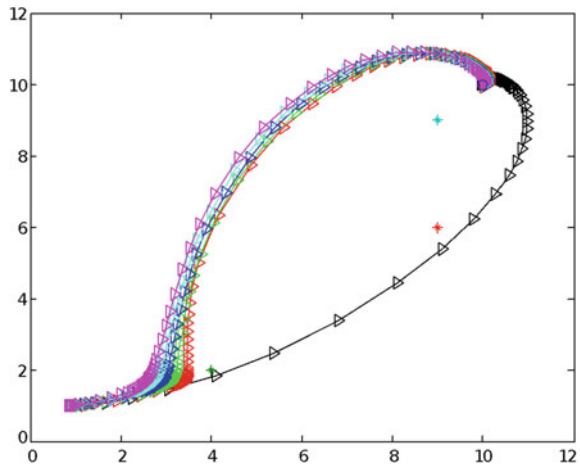


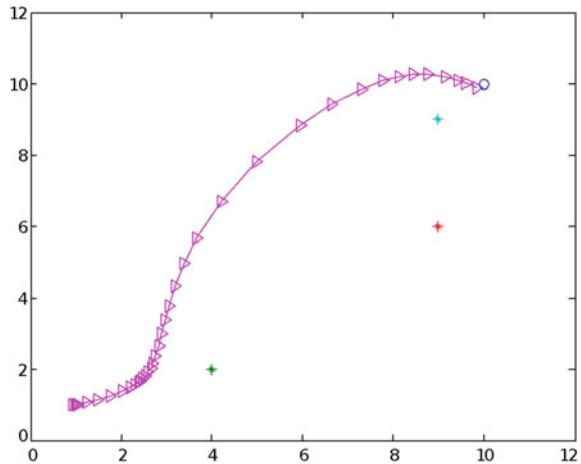
Table 4 Time consumption on different k_o (with obstacle)

Colour	k_o	Elapsed time, t(s)			
		L = 10	L = 15	L = 20	L = 25
Black	10	0.006099	0.004762	0.004747	0.004834

5 Conclusion

In this paper, a possible mathematical model of a Ackermann steering four-wheeled car-like mobile robot have been studied. A mobile robot kinematic model has been successfully been simulated via MATLAB to demonstrate a path planning. A potential field method is proposed for the path planning of autonomous mobile robots by using repulsive and attractive forces. The potential functions defines the relative

Fig. 15 Wheel base, $L = 10$,
velocity = 0.63



positions and velocities of the robot with respect to the goal and the obstacles into account. The virtual force exhibits its effect to keep the robot to follow the goal with the similar moving trend and avoid obstacles with contrary moving trends. By choosing the suitable parameters for the potential function, the reasonable planning path can be produced successfully. Finally, some methodic simulations are completed to confirm and show the performance of the potential field method for mobile robot path planning.

Acknowledgements The authors would like to thank Ministry of Higher Education and Universiti Malaysia Pahang for supporting this research under RDU160145 and RDU160379.

References

1. Japan Robot Association. Summary report on technology strategy for creating a robot society in the 21st century. Japan. May 2001
2. Borenstein, J., Koren, Y.: Real-time obstacle avoidance for fast mobile robots. *IEEE Trans. Syst. Man, Cybern.* **19**(5), 1179–1187 (1989)
3. Borenstein, J., Koren, Y.: The vector field histogram-fast obstacle avoidance for mobile robots. *IEEE Trans. Robot. Autom.* **7**(3), 278–288 (1991)
4. Latombe, J.: *Robot Motion Planning*. Kluwer, Norwell, MK (1991)
5. Zahra, E., Mehmet O.E.: Multi-objective grasshopper optimization algorithm for robot path planning in static environments. In: 2018 IEEE International Conference on Industrial Technology, pp. 244–249 (2018)
6. Safdar, Z., Mehreen, S., Ayesha, B., Foqia, H., Kaleem, A.: Planning-based optimized path for automatic robot navigation. In: 2018 IEEE International Conference on Computing, Mathematics and Engineering Technologies, pp. 1–6 (2018)
7. Mehmet, K., Akif, D.: Comparison of optimal path planning algorithm. In: 2018 International Conference on Advanced Trends in Radioelectronics, Telecommunications and Computer Engineering, pp. 255–258 (2018)

8. Yuhong, L., Fating, H., Winjie, L., Sheng, B., Liqian, F.: Optimization of robot path planning parameters based on genetic algorithm. 2017 IEEE International Conference on Real-time Computing and Robotics, pp. 529–534 (2017)
9. Asma, A., Sadok, B.: A new multi-robot path planning algorithm: dynamic distributed particle swarm optimization, In: 2017 IEEE International Conference on Real-Time Computing and Robotics, pp. 437–442 (2017)
10. Farid, B., Denis, G., Herve, P., Dominique, G.: Modified artificial potential field method for online path planning applications. In: 2017 IEEE Intelligent Vehicle Symposium, pp. 180–185 (2017)
11. H. Asadi, S. Ozgoli.: A novel approach to reduce oscillations in path planning based on potential field approach. In: 2017 Iranian Conference on Electrical Engineering, pp. 603–608 (2017)
12. Hendri, H.T., Oyas, W., Teguh, B.A., Adha, I.C.: Framework transformation for local information on artificial potential field path planning. In: 2016 8th International Conference on Information Technology and Electrical Engineering, pp. 1–6 (2016)
13. Yadollah, R., Amir, K., Shih-Ken, C., Bakhtiar, L.: A potential field based model predictive path planning controller for autonomous road vehicles. *IEEE Trans. On Intelligent Transportation System* **18**(5), 1255–1267 (2017)
14. Youcef, H., Adel, M., Abdelfetah, H., Ourda, H., Brahim, B.: Mobile manipulator path planning based on artificial potential field: application on RobuTER/U LM, 2015 IEEE International Conference on Electrical Engineering, pp. 1–6 (2015)
15. Hossein, K., Poria, N.P., Mehdi, T.M., Roya, S.N.: Path planning of 3-RRR parallel robot by avoiding mechanical interference via artificial potential field. In: 2015 3rd RSI International Conference on Robotics and Mechatronics, pp. 240–245 (2015)

Data-Driven PID Tuning for Liquid Slosh-Free Motion Using Memory-Based SPSA Algorithm



Nik Mohd Zaitul Akmal Mustapha, Mohd Zaidi Mohd Tumari,
Mohd Helmi Suid, Raja Mohd Taufika Raja Ismail
and Mohd Ashraf Ahmad

Abstract This study proposes a data-driven PID tuning for liquid slosh suppression based on enhanced stochastic approximation. In particular, a new version of Simultaneous Perturbation Stochastic Approximation (SPSA) based on memory type function is introduced. This memory-based SPSA (M-SPSA) algorithm has the capability to obtain a better optimization accuracy than the conventional SPSA since it is able to keep the best design parameter during the tuning process. The effectiveness of this algorithm is tested to data-drive PID tuning for liquid slosh problem. The achievement of the M-SPSA based algorithm is assessed in terms of trajectory tracking of trolley position, slosh angle reduction and also computation time. The outcome of this study shows that the PID-tuned M-SPSA is able to provide better control performance accuracy than the other variant of SPSA based method.

Keywords Data-driven control · PID controller · Stochastic approximation

1 Introduction

Recently, liquid slosh problems have become attractive research topics due to their safety issue in vehicle transportations and a numerous number of applications in various industries. Nevertheless, there are still a lot of challenges that need to be considered in controlling such systems. The control strategies for liquid slosh reduction can be clustered into two main parts, which are mechanical design part and control design part. In mechanical design part, researchers are interested to improve the whole mechanical structure of the tank or the vehicle to reduce liquid slosh motion. For example, they may propose different shapes of tank or introduce some

N. M. Z. A. Mustapha · M. H. Suid · R. M. T. Raja Ismail · M. A. Ahmad (✉)
Faculty of Electrical and Electronics Engineering, Universiti Malaysia Pahang, Pekan, Malaysia
e-mail: mashraf@ump.edu.my

M. Z. Mohd Tumari
Faculty of Engineering Technology, Universiti Teknikal Malaysia Melaka, Durian Tunggal,
Malaysia

kinds of damper inside the tank. Meanwhile, in the control design part, they are interested in developing an efficient control algorithm to suppress the slosh. For such a case, they must clearly observe the slosh behaviour through available sensors to detect the slosh. Perhaps, the sensor design for detecting slosh also became very interesting topics to be discovered.

Research on improving the mechanical design of tanks or carriers has started earlier than the controller design part. It is started in 1960 by Budiansky [1], which is the first researcher studied the liquid slosh impact on the circular canal and spherical tanks. Other earlier work is reported by Fischer [2], which focused on the cylindrical tank. In parallel with software advancement in the past few decades that can simulate the fluid dynamics of slosh with different types of tank shapes, many researchers have further improved and optimized the shapes of the tanks or carriers. Recent works on improving the tank shapes are reported in [3–9]. On the other hand, instead of proposing an improved shape of the tank, there is also research work on introducing a kind of damper or baffles inside the tank to reduce the liquid slosh. This kind of baffles is promising strategy since it is widely applied for a long type cylindrical tank such as in fuel tank lorry or vessel. Their works are reported in [10–18].

The controller design part of liquid slosh motion mostly focused on regulating the cart or trolley (that carrying the liquid) such that it can follow a given cart position tracking precisely with less liquid slosh level inside the tank. So far, various control techniques have been introduced to achieve these objectives. Bridgen et al. [19] and Aboel-Hassan et al. [20] proposed the input shaping controller, which is in the class of feed-forward control design. This method can also be considered as a data-based or model-free control scheme since it is designed based on the frequency of slosh oscillation data. The relevant work has also been done by Baozeng and Lemei [21]. However, the feed-forward control scheme has a drawback of handling any unexpected disturbance since there is no feedback signal to be controlled. Therefore, many researchers are focused on developing numerous feedback control strategies for liquid slosh suppression, such as Sliding Mode Controller [22–27], Linear Quadratic Regulator [28–30], H-infinity [31, 32], and Variable Structure Control [33]. Those mentioned methods heavily depend on the state space model of the system, which may not represent the chaotic nature of slosh motion and also may not consider the unmodeled dynamics. A similar class of model-based feedback controller has been reported by Nair et al. [34] and Sira-Ramirez [35]. Here, a nonlinear higher order Sliding Mode Controller and a flatness generalized PI control have been introduced in [34] and [35], respectively. Meanwhile, in [36], an active force control (AFC) has been proposed by combining it with a conventional PID control scheme. It is shown that the composite PID-AFC provides better slosh reduction than the standalone PID. On the other hand, intelligent control methods—such as fuzzy logic controllers and artificial neural networks—have been investigated in a variety of applications that capable of obtaining robust controllers for mathematically ill-defined systems. This merit has brought to recent advances in the area of intelligent design in tank shape [37, 38]. Various fuzzy based controllers have been credited in the control of liquid slosh which have brought to promising performances [39–42]. Grundelius [43] used

an iterative learning control technique for controlling liquid slosh in an industrial packaging machine.

Based on the above survey, most of the control designs are highly dependent on the developed model. In other words, they need to use the information of the plant's model to obtain the parameters of the controller. However, the obtained control coefficients may not accurately control the real slosh system due to unmodeled dynamics feature in the model and also some simplifications to the model. Therefore, it is necessary to develop the control strategy using the real input-output data of the system instead of using the model, which is called data-driven control. Besides that, a norm-limited simultaneous perturbation stochastic approximation (SPSA) [44–46] already shown a satisfactory finding for the data-driven method. The reason is that the SPSA method has been proven to be powerful for various data-driven tuning problems in the absence of any straightforward form of the loss function. Moreover, this method is also useful for data-driven approach framework since it can guarantee the stable convergence by using a saturation function to limit the updated control parameter. However, the norm-limited SPSA and its variants are still not able to produce better control accuracy due to its memory less structure. In particular, the norm-limited SPSA and its variants only produce the optimal design parameters at the final iteration while it may keep better design parameters during the tuning process if they have memory. Therefore, the SPSA with memory feature has a good potential to keep the best design parameters during the controller tuning process.

This paper proposed an enhanced SPSA with the memory feature for PID control tuning of liquid slosh problem. Here, we adopt a liquid slosh mathematical model in [47], which is derived from a motor-driven with partially liquid in the rectangular tank which performing a rectilinear motion. The aim of this study is to apply the proposed memory-based SPSA in tuning the given PID controller such that the cart position follows the desired tracking while minimizing the slosh motion. Finally, the effectiveness of the proposed method is evaluated regarding the trajectory tracking of cart position and level of slosh reduction.

The organization of the paper is structured as follows. The formulation of the problem of data-driven PID controller for liquid slosh control is described in Sect. 2. In Sect. 3, a review on standard SPSA and the explanation on the memory-based SPSA method is discussed. The application of memory-based SPSA for model-free PID controller design is also presented. Section 4 presents the simulation results and discussion. Section 5 concludes the findings of our study.

Notation: The symbol \mathbf{R} is denoted as a set of real numbers and the symbol \mathbf{R}_+ is denoted as a set of positive real numbers. The probability of event $Q = a$ is denoted by $\mathbf{P}_r(Q = a)$, where Q is the random variable.

2 Formulation of Data-Driven PID Problem

The control system block diagram of the liquid slosh problem is given in Fig. 1. Here, the reference is defined as $Y_R(t)$, the control input is $V(t)$, the trolley position is $Y(t)$ and the slosh angle is $\theta(t)$. The liquid slosh plant is denoted by the symbol G .

The symbols $K_1(s)$ and $K_2(s)$ are the PID controller that are fed back from the trolley position and the slosh angle, respectively. Here,

$$K_1(s) = p_1 \left(1 + \frac{1}{i_1 s} + \frac{d_1 s}{1 + (d_1/n_1)s} \right), \quad (1)$$

$$K_2(s) = p_2 \left(1 + \frac{1}{i_2 s} + \frac{d_2 s}{1 + (d_2/n_2)s} \right), \quad (2)$$

where $p_1, p_2 \in \mathbf{R}$ are the proportional gains $i_1, i_2 \in \mathbf{R}$ are the integral time gains, $d_1, d_2 \in \mathbf{R}$ are the derivative time gains and $n_1, n_2 \in \mathbf{R}$ are the filter parameter. The performance indicator is to track the given reference trolley position while producing minimum liquid slosh. Firstly, let

$$\hat{E} = \int_{t_0}^{t_f} |Y_R(t) - Y(t)|^2 dt, \quad (3)$$

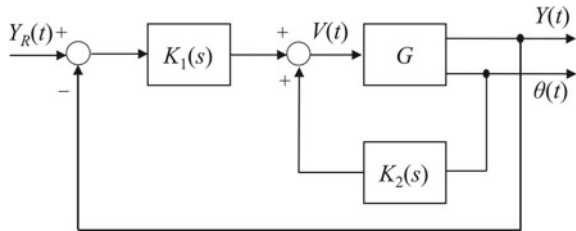
$$\hat{\theta} = \int_{t_0}^{t_f} |\theta(t)|^2 dt, \quad (4)$$

$$\hat{V} = \int_{t_0}^{t_f} |V(t)|^2 dt, \quad (5)$$

where the time span $[t_0, t_f]$ is denoted as the performance evaluation span, and $t_0 \in \{0\} \cup \mathbf{R}$ and $t_f \in \mathbf{R}_+$. Then, the performance indicator is given by

$$J(\mathbf{p}, \mathbf{i}, \mathbf{d}, \mathbf{n}) = w_1 \hat{E} + w_2 \hat{\theta} + w_3 \hat{V}, \quad (6)$$

Fig. 1 Control system block diagram for liquid slosh



where $\mathbf{p} = [p_1 \ p_2]^T$, $\mathbf{i} = [i_1 \ i_2]^T$, $\mathbf{d} = [d_1 \ d_2]^T$, and $\mathbf{n} = [n_1 \ n_2]^T$. The symbols $w_1 \in \mathbf{R}$, $w_2 \in \mathbf{R}$ and $w_3 \in \mathbf{R}$ are pre-defined weighting coefficients, which are to be determined by the designer. Thus, the problem statement for data-driven PID controller can be stated by.

Problem 1 Given the PID control system in Fig. 1. Then, find the controllers $K_1(s)$ and $K_2(s)$, PID controllers where the control objective $J(\mathbf{p}, \mathbf{i}, \mathbf{d}, \mathbf{n})$ corresponds to the control vector gain $\mathbf{p}, \mathbf{i}, \mathbf{d}$, and \mathbf{n} is minimizes in corresponded with the input and output data ($V(t), Y(t), \theta(t)$).

3 Data-Driven PID Using Memory-Based SPSA

Now, the proposed memory-based SPSA algorithm is applied to data-driven PID tuning of liquid slosh problem. Firstly, we review the basic algorithm of Simultaneous Perturbation Stochastic Approximation that was firstly introduced by Spall [48]. Secondly, the improved version of SPSA, which is called memory-based SPSA is explained. Finally, it is shown on how to apply this new algorithm as a tool form data-driven PID controller design for liquid slosh problem.

3.1 A Review on Basic SPSA Algorithm

This section briefly shows the basic algorithm of SPSA introduced by Spall [48]. Since the liquid slosh problem involves minimizing the tracking error and control input energy, we consider the minimization optimization problem given by

$$\min_{z \in \mathbf{R}^n} L(z) \quad (7)$$

where $L: \mathbf{R}^n \rightarrow \mathbf{R}$ is an unknown loss function with the design parameter vector $z \in \mathbf{R}^n$. The SPSA algorithm [48] updates $z \in \mathbf{R}^n$ to find an optimal solution $z^* \in \mathbf{R}^n$ of (7) by using

$$z(j+1) = z(j) - g_1(j)\sigma(z(j)) \quad (8)$$

for $j=0, 1, \dots$ where $g_1(j)$ is the gain sequence such that $g_1(j) \rightarrow 0$ when $j \rightarrow \infty$, and $\sigma(j)$ is the vector for gradient approximation denoted by

$$\sigma(z(j)) = \frac{L(z(j) + g_2(j)\delta(j)) - L(z(j) - g_2(j)\delta(j))}{2g_2(j)} \begin{bmatrix} \delta_1(j) \\ \delta_2(j) \\ \vdots \\ \delta_n(j) \end{bmatrix}. \quad (9)$$

In (9), $g_2(j)$ is another gain sequence that follows $g_2(j) \rightarrow 0$ when $j \rightarrow \infty$, and $\delta(j)$ is the random vector with n dimension. The symbol $\delta_i(j)$ is the i -th element of the random vector $\delta(j)$. In this algorithm, both gain sequences $g_1(j)$ and $g_2(j)$ are normally expressed by $g_1(j) = a/(j+1+A)^\alpha$ and $g_2(j) = c/(j+1)^\gamma$, respectively. The guidance to select the nonnegative values of a, A, α, c and γ are explained in [48]. Next, the $\delta(j)$ is generated using the component-wise Bernoulli distribution

$$\begin{cases} \mathbf{P}_r(\delta_i(j) = 1) = 0.5, \\ \mathbf{P}_r(\delta_i(j) = -1) = 0.5. \end{cases} \quad (10)$$

Then, the SPSA algorithm is shown in **Algorithm 1** as follow:

Algorithm 1 Basic SPSA [48]

- S1:** Determine the values a, A, α, c and γ for the gain sequences $g_1(j)$ and $g_2(j)$. Select the initial design parameter $z(0)$ and j_{\max} , and set $j = 0$
- S2:** Produce random vector $\delta(j)$
- S3:** Acquire two values of the $L(z(j) + g_1(j)\delta(j))$ and $L(z(j) - g_1(j)\delta(j))$
- S4:** Approximate the gradient $\sigma(j)$ in (9)
- S5:** Obtain $z(j+1)$ by calculating the updated law in (8)
- S6:** If j_{\max} is achieved, the algorithm stops with the solution $z^* = z(j_{\max})$. Otherwise, set $j = j + 1$ and repeat Step S2.

3.2 Memory-Based SPSA Algorithm (M-SPSA)

This section demonstrates the enhanced SPSA by adopting the memory feature. In particular, the memory function is introduced after Step S3 and Step S5 in **Algorithm 1**. The detail of the M-SPSA algorithm is shown in **Algorithm 2** as follow:

Algorithm 2 M-SPSA

- S1:** Determine the values a, A, α, c and γ for the gain sequences $g_1(j)$ and $g_2(j)$. Select the initial design parameter $z(0)$ and j_{\max} , and set $j = 0$. Obtain $L_{\text{best}} = L(z(0))$ and $z_{\text{best}} = z(0)$
- S2:** Produce random vector $\delta(j)$
- S3:** Acquire two values of $L(z(j) + g_1(j)\delta(j))$ and $L(z(j) - g_1(j)\delta(j))$
- S4:** If $L(z(j) + g_1(j)\delta(j)) < L_{\text{best}}$, update $L_{\text{best}} = L(z(j) + g_1(j)\delta(j))$ and $z_{\text{best}} = z(j) + g_1(j)\delta(j)$. Otherwise, go to Step S5.
- S5:** If $L(z(j) - g_1(j)\delta(j)) < L_{\text{best}}$, update $L_{\text{best}} = L(z(j) - g_1(j)\delta(j))$ and $z_{\text{best}} = z(j) - g_1(j)\delta(j)$. Otherwise go to Step S6.
- S6:** Approximate the gradient $\sigma(j)$ in (9)
- S7:** Obtain $z(j+1)$ by calculating the updated law in (8)
- S8:** Execute $L(z(j+1))$. If $L(z(j+1)) < L_{\text{best}}$, update $L_{\text{best}} = L(z(j+1))$ and $z_{\text{best}} = z(j+1)$. Otherwise, $z(j+1) = z_{\text{best}}$

S9: If j_{\max} is achieved, the algorithm stops with the solution $z^* = z_{\text{best}}$. Otherwise, set $j = j + 1$ and repeat Step S2

Based on the **Algorithm 2** above, the parameter L_{best} and z_{best} are introduced to keep the best loss function and its corresponding design parameter at each iteration. In particular, the value of L_{best} is compared with the perturbed loss function values $L(z(j) + g_1(j)\delta(j))$ and $L(z(j) - g_1(j)\delta(j))$ and the updated $L(z(j+1))$ in Steps S4, S5 and S8, respectively, to seek for the best loss function and its best design parameter along the tuning process. Finally, in Step S9, the optimal design parameter z^* is set as z_{best} .

3.3 Application of M-SPSA for Data-Driven PID Controller Design

Furthermore, the M-SPSA algorithm explained in Sect. 3.2 is applied for data-driven PID control scheme. Firstly, let the design parameter is defined as follows:

$$\zeta = [p_1 \ p_2 \ i_1 \ i_2 \ d_1 \ d_2 \ n_1 \ n_2]^T \in \mathbf{R}^8. \tag{11}$$

Here, the design parameter tuning based on logarithmic scale is adopted to enhance the exploration of the design parameter by setting $\zeta = 10^{z_i}$ ($i = 1, 2, \dots, 8$). Then, the modified representation of the loss function is written as $J = [10^{z_1} \ 10^{z_2} \ \dots \ 10^{z_8}]$. Finally, the data-driven PID controller is shown in **Algorithm 3** as follows:

Algorithm 3 Data-driven PID controller design

- S1:** Select the PID control parameter according to (1) and (2), and set the design parameter $z_i = \log \zeta_i$
- S2:** Execute the **Algorithm 2** (M-SPSA algorithm) using the loss function in (6) by setting J as L
- S3:** Record the optimal design parameter and apply $\zeta^* = [10^{z_1^*} \ 10^{z_2^*} \ \dots \ 10^{z_8^*}]^T$ to $K_1(s)$ and $K_2(s)$ in Fig. 1

4 Implementation and Findings

This section demonstrates our findings on the data-driven PID using M-SPSA based method. Initially, the mathematical model of liquid slosh in [47] is explained. Next, the M-SPSA based method is applied to the liquid slosh model.

The liquid slosh system’s dynamic equation is derived based on the Euler-Lagrange formulation and the parameter of the model is obtained from the quick

Table 1 Parameters of liquid slosh model

Parameter	Value	Unit
M	6.0	kg
m	1.32	kg
l	0.052126	m
d	3.0490×10^{-4}	kg m ² /s
g	9.81	m/s ²

stop experiment of liquid slosh plant executing straight line motion [47]. The mathematical model of liquid slosh is given by:

$$M\ddot{Y} + ml \cos \theta \ddot{\theta} - ml\dot{\theta}^2 \sin \theta = V, \quad (12)$$

$$ml \cos \theta \ddot{Y} + ml^2 \ddot{\theta} + d\dot{\theta} - mgl \sin \theta = 0, \quad (13)$$

where M is the mass of tank, m is mass of liquid, l is hypotenuse distance of slosh, d is damping coefficient and g is gravity. These parameters are depicted in Table 1.

Based on the obtained liquid slosh model in (12) and (13), we apply the proposed data-driven PID based M-SPSA using the Matlab environment. In order to evaluate the performance of the M-SPSA based method, we also compare with norm-limited SPSA in [44]. In order to handle the stochastic nature of both methods, 30 independent trials are adopted to assess their performances from the statistical point of view. Then, after the termination criterion is satisfied, the proposed method is evaluated based on the following performance criteria:

- (i) The statistical analysis of the loss function $J(\mathbf{p}, \mathbf{i}, \mathbf{d}, \mathbf{n})$, total norm of the error \hat{E} , the slosh angle $\hat{\theta}$ and total norm of the input \hat{V} . Specifically, the mean, best, worst, and standard deviation values of them are observed from 30 independent trials.
- (ii) The average computation time from 30 independent trials.

The corresponding design parameters for the PID controllers $K_1(s)$ and $K_2(s)$ are tabulated in Table 2. In this study, the reference of the trolley position is expressed by:

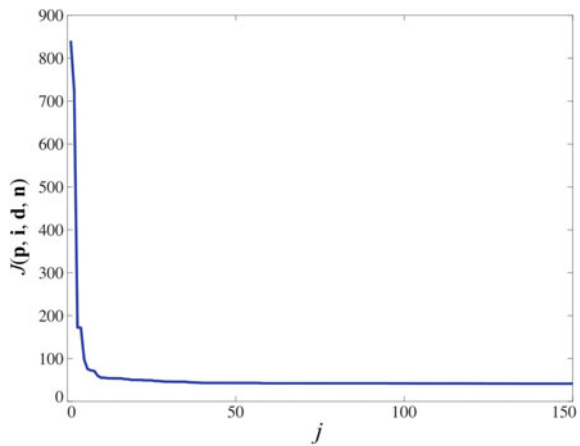
$$Y_R(t) = \begin{cases} 0, & 0 \leq t \leq 0.5, \\ 0.5, & 0.5 < t \leq 20, \end{cases} \quad (14)$$

for $t_0 = 0$ s and $t_f = 20$ s. Our goal is to find $z \in \mathbf{R}^8$ such that the control performance J in (6) is minimized for $w_1 = 100$, $w_2 = 100$, $w_3 = 5$. The gain sequences of the M-SPSA based method is set as $g_1(j) = 0.001/(j+29)^{0.6}$, $g_2(j) = 0.1/(j+1)^{0.1}$, while the norm-limited SPSA is set as $g_1(j) = 0.005/(j+24)^{0.6}$, $g_2(j) = 0.2/(j+1)^{0.1}$ and $d = 0.1$. Note that the parameter d is an additional parameter introduced in norm-limited SPSA for saturation function. Please refer [44] for the detailed of the norm-limited SPSA algorithm. Note that in the M-SPSA based method, it requires three loss

Table 2 Design parameters

ζ	PID gain	$z(0)$	ζ corresponding to $z(0) (\times 10^3)$	z^*	ζ^* corresponding to z^*
ζ_1	p_1	1.0	0.0100	-0.6564	0.2206
ζ_2	i_1	3.5	3.1623	2.7047	506.6536
ζ_3	d_1	0.0	0.0010	1.2867	19.3507
ζ_4	n_1	1.0	0.0100	1.4220	26.4211
ζ_5	p_2	2.0	0.1000	1.1228	13.2665
ζ_6	i_2	1.0	0.0100	0.5653	3.6753
ζ_7	d_2	0.0	0.0010	-0.8518	0.1407
ζ_8	n_2	1.0	0.0100	1.1584	14.4029

Fig. 2 Response of the loss function



function evaluations as compared to norm-limited SPSA, which requires only two loss function evaluations. Therefore, in order to have a fair number of loss function evaluations, we set $k_{\max} = 150$ and $k_{\max} = 225$ for M-SPSA and norm-limited SPSA, respectively. The initial design parameter $z(0)$ is also set to be the same for both methods, which is given in Table 2. Here, $z(0)$ is selected such that a stable closed-loop system is produced during the given time span.

Figure 2 exhibits the convergence curve of the loss function for 150 iterations and the optimal design parameter z^* is tabulated in Table 2. Note that z^* in Table 2 is corresponded to the best total norm of error and slosh angle from 30 trials. It shows that the M-SPSA based method successfully produces the optimal PID parameters by minimizing the loss function. Besides that, the results of $Y(t)$, $\theta(t)$ and $V(t)$ are demonstrated in Figs. 3, 4 and 5. Here, the thin red line represents the responses at $k = 0$ and the thick blue line represents the responses at $k = 150$, which is the optimal design parameters. It demonstrates that the trolley settles to the reference position around 3 s (see Fig. 3) with slightly minimum overshoot, which is 3.16%.

Fig. 3 Response of the trolley position

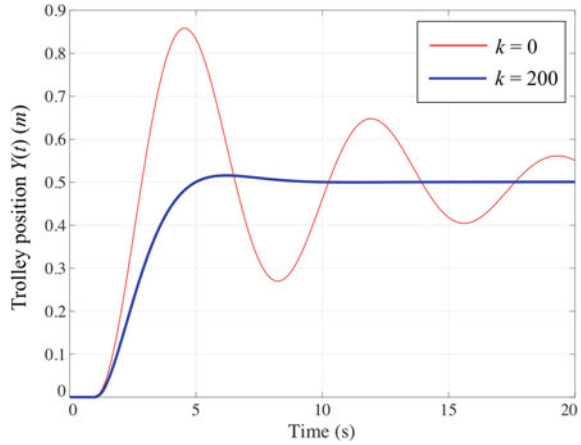
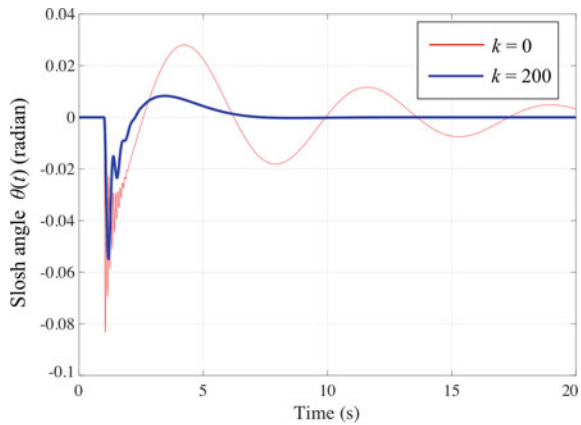


Fig. 4 Response of the slosh angle



Meanwhile, the proposed controller is also able to suppress the slosh angle after 150 iterations. The obtained slosh angle amplitude range has been reduced from -0.083 to 0.028 rad (at $k = 0$) to only -0.055 to 0.008 rad (at $k = 150$), which is almost 73.55% of slosh amplitude reduction. Moreover, the liquid slosh oscillation is able to settle down at nearly 6 s, which is better than the initial PID parameters. Moreover, a satisfactory control input (see Fig. 5) is utilized to fulfill the given control objective. It shows that the range of control output amplitude has been reduced from -39 to 55 N to -0.48 to 3.02 N. Therefore, it is confirmed that the data-driven PID tuning based on M-SPSA method has a high potential in suppressing the liquid slosh while maintaining the desired trolley position and used minimum input energy.

Remark 2 Note that, in this underactuated system control framework, one might produce a faster settling time in the cart position response. However, it may come at the cost of higher amplitude response in the slosh angle with may also produce higher oscillation and longer settling time. Therefore, in this data-driven control scheme,

Fig. 5 Response of the control input

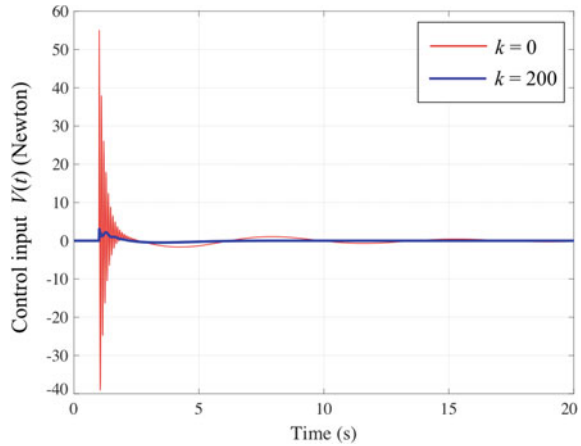


Table 3 Statistical performance comparison between M-SPSA and norm-limited SPSA [44] based methods

Algorithm		Norm-limited SPSA [44]	M-SPSA
$J(\mathbf{p}, \mathbf{i}, \mathbf{d}, \mathbf{n})$	Average	42.2984	41.8345
	Best	41.3127	41.1081
	Worst	43.2125	42.7285
	Std.	0.4633	0.5136
Total norm of error and slosh angle	Average	0.3189	0.3146
	Best	0.3030	0.3040
	Worst	0.3402	0.3297
	Std.	0.0096	0.0072
Total norm of input	Average	2.1965	2.1693
	Best	1.8021	1.9103
	Worst	3.1634	3.2530
	Std.	0.2950	0.2431
Mean computation time, second		84.2601	98.1404

Results in bold in Table 3 is considered as the best performance

the chosen weights for both slosh angle reduction and cart trajectory tracking also play an important role to obtain optimum results. This is also similar to the chosen weight of control output since one might consider an effective input energy to the system.

Table 3 tabulated the statistical comparative assessment between M-SPSA and norm-limited SPSA based algorithms. The performance of the algorithms is compared through the loss function, total norm of error, total norm of slosh angle and total norm of input, in terms of average, best, worst and standard deviation. More-

over, the computation time of each algorithm is also observed. In terms of the loss function, the M-SPSA based algorithm slightly produce better average and best values than the norm-limited SPSA. The similar pattern is also observed in total norm of input, where the GSPSA slightly produce lower average and best values. However, in terms of total norm of error and slosh angle, the M-SPSA based algorithm produce the lowest average values, while, the norm-limited SPSA based algorithm produce the lowest best values. In terms of the computation time, the norm-limited SPSA based method slight produce the lowest value as compared to the M-SPSA based method. In overall, it is proven that the M-SPSA based method, capability to memorize the best optimal parameter during its tuning process, is able to produce slightly better control performance than norm-limited SPSA based approach.

5 Conclusion

In this paper, a framework of data-driven PID control scheme based on the memory simultaneous perturbation stochastic approximation (M-SPSA) has been established. Based on the step-by-step procedure of this framework in Algorithm 2 and Algorithm 3, the effectiveness of the M-SPSA-based method has been investigated for liquid slosh control problem. The goal is to obtain the optimal PID control parameter based on only input and output data such that the liquid slosh is suppressed while the trolley position follows the desired trajectory. As a result, it is proven that the M-SPSA-based method has a high potential in obtaining promising results within a few minutes through iterative simulation works. In particular, from the control performance and the statistical results indicate that the M-SPSA-based algorithm outperforms the norm-limited SPSA based method.

Acknowledgements The study was funded by Research Grant RDU170104 from the University of Malaysia Pahang under Research and Innovation Department, and Ministry of Higher Education with reference no. JPT.S (BPKI) 2000/09/01 Jld.25 (29).

References

1. Budiansky, B.: Sloshing of liquids in circular canals and spherical tanks. *J. Aerosp. Sci.* **27**(3), 161–173 (1960)
2. Fischer, D.: Dynamic fluid effects in liquid-filled flexible cylindrical tanks. *Earthquake Eng. Struct. Dyn.* **7**(6), 587–601 (1979)
3. Dutta, S., Laha, M.K.: Analysis of the small amplitude sloshing of a liquid in a rigid container of arbitrary shape using a low-order boundary element method. *Int. J. Numer. Methods Eng.* **47**(9), 1633–1648 (2000)
4. Kang, X., Rakheja, S., Stiharu, I.: Effects of tank shape on the roll dynamic response of a partly filled tank vehicle. *Veh. Syst. Dyn.* **35**(2), 75–102 (2001)
5. Hasheminejad, S.M., Aghabeigi, M.: Liquid sloshing in half-full horizontal elliptical tanks. *J. Sound Vib.* **324**(1–2), 332–349 (2009)

6. Rebouillat, S., Liksonov, D.: Fluid–structure interaction in partially filled liquid containers: a comparative review of numerical approaches. *Comput. Fluids* **39**(5), 739–746 (2010)
7. Azadi, S., Jafari, A., Samadian, M.: Effect of tank shape on roll dynamic response of an articulated vehicle carrying liquids. *Int. J. Heavy Veh. Syst.* **21**(3), 221–240 (2014)
8. Kolaie, A., Rakheja, S., Richard, M.J.: Three-dimensional dynamic liquid slosh in partially-filled horizontal tanks subject to simultaneous longitudinal and lateral excitations. *Eur. J. Mech. B/Fluids* **53**, 251–263 (2015)
9. Park, J.J., Kim, S.Y., Kim, Y., Seo, J.H., Jin, C.H., Joh, K.H., Kim, B.W., Suh, Y.S.: Study on tank shape for sloshing assessment of LNG vessels under unrestricted filling operation. *J. Mar. Sci. Technol.* **20**(4), 640–651 (2015)
10. Hasheminejad, S.M., Mohammadi, M.M.: Effect of anti-slosh baffles on free liquid oscillations in partially filled horizontal circular tanks. *Ocean Eng.* **38**(1), 49–62 (2011)
11. Biswal, K.C., Bhattacharyya, S.K., Sinha, P.K.: Free-vibration analysis of liquid-filled tank with baffles. *J. Sound Vib.* **259**(1), 177–192 (2003)
12. Modaresi-Tehrani, K., Rakheja, S., Stiharu, I.: Three-dimensional analysis of transient slosh within a partly-filled tank equipped with baffles. *Veh. Syst. Dyn.* **45**(6), 525–548 (2007)
13. Biswal, K.C., Bhattacharyya, S.K., Sinha, P.K.: Non-linear sloshing in partially liquid filled containers with baffles. *Int. J. Num. Methods Eng.* **68**(3), 317–337 (2006)
14. Kolaie, A., Rakheja, S., Richard, M.J.: A coupled multimodal and boundary-element method for analysis of anti-slosh effectiveness of partial baffles in a partly-filled container. *Comput. Fluids* **107**, 43–58 (2015)
15. Wang, W., Guo, Z., Peng, Y., Zhang, Q.: A numerical study of the effects of the T-shaped baffles on liquid sloshing in horizontal elliptical tanks. *Ocean Eng.* **111**, 543–568 (2016)
16. Wang, Q.Y., Rakheja, S., Shangguan, W.B.: Effect of baffle geometry and air pressure on transient fluid slosh in partially filled tanks. *Int. J. Heavy Veh. Syst.* **24**(4), 378–401 (2017)
17. Liu, Z., Li, C.: Influence of slosh baffles on thermodynamic performance in liquid hydrogen tank. *J. Hazard. Mat.* **346**, 253–262 (2018)
18. Cheng, X., Jing, W., Gong, L.: Liquid sloshing problem in a concrete rectangular LSS with a vertical baffle. *Arab. J. Sci. Eng.* 1–12 (2018)
19. Pridgen, B., Bai, K., Singhose, W.: Slosh suppression by robust input shaping. In: *Proceedings of IEEE Conference on Decision and Control*, pp. 2316–2321 (2010)
20. Aboel-Hassan, A., Arafa, M., Nassef, A.: Design and optimization of input shapers for liquid slosh suppression. *J. Sound Vib.* **320**(1–2), 1–15 (2009)
21. Baozeng, Y., Lemei, Z.: Hybrid control of liquid-filled spacecraft maneuvers by dynamic inversion and input shaping. *AIAA J.* **52**(3), 618–626 (2014)
22. Kurode, S., Spurgeon, S.K., Bandyopadhyay, B., Gandhi, P.S.: Sliding mode control for slosh-free motion using a nonlinear sliding surface. *IEEE/ASME Trans. Mech.* **18**(2), 714–724 (2013)
23. Acarman, T., Ozguner, U.: Rollover prevention for heavy trucks using frequency shaped sliding mode control. In: *Proceedings of 2003 IEEE Conference on Control Applications*, pp. 7–12 (2003)
24. Bandyopadhyay, B., Kurode, S., Gandhi, P.S.: Sliding mode control for slosh-free motion—a class of underactuated system. *Int. J. Adv. Mech. Syst.* **1**(3), 203–213 (2009)
25. Acarman, T., Ozguner, U.: Rollover prevention for heavy trucks using frequency shaped sliding mode control. *Veh. Syst. Dyn.* **44**(10), 737–762 (2006)
26. Richter, H.: Motion control of a container with slosh: constrained sliding mode approach. *J. Dyn. Syst. Meas. Control* **132**(3), 031002 (2010)
27. Shtessel, Y.B., Hall, C.E.: Multiple time scale sliding mode control of reusable launch vehicles in ascent and descent modes. In: *Proceedings of the American Control Conference*, pp. 4357–4362 (2001)
28. De Souza, L.C., De Souza, A.G.: Satellite attitude control system design considering the fuel slosh dynamics. *Shock Vib.* (2014)
29. De Souza, A.G., De Souza, L.C.: Satellite attitude control system design taking into account the fuel slosh and flexible dynamics. *Math. Prob. Eng.* (2014)

30. De Souza, A.G., De Souza, L.C.: Design of satellite attitude control system considering the interaction between fuel slosh and flexible dynamics during the system parameters estimation. *Appl. Mech. Mat.* **706**, 14–24 (2015)
31. Zhang, T., Yang, J.: Nonlinear dynamics and robust control of sloshing in a tank. *J. Vib. Control*, 1077546318772256 (2018)
32. Kuang, J., Leung, T.: H-infinity feedback for attitude control of liquid-filled spacecraft. *J. Guidance Control Dyn.* **24**(1), 46–53 (2001)
33. Mishra, J.P., Kurode, S.R.: Robust output-feedback control for container-slosh system using variable gain super-twisting algorithm. In: 13th International Workshop on Variable Structure Systems, pp. 1–6 (2014)
34. Nair, A.P., Selvaganesan, N., Lalithambika, V.R.: Lyapunov based PD/PID in model reference adaptive control for satellite launch vehicle systems. *Aerosp. Sci. Technol.* **51**, 70–77 (2016)
35. Sira-Ramirez, H.: A flatness based generalized PI control approach to liquid sloshing regulation in a moving container. In: Proceedings of the American Control Conference, pp. 2909–2914 (2002)
36. Purnomo, D.S., Besari, A.R.A., Darojah, Z.: Control of liquid sloshing container using active force control method. In: IOP Conference Series: Materials Science and Engineering, p. 012007 (2017)
37. Terzic, E., Nagarajah, R., Alamgir, M.: A neural network approach to fluid quantity measurement in dynamic environments. *Mechatronics* **21**(1), 145–155 (2011)
38. Hyun-Soo, K., Young-Shin, L.: Optimization design technique for reduction of sloshing by evolutionary methods. *J. Mech. Sci. Technol.* **22**(1), 25–33 (2008)
39. Mazmanyan, L., Ayoubi, M.A.: Takagi-Sugeno fuzzy model-based attitude control of spacecraft with partially-filled fuel tank. In: AIAA/AAS Astrodynamics Specialist Conference, p. 4215 (2014)
40. Mazmanyan, L., Ayoubi, M.A.: Fuzzy attitude control of spacecraft with fuel sloshing via linear matrix inequalities. *IEEE Trans. Aerosp. Electron. Syst.* (2018)
41. Shen, Y., Wang, Z.: Fuzzy control of liquid surface sloshing in liquid delivery. *J. Shenyang Jianzhu Univ. (Natural Science)* **4**, 031 (2013)
42. Wang, Z., Wang, Q., Zhang, X.J.: An adaptive fuzzy sliding-mode technique for attitude control of launch vehicle. In: International Conference on Mechatronics and Automation, pp. 1587–1592 (2007)
43. Grundelius, M., Bernhardsson, B.: Constrained iterative learning control of liquid slosh in an industrial packaging machine. In Proceedings of IEEE Conference on Decision and Control, pp. 4544–4549 (2000)
44. Ahmad, M.A., Rohani, M.A., Raja Ismail, R.M.T., Mat Jusof, M.F., Suid, M.H., Nasir, A.N.K.: A model-free PID tuning to slosh control using simultaneous perturbation stochastic approximation. In: Proceedings of 5th IEEE International Conference on Control Systems, Computing and Engineering, pp. 343–347 (2015)
45. Ahmad, M.A., Azuma, S., Sugie, T.: Performance analysis of model-free PID tuning of MIMO systems based on simultaneous perturbation stochastic approximation. *Expert Syst. Appl.* **41**(14), 6361–6370 (2014)
46. Ahmad, M.A., Raja Ismail, R.M.T.: A data-driven sigmoid-based PI controller for buck-converter powered dc motor. In: Proceedings of IEEE Symposium on Computer Applications and Industrial Electronics (2017)
47. Bandyopadhyay, B., Gandhi, P.S., Kurode, S.: Sliding mode observer based sliding mode controller for slosh-free motion through PID scheme. *IEEE Trans. Ind. Electron.* **56**(9), 3432–3442 (2009)
48. Spall, J.C.: Multivariate stochastic approximation using a simultaneous perturbation gradient approximation. *IEEE Trans. Autom. Control* **37**(3), 332–341 (1992)

Barnacles Mating Optimizer Algorithm for Optimization



Mohd Herwan Sulaiman, Zuriani Mustaffa, Mohd Mawardi Saari, Hamdan Daniyal, Ahmad Johari Mohamad, Mohd Rizal Othman and Mohd Rusllim Mohamed

Abstract This article proposes a new technique to solve optimization problems based on barnacles' mating behavior namely Barnacles Mating Optimizer (BMO). Barnacles are micro-organisms existed since Jurassic times and they attach themselves to objects in the water and grow shell. They are also known as hermaphroditic micro-organisms and one of the special characters of barnacles is they have long penises which is the longest in animal kingdom relative to their body size. The Hardy-Weinberg principle is adopted in BMO to generate new off-springs and the mating process is performed randomly based on the length of the barnacle's penis. The effectiveness of BMO is tested through a set of 23 benchmark functions in finding the optimal solutions. Some impactful and reliable results are presented compared with other techniques in this paper.

Keywords Barnacles mating optimizer · Benchmark functions · Optimization

1 Introduction

Metaheuristic algorithms have become notably common to solve optimization problems since they are plainness, flexible, derivative-free mechanism and able to avoid from local optima [1]. In addition, the factor of No Free Lunch (NFL) theorem has pushed the invention of new algorithms inspired by nature to the new level. Thus, there are sudden increment of new algorithms that have been proposed in literature

M. H. Sulaiman (✉) · M. M. Saari · H. Daniyal · A. J. Mohamad · M. R. Othman
M. R. Mohamed
Faculty of Electrical and Electronics Engineering, Universiti Malaysia Pahang,
26600 Pekan, Pahang, Malaysia
e-mail: mherwan@ieee.org

Z. Mustaffa
Faculty of Computer Systems and Software Engineering, Universiti Malaysia Pahang,
26300 Gambang, Pahang, Malaysia

© Springer Nature Singapore Pte Ltd. 2019
Z. Md Zain et al. (eds.), *Proceedings of the 10th National Technical Seminar on Underwater System Technology 2018*, Lecture Notes in Electrical Engineering 538,
https://doi.org/10.1007/978-981-13-3708-6_18

since the last decade such as Grey Wolf Optimizer (GWO) [2], Firefly Algorithm (FA) [3], Moth-Flame Optimizer (MFO) [4] and many more.

This paper proposes a new nature-inspired algorithm to solve optimization problems namely Barnacles Mating Optimizer (BMO). This algorithm mimics the mating concepts of barnacles. To the knowledge of authors, there is no studies on this area of solving optimization that has been proposed in literature. This paper is organized as follows: Sect. 2 discussed in brief the BMO concept and development, it follows by the results and discussion in Sect. 3. Lastly, Sect. 4 concludes the paper.

2 Barnacles Mating Optimizer

2.1 Inspiration

Barnacles are known as sessile organisms where they are normally attached to rocks, corals and even to the ships permanently. They are also known as hermaphroditic organisms and have long penises for mating which can stretch to up to seven or eight times the length of their body. For the isolated barnacles, sperm-cast is happened for mating process where the eggs are fertilized by sperms that released into the water. The process of generating new off-springs of barnacles becoming the inspiration in the proposed BMO for solving optimization problems.

2.2 Hardy-Weinberg Principle

Hardy-Weinberg principle is used in the generation of new off-springs of barnacles. The simplest case with two alleles of parents denoted as *Dad* (D) and *Mum* (M) with frequencies $f(D) = p$ and $f(M) = q$ respectively is depicted in Fig. 1. From this figure, the expected genotype frequencies under normal mating can be expressed as $f(DD) = p^2$ for DD homozygotes, $f(MM) = q^2$ for the MM homozygotes and $f(DM) = 2pq$ for heterozygotes. The sum of the entries is $p^2 + 2pq + q^2 = 1$. It also can be noted that $p + q = 1$, hence for the simplification, the generation of new off-spring is referring to the p and q of the barnacles' parents.

2.3 Selection Process

The selection process in BMO mimics the behavior of barnacles. For simplification, the selection is made based on the following rules:

- i. Selection of *Mum* and *Dad* is done randomly and limited to the length of the penis of barnacle, pl that has been set initially.

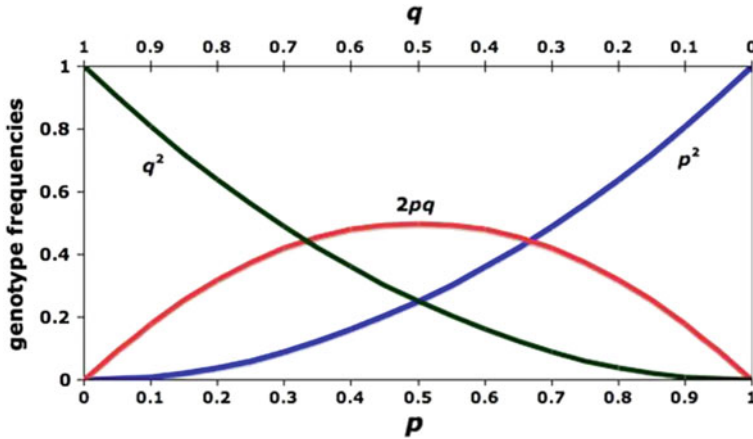


Fig. 1 Hardy-Weinberg principle for two alleles [5]

- ii. It is assumed that each barnacle can be fertilized by one other barnacle only at one time even though in real life, the female barnacle can probably be fertilized by more than one male [6].
- iii. If the selection of *Mum* and *Dad* is out of the range of pl , the new off-springs are produced by sperm-cast process.

2.4 Off-Springs Generation

The new off-springs generation is based on Hardy-Weinberg principle which are expressed as follow:

$$x_i^{N-new} = px_{barnacle_d}^N + qx_{barnacle_m}^N \quad \text{for } k \leq pl \tag{1}$$

$$x_i^{N-new} = rand() \times x_{barnacle_m}^N \quad \text{for } k > pl \tag{2}$$

where $k = |barnacle_d - barnacle_m|$, p is the normally distributed pseudo random number, $q = (1 - p)$, $x_{barnacle_d}^N$ and $x_{barnacle_m}^N$ are the variables selected randomly for barnacle's *Dad* and *Mum* respectively and $rand()$ is the random number between [0, 1]. From these equations, it can be noted that p and q represent the percentage of inheritance from respective barnacles' parents. For easy illustration, let's say p is 0.75 (randomly generated), it means that 75% of the *Dad*'s character or behavior and 25% of *Mum*'s behavior are embedded in the new off-springs generation. It is also can be seen that Eq. (1) represents the exploitation process while Eq. (2) represents the exploration process. For exploration process, only *Mum*'s barnacle is involved due to the new offspring is produced by *Mum*'s barnacle since its receiving the sperm from the water that has been released by the other barnacles elsewhere.

2.5 *Sorting*

To control the matrix expansion from the population size, each new off-springs of barnacles are evaluated and merged with the parents. From here, the sorting process is done to select the half of the top solution that fit the population size. The poor results are assumed to be dead and eliminated. Pseudo code for BMO is exhibited in the Fig. 2.

3 Results and Discussion

To show the effectiveness of proposed BMO, 23 benchmark functions (F1–F23) [1, 2, 4] have been used for testing and verification. Only selected results will be presented in this paper, which is multi modal benchmark functions. The performance of BMO is evaluated on function F12 for multi modal benchmark function to show the effect of pl in terms of exploitation and exploration processes of BMO in searching the global optima. Figures 3 and 4 show the effect of $pl = 5$ and 7 for barnacle's population of 10 until 10th iterations. After 10th iteration, it is expected that the results will be converged. The dimension is set to 2 for simple visualization. From these figures, it can be concluded that the selection of $pl = 5$ gave the best results compared to $pl = 7$. This means that the proposed selection for pl for balancing the exploitation and exploration can be set to 50% from the total population for this case (F12). However, the selection of pl is depending on the different set of problems to be solved. Thus, it can be said that it will need to be tuned properly for the value of pl in order to obtain good results in solving optimization problems.

Details of results for BMO tested on multi modal benchmark functions are tabulated in Table 1. It can be seen that BMO obtained the best performance overall compared to Genetic Algorithm (GA) and MFO. The best results are marked in bold for better comparison. For these multi modal test functions (F8–F13), they are supposed to have significant number of local optima. From the results shown, it can be concluded that proposed BMO is efficient in avoiding local optima, as good as GA. Detail results for unimodal (F1–F7) and composite functions (F14–F23) using BMO can be obtained in [7].

Initialize the population of barnacles X_i
Calculate the fitness of each barnacle
Sorting to locate the best result at the top of the population (T =the best solution)
while ($l < \text{Maximum iterations}$)
 Set the value of pl
 Selection using the following equations:
 barnacle_d = randperm(n)
 barnacle_m = randperm(n)

 if selection of Dad and Mum = pl
 for each variable
 Offspring generation using equation (1):

$$x_i^{N-\text{new}} = px_{\text{barnacle}_d}^N + qx_{\text{barnacle}_m}^N \text{ for } k \leq pl$$

 end for
 else if selection of Dad and Mum $> pl$
 for each variable
 Offspring generation using equation (2):

$$x_i^{N-\text{new}} = \text{rand}() \times x_{\text{barnacle}_m}^N \text{ for } k > pl$$

 end for
 end if
 Bring the current barnacle back if it goes outside the boundaries
 Calculate the fitness of each barnacles
 Sorting and update T if there is a better solution
 $l = l + 1$
 end while
 Return T

Fig. 2 Pseudo code for proposed BMO algorithm

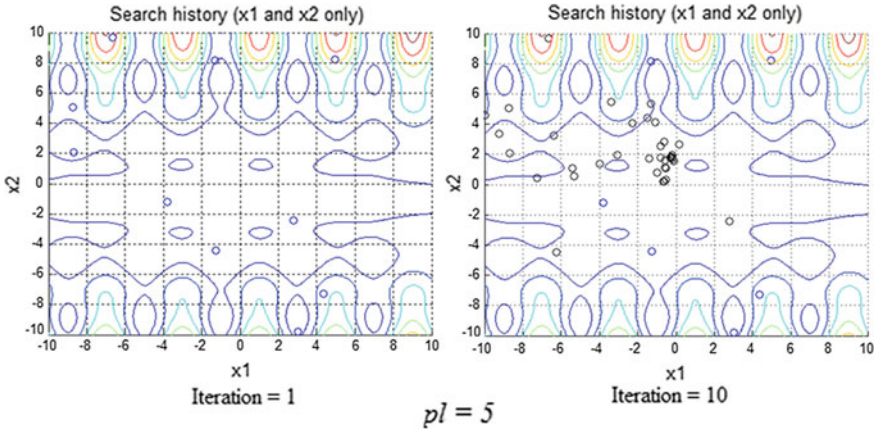


Fig. 3 Effect of $pl = 5$

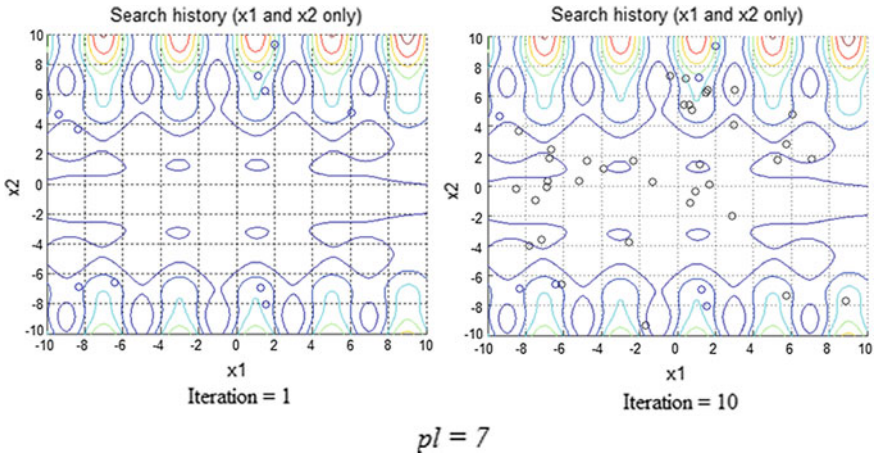


Fig. 4 Effect of $pl = 7$

4 Conclusion

A new novel algorithm namely Barnacles Mating Optimizer has been proposed in this paper. The concept of mating behavior of barnacles together with the Hardy-Weinberg principle have been adopted in the proposed BMO. The performance of BMO has been evaluated through 23 test benchmark functions. Only the results of multi modal are presented in this paper. The results show that BMO is able to compete and produce better results compared to other selected algorithms.

Table 1 Results of multi modal benchmark functions

Function		GA	MFO	BMO
F8	Best	-1.76E+03	-1.62E+03	-1.74E+03
	Worst	-1.32E+03	-1.08E+03	-1.64E+03
	Mean	-1.53E+03	-1.38E+03	-1.68E+03
	Std	1.11E+02	1.35E+02	2.67E+01
F9	Best	5.85E-01	8.50E+01	0.00E+00
	Worst	8.91E+00	3.95E+02	0.00E+00
	Mean	3.68E+00	1.98E+02	0.00E+00
	Std	1.86E+00	8.18E+01	0.00E+00
F10	Best	2.00E+01	2.00E+01	8.88E-16
	Worst	2.00E+01	2.00E+01	8.88E-16
	Mean	2.00E+01	2.00E+01	8.88E-16
	Std	7.76E-04	0.00E+00	4.01E-31
F11	Best	1.83E-02	2.70E-02	0.00E+00
	Worst	1.38E-01	3.50E+00	0.00E+00
	Mean	4.94E-02	1.05E+00	0.00E+00
	Std	2.32E-02	1.31E+00	0.00E+00
F12	Best	1.67E-05	1.93E-01	5.72E-03
	Worst	1.04E-01	1.28E+01	2.13E-01
	Mean	3.61E-03	4.90E+00	4.17E-02
	Std	1.89E-02	2.81E+00	4.02E-02
F13	Best	8.52E-02	1.38E+01	4.64E-02
	Worst	8.96E-01	1.11E+05	2.97E+00
	Mean	2.58E-01	7.23E+03	5.49E-01
	Std	1.94E-01	2.33E+04	6.74E-01

Bold values are defined by the best results

Acknowledgements This work was supported by the Ministry of Higher Education (MOHE) Malaysia and Universiti Malaysia Pahang under Fundamental Research Grant Scheme (FRGS) RDU#170105.

References

1. Moghdani, R., Salimifard, K.: Volleyball premier league algorithm. *Appl. Soft Comput.* **64**, 161–185 (2018)
2. Mirjalili, S., Mirjalili, S.M., Lewis, A.: Grey wolf optimizer. *Adv. Eng. Softw.* **69**, 46–61 (2014)
3. Yang X.-S.: Firefly algorithm, Lévy flights and global optimization. In: *Research and Development in Intelligent Systems XXVI*, pp. 209–218, London (2010)
4. Mirjalili, S.: Moth-flame optimization algorithm: a novel nature-inspired heuristic paradigm. *Knowl. Based Syst.* **89**, 228–249 (2015)
5. Andrew, C.: The Hardy-Weinberg principle. *Nat. Educ. Knowl.* **3**, 65 (2010)

6. Barazandeh, M., Davis, C.S., Neufeld, C.J., Coltman, D.W., Palmer, A.R.: Something Darwin didn't know about barnacles: spermcast mating in a common stalked species. In: Proceedings of the Royal Society B: Biological Sciences, vol. 285 (2013)
7. Sulaiman, M.H., Mustaffa, Z., Saari, M.M., Daniyal, H., Daud, M.R., Razali, S., Mohamed, A.M.: Barnacles mating optimizer: a bio-inspired algorithm for solving optimization problems. In: 9th IEEE/ACIS International Conference on Software Engineering, Artificial Intelligence, Networking and Parallel/Distributed Computing (SNPD 2018), Busan, Korea (2018)

Random Search in Energy Management Strategy (EMS) for Hybrid Electric Vehicles



Muhammad Syahmi Ghazali and Muhammad Ikram Mohd Rashid

Abstract The aim of this project is to optimize the total energy used (summation fuel and electricity) from vehicle utilization with the initial result in hybrid electric car (HEV) by using an optimization called Random Search Optimization. Nowadays, the developments of hybrid electric cars are not something new. There are a lot of research are being done on how to increase the effectiveness of hybrid electric cars. One of the main aspects that are being aim is to reduce the electricity consumption while increasing the HEV performance. This is for maintain or increase the HEV performance which is increase the efficiency. Thus, Random Search Optimization was applied to optimize the HEV source output which is from electricity system. This method also had already been applied to solve several other problems. But for HEV optimization more research is needed so that it can be applied for real HEV development in industry not for simulation purpose only.

Keywords HEV · Random search · Optimization

1 Introduction

Nowadays, hybrid electric vehicles (HEV) is used very popular among the car industries. The industries very busy to make sure their models are the best to sell for the customers based on their best energy management strategy of hybrid. All of the HEV need to improve energy management performances for make sure the car has high efficiency and economic for customers. This project proposes an energy management approach based on single agent optimization logarithm which is Random Search Method. The optimization objective is to minimize total energy cost for summation of fuel and electricity from vehicle utilization. The single agent optimization (Random Search Method) will be analysis to increase the efficiency in the energy management strategy as a single agent. Thus, the minimum optimization based on the

M. S. Ghazali (✉) · M. I. Mohd Rashid
Faculty of Electrical and Electronic Engineering, University Malaysia Pahang, Pekan, Malaysia
e-mail: syahmiesyahmi@gmail.com

© Springer Nature Singapore Pte Ltd. 2019
Z. Md Zain et al. (eds.), *Proceedings of the 10th National Technical Seminar on Underwater System Technology 2018*, Lecture Notes in Electrical Engineering 538,
https://doi.org/10.1007/978-981-13-3708-6_19

Random Search Method will help the energy management strategy become smooth and economic for the fuel and electricity utilization. Therefore, the Random Search Method optimization needed in this limitation and the ideal way to solving all the problem and helpful in the application of this project. This project needed to comes with the understanding of the hybrid vehicle design through modeling, simulation, and optimization.

The basics rules to determine the base of the hybrid electric vehicle system need to be concern. Hybrid electric vehicle assumes an essential part in the automotive industries improvement for driving distance, low fuel utilization and pollution, driving cycles, and so on [1]. The battery execution for hybrid electric vehicle straightforwardly influences the performance of vehicle [2]. Hybrid Electric Vehicles (HEV) offer many improvements over conventional vehicles in terms of a variety of societal and environmental benefits as implemented in a variety of demonstration, concept and production vehicles. Relative to conventional vehicles, these benefits include reduced vehicle and societal greenhouse gas emissions, reduced vehicle and societal petroleum consumption, reduced regional criteria emissions, improved national energy security, reduced vehicle fueling costs, and improved transportation system robustness to fuel price and supply volatility [1]. The implements to the HEV can be introduce for overall systems include the methods, developing key components, energy management strategy, drive cycles, optimization algorithms, economic analysis and decision making, system test and evaluation. As we know, every part of the parameters is need to determine before the optimization simulate because the parameters obtained the value that will changes when Random Search applied.

Based on the optimization approached, a simulation environment was developed to evaluate the changes. This study considered the power-split HEV type, which employs an electric continuously variable transmission (E-CVT). The HEV model consists of an ICE, two EMs, a battery, a regenerative brake system, vehicle resistance loads, a planetary gear set and a driver model, as shown in schematic diagram of power split type HEV simulation environment [3].

This parameters study will be compared with our model of the HEV power-split for fix with our model and objectives. The power-split can define as a controller because in every vehicle model's controller consists of algorithms and equations based on defined system parameters and desired control style, which dictates commands to each of the components within the vehicle's subsystems [1]. The control system of the benchmark problem also displayed in Fig. 2. For complete task, all of the of the reference input, control input and the output of HEV systems describe in Table 1 [4]. All of the parameter will be applied to the iterations of the optimization algorithm via direct search algorithm. Besides that, the parameters optimization values obtained from the real test vehicle and the adequacy of the proposed will discuss based on the analysis.

Table 1 Gain value for each parameter

Iterations	Gain	Y	L	H	U
1st	x(1)	1.8147	1.8147	1.8147	1.8147
	x(20)	1.9595	1.9595	1.9595	1.9595
2nd	x(1)	1.6557	1.6557	1.6557	1.6557
	x(20)	1.0344	1.0344	1.0344	1.0344
3rd	x(1)	1.4387	1.4387	1.4387	1.4387
	x(20)	1.2238	1.2238	1.2238	1.2238
4th	x(1)	1.7513	1.7513	1.7513	1.7513
	x(20)	1.4733	1.4733	1.4733	1.4733
5th	x(1)	1.3517	1.3517	1.3517	1.3517
	x(20)	1.3371	1.3371	1.3371	1.3371
6th	x(1)	1.1622	1.1622	1.1622	1.1622
	x(20)	1.4427	1.4427	1.4427	1.4427
7th	x(1)	1.1067	1.1067	1.1067	1.1067
	x(20)	1.1450	1.1450	1.1450	1.1450
8th	x(1)	1.8530	1.8530	1.8530	1.8530
	x(20)	1.1112	1.1112	1.1112	1.1112
9th	x(1)	1.7803	1.7803	1.7803	1.7803
	x(20)	1.4509	1.4509	1.4509	1.4509
10th	x(1)	1.5470	1.5470	1.5470	1.5470
	x(20)	1.7948	1.7948	1.7948	1.7948

2 HEV Model

A hybrid electric vehicle model is chosen due to its simplicity and practicality. This model consists of functioning circuit that will be able to produce output such as vehicle velocity, power loss, and etc. Many subsystems created in the model to combine the part of hybrid source. It is also made up from electrical and physical part. The block diagram of the simple HEV model as shown in Fig. 1.

In order to tune our output which are power loss and fuel consumption, there are four parameter that are being tune which are the engine, electric generator, electric motor, and battery. There are one gain that are being place inside each of the four parameter. Gain is being named by L, Y, H, and U were placed inside the four parameter and been given initial value of 1. With this initial value, first simulation will be run and the output will be recorded. Using Random Search Algorithm, the initial value of power loss and the gain value will optimize the value. Thus new output performance will be produce for the value of power loss and gain. The gain location in the simulink (Figs. 2, 3, 4 and 5).

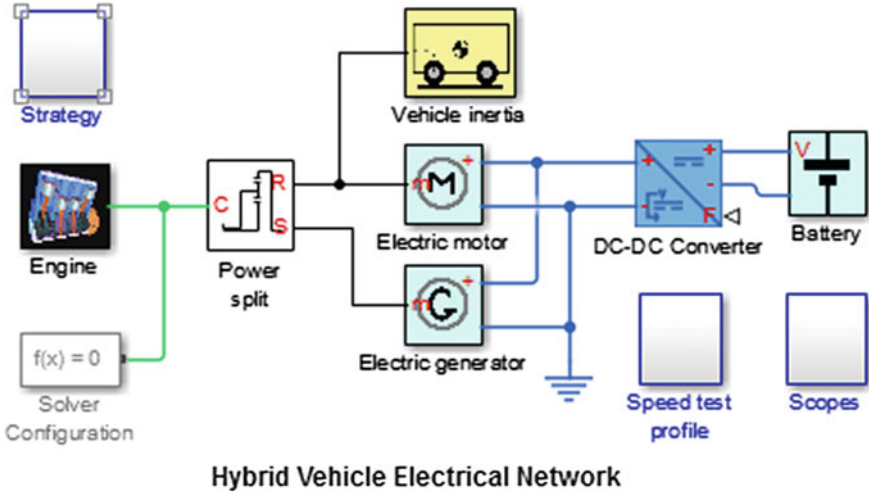


Fig. 1 HEV models MATLAB Simulink

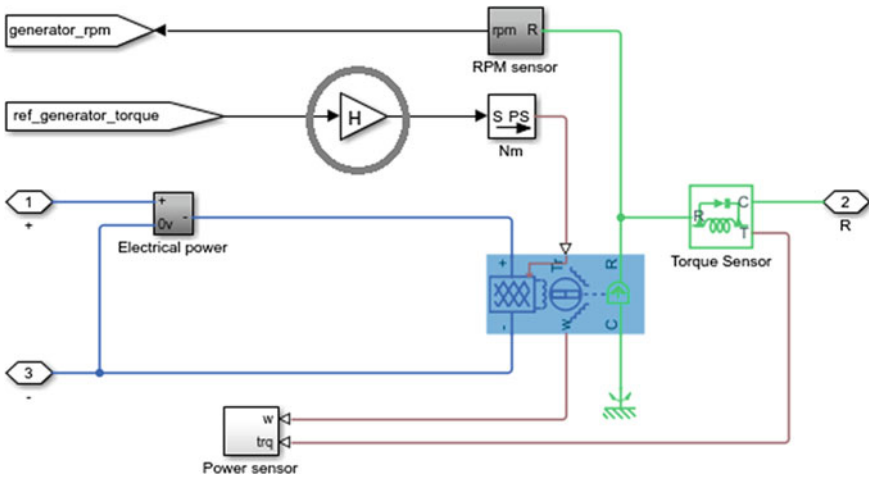


Fig. 2 Gain H in generator

3 Random Search

Random Search method can handle a large class of optimization problems. Beginning with the basics of the algorithm, direct random search is a large subject into the optimization steps. Only a small selection of algorithms is being presented here to keep this subsection of manageable length. The three algorithms here are intended

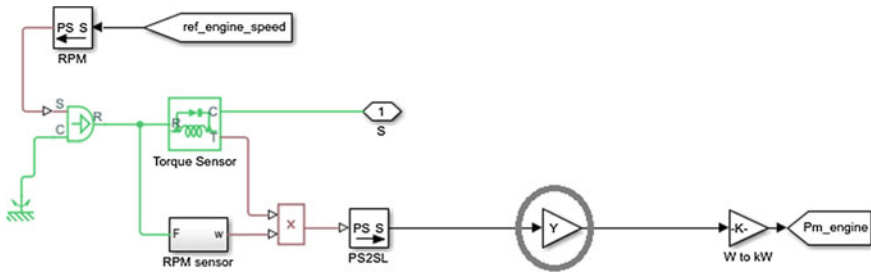


Fig. 3 Gain Y in engine

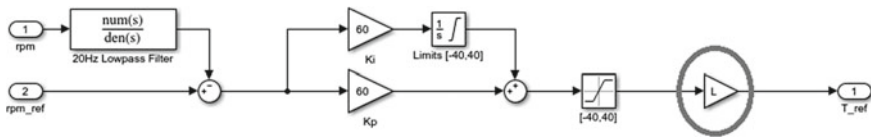


Fig. 4 Gain L in electric motor

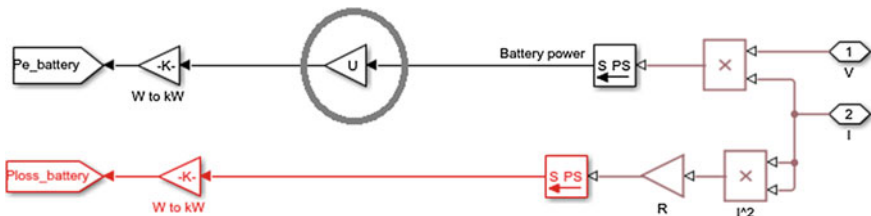


Fig. 5 Gain U in battery

to convey the essential flavour of the most available direct search algorithms [5]. In support of this, a few references are seen to be compared the similarity of the steps is used [5].

The complexity is how to compile the Random Search algorithm of single agent with the hybrid systems because many types of the Random Search algorithm like Genetic algorithm and particle swarm optimization is multi-agent optimization which is have a problem when there are parameter values that define the operating conditions of each of the algorithms differently and affect their performance. So, for reach their goals, they combined the techniques with other techniques working examine multiple optimization [1]. However, this literature showed a single point search which is more effective and accurate but the single point search method will take more convergence time or it can converge to a local maxima or local minima [6]. The Random search algorithm can find in many symbols they used but basically all the steps are the same. The concept of Random search algorithm is described as:

Conceptual algorithm

Step 0 (initialization)

Choose an initial value of $\theta =$ inside of Θ . Set $k = 0$.

- If random, usually a uniform distribution on Θ is used.
- Calculate $L(\theta_0)$.

Step 1 (candidate value)

Generate a new independent value $\theta_{\text{new}}(k+1) \in \Theta$, according to the chosen probability distribution.

If $L(\theta_{\text{new}}(k+1)) < L(\theta^k)$. Set $\theta^k + 1 = \theta_{\text{new}}(k+1)$. Else take $\theta^k + 1 = \theta^k$.

- New input is a member of the Θ .
- Compare the conditions for the estimation.

Step 2 (return or stop)

Stop if maximum number of L evaluations has been reached or user is otherwise satisfied with the current estimate for θ ; else, return to step 1 with the new k set to the former $k + 1$.

where

θ	Input
n	Small positive number
L	Loss Functions
N	Number of iterations
$L(\theta_0)$	Noise free output
$\theta^k + 1$	Estimate for θ at iteration k .

4 Result and Discussion

The project gives several results that can be obtain. This result is important for the data collection and analysis part. This is because comparison for the data before and after optimization will indicate the result. The results divided into two part which is in the Tables 1 and 2 for estimate the real result. For the initial result, the gain was setting by the value for L:1, Y:1, H:1, U:1 and the CostFunction (Power Loss) show the initial value which is 11.1157. This CostFunction value was optimized when the Random Search Algorithm applied and find the best value. The result of the iterations for power loss and the gains tuning value are shown in Table 1.

After iterations was applied ten times to make the analysis can be compared between all of the iterations value of the power loss and gains. The second iteration is the lowest value which is 0.6428 in Table 2 and the worst is first iteration with value of 8.2481. By compare with the initial gain setup which is 11.1157 of power losses, this deduction shows the optimization. Graph Power losses against time show a different value through the optimization.

Table 2 Power loss value

Iteration	Power loss
1st	8.2481
2nd	0.6428
3rd	1.4866
4th	3.1546
5th	2.1649
6th	2.9153
7th	1.0914
8th	0.9414
9th	2.9788
10th	6.2465

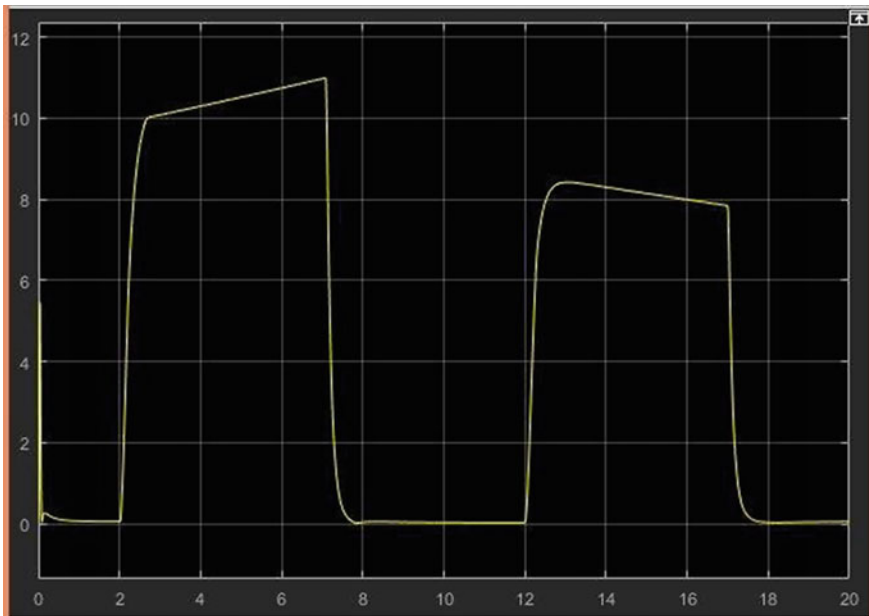


Fig. 6 Initial time against power loss graph

When optimization complete, the analysis continued with the graph curve which is show power loss curve. The graph was compared between the initial and lowest value in the iteration which is graph of second iteration and show a different curve between before and after optimization. The graph curve shown below in Figs. 6 and 7.

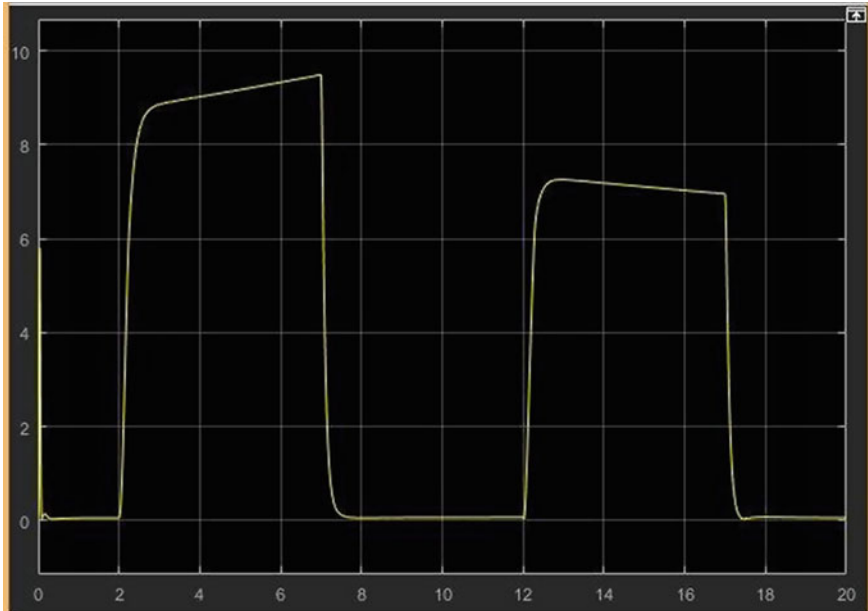


Fig. 7 Optimized time against power loss graph model

5 Conclusion

In this paper, Random Search in Energy Management Strategy (EMS) for HEV system has been addressed. The optimal power loss value shows a potential for improving the electric efficiency compared to the initial value. It has been also shown that this performance also can be more efficient when this method proposed to tuning the gain value for HEV systems than the normal system. This single agent method needed to compare to others method to prove its better or not with others single agent method.

References

1. Geller, B.M.: Increased understanding of hybrid vehicle design through modeling, simulation, and optimization. Colorado State University, Colorado (2010)
2. Yongqin, Z.J.: Power Battery Charging State-of-Charge Prediction Based on Genetic Neural Network (2010)
3. Park, J., Park, J.H.: Development of equivalent fuel consumption minimization strategy for hybrid electric vehicles. *Int. J. Autom. Technol.* **13**(5), 835–843 (2002)
4. Ahmad, M.A.: Model Free Tuning of Variable State of Charge Target of Hybrid Electric Vehicles (2013)

5. Spall, J.C.: Introduction To Stochastic Search And Optimization: Estimation, Simulation, and Control. Wiley Interscience (2003)
6. Sankar, P., Kruthiventi, K.K.P.: A New Random Search Algorithm: Multiple Solution Vector Approach (2016)

Extended Bat Algorithm (EBA) as an Improved Searching Optimization Algorithm



Dwi Pebrianti, Nurnajmin Qasrina Ann, Luhur Bayuaji,
N. R. Hasma Abdullah, Zainah Md. Zain and Indra Riyanto

Abstract This paper presents a new searching technique by using a new variant of Bat Algorithm (BA) known as Extended Bat Algorithm (EBA). EBA introduces the spiral searching method instead of randomly searching used in original BA. Spiral searching method taken from Spiral Dynamic Algorithm (SDA) is performed to improve the accuracy and efficiency of the original algorithm such as stabilizing the convergence when reaching ideal value. EBA conserves the robustness of BA and SDA and increases the performance of the proposed algorithm. The proposed algorithm is tested by using numerical experiments with three different objective functions. The results show that EBA outperforms original Bat Algorithm (BA) and Particle Swarm Optimization (PSO) in almost test functions and successfully optimizes the numerical problems.

Keywords Extended bat algorithm · Spiral searching method
Engineering optimization

D. Pebrianti (✉) · N. Q. Ann · N. R. H. Abdullah · Z. Md. Zain
Faculty of Electrical and Electronics Engineering, Universiti Malaysia Pahang, 26600 Pekan,
Malaysia
e-mail: dwipebrianti@ump.edu.my

L. Bayuaji
Faculty of Computer Science and Software Engineering, Universiti Malaysia Pahang, Pekan,
Malaysia

D. Pebrianti · L. Bayuaji
Magister of Computer Science, Universitas Budi Luhur, South Jakarta, Indonesia

I. Riyanto
Department of Electronics Engineering, Faculty of Engineering, Universitas Budi Luhur, South
Jakarta, Indonesia

1 Introduction

Metaheuristic optimization algorithms have acquired more interest from a lot of researchers globally. These algorithms are inspired by biological phenomena or natural phenomena. For example, focused spiral phenomena are approximated to logarithmic spirals which frequently appear in nature, such as whirling current, a low pressure, a nautilus shell, arms of spiral galaxies and so on [1].

This paper proposed a new variant of Bat Algorithm (BA) [2] that uses the search method from Spiral Dynamic Algorithm (SDA) [1, 3]. Motivation of these algorithms came from the searching method of most metaheuristic algorithms such as Bat Algorithm (BA) and Particle Swarm Optimization (PSO) which are spreading the particles randomly in search space. It is expected that by adding the spiral searching technique, it makes the algorithm becomes more accurate and efficient.

Hybridization is a popular approach used in metaheuristic to magnify ability of optimization algorithms [4]. It may lead to better performance with simple and better structure. Besides, with the fast changing of computing tools and efficient in current technology, hybrid approaches have become increasingly popular to explore. In literature, there are two major hybrid algorithm with Bat Algorithm (BA) which are BA with different evolution strategies [5], BA with Mutation [6] and BA with Harmony Search [7]. The original BA using Differential Evolutions (DE) strategies known as Hybrid Bat Algorithm (HBA) is explained in [5]. HBA is added by using DE strategy from the original BA to improve the original BA. In [7], the improvement of the algorithm is about inclusion of pitch adjustment operation in Harmony Search (HS) to increase the speed of convergence time. HS serve as a mutation operator making the approach more practical for a broader scope of real-world applications. Based on literature, in [4], the paper presented a new hybrid algorithm called Hybrid Spiral Dynamics Bacterial Chemotaxis (HSDBC) algorithm based on SDA and Bacterial Foraging Algorithm (BFA). The hybrid is done due to the reason that the original BFA has higher convergence speed and SDA has better accuracy.

Azmi et al. in [8] has applied the natural selection as the searching algorithm in BA. This natural searching algorithm is inspired by the Genetic Algorithm (GA). Six different natural selections are investigated, which are global-best, tournament, proportional, linear rank, exponential rank and random. The results suggest that there are positive effects of the selection mechanisms on the performance of the classical bat-inspired algorithm.

The enhancement of local and global search characteristic in BA has been enhanced with three different methods in [9]. The three different methods are inertia weight modification (IS1), distribution of the population modification (IS2) and hybridization with invasive weed optimization (IS3). The proposed methods are claimed to be more effective than the original BA.

Xie et al. in [10] proposed a method to overcome the slow convergence rate and low accuracy of bat algorithm. Differential operator and Levy flights trajectory are used to modify the original bat algorithm. Differential operator is introduced to accelerate the convergence speed of proposed algorithm, which is similar to mutation strategy

“DE/best/2” in differential algorithm. Lévy flights trajectory can ensure the diversity of the population against premature convergence and make the algorithm effectively jump out of local minima. The simulation results not only show that the proposed algorithm is feasible and effective, but also demonstrate that the proposed algorithm has superior approximation capabilities in high-dimensional space.

In this paper, combination of BA and spiral searching method is performed intensively. Even though this algorithm is extended from original BA, but how both algorithms, BA and SDA combine is like a hybrid process.

2 Methodology

Bat Algorithm (BA) is developed by Xin-She Yang and explained in detail in [11]. The theory of the algorithm is based on the echolocation behavior of bats. Such echolocation behavior of microbats is formulated in such a way that it can be associated with the objective function to be optimized.

The Spiral Dynamic Algorithm (SDA) is developed by Tamura et al. in [12]. SDA is known as fast computing algorithm according to its simplicity in the structure and it has stable convergence response when approaching the optimum point in the search space.

Figure 1 shows flowchart of Extended Bat Algorithm (EBA). EBA consists of original BA algorithm and searching technique by SDA. The dotted rectangle in Fig. 1 represents the searching technique by SDA. The combination of both algorithms is expected to perform very well together and could improve the performance of the original BA. The only part taken from SDA is for updating the x value, and the remaining algorithm is from BA. How this SDA part improves the EBA will be further discussed.

In simulations, firstly, frequency, f , positions, x and velocities, v are defined in a search area. The updated x and v are updated at time, t as below.

$$f_i = f_{\min} + (f_{\max} - f_{\min})\beta \tag{1}$$

$$v_i = v_i + (x_i - x_*)f \tag{2}$$

$$solution = x_i^{k+1} + v_i \tag{3}$$

where $\beta \in [0, 1]$ is a random vector between 0 to 1 only. Here x_* is the current global best value after comparing all the solutions among all the bats.

Before the result is updated by using Eq. (3), the searching method of BA is changed from random to spiral searching technique by using Eq. (4). This is the important part which changes the searching technique from random method to spiral method. The equation is taken from spiral equation SDA.

$$x_i^{k+1} = A_{spiral_i} x_i^k - (A_{spiral_i} - I_d)x^* \tag{4}$$

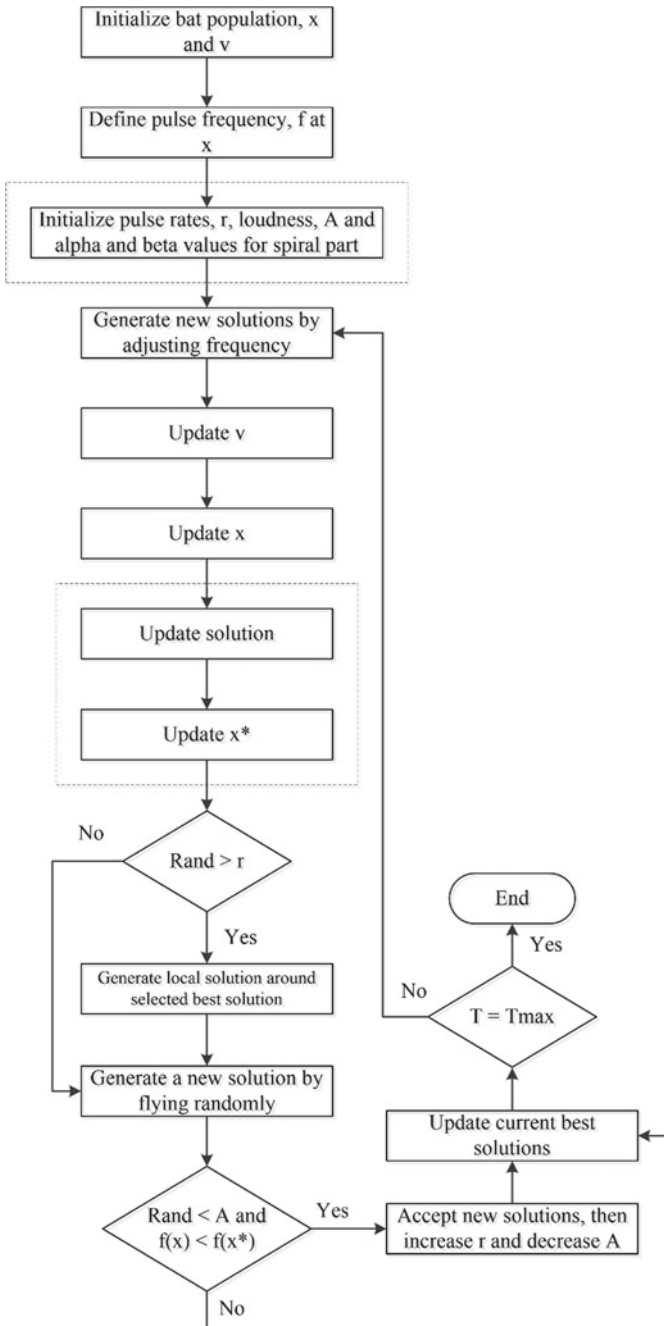


Fig. 1 Flowchart of extended bat algorithm

The final step of BA that should be considered in EBA implementation is the loudness and pulse emission that are also updated correspondingly as the iterations increased. As the loudness normally lessen once a bat has found its prey, the rate of pulse emission increases, the loudness can be chosen as any appropriate value.

$$A_i^{t+1} = \alpha A_i^t, r_i^{t+1} = r_i^0 [1 - \exp(-\gamma t)] \quad (9)$$

where α and γ are constants. For any $0 < \alpha < 1$ and $\gamma > 0$,

$$A_i^t \rightarrow 0, r_i^t \rightarrow r_i^0, t \rightarrow \infty \quad (10)$$

Lastly, the algorithm will continue the searching until meet the termination condition and in this case, until the maximum iteration achieved.

3 Result and Discussion

In this study, Extended Bat Algorithm (EBA) will be compared with Particle Swarm Optimization (PSO) algorithm and also original BA to evaluate its performance. Table 1 shows three different values of r and θ values that had been applied in EBA.

There are three different objective functions that have been used for the comparison, which are Ackley, Hyperellipsoid and Rosenbrock functions. Table 2 shows simulation results of the proposed methods, original PSO and BA after 300 iterations. PSO used in this study is the original PSO with randomness. The asterisks (*) in Table 2 marks the best values obtained for each case.

These results extensively show that the proposed method has best searching performance compared to BA and PSO. Mainly, EBA#3 gives the highest performance. It is shown by the lowest fitness value obtained compared to another four algorithms. In our case study, the objective is to find the minimum value of each function. BA, PSO, EBA#1 and EBA#2 outputs are in the moderate performances.

The convergence graph for each function is shown in Figs. 2, 3 and 4. In Fig. 2, convergence curve for Hyperellipsoid function, it is seen that the proposed algorithm EBA#1, EBA#2 and EBA#3 have the best fitness value compared to BA and PSO. The exploration phase in EBA is until around iteration 40. Meanwhile, the exploration phase of PSO is still running until the end of maximum iteration.

Figure 3 shows the convergence curve of Ackley function. It is shown that the exploration and exploitation phases among BA, PSO and 3 different EBA have the same movement. However, EBA has the best fitness value compared to PSO and original BA.

Table 2 Results of Numerical Experiment

Function	Algorithm	Max	Min	Mean
Ackley	BA	17.2919	9.2850	16.5730
	PSO	18.0746	4.8686	13.2091
	EBA#1	12.3883*	4.1671*	9.5653*
	EBA#2	12.3883*	4.1671*	9.5653*
	EBA#3	12.3883*	4.1671*	9.5653*
Hyperellipsoid	BA	17.2919*	8.1917	16.4880
	PSO	1030.184	16.36137	333.7813
	EBA#1	20.5999	4.1671*	14.5214
	EBA#2	20.7218	4.1671*	13.9454*
	EBA#3	20.4815*	5.6497	14.2200
Rosenbrock	BA	17.2919	8.1917	16.4880
	PSO	979,569	0.01857*	24748.6024
	EBA#1	20.79878	0.216619	14.08558
	EBA#2	20.73878	0.593442	14.5011
	EBA#3	20.7186*	0.604328	13.38932*

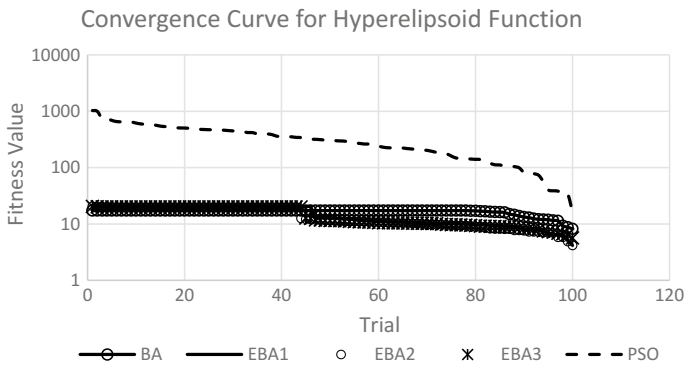


Fig. 2 Convergence curve for hyperellipsoid function

Figure 4 shows the result of convergence curve for Rosenbrock function. From the graph, it is clearly seen that the exploration phase of PSO is longer than EBA and BA. However, EBA#3 has the best fitness values among all algorithms for Rosenbrock function.

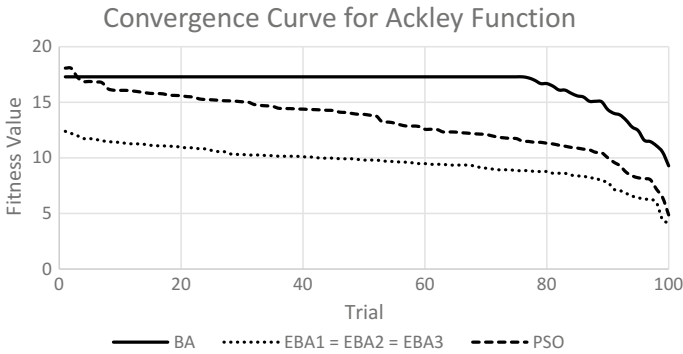


Fig. 3 Convergence curve of Ackley Function

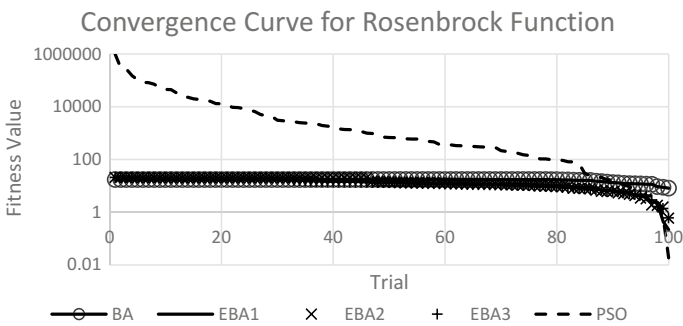


Fig. 4 Convergence curve of Rosenbrock Function

4 Conclusion

As conclusion, this paper proposed a new searching technique to improve the performance of Bat Algorithm (BA). Extended Bat Algorithm (EBA) introduces spiral searching method instead of particles spreading randomly for standard BA. For some benchmark problems, EBA gives the good numerical performance compared to PSO. The potential of the proposed method was confirmed from simulation results.

Acknowledgements This works is supported by Universiti Malaysia Pahang (UMP), under Universiti Malaysia Pahang Research Grant RDU 170378.

References

1. Tamura, K., Yasuda, K.: Spiral dynamics inspired optimization. *J. Adv. Comput. Intell. Intell. Inf.* **15**, S98–S100 (2010)
2. Yang, X.S.: A new metaheuristic bat-inspired algorithm. *Stud. Comput. Intell.* **284**, 65–74 (2010)
3. Tamura, K., Yasuda, K.: Spiral optimization—a new multipoint search method. In: *Conference Proceedings IEEE International Conference Systems Man Cybernetics*, pp. 1759–1764, IEEE, USA (2011)
4. Ahmad Nor Kasruddin, N., Normaniha, A.G., Mohd Ashraf, A.: A novel hybrid spiral-dynamics bacterial-foraging algorithm for global optimization with application to control design. In: *12th UK Workshop on Computational Intelligence*, pp. 3–5, IEEE, UK (2012)
5. Fister, I., Fister, D., Yang, X.S.: A hybrid bat algorithm. *Elektroteh. Vestnik/Electrotechnical Rev.* **80**, 1–7 (2013)
6. Zhang, J., Wang, G.: Image matching using a bat algorithm with mutation. **203**, pp. 88–93. (2012)
7. Wang, G., Guo, L.: A novel hybrid bat algorithm with harmony search for global numerical optimization. *J. Appl. Math.* p. 21 (2013)
8. Al-Betar, M.A., Awadallah, M.A., Faris, H., Yang, X.-S., Khader, A.T., Alomari, O.A.: Bat-inspired algorithm with natural selection mechanism for global optimization. *Neurocomputing* **273**, 448–465 (2018)
9. Yilmaz, S., Kucuksille, E.U.: A new modification approach on bat algorithm for solving optimization problem. *Appl. Soft. Comput.* **28**, 259–275 (2015)
10. Xie, J., Zhou, Y., Chen, H.: A novel bat algorithm based on differential operator and levy flights trajectory. *Comput. Intell. Neurosci.* p. 13 (2013)
11. Yang, X-S.: A new metaheuristic bat-inspired algorithm. *Nature Inspir. Cooperative Strat. Optim. (NICSO 2010)*, pp. 65–74 (2010)
12. Tamura, K., Yasuda, K.: Primary study of spiral dynamics inspired optimization. *IEEJ Trans. Electrical Electron. Eng.* **6(S1)**, 98–100 (2011)

Performance Comparison of Perturbation Signals for Time-Varying Water Temperature Modeling Using NARX-Based BPSO



Najidah Hambali, Mohd Nasir Taib, Ahmad Ihsan Mohd Yassin and Mohd Hezri Fazalul Rahiman

Abstract There is an increasing concern on the perturbation signal analysis on nonlinear modeling for nonlinear systems. Several studies have shown the importance of suitable perturbation signal for the real nonlinear system applications. This study systematically reviews the performance comparison for nonlinear modeling using two perturbation signals, namely as Pseudo Random Binary Signal (PRBS) and Multi-level Pseudo Random Sequence (MPRS) for a time-varying water temperature of Steam Distillation Pilot Plant (SDPP). A Binary Particle Swarm Optimization (BPSO) algorithm was utilized in the model structure selection for polynomial Nonlinear Auto-Regressive with eXogenous (NARX) input. Three model's selection criteria were examined; Akaike Information Criterion (AIC), Model Descriptor Length (MDL), and Final Prediction Error (FPE) for performance analysis that included model validation. The results presented lesser number of input and output lags, also fewer output model parameters for MPRS perturbation signal. Further analysis of the nonlinear model has demonstrated high R-squared and low MSE for model validation for both models using PRBS and MPRS perturbation signals.

Keywords System identification · Time-varying temperature · Nonlinear model Particle swarm optimization · Distillation column · Perturbation signal

1 Introduction

System identification plays an importance role in representing the process plant and instrumentation system [1]. A linear and nonlinear modeling are included in the system identification [2–6]. An alternative perturbation signal approach is necessary

N. Hambali · M. N. Taib · A. I. M. Yassin · M. H. F. Rahiman (✉)
Faculty of Electrical Engineering, Universiti Teknologi MARA, 40450 Shah Alam, Selangor, Malaysia
e-mail: hezrif@ieee.org

© Springer Nature Singapore Pte Ltd. 2019
Z. Md Zain et al. (eds.), *Proceedings of the 10th National Technical Seminar on Underwater System Technology 2018*, Lecture Notes in Electrical Engineering 538, https://doi.org/10.1007/978-981-13-3708-6_21

for nonlinear system identification since it might be dissimilar from those demanded for linear system.

A NARX modeling was implemented for several systems with good standing performance [7–9]. Over the past two decades, a new NARX model with optimization has recorded an effective improvement of disturbances compensation [10, 11]. Besides that, numerous studies have reported on the ease of implementation and autocorrelation function that is similar to the white noise. This is among the advantages of the PRBS perturbation signal [12–15]. Moreover, previous studies have explored the application of PRBS through NARX modeling which provides highly accurate outcomes [16–19]. In addition, the PRBS perturbation input signals have been implemented for the distillation column that recorded the effectiveness of the proposed technique [11].

However, there is growing concerns in [20–23] whose claimed that the PRBS may not provides sufficient information to identify the nonlinear behavior [9]. Thus, this signal cannot excite certain nonlinearities of the system. Interestingly, all the comparison analysis reviewed between the PRBS and Multi-level Pseudo Random Sequence (MPRS) perturbation signal application in the nonlinear modeling so far, despite the facts that PRBS signal was not appropriate for the nonlinear system identification [24]. Such approaches also have failed to address the important of time varying factor that related to this nonlinear behavior of the distillation column in their investigation as resolved clearly by other researchers [25–28].

Several perturbation input signals allow the system to explore its nonlinearity behavior include MPRS signal. Keith Godfrey described the MPRS perturbation input signal's theoretical development in the system identification [29, 30]. Besides that, the MPRS perturbation signal is not only operates at numerous level but also have no limitations on the levels amount within the input range ability. A much more better approach in the performance of the nonlinear modeling has revealed the consistently evaluation through the usage of MPRS perturbation signal in contrast to the PRBS [31–33]. A number of studies has suggested MPRS perturbation signal for the nonlinear system which allow the nonlinearity behavior to be highlighted [34–36].

More recent attentions have focused on the provision of the time-varying feature for the nonlinear system [37–40]. The nonlinear and time-varying NARX model have been successfully developed for semisubmersible platform, dielectric elastomer actuators, human EEG data; and induced muscular dynamics respectively [25–28]. Besides that, there has been a wide increase in investigation of a distillation column in the last more than two decades [41–46]. The optimization approach in NARX modeling for the distillation column has effectively improved to optimum stage besides reduced the computational time [47]. Furthermore, a great deal of earlier research into Binary Particle Swarm Optimization (BPSO) has focused on provided excellent result for the time-varying process [48, 49].

The promising choice of BPSO method to other established exploratory techniques is designed for optimization problem solving. Kennedy and Eberhart have designed a discrete version of the PSO algorithm [47]. Besides that, model parsimony aims the best model with the least complexity between multiple model structures.

Information criteria such as Akaike Information Criterion (AIC), Final Prediction Error (FPE) and Model Descriptor Length (MDL) are used to impose parsimony by integrating difficulty drawbacks in accession to residual fit [50–52].

The aim of this study is to demonstrate the performance comparison of PRBS and MPRS perturbation signals for time-varying water temperature of the SDPP. On the basis of the polynomial Nonlinear Auto-Regressive with eXogenous input (NARX), the BPSO algorithm was employed for model structure selection. Then, several models selection criteria such as Akaike Information Criterion (AIC), Model Descriptor Length (MDL), and Final Prediction Error (FPE) were investigated for model validation. The comparison analysis was presented for model validation of both perturbation signals.

This paper has been divided into six parts. The second part deals with the theoretical background. In the third part, the experimental design is presented. The methodology that has been used in this paper is also reported in part four. All the results and discussion has been shown in part five. Lastly, the conclusion is discussed in the final part.

2 Theoretical Background

2.1 NARX Model

The NARX model is presented as

$$y(t) = f^d \left[\begin{array}{l} y(t-1), y(t-2), \dots, y(t-n_y), \\ u(t-n_k), u(t-n_k-1), \dots, u(t-n_k-n_u) \end{array} \right] + \varepsilon(t) \quad (1)$$

f^d is the estimated model with corresponding maximum lags and input signal time delay, n_y , n_u , and n_k while $y(t)$ and $u(t)$, are the output and input, respectively. The pick of model structures is required for parameter prediction of y that depends on lagged y , u and ε , the white noise residuals terms.

NARX polynomial model representation is given by

$$y(t) = \sum_{m=1}^{n_p} P_m \theta_m + \varepsilon(t) \quad (2)$$

The m -th regression term, P_m and the m -th regression parameter, θ_m are presented in the polynomial expansion for n_p the number of terms.

The Least Squares (LS) problem's formulation and solution have been involved in identification. The matrix form is

$$P\theta + \varepsilon = y \quad (3)$$

where y is the real reflections, θ is a coefficient vector and P is a regressor matrix.

2.2 BPSO

The PSO technique is established on evolutionary computation and swarm philosophy. The convergence quality improvement and the algorithm adaptation in problems solving contributed to numerous established variants such as Vanilla [53] and Binary [47] PSO algorithms.

The velocity and position update equations are among the Vanilla PSO algorithm,

$$V_{id} = V_{id} + C_1(P_{best} - X_{id}) \times rand_1 + C_2(G_{best} - X_{id}) \times rand_2 \quad (4)$$

The best particle's fitness, P_{best} and the best particle's solution, G_{best} attained by the swarm with compounding of C_1 and C_2 , the cognition and social learning rate, respectively. While the particle velocity, V_{id} and the particle position X_{id} , are used together with uniformly-distributed random numbers, $rand_1$ and $rand_2$ which is between 0 and 1.

The value of V_{id} has been employed for a particle positions alteration.

$$X_{id} = X_{id} + V_{id} \quad (5)$$

In binary optimization problem solving, the probabilities of change have been demonstrated in the BPSO particle positions rather than the actual solution as in (4) and (5) [54]. The bit change process is between 0 and 1, as stated below;

$$bin\ string = \begin{cases} 1, & X_{id} \geq 0.5 \\ 0, & X_{id} < 0.5 \end{cases} \quad (6)$$

The bit will vary from its current condition to another (either 0–1 or 1–0) for probability value bigger than 0.5. Otherwise, the bit will sustain for the particle value is smaller than 0.5.

BPSO convergence is affected by various parameters such a velocity bounding parameters (V_{min} and V_{max}), position bounding parameters (X_{min} and X_{max}) and parameters (C_1 and C_2) for the influence control of the swarm and self-cognition.

In the swarm of BPSO for polynomial NARX structure selection, it involves a linear least squares solution. A $1 \times m$ solutions vector, X_{id} has been transmitted for each one particle. QR factorization has been employed for the forecasting of the parameter value, θ_R for the reduced P matrix (θ_R).

$$P_R\theta_R + \varepsilon = y \quad (7)$$

$$P_R = \theta_R R_R \quad (8)$$

$$g_R = Q_R^T y \quad (9)$$

$$R_R \theta_R = g_R \quad (10)$$

Next, the value of θ_R can be estimated by reorganizing and solving (10).

$$\theta_R = R_R^T g_R \quad (11)$$

2.3 Model Estimation

Based on the model parameters, θ , the residuals Normalized Sum Squared Error (NSSE), $V_{NSSE}(\theta, Z^N)$ is;

$$V_{NSSE}(\theta, Z^N) = \frac{1}{2N} \sum_{t=1}^N \varepsilon^2(t, \theta) \quad (12)$$

The selection of model order can be done by using several established model selection criteria such as Akaike Information Criterion (AIC), Model Descriptor Length (MDL), and Final Prediction Error (FPE) as shown in (13), (14) and (15) respectively.

$$V_{AIC} = \left(1 + 2\frac{d}{N}\right) V_{NSSE}(\theta, Z^N) \quad (13)$$

$$V_{MDL} = \left(1 + \log(N)\frac{d}{N}\right) V_{NSSE}(\theta, Z^N) \quad (14)$$

$$V_{FPE} = \left(\frac{1 + \frac{d}{N}}{1 - \frac{d}{N}}\right) V_{NSSE}(\theta, Z^N) \quad (15)$$

where the number of estimated parameters and the data points amount are presented as d and N , respectively. $V_{NSSE}(\theta, Z^N) \rightarrow 0$ will leads to minimum values of V_{AIC} , V_{MDL} and V_{FPE} when $d \rightarrow 1$. Models with the lowest V_{AIC} , V_{MDL} and V_{FPE} scores or fitness values conform the principle of parsimony as the smallest quantity of parameters were necessary to supply the most beneficial fit for the data.

The collected data using SDPP will be separated into two divisions; training set for model estimation and testing set for model validation. For model estimation, the sample data are utilized for estimation to fit the NARX model. The interlacing method that has been used divides the dataset based on the position of the data into training and testing sets. The training set contains odd positions data, while even positions data are allotted for the testing set.

For odd N case, $D_{1,3,5,\dots,N} = D_{training}$ and $D_{2,4,6,\dots,N} = D_{testing}$. Otherwise, for even N case, $D_{2,4,6,\dots,N} = D_{training}$ and $D_{1,3,5,\dots,N} = D_{testing}$.

2.4 Model Validation

A measurement of the model's ability for future value prediction in One-Step Ahead (OSA) prediction is based on its previous data as given by;

$$\hat{y} = \hat{g}(z(t)) \quad (16)$$

The estimated nonlinear model, \hat{g} and the regressors, $z(t)$ are utilized in (16). For the NARX model, the $z(t)$ representation is given below.

$$z(t) = \begin{bmatrix} y(t-1), y(t-2), \dots, y(t-n_y) \\ u(t-n_k-1), u(t-n_k-2), \dots, u(t-n_k-n_u) \end{bmatrix} \quad (17)$$

The magnitude testing of residuals for regression and model fitting problems are solved by employing the standard methods, Sum Squared Error (SSE) and Mean Squared Error (MSE).

The SSE equation of length n for a residual vector ε is given by;

$$SSE = \sum_{i=1}^n (e_i)^2 = \sum_{i=1}^n (y_i - \hat{y}_i)^2 \quad (18)$$

where y_i is the discovered value, and \hat{y}_i is the projected value at point i .

Similar to the SSE equation, but the MSE equation is divided by n , the number of samples as stated below;

$$MSE = \frac{\sum_{i=1}^n (e_i)^2}{n} = \frac{\sum_{i=1}^n (y_i - \hat{y}_i)^2}{n} \quad (19)$$

A good model fit results from low values of SSE and MSE from the residuals magnitude.

The R-Squared technique is employed for the goodness of fit model measurement. The R-Squared is reported as;

$$R^2 = 1 - \frac{\sum_{i=1}^n (y_i - \hat{y}_i)^2}{\sum_{i=1}^n (y_i - \bar{y})^2} \quad (20)$$

where the actual and estimated observations at interval i , are described as y_i and \hat{y}_i , respectively. n is the number of observations and \bar{y} is the mean value of n .

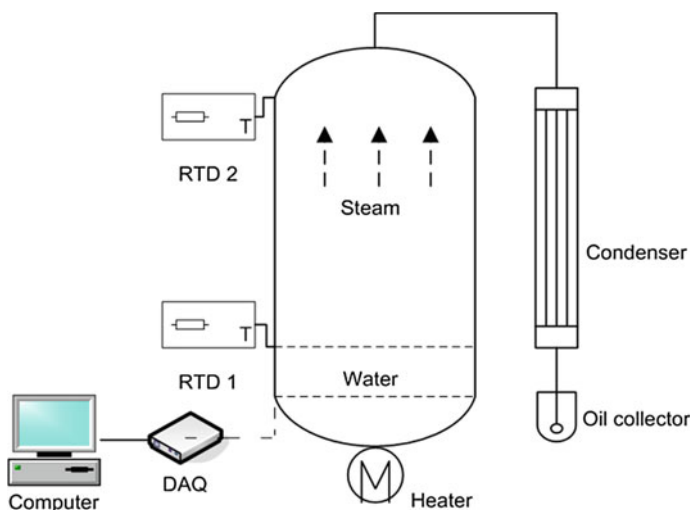


Fig. 1 Steam distillation pilot plant (SDPP) system

3 Experimental Design

The SDPP system used coil-type water immersion heater to generate steam with two resistive temperature detectors (RTD) PT-100. The water and steam temperature are monitored using both RTDs. 1–5 V signals are obtained from the RTDs' resistance output for specific several temperature series. The boiling water allows steam to exceed through the raw material during the extraction process. Then, the condenser condenses the steam first before it changes into oil and hydrosol in the collector. A plant with a 1.5 kW, 240 V and 50 Hz power has been used for immersion heating element with specific sampling time. For modeling purposes, a MATLAB software is utilized for plant integration and data collection.

In this study, two different perturbation input signals are described; PRBS and MPRS. The PRBS perturbation signal consists of two conditions signal which changes between high and low values. The probability band of 0.1 was utilized in this study for PRBS perturbation input signal representation. The 5 and 0 V values represented the maximum and minimum levels respectively of the PRBS perturbation input signal. Besides that, the maximum value of MPRS applied in this study was 5 with one second sampling time for 18,000 s. Figure 1 illustrates a pilot plant of the essential oil extraction system.

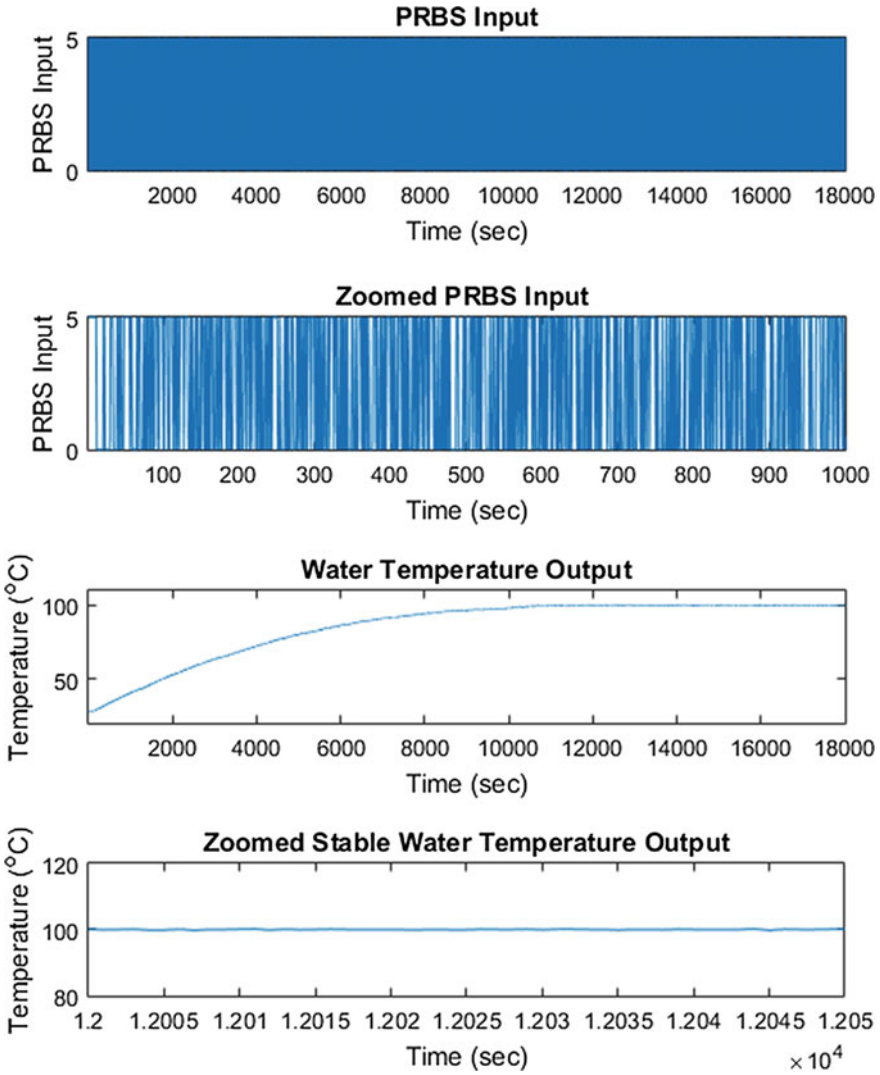


Fig. 2 Water temperature dataset using PRBS input

4 Methodology

The time-varying water temperature dataset that consists of 18,000 data points from the SDPP with the implementation of the PRBS perturbation input is presented in Fig. 2.

The application of MPRS perturbation input signals for the water temperature system is illustrated by Fig. 3.

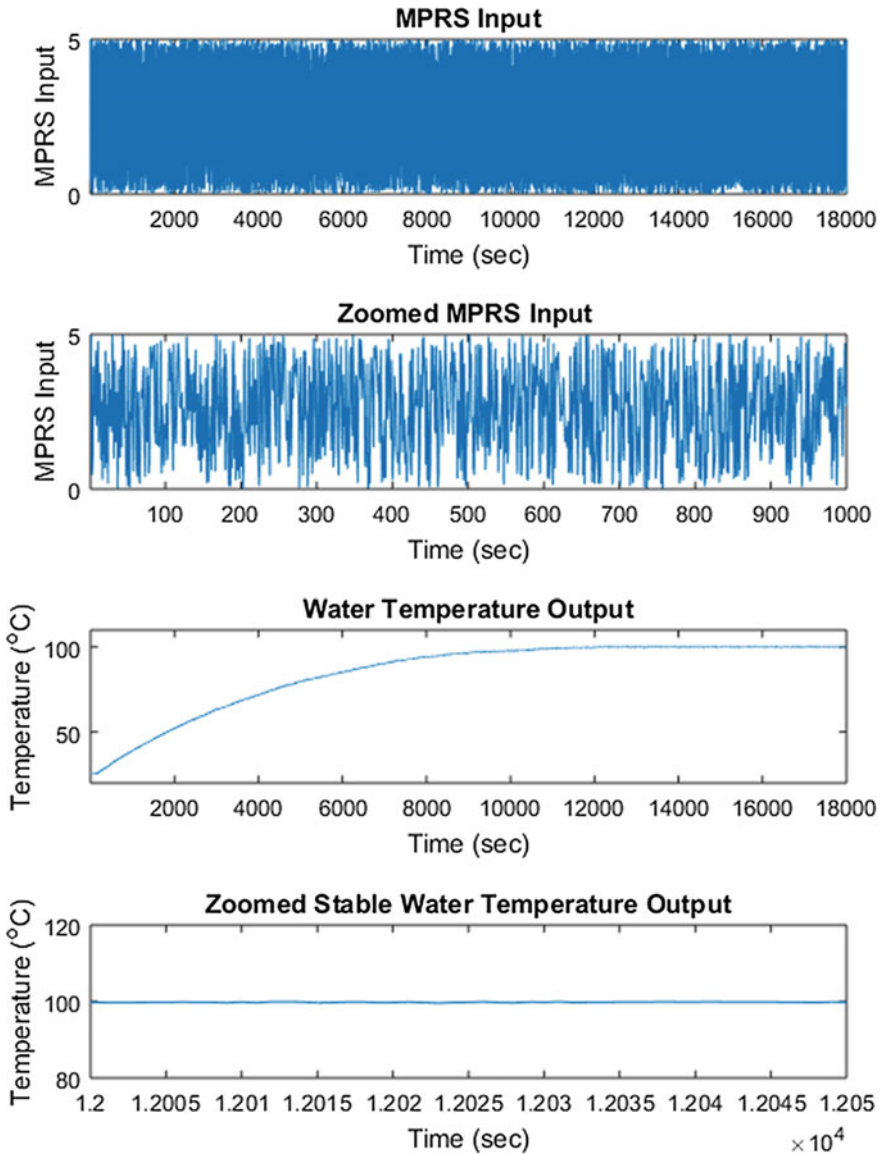


Fig. 3 Water temperature dataset using MPRS input

For optimization purposes, various swarm sizes, maximum iterations, and random seeds parameters have been combined. Higher swarm sizes create larger potential in global minima searching by the number of agents based on optimization time and computational cost. Termination of the PSO search will be driven by the achievement of the objective or the finding of maximum iterations for each experiment. In addition,

Table 1 BPSO parameter settings for structure selection

Parameter	Value
Fitness criterion	AIC, FPE, MDL
Swarm size	10, 20, 30, 40, 50
Maximum iterations	500, 1000, 1500
Initial random seed	0, 10 000, 20 000
X_{min}	0
X_{max}	1
V_{min}	-1
V_{max}	+1
C_1	2.0
C_2	2.0

the initial random seed for each V_{id} and X_{id} particles have influence on the final optimization PSO result. The consistency of the results will be decided by different initial random seeds for repeated experiments. The selected parameter values as listed in Table 1 are examined which has been implemented by Yassin et al. [52, 54] for the fitness function optimal convergence exploration.

5 Results and Discussion

The order of the model of the input and output (maximum lags) for each dataset has been chosen based on the low fitness values. The input and output model order of the maximum lags have been tested from the lowest value of 1 and it was continuously increased by one until the minimum fitness values have been found. The selected input and output lags will be utilized for further analyzed using NARX-based BPSO modeling.

As can be seen in Figs. 4 and 5 the fitness and CRV measures for water temperature using PRBS perturbation input signal were decreased as the number of input and output lags were increased. Input and output lags of 4 was selected as both fitness and CRV provided the lowest amount.

Next, the fitness values of the water temperature modeling using MPRS perturbation input signal in Fig. 6 declined steadily starting at input and output lags of 3 onwards. Besides that, Fig. 7 presents the CRV amount that reached the lowest point at input and output lags of 3. Therefore, input and output lags of 3 was chosen for this dataset.

The Water Temperature NARX-based BPSO models of AIC, FPE and MDL using PRBS and MPRS perturbation input signals are presented in Tables 2 and 3 respectively.

Based on Table 2, the output models selected using PRBS were reported. All the output models for water temperature NARX-based BPSO model considered past

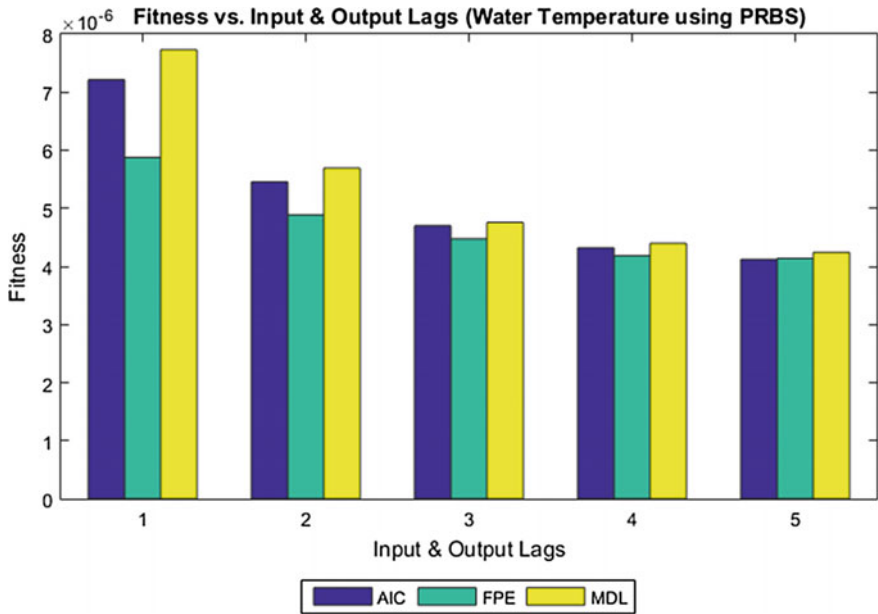


Fig. 4 Minimum fitness of input and output lags using PRBS

Table 2 Water temperature output model using PRBS

Criterion	Output model
AIC	$y(t) = 2.0880 \times 10^{-4} u(t - 4) + 1.0017 y(t - 2) + 8.3542 \times 10^{-3} y(t - 1) * y(t - 3) - 2.8747 \times 10^{-3} y(t - 1) * y(t - 2) - 5.4969 \times 10^{-3} y(t - 2) * y(t - 3) + \varepsilon(t)$
FPE	$y(t) = 1.7413 \times 10^{-4} u(t - 4) + 1.0019 y(t - 2) + 2.1629 \times 10^{-7} u(t - 1) * y(t - 4) + 1.9333 \times 10^{-3} y(t - 1) * y(t - 4) + 3.0495 \times 10^{-3} y(t - 1) * y(t - 3) - 5.8121 \times 10^{-4} y(t - 3) * y(t - 3) - 4.4207 \times 10^{-3} y(t - 2) * y(t - 2) + \varepsilon(t)$
MDL	$y(t) = 1.0019 y(t - 2) - 8.1381 \times 10^{-5} u(t - 2) * u(t - 3) + 1.9125 \times 10^{-3} y(t - 3) * y(t - 4) + 6.9128 \times 10^{-3} y(t - 1) * y(t - 1) - 8.8446 \times 10^{-3} y(t - 1) * y(t - 2) + \varepsilon(t)$

outputs which resulted as good fitting OSA outcomes. Besides that, both AIC and FPE models included input terms 4, $u(t - 4)$ in the output model. In addition, there were additional term $u(t - 1) * y(t - 4)$ for FPE and $u(t - 2) * u(t - 3)$ for MDL output models. Consequently, the AIC and MDL models were found to be more effective with lesser number of parameters in the output model.

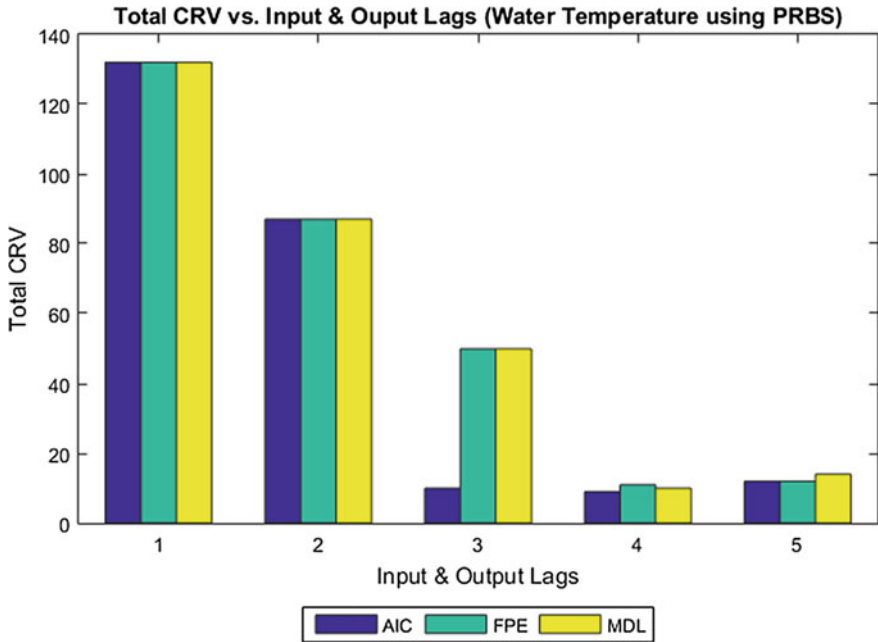


Fig. 5 Minimum total CRV of input and output lags using PRBS

Table 3 Water temperature output model using MPRS

Criterion	Output model
AIC	$y(t) = 1.0015 y(t - 1) - 3.2277 \times 10^{-3} y(t - 1) * y(t - 1) + 3.2128 \times 10^{-3} y(t - 2) * y(t - 3) + \varepsilon(t)$
FPE	$y(t) = 1.0015 y(t - 1) - 3.2277 \times 10^{-3} y(t - 1) * y(t - 1) + 3.2128 \times 10^{-3} y(t - 2) * y(t - 3) + \varepsilon(t)$
MDL	$y(t) = 1.0015 y(t - 1) - 3.2277 \times 10^{-3} y(t - 1) * y(t - 1) + 3.2128 \times 10^{-3} y(t - 2) * y(t - 3) + \varepsilon(t)$

Next, evidence of the output model using MPRS can be observed from Table 3 which provided strong parsimonious model structures of all the criterion models. This finding validates identical output model for the AIC, FPE, and MDL models. All the output models included previous outputs which leads to beneficial fitting OSA outcomes. Some noticeable determinations were revealed in the output model of the water temperature modeling using MPRS perturbation input signal. These findings demonstrated that improved parameter numbers of the output model were achieved using MPRS perturbation signal with three parameters. This is better than the output model of the water temperature using PRBS perturbation signal that provided five to seven parameters as can be identified from Table 2.

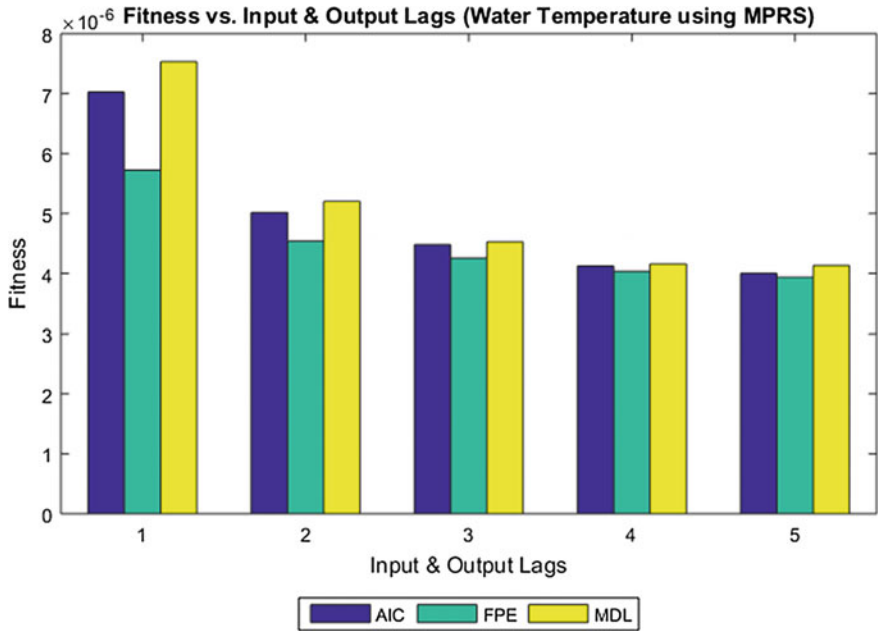


Fig. 6 Minimum fitness of input and output lags using MPRS

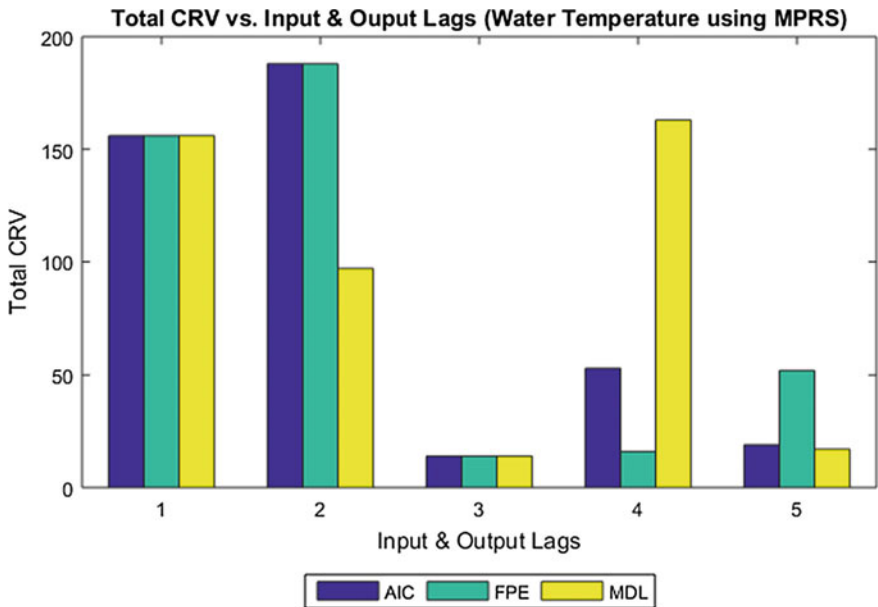


Fig. 7 Minimum total CRV of input and output lags using MPRS

Table 4 Performance comparison of water temperature modeling

Performance criterion	Models criterion	PRBS signal	MPRS signal
Input and output lags	AIC	4	3
	FPE		
	MDL		
Output model parameter	AIC	5	
	FPE	7	3
	MDL	5	
R-squared	AIC	99.9974%	99.9975%
	FPE	99.9975%	
	MDL	99.9975%	
MSE	AIC	1.0579×10^{-2}	1.0723×10^{-2}
	FPE	1.0317×10^{-2}	
	MDL	1.0321×10^{-2}	

The comparison of water temperature modeling using PRBS and MPRS perturbation input signals is summarized in Table 4.

It is also evident that high R-Squared, and small MSE were produced for both models using PRBS and MPRS. In the development of water temperature NARX-based BPSO model, the second-order terms were chosen thus indicating that there exist second-order influences in the nonlinear system of SDPP. These differences can be explained by the inclusion of the past outputs only from the first and second order terms in the output models.

6 Conclusion

The performance comparison of perturbation signals between PRBS and MPRS for time-varying water temperature modeling was identified using NARX-based BPSO. The implementation of MPRS perturbation signal provided better model than PRBS perturbation signal implementation. It is apparent that the output model parameters number using MPRS perturbation signal were reduced for all the criterion models compared with PRBS perturbation signal, besides lower input and output lags. This is essential to match the parsimonious principle of the model in system identification. In the development of water temperature NARX-based BPSO model, the second-order terms were chosen thus indicating that there exist second-order influences in the nonlinear system of SDPP.

Acknowledgements This project was funded by Institute of Research Management & Innovation (IRMI), Universiti Teknologi MARA (UiTM) Shah Alam, Selangor, Malaysia [grant number 600-IRMI/DANA 5/3 BESTARI 9049/2017)] and Kementerian Pendidikan Tinggi Malaysia [SLAI

Scholarship] for the first author. The first author would like to thank Jabatan Pengurusan Sumber Manusia (JPSM), Universiti Teknologi MARA (UiTM) Shah Alam, Selangor, Malaysia for the scholarship management.

References

1. Lu, S., Hogg, B.W.: Dynamic nonlinear modelling of power plant by physical principles and neural networks. *Int. J. Electr. Power Energy Syst.* **22**(1), 67–78 (2000)
2. Bachnas, A.A., Tóth, R., Ludlage, J.H.A., Mesbah, A.: A review on data-driven linear parameter-varying modeling approaches: a high-purity distillation column case study. *J. Process Control* **24**(4), 272–285 (2014)
3. Billings, S.A., Chen, S., Backhouse, R.J.: The identification of linear and non-linear models of a turbocharged automotive diesel engine. *Mech. Syst. Signal Process.* **3**(2), 123–142 (1989)
4. Paduart, J., Lauwers, L., Swevers, J., Smolders, K., Schoukens, J., Pintelon, R.: Identification of nonlinear systems using Polynomial Nonlinear State Space models. *Automatica* **46**(4), 647–656 (2010)
5. Wang, S., Han, Z., Liu, F., Tang, Y.: Nonlinear system identification using least squares support vector machine tuned by an adaptive particle swarm optimization. *Int. J. Mach. Learn. Cybern.* **6**(6), 981–992 (2015)
6. Silva, N., Bispo, H., Brito, R., Manzi, J.: Auto tuning applied to distillation column based on Armax model parameter estimation, pp. 261–272. Springer, Cham (2015)
7. Ohno, Y., Inoue, J., Iwase, M., Hatakeyama, S.: Motion and force estimation based on the NARX with an EMG signal. In: *International Conference on Advanced Engineering Theory and Applications*, pp. 288–298 (2017)
8. Jiang, J., Wang, F., Zhang, Y., Qin, Y., Gao, X.: Estimation of vertical track irregularity based on NARX neural network. In: *Proceedings of the 2015 International Conference on Electrical and Information Technologies for Rail Transportation*, pp. 167–175 (2016)
9. Ravi Srinivas, G., Arkun, Y., Chien, I.-L., Ogunnaike, B.A.: Nonlinear identification and control of a high-purity distillation column: a case study. *J. Process Control* **5**(3), 149–162 (1995)
10. Soni, A.: Control-relevant system identification using nonlinear Volterra and Volterra-Laguerre models, Doctor Dissertation University Pittsburgh (2006)
11. Godfrey, K.R., Tan, A.H., Barker, H.A., Chong, B.: A survey of readily accessible perturbation signals for system identification in the frequency domain. *Control Eng. Pract.* **13**(11), 1391–1402 (2005)
12. Drescher, U., Koschate, J., Schiffer, T., Schneider, S., Hoffmann, U.: Analysis of heart rate and oxygen uptake kinetics studied by two different pseudo-random binary sequence work rate amplitudes. *Respir. Physiol. Neurobiol.* **240**, 70–80 (2017)
13. Nguyen, S.T.N., Gong, J., Lambert, M.F., Zecchin, A.C., Simpson, A.R.: Least squares deconvolution for leak detection with a pseudo random binary sequence excitation. *Mech. Syst. Signal Process.* **99**, 846–858 (2018)
14. Alonge, F., D’Ippolito, F., Raimondi, F.M., Tumminaro, S.: Identification of nonlinear systems described by Hammerstein models. In: *42nd IEEE International Conference on Decision and Control (IEEE Cat. No. 03CH37475)*, pp. 3990–3995 (2003)
15. Safarinejadian, B., Kianpour, N., Asad, M.: A novel identification method for fractional-order wiener systems with PRBS input. In: *2016 4th International Conference on Control, Instrumentation, and Automation ICCIA 2016*, pp. 290–295, Jan 2016
16. Karacan, S., Hapoğlu, H., Alpbaz, M.: Application of optimal adaptive generalized predictive control to a packed distillation column. *Chem. Eng. J.* **84**(3), 389–396 (2001)
17. Misra, S., Nikolaou, M.: Adaptive design of experiments for model order estimation in subspace identification. *Comput. Chem. Eng.* **100**, 119–138 (2017)

18. Häggblom, K.E.: A new optimization-based approach to experiment design for dynamic MIMO identification. *IFAC-Papers OnLine* **50**(1), 7321–7326 (2017)
19. Karacan, S., Moslempour, Z., Hapoğlu, H., Albaz, M.: Application of multivariable nonlinear adaptive generic model control to a packed distillation column. *Chem. Eng. Commun.* **193**(12), 1635–1659 (2006)
20. Rivera, D., Lee, H., Mittelmann, H., Braun, M.: High-purity distillation. *IEEE Control Syst. Mag.* **27**(5), 72–89 (2007)
21. Deflorian, M., Zaglauer, S.: Design of experiments for nonlinear dynamic system identification. In: *IFAC 18th World Congress* (2011)
22. Nelles, O.: *Nonlinear System Identification: from Classical Approaches to Neural Networks and Fuzzy Models*. Springer (2001)
23. Braun, M.W., Rivera, D.E., Stenman, A., Foslien, W., Hrenya, C.: Multi-level pseudo-random signal design and ‘model-on-demand’ estimation applied to nonlinear identification of a RTP wafer reactor. In: *Proceedings of the 1999 American Control Conference* (Cat. No. 99CH36251), vol. 3, pp. 1573–1577 (1999)
24. Leontaritis, I.J., Billings, S.A.: Experimental design and identifiability for non-linear systems. *Int. J. Syst. Sci.* **18**(1), 189–202 (1987)
25. Yazid, E., Liew, M.S., Parman, S., Kurian, V.J.: Identification of transfer functions from surge motion response of a semisubmersible platform using time-varying NARX model. *Appl. Ocean Res.* **54**, 53–66 (2016)
26. Jacobs, W.R., et al.: Control-focused, nonlinear and time-varying modelling of dielectric elastomer actuators with frequency response analysis. *Smart Mater. Struct.* **24**, 055002 (2015)
27. Zhao, Y., Billings, S.A., Wei, H., He, F., Sarrigiannis, P.G.: A new NARX-based Granger linear and nonlinear casual influence detection method with applications to EEG data. *J. Neurosci. Meth.* **212**(1), 79–86 (2013)
28. Li, Z., Hayashibe, M., Fattal, C., Guiraud, D.: Muscle fatigue tracking with evoked EMG via recurrent neural network: toward personalized neuroprosthetics. *IEEE Comput. Intell. Mag.* **9**(2), 38–46 (2014)
29. Godfrey, K.: *Perturbation Signals For System Identification*. Prentice Hall (1993)
30. Braun, M., Rivera, D., Stenman, A.: Identification of a RTP wafer reactor multi-level pseudo-random signal design and ‘model-on-demand’ estimation applied to nonlinear identification of a RTP wafer reactor. *Am. Control Conf.* **1999**(3), 1573–1577 (1999)
31. Lara, J.M.V., Milani, B.E.A.: Identification of neutralization process using multi-level pseudo-random signals. In: *Proceedings of the 2003 American Control Conference*, vol. 5, pp. 3822–3827 (2003)
32. Deshpande, S., Rivera, D.E.: A data-centric system identification approach to input signal design for Hammerstein systems. In: *52nd IEEE Conference on Decision and Control*, pp. 5192–5197 (2013)
33. Jin, H., Chen, X., Wang, L., Yang, K., Wu, L.: Dual learning-based online ensemble regression approach for adaptive soft sensor modeling of nonlinear time-varying processes. *Chemom. Intell. Lab. Syst.* **151**, 228–244 (2016)
34. Barker, H.A., Godfrey, K.R., Tucker, A.J.: Nonlinear system identification with multilevel perturbation signals. *IFAC Proc.* **33**(15), 1175–1178 (2000)
35. Barker, H.A., Tan, A.H., Godfrey, K.R.: The performance of multilevel perturbation signals for nonlinear system identification. *IFAC Proc.* **36**(16), 663–668 (2003)
36. Braun, M.W., Ortiz-Mojica, R., Rivera, D.E.: Application of minimum crest factor multi-sinusoidal signals for ‘plant-friendly’ identification of nonlinear process systems. *Control Eng. Pract.* **10**(3), 301–313 (2002)
37. Choung, Y.J., Kang, J., Kim, S.B.: Process control of time-varying systems using parameter-less self-organizing maps. *J. Process Control* **52**, 45–56 (2017)
38. Ghasemi, M., Aghaei, J., Hadipour, M.: New self-organising hierarchical PSO with jumping time-varying acceleration coefficients. *Electron. Lett.* **53**(20), 1360–1362 (2017)
39. Lee, J.-Y., Jung, K., Hong, B., Cho, S.: Method of extended input/output linearization for the time-varying nonlinear system. In: *Future Information Technology*, pp. 37–46 (2014)

40. Lee, J.-S., Lee, J.-S.: The cluster algorithm for time-varying nonlinear system with a model uncertainty. In: *Advances in Parallel and Distributed Computing and Ubiquitous Services*, pp. 173–177 (2016)
41. Lee, Q., Ahmad, Z.: Development of model based decoupler for methanol water distillation column. In: *1st National Colloquium on Process Control Colloquium* (2013)
42. Muralidharan, G., Abraham, A., Pappa, N.: Estimation of variation in vapour liquid equilibrium constants for modeling a multicomponent crude distillation column. *IFAC-Papers OnLine* **49**(13), 199–204 (2016)
43. Yildirim, Ö., Kenig, E.Y.: Rate-based modelling and simulation of distillation columns with sandwich packings. *Chem. Eng. Process. Process Intensif.* **98**, 147–154 (2015)
44. Fernandez, M.F., et al.: Experiments and dynamic modeling of a reactive distillation column for the production of ethyl acetate by considering the heterogeneous catalyst pilot complexities. *Chem. Eng. Res. Des.* **91**(12), 2309–2322 (2013)
45. Liu, X., Zhou, Y., Cong, L., Ding, F.: High-purity control of internal thermally coupled distillation columns based on nonlinear wave model. *J. Process Control* **21**(6), 920–926 (2011)
46. Balasubramhanya, L.S., Doyle, F.J.: Nonlinear model-based control of a batch reactive distillation column. *J. Process Control* **10**, **2**(3), 209–218 (2000)
47. Kennedy, J., Eberhart, R.C.: A discrete binary version of the particle swarm algorithm. In: *1997 IEEE International Conference on Systems, Man, and Cybernetics. Computational Cybernetics and Simulation*, vol. 5, pp. 4104–4108 (1997)
48. Islam, M.J., Li, X., Mei, Y.: A time-varying transfer function for balancing the exploration and exploitation ability of a binary PSO. *Appl. Soft Comput.* **59**, 182–196 (2017)
49. Chih, M., Lin, C.-J., Chern, M.-S., Ou, T.-Y.: Particle swarm optimization with time-varying acceleration coefficients for the multidimensional knapsack problem. *Appl. Math. Model.* **38**(4), 1338–1350 (2014)
50. Mendes, E.M.A.M., Billings, S.A.: alternative solution to the model structure selection problem. *IEEE Trans. Syst. Man Cybern. Part A Syst. Hum.* **31**(6), 597–608 (2001)
51. Yassin, I.M.: *Nonlinear Auto-Regressive Model Structure Selection Using Binary Particle Swarm Optimization Algorithm*, Ph.D. Thesis, vol. 1, pp. 1–5 (2014)
52. Yassin, I., Taib, M., Adnan, R., Alam, S.: Extended analysis of bpsso structure selection of nonlinear auto-regressive model with exogenous inputs (NARX) of direct current motor. *Songklanakarinn J. Sci. Technol.* **36**(6), 683–699 (2014)
53. Kennedy, J., Eberhart, R.: Particle swarm optimization. In: *Proceedings of ICNN'95—International Conference on Neural Networks*, vol. 4, pp. 1942–1948 (1995)
54. Yassin, I.M., Taib, M.N., Adnan, R., Salleh, M.K.M., Hamzah, M.K.: Effect of swarm size parameter on Binary Particle Swarm optimization-based NARX structure selection. In: *2012 IEEE Symposium on Industrial Electronics and Applications*, pp. 219–223 (2012)

Adaptive Fuzzy-PID Controller for Quad-Rotor MAV with Mass Changes



Goh Ming Qian, Dwi Pebrianti, Luhur Bayuaji, Rosdiyana Samad, Mahfuzah Mustafa and Mohammad Syafrullah

Abstract Micro Aerial Vehicle (MAV) has become famous to be used in agricultural application such as for spraying operation, for watering plantation or spraying the pesticide, 2-D flow visualization image to measure the droplet distribution and so on. Due to the need to sustain food for all human population, there is need for the development of effective spraying to increase the productivity. In crop spraying, the payload changes against time is the big challenge on the development of MAV. This is because the payload change problem could affect the altitude which is the position along z-axis of the MAV. In this research, a quad-rotor MAV is used as the platform. Then, an adaptive Fuzzy-PID controller for the altitude control by considering payload change is presented. The performance of altitude control by using adaptive Fuzzy-PID controller and PID controller are validated in this research study through simulation. The adaptive Fuzzy-PID controller is successfully designed for the changing of payload. The result shows the performance of adaptive Fuzzy-PID controller is better than PID controller on quad-rotor MAV control considering payload changes.

Keywords Adaptive Fuzzy-PID controller · Quad-rotor MAV · Payload change

G. M. Qian · D. Pebrianti (✉) · R. Samad · M. Mustafa
Faculty of Electrical & Electronics Engineering, Universiti Malaysia Pahang, Campus Pekan,
Pekan 26600, Pahang, Malaysia
e-mail: dwipebrianti@ump.edu.my

G. M. Qian
e-mail: gohmingqian@gmail.com

L. Bayuaji
Faculty of Computer Science and Software Engineering, Universiti Malaysia Pahang, Pekan,
Malaysia

D. Pebrianti · L. Bayuaji · M. Syafrullah
Magister of Computer Science, University Budi Luhur, Jakarta, Indonesia

© Springer Nature Singapore Pte Ltd. 2019
Z. Md Zain et al. (eds.), *Proceedings of the 10th National Technical Seminar on Underwater System Technology 2018*, Lecture Notes in Electrical Engineering 538,
https://doi.org/10.1007/978-981-13-3708-6_22

1 Introduction

Recently, the viability of UAVs as a multipurpose research vehicle have been widely used in many practical applications such as military, rescue operation, photographing, payload carrier, agricultural and transportation [1]. The common types of UAVs are fixed-wing, rotary-wing UAVs that includes helicopters and quad-rotor MAV [2]. Fixed-wing UAVs can fly at high speed and efficient in long distance travelling compared to rotary-wing UAVs. However, it requires a long runway take-off and landing [3]. The rotary-wing UAVs has advantages which are high maneuverability, vertical take-off and landing (VTOL) and hovering [4]. By comparing the maintenance cost and system design of rotary wing UAV, quad-rotor MAV has a simple design and low maintenance cost. Therefore, quad-rotor MAV as shown in Fig. 1 is chosen in this research because the size and safety is most practical for experimental testing.

The major challenge is the design in flight controller due to the non-linearity associated with the mathematical model system included in quad-rotor MAV [5]. Therefore, many researchers have been more interested in developing new controllers from linear to non-linear for quad-rotor MAV to enhance its performance under many different conditions such as wind disturbances and mass disturbance. Among the controllers, Proportional-Integral-Derivative (PID) controller is mostly used in practical industry to achieve task. In [6], a waypoint navigation of quad-rotor MAV by using PID controller is proposed. The performance of real flight experiment by using PID controller is satisfied in term of overshoot percentage (%OS) which are for x position is 13%, y position is 11.89% and altitude z is 2.34%. However, PID is a fixed gain algorithm that is unadaptable to the physical changes.

By considering the problem of unadaptable to the physical changes, many researchers solved this physical change by using non-linear controller or a combination of two or more algorithms from linear and non-linear controllers, that is commonly known as hybrid controller. In paper [7], Huseyin Demircioglu et al. proposed an adaptive controller for the attitude and altitude control of quadrotor

Fig. 1 Quad-rotor MAV



considers unknown wind disturbances. The stability of the designed adaptive controller in a windy environment is proved by the equilibrium of closed loop error system. Besides, Qian et al. [8] proposed Fuzzy-PID controller for controlling the position of quad-rotor MAV to complete waypoint-navigation. Hence, we proposed an adaptive Fuzzy-PID controller on quad-rotor MAV considers payload change for controlling altitude, z position in this paper.

The organization of this paper is described as follows, the modelling of quad-rotor MAV is presented in Sect. 2. Section 3 clarifies the development of adaptive Fuzzy-PID controller considers payload changes on the quad-rotor MAV. The validation of simulation results between PID controller and adaptive Fuzzy-PID controller for altitude z control is discussed in Sect. 4. Finally, Sect. 5 provides conclusion and future works.

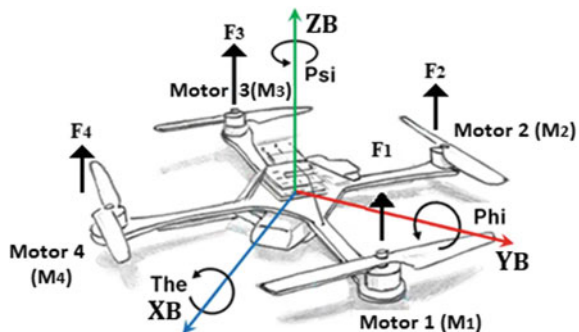
2 Modelling of Quad-Rotor MAV

The force of rotor and torque, gyroscopic effect and aerodynamic forces and moments are considered in quad-rotor MAV modelling. The modelling of quad-rotor MAV system is developed based on [8]. Figure 2 shows full design of ‘X’ configuration quad-rotor MAV. The body axis of quad-rotor MAV is related to the inertia frame and alter its position setting by incorporating rotational motions roll (θ), pitch (ϕ) and yaw (φ) and translation motion are x , y and z position as shown in Fig. 3 [9].

The total forces of the quad-rotor MAV are presented in Eq. 1 while the rotation matrix of quad-rotor MAV as shown in Eq. 2 where C , S are cosine and sine function, respectively. The general translation motion is presented in Eq. 3 where \ddot{x} , \ddot{y} , \ddot{z} are linear acceleration of quad-rotor MAV in each axis.

$$F_{total} = \sum_{i=1}^4 F_i \tag{1}$$

Fig. 2 An ‘X’ configuration of quad-rotor MAV



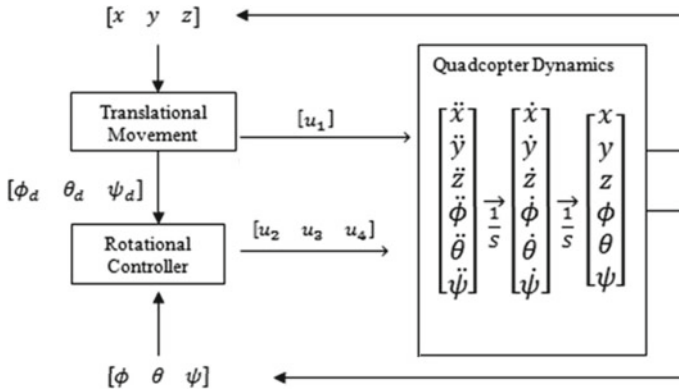


Fig. 3 The system of quad-rotor MAV

$$R = \begin{bmatrix} C\theta C\phi & C\theta S\phi S\varphi - C\varphi S\theta & S\theta S\phi S\varphi + C\theta C\varphi S\phi \\ C\phi S\theta & C\theta C\varphi + S\theta S\phi S\varphi & C\varphi S\theta C\phi - C\theta S\varphi \\ -S\phi & C\phi S\varphi & C\phi C\varphi \end{bmatrix} \tag{2}$$

$$m \begin{bmatrix} \ddot{x} \\ \ddot{y} \\ \ddot{z} \end{bmatrix} = R \begin{bmatrix} 0 \\ 0 \\ F_{total} \end{bmatrix} - \begin{bmatrix} 0 \\ 0 \\ mg \end{bmatrix} \tag{3}$$

The translation motion on x , y and z position is presented in Eqs. 4, 5 and 6 based on substitution of Eqs. 1 and 2 into Eq. 3.

$$m\ddot{x} = (\sin\theta \sin\varphi + \sin\phi \cos\theta \cos\varphi)U_1 \tag{4}$$

$$m\ddot{y} = (\sin\phi \cos\theta \sin\varphi - \sin\theta \cos\varphi)U_1 \tag{5}$$

$$m\ddot{z} = mg - (\cos\theta \cos\phi)U_1 \tag{6}$$

where mg is the total weight force of the quad-rotor MAV. U_1 is the total force to control input. θ , ϕ and yaw φ are roll, pitch and yaw, respectively.

The dynamic equations are summarized in equation are summarized in equation as follows:

$$\ddot{x} = \frac{(S\phi S\varphi + C\phi C\varphi S\theta)U_1}{m} \tag{7}$$

$$\ddot{y} = \frac{(S\varphi S\phi C\theta - S\phi C\varphi)U_1}{m} \tag{8}$$

$$\ddot{z} = g - \frac{(C\theta S\varphi)U_1}{m} \tag{9}$$

The mass of quad-rotor MAV is variable due to weight variation of payload. The equation of total mass of quad-rotor MAV is in Eq. 10.

$$\dot{m} = M_Q + M_P - \delta t \tag{10}$$

where \dot{m} represents rate of total mass of quad-rotor MAV that include mass of payload. M_Q and M_P denotes mass of quad-rotor MAV and mass of payload, respectively. While δ represents rate of liquid flow, $0 < \delta < M_P$ and t represents time.

3 Controller Development

The main function of the controller is to reduce a specific error and known as a device or logical unit used to adjust the output value compared with a reference value. This paper focuses on comparison of PID control and Fuzzy-PID control algorithm by considering payload changes that will be implemented on altitude, z position.

3.1 Proportional-Integral-Derivative (PID) Controller

PID controller has three gains which are proportional gain K_p , integral gain K_i and derivative gain K_d . Based on the method of Ziegler-Nichols [10], the parameters of PID gains are calculated to correct the response of system. The equation of a PID controller is shown in Eq. 11.

$$U(t) = K_p e(t) + K_i \int_0^t e(t) dt + K_d \frac{d}{dt} e(t) \tag{11}$$

The PID controller of altitude z that has been tuned with optimum gains is shown in Table 1 [6].

3.2 Adaptive Fuzzy-PID Controller

Figure 4 shows the block diagram of adaptive Fuzzy-PID overall system controller considers payload change where desire input of x, y, z, θ and ϕ are represented by

Table 1 Parameters tuned by using PID controller

Parameter	Gain		
	K_p	K_i	K_d
Altitude z	-2.625	-0.153	-9.996

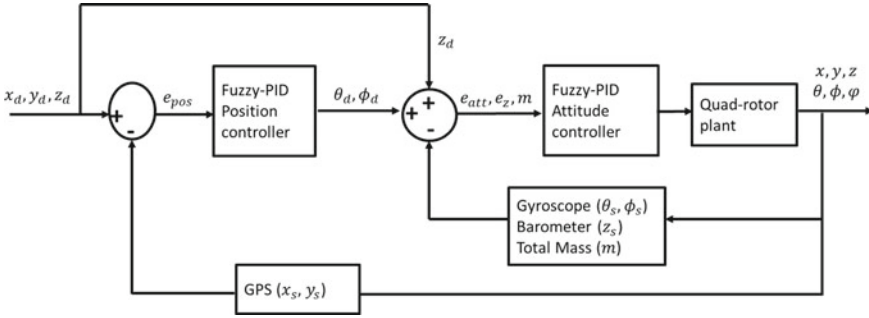


Fig. 4 The block diagram of adaptive Fuzzy-PID overall system controller considers payload change

x_d, y_d, z_d, θ_d and ϕ_d , respectively. Meanwhile state input of x, y, z, θ and ϕ are represented by x_s, y_s, z_s, θ_s and ϕ_s , respectively. e_{pos}, e_{att} and e_z represent the error of position, attitude and altitude control, respectively. While m is the total mass of quad-rotor MAV that includes the mass of payload. x, y, z, θ, ϕ and φ represent the output of quad-rotor MAV. The block diagram of adaptive Fuzzy-PID for altitude z control by considering payload changes is shown in Fig. 5.

The adaptive Fuzzy-PID controller is designed to overcome the problem of payload change in real time. Here, the Fuzzy controller is adjusting the gains of PID (K_p, K_i, K_d) according to the total mass (m), error of z (e_z) and rate of error (\dot{e}_z) by evaluating the feedback from GPS sensor, barometer and gyroscope and the reference of position and attitude given by the user. Additionally, the gains of PID are calculated based on centroid algorithm [11] as shown in Eqs. 12, 13 and 14.

$$K_p = K_{p_{min}} + (K_{p_{max}} - K_{p_{min}}) \times \alpha \tag{12}$$

$$K_i = \frac{K_p^2}{K_d \times \gamma} \tag{13}$$

$$K_d = K_{d_{min}} + (K_{d_{max}} - K_{d_{min}}) \times \beta \tag{14}$$

where K_p, K_i and K_d denote the gain of proportional, integral and derivative, respectively. $K_{p_{min}}$ and $K_{d_{min}}$ denote the minimum gain of proportional, integral and derivative, respectively. Meanwhile $K_{p_{max}}$ and $K_{d_{max}}$ denote the maximum gain of pro-

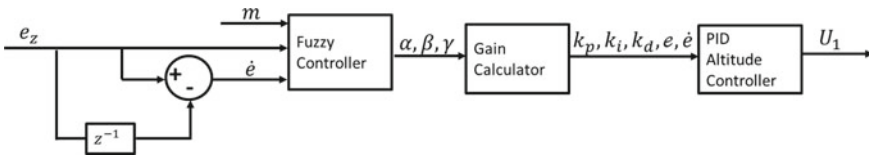


Fig. 5 The block diagram of adaptive Fuzzy-PID for altitude z control considers payload change

Table 2 The minimum and maximum for proportional and derivative gain of altitude, z position

Parameters	Gain			
	K_p		K_d	
	Min	Max	Min	Max
Altitude z	-3.625	-1.625	-10.996	-8.996

Table 3 a Fuzzy Rules for alpha (α) with small mass b Fuzzy Rules for alpha (α) with big mass

(a) Mass = small	(b) Mass = big

\dot{e} e	N	P
N	B1	S2
P	S2	B1

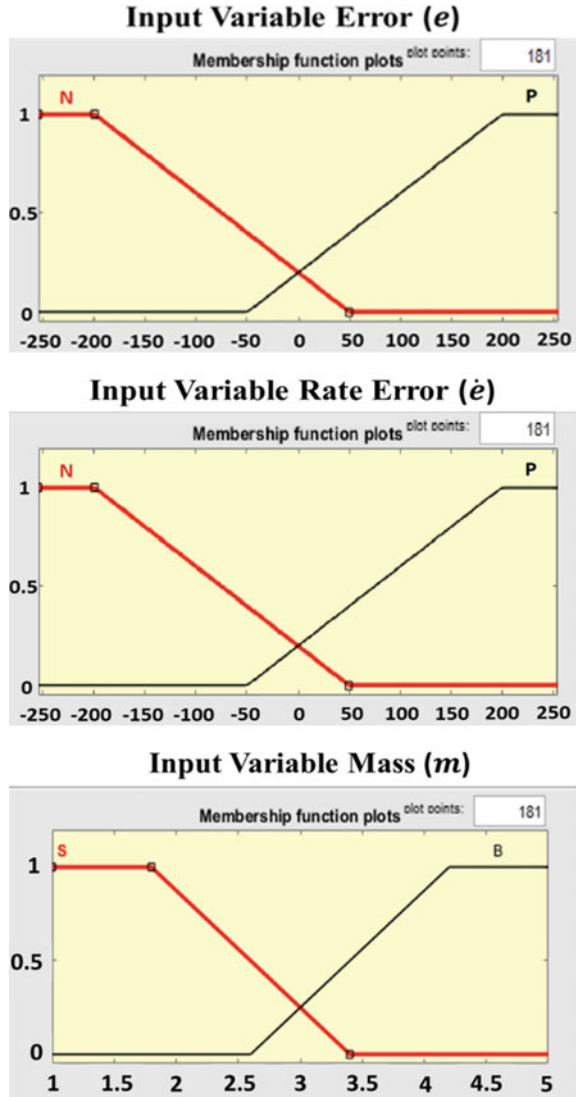
\dot{e} e	N	P
N	B2	S1
P	S1	B2

portional, integral and derivative, respectively. α , β and γ represent alpha, beta and gamma, respectively.

Table 2 represents the minimum and maximum for proportional and derivative gain of altitude, z position. The minimum and maximum proportional gain value of altitude, z position is assumed based on the deviation range/tolerance of ± 1 from the obtained proportional gain, -2.625. While the minimum and maximum derivative gain value of altitude z is assumed based on the deviation range of ± 1 from the obtained derivative gain, -9.996.

The method of Fuzzy controller used in the system is Mamdani method with Min-Max operation to conduct the combination of fuzzy logic system. The Fuzzy Logic controller consists of three inputs which are error (e), error of rate (\dot{e}) and mass (m) while three outputs are alpha (α), beta (β) and gamma (γ). The input of error (e), rate error (\dot{e}) and mass (m) are trapezoidal membership function with two variable fuzzy sets as shown in Fig. 6, respectively where N and P denote Negative and Positive within the range of -255 to 255 while S and B represent Small and Big within the range of 1-5. Figure 7 shows the output of alpha (α), beta (β) and gamma (γ). The output of alpha (α) and gamma (γ) use trapezoidal membership function with four variable fuzzy sets where S2, S1, B1, B2 represent small 2, small 1, Big 1 and Big 2, respectively and the range is between 0 and 255. Meanwhile the output of beta (β) uses three variable fuzzy sets with trapezoidal and triangle membership function where NM, NS and Z represent Negative Medium, Negative Small and Zero, respectively in range of 40-160. There are 8 rules used in Fuzzy Inference System (FIS) based on [12] for alpha (α), beta (β) and gamma (γ) which are represented in Tables 3, 4 and 5.

Fig. 6 The input membership function of error (e), rate error (\dot{e}) and mass (m)

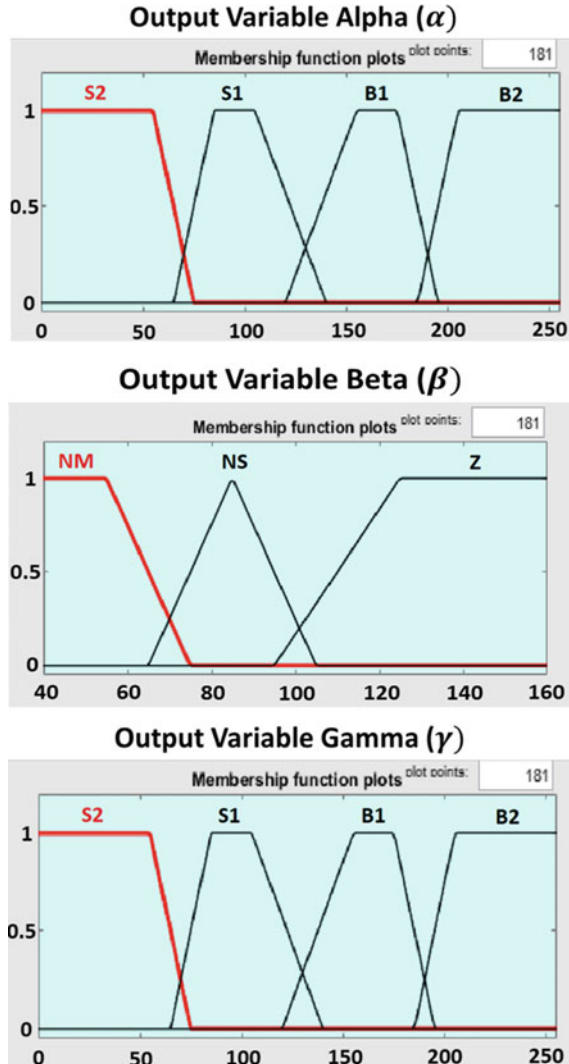


4 Discussion and Results

In this section, the performance results of the proposed adaptive Fuzzy-PID controller is compared with PID controller for controlling the altitude z by considers payload changes. Table 6 shows the desired altitude z which is set at 7meters of height against time from 20 s until 100 s.

The rate of change of payload is illustrated in Fig. 8. The total weight of the quad-rotor MAV is started at 2 kg where the weight of quad-rotor MAV is 1 kg and the

Fig. 7 The output membership function of alpha (α), beta (β) and gamma (γ)



weight of payload is 1 kg. Then, the mass of payload starts to change after 30 s when the quad-rotor MAV is ready to start the spraying operation. The rate of change is 0.1 kg/s. Therefore, after 10 s, the liquid-base substance is fully sprayed out and the container is empty, where the remaining 1 kg is the weight of the quad-rotor MAV itself.

Figure 9 shows the performance of altitude z control using adaptive Fuzzy-PID controller by considering payloads changes and the detail of adaptive Fuzzy-PID during spraying operation showed within 30–40 s. The performance of altitude z control using PID controller considers payload is shown in Fig. 10 and the detail of

Table 4 a Fuzzy rules for beta (β) with small mass b Fuzzy Rules for beta (β) with big mass

(a) Mass = small			(b) Mass = big		
$e \backslash \dot{e}$	N	P	$e \backslash \dot{e}$	N	P
N	NM	NS	N	NM	NS
P	Z	Z	P	Z	Z

Table 5 a Fuzzy rules for gamma (γ) with small mass b Fuzzy rules for gamma (γ) with big mass

(a) Mass = small			(b) Mass = big		
$e \backslash \dot{e}$	N	P	$e \backslash \dot{e}$	N	P
N	B1	S2	N	B2	S1
P	S2	B1	P	S1	B2

Table 6 Desired altitude z

Time	0	10	20	30	40	50	60	70	80	90	100
Altitude z (m)	0	0	7	7	7	7	7	7	0	0	0

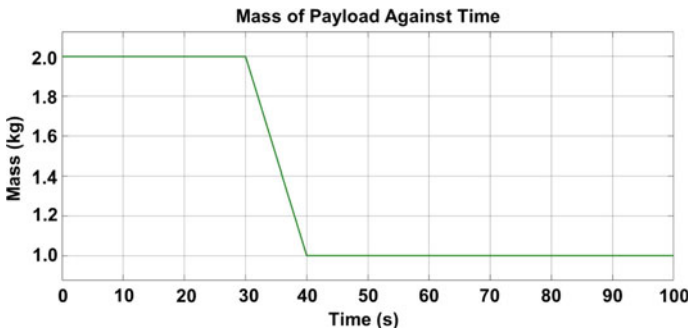


Fig. 8 The result of payload changes against time

PID controller during spraying operation within 30–40 s. The dot line is desired of altitude, z position while the dash line is actual value of altitude, z position.

Table 7 shows the performance of adaptive Fuzzy-PID controller and PID controller in terms of overshoot percentage (%OS), settling time (T_s) and rise time (T_r) and steady-state error (e_{ss}) by considering payload change.

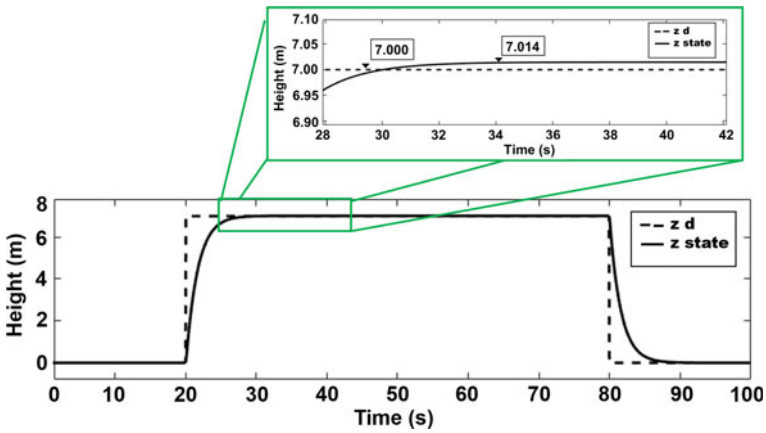


Fig. 9 The performance of altitude z control using adaptive Fuzzy-PID controller with payload change

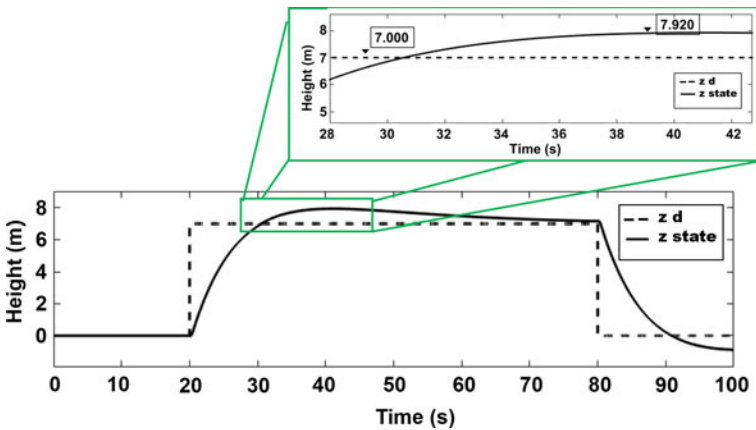


Fig. 10 The performance of altitude z control using PID controller with payload change

Based on Table 7, the performance is acceptable since the percentage overshoot ($\%OS$) of altitude z in adaptive Fuzzy-PID controller is 0% while the percentage overshoot ($\%OS$) in PID controller is 13.14%. The rise time of adaptive Fuzzy-PID controller is 3.77 s but PID controller required 8.26 s for the rise time. The PID controller requires more time about 60 s compared with adaptive Fuzzy-PID controller that needs only 14.10 s to achieve steady-state. The steady-state error of PID controllers is 2.16% at 60 s after input signal. While the steady-state error of adaptive Fuzzy-PID controller is 0.2%.

Table 7 The output responses of altitude z control between PID and adaptive Fuzzy-PID controller with payload change

Responses	Adaptive Fuzzy-PID	PID
%OS	0	13.14
T_s (s)	14.10	14.10
T_r (s)	3.77	8.26
e_{ss} (%)	0.20	2.16 ^a

^aat 60 s after input signal

5 Conclusion and Future Work

As conclusion, the proposed adaptive Fuzzy-PID controller is successfully adapted the changes of quad-rotor MAV weight. The performance is compared with conventional PID and the results shows that adaptive Fuzzy-PID can produce more responsive output than PID in all range of payload change from 2 to 1 kg. Here, the overshoot, settling time, rise time and steady error obtained from Fuzzy-PID for altitude z are 0%, 14.10 s, 3.77 s and 0.2%, respectively. On the other hand, the output responses of PID is less responsive because the overshoot, settling time, rise time and steady error obtained for altitude z are 13.14%, more 60 s, 8.26 s and 2.16% at 60 s after input signal, respectively. Therefore, adaptive Fuzzy-PID controller is performing better than PID controller on quad-rotor MAV control consider payload change.

In the future, the adaptive Fuzzy-PID controller will be implemented on quad-rotor MAV hardware and experiment will be carried out based on the quad-rotor MAV hardware. The experiment will be conducted for both adaptive Fuzzy-PID controller and PID controller and the performance will be evaluated.

Acknowledgements This work is supported by Universiti Malaysia Pahang (UMP), under Universiti Malaysia Pahang Research Grant RDU 170378.

References

1. Al-Younes, Y.M., Al-Jarrah, M.A., Jhemi, A.A.: Linear versus nonlinear control techniques for a quadrotor vehicle. In: Mechatronics and its Applications (ISMA), 2010 7th International Symposium, pp. 1–10 (2010)
2. Budiyo, A.: Advances in unmanned aerial vehicles technologies. Chinese Sci. Bull. **52**(1), 1–13 (2007)
3. Ni, J., Yao, L., Zhang, J., Cao, W., Zhu, Y., Tai, X.: Development of an unmanned aerial vehicle-borne crop-growth monitoring system. Sensors (Switzerland) **17**(3) (2017)
4. Zou, Y., Huo, W.: Nonlinear robust controller for miniature helicopters without singularity. IEEE Trans. Aerosp. Electron. Syst. **53**(3), 1402–1411 (2017)

5. Li, L., Sun, L., Jin, J.: Survey of advances in control algorithms of quadrotor unmanned aerial vehicle. In: International Conference on Communication Technology Proceedings, pp. 107–111 (2016)
6. Qian, G.M., Pebrianti, D., Chun, Y.W., Hao, Y.H., Bayuaji, L.: Waypoint navigation of quadrotor MAV. In: 2017 7th IEEE International Conference on System Engineering and Technology (ICSET), pp. 38–42 (2017)
7. Demircioglu, H., Basturk, H.I.: Adaptive attitude and altitude control of a quadrotor despite unknown wind disturbances. In: 2017 IEEE 56th Annual Conference on Decision and Control, pp. 274–279(2018)
8. G.M. Qian et al.: Waypoint navigation of quad-rotor MAV using Fuzzy-PID control. In: Lecture Notes in Mechanical Engineering, pp. 271–284 (2018)
9. Bouabdallah, S.: Design and control of quadrotors with application to autonomous flying. *École Polytech. Fédérale Lausanne, À La Fac. Des Sci. Tech. L'Ingénieur* **3727(3727)**, 61 (2007)
10. Ziegler, J.G., Nichols, N.B.: Optimum settings for automatic controllers. *InTech* **42(6)**, 94–100 (1995)
11. Fahmizal, Surriani, A., Budiyanto, M., Arrofiq, M.: Altitude control of quadrotor using fuzzy self tuning PID controller. In: 2017 5th International Conference on Instrumentation, Control, and Automation (ICA), pp. 67–72 (2017)
12. Mehranpour, M.R., Mohammad Shahri, A., Emamgholi, O., Farrokhi, M.: A new fuzzy adaptive control for a quadrotor flying robot. In: 2013 13th Iranian Conference Fuzzy Systems, pp. 1–5 (2013)

Investigating State Covariance Properties During Finite Escape Time in H_∞ Filter SLAM



Hamzah Ahmad, Nur Aqilah Othman, Mawardi Saari
and Mohd Syakirin Ramli

Abstract This paper deals with the investigation of finite escape time problem in H_∞ Filter based localization and mapping. Finite escape time in H_∞ Filter has restricted the technique to be applied as the mobile robot cannot determine its location effectively due to inconsistent information. Therefore, an analysis to improved the current H_∞ Filter is proposed to investigate the state covariance behavior during mobile robot estimation. Three main factors are being considered in this research namely the initial state covariance, the γ values and the type of noises. This paper also proposed a modified H_∞ Filter to reduce the finite escape time problem in the estimation. The analysis and simulation results determine that the modified H_∞ Filter has better performance compared to the normal H_∞ Filter as well as to Kalman Filter for different γ , initial state covariance and works well in non-gaussian noise environment.

Keywords H_∞ filter · Finite escape time · Estimation

1 Introduction

Mobile robot has been one of the technologies to make human life comfortable and safe. Its applications covers various industries, explorations, mining and military to achieve a particular task. Even now, the job of cleaning the house can be performed by an autonomous mobile robot as a vacuum cleaner or lawn mower. These technologies requires a study of mobile robot kinematics, dynamical system, behavioural based decisions and some other aspects to be considered prior to the mobile robot design and applications.

To operate a mobile robot in a remote area with less human monitoring system is a challenging task which includes various factors to be considered. To list a few of it are such as the environment conditions, sensory devices, communications sys-

H. Ahmad (✉) · N. A. Othman · M. Saari · M. S. Ramli
Faculty of Electrical & Electronics Engineering, University Malaysia Pahang, Pekan, Pahang,
Malaysia
e-mail: hamzah@ump.edu.my

© Springer Nature Singapore Pte Ltd. 2019
Z. Md Zain et al. (eds.), *Proceedings of the 10th National Technical Seminar on Underwater System Technology 2018*, Lecture Notes in Electrical Engineering 538,
https://doi.org/10.1007/978-981-13-3708-6_23

271

tem, intelligent system and a suitable mobile robot design. Generally, these issues requires a truly autonomous mobile robot to perform the operations which is capable to identify its location and any related decisions respectively to the surroundings. This condition is known as localization and mapping where mobile robot needs to localize itself concurrently with the construction of environment. The problem is also alternatively known as Simultaneous Localization and Mapping (SLAM) since it was presented earlier two decades before after a series of conferences [1, 2].

One of the conventional way to perform SLAM is by calculating the kinematic model accurately by taking into account the measurement by the mobile robot sensors [3–6]. By doing this, the mobile robot is able to define its location at each time by referring to a global coordinate system. Another reliable method to achieve the whole task is by utilizing a probabilistics method to infer the situations of the environment during mobile robot observations such as Extended Kalman Filter [7, 8], Unscented Kalman Filter [9] and FastSLAM [10]. This approach has gain a lot of attentions due to only certain information are necessary prior to the developed system.

Kalman Filter as one of the celebrated techniques in probabilistic approach has been successfully applied in real applications that covers manufacturing industries, military and even in household appliances. Even more accurate estimation results can be achieved if particle filter is chosen which works effectively in unknown noise condition. Unfortunately, Kalman Filter is facing problem in non-gaussian noise and particle filter at the time being has higher computational cost. Besides, particle filter is still incapable to be operated online which eventually makes its appearance still under development stages. Hence, analyzing a technique that proven to work, more robust than Kalman Filter and has less computational cost as well as complexity is the main objective to be pursued of this paper. Therefore, H_∞ Filter is selected for analysis purposes to recognize its capability and efficiency in estimation. There has been a lot of reports applying the techniques in various application in biology, power system and mobile robot [11–15].

Some works on H_∞ Filter based localization and mapping have been studied regarding its capability and conditions [16–18]. This paper attempts to discuss and analyze on the finite escape time in H_∞ Filter during mobile robot observation. The problem has makes the estimation becomes inconsistency due to the state covariance can be unexpectedly infinite in both positive and negative directions. Remark that the state covariance defines the information of the uncertainties at a particular time during measurements. Hence even best estimation results can be obtained, the robot do not has confidence on it.

The rest of the paper is organized as follow. Section 2 describes the system modeling that includes the H_∞ Filter technique. This is followed by Sect. 3 which explains the analysis of finite escape time and then Sect. 4 for some preliminary simulation results. Finally, Sect. 5 concludes the paper.

2 Mathematical Modelling of the Proposed System

In analyzing the behavior of mobile robot in localization and mapping, there are two general models to be applied i.e. the kinematic and measurement models. These two models defines the kinematics motions and the information of environment measured by sensors during observations respectively.

The process model is defined as

$$X_k = f_k(X_{k-1}, u_{k-1}, \omega_{k-1}) \quad (1)$$

where X_k is the augmented state containing the mobile robot states (θ, x_r, y_r) and identified landmarks (x_{m_i}, y_{m_i}) . u_k, ω_k are the control input and its associated control noise.

The measurement process holds the following condition.

$$y_k = \begin{bmatrix} r_i \\ \phi_i \end{bmatrix} = H_k X_{k-1} + v_k \quad (2)$$

where r_i, ϕ_i defines the measured relative distance and angle between mobile robot and any observed landmarks. H_k is the measurement matrix and v_k acts as the measurement noise.

Similar to Kalman Filter, H_∞ Filter has both predict and update stages. The predicted stage becomes

$$X_k^- = f_{k-1} X_{k-1} \quad (3)$$

$$P_k^- = f_{k-1} P_{k-1} f_{k-1}^T + Q_k \quad (4)$$

where Q_k is the process noise covariance. The updated stage on the other hand has the following results.

$$X_k^+ = X_{k-1} + K (y_{k-1} - H_k X_{k-1}) \quad (5)$$

$$P_k^+ = f_{k-1} P_k^- (I - \gamma^{-2} P_k^- + H_{k-1}^T R_{k-1}^{-1} H_{k-1} P_k^-)^{-1} f_{k-1}^T \quad (6)$$

where $K = P_k^- H_{k-1}^T (H_{k-1} P_k^- H_{k-1}^T + R_{k-1})^{-1}$. R_k is the measurement noise covariance. Note that the measurement and process noise covariances are uncorrelated. The H_∞ Filter attempts to minimize the error based on these information.

3 Finite Escape Time Analysis and Discussion

It is important to understand why finite escape time occurred in H_∞ Filter but not in Kalman Filter even though they are classified in one family. Through the observations of differences between those two techniques, it can be recognized that the updated

Table 1 Kalman Filter and H_∞ Filter differences

Technique	Gain	State covariance
Kalman Filter	$K = P(I + H^T R^{-1} H P)^{-1}$	$P = f P(I + H^T R^{-1} H P)^{-1} f^T + Q$
H_∞ Filter	$K = P(I - \gamma^{-2} H^T R^{-1} H P)^{-1}$	$P = f P(I - \gamma^{-2} P + H^T R^{-1} H P)^{-1} f^T + Q$

state covariance for H_∞ Filter is modified to include γ as a tuning parameters to obtain better estimation results. Table 1 describes the differences between H_∞ Filter and Kalman Filter.

As been presented in Table 1, it can be noticed that there is an existence of $\gamma^{-2}P$ in H_∞ Filter compared to Kalman Filter. This implies that, this parameter contributes the reason why finite escape time appear in H_∞ Filter. Further analysis based on $\gamma^{-2}P$ is required to identify why this is happening with consideration to the associated parameters in the state covariance. Let

$$\psi = I - \gamma^{-2}P + H^T R^{-1} H P \tag{7}$$

Based on Eq. 7 without the $\gamma^{-2}P$, the equation is guaranteed to hold a positive semidefinite matrix as demonstrated by Huang et al. [7]. Therefore, further analysis on this matter is needed. ψ can produce a negative definite or negative semidefinite matrix that depends on the selection on the tuning parameter, γ . Before going further, each of the component in above equation is examined.

Note that, if $\psi \rightarrow 0$, then the equation simply becomes KF equation and guaranteed to be converged. In H_∞ Filter, the noises are assumed to be bounded [12] and therefore the measurement noise covariance is priori known. The remaining variables are the measurement matrix with the state covariance. The measurement matrix depends heavily on the information of relative angle and distance measurements. It contains particular information at a specific measurement time. The nearer the objects to the mobile robot, then the smaller value the measurement matrix exhibits to the system. To demonstrate this, the following situation is shown.

At time k, the measurement matrix pose the following information.

$$H_k = \begin{bmatrix} 0 & -\frac{dx}{r} & -\frac{dy}{r} & \frac{dx}{r} & \frac{dy}{r} \\ -1 & \frac{dx}{r^2} & \frac{dy}{r^2} & \frac{dx}{-r^2} & \frac{dy}{r^2} \end{bmatrix} = \begin{bmatrix} -a & -l & l \end{bmatrix} \tag{8}$$

where $l = \begin{bmatrix} \frac{dx}{r} & \frac{dy}{r} \\ \frac{dx}{-r^2} & \frac{dy}{r^2} \end{bmatrix}$ $dx = x_m - x_r, dy = y_m - y_r, r = \sqrt{dx^2 + dy^2}$.

Consider a case of a linear and stationary monobot observing a landmark A. From the measurement matrix in Eqs. (2) and (8), $H^T R^{-1} H P$ produced a very small amount of information such that it is smaller than 1 i.e. the identity matrix such that $I \gg H^T R^{-1} H P$. Assume also that the noise covariance is so small such that

Table 2 Updated state covariance with different γ for stationary monobot case

Updated state covariance	P_1	P_2	P_3	P_4	P_5
$\gamma = 2$	1.333	1.500	1.600	1.667	1.714
$\gamma = 3$	1.125	1.143	1.145	1.146	1.146
$\gamma = 4$	1.067	1.071	1.071	1.072	1.072
$\gamma = 5$	1.042	1.043	1.044	1.044	1.044

it can be neglected since the mobile robot is stationary. Remark that without the existence of γ , the equation is similar to KF. In this condition, the remaining parts to be assessed is $I - \gamma^{-2}P$. Select and compare the case of having $\gamma = 0.02, 1.2$ and initial state covariance $P = 1$ for instance. Then the following are obtained.

$$\psi_1 \approx I - 0.02^{-2}(1) = -2499$$

$$\psi_1^{-1} = -4 \times 10^{-4}$$

At time $k = 1[s]$, the system has exhibit a negative definite matrix from 1 to -4×10^{-4} . From Eq. (6) and following the filter algorithm, the updated state covariance applies this value for next measurement step.

$$\psi_2 \approx I - [0.02^{-2}(-4 \times 10^{-4})] = 2$$

$$\psi_1^{-1} = 0.5$$

Interestingly at $k = 2[s]$, the state covariance is now producing a positive value. This is actually a case of finite escape time where the state covariance drastically changed from negative to positive. The value will be more significant if the initial state covariance is set to be higher such as 100 or 10,000 where the value of ψ becomes infinite.

Now lets move to consider a case when $\gamma = 1.2$.

$$\psi_1 \approx I - 1.2^{-2}(1) = 0.31$$

$$\psi_1^{-1} = 3.273$$

The updated state covariance for next measurement yields

$$\psi_2 \approx I - 1.2^{-2}(3.273) = -1.273$$

$$\psi_1^{-1} = -0.786$$

Again, the finite escape time occurs but in opposite way if compared to the first case of $\gamma = 0.02$. Using similar calculation for different γ provides the following characteristics of ψ shown in Table 2.

Looking on the updated state covariance, the results are now more promising and do not exhibit finite escape time at all from $k = 1-5[s]$. Therefore the findings also suggest that designer must choose γ with respect to the initial condition of state covariance as well as the noise covariance even though their existence was not demonstrated in the explanations above. In fact, the result of updated state covariance shows consistency and agrees with preceding research [Huang et al.] and conforms that the updated state covariance converge to its initial conditions i.e. 1.

Now, refer to Eq. 7 on the right side of the variable focusing on the $H^T R^{-1} H P$. For simplicity without loss of general information of the states, assume the robot starts at initial position with the initial state covariance and measurement noise covariance are both 1. This will simply yields

$$\begin{aligned}
 H^T R^{-1} H P &= H^T H = \begin{bmatrix} -a & -l & l \end{bmatrix}^T \begin{bmatrix} -a & -l & l \end{bmatrix} \\
 &= \begin{bmatrix} a^2 & * & * \\ * & l^2 & * \\ * & * & l^2 \end{bmatrix} \geq 0
 \end{aligned}
 \tag{9}$$

Based on Schur complement, the above result can be defined as a positive semidefinite matrix. As a results, to guarantee a positive semidefinite matrix and producing reliable estimation, Eq. 7 must also exhibits a positive semidefinite matrix at all time [Huang et al.]. Hence this equation needs further analysis. Remember that ψ in Eq. 7 plays an important role for efficient estimation. In the equation, the selection of γ can guarantee a positive semidefinite matrix and can also produce a negative definite or negative semidefinite matrix. One more thing to realize is that based on Eq. (9), $I + H^T R^{-1} H P \geq 0$ can be simply understood.

Suppose that $\gamma, P > 0$ and $\gamma, P \in 0$. For any value of γ, P , the following can be derived.

$$\psi = \begin{cases} \psi & \text{for } \psi \geq 0 \\ -\psi & \text{for } \psi < 0 \end{cases}
 \tag{10}$$

Based on above definition, the following theorem explains the condition of the state covariance in specified situation.

Theorem 1 Assume that $\gamma, P > 0$ and $\gamma, P \in R$. Then $|I - \gamma^{-2} P + H^T R^{-1} H P| \leq |I - \gamma^{-2} P| + |H^T R^{-1} H P|$.

Proof It is known that I is positive definite matrix at all time. Assume that $I - \gamma^{-2} P < 0$ such that $|I - \gamma^{-2} P| = -(I - \gamma^{-2} P)$

i. if $I - \gamma^{-2} P + H^T R^{-1} H P \geq 0$, then

$$\begin{aligned}
 |I - \gamma^{-2} P + H^T R^{-1} H P| &= I - \gamma^{-2} P + H^T R^{-1} H P \\
 &\leq -(I - \gamma^{-2} P) + H^T R^{-1} H P
 \end{aligned}$$

$$= |I - \gamma^{-2}P| + |H^T R^{-1}HP|$$

ii. if $I - \gamma^{-2}P + H^T R^{-1}HP < 0$, then

$$\begin{aligned} |I - \gamma^{-2}P + H^T R^{-1}HP| &= -(I - \gamma^{-2}P) - H^T R^{-1}HP \\ &\leq -(I - \gamma^{-2}P) + H^T R^{-1}HP \\ &= |I - \gamma^{-2}P| + |H^T R^{-1}HP| \end{aligned}$$

■

Theorem 1 denotes that, there is a possibility that ψ can produce a negative definite matrix. Next is to understand what happens when ψ is a negative definite matrix. As shown in the proof, there are two conditions that occurs when a part of the equation is less than 0. An intuitive way to present this is by simulating a specific conditions that describing the situation.

Inspired by Theorem 1, the normal H_∞ Filter is then modified to ensure that it will always exhibits a positive semidefinite matrix in each measurement. As been explained earlier, due to the selection of γ and initial state covariance, the system can produce finite escape time problem i.e. there are situation that the state covariance accidentally becomes $I - \gamma^{-2}P + H^T R^{-1}HP \leq 0$. As a consequences, the estimation results in unreliable prediction results for both mobile robot and landmarks locations. Interestingly the proposed technique is a simple method that attempts to make the first and second component of $I - \gamma^{-2}P + H^T R^{-1}HP$ which are $I - \gamma^{-2}P$ to be positive at all time such that by applying $|I - \gamma^{-2}P|$ only when this equation exhibit negative. Hence, the algorithm of the H_∞ Filter especially for the updated state becomes as follow.

$$P_k^+ = f_{k-1} P_k^- (|I - \gamma^{-2}P_k^-| + H_{k-1}^T R_{k-1}^{-1} H_{k-1} P_k^-)^{-1} f_{k-1}^T \quad (11)$$

By applying this equation, the simulation will examine whether this modified version of the filter can further improved the inference to the SLAM problem.

4 Preliminary Simulation Results and Analysis

This section demonstrates the results and analysis of H_∞ Filter with comparison to the normal H_∞ Filter and Extended Kalman Filter (EKF). The analysis considers the initial state covariance, the environment noise types as well as the value of γ . Most of the analysis are referring to the proposed conditions stated earlier to evaluate their performance. The simulation settings is presented in Table 3 to demonstrates the conditions of both mobile robot and the environment to be observed.

Figure 1 shows the proposed H_∞ Filter in comparison to the EKF in non-gaussian noise environment. The state covariance is set initially at 100 for both mobile robot

Table 3 Simulation parameters

Variables	Parameters
Landmarks (x_{m_i}, y_{m_i})	$\begin{bmatrix} -20 & 60 \\ -2 & 6 \\ 6 & 12 \\ -3 & 15 \\ -20 & 23 \\ -22 & 6 \\ -20 & 16 \end{bmatrix}, \begin{bmatrix} -19 & -4 \\ 17 & 5 \\ 2 & 24 \\ -1 & -20 \\ -8 & -6 \\ 1 & 13 \end{bmatrix}$
Mobile robot initial pose (θ, x_r, y_r)	[0, 0, 0]
Gaussian noise covariance	0.000001
Non-Gaussian noise covariance	$Q_{max} = 0.001$ $Q_{min} = -0.001$ $R_{\theta_{max}} = 0.16$ $R_{\theta_{min}} = -0.08$ $R_{distance_{max}} = 0.5$ $R_{distance_{min}} = -0.5$
γ	0.07 and 0.7
Initial state covariance	$\begin{bmatrix} P_r & 0 \\ 0 & P_m \end{bmatrix} = \begin{bmatrix} 100 & 0 \\ 0 & 100 \end{bmatrix}$ $\begin{bmatrix} P_r & 0 \\ 0 & P_m \end{bmatrix} = \begin{bmatrix} 10000 & 0 \\ 0 & 10000 \end{bmatrix}$

and environment to describe that the system do not pose many information about the surroundings. From the figure, the estimation of the proposed H_∞ Filter has improved compared to EKF especially about the mobile robot estimation, thus showing possibility to be a solution for estimation.

With the same settings, the performance is also viewable between the normal H_∞ Filter and the new H_∞ Filter as presented in Figs. 2 and 3. Surprisingly, the new proposed H_∞ Filter surpassed the normal H_∞ Filter for different noises. Based on investigation for these figures, Eq. 7 has exhibit finite escape time for the normal H_∞ Filter which eventually makes the estimation becomes erroneous. The updated state covariance is presented in Fig. 4 which demonstrates both techniques still converging to a steady state behaviour. Nevertheless, the new H_∞ Filter is still producing finite escape time but lesser than the normal H_∞ Filter. Therefore, further investigations are needed.

Changing the value of γ and the initial state covariance also reflecting the same performance when the proposed technique is compared to the normal H_∞ Filter as shown in Fig. 5. Higher values of both parameters do not effect the proposed technique but the normal H_∞ Filter estimation becomes erroneous. For evaluation purposes, Fig. 6 is included to illustrate the performance of the updated state covariance. Similar

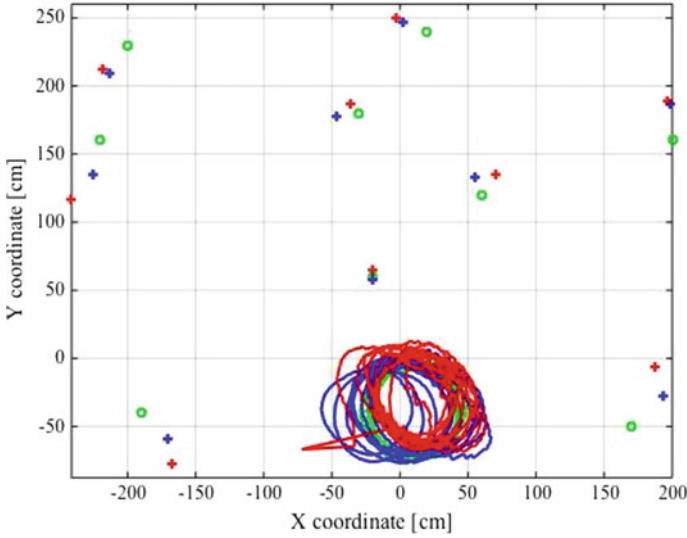


Fig. 1 Comparison between true (green), improved H_∞ Filter (red) and EKF (blue) with non-Gaussian Noise with initial state covariance of 100 and $\gamma=0.7$

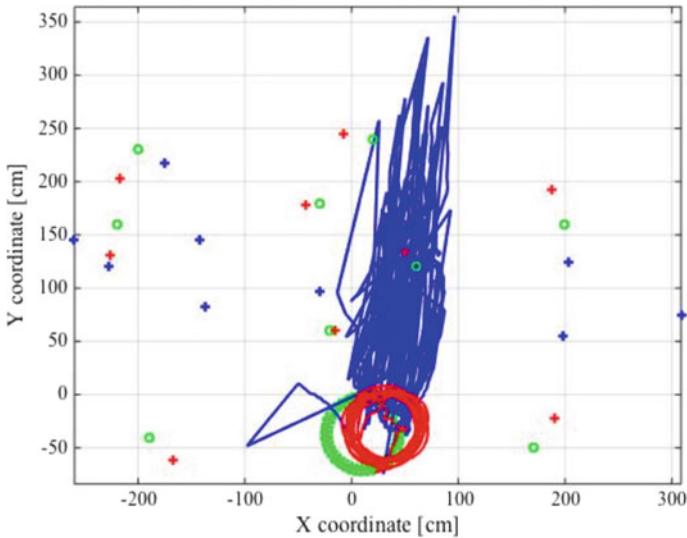


Fig. 2 Comparison between true (green), normal H_∞ Filter (blue) and improved H_∞ Filter (red) with Gaussian Noise

to the previous case of smaller γ and initial state covariance, the proposed method surpassed the normal H_∞ Filter. Besides in Fig. 7, further analysis with EKF also confirms that the proposed technique still offers better estimation than EKF. Thus,

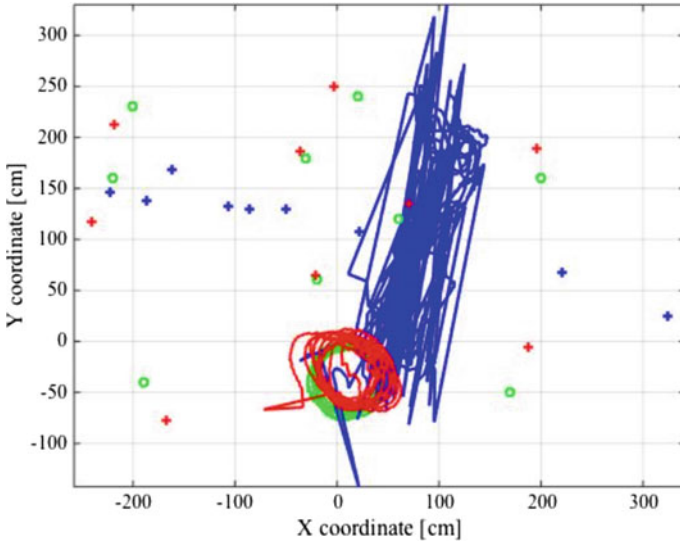


Fig. 3 Comparison between true (green), normal H_∞ Filter (blue) and improved H_∞ Filter (red) with non-Gaussian Noise

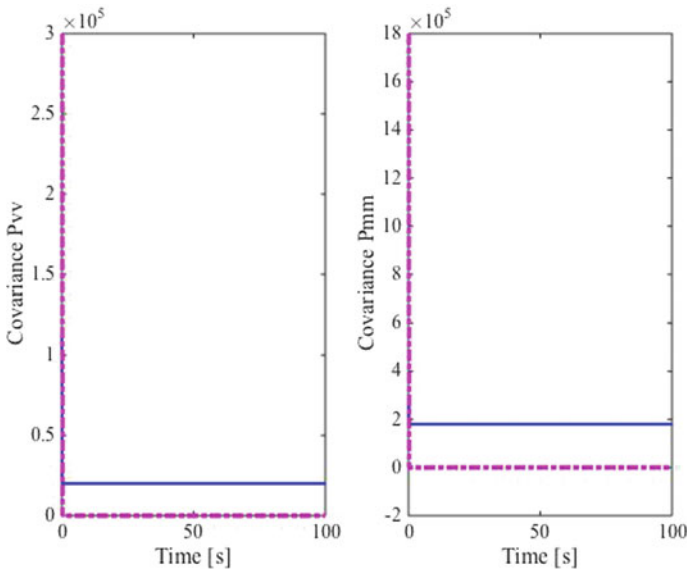


Fig. 4 State covariance performance between normal H_∞ Filter (blue) and improved H_∞ Filter (magenta) with non-Gaussian Noise

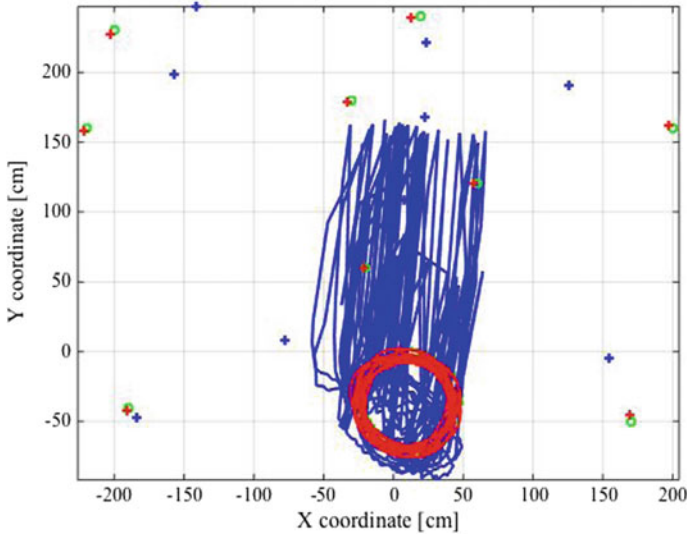


Fig. 5 SLAM performance between normal H_{∞} Filter (blue) and improved H_{∞} Filter (red) with non-Gaussian Noise, initial state covariance of 10,000 and $\gamma=0.07$

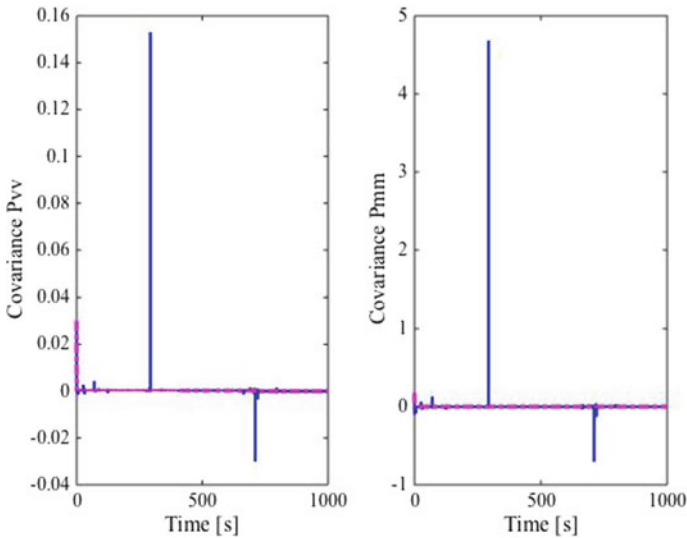


Fig. 6 State covariance performance between improved H_{∞} Filter (magenta) and normal H_{∞} Filter (blue) with non-Gaussian Noise, initial state covariance of 10,000 and $\gamma=0.07$

this achievement has opens new perspective of the filter and offers better results of estimation and possibilities for reliable estimation than its existing conventional type.

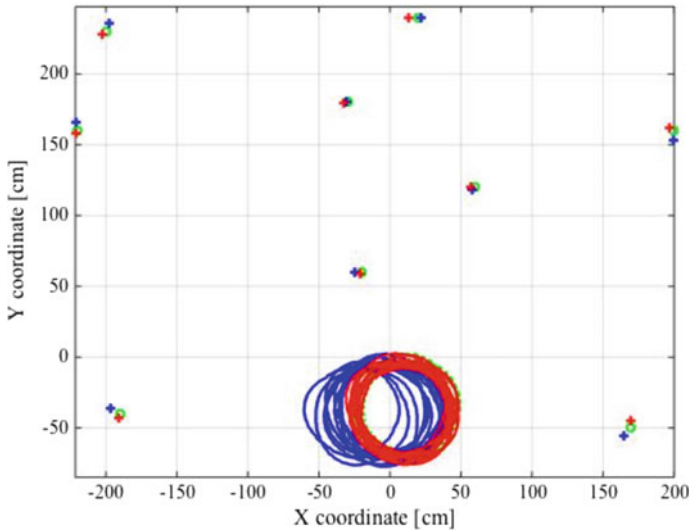


Fig. 7 SLAM performance between true (green), improved H_∞ Filter (red) and EKF (blue) with non-Gaussian Noise, initial state covariance of 10,000 and $\gamma=0.07$

5 Conclusion

This paper presented the investigation of H_∞ Filter based mobile robot localization and mapping considering the finite escape time problem. Three main aspects are analyzed which includes, the initial state covariance, environmental noise and the tuning parameters to understand their influences to the H_∞ Filter performance. The current H_∞ Filter is being modified to achieve better estimation results as well as to reduce the effect of finite escape time. The results have shown a consistency to the preceding works and offers better solution than the conventional method or normal H_∞ Filter in different noise characteristics. Even though there is still some finite escape time issues observed in the estimation, the results are convincing and has similar performance compared to Kalman Filter.

Acknowledgements The authors would like to thank Ministry of Higher Education and Universiti Malaysia Pahang for supporting this research under RDU160145 and RDU160379.

References

1. Durrant-Whyte, H., Bailey, T.: Simultaneous localization and mapping: part I. *IEEE Robot. Autom. Mag.* **13**(2), 99–110 (2006)
2. Bailey, T., Durrant-Whyte, H.: Simultaneous localization and mapping (SLAM): part II. *IEEE Robot. Autom. Mag.* **13**(3), 108–117 (2006)

3. Smith, R.C., Cheeseman, P.: On the representation and estimation of spatial uncertainty. *J. Robot. Res.* **5**(4), 56–68 (1987)
4. Porta, J.M.: CuikSLAM: a kinematics-based approach to SLAM. In: *Proceeding of the 2005 IEEE International Conference on Robotics and Automation*, pp. 2425–2431, Spain (2005)
5. Thallas, A., Tsardoulias, E., Petrou, L.: Particle filter-scan matching SLAM recovery under kinematic model failures. In: *24th Mediterranean Conference on Control and Automation*, pp. 232–237, Greece (2016)
6. Johansen, T.A., Brekke, E.: Globally exponential stable Kalman Filtering for SLAM with AHRS. In: *19th International Conference on Information Fusion (FUSION)*, pp. 909–916, Germany (2016)
7. Huang, S., Dissayanake, G.: Convergence and consistency analysis for extended Kalman Filter based SLAM. *IEEE Trans. Robot.* **23**(5), 1036–1049 (2007)
8. Dissayanake, G., Newman, P., Clark, S., Durrant-Whyte, H., Csorba, M.: A solution to the simultaneous localization and map building (SLAM). *IEEE Trans. Robot. Autom.* **17**(3), 229–241 (2001)
9. Kurt-Yavuz, Z., Yavuz, S.: A comparison of EKF, UKF, FastSLAM2.0, and UKF based FastSLAM algorithm. In: *IEEE 16th Conference on Intelligent Engineering System (INES)*, pp. 37–43, Portugal (2012)
10. Buonocore, L., Barros dos Santos, S.R., Neto, A.A., Nascimento, C.L.: FastSLAM filter implementation for indoor autonomous robot. In: *2016 IEEE Intelligent Vehicles Symposium*, pp. 484–489, Sweden (2016)
11. Guo, L., Song, C., Mao, Y.: H infinity filter in maneuvering target tracking of military guidance field. In: *International Conference on Automatic Control and Artificial Intelligence (ACAI2012)*, pp. 1114–1116, China (2012)
12. Hur, H., Hyo-Sung, A.: Discrete-time H_∞ filter for mobile robot localization using wireless sensor network. *IEEE Sens. J.* **13**(1), 245–252 (2013)
13. Charkhgard, M., Haddad Zarif, M.: Design of adaptive H_∞ filter for implementing on state-of-charge estimation based on battery state-of-charge varying modelling. *IET Power Electron.* **8**(10), 1825–1833 (2015)
14. Zhao, F., Zhang, Q., Zhang, Y.: H_∞ filtering for a class of singular biological systems. *IET Control Theory Appl.* **9**(13), 2047–2055 (2015)
15. Nazamzade, P., Fontanelli, D., Macii, D., Palopoli, L.: Indoor localization of mobile robots through QR code detection and dead reckoning data fusion. *IEEE/ASME Trans. Mechatron.* **22**(6), 2588–2599 (2017)
16. Bolzern, P., Colaneri, P., De Nicolao, G.: H_∞ differential Riccati equations: convergence properties and finite escape phenomena. *IEEE Trans. Autom. Control* **42**(1), 113–118 (1997)
17. Bolzern, P., Maroni, M.: New conditions for the convergence of H/sub/spl infin//filters and predictors. *IEEE Trans. Autom. Control* **44**(8), 1564–1568 (1999)
18. Ahmad, H., Namerikawa, T.: Feasibility study of partial observability in H_∞ filtering for robot localization and mapping problem. In: *American Control Conference (ACC) 2010*, pp. 3980–3985 (2010)

Diagonalization of Covariance Matrix in Simultaneous Localization and Mapping of Mobile Robot



Maziatun Mohamad Mazlan, Nur Aqilah Othman and Hamzah Ahmad

Abstract The purpose of this study is to analyze the effects of covariance state update by means of modified algorithm of diagonal matrix using eigenvalue, and diagonalization function in MATLAB on the computational cost of extended Kalman filter based Simultaneous Localization and Mapping (SLAM). The multiplications of the covariance matrix with other parameters increase its dimension, which is twice the number of landmarks and might result in erroneous estimation. This motivates this study in searching for ways to reduce the computational cost of the covariance matrix without minimizing the accuracy of the state estimation using eigenvalue method. The matrix diagonalization strategy which is applied to the covariance matrix in EKF-based SLAM must be examined to simplify the multiplication procedure. Therefore, improvement is needed to find better diagonalization method. Simulation results demonstrate that MATLAB's built-in diagonalization function can reduce the computational cost.

Keywords Covariance · Diagonalization · Eigenvalue · Extended Kalman filter Localization

1 Introduction

These days, there has been expanding business enthusiasm for new utilizations of a robot other than modern creation. Not restricted to just mechanical robots, portable robots have broadening their applications in various distinctive areas from indoor robots to outside, space, in military or unsafe region, submerged, and airborne frame-

M. M. Mazlan
Electrical Engineering Department, Politeknik Sultan Haji Ahmad Shah, 25350 Kuantan,
Pahang, Malaysia

N. A. Othman (✉) · H. Ahmad
Faculty of Electrical and Electronics Engineering, Universiti Malaysia Pahang, 26600 Pekan,
Pahang, Malaysia
e-mail: nuraqilah@ump.edu.my

work. Nevertheless, it has shown a great deal of difficulties to defeat in seeking after a genuinely self-governing robot. One of the investigation districts that is acknowledged to give a response for this issue is known as Simultaneous Localization and Mapping (SLAM) issue.

The Simultaneous Localization and Mapping (SLAM) problem asks if it is possible for a mobile robot to move autonomously and observing its surrounding in an obscure situation with no earlier data on its area, and have it simultaneously decided its location.

In realizing a solution for SLAM problem, researcher has to deal with several issues such as uncertainties, data association, and feature extraction. This examination reveals the vulnerabilities impact to the covariance state as it adds to computational cost of Extended Kalman Filter based Simultaneous Localization and Mapping issue.

In recent years, there are few methodologies have been presented, for example, extended Kalman filter (EKF), unscented Kalman filter (UKF), and Particle filter for estimation purposes. A large portion of those strategies share the indistinguishable specialized properties where they depend on Bayesian strategy. Between previously mentioned approaches, EKF are the most commended technique for SLAM arrangement. The reason could be because of the channel offers simpler calculation to take after and has brought down computational cost contrasted with others.

Extended Kalman filter (EKF) is a good way to learn about SLAM because of simplicity whereas probabilistic method is complex, but they handle uncertainty better contrasted with different methodologies, for example particle filter. Nevertheless, the entire covariance matrix in EKF-based SLAM should be refreshed each time another point of interest is identified. This methodology includes bunches of numerical tasks, subsequently will raise the computational cost. Besides, the measurement of covariance matrix will increase to double the quantity of historic point, as more landmarks are detected. It is known that the cost of $O(m^2)$, in which m is a total landmark of the map in EKF-based SLAM. For large environment the used of EKF is limited (only hundred landmarks). As the landmarks increase it will affect the full covariance structure which is responsive to the effects of linearization errors which build up through time.

Therefore, this study is focused on MATLAB simulation coding modification where the MATLAB command for finding eigenvalue and diagonal matrix directly used without changing the structure of diagonal matrix. One of the process of finding the eigenvalue is done by some MATLAB simulation coding modification that designs so that the structure of covariance matrix will be diagonalized.

Guivant and Nebot developed a decorrelation calculation with improve the covariance matrix [1]. A subset of the states will decorrelate the calculation that is feebly associated and drop the pitifully cross-relationship terms in the covariance matrix. To diminish both computational and capacity costs in SLAM a positive semi definite matrix is added to the covariance matrix.

Besides decorrelation algorithm, Julier and Uhlmann presented a covariance convergence strategy for SLAM, a combination system that consolidates two covariances when the relationships between them are obscure [2], and this technique has been

implemented not only in SLAM, but also in other applications [3] and this procedure has been executed in SLAM, as well as in different applications. In this strategy, the refresh procedure is completed in two autonomous advances; refreshing the robot, at that point refreshing the historic point. In addition, there exists a parameter ω in the calculation that should be defined beforehand.

Besides in Kalman filter, a method of decorrelating some of the updated state covariance of the H infinity filter has been suggested by Ahmad and Othman [4], in order to reduce the cost computation. This is due to Finite Escape Time problem in H infinity filter based Simultaneous Localization and Mapping problem as the Finite escape time has been one of the obstacles that holding the realization of H infinity Filter in many applications. As their discoveries, they proposed an outcome if the full rank of delta P is added to the covariance and without association with the other state components. However, there is also a possibility that may result unbounded uncertainties in the estimation of SLAM problem.

This study is conducted to analyze the behavior effects of covariance state update of different MATLAB simulation coding between modification algorithm of diagonal matrix using eigenvalue [5] and using algorithm build-in function of diagonalization directly. The results of the cause on the estimation and covariance behavior are presented, which have been obtained through simulations.

2 Issue of Formulation

2.1 Model of Simultaneous Localization and Mapping (SLAM)

The equation of discrete time dynamic system can be represented for SLAM concerning process and observation model. The movements of the mobile robot illustrated from process model while the measurement of the map features described by the observation model with reference to the mobile robot position. Both models (i.e. process and observation model) of SLAM depicts on Fig. 1. An equation that represent SLAM process model from time k to time $k + 1$ for linear system is stated as

$$X_{k+1} = F_k X_k + G_k U_k + w_k \quad (1)$$

in which the state of landmarks and mobile robot represented by X_k , the state transition matrix represented by F_k , the control matrix represented by G_k , the control inputs represented by U_k , and the zero-mean Gaussian process noise with covariance Q represented w_k .

A combined state vector of landmarks X_m and robot X_r represent the state vector of 2D SLAM at time k as follows

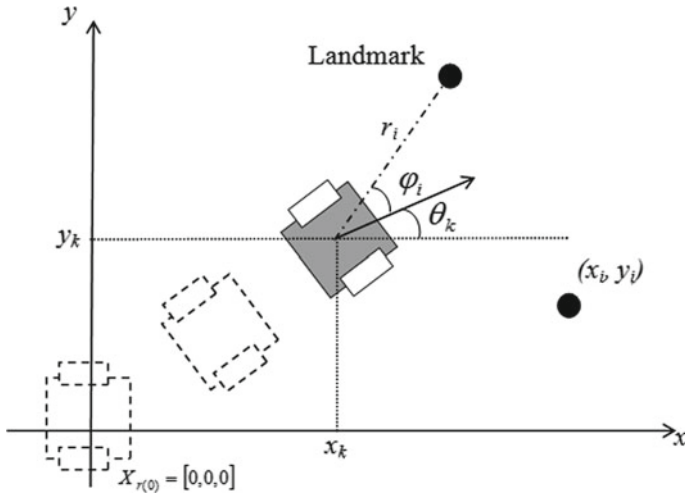


Fig. 1 SLAM model

$$X_k = \begin{bmatrix} X_r \\ X_m \end{bmatrix} = \begin{bmatrix} \theta_k \\ x_k \\ y_k \\ x_i \\ y_i \end{bmatrix} \tag{2}$$

where the middle location of the mobile robot with reference to global coordinate frame represented by x_k and y_k and the direction angle of the mobile robot represented by θ_k . The Cartesian coordinate (x_i, y_i) , $i = 1, 2, \dots, m$ is correspond to the landmark model where m is number of landmarks. A model of two-wheel mobile robot is applied through this study. $X_r = [\theta_k \ x_k \ y_k]^T$ is applied to signify the robot position or in this study sometimes we denote it as robot pose. The kinematic movement of mobile robot that illustrate the process form defined as $X_{r(k+1)} = f(X_{r(k)}, u_k, \delta\omega, \delta\nu)$ and $u_k = [\omega_k \ v_k]^T$ in which

$$\begin{aligned} \theta_{k+1} &= \theta_k + (\omega_k + \delta\omega)T \\ x_{k+1} &= x_k + (v_k + \delta\nu)T \cos(\theta_k) \\ y_{k+1} &= y_k + (v_k + \delta\nu)T \sin(\theta_k) \end{aligned} \tag{3}$$

with mobile robot angular acceleration control inputs defined as ω_k and mobile robot velocity with related process noises, $\delta\omega$ and $\delta\nu$ represent by v_k . The time interval of one movement step defined as T . As landmarks are assumed to be static, the process model for the landmarks $[x_i, y_i]^T$ for $i = 1, 2, \dots, m$ is unaffected with zero noise.

$$X_{m(k+1)} = X_{m(k)} \quad (4)$$

State observation or measurement processes are represented using an observation model

$$z_{(k+1)} = \begin{bmatrix} r_i \\ \phi_i \end{bmatrix} = H_{k+1} X_{k+1} + V_{r_i} \phi_i \quad (5)$$

where the measurement matrix represented by H_k and the zero-mean Gaussian noise with covariance matrix R represented by $V_{r_i} \phi_i$. At time $k + 1$, the observation of i th landmark is a range r_i and bearing ϕ_i which shows the relative distance and angle of the mobile robot to the observed landmarks. It is assumed that the sensor in the robot operates with a range sensor and a bearing that keeps the observation of the landmark in the environment as well as the encoder on the wheel for vehicle speed measurement. Range and bearing are defined as

$$r_i = \sqrt{(y_i - y_{k+1})^2 + (x_i - x_{k+1})^2} + v_{r_i} \quad (6)$$

$$\phi_i = \arctan\left(\frac{y_i - y_{k+1}}{x_i - x_{k+1}}\right) - \theta_{k+1} + v_{\theta_i} \quad (7)$$

where $(x_{k+1}, y_{k+1}, \theta_{k+1})$ is current robot position, (x_i, y_i) is position of observed landmark, v_{r_i} and v_{θ_i} are the noises on the measurements.

2.2 SLAM Based on Extended Kalman Filter

In this study the extended Kalman filter (EKF) is applied to estimate the location of mobile robot and landmarks. First, based on the earlier system information, the state vector is predicted. After that using the measurement data received from the sensors, the state vector will be estimated. Parameters of interest are the updated state vector \hat{X}_k and the covariance matrix of the estimation P_k . The elaborations of prediction and estimation of EKF are stated as follows.

A. Prediction (update of time)

The estimation of the state vector at the instant k stated as

$$\hat{X}_k = \left[\hat{X}_r \ \hat{X}_1 \ \hat{X}_2 \ \dots \ \hat{X}_m \right]^T \quad (8)$$

and P_k is the covariance matrix of the estimation error. The process model (Eqs. 1–4) is linearized as an extension of the Taylor series about \hat{X}_k and thus leads to the next predicted state vector \hat{X}_{k+1}^- and error covariance matrix P_{k+1}^-

$$\begin{aligned}\hat{X}_{k+1}^- &= f(X_k, u_k, 0, k) \\ P_{k+1}^- &= \nabla F_X P_k \nabla F_X^T + \nabla F_w Q_k \nabla F_w^T\end{aligned}\quad (9)$$

where the Jacobian of f with respect to X_k is represented by ∇F_X and the Jacobian with respect to ω_k is represented by ∇F_ω the Jacobian with respect to ω_k . These Jacobians are valued from Eq. 3 at \hat{X}_k and have the subsequent expressions:

$$\nabla F_X = \begin{bmatrix} 1 & 0 & 0 & 0 \\ -\omega T \sin \hat{\theta}_k & 1 & 0 & 0 \\ \omega T \cos \hat{\theta}_k & 0 & 1 & 0 \\ 0 & 0 & 0 & I_m \end{bmatrix}, \quad \nabla F_\omega = \begin{bmatrix} \nabla F_{\gamma\omega} \\ 0_m \end{bmatrix}\quad (10)$$

I_m and 0_m is the character and null matrix individually with fitting measurements relying upon the quantity of points of landmark watched while the inspecting rate is T . There is no procedure noise for the landmarks as they are assumed to be stationary constantly

B. Updated (update estimation)

The equation of the state vector and the error covariance matrix in the update procedure is framed by linearizing the observation model (Eq. 5) through the Taylor series development about \hat{X}_{k+1}^- . With the accessibility of estimation data information z_{k+1} , the mobile robot updates its current position relative to the position of observed landmarks

$$P_{k+1}^+ = P_{k+1}^- - K_{k+1}(\nabla H_i P_{k+1}^- \nabla H_i^T + R_k)K_{k+1}^T$$

K_{k+1} is a Kalman gain and has the following definition:

$$K_{k+1} = P_{k+1}^- \nabla H_i^T (\nabla H_i P_{k+1}^- \nabla H_i^T + R_k)^{-1}\quad (11)$$

The Jacobian is represented by ∇H_i in Eq. 5 with refer to X_k assessed at \hat{X}_{k+1}^- and expressed as follows:

$$\nabla H_i = \begin{bmatrix} 0 & -\frac{dx}{r} & -\frac{dy}{r} & \frac{dx}{r} & \frac{dy}{r} \\ -1 & \frac{dy}{r^2} & -\frac{dx}{r^2} & -\frac{dy}{r^2} & \frac{dx}{r^2} \end{bmatrix}\quad (12)$$

with

$$dx = \hat{x}_i^- - \hat{x}_{k+1}^-, \quad dy = \hat{y}_i^- - \hat{y}_{k+1}^-, \quad r = \sqrt{dx^2 + dy^2}\quad (13)$$

2.3 State Error Covariance Matrix

Commonly, the covariance of two variants is the measure of the correlation between two variables. The amount of linear dependence between variables can be measured by the correlation theory. Matrix arrangement of robot position and landmarks covariance matrices and correlation among the robot and landmarks is the covariance matrix of a state estimate in SLAM. In SLAM the covariance matrix, P is defined as

$$P = \begin{bmatrix} P_{RR} & P_{RM} \\ P_{RM}^T & P_{MM} \end{bmatrix} \quad (14)$$

Covariance matrix of robot position is represented P_{RR} , covariance matrix of the landmark position is represented by P_{MM} and cross-covariance matrix of the robot and landmarks or cross-correlation between them is represented by P_{RM} .

In SLAM, the covariance matrix indicates the error associated with the estimates of the state of the robot and of the reference point. As of the covariance matrix information, the uncertainties and errors of estimation can be monitor either raise or decrease, in which they stand for the accuracy and consistency of the estimate. Consequently, it is very crucial to research the behavior of the covariance matrix as it contributes significant issue in SLAM.

Proposition 1 *The determinant of the error covariance matrix is a measure of the volume of the uncertainty ellipsoid associated with the state estimate, which indicate the total uncertainty of that particular state estimation [6].*

The state error covariance in SLAM having dimension of $(3 + 2m)^2$, where m is a landmark. As robot detected the latest landmarks in its area the size of state error covariance will be increased. Equation 15 represents the state error covariance matrix for SLAM. The covariance of the state error indicates the error associated with the estimates of the status of the reference points and of the robot, as defined in Proposition 1. The precision and consistency of the estimation could be represented by the state error covariance where the increment and decrement of uncertainties could be observed. The smaller covariance value shows the better estimation. Nevertheless, if the actual value is bigger than the covariance value, the estimation is look like to have an inaccuracy, but the covariance indicates lesser value, then the estimation in this condition is said to be an optimistic estimation. The optimistic estimation is one of the problems in SLAM which have to take into account in EKF-based SLAM.

$$\begin{bmatrix}
 P_{\theta\theta} & P_{\theta X} & P_{\theta y} & P_{\theta m_{1,x}} & P_{\theta m_{1,y}} & \dots & P_{\theta m_{n,x}} & P_{\theta m_{n,y}} \\
 P_{x\theta} & P_{xx} & P_{xy} & P_{xm_{1,x}} & P_{xm_{1,y}} & \dots & P_{xm_{n,x}} & P_{xm_{n,y}} \\
 P_{y\theta} & P_{yx} & P_{yy} & P_{ym_{1,x}} & P_{ym_{1,y}} & \dots & P_{ym_{n,x}} & P_{ym_{n,y}} \\
 P_{m_{1,x}\theta} & P_{m_{1,x}x} & P_{m_{1,x}y} & P_{m_{1,x}m_{1,x}} & P_{m_{1,x}m_{1,y}} & \dots & P_{m_{1,x}m_{n,x}} & P_{m_{1,x}m_{n,y}} \\
 P_{m_{1,y}\theta} & P_{m_{1,y}x} & P_{m_{1,y}y} & P_{m_{1,y}m_{1,x}} & P_{m_{1,y}m_{1,y}} & \dots & P_{m_{1,y}m_{n,x}} & P_{m_{1,y}m_{n,y}} \\
 \vdots & \vdots & \vdots & \vdots & \vdots & \dots & \vdots & \vdots \\
 \vdots & \vdots & \vdots & \vdots & \vdots & \dots & \vdots & \vdots \\
 P_{m_{n,x}\theta} & P_{m_{n,x}x} & P_{m_{n,x}y} & P_{m_{n,x}m_{1,x}} & P_{m_{n,x}m_{1,y}} & \dots & P_{m_{n,x}m_{n,x}} & P_{m_{n,x}m_{n,y}} \\
 P_{m_{n,y}\theta} & P_{m_{n,y}x} & P_{m_{n,y}y} & P_{m_{n,y}m_{1,x}} & P_{m_{n,y}m_{1,y}} & \dots & P_{m_{n,y}m_{n,x}} & P_{m_{n,y}m_{n,y}}
 \end{bmatrix} \tag{15}$$

3 Matrix Diagonalization

A matrix in which the top and bottom elements are all null is called the diagonal matrix. The contents of diagonal elements may fill up either with value or also null. For a $n \times n$ square matrix is said to be diagonal matrix if it stated as

Let the elements of $D = (d_{i,j})$

$$(d_{i,j}) = 0 \text{ if } i \neq j \forall i, \quad j \in \{1, 2, \dots, n\} \tag{16}$$

The multiplication step of the matrix is easier for a diagonal matrix where just diagonal elements are concerned and this will make the operation faster and will require a lower computational cost if applied in SLAM. Let A be a $n \times n$ square matrix. It is believed that there be present a number and a column matrix B with dimension of such that

$$AB = \lambda B$$

With the matching eigenvector B , λ is define as an eigenvalue of A . Then A is diagonalizable to a matrix D . There will usually be n number of eigenvalues for each $n \times n$ matrix, in which the eigenvalues could be actual, complex or the join of mutually numbers.

Definition 1 Let A be a $n \times n$ square matrix and D is a diagonal matrix in which its diagonal elements are the eigenvalues of A , such as follows:

$$D = \begin{bmatrix} \lambda_1 & 0 & 0 & 0 \\ 0 & \lambda_2 & 0 & 0 \\ 0 & 0 & \ddots & 0 \\ 0 & 0 & 0 & \lambda_n \end{bmatrix} \quad (17)$$

Therefore, there exists the following relationship between matrix A and matrix D:

$$\begin{aligned} \det(A) &= \det(D) \\ \text{norm}(A) &= \text{norm}(D) \end{aligned} \quad (18)$$

Therefore, referring to Proposition 1 and to the behavior of the diagonal matrix presented by Eq. 18, the possibility exists that the diagonalization through eigenvalues may be one of the alternative techniques to minimize the computational cost of SLAM based on EKF. The method was also motivated by the earlier works of [1, 7] that mainly investigated and discussed about the diagonalization of the updated state covariance matrix.

3.1 Diagonalization of Covariance Matrix for EKF-Based SLAM

The behavior of covariance and estimation performance is examined through simulation by the effect of diagonalizing the covariance matrix. This is because the multiplication steps in covariance calculation become simple, as an effort to decrease the computational difficulty as well as computational cost. As the only diagonal elements involve in multiplication of a matrix with another diagonal matrix, it is much simpler and quicker. The study has been conducted based on two case studies:

- (1) Estimated covariance for both (robot and landmark) is diagonalized using eigenvalue MATLAB function and reconstruction of diagonal matrix as in [5].
- (2) Estimated covariance for both (robot and landmark) is diagonalized using MATLAB function of diagonalization directly.

For the case study 1 the eigenvalue of estimated covariance is first calculated using the function stated as follows:

$$\lambda_n = \text{eig}(P_{k+1}^+)$$

where λ_n represent the eigenvalue and (P_{k+1}^+) represent the estimated covariance. Then the diagonal matrix will be build using the next function stated as follows:

$$P_{(D),k+1}^+ = \text{diag}(\lambda_n)$$

where $P_{(D),k+1}^+ = \text{diag}(\lambda_n)$ is a diagonal matrix that built from eigenvalue.

For the case study 2 the eigenvalue of estimated covariance is directly calculated using the MATLAB function stated as follows:

$$[V, D] = \text{eig}(P_{k+1}^+)$$

where $[V, D]$ is the MATLAB function of finding diagonal matrix directly. Next the diagonal matrix will be build using the function stated as follows:

$$P_{(D),k+1}^+ = D$$

The above two cases are analyzed separately to find out the consistency and reliability of the proposed method.

4 Simulation Results and Discussions

The analyses through simulation for two case studies of different diagonalization algorithm coding are presented to examine the behavior of the estimation and covariance matrix of EKF-based SLAM.

Figure 2 depicts the estimation of the landmarks and mobile robot position under normal condition, (i.e. using normal covariance matrix). The simulation time for the mobile robot is 1000 s and continuously detects the landmarks for every loop of motion, with constant speed. The uncertainties of the estimation are represented by the covariance-ellipses. Better estimation will show smaller ellipse.

The simulations for two case studies as defined in Sect. 3 are conducted using the same parameters. The behavior of covariance through estimation in the first case as depicted in Fig. 3, while Fig. 4 shows the result of the second case study. It is apparent in the previously mentioned figures, that the estimation of the position of mobile robot and landmarks is possible even when the whole covariance is diagonalized through the technique defined in Sect. 3. However, the estimations demonstrated some acceptable errors. Estimation of landmark position in case 2 is better than that of in case 1. Moreover, this shows that the diagonalization method through finding of eigenvalues and rebuilding a diagonal matrix as defined in [5], is able to produce similar prediction behavior as compared to build-in MATLAB function of matrix diagonalization.

On the other hand, the covariance behaves unusual in both cases, where the covariance decreases suddenly, and it is too tiny compared to the normal covariance as illustrated in Fig. 2. This situation illustrates the optimistic estimation as described in Sect. 2.3 of this paper.

The comparison of processing time of all methods is depicted in Table 1. Diagonalization method using built-in function in MATLAB (Case 2) was found to be the fastest among all cases, about 15% faster than the normal condition. Case 1 also completed about 13% faster than the normal condition, despite additional steps taken in diagonalizing the covariance matrix. Furthermore, Case 2 produces more accurate

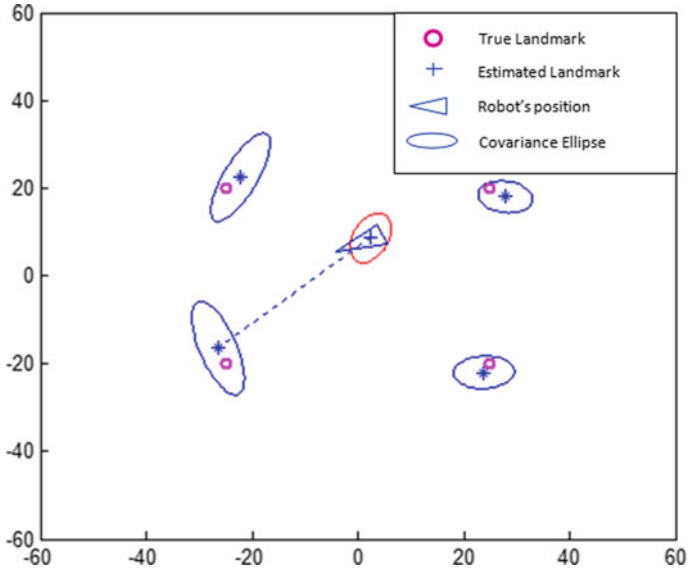


Fig. 2 Position estimation and covariance under normal condition

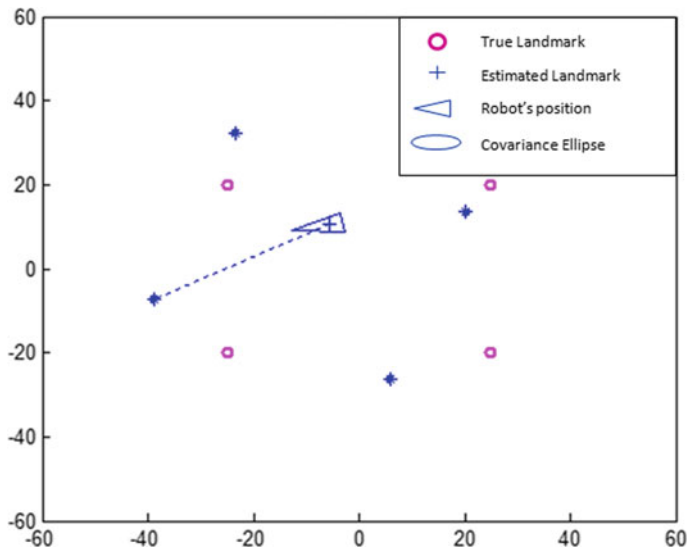


Fig. 3 Estimation of the state and covariance behavior of case one

estimation compared to Case 1 as shown in Figs. 3 and 4. This is demonstrated by the true landmark being closer to the estimated landmark in Case 2.

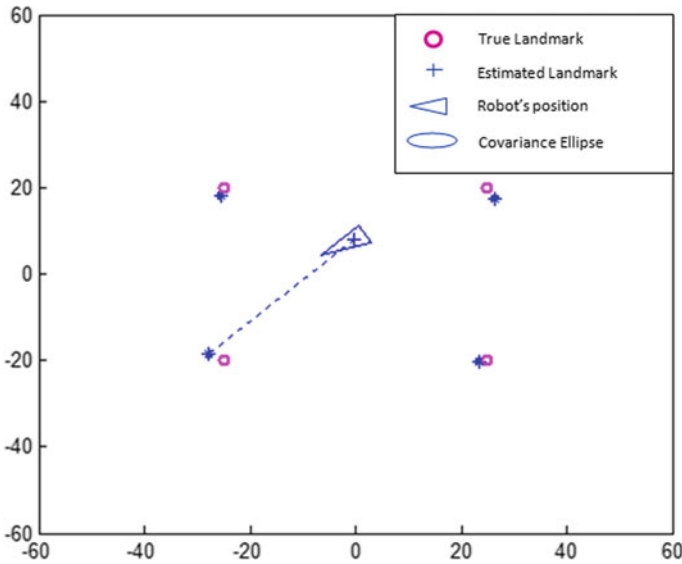


Fig. 4 Estimation of the state and covariance behavior of case two

Table 1 Processing time for all cases

Covariance type	Simulation time (s)	Total processing time (s)	Percentage of processing time reduction (%)
Normal	1000	96.3977	
Case 1	1000	83.9984	12.86
Case 2	1000	81.639	15.31

5 Conclusion

This paper presented an analysis of EKF-based SLAM execution under the states of diagonalized covariance of two cases as discussed in Sect. 3. Case 1 diagonalizes the covariance matrix through eigenvalues, while Case 2 makes use of built-in diagonalization function in MATLAB. It was found that Case 2 completed the fastest compared to Case 1 and the normal condition. In addition, it was found that Case 2 produces more accurate estimation than Case 1. Future work will be using the build-in MATLAB function to further investigate on how to reduce computational cost of mobile robot SLAM. In addition, correction of optimistic value of covariance matrix is the subject of future investigation.

Acknowledgements This study was supported by the Universiti Malaysia Pahang (UMP) internal grant RDU170369.

References

1. Guivant, J.E., Nebot, E.M.: Solving computational and memory requirements of feature-based simultaneous localization and mapping algorithms. *IEEE Trans. Robot. Autom.* **19**(4), 749–755 (2003)
2. Julier, S.J., Uhlmann, J.K.: Using covariance intersection for SLAM. *Robot. Auton. Syst.* **55**(1), 3–20 (2007)
3. Jiang, Y., Xiao, J.: Target tracking based on a multi-sensor covariance intersection fusion Kalman Filter. *Eng. Rev.* **34**(1), 47–54 (2014)
4. Ahmad, H., Othman, N.A.: A solution to finite escape time for H_∞ filter based SLAM. *J. Telecommun. Electron. Comput. Eng.* **8**(11), 7–13 (2016)
5. Othman, N.A., Ahmad, H.: Examining the eigenvalues effect to the computational cost in mobile robot simultaneous localization and mapping. *Comput. Electr. Eng.* **56**, 659–673 (2016)
6. Gamini Dissanayake, M.W.M., Newman, P., Clark, S., Durrant-Whyte, H.F., Csorba, M.: A solution to the simultaneous localization and map building (SLAM) problem. *IEEE Trans. Robot. Autom.* **17**(3), 229–241 (2001)
7. Andrade-Cetto, J., Sanfeliu, A.: The effects of partial observability in SLAM. In: *Robotics and Automation (ICRA)*, pp. 397–402 (2004)

Development and Control of Biped Walking Robot Using PI Control



K. H. Tan, N. S. M. Nor and M. Z. Md Zain

Abstract Biped walking robot is a humanoid robot which move, act and behaves like human. In this project, a control system named PI is studied and implemented into a simple biped robot with only bottom body. PI control is research and implement into the biped robot to increase the accuracy of the actuators performance in each robot's joint. The whole project is started by studying the Degree of freedom (DOF) and control system of biped robot. According to the requirement of the PI control, a mechanical design is proposed to coordinate all sensors and actuators together. In this project, a preliminary experiment of PI is done to test the function and effect of PI on the actuator (servo) accuracy before all components are assemble to build up the biped robot. The most critical part in this project is about the calibration of sensors and actuators. The failure in calibration may induced errors and its magnitude depend on how well the calibration is done. According to sensors feedback, angle deviation of 5° is solved after PI control. Therefore, PI control is successfully implemented and the biped robot build is able to perform walking and downstairs action with higher accuracy.

Keywords Degree of freedom (DOF) · Proportional-integral control (PI) · Biped walking robot · Calibration · Servo

1 Introduction

Humanoid robot is a robot which behaves like a human. Humanoid robot replicates the walking style of a human particularly walking upright. Humanoid biped robot is a robot with two legs and certain joints to perform walking actions like human.

K. H. Tan

Faculty of Mechanical Engineering, Universiti Teknologi Malaysia, 81310
Johor Bahru, Johor, Malaysia

N. S. M. Nor (✉) · M. Z. Md Zain

Department of Applied Mechanics & Design, Faculty of Mechanical Engineering,
Universiti Teknologi Malaysia, 81310 Johor Bahru, Johor, Malaysia
e-mail: nursafwati@utm.my

© Springer Nature Singapore Pte Ltd. 2019

Z. Md Zain et al. (eds.), *Proceedings of the 10th National Technical Seminar*

on Underwater System Technology 2018, Lecture Notes in Electrical Engineering 538,

https://doi.org/10.1007/978-981-13-3708-6_25

The term “biped” means two. Biped walking robot can be designed to have many different numbers of DOF. The design of robot with higher degree of freedom also mean a higher hardness of coordinating and controlling of the motion of the robot. The optimize number of DOF allow the robot to move smoothly.

In general, the lowest allowable DOF for a very simple biped walking robot is 4 DOF. There are a lot of biped walking robot designed with others depend on the usage and the movement the designer want their robot to achieve. Lim and Tajima [1–3] having their biped walking robot designed with two 6 DOF legs and 3 DOF waist. Its leg system consists of two 2 DOF ankles, two 1 DOF knees and two 3 DOF hips. The DOF for both legs are normally designed to have the same number and same design to ease the process of programming and mechanical design.

There are a lot of control system used in for biped walking robot to perform walking action. For example, Zero Moment Point (ZMP), PID, torque controlled and many others depend on the design of the robot. ZMP is one of the famous control method which applied in a few high end robot product such as ASIMO and TORO. High end biped robots having a lot of sensors and complicated control system. Other than that, to control the stiffness of the robot, a particular spring with non-linear elasticity such as SAT (Stiffness Adjustable Tendon) is utilized with antagonistic actuator together with control algorithm for walking motion [4, 5].

Control system is the core of a biped robot. Some of the control system implemented is function to maintain the accuracy of the biped walking action especially the biped robot with a poor quality actuator. PI control apply in any field to eliminate the errors of the system and it is suitable to remove the error between the theoretical and real angle error caused by the poor actuator. Thus, PI control is commonly used in controlling to adjust the system to the set point.

2 Model of Biped Walking Robot

2.1 PID Controller

A proportional–integral–derivative controller is a control loop feedback mechanism widely used in control systems and a variety of other applications requiring continuously modulated control [6, 7] (Fig. 1).

There are three important terms in PID control system which is P (proportional), I (Integral) and D (derivative) [9–11].

- (1) Term P is proportional to $e(t)$. For instance, if the value of $e(t)$ is large and positive, the control output will also be large and positive. Residual will be occurred if proportional control, P is used alone in the system.
- (2) Term I is account for the past values of the $e(t)$ and integrates them over time to produce the control output. If there is residual error occurred after application of proportional control, the integral term seeks to eliminate the residual error by

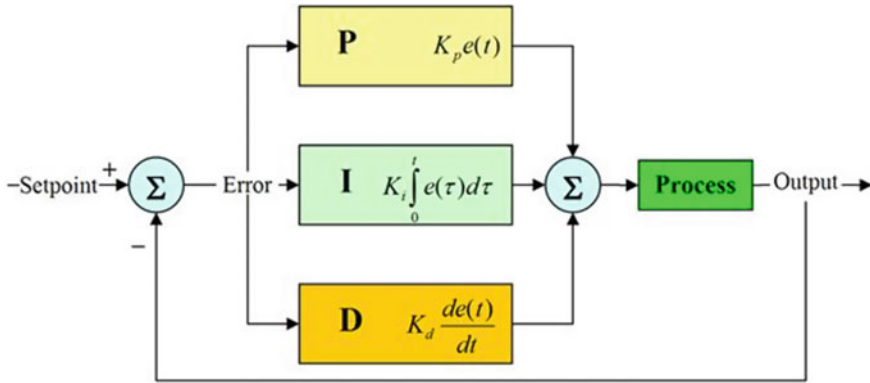


Fig. 1 Block diagram of a PID controller in a feedback loop [8]

adding a control effect due to the historic cumulative value of the error. When the error is eliminated, the integral term will stop to grow.

- (3) Term D is the estimate of the future trend of $e(t)$ based on the current rate of change of error. It will exerting a control to the system depend on the rate of error change. The more rapid the change, the greater the controlling and damping effect.

$$u(t) = K_p e(t) + K_i \int_0^t e(\tau) d\tau + K_d \frac{de(t)}{dt} \tag{1}$$

where K_p is proportional gain, K_i is integral gain, K_d is derivative gain, $u(t)$ is total control output and t is the time variable. Total control output, $u(t)$ will be used to compensate and adjust the system back to its desired position.

2.2 Control Method

In this project, PI control is used instead of PID. K_p and K_i value are tune using trial-and—error method [11]. There are a few step need to be follow to obtain PI parameter for stable PI control. The tuning methodology is as shown below [12]:

Methodology (Tuning):

1. At first, all of the parameters, K_p , K_i and K_d is set at zero.
2. Then, run a program to the Arduino board with K_p equal to 1 and see its output.
 - a. At most of the time, the output is an oscillation with certain amplitude and time required to reach the desired angle.
 - b. At this time, K_i and K_d is set to zero.

3. The K_p value is vary until a the oscillation is in a very small amplitude or oscillation with standard deviation of only 1° . (This is a trial-and-errors method in which the value of K_p can be increase or decrease depend on the oscillation.)
4. Step 3 is repeated until the system is oscillate with a very small amplitude.
5. After getting the right value of K_p , the tuning is continue with K_i parameter.
6. The value of K_p is remain and the program is run with K_i equal to 0.2.
 - a. At this time, K_d is set to zero.
7. After step 6, the system may oscillate with a higher amplitude or remain unchanged.
8. If the system remained unchanged, it mean that the K_i value is too small to activate its function. At this time, the value of K_i will be increase with 0.05 increment until it oscillate with certain amplitude.
 - a. The oscillation amplitude can be low or high.
 - b. Once, the system start to oscillate, it means that K_i parameter start to function in that PI control system. At this time, the amplitude of oscillation is reduced by better tuning of the value, K_i .
9. The value of K_i is vary until the system is oscillate with a very low amplitude or no oscillation.
10. The tuning process is finish after obtaining control parameter value of K_p and K_i .

2.3 Mechanism of Biped Walking Robot

Simple biped walking robot is fabricated as a hardware to test the function of PI control system. To minimize the complexity of the control system and reduce the errors during the implementation, the design of robot is prefer to have low number of degree of freedom as long as it can perform walking and downstairs action. The total DOF for the biped walking robot of this project is 3 DOF for each leg.

Reason of choosing 3 DOF for each leg:

- Easy to control
- Least number of DOF that still manage to performs downstairs action
- Reduce the use of servo for cost saving
- Reduce the use of servo to reduce failure occur due to low quality servo (cheaper)
- Reduce the weight of the robot since one DOF equal to one servo and servo is heavy in term of small robot (Fig. 2).

Limitation of 3 DOF leg:

- The movement is less simulated as human.
- Some of the actions such as climbing upstairs is hardly to perform.

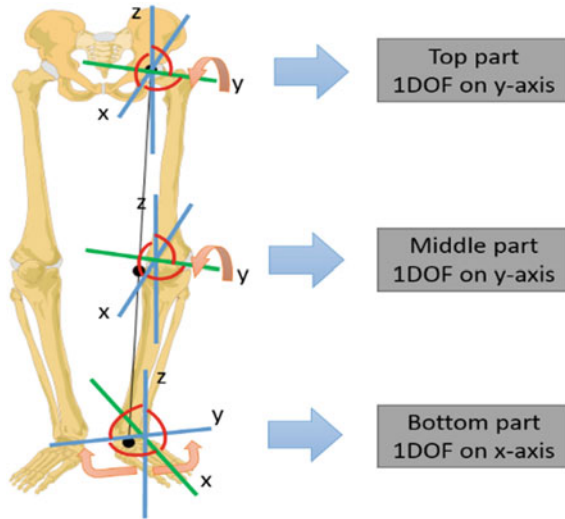


Fig. 2 Location of each DOF

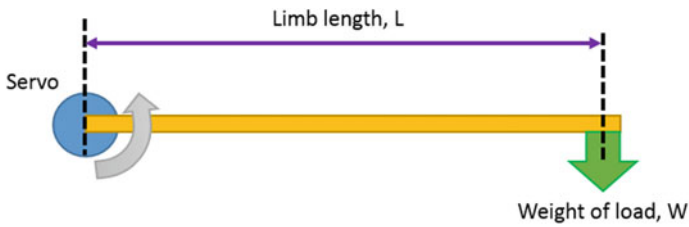


Fig. 3 Relationship between limb length, weight of load and torque from servo

- The center of mass (COM) is easily deviated from the support polygon since some of the stable posture cannot be performed due to lack of degree of freedom.

2.4 Servo Selection Based on the Stall Torque Required

$$\text{Stall torque required} = W \times L \times SF \tag{2}$$

where W is weight of load, L is the limb length and SF is the safety factor (Fig. 3).

The weight of load depends on the weight of a robot's leg, whereas limb length is based on the design. The servo selected needs to have a stall torque higher than the required stall torque calculated so that it is able to lift the leg upward [13].

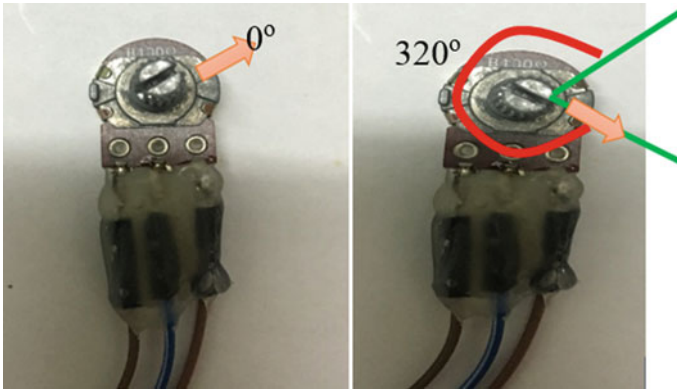


Fig. 4 Potentiometer calibration

2.5 Center of Mass Calculation

Center of mass is calculated for walking gait planning. To maintain stability, robot need to have its center of mass above its current support polygon when it is performing any action [14–16].

$$\text{Centre of mass} = \frac{m_1x_1 + m_2x_2 + m_3x_3 + \dots}{m_1 + m_2 + m_3 + \dots} \tag{3}$$

where m_1 is mass 1, m_2 is mass 2, m_3 is mass 3, x_1 , x_2 and x_3 is the distance from reference point.

2.6 Calibration of Servo and Potentiometer

Potentiometer used is not able to perform 360° of rotation. Therefore, calibration required to obtain the maximum and minimum value of bytes that can be read by Arduino through computer for calculation of actual angle of the joint at particular time (Fig. 4).

$$\text{Actual angle} = \frac{\text{Signal value at certain angle} - \text{minimum value (potentiometer)}}{\text{Maximum value (potentiometer)} - \text{minimum value (potentiometer)}} \times 180^\circ \tag{4}$$

Servo brand MG996R have angle variation. They are not able to move to the same angle position even the same bytes value is given. Therefore, calibration is done to obtain the value of bytes per 1° for each of the servo (Fig. 5).

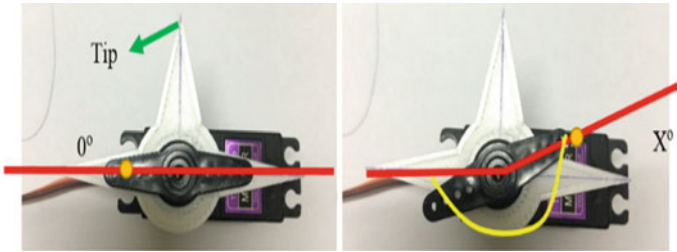


Fig. 5 Servo calibration

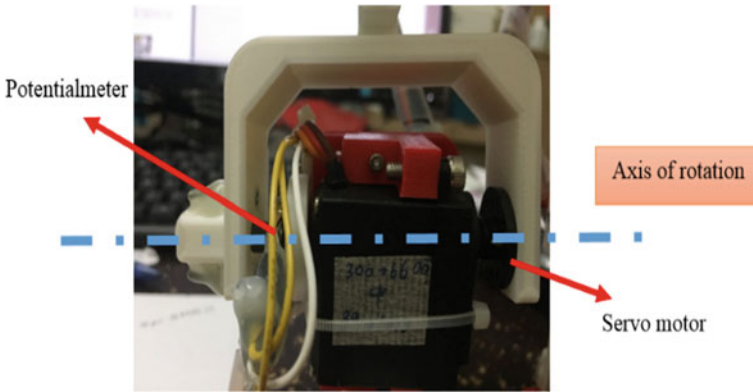


Fig. 6 Position of servo and potentiometer

$$\text{Value of bytes per } 1^\circ = \frac{\text{Maximum value (servo)} - \text{minimum value (servo)}}{X} \tag{5}$$

where X° is the angle measured from 0° to random angle position greater than 180° .

The calibration result for potentiometer and servo is involved in mathematical equation of PI control algorithm. During the fabrication, servo (actuator) and potential meter (sensor) need to attach with their rotating part located at the same axis for PI control to function (Fig. 6).

3 Experimental Result

3.1 Calibration Result of Servo and Potentiometer

Tables 1 and 2 provide the information for mathematical equation in PI control programming code.

Table 1 Calibration result of servo

SERVO	Minimum value (servo)	Maximum value (servo)	Angle, X°	Value of bytes per 1°
Servo 1	110	7000	181	38.0663
Servo 2	150	6900	174	38.7931
Servo 3	120	6900	189	35.8730
Servo 4	110	6800	179	37.3743
Servo 5	105	6900	189	35.9524
Servo 6	110	6900	189	35.9259

Table 2 Calibration result of potentiometer

Potentiometer	Minimum value (PM)	Maximum value (PM)	Bytes value read from sensor when it is in position of 90°
PM 1	13	1010	512
PM 2	7	1012	510
PM 3	7	1009	508
PM 4	14	1002	508
PM 5	7	1016	512
PM 6	19	1008	514

Values of bytes per 1° will multiply by the desired angle value and this output bytes value will move servo motor to that desired angle with poorer angle accuracy. From Table 1, value of bytes per 1° are varies between each servo but it is not able to affect the angle accuracy with PI control. With PI control, servo will only move to the position according to the angle position detected by potentiometer.

Similar to servo, each potentiometer detected different bytes value at different angular position. Even there is an error range of 6 bytes, but this is too small to affect the control system. Therefore, this error can be negligible. Calibration of potentiometer is the most critical part for angle accuracy. If the desired angle is 90°, with PI control, servo 1 will continue to move and adjust until potentiometer, PM 1 read a bytes value of 512. This is the concept how servo coordinating with servo to perform angular movement with high angle accuracy.

3.2 Error of Angle Accuracy After PI Control

After applying PI control, the angle move by the servo will be more accurate. The output angle will be approaches to the theoretical angle (desired angle). In this project, PI control coding is wrote to the servo to allow it to move to certain angle which are 60°, 70°, 80° and 90° and the errors are measured using two methods which are by protractor and through the potentiometer bytes reading.

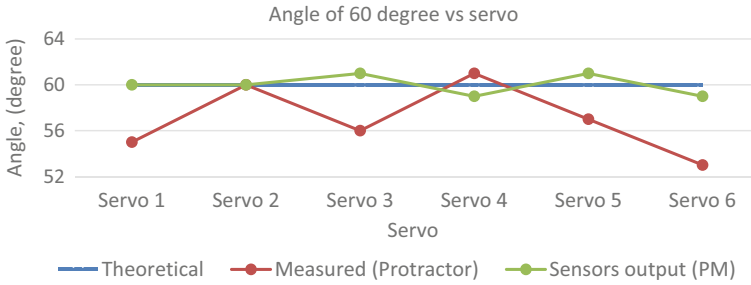


Fig. 7 Angle of 60° versus servo

From Fig. 7, the angle detected by the sensors is only plus minus 1° standard deviation between the theoretical values. In this project, the servo is calibrated together with the potentiometer (sensor). The servo will continue to rotate to allow the sensors output to be exactly the same as the theoretical angle. This is the main purpose of applying PI control in the angle accuracy control of servo. Even there is a small angle different of 1°, but the PI control is still considered successful. PI control is not able to totally make the system to be stable only at one point, there will be a very small fluctuation which is small enough to be neglected. The amplitude of small fluctuation at the stable condition is depend on precision and accuracy of the actuator and sensors used. In this project, the small fluctuation is about 1°. This is also caused by limitation of the precision of the servo and servo controller. The bytes value need to write into the servo controller is accurate but the servo do not move with a very small increment of bytes value. For example, servo currently is in 59° with a bytes value input of 2333 bytes. To achieve 60°, PI control give 39 bytes more to 2333 bytes which is 2372 to the servo but servo do not move and maintain at 59°. The calculation of PI control is correct and appropriate but it may not enough to move the servo for 1° more. Integral term in PI control allow the system to increase the bytes value input until the servo move for 1°–60°. In practically, the servo which need to move to 60° will keep the chance to move to 59°, 60° or 61°. The 1° fluctuation may occur due to a few external and internal effect. Internal effect is regarding the design limitation of the servo whereas the external effect can be wind condition and external force applied. The external force is the normal reaction force of biped robot itself, inertia during motion and weight of the body. Furthermore, PI is not able to reduce completely the remained very small fluctuation when the system order is high. Unfortunately, this statement cannot be justify in this project because the project is done by practical method of trial-and-error and some simple calculations. There are no evidence to prove that the system used for the biped robot is in high order or low order. Other than 60°, the 70°, 80° and 90° also show the same trend of error as 60°. The result is as shown in Figs. 8, 9 and 10.

From Fig. 11, there is a great range of error between measured angle and theoretical angle at 60° which is 8°, follow by 9° for analysis at 70°, 8° for analysis at 80° and 10° for analysis at 90°. This error is a zero error. It can be caused by human error

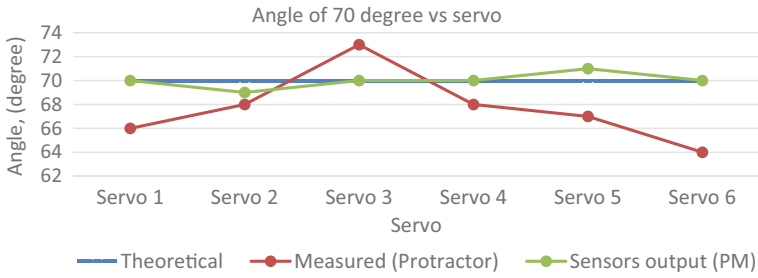


Fig. 8 Angle of 70° versus servo

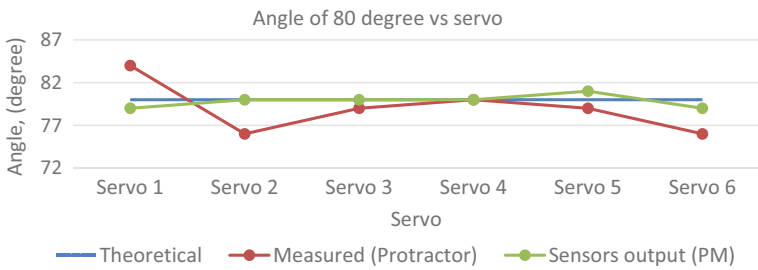


Fig. 9 Angle of 80° versus servo

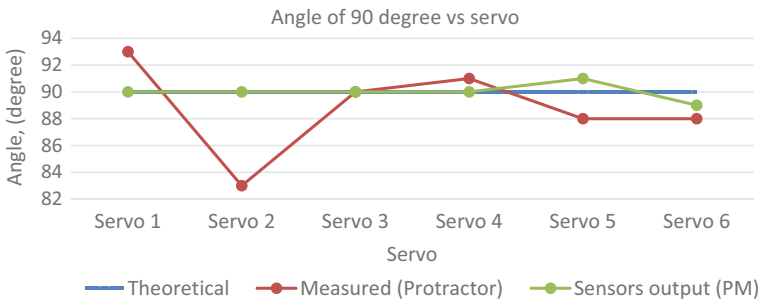


Fig. 10 Angle of 90° versus servo

when measuring the angle using protractor. The human errors involve parallax error and misalign during measurement. From the observation during the trial-and-error coding method, the limb do not go to the 90° position when the coding for 90° is given. There is some obvious angle deviation shown between actual and theoretical position. The major error of this deviation is actually caused by the failure during calibration. The 90° calculated from the input of the sensors is not equal to the theoretical 90° that need to be achieved by the robot. This error can be reduced or become zero by adjusting the position of the potentiometer to make sure that calculated value from sensors input for 90° is exactly the same as the desired position at 90° for that joint.

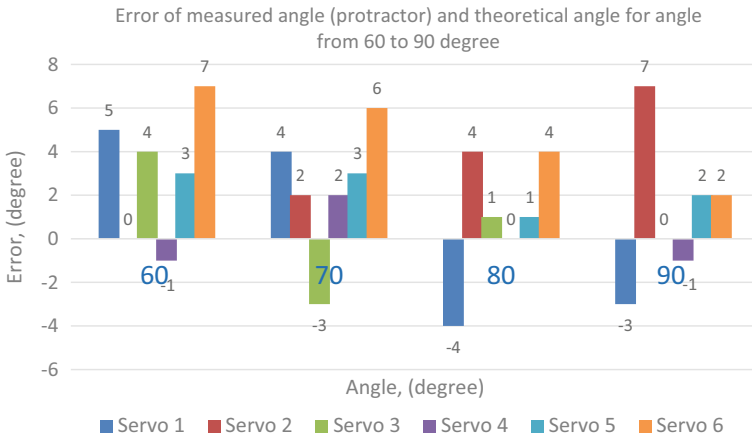


Fig. 11 Error of measured angle (protractor) and theoretical angle for angle from 60° to 90°

In this project, the problem is solve by involving this zero error into the programming code and test it using trial-and-error method.

3.3 Effect of PI Control on the Angle Accuracy

In this project, PI control system is used instead of PID. From the research, derivative control is rarely used in controlling process. It is not absolutely required because it is very sensitive to the noise and very hard to tune [17]. Derivative control can function to make the control loop respond a little faster than PI control alone. Nevertheless, PI control is enough for controlling servo accuracy since servo itself can react very fast to the designated position. The PI control is an enhancement of the servo function to make sure servo move to a theoretical angle accurately. In this subtopic, we will discussed about the effect of PI control toward the servo angle accuracy as well as the fluctuation of the system at different value of K_p and K_i . Figure 12 show the servo output before the implementation of PI control. Inside the figure, six of the servos are allowed to move to 90° and the angle position is calculated from the bytes value obtained from potentiometer (sensors) of each set of servo.

From the graph, six of the servos show $\pm 5^\circ$ of offset from the theoretical value of 90°. These different are caused by the error of the servo in performing its function. This is the reason why PI control need to be implemented to eliminate the offset error of the servo and allow servo always move to the desired angle accurately. Figure 13 shows the implementation of proportional control alone and the effect of different K_p value to the system.

High K_p value of 2.45 making the system fluctuating with a high amplitude. When K_p value is reduce to 1.85, the system continue to fluctuate with high amplitude but

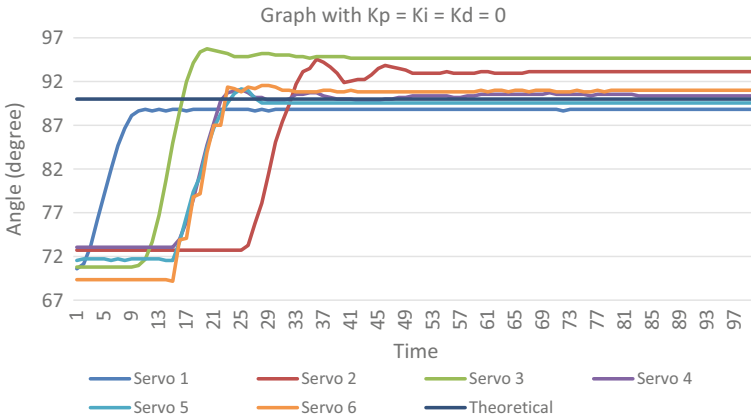


Fig. 12 Graph with $K_p = K_i = K_d = 0$

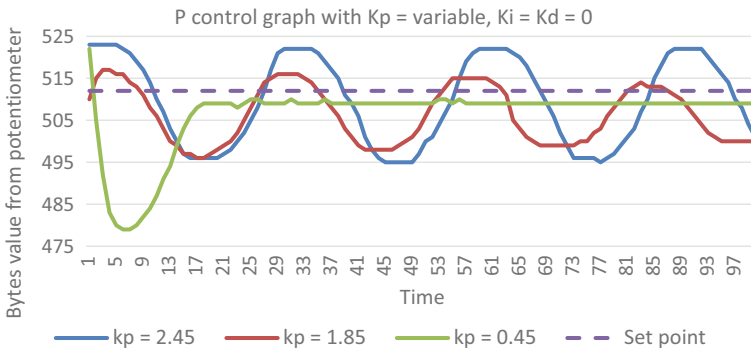


Fig. 13 P control graph with $K_p = \text{variable}, K_i = K_d = 0$

smaller magnitude when compare to $K_p = 2.45$. The value of K_p is continue to reduce until it reach a stable state in which the system is not oscillated [18]. After tuning, the optimum K_p value is 0.45. In this project, servo is attach with potentiometer, the bytes value detected by the potentiometer is instantly changed according to the movement of the servo, offset is less likely to occur even only proportional control is used. Nevertheless, the proportional control graph continue to show the occurrence of "Offset". From Table 1, servo need 35–39 bytes for 1° of rotation. Nevertheless, Fig. 13 show a very small offset value of 3 bytes and this bytes value is actually not enough to move the servo. This is a hardware limitation in which a very small offset cannot be completely eliminated. Other than that, there might have chance that servo already move with an extremely small angle but not detected by potentiometer since it is too small for the potentiometer to rotate. The potentiometer remain the same position. This is another hardware limitation of potentiometer. In calculation, 3 bytes is also too small to affect the angle calculated. Therefore, we can conclude

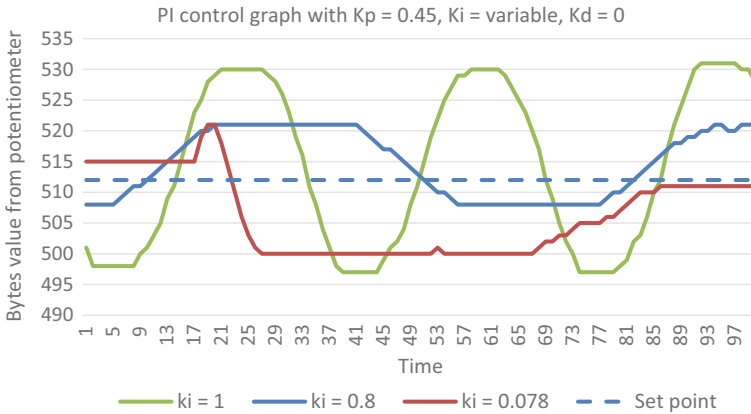


Fig. 14 PI control graph with $K_p=0.45$, $K_i = \text{variable}$, $K_d=0$

that the proportional control is actually enough for servo angle accuracy controlling. In this project, the effect of integral term toward the system is also studied [17, 19]. Figure 14 shows the effect of Proportional-Integral (PI) control with correctly tune K_p value and variable K_i value.

From the graph, when K_i value is large, the fluctuation is large [20]. This is due to the overshoot effect in which the PI output is large enough to exceed the desired value back and for. PI output is reduced when lower value of K_i is used. Therefore, K_i value is continuously reduced until an optimum value in which the system is stable and not oscillate. In this project, the optimum value for K_i is 0.078. From the graph, after applying $K_p=0.45$ and $K_i=0.078$, the system is stable in 1–2 s and approaches to the desired value. Nevertheless, there is an extremely small offset of 1 bytes occur in the system. Similar to P control, PI control show the same offset error with a same reason as P control system. Therefore, we can conclude that P control or PI control are suitable for angle accuracy control [21].

4 Conclusion

Proportional-Integral (PI) control system is successfully implemented. The robot is designed with six degree of freedom (6DOF) and able to perform walking and downstairs action. From the result of calibration, each of the servo and potentiometer having their own minimum and maximum limits. All of the data are tabulated and involved in mathematically calculation of PI control to reduce the angle error. According to the type of servo used, a draft dimension of robot is drawn and calculation is done on center of mass (COM) and stall torque required by servo. From the calculation, the COM is about (47.5, 105, 177.66) mm from the reference point

and the servo (MG996R) is suitable. Beside, the whole robot body is built by using additive 3D printing technology for a lighter weight.

Proportional control alone and proportional-integral control are studied to know the effect of these PI control toward the servo angle accuracy. The angle accuracy is studied for before and after the implementation of the control system. From the result, the angle may deviate $\pm 5^\circ$ from the desired angle when there is no control system implemented to better control the rotation angle of the servo. Nevertheless, the servo able to move to the desired angle position after implemented proportional control or proportional-integral control. According to the angle position detected from the sensors of the robot, both proportional control and proportional-integral control show the similar output. Due to the design of position of the hardware, there are no offset occur even proportional control alone is implemented. In conclusion, the design of biped walking robot in this experiment is able to function well in proportional control or proportional-integral control.

After implementation of PI control and error analysis, a simple walking gait is designed and programming code for walking and downstairs action are write and uploaded to the robot. From the observation, the robot can function well with a more accurate joint angle especially the leg lifting action. The project of PI control on biped walking robot servo angle accuracy control is considered successfully implemented.

Acknowledgements The author acknowledges the technical support and guidance from supervisor, Prof. Madya Dr. Mohd Zarhamdy bin Md. Zain and appreciates Universiti Teknologi Malaysia (UTM) for providing facilities and education.

References

1. Lim, H.O., Tajima, K.: Mechanism and control of biped walking robot with 3 DOF waist. In: International Conference on Control, Automation and Systems, pp. 2026–2031 (2008)
2. Ogura, Y., Aikawa, H., Lim, H.O., Takanishi, A.: Development of a human-like walking robot having two 7-DOF legs and a 2-DOF waist. In: Proceedings of IEEE International Conference on Robotics and Automation, pp. 134–139 (2004)
3. Inoue, H., Tachi, S., Nakamura, Y., Hirai, K., Ohyu, N., Hirai, S., Hirukawa, H.: Overview of humanoid robotics project of METI. In: Proceedings of the 32nd International Symposium on Robotics, pp. 1478–1482 (2001)
4. Kaneko, K., Kajita, S., Kanehiro, F., Yokoi, K., Fujiwara, K., Hirukawa, H., Iozumi, T.: Design of advanced leg module for humanoid robotics project of METI. In: Robotics and Automation Proceedings, pp. 38–45 (2002)
5. Yano, T., Lee, J.H., Okamoto, S.: Walking experiment of biped robot with antagonistic actuation using non linear spring. In: Proceedings of Multi Conference of Engineers and Computer Scientists, vol. 1 (2016)
6. PID Controller, https://en.wikipedia.org/wiki/PID_controller. Last accessed 2018/05/22
7. Honeywell, D.: PID Control. Industrial Control (2000)
8. Astrom, K.J.: PID Control. Control System Design (2002)
9. Different PID Equations, <http://amechatronics.com/notes/general-engineering/449-different-pid-equations>. Last accessed 2016/06/15
10. Zhang, J., Cao, W.: Analysis of PID control based on the balance equation. In: IEE Control Conference (CCC), pp. 6472–6477 (2017)

11. Hing, M.M.: Introduction to Robotic Systems & Control. Penerbit UTM Press (2017)
12. What are good strategies for tuning PID loops, <https://robotics.stackexchange.com/questions/167/what-are-good-strategies-for-tuning-pid-loops>. Last accessed 2012/10/2009
13. PID controllers in bestune, <http://bestune.50megs.com/PIDs.htm>. Last accessed 2012/10/12
14. How to calculate servo torque, <https://www.rcgroups.com/forums/showthread.php?1194285-How-To-Calculate-Servo-Torque>. Last accessed 2010/02/15
15. Center of mass, https://en.wikipedia.org/wiki/Center_of_mass. Last accessed 2018/04/25
16. What is center of mass, <https://www.khanacademy.org/science/physics/linear-momentum/center-of-mass/a/what-is-center-of-mass>. Last accessed 2016/05/06
17. Center of mass, https://isaacphysics.org/concepts/cp_centre_mass. Last accessed 2018/02/05
18. Smuts, J.: PID control modes. In: Smuts, J.F. (ed.) Process Control for Practitioners, pp. 77–96 (2011)
19. PID Control (with code), Verification, and Scheduling, <http://robotsforroboticists.com/pid-control/>. Last accessed 2014/09/22
20. PID Theory Explained, <http://www.ni.com/white-paper/3782/en/>. Last accessed 2011/03/29
21. Sena Temel, S.Y.: PI Controller. P, PD, PI, PID Controllers, 3–6, 14–30 (2013)

Improved Generalized Cross Correlation Phase Transform Algorithm for Time Difference of Arrival Estimation



Chee Sheng Tan, Rosmiwati Mohd-Mokhtar and Mohd Rizal Arshad

Abstract In this paper, we proposed an improved Generalized Cross-Correlation Phase Transform (GCC-PHAT) based on segmentation to estimate a time difference of arrival (TDOA). Traditionally, a GCC-PHAT computes the TDOA between two signals for a given segment in a complete signal. A computation of the TDOA is repeated on every segment between a pair of sensors. A time delay is estimated after a cross-correlation between two segments of signals in the frequency domain. However, in this study instead of the cross-correlation between two signals from segment to segment, this approach is selecting a segment that contains a frequency of interest within the signals. Both selected segments do not need to be aligned for implementation of the cross-correlation. The TDOA estimation is derived based on an intensity of a received signal with the frequency of interest after computing the GCC-PHAT. According to an experimental result, a proposed method is successfully validated on a real data containing a base signal that are recorded from a hydrophone.

Keywords Generalized cross-correlation phase transform (GCC-PHAT) · Segmentation · Time difference of arrival (TDOA)

1 Introduction

The TDOA estimation based on the generalized cross-correlation (GCC) has been widely utilized in an underwater positioning and localization system [1]. A sharpen peak of correlation between two signals represent a time lag between them. An

C. S. Tan · R. Mohd-Mokhtar (✉) · M. R. Arshad
Underwater Control Robotics Research Group, School of Electrical and Electronic Engineering,
Engineering Campus, Universiti Sains Malaysia, 14300 Nibong Tebal, Seberang Perai Selatan,
Pulau Pinang, Malaysia
e-mail: eeerosmiwati@usm.my

C. S. Tan
e-mail: tancheesheng@hotmail.com

M. R. Arshad
e-mail: eerizal@usm.my

accuracy is improved as compared to a traditional cross-correlation [2]. However, a disadvantage of utilizing the GCC on the TDOA estimation is that it is easily influenced by a noise and reverberation [3]. It is the most significant challenge for the TDOA estimation.

There are various weighting functions that can be selected to optimize the sharp edge performance. Typically, two input signals are converted into the frequency domain and its cross-spectrum between two signals is applied by an interested weight. Then, the generalized cross-correlation function (GCCF) is obtained after an inverse is transformed back to the time domain. The generalized cross-correlation with phase transform (PHAT) weighting is the most accurate in a low noise environment [4, 5].

In this paper, the improved GCC-PHAT based on segmentation is proposed. The aim is to improve the accuracy for time difference of arrival estimation during the underwater positioning or localization. Overall, this paper will be discussed as follows. Section 2 will elaborate on the Cross Correlation (CC) and the GCC-PHAT approach as well as method to be used and the segmentation based procedure. Results and discussion will be shown in Sect. 3. Finally, Sect. 4 gives a conclusion of the paper.

2 Approach and Methods

2.1 CC and GCC-PHAT

The cross-correlation refers to a similarity between two signals received from the hydrophones. The GCC-PHAT based sound source tracking is the most famous in the time delay estimation due to advantage of reducing computational load [6, 7]. The GCC-PHAT method is briefly described as follows. Let $x_1(t)$ and $x_2(t)$ are the signals received from two hydrophones, continuous time signals are converted into discrete signals, $x_1[n]$ and $x_2[n]$ by sound cards as shown in Eqs. 1 and 2.

$$x_1[n] = s[n] + \gamma_1[n] \quad (1)$$

$$x_2[n] = s[n - t_d] + \gamma_2[n] \quad (2)$$

where t_d is the time delay in discrete form, $s[n]$ is a source signal, $\gamma_1[n]$ and $\gamma_2[n]$ are noises that induced by surrounding. The discrete signals are implemented with a Hanning window as to reduce a spectral leakage. The time domain signals are converted into the frequency domain by a Fast Fourier Transform (FFT) for cross-correlation. The cross-correlation equation is obtained by Eq. 3 after implementing the inverse Fourier transform. $\vartheta(\omega)$ is the frequency weighting function where $\vartheta(\omega) = 1$ for CC method.

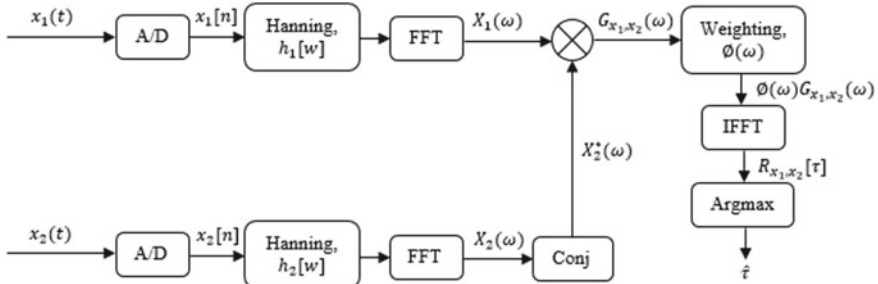


Fig. 1 Block diagram of GCC-PHAT

$$R_{x_1, x_2}(\tau) = \frac{1}{2\pi} \int_{-\infty}^{\infty} \phi_{\omega} G_{x_1, x_2}(\omega) e^{i\omega\tau} d\omega \quad (3)$$

$$\phi(\omega) = \frac{1}{|G_{x_1, x_2}(\omega)|} \quad (4)$$

$$\hat{\tau} = \arg \max R_{x_1, x_2}(\tau) \quad (5)$$

In GCC-PHAT, a weighting function to estimate the time delay is expressed as Eq. 4. However, an error will be increased as a denominator tends to be zero under the low signal to noise ratio (SNR). The delay time between two signals, $\hat{\tau}$ is determined by a maximum value of correlation as shown in Eq. 5. The block diagram of the generalized cross-correlation and the TDOA estimation between two hydrophones is shown in Fig. 1.

2.2 Segmentation

The proposed method requires two additional steps to compute the TDOA as shown in Fig. 2. Two signals are split into several segments and each segment is converted into the frequency domain by performing the FFT. For each signal, two segments that involve the frequency of interest are selected to implement the GCC-PHAT. 2048 samples are required from each signal for computing the cross-correlation. A correlation peak can be obtained after implementing the inverse FFT. The time delay of the hydrophone pair of the received signals can be estimated by using Eq. 6.

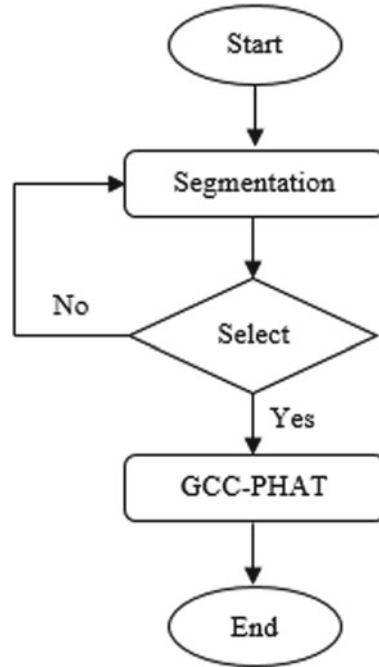


Fig. 2 Flow chart of GCC-PHAT based on segmentation

$$TDOA = \frac{N(S_{FFT2} - S_{FFT1}) + \varphi}{f_s} \quad (6)$$

where S_{FFT1} and S_{FFT2} are the first segment within two segments that involved the frequency of interest with respective the hydrophone 1 and the hydrophone 2, N is a number of samples based on segmentation and φ is a lag between the hydrophone pairs.

3 Results and Discussions

For experimental verification, the improved GCC-PHAT algorithm based on segmentation is tested to estimate the TDOA. Two input signals are generated and recorded in a real environment and they are shown in Fig. 3. The whole signals are sampled using a sampling rate of 96 kHz within the time period of 0.1 s (9600 samples). The frequency of a base signal (without noise) is 16.5 kHz and it is continuously emitted for 0.01 s.

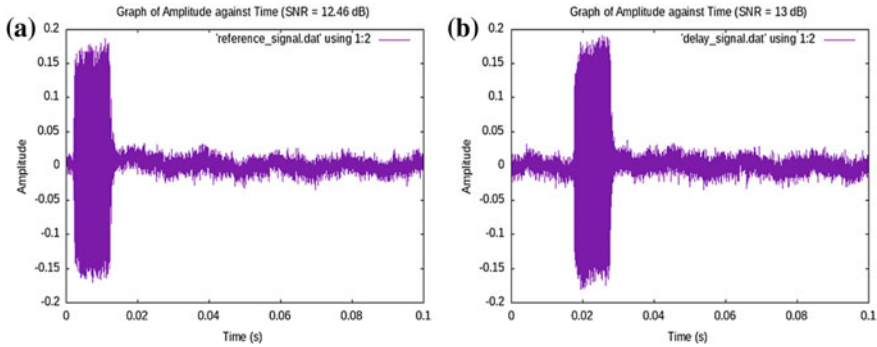


Fig. 3 Amplitude against time signal recorded in the real environment. **a** Reference signal (SNR = 12.46 dB), **b** delay signal (SNR = 13 dB)

Table 1 The comparison of computational time in millisecond

TDOA algorithms	Number of correlation	Computational time (ms)
Traditional GCC-PHAT	4	44.133
Proposed GCC-PHAT	1	29.012

The segmentation method is applied to a reference signal and a delay signal as shown in Fig. 4. Each segment is processed by the FFT with 1024 samples and a spectrum of an output signal is shown in Fig. 5. This method is used to obtain a local maximum of the frequency of interest. The results show that only the first segment and a second segment contain the base signal for the reference signal, whereas the second segment and a third segment contain the base signal for the delay signal.

The GCC-PHAT is carried out on the segments from two signals that contain the base signal (2048 samples). In Fig. 6a, there is a peak of correlation that represents the maximum of phase delay after comparing two segments. The figure shows that the position of the maximum peak is located at 459. The delay time can be determined by using Eq. 6 since both segments are not aligned. Figure 6b shows that the delay time between the reference signal and the delay signal is 0.015448 s. An actual TDOA is 0.015 s, which means that a measurement error of 2.99% is observed. This indicates that the proposed GCC-PHAT able to give almost accurate TDOA estimation for the tested signals. Table 1 shows the comparison of computational time between the traditional GCC-PHAT and the proposed method. It can be seen that the computational time has been reduced by 34.26%. The reduced computational time while maintaining good accuracy of estimation, is very important for improved performance during underwater positioning and localization.

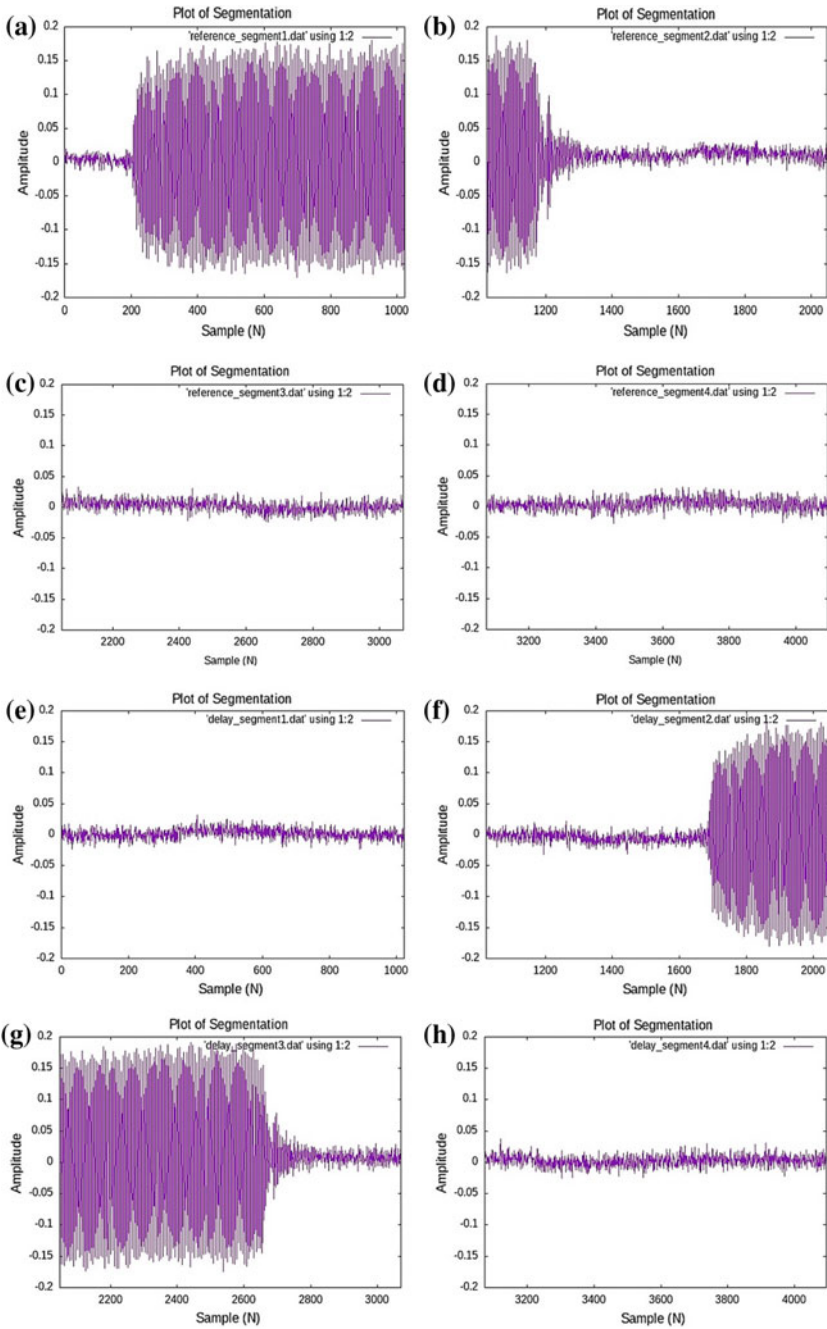


Fig. 4 Signals are divided into several segments with 1024 samples. Reference signal, **a** 1st segment (0–1023 samples), **b** 2nd segment (1024–2047 samples), **c** 3rd segment (2048–3071 samples), **d** 4th segment (3072–4095 samples), and Delay signal, **e** 1st segment (0–1023 samples), **f** 2nd segment (1024–2047 samples), **g** 3rd segment (2048–3071 samples), **h** 4th segment (3072–4095 samples)

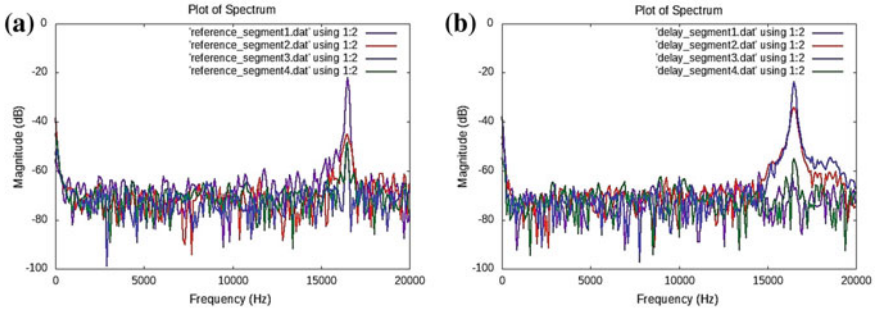
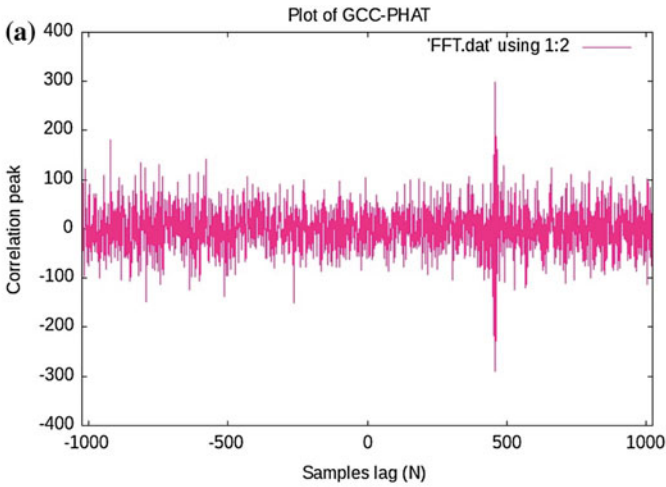


Fig. 5 Performing FFT processing on all segments. **a** Frequency spectrum of reference signal, **b** frequency spectrum of delay signal



(b)

```
Segmentation
Reference signal --> 1st highest peak : 1 th segment
                  --> 2nd highest peak : 2 th segment
Delay signal    --> 1st highest peak : 3 th segment
                  --> 2nd highest peak : 2 th segment
S_FFT1 = 1 th, S_FFT2 = 2 th

GCC PHAT
lag = 459, delay = 0.015448 s
```

Fig. 6 Experimental result. **a** Improved GCC-PHAT, **b** TDOA

4 Conclusion

This paper proposed the time difference of arrival estimation by using the improved GCC-PHAT based on segmentation. From this study, the method has successfully reduced a computational time for the system as well as it can provide the low latency of the delay time estimation after the signals are received. In this project, the experimental results have indicated that the proposed system able to provide with accurate TDOA estimation in the real underwater environment.

Acknowledgements This project is supported by a FRGS Grant: 203/PELECT/6071291. Authors would like to thank Universiti Sains Malaysia for providing a necessary tools and an instrumentation to conduct a research. A permission given especially during the experimental testing is truly appreciated.

References

1. Valente, J.F., Alves, J.C.: Real-time TDOA measurements of an underwater acoustic source. In: Proceedings of the OCEANS 2016 MTS/IEEE Monterey, CA, USA, pp. 1–7, (2016)
2. Chen, J., Benesty, J., Huang, Y.: Time delay estimation in room acoustic environments: an overview. *EURASIP J. Appl. Sig. Process.* 1–19 (2006)
3. Abutalebi, H.R., Momenzadeh, H.: Performance improvement of TDOA-based speaker localization in joint noisy and reverberant conditions. *EURASIP J. Adv. Signal Process.* 1–13 (2011)
4. Shome, S.: On methods to improve time delay estimation for underwater acoustic source localization. *Indian J. Geo-Marine Sci.* **44**(2), 237–244 (2015)
5. Arifianto, D., Wirawan, Atmaja, B.T., Dhanardhono, T., Rahman, S.A.: Azimuth tracking of underwater moving sound source based on time delay estimation using hydrophone array. *Procedia Eng.* **170**, 169–176 (2017)
6. Hoseini, S., Rezaie, A., Zanjireh, Y.: Time difference of arrival estimation of sound source using cross correlation and modified maximum likelihood weighting function. *Sci. Iran.* **24**(6), 3268–3279 (2017)
7. Perez-Lorenzo, J.M., Viciano-Abad, R., Reche-Lopez, P., Rivas, F., Escolano, J.: Evaluation of generalized cross-correlation methods for direction of arrival estimation using two microphones in real environments. *Appl. Acoust.* **73**(8), 698–712 (2012)

Performance Evaluation of PID Controller Parameters Gain Optimization for Wheel Mobile Robot Based on Bat Algorithm and Particle Swarm Optimization



Nur Aisyah Syafinaz Suarin, Dwi Pebrianti, Nurnajmin Qasrina Ann,
Luhur Bayuaji, Muhammad Syafrullah and Indra Riyanto

Abstract Tuning Proportional Integral Differential (PID) controller to the best value of gains is essential to develop a reliable controller for wheel mobile robot (WMR). WMR is a nonlinear system that falls into category of underactuated system where the inputs number is less than output number. The selection of PID gains for such system is highly difficult. Optimization of PID controller using Bat Algorithm (BA) is presented in this paper. BA as a nature inspired algorithm is used to search the optimum PID gains for wheel mobile robot i.e. an off-the-shelf mobile robot called mBot so that the system will have good performance in term of steady state error and time response. Kinematic model of mBot robot is used to develop a simulation model to simulate the system. The result of tuning and optimizing PID gains using BA is compared with Particle Swarm Optimization (PSO). The tuning result by using BA outperformed PSO methods with faster processing time and best values of gain K_p and K_d to be applied in the WMR. The PID gain values obtained from the BA and PSO are then applied on the WMR model. The performance of BA shows better result compared to PSO. Settling time for BA is 10.62 s compared with PSO 11.1 s, rise time for BA is 3.24 s while PSO 2.68 s, percentage overshoot of BA 28.2% compared with PSO 28.4%. Thus, the result proven that BA is able to optimize gain of PID controller better than PSO.

N. A. S. Suarin · D. Pebrianti (✉) · N. Q. Ann
Faculty of Electrical and Electronics Engineering, Universiti Malaysia Pahang, Pekan, Malaysia
e-mail: MEG18002@stdmail.ump.edu.my; dwi Pebrianti@ump.edu.my

N. A. S. Suarin
e-mail: syahfinaz01@gmail.com

L. Bayuaji
Faculty of Computer Science and Software Engineering, Universiti Malaysia Pahang, Pekan,
Malaysia

D. Pebrianti · L. Bayuaji · M. Syafrullah
Magister of Computer Science, Universitas Budi Luhur, Jakarta 12260, Indonesia

I. Riyanto
Faculty of Engineering, Universitas Budi Luhur, Jakarta 12260, Indonesia

Keywords Bat algorithm · Underactuated system
Proportional integrated differential controller

1 Introduction

Recently, research on underactuated system becomes increasing rapidly. This is because most of systems existing in human life fall into this category. Underactuated system refers to a system that has more Degree of Freedom (DoF) compared to the existing actuators in the system. Wheel Mobile Robot (WMR) is one of the examples of the underactuated system. In WMR, there are two actuators which are left and right motors. Meanwhile, the output of the system is the movement of forward – backward, movement of left – right and also attitude or known as heading.

Based on the literatures, it is clearly seen that to control an underactuated system is a highly difficult task. This is because most of the controller has some parameters need to be tuned precisely. The tuning process is considered to be an optimization problem. Some of swarm intelligence optimization algorithms used for controller design are Genetic algorithm [1], Particle Swarm Optimization [2, 3], Bacteria Foraging Optimization [4], Cuckoo [5], Ant Colony Algorithm [6, 7], etc. Most of these algorithms are designed to solve the optimization in controller design by considering the system is Single Input Single Output (SISO) system. Underactuated system is considered as a Multi Input Multi Output (MIMO) system where the input and output numbers are more than one. Therefore, in this study, Bat Algorithm (BA) is proposed to deal with the controller design of underactuated system.

PID controller is a classical controller and frequently applied in underactuated control system. Process control, motor drivers and instrumentation prefer the application of PID controller on the system due to its simple structure which can be easily understood and implemented. Chia et al. [8] introduced an educational method by develop a portable PID control learning tool to tune PID for mobile robot. The method is good for beginner and student to learn the basic of PID tuning. However, in order to apply PID to other application with high complexity, obtaining optimized value of gains during PID tuning in short time is necessary.

Bat Algorithm is effectively applied in solving optimization problem including engineering design, image processing and feature selection. BA is applied in fuel arrangement optimization of reactor core which was researched by Kashi et al. [9] The result is promising to implement BA into loading pattern optimization of nuclear core. Some modification to the original BA was proposed by Latif and Palensky [10] and applied to optimize the economic dispatch problem. Sambariya and Prasad [11] applied BA to optimize the design of conventional power system stabilizer. Thus, BA is convincing and worth to try and apply to optimizing PID controller.

The paper will be divided into 4 sections. Section 1 is the introduction. Section 2 will discuss about the research method. The detail explanation about the WMR mathematical model, PID controller design and BA will be presented. Section 3 is the simulation result and discussion. The result of BA tuning process, the performance

of PSO tuning process, time response analysis and steady state error analysis will be discussed in this section. Section 4 will be the conclusion and future works.

2 Research Method

This section will cover the Wheel Mobile Robot (WMR) mathematical modeling, Proportional Integral Differential (PID) controller design and Bat Algorithm (BA) optimization for the tuning process and last but not least is how the simulation is conducted. Kinematic model is used in this study. Some modification in fitness function that is used by BA to search for the optimum values of PID gain is also explained in this section.

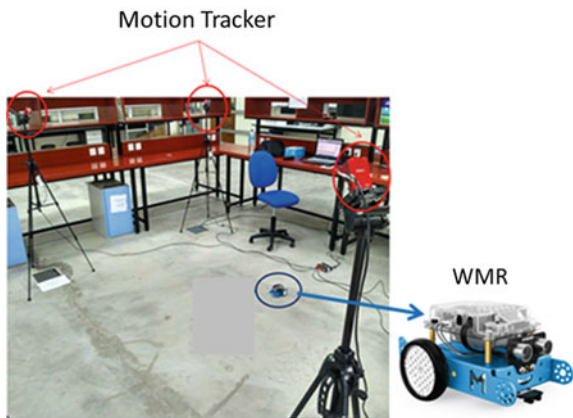
2.1 Wheel Mobile Robot Mathematical Model—Kinematic Model

In previous study, Pebrianti et al. [12] have developed kinematic model of mBot robot and verified the model through experimentation by using mBot robot and Flex 3 cameras. The setup to obtain and verify the model is shown in Fig. 1. The result of kinematic model from the study is 95% accuracy. Thus, by implementing the well-developed kinematic model in this research study, a simulation to tune and optimize the PID gains will be easily constructed.

The configuration of the mBot is indicated by the three generalized coordinates as stated below:

$$Q = (x, y, \theta) \tag{1}$$

Fig. 1 Experimental setup to develop kinematic model of mBot robot



where x and y is the position of the mBot and θ is the orientation angle of the mBot. In order to analyse the data collected form Flex 3 cameras, a mathematical model is derived as follow:

$$\dot{x} = \frac{r}{2}(\omega_r + \omega_l) \cos \theta \quad (2)$$

$$\dot{y} = \frac{r}{2}(\omega_r + \omega_l) \sin \theta \quad (3)$$

$$\dot{\theta} = \frac{r}{D}(\omega_r - \omega_l) \quad (4)$$

where r is the radius of the mBot's wheel, ω_r is the right wheel angular velocity, ω_l is the left wheel angular velocity and D is the distance between the mBot's wheels.

$$\dot{x} = v \cos \theta \quad (5)$$

$$\dot{y} = v \sin \theta \quad (6)$$

$$\dot{\theta} = \omega \quad (7)$$

By rearranging the inputs Eqs. (2)–(7) we get:

$$\omega_r = \frac{2v + \omega D}{2r} \quad (8)$$

$$\omega_l = \frac{2v - \omega D}{2r} \quad (9)$$

where ω_r is the right wheel velocity of the vehicle mBot and ω_l is the left wheel velocity of the vehicle mBot.

The output of ω_r and ω_l are formed from the inputs of v and ω . A constant number 0.113 m is used in the model. This constant number is the distance between two mBot's wheels and R referred to the radius of the mBot's wheel which is 0.03 m.

2.2 PID Controller Design

The block diagram of the system is shown in Fig. 2. In this study, Wheel Mobile Robot (WMR) is considered as an underactuated system. This is because WMR consists of two inputs which are velocity (v) and angular velocity (ω) and three outputs which are position of x , y and attitude θ . As the preliminary study, the controller for angular velocity (ω) used in this study is set to be one.

The velocity of WMR contains velocity along x-axis and y-axis as shown in Eq. (10).

$$v = \sqrt{v_x^2 + v_y^2} \quad (10)$$

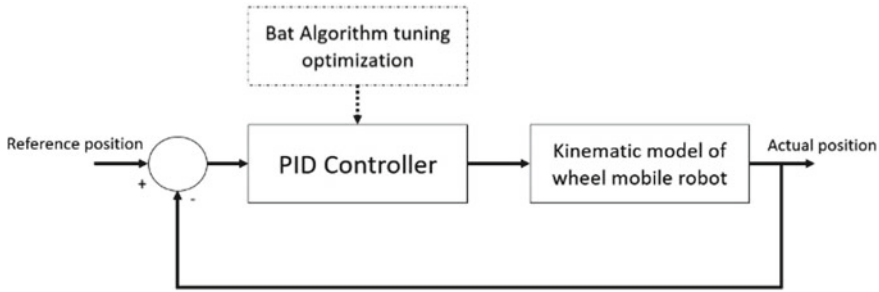


Fig. 2 Block diagram of wheel mobile robot using PID-BA controller

where v_x and v_y are velocity along x- and y-axis, respectively.

The path x and path y are set with a certain desired input values. These values will be compared with the actual values to generate an error signal. However, since the input to the system is velocity and angular speed, there is a need to construct the error so that it will be acceptable to the system. Two different functions are designed to transform these error values into the two inputs of TWMR system, as shown in Eqs. (11) and (12).

$$\tilde{v} = \sqrt{(x_{desired} - x_{actual})^2 + (y_{desired} - y_{actual})^2} \tag{11}$$

$$\tilde{w} = atan2((y_{desired} - y_{actual}), (x_{desired} - x_{actual})) \tag{12}$$

where \tilde{v} is modified error signal for velocity controller, \tilde{w} is modified error signal for angular speed controller, $x_{desired}$ is target of x position, $y_{desired}$ is target of y position, x_{actual} is actual value of x position, y_{actual} is actual value of y position, and $atan2$ is four-quadrant inverse tangent, where it will return values in the closed interval $[-\pi, \pi]$.

Control input for the controller used in this study is shown in Eq. (13).

$$v = K_p \tilde{v} + K_d \frac{d\tilde{v}}{dt} \tag{13}$$

where K_p and K_d are proportional and derivative gain, respectively.

2.3 Optimization by Bat Algorithm

To evaluate the performance of the designed controller, certain criteria need to be considered in advance. When the reference input is the unit step function, typical indices which are often used to characterize the transient response in the time domain include the delay time, rise time, maximum overshoot, settling time, etc. For general PID controller design, there are three commonly used performance criteria, includ-

ing the integral square error (*ISE*), integral absolute error (*IAE*), and integral time absolute error (*ITAE*). In a MIMO system, they are defined by

$$ISE = \int_0^{\infty} (e_1^2(t) + e_2^2(t) + \dots + e_n^2(t))dt \tag{14a}$$

$$IAE = \int_0^{\infty} (|e_1(t)| + |e_2(t)| + \dots + |e_n(t)|)dt \tag{14b}$$

$$ITAE = \int_0^{\infty} t \cdot (|e_1(t)| + |e_2(t)| + \dots + |e_n(t)|)dt \tag{14c}$$

where $e(t)$ is the error which is the difference between reference and measurement values.

Bat Algorithm was developed in 2010 by Xin-She Yang [13]. It is a nature inspired algorithm based on echolocation behavior of microbats. Each bat is encoded with a velocity and location in a dimensional space at iteration. What makes BA different from others nature inspired algorithm is the presence of loudness and pulse emission rates parameter. The mathematical equations for updating the locations (x), velocities (v), loudness (A) and pulse emission rates (r) are shown in Eq. 15. The BA procedure is presented as well.

$$f_i = f_{min} + (f_{max} - f_{min})\beta \tag{15a}$$

$$v_i^t = v_i^t + (x_i^{t-1} - x^*)f_i \tag{15b}$$

$$x_i^t = x_i^{t-1} + v_i^t \tag{15c}$$

$$x_{new} = x_{old} + EA^t \tag{15d}$$

$$A_i^{t+1} = \alpha A_i^t \tag{15e}$$

$$r_i^{t+1} = r_j^0 [1 - \exp(-\gamma t)] \tag{15f}$$

The procedure of Bat Algorithm is described as follows and Fig. 3. shows the pseudo code of BA.

- Step 1 Initialization. Initialize the parameters of algorithm i.e. bat population, number of iteration and then determine the best solution in the population.
- Step 2 Generate new solution. At this step, virtual bats fly randomly in the search space to updating rules of BA.
- Step 3 Local search step. The best solution improved using random walk.
- Step 4 evaluate new solution. The evaluation of new solution is carried out.
- Step 5 Save the best solution.
- Step 6 the current best solution is updated for each iteration

```

Objective function  $f(x), x = [x_1, x_2, \dots, x_d]^T$ 
Initialize the bat population  $x_i (i = 1, 2, \dots, n)$  and  $v_i$ 
Define pulse frequency  $f_i$  at  $x_i$  Initialize pulse rates  $r_i$  and the loudness  $A_i$ 
While ( $t < \text{Max number of iterations}$ )
    Generate new solutions by adjusting frequency,
    and updating velocities and locations/solutions [(1)]
    if ( $\text{rand} > r_i$ )
        Select a solution among the best solutions
        Generate a local solution around the selected best solution
    end if
        Generate a new solution by flying randomly
    if ( $\text{rand} < A_i \ \& \ f(x_i) < f(x_*)$ )
        Accept the new solutions
        Increase  $r_i$  and reduce  $A_i$ 
    end if
        Rank the bats and find the current best  $x_*$ 
end while
    Postprocess results and visualization.

```

Fig. 3 Pseudo code of Bat Algorithm

2.4 Simulation

Simulation to optimize the controller parameters is constructed by using Simulink software. The procedure of simulation is described as follows. Firstly, bat algorithm is prepared with all initialization parameters. The initialize values of K_p , K_i and K_d computed from BA are feed into Simulink model. Next, Simulink model as illustrated in Fig. 4 is executed and error is calculated from the closed loop system. Tuning of PID will keep running until number of iterations initialized in the BA is meet. Lastly, the simulation is recorded all the value and determine the best fitness value from the simulation and PID gains to be fed to the wheel mobile robot.

The result from the BA is compared with PID controller parameters tuned by using PSO. In previous study, PSO has been used to tune PID by Solihin et al. [10] which proven its potential to tune gain of PID controller. Thus, in this paper, the technique of PSO is being experimented as well with BA.

3 Result and Analysis

The parameters used in BA and PSO are listed below.

- The member of each individual is set to be $\theta = [K_p \ K_d]$.
- Population size = 20.

- Range of frequency = [0,2]
- Maximum iteration is set to 300.

(a) BA

- Loudness = 0.5
- Pulse rate = 0.5
- Weights for α and β in fitness function are 10 and 1, respectively.

(b) PSO

- Inertia weight factor w is set to be 0.9.
- Acceleration constants $c_1 = 2$ and $c_2 = 2$.

The convergence curve of the fitness function for PSO and BA is shown in Fig. 5. BA showed better performance in exploration and exploitation for searching the best value of K_p and K_d . In a meanwhile, PSO has been trapped in local minima at iteration 25th which make the particles unable to widen their exploratory area.

Table 1 shows the value of K_p and K_d gain. Both of the tuning obtain different values of K_p and K_D . $K_p = 1.6625$, $K_D = 0.4465$ for PSO and $K_p = 1.6557$, $K_D = 3.0034$ for BA. Due to the low differences of value for PSO and BA, both of the value give out the same position response graph for X and Y. However, the tuning time to tune the value for both algorithm give out different value. BA is faster than PSO. BA is completed the tuning process in 25 min 11 s while PSO is completed in 40 min 36 s. The tuning time might be different for different processor used by the simulation. In this study, PSO and BA were tested using Intel Core i7 processor.

The next is to apply the obtained PD gains and test it on Wheel Mobile Robot (WMR) system. The values obtained from each trial is used and the analysis is conducted to evaluate the time response performance and also the steady state error

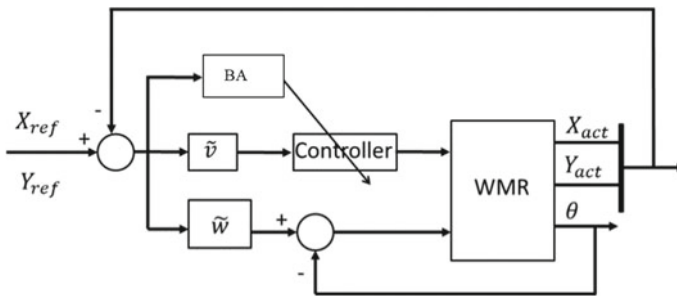


Fig. 4 Illustration of Simulink model

Table 1 Statistical analysis for PD Gain optimization

Algorithm	PSO	BA
Gain K_p	1.6625	1.6557
Gain K_d	0.4465	3.0034

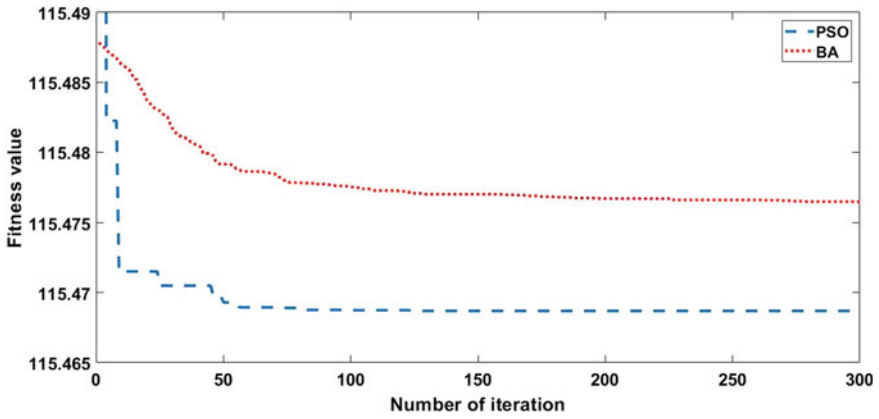


Fig. 5 Convergence curve fitness function of PSO and BA

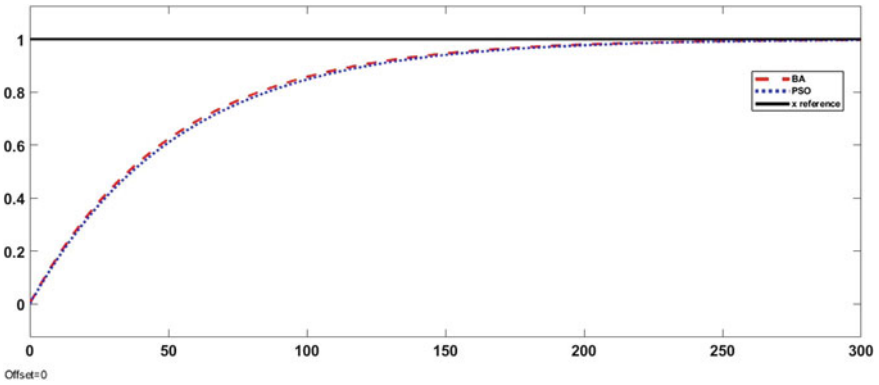


Fig. 6 X position time response BA and PSO

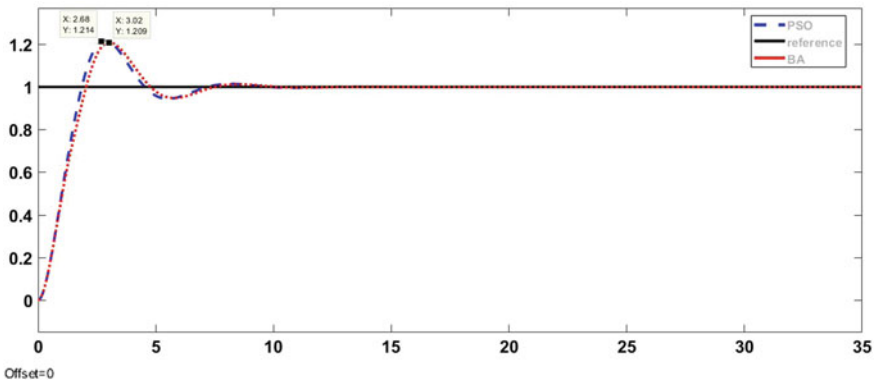


Fig. 7 Y position time response for BA and PSO

Table 2 Statistical analysis for PD gain optimization

Algorithm	PSO	BA
Best fitness value	115.468	115.476
Gain K_p	1.6625	1.6557
Gain K_d	0.4465	3.0034
Tuning time	40 min 36 s	25 min 11 s
Time response (s)	230.3	223.4
% overshoot	28.4	28.2
Settling time (s)	11.1	10.62
Rise time (s)	2.68	3.24
Steady state error	0	0

analysis for each position x and y of the robot. Figures 6 and 7 shows the time response of x and y position, respectively.

Table 2 shows the differences between PSO and BA algorithm in optimize PID controller parameters.

4 Conclusion

Optimization of PID gain controller for Wheel Mobile Robot (WMR) is proposed in this study. The proposed algorithm, Bat Algorithm (BA) showed its ability to optimize the PID controller parameters and outperformed the performance of PSO in term of processing time. Besides, percentage for optimizing PID controller parameters by using BA produced better result in overshoot per percentage which is 0.2% better than PSO. Additionally, the PID controller gain values obtained by BA has lower settling time, 0.48 s better than PSO. The searching method of BA in avoiding to be trapped in local minima showed its potentiality to obtain good result for solving optimization problem.

Acknowledgements This works is supported by Universiti Malaysia Pahang (UMP), under Universiti Malaysia Pahang Research Grant RDU 170378

References

1. Sontag, E.D.: Mathematical control theory: Deterministic finite dimensional systems. Springer (1998)
2. Kwakernaak, H., Sivan, R.: Linear optimal control systems. Wiley Interscience (1972)
3. Kennedy, J., Eberhart R.: Particle swarm optimization. In: Proceeding of the IEEE International Conference Neural Networks, Vol. IV, pp. 1942–1948 (1995)
4. Chow, G.C.: Analysis and control of dynamic economic systems. Krieger Pub Co (1 Sept 1986)

5. Oryschuk, P., Salerno, A., Al-Husseini, A.M., Angeles, J.: Experimental validation of an under-actuated two-wheeled mobile robot, *IEEE/ASME Transaction on Mechatronics*, Vol. 14, No. 2, pp. 252–257 (April 2009)
6. Tian, Y., Sarkar, N.: Control of a mobile robot subject to wheel slip. *J. Intell. Robot. Syst.* **74**, 915–929 (2014)
7. Juang, C.F.: Ant colony optimization algorithm for Fuzzy controller design and its FPGA implementation. *IEEE Trans. Ind. Electron.* **55**(3), 1453–1462 (2008)
8. Chia, K. S.: Ziegler-nichols based proportional-integral-derivative controller for a line tracking robot. *Indonesian J. Electr. Eng. Comput. Sci.* **9**(1), 221–226 (2018)
9. Kashi, S., Minuchehr, A., Poursalehi, N., Zolfaghari, A.: Bat algorithm for the fuel arrangement optimization of reactor core. *Ann. Nucl. Energy.* **64**, 144–151 (2014)
10. Fister, I.Jr., Yang, X.: Bat algorithm: Recent advances, pp. 163–167 (2014)
11. Sambariya, D.K., Prasad, R.: Robust tuning of power system stabilizer for small signal stability enhancement using metaheuristic bat algorithm. *Int. J. Electr. Power & Energy Syst.* **61**, 229–238 (2014)
12. Pebrianti, D., et al.: Motion tracker based wheeled mobile robot system identification and controller design. In: Hassan, M. (ed.) *Intell. Manuf. Mechatron.*, pp. 241–258. Singapore, Lecture Notes in Mechanical Engineering. Springer (2018)
13. Rajanioun, R.: Cuckoo optimization algorithm. *Appl. Soft Comput.* **11**, 55085–5518 (2011)

Restoration of Kids Leg Function Using Exoskeleton Robotic Leg (*ExRoLEG*) Device



Mohd Azrul Hisham Mohd Adib, Szeto Yang Han, Prashant Raj Ramani,
Low Jian You, Law Ming Yan, Idris Mat Sahat
and Nur Hazreen Mohd Hasni

Abstract The neurological disorder normally happens to a child's brain due to injury or malfunction during growth. This primarily affects muscle coordination and body movement. This paper focuses on restoration of cerebral palsy kids using exoskeleton robotic leg (*ExRoLEG*) device. These include strengthening, walking pattern and walking posture. As a part of rehabilitation, *ExRoLEG* device aims to achieve early walking independent age compared to conventional methods where the patient undergoes physiotherapy daily to improve their walking pattern. Every factor is considered to avoid risk or failure including materials, safety and user friendly. This study is to use simple and low cost mechanism to serve that purpose. By doing this, every patient can afford the exoskeleton and speed up their recovery.

Keywords Exoskeleton · Robotic leg · Kids · Neurological disorder
Rehabilitation · Brain injury

1 Introduction

Cerebral palsy is mainly divided into two groups, spastic and non-spastic. *ExRoLEG* [1] will be built based on patients with spastic cerebral palsy, which also accounts to almost 70–80% of all diagnosed cerebral palsy cases [2]. Severity of the cerebral palsy is classified based on Gross Motor Function Classification System (GMFCS). There are a total of 5 levels [3, 4], GMFCS Level I—gaits without any limitations. GMFCS Level II—gaits with limitations that include walking for long distances. Patients may

M. A. H. Mohd Adib (✉) · S. Y. Han · P. R. Ramani · L. J. You · L. M. Yan · I. Mat Sahat
Medical Engineering and Health Intervention Team (MedEHIT),
Human Engineering Group, Faculty of Mechanical Engineering,
Universiti Malaysia Pahang, 26600 Pekan, Pahang, Malaysia
e-mail: azrul@ump.edu.my

N. H. Mohd Hasni
Klinik Kesihatan Kurnia, Ministry of Health Malaysia (MOH), Batu 3,
25150 Kuantan, Pahang, Malaysia

need the use of mobility devices when first learning to walk, usually prior to age 4; and may rely on wheeled mobility equipment when outside of home for traveling long distances. GMFCS Level III—gaits with adaptive equipment assistance. Requires hand-held mobility assistance to walk indoors, while utilizing wheeled mobility outdoors, can sit on own with limited external support. GMFCS Level IV—self-mobility with use of power mobility assistance. Usually supported when sitting; self-mobility is restricted; and likely to be transported in manual wheelchair or powered mobility. GMFCS Level V—This is the most severe category where patients experience head and trunk control restrictions. Requires extensive use of assisted technology and physical assistance; and transported in a manual wheelchair [5], unless self-mobility can be achieved by learning to operate a powered wheelchair. Another one of the biggest issues for many people with cerebral palsy is known as “crouch gait,” or walking while the knees are excessively bent [2]. Therefore, the focus of the project to innovate a design to improve and alleviate walking posture of affected individuals. The design is intend to have the robotic exoskeleton leg to operate according to the gait cycle, which will then be strapped to the patients, desired to readjust their walking or standing posture after a few rehabilitation sessions. Conventional rehabilitation suggests that the patient undergoes physiotherapy weekly or even daily to improve their walking pattern. However, studies show that by using automation or exoskeleton it decreases the duration of physiotherapy and aids the patient to be walking independently. This is because their movement is supported by the exoskeleton rather than applying a huge stress on the patient’s leg, which could cause pain and discomfort in patient. There are products in the market but the cost is very expensive. Many rehabilitation centers do not have the budgets to buy this kind of devices. Therefore, they are more opted to using the conventional method as it is very cheap.

This paper focus on restorable the low cost mechanism of a *ExRoLEG* device where achieved the Level II and III. The target is on patients with limitation to walk for long distances and who requires mobility devices when first learning to walk. So, with this *ExRoLEG* device, every patient can afford the exoskeleton and speed up their recovery.

2 Methodology

2.1 Development of *ExRoLEG* Device

The *ExRoLEG* is designed using *SolidWorks 2017*. Every components and parts of the product are designed and drawn with precise dimension as the real product. The components and parts that are required to fabricate are clearly drawn in detail. Figure 1 shows the isometric view of the final design and the full dimension of the *ExRoLEG* is shown in the top box. The actual prototype consists of a lot of joint parts and connectors. Since the prototype requires itself to be able to withstand high load, the connectors used to assemble other parts into one needs to be loaded

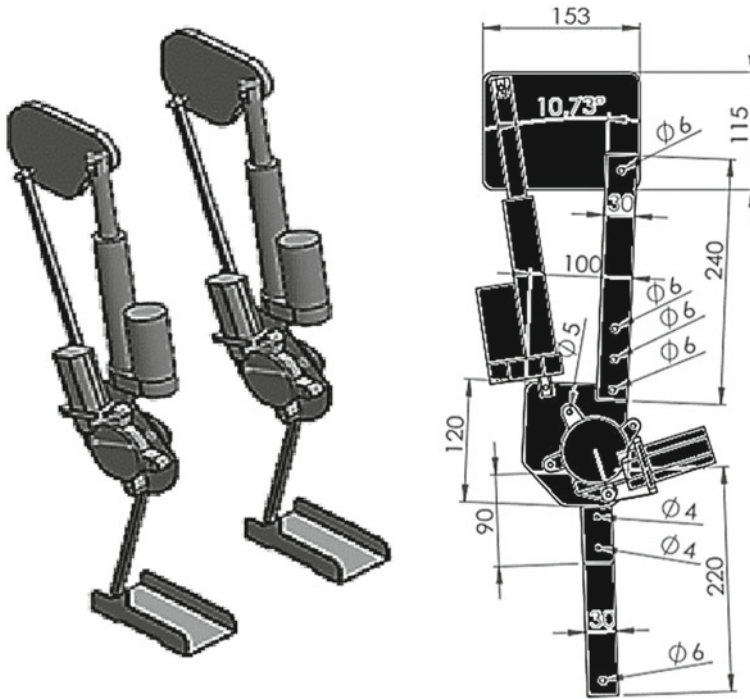
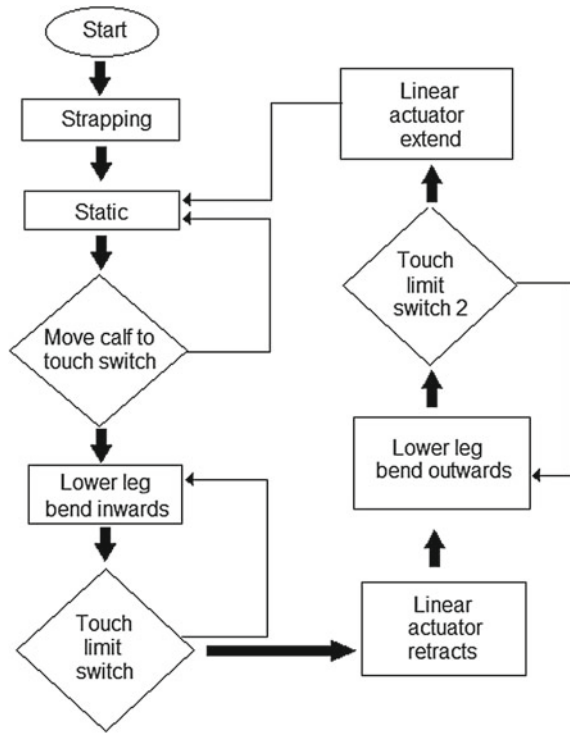


Fig. 1 Design development of *ExRoLEG* device with full dimension [unit: mm]

withstanding. Thus, bolts and nuts were used mainly to link other parts together into a tight connection. In SolidWorks, all parts are mated tightly together to form the design of the product. Features of mating like concentric mate between two surfaces and coincident mate between surfaces and edges represent the fabrication of the real product case. Every single dimension is taking into account throughout the fabrication process.

ExRoLEG is mainly built up by metals and micro-controlled by Arduino. The Arduino is used as a controller to code and execute the requested command in the system. The coding is done to mimic the movement of the human walking. For the metals used in this project are 2 mm galvanized iron sheet metal and aluminum plate. Aluminum plate is cut into the dimension of 30 mm × 220 mm for upper leg and 30 mm × 240 mm for lower leg. The sheet metal is cut into various designs for waist plate, foot plate, upper knee joint and lower knee joints. The processes involved in fabrication are sheet metal shearing, bending, drilling, cutting and finishing. Most of the cutting processes are done by abrasive cutting with a grinder. All the parts are joined by a bolt and nut. Linear actuator and power window motor are assembled at the knee joint to control the motion. The Velcro brand is used as a strap because easy to use as it can attach and detach according to preference. Velcro also not expensive light in weight and durable. In Arduino system, EMG or limit switch (optional) is functioning

Fig. 2 The operation of the *ExRoLEG* device



as the control mechanism that gives analog input. The *ExRoLEG* operation mainly control by two transmission actuators that are electric linear actuator with 500 N linear force and power window motor with 30 kg.cm or 2.9 Nm rated torque [see Fig. 2 for the overall operation system of *ExRoLEG*]. The cost of the electric linear actuator is three times higher than power window motor. In order to cut the cost, torque is calculated on the motion of the leg of a child with the assumption that he/she has a 50 cm long leg and weighted with 4 kg. Details of the bill of materials is showed in Table 1.

3 Result and Discussion

In Fig. 3, the rectangular sheet metal will be attached to the waist belt, which is connected to aluminum bar that acts as a support for the thigh. The following heptagonal sheet metal represents the knee joint that is fixed to another aluminum bar that will reach all the way to the feet. An electric actuator will be responsible to lift the weight of the entire leg, and a power motor will be used to bend the knees. The movement of our exoskeleton will be mostly automated, controlled by an Arduino system.

Table 1 Bill of material (BOM)

No.	Part name	Measurement and features
1	Aluminium angle bar	5 cm × 100 cm × 0.5 cm (W × L × T)
2	Aluminium sheet metal	100 cm × 100 cm × 0.2 cm (W × L × T)
3	Velcro	2.5 cm × 500 cm (W × L)
4	Electrical actuator	12 V, 4 in stroke
5	EMG sensor	9 V
6	Electric power motor	12 V
7	Arduino mega 2560	5–12 V
8	Relay module	4 slotted
9	Knee guard	Strap on
10	Bolt and nuts	M5
14	EVA foam	20 cm × 30 cm × 0.2 cm (W × L × T)
15	Rechargeable motor battery	12 V

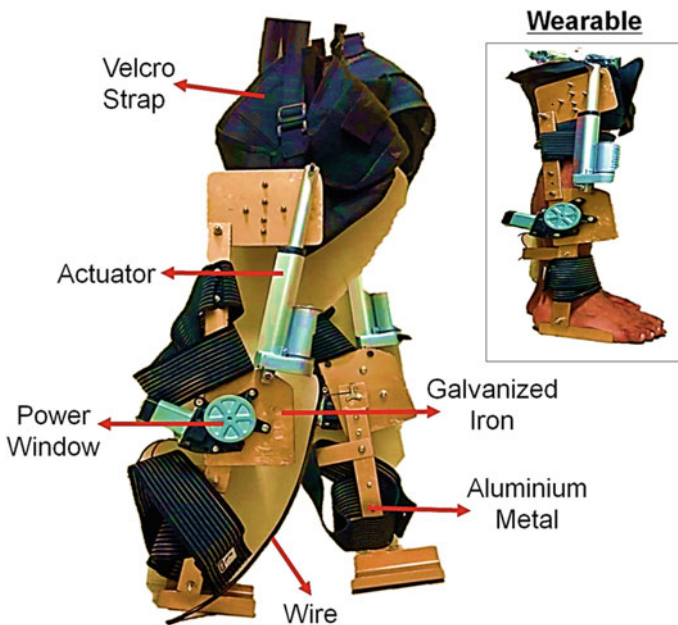


Fig. 3 Final design of *ExRoLEG* device. *Top box*: Expression the right way of wearable the *ExRoLEG* device

Electric actuator and power motor are power hungry devices. Therefore, it requires more DC power supply to operate. Besides, this requires a better motor driver module to withstand the high power rating. If lower specifications are used, the circuit might burn or the devices will not operate optimally due to lack of power supply.

By default, the entire transmission mechanism can be simply works by 2 electric actuators. The assembly will be much easier compared to the current design. However, in terms of cost, the cost of a unit of electric actuator is 3 times the cost of a unit of power motor. In addition to the engineering calculation we conducted, electric actuator can support a higher load in comparison to power motor, but the possible load applied to the power motor will be sufficient enough for its function.

3.1 Restoration Perspective

In structural aspects, design is always updated due to errors during fabrication. Most of the metal works involve simple geometry, but there are some parts that require skills and innovation to produce the specific parts shape. Last but not least, the weight of the total product itself is approximately 4 kg per *ExRoLEG*. This is pretty heavy and assistance is needed to utilize this product. Figure 4 shows the three main views when restoring the kid's leg using *ExRoLEG* device.

3.2 Functionality Validation

To validate the functionality of the proposed device the first prototype has been manufactured as presented in Fig. 4. Preliminary investigation has been completed focusing on evaluating of kinematic and dynamic parameters required for proper

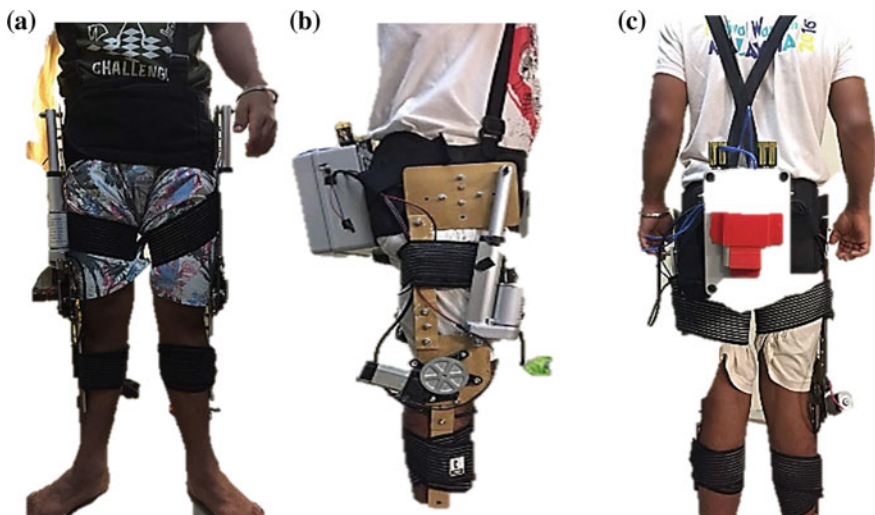


Fig. 4 Represented the main view of *ExRoLEG* device; a front view; b side view; and c back view

Fig. 5 The comfortable and discomfortable feel of the patient when used the *ExRoLEG* device

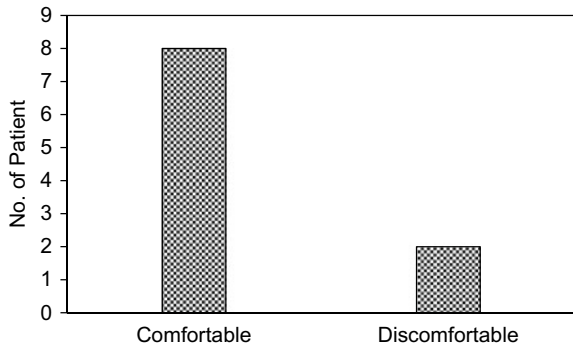


Fig. 6 The compliant handles link mechanisms of the *ExRoLEG* device for kids with cerebral palsy



functional use of the designed *ExRoLEG* device. The device well reproduced the subject movement, thus demonstrating repetitive walking exercise. Figure 5 shows out of 8 patients presented comfortable feeling when used the *ExRoLEG* device and Fig. 6 shows only four patients compliant bad in handling the *ExRoLEG* device. The same preliminary tests conducted on kids with cerebral palsy confirm that the compliant handle link mechanism of the *ExRoLEG* device shows well in walking movement bending during active exercises. The subjects did not feel any discomfort or applied interaction forces imposed by the device and could freely work with the device.

4 Conclusion

The new era of technologies is being generated every day to enhance the living quality of human life which makes this project an appropriate and crucial innovation to mankind. The main objectives of this paper has been achieved as we were able to restore a kids leg function with a prototype of *ExRoLEG* device and able to function satisfyingly. One of the highlights is the extremely low cost of manufacture

compared to the available similar devices in the market. However, there are still much improvements that can be made towards this device for a greater performance in the future.

In the future works, the authors plan to improve the design and functionality of the device, exclusively for the operation and safety aspects. Additionally, to conduct the clinical study and expand the efficiency of therapy treatments as patients will remain more focused through the frequently extended rehabilitation process.

Acknowledgements The support of the University Malaysia Pahang under grant RDU180330 and MedEHIT are gratefully acknowledged. The authors of this paper also would like to express their gratitude to Dr. Nor Shahizan Mohd Redzuan for supporting these research activities.

References

1. Adib, M.A.H.M., Han, S.Y., Ramani, P.R., You, L.J., Yan, L.M., Zabudin, N.F., Hasni, N.H.M.: Development of Exoskeleton Robotic Leg (ExRoLEG) for Kids with Cerebral Palsy, Innovative Research and Industrial Dialogue IRID18. UTEM, Malaysia (2018)
2. Matchar, E.: This Robotic Exoskeleton Helps Kids with Cerebral Palsy Walk Upright Homepage, <https://www.smithsonianmag.com/innovation/this-robotic-exoskeleton-helps-kids-cerebral-palsy-walk-upright-180964750/>, (2017). Last Accessed 19 July 2018
3. Cerebral Palsy Guide, Assistive Technology for Limited Clinical Mobility Issues Homepage, <https://www.cerebralpalsyguide.com/treatment/mobility-aids/>. Last Accessed 19 July 2018
4. Cerebral Palsy Guidance, Cerebral Palsy and Pain Homepage, <https://www.cerebralpalsyguidance.com/cerebral-palsy/associated-disorders/pain/>. Last Accessed 19 July 2018
5. Lerner, Z.F., Damiano, D.L., Bulea, T.C.: A lower-extremity exoskeleton improves knee extension in children with crouch gait from cerebral palsy. *Sci. Transl. Med.* **9**(404), (2017)

Simulated Kalman Filter Algorithm with Improved Accuracy



Mohd Falfazli Mat Jusof, Ahmad Azwan Abd Razak,
Shuhairie Mohammad, Ahmad Nor Kasruddin Nasir, Mohd Helmi Suid,
Mohd Ashraf Ahmad and Zuwairie Ibrahim

Abstract This paper presents an improved Simulated Kalman Filter optimization algorithm. It is a further enhancement of a Simulated Kalman Filter (SKF) optimization algorithm. SKF is a random based optimization algorithm inspired from Kalman Filter theory. An exponential term is introduced into Estimation stages of SKF to speed up the searching process and gain more chances in finding better solutions. Cost function value that represents an accuracy of a solution is considered as the ultimate goal. Every single agent carries an information about the accuracy of a solution in which will be used to compare with other solutions from other agents. A solution that has a lower cost function is considered as the best solution. The algorithm is tested with various benchmark functions and compared with the original SKF algorithm. The result of the analysis on the accuracy tested on the benchmark functions shows that the proposed algorithm outperforms SKF significantly. Graphical results of the test show that the SKFIA has faster convergence speed as compared to SKF.

Keywords Simulated Kalman filter · Optimization algorithm · CEC2014

1 Introduction

Most of the real world problems are complex in its structure or landscape, have different properties and consist of various dimensions. Naturally, a problem that encountered in real life might consists of unimodal, multimodal, or dynamic fitness landscapes. Therefore, a good optimization algorithm is needed to solve this kind

M. F. Mat Jusof · A. A. Abd Razak · S. Mohammad · A. N. K. Nasir (✉) · M. H. Suid
M. A. Ahmad
Faculty of Electrical and Electronics Engineering, Universiti Malaysia Pahang,
26600 Pekan, Pahang, Malaysia
e-mail: kasruddin@ump.edu.my

Z. Ibrahim
Faculty of Manufacturing Engineering, Universiti Malaysia Pahang,
26600 Pekan, Pahang, Malaysia

© Springer Nature Singapore Pte Ltd. 2019
Z. Md Zain et al. (eds.), *Proceedings of the 10th National Technical Seminar on Underwater System Technology 2018*, Lecture Notes in Electrical Engineering 538,
https://doi.org/10.1007/978-981-13-3708-6_29

of problem. Optimization algorithm is regarded as a tool for many researchers and scientists in academia in solving various real life and complex problems. It is also a trend for many engineers in the industry to use the algorithm. This is due to the solution offers by the algorithm is reliable and optimal.

The main challenge of optimization algorithm is to find the best global solution for problems that has all the features mentioned above with fastest speed and low computation cost. All these performances are crucial and important when it comes to a real time processing for solving various real life problems. An algorithm might capable of searching for a near optimal solution but its performance on the convergence speed might be poor and vice versa. In the literature, also it is hard to find an algorithm that can perform relatively the best as compared to other algorithms on all problems that have different landscapes and complexities. Most of the cases a certain algorithm is only capable to outperform for some problems that have certain landscapes, but loses to other problems with different landscapes. A lot of optimization algorithms have been introduced by many researchers worldwide.

Simulated Kalman Filter (SKF) [1] is a relatively new optimization algorithm. It is formulated inspired from the theory of Kalman filtering technique. Today, the SKF has been applied to solve various real life problems. The SKF however, still has a certain drawback. For some problems, it's unable to find the optimal and accurate solution. The research on improving the SKF is still ongoing. Many modifications have been made to improve SKF accuracy. Jusof et al. [2] developed an Exponential-based SKF in which the Kalman gain, K is formulated with respect to the algorithm iteration. The algorithm was applied to solve a liquid slosh problem on a moving platform. Azwan et al. [3] introduced the first multiobjective type SKF. The algorithm was tested on various benchmark problems and compared with NSGA2 algorithm. Result from the test showed the algorithm has a competitive performance. This paper proposes an SKF algorithm with improved accuracy, namely as SKFIA. An exponential term is incorporated into several equations in the Estimation stage of the SKF algorithm.

2 Kalman Filter, Simulated Kalman Filter and Simulated Kalman Filter with Improved Accuracy

2.1 Kalman Filter

Two main stages in Kalman Filter (KF) are known as Prediction and Measurement stages. Prediction stage is a process to predict state variables of a system of interest based on prior information of the state variables at a previous time and their corresponding prediction noise. It also involves the calculation of a variance associated with the prediction of the state variables. On the other hand, the Measurement stage is a process to read information about the state variables at the current time with consideration of measurement noise. The combination of the information from the

prediction and measurement stages is then used to estimate the next state variable of the system of interest. It also involves the calculation of a variance associated with the measurement of the state variables. The process is recursively occurred.

2.2 Simulated Kalman Filter Algorithm

SKF algorithm is developed inspired from a theory of a KF. There are three main stages of the SKF algorithm, which is known as Prediction, Measurement and Estimation. Prediction and Measurement of SKF and KF are the same. However, the combination of Prediction and Measurement data in KF is known as an Estimation stage in SKF.

In developing an optimization algorithm, a KF is considered as an individual agent in which acts to search theoretical global optimal solution. Every agent carries information about a system's state variable. It reflects the position of an individual agent in search space. This is shown in Eq. (1):

$$X_i(t - 1) = \{x_i^1(t - 1), x_i^2(t - 1), x_i^3(t - 1) \dots x_i^D(t - 1)\} \tag{1}$$

where $x_i^D(t - 1)$ is a position of an agent, i is a number of an agent, D is a search space dimension and t is a number of iterations. In the prediction stage, the Eqs. (2) and (3) take place.

$$\hat{X}_i(t) = X_i(t - 1) \tag{2}$$

$$\hat{P}(t) = \hat{P}(t - 1) + \hat{Q} \tag{3}$$

where $\hat{X}_i(t)$ is a predicted position of an agent. $\hat{P}(t)$, $\hat{P}(t - 1)$ and \hat{Q} are a current variance associated with the prediction, a previous variance associated with the prediction and prediction noise covariance which is defined as a constant respectively. In the Measurement stage, the search agents are set to move in a random manner through the utilization of the predicted position and it is implemented by using Eq. (4).

$$z_i(t) = \hat{X}_i(t) + \sin(rand \times 2\pi) \times \left(\left| \hat{X}_i(t) - \hat{X}_{best}(t) \right| \right) \tag{4}$$

where $\sin(rand \times 2\pi) \times \left(\left| \hat{X}_i(t) - \hat{X}_{best}(t) \right| \right)$ is to introduce random behavior in the agents movement. Equation (4) also measures a new position of the search agents. Information from Eqs. (2)–(4) is then used in the final stage of SKF algorithm to estimate and update the agents' position. Equations (5), (6) and (7) are applied and thus complete the algorithm's cycle.

$$X_i(t) = \hat{X}_i(t) + K \times (z_i(t) - \left(\left| \hat{X}_i(t) \right| \right)) \tag{5}$$

where $X_i(t)$ is the i agent's current position and K is a Kalman gain and is defined as (6).

$$K(t) = \frac{\hat{P}(t)}{\hat{P}(t) + R} \quad (6)$$

where R is an estimation noise covariance which is defined as a constant.

$$P(t) = (1 - K(t)) \times \hat{P}(t) \quad (7)$$

where $P(t)$ is the a current variance associated with the estimation.

2.3 Simulated Kalman Filter with Improved Accuracy Algorithm

An improved version of the SKF is proposed and it is named as Simulated Kalman Filter with Improved Accuracy (SKFIA). The proposed SKFIA has the same structure as the SKF. The difference is on the formulation in the Estimation stage. An exponential term is introduced into Eqs. (6) and (7). The exponential term is included into the equations to speed up agents movement from one location to another at the beginning of the search process. On the contrary the agents search slower with smaller step size in a more confined space at the end of the process. The newly formulated equations are represented as Eqs. (8) and (9).

$$K(t) = \exp\left(\frac{\hat{P}(t)}{\hat{P}(t) + R}\right) \quad (8)$$

$$P(t) = \exp\left((1 - K(t)) \times \hat{P}(t)\right) \quad (9)$$

Instead of using R as a constant, in SKFIA, it is now formulated such that it is exponentially changed with respect to P . This is shown in (10).

$$R = \exp\left(0.5 \times \hat{P}(t)\right) \quad (10)$$

3 Benchmark Functions and Test Setup

The proposed SKFIA is tested with four standard benchmark functions in comparison to SKF. Functions 1–4 represent High Condition Elliptic, Bent Cigar, Ackley, and Rosenbrock functions respectively [4]. All the functions are set to have 10 variables

Table 1 CEC2014 benchmark functions

Function no.	Mathematical representation
<i>F1</i>	$f_1(x) = \sum_{i=1}^D (10^6)^{\frac{i-1}{D-1}} x_i^2$
<i>F2</i>	$f_2(x) = x_1^2 + 10^6 \sum_{i=2}^D x_i^2$
<i>F3</i>	$f_3(x) = -20 \exp(-0.2) \sqrt{\frac{1}{D} \sum_{i=1}^D x_i^2} - \exp\left(\frac{1}{D} \sum_{i=1}^D \cos(2\pi x_i)\right) + 20 + e$
<i>F4</i>	$f_4(x) = \sum_{i=1}^{D-1} (100(x_i^2 - x_{i+1})^2 + (x_i - 1)^2)$

or dimensions and their search range is [-100, 100]. Mathematical representations of the functions are summarized in Table 1.

Both SKFIA and SKF are set such that they have 100 search agents in total. They are allowed to search the theoretical optimal solution up to a maximum of 100,000 number of cost function evaluation (NFE). If the solution reaches a minimum error of 10^{-8} , the algorithm is set to stop and the error is recorded as zero. Therefore, the stopping condition for the algorithms is set based on maximum NFE or the minimum accuracy. The algorithms are set to 51 repeated runs and the average value is taken for analysis purpose. Initial error covariance, prediction error and measurement error for the SKFIA and SKF are set as 1000, 0.5 and 0.5 respectively.

4 Results and Discussion

Assessment of the performance is done in terms of the accuracy of the solution to reach the theoretical global optimal solution. The average value of the cost function value, best and worst solution from the 51 runs for the SKFIA and KSF are recorded in Tables 2 and 3 respectively. Result with the lowest cost function value is considered as the best solution. From the tables, it is noted that for all four test functions, SKFIA has presented the lowest average value. In other words, SKFIA has achieved a better accuracy compared to SKF.

Graphical results of both SKF and SKFIA tested on benchmark functions are shown in Figs. 1, 2, 3 and 4. Graphical result of the SKF is shown in red-dotted line while the result of SKFIA is shown as blue-smoothed line. The horizontal x-

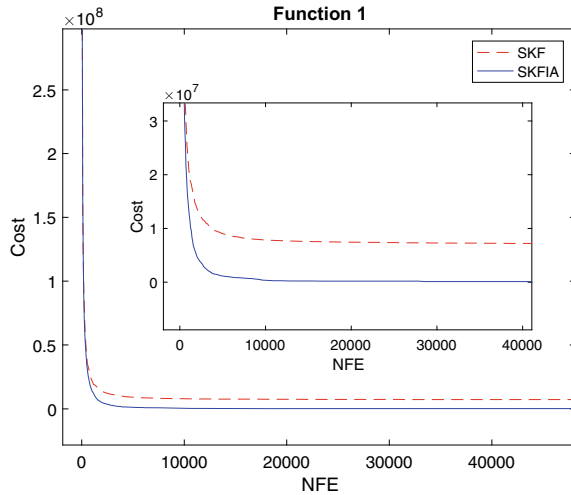
Table 2 Cost function attainment for the SKFIA

Function no.	Best	Worst	Average
<i>F1</i>	4.10×10^2	3.14×10^5	5.51×10^6
<i>F2</i>	2.02×10^2	1.19×10^4	1.37×10^7
<i>F3</i>	3.01×10^2	9.29×10^3	2.93×10^3
<i>F4</i>	400.00	438.41	4.36×10^2

Table 3 Cost function attainment for the SKF

Function no.	Best	Worst	Average
<i>F1</i>	4.70×10^4	1.81×10^7	5.71×10^6
<i>F2</i>	2.26×10^2	1.21×10^8	6.81×10^6
<i>F3</i>	3.55×10^2	1.72×10^4	4.16×10^3
<i>F4</i>	400.06	470.55	433.52

Fig. 1 Comparison of the graphical result for function 1



axis of the graph represents NFE while the vertical y-axis represents cost function value. Noted from the graph of Fig. 1, both SKF and SKFIA graphs shows a sharp convergence before NFE of 4000. Both graph unable to converge drastically after that point. However, it shows that the SKFIA graph has converged to a better cost function value.

On the hand, it is noted from Fig. 2 that both SKF and SKFIA graphs show a pretty identical convergence trend. However, by zooming-in the graph, it can be obviously seen that the SKFIA graph has a lower cost value. It also noted from the zoomed-in picture that the SKFIA graph has achieved at almost 0 cost at NFE 5000 while the SKF graph was still converging toward cost value of 6×10^6 . Similarly for function 3 from Fig. 3, both SKF and SKFIA graphs show almost identical convergence pattern. However it is noted that the SKF graph shows a slower convergence speed starting from a cost value of 450 towards the end of searching operation. On the contrary, result of function 4 as shown in Fig. 4 shows that the SKFIA graph significantly outperformed the SKF graph in terms of convergence speed. The SKFIA graph was converging smoothly toward the optimal value while the SKF graph was facing a problem starting at a cost value of 520.6. Both SKFIA and SKF achieved almost the same cost value at the end of the operation.

Fig. 2 Comparison of the graphical result for function 2

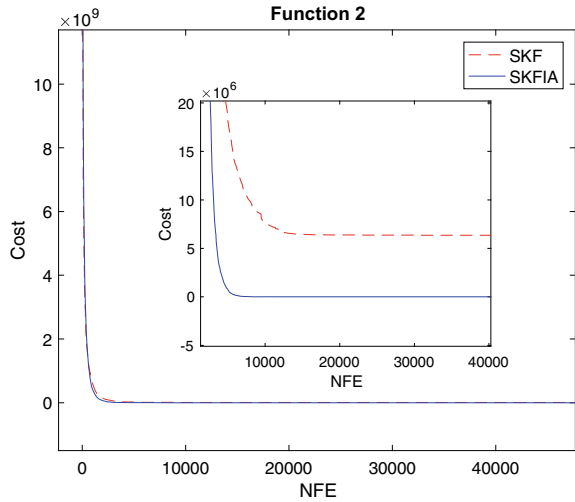


Fig. 3 Comparison of the graphical result for function 3

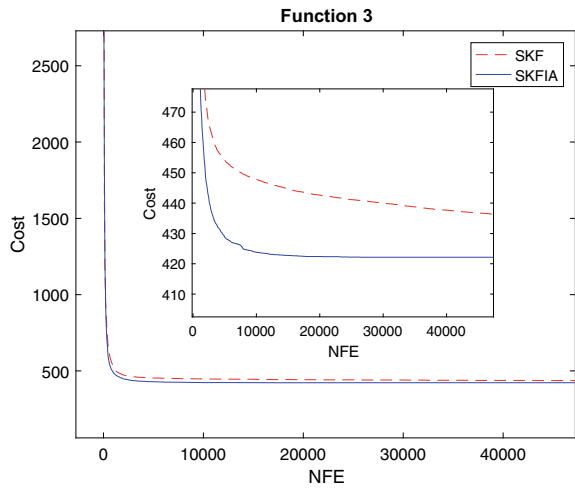


Table 4 shows result of the Wilcoxon Signed Rank test. The improvement of SKFIA is said as significant if p -value of the Wilcoxon Signed Rank test is below 5%. It is noted from the table, all the p -value are recorded as below 5% and this indicates that the accuracy performance of the SKFIA is significantly improved.

Fig. 4 Comparison of the graphical result for function 4

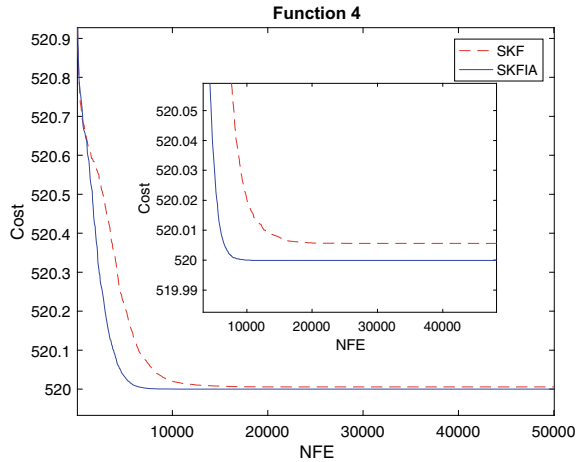


Table 4 Result of Wilcoxon signed rank test of 10 DIM CEC2014 functions

Function no.	Sum of +ve rank	Sum of -ve rank	z-value	p-value
<i>F1</i>	1326	0	-6.2146	<0.05
<i>F2</i>	1270	56	-5.6897	<0.05
<i>F3</i>	1160	166	-4.6586	<0.05
<i>F4</i>	1033	293	-3.4682	<0.05

5 Conclusion

An improved version of Simulated Kalman Filter (SKF) optimization algorithm which is known as SKFIA has been proposed in this paper. It is a modification in the Estimation stage of the SKF. Exponential term has been incorporated to balance exploration and exploitation. The proposed SKFIA has been tested with several standard benchmark functions and compared with SKF. The accuracy performance of the algorithms have been analyzed and discussed. Graphical plots have been included to portray convergence trend as well as the accuracy achievement. Results of the test have shown that the SKFIA graphs have outperformed the SKF graphs in both convergence speed and accuracy for most of the functions. In the future, the algorithm will be used to solve and optimize modelling and control problem of a robotic system.

Acknowledgements This work is supported by Fundamental Research Grant Scheme RDU160103 which is awarded by the Ministry of Higher Education Malaysia (MOHE) through Research and Innovation Department and Faculty of Electrical and Electronics Engineering of the Universiti Malaysia Pahang, Malaysia.

References

1. Ibrahim, Z., Aziz, N.H.A., Aziz, N.N.A., Razali, S., Shapiai, M.I., Nawawi, S.W., Mohamad, M.S.: A Kalman filter approach for solving unimodal optimization problems. *ICIC Express Lett.* **9**(12), 3415–3422 (2015)
2. Jusof, M.F.M., Nasir, A.N.K., Ahmad, M.A., Ibrahim, Z.: An exponential based simulated Kalman filter algorithm for data-driven PID tuning in liquid slosh controller. In: *Proceeding of 2018 IEEE International Conference on Applied System Invention (ICASI)*, pp. 984–987. IEEE, Chiba Japan (2018)
3. Azwan, A., Razak, A., Jusof, M.F.M., Nasir, A.N.K., Ahmad, M.A.: A multiobjective simulated Kalman filter optimization algorithm. In: *Proceeding of 2018 IEEE International Conference on Applied System Invention (ICASI)*, pp. 23–26. IEEE, Chiba Japan (2018)
4. Liang, J.J., Qu, B.Y., Suganthan, P.N.: Problem definitions and evaluation criteria for the CEC 2014 special session and competition on single objective real-parameter numerical optimization. In: *Zhengzhou University and Nanyang Technological University, Technical Report, Singapore* (2013)

Initial Study of Multiple Excitation Source for Electrical Resistance Tomography in Steel Pipe Application



Yasmin Abdul Wahab, Syazwani Amanina Syakyeen, Zainah Md. Zain, Normaniha Abd Ghani and Maziyah Mat Noh

Abstract Tomography is a method of reconstructing the image of an object's interest within the sensing zone. Electrical Resistance Tomography (ERT) system operates when using current as an excitation source and output voltage is measured at the detection electrode and the research will result in the changes of electric potential distribution. A lot of researches have been made using ERT to identify a liquid-gas regime in the steel pipe focused on improving image resolution of the regime. However, a common excitation source of ERT used only a single excitation. Thus, this research uses COMSOL Multiphysics as a platform for simulation of multiple excitations of electrical resistance tomography for liquid-gas regime identification in steel pipe. The analysis and performance of new simulation which applies multiple excitation sources have been compared with the single excitation. Besides, the project is limited to 54 mm inner diameter of a steel pipe. As a conclusion, 50% of the excitation source can increase the image resolution of those regimes especially in the middle of the steel pipe.

Keywords ERT · Multiple excitation source · Steel pipe

1 Introduction

Tomography comes from Greek word, 'Tomos' means section and 'graphy' means image [1]. In other words, tomography can be a method of reconstructing the image of an object's interest within the sensing zone. Industrial process tomography involves the measured signal from sensors located around an object such as a pipeline that can be implemented for industry purpose. By using an array of sensor, it can identify the medium concentration and a movement of an object interest inside the vessel by forming a cross-sectional image. One of the most favourite popular technique of

Y. Abdul Wahab (✉) · S. A. Syakyeen · Z. Md. Zain · N. Abd Ghani · M. Mat Noh
Faculty of Electrical and Electronic Engineering, Universiti Malaysia Pahang, 26600 Pekan,
Pahang, Malaysia
e-mail: yasmin@ump.edu.my

© Springer Nature Singapore Pte Ltd. 2019
Z. Md Zain et al. (eds.), *Proceedings of the 10th National Technical Seminar on Underwater System Technology 2018*, Lecture Notes in Electrical Engineering 538,
https://doi.org/10.1007/978-981-13-3708-6_30

tomography is Electrical Resistance Tomography (ERT). It is safe and inexpensive to operate and enabling real-time monitoring of the process.

In ERT, measurement strategy is important to define the experiment of a metal. There are four main strategies in ERT which is an adjacent strategy, diagonal strategy, opposite strategy and conducting boundary strategy [2]. Quantitative data explains the condition of the conductivity distribution inside the vessel. Thus, a chosen of suitable strategy is important since it can mislead the image construction. But, mostly current researches in ERT [3–5] only uses a single excitation to test the regime. Hence, when the number of electrodes increased, the area of electrode size become smaller and decreasing the signal level. Hence, the resolution image at the center region of interest also decreasing. In this paper, electrical resistance tomography sensor structure is presented by applying multiple excitations of conducting boundary strategy to identify the regime of liquid gas. By using multiple excitations, it is expected that more internal information can be obtained and improved. To test the expectation, the simulation of the system is built up using COMSOL Multiphysics software.

2 Basic Principle of ERT in Steel Pipe

The operation mode of ERT applies a current or voltage on an excitation electrode and measure a potential difference or a current at the detection electrodes [6]. Commonly, ERT system operates when using current as excitation source and output voltage is measured at the detection electrode since the project will results in the changes of electric potential distribution. The measured voltage consists of information on the conductivity in the sensing field and from processed information will figure out the internal flow status. In the case of conduction pipe, the electrodes need to be insulated from the conducting wall.

A common current strategy used for metallic pipe is named as conducting boundary strategy [7]. This strategy is proposed to replace the adjacent strategy in conducting vessel to overcome grounding effect as shown. It uses the wall itself as the ground electrode. This strategy considers each electrode operate sequentially as a current source while all the metallic vessel as a grounded current sink [6]. Since this research is using metal pipe, this strategy is suitable to be applied in. This approach is applied as a basis for multiple excitation sources in this paper.

3 Methodology

The simulation in 2D has been done by using COMSOL Multiphysics software. This simulation aimed to investigate and analyse the effect of multiple excitation sources

Fig. 1 Sixteen electrodes of ERT

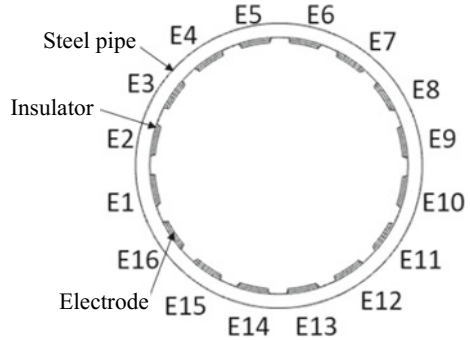


Table 1 Properties and specific dimension

Item	Value	Item	Value
Inner diameter of steel pipe	54 mm	Number of electrodes	16
Thickness of wall	3 mm	Excitation current	20 mA
Type of electrode	Silver	Electrode's width	6.4 mm

of ERT for liquid-gas identification in steel pipe. In building a model using COMSOL Multiphysics, a specific dimension, physics interphase, and study type need to be specified. This simulation study uses Electric Current (ec) interface under a branch of AC/DC model. It produces an electrical field and has the electrical potential required for the analysis.

Sixteen rectangular electrodes (E1–E16) were implemented and attached along the circumference of the steel pipe wall as shown in Fig. 1. The electrodes need to be positioned equidistantly to ensure the system can abstract maximum amount of information. Size of electrodes covers 60% of the surface of the region of interest to provide a high signal-to-noise ratio [3]. The electrode has been insulated from the metal wall. The applied parameters in the simulation are shown in Table 1.

After the physical model is built up, each of the domain needs to be defined based on its material to ensure the simulation synchronise with the real application. The details of each material used are shown in Table 2. To overcome the grounding effect of the vessel, the measurement strategy applied to the model is basically using conducting boundary strategy and then improved by using multiple excitation sources.

Table 2 Parameter of material used in the simulation

Material	Electrical conductivity, S/m	Electrical permittivity
Steel	132×10^6	1
Silver	628×10^7	
Plastic (ABS)	3.0×10^{-14}	2.0
Distilled water	5×10^{-3}	80

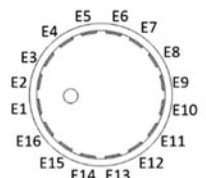
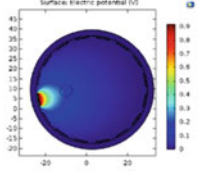
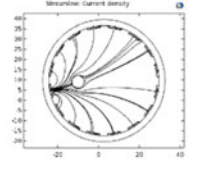
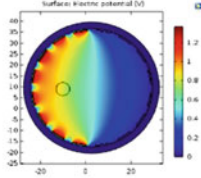
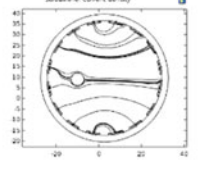
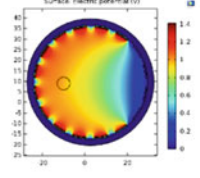
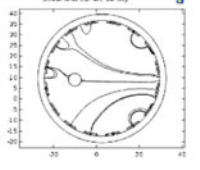
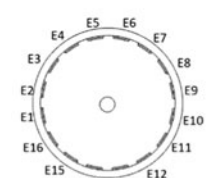
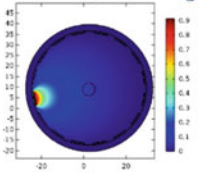
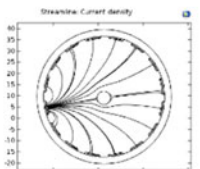
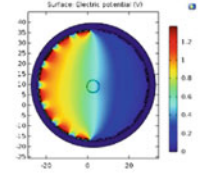
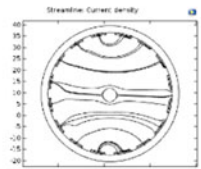
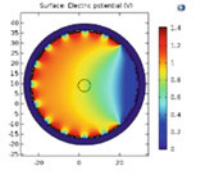
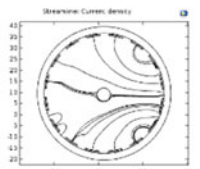
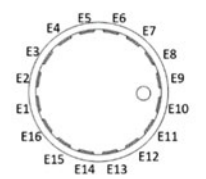
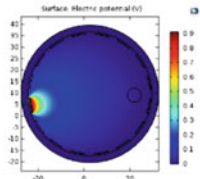
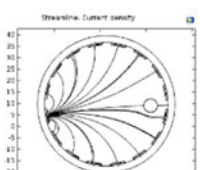
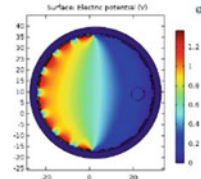
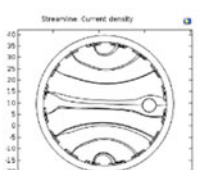
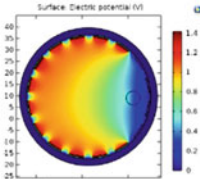
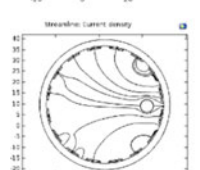
The whole conducting vessel is grounded and acted as current sink and the electrode acts sequentially as a current source. The voltage measurements were referenced to the same earth potential of the conducting boundary [3]. The source electrode is a constant current and measured data is from the output voltage of the detection electrodes. In this simulation, the single excitation source will be compared with the multiple excitation sources. These will investigate the theory mentioned beforehand.

4 Results and Discussions

The result of 3.0 mm in diameter bubble with 6.25, 50 and 75% of excitation source at distinguishing locations is presented in Table 3. The 6.25% means only 1 channel was set as the excitation source and the remaining channels as the receiver. It is also a common practice of conducting boundary strategy approach in ERT. Then, the excitation was improved by implementing multiple channels as the excitation sources which are 8 channels (50%) and then 12 channels (75%). The chosen of the percentage of excitation sources was based on a trial and error method. Each of excitation source shows a present of surface and streamline results for each position. The surface result means the penetration of the excitation signal while streamline is referred to the propagation of the electric field inside the pipe. Consequently, the surface results show an increment of penetration of the excitation signal inside the pipe with the increment numbers of excitation sources used at a time. However, an obstacle (bubble) was placed inside the pipe to observe the limitation of a number of multiple sources that can be applied to the ERT system. The origin (0, 0) position was the center of the pipe drawn in the COMSOL Multiphysics. Simultaneously, the results of sensor reading performance for each excitation is shown in Fig. 2.

In comparison, the left position (-10, 9) of the bubble is the closest position with the excitation source. Looking into the streamline and surface results, the bubble near to the excitation channels would affect more on the system. It gave a low penetration of the entire excitation signal into the pipe when the bubble placed near the source. This bubble will affect as an obstacle to the signal. Simultaneously, the electric field that represented the soft-field behavior could also be seen when the system consists of the bubble. Conversely, the 75% of excitation produce less streamline at the transmitter as the receiver less than the transmitter. In short, this part shows that 50% of excitation give enough current to detect the bubble since the number of excitation and receiver were equally transmit and receive the signal.

Table 3 Result of distinguish locations of 3.0 mm bubble

Geometry (size bubble 3 mm)	Excitation		
	Single (6.25%)	50%	75%
 <p>At position (-10, 9)</p>	 	 	 
 <p>At position (0, 0)</p>	 	 	 
 <p>At position (22, 9)</p>	 	 	 

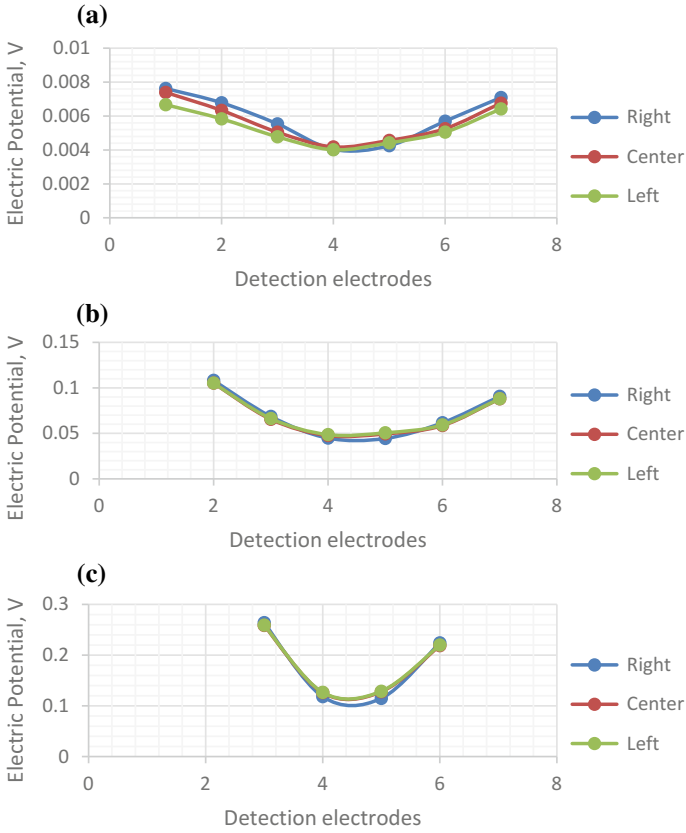


Fig. 2 Sensor reading performance at the detection electrodes E6 till E12 at different excitation: **a** 6.25%, **b** 50% and **c** 75%

5 Conclusion

In short, the objective of this paper is achieved. It is proved that there is an increment for the signal that received by the detection electrodes when the number of sources increased. 50% of the excitation source is believed to be enough for implementing in the ERT system. Future work will focus on hardware design and image reconstruction.

Acknowledgements The authors thank the Universiti Malaysia Pahang (RDU170368) for the support of this project.

References

1. Abdul, Y.A., Abdul Rahim, R., Fazalul Rahiman, M.H., Abdul Rahim, H., Ridzuan Aw, S., Mohd Fadzil, N.S., Jamaludin, J.: A review of process tomography application in inspection system. *Jurnal Teknologi*. **70**, 35–39 (2014)
2. Wahab, Y.A., Abdul Rahim, R., Pei Ling, L., Fazalul Rahiman, M.H., Ridzuan Aw, S., Mohd Yunus, F.R., Abdul Rahim, H.: Optimisation of electrode dimensions of ERT for non-invasive measurement applied for static liquid–gas regime identification. *Sens. Actuators, A* **270**, 50–64 (2018)
3. Ridzuan, Aw., S., Abdul Rahim, R., Fazalul Rahiman, M.H., Mohd Yunus, F.R., Goh, C.L.G.: Electrical resistance tomography: a review of the application of conducting vessel walls. *Powder Technol.* (2014)
4. Ridzuan Aw, S., Abdul Rahim, R., Fazalul Rahiman, M.H., Mohamad, E.J., Mohd Yunus, F.R., Wahab, Y.A., Fadzli, N.S., Jamaludin, J.: Study on bubble detection in a metallic bubble column using electrical resistance tomography. *8*, 19–25 (2014)
5. Yang, C., Wang, H., Cui, Z.: Application of electrical resistance tomography in bubble columns for volume fraction measurement. In: *Proceedings of the 2012 IEEE International Conference on Instrumentation and Measurement Technology*. pp. 1199–1203 (2012)
6. Dickin, F., Wang, M.: Electrical resistance tomography for process applications. *Meas. Sci. Technol.* **7**, 247–260 (1996)
7. Ridzuan Aw, S., Abdul Rahim, R., Mohd Yunus, F.R., Fazalul Rahiman, M.H., Wahab, Y.A., Nor Shah, M.B., Puspanathan, J., Mohamed, E.J.: Sensitivity map generation for conducting strategy in electrical resistance tomography. *Jurnal Teknologi*. **17**, 91–97 (2015)

Simultaneous Perturbation Stochastic Approximation Optimization for Energy Management Strategy of HEV



Muhammad Fadhlán Afif Nazri and Muhammad Ikram Mohd Rashid

Abstract This paper addresses optimization for hybrid electric vehicle (HEV). This project is using a single agent method to optimize the power losses under a specific driving cycle which is simultaneous perturbation stochastic approximation (SPSA) based method. For optimization process, four gain are added in four main parts of the HEV system. Those main parts are engine, motor, generator and battery. These four gain is controlled the output for each component to give the minimum power losses. The design method is applied to free model of HEV by using Simulink/MATLAB software while M-File/MATLAB is used to apply the SPSA method. The result from design method achieved a minimum reduction of power losses compared to original system. Thus, the comparison of result has been done to show the different before and after optimization.

Keywords Simultaneous perturbation stochastic approximation (SPSA) Optimization

1 Introduction

Hybrid electric vehicles (HEV) is introduce to help user reduce their daily cost when using vehicle as fuel consumption can be minimize with help of electric system. This is because HEV is using hybrid of two sources which are Internal Combustion Engine (ICE) and an electric generator as alternate energy source. ICE consume fuel (petrol/diesel) to generate energy to move the vehicle while electric motor use electricity that generate by generator. HEV give a minimum fuel consumption as the electric motor used to move the vehicle from the rest and ICE support the vehicle

M. F. A. Nazri (✉) · M. I. Mohd Rashid
Faculty of Electrical and Electronic Engineering, University Malaysia Pahang,
Pekan, Pahang, Malaysia
e-mail: mfadhlanaif@gmail.com

M. I. Mohd Rashid
e-mail: mikram@ump.edu.my

© Springer Nature Singapore Pte Ltd. 2019
Z. Md Zain et al. (eds.), *Proceedings of the 10th National Technical Seminar on Underwater System Technology 2018*, Lecture Notes in Electrical Engineering 538,
https://doi.org/10.1007/978-981-13-3708-6_31

when it start to accelerate. This fuel economic give an advantage to HEV compare to ICE vehicle. Energy Management Strategy (EMS) is a method to optimize the split usage between electric motor and fuel in order to give the best optimization of the fuel consumption. The main function of the EMS is power management. Automotive and communication control make a joint research that focusing on fuel consumption optimization [1]. Many approach has been proposed to optimize the fuel consumption which are consider many aspects in HEV model based on the method as optimal control and input control.

There are some aspect that can be optimize in HEV model. One of them is optimize the power usage in four main components in HEV which are ICE, generator, motor and battery. Most HEV research is focusing on optimization using advanced control algorithms which lead to minimization of the energy circulation loss [2]. The power usage can be optimize by reducing the power losses in those component to give a high performance to HEV.

One of method that can used to optimize the HEV model is using simultaneous perturbation stochastic approximation (SPSA). This method is one of stochastic approximation group method. This type of SA has potential applications in a number of areas relevant to statistical modelling and control [3]. Thus, this method can be most suitable for this project.

As conclusion, EMS is needed to help the development of HEV in future for a better performance to compute with others type of vehicles. This optimization is important to give more advantage to the HEV model. This paper presented SPSA technique to solve the EMS problem for HEV free model.

2 Free Model of HEV

A simple hybrid electric vehicle model is chosen due to its simplicity and practicality. The model is taken from MATLAB library archive to be apply in the simulation. This model consists of functioning circuit that will be able to produce output such as vehicle velocity, power loss, and etc. It is also made up from electrical and physical part. Hybrid Electric Vehicles (HEVs) consist of two power sources, that is, (1) Internal Combustion Engine (ICE) and (2) battery [4]. The block diagram of the simple HEV model as below: (Fig. 1).

In order to tune our output which are power loss and fuel consumption, there are four parameters that are being tune which are the engine, electric generator, electric motor, and battery. There is one gain that are being place inside each of the four parameter. Before the tuning is done, the initial output is being taken. The power loss and power graph is the being recorded so it will be compare to the final result.

Gain is being used. L, H, Y, and U gain is placed inside the four parameter and been given initial value of 1. With this initial value, first simulation will be run and the output will be recorded. Then using Simulated Annealing Algorithm, new number will be generated and replace the initial value. Thus new output performance will be produce.

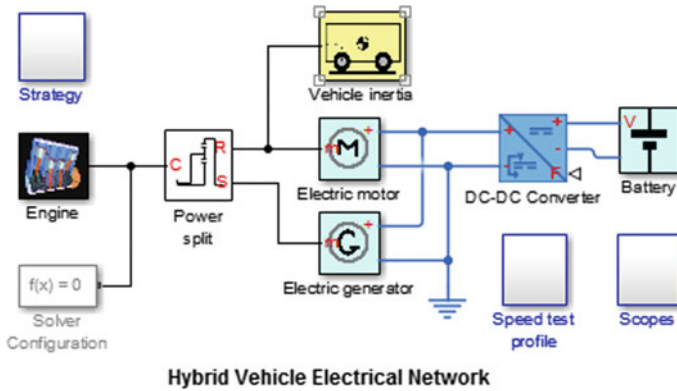


Fig. 1 HEV models MATLAB Simulink

3 Methodology

In this section, it is presented how to implement the design into the HEV system. Combination of Simulink and M-File in MATLAB software is used. The Simulink used to for HEV model while M-File used to optimize the gains in the Simulink based on SPSA method. SPSA algorithm is as below:

A general optimization problem is given by

$$\max_{x \in R^n} f(x) \text{ --- numbering?}$$

where $f: R^n \rightarrow R$ is the objective function and $x \in R^n$ is the design variable.

The SPSA algorithm updates the values of design parameter for each iteration to achieve $x^* \in R^n$. The update law is:

$$x(k + 1) = x(k) + ak g(x(k)) \tag{1}$$

For $(k=0, 1, \dots)$. $g(x(k))$ is the estimation of the gradient at the iterate k, which is given by

$$g(x(k)) = \frac{f(x(k) + c_k \Delta_k) - c_k \Delta_k}{2c_k} \begin{pmatrix} \Delta_{k1}^{-1} \\ \vdots \\ \Delta_{kn}^{-1} \end{pmatrix} \tag{2}$$

where $\in R^+$ and $\in R^+$ for some given non-negative numbers $a, A, \alpha, c,$ and γ and Δ_{ki} is the random number drawn from the Bernoulli distribution.

Step for SPSA algorithm is as below:

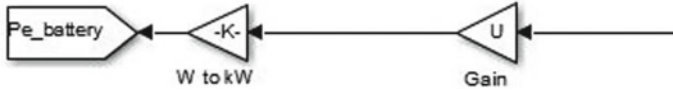


Fig. 2 Gain in battery

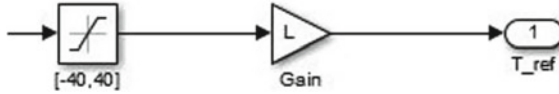


Fig. 3 Gain in motor

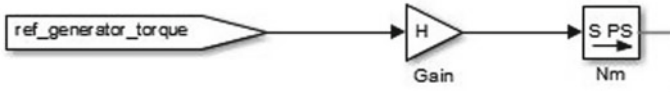


Fig. 4 Gain in generator

- Step 1: Enter non-negative coefficients a , c , A , α and γ for SPSA gain. Initial condition of design parameters is set as $\theta(0)$ and $k=0$.
- Step 2: Generate n -dimensional random perturbation vector Δk .
- Step 3: Obtain two values of the objective functions $f(\theta(k) + c(k) \Delta(k))$ and $f(\theta(k) - c(k) \Delta(k))$
- Step 4: Calculate the vector $g(\theta(k))$.
- Step 5: Execute the update law in first equation and get $\theta(k+1)$.
- Step 6: If a pre-specified termination criterion is satisfied, the algorithm terminates. Otherwise, repeated step 2

Based on the SPSA algorithm above, summary of our design procedure is as follow:

- Step 1: Get the number of maximum iterations. Identify the four gain in the system with initial value of 1.
- Step 2: Determine value of objective function for each iterations by performing SPSA algorithm as shown above.
- Step 3: After reach the maximum iteration, the lowest value of power losses is selected and compare to the original system for the result.

Algorithm of SPSA is implement in M-file (Matlab) to generate the value for parameters for each iteration while running. The value will sent to Simulink (Matlab) block diagram of HEV where the parameters are placed. M-file also used to call the HEV in Simulink to run over and over again according to iteration until it reach maximum iteration. So, the value or four parameter will change continuously and give a different output value of power losses. The four parameters is as below: (Figs. 2, 3, 4, 5, Table 1).

Fig. 5 Gain in engine



Table 1 Gain name and parameter

Gain name	Parameter
L	Electric motor
Y	Internal combustion engine
U	Battery
H	Electric generator

4 Result

In this section, we discuss about the value of parameters that most suitable to use for this free model HEV. There are many value that we get from the iterations that we have done. Each of value that came out is generated by SPSA algorithm that we implement in coding (m-file Matlab). Each of the parameter give a different value for each iteration to minimize the power losses. After we get the lowest value of power loss, the analysis is taking place as to determine the gain values. SPSA-based method may be extended to a more complicated situation as long as the objective function can be measured [5]. Also, comparison between the original and the optimize model for the analysis part. Tables 2 and 3 show value for all gains (L, Y, H and U) and power losses (Ploss).

Finally, a comparative assessment between the proposed scheme and power loss problem is presented [6].

5 Discussion

In this section, we will discuss about the result we get. Based on table in result above, the lowest power loss that we get at 8th iteration with 0.1407 while the worst is 0.2282 at 3rd iteration. By comparing with the original model which is 852.7655 value of power losses, this deduction is quite large margin between them. As we determine the lowest power loss, we obtain the gain value for each of parameter. All the value for gain parameter is shown in Table 4.

For more information about the different between the optimize model and the original model, Table 5 show the comparison.

Since the shaft speed is maintained as the same, it is mean that both of model moving at the same speed and reducing the power consumption and power loss by the HEV model.

Table 2 Gains value for each iteration

Gain iteration		Y	L	H	U
1st	x(1)	0.8134	0.8134	0.8134	1.1866
	x(50)	1.2764	0.1480	0.4138	0.8754
2nd	x(1)	0.8134	1.1866	0.8134	1.1866
	x(50)	1.1464	-0.0961	1.1692	0.8824
3rd	x(1)	0.8134	0.8134	1.1866	1.1866
	x(50)	1.3188	1.9521	-0.0932	1.5265
4th	x(1)	0.8134	0.8134	0.8134	1.1866
	x(50)	1.1227	-0.1245	0.4087	1.1515
5th	x(1)	1.1866	0.8134	0.8134	1.1866
	x(50)	1.1004	0.1666	0.9755	1.1474
6th	x(1)	0.8134	1.1866	1.1866	1.1866
	x(50)	1.9611	0.1621	1.0608	1.1473
7th	x(1)	0.8134	1.1866	0.8134	1.1866
	x(50)	0.5298	-0.1032	1.2758	1.1541
8th	x(1)	1.1866	0.8134	1.1866	0.8134
	x(50)	1.5232	0.1594	1.0878	0.8821
9th	x(1)	1.1866	0.8134	0.8134	1.1866
	x(50)	0.5478	0.1552	0.8911	0.8750
10th	x(1)	1.1866	0.8134	0.8134	0.8134
	x(50)	0.3190	0.1472	0.6851	0.8792

Table 3 Value of power loss for each iteration

Iteration	Power loss
1st	0.1983
2nd	0.1860
3rd	0.2282
4th	0.1753
5th	0.1634
6th	0.1779
7th	0.1581
8th	0.1407
9th	0.1721
10th	0.1673

Table 4 Gain value for parameter at lowest power loss

Gain parameter	Value
Internal combustion engine	1.5232
Electric motor	0.1594
Electric generator	1.0878
Battery	0.8821

Table 5 Comparison between graph of original and optimize HEV model

Model	Original model	Optimize model
Graph		
Power loss		
Power		
Shaft speed		

6 Conclusion

This paper has presented optimization of a free model HEV by using simultaneous perturbation stochastic approximation method to reduce power loss as a cost function. This project work properly and a minimize power loss value as the output that can give advantage to HEV users. SPSA is an efficient gradient-free SA algorithm that has performed well on a variety of complex optimization problems [7]. The technologies of HEV can be develop further more in the future to compete in automotive industry. As the result is positive for development, this project can be considered as successful and the innovation apply to the HEV is suitable. Since this is a free model HEV, there are many aspects that can be optimize for future uses.

References

1. Ahmad, M.A.: Switching controller design for hybrid electric vehicles. *SICE J.* **7**(5), 273–282 (2014)
2. Wang, A.A.F.Q.: Plug-in HEV with CVT: configuration, control, and its concurrent multi-objective optimization by evolutionary algorithm. *Int. J. Autom. Technol.* **15**(1), 103–115 (2014)
3. Spall, J.C.: Multivariate stochastic approximation using a simultaneous perturbation gradient approximation. *IEEE Trans. Autom. Control.* **37**(3), (1992)
4. Bansal, H.O.: A review of optimal energy management strategies for hybrid electric vehicle. *Int. J. Veh. Technol.*, (2014)
5. Ahmad, M.A.: Model free tuning of variable state of charge target of hybrid electric vehicles. *The International Federation of Automatic Control*, (2013)
6. Spall, J.C.: An overview of simultaneous perturbation method for efficient optimization, *John Hopkins APL Technical Digest*, **19**(4), (1998)
7. Prokhorov, D.: Toyota Prius HEV neuro control, In: *Proceedings of International Joint Conference on Neural Networks* (2007)

Part III
Applied Electronics and Computer
Engineering

Image Processing-Based Flood Detection



Angga Ariawan, Dwi Pebrianti, Ronny, Yudha Maulana Akbar,
Lestari Margatama and Luhur Bayuaji

Abstract This paper discusses about the design of an online flood detection and early warning system which integrated to using Raspberry-PI and optical sensor. Raspberry-PI is a single board of computer which in this case we design as an image processor to process image obtained from the webcam and update the result to the twitter. This research can help some of the citizens who live near the river to get the updated information regarding water conditions and the possibility of flooding so that they can take action to secure their properties and families as soon as possible. We use OpenCV as an image processing application. The steps are as follows: (1) Region of Interest to create a portion of an image to filter or perform some other operation. (2) Brightness and contrast adjustment in order to get brighter and better image before the next process. (3) Grayscale and threshold to create segmentation object with Otsu-thresholding. (4) Edge detection algorithm to find edge points on a roughly horizontal water line and riverbank height. By using the above method, the system can read and monitor the water level of a river or other water bodies. If the water level exceeds the specific threshold, the system will generate notification as early warning for the possibility of flooding by uploading the text and image to the twitter regarding that condition. The citizens will get the information if they follow that account (early warning system) on Twitter. The result of this simulation using prototype that we have made is that the system can read the water conditions with an increase in accuracy reaching 99.6%.

A. Ariawan (✉) · D. Pebrianti · L. Bayuaji
Magister of Computer Science, Universitas Budi Luhur, Jakarta 12260, Indonesia
e-mail: anggaarial@gmail.com

Ronny · Y. M. Akbar
Faculty of Engineering, Universitas Budi Luhur, Jakarta 12260, Indonesia

L. Margatama
Faculty of Information Technology, Universitas Budi Luhur, Jakarta 12260, Indonesia

L. Bayuaji
Faculty of Computer Science and Software Engineering, Universiti Malaysia Pahang, Pekan,
Malaysia

D. Pebrianti
Faculty of Electrical and Electronics Engineering, Universiti Malaysia Pahang, Pekan, Malaysia

© Springer Nature Singapore Pte Ltd. 2019

371

Z. Md Zain et al. (eds.), *Proceedings of the 10th National Technical Seminar*

on Underwater System Technology 2018, Lecture Notes in Electrical Engineering 538,

https://doi.org/10.1007/978-981-13-3708-6_32

Keywords Flood detection • Early warning system • Optical sensor
Image processing

1 Introduction

Jakarta is a land that is geographically located in the lowlands. Jakarta is also a city where 13 rivers flow. Flooding is a phenomenon that almost always happens every year in Jakarta. One aspect that is often overlooked is that floods are closely related to the unity of the so-called watersheds (Watershed or Watershed) [1]. Floods cause losses that are not small, both moral and material, and cause various post-disaster problems such as health problems. Various ways have been carried out by both the government and the independent community to deal with this problem. However, various efforts made to overcome flooding will not be effective without an early warning system of floods. Without an adequate early warning system, the surrounding population will find it difficult to find out if the flood comes suddenly. Such conditions can exacerbate the impact caused by flooding, such as loss of property, securities, and even loss of life because of people are not aware that floods will come [1]. Therefore, it must be realized, that a flood early warning system needs to be built so that it can be used as a tool for integrated flooding forecasts and minimize the impact or risk that occurs in the community.

Along with the rapid development of technology and supported by several devices that have easily access, a tool is made to detect flood in an early stage. Broadly speaking, this tool will include a camera which will take pictures in real time. Then the image will be processed by digital image processing. Digital image processing is done by utilizing Raspberry-PI single board to produce a valid information about how high the water debit changes are updated. In addition to processing with digital images, this system will also send the updated image capture on Twitter. This will make people more aware about flood detection information.

The outline of the paper will be as follows. Section 2 is the literature review. Section 3 will discuss the detail method used in this study. Section 4 will be the result and discussion. Conclusion and future works will be explained in Sect. 5.

2 Literature Review

Several methods to detect early flooding in previous research have been carried out. Some of the methods use in literature review are electronic sensors and remote sensing.

2.1 Water Level Sensor Detector

There are various ways have been done either by the government or by the non-government community to understand and solve this problem [2]. To give an early warning, many electronics systems have been developed by using a microcontroller or microprocessor and sensors for detecting the level of the water surface. In most cases, water level control system still uses physical contact between the sensor and the water. One example is by using water as a conductor of the sensor systems. This is the same method as in the automatic water pump [3]. When the water reaches a certain level, then the sensor will be connected to the water and the water pump will stop or triggers the alarm in case of flood detection. Other systems were developed by using ultrasonic sensors for measuring the depth of water by calculating the time when sensors transmit ultrasonic waves until the signal is received back by the sensor, while not directly contact the water, the sensor still uses float as detection surface [4]. In either case, especially for trash-ridden rivers in Jakarta, these systems are prone to damage by floating debris; therefore, a non-contact method by using optical sensor is proposed [5].

2.2 Remote Sensing Satellite Detection

Revilla-Romero et al. [6] proposed flood detection by evaluating images from satellite. The aim of his study is to test the potentials and constraints of the remote sensing signal of the Global Flood Detection System for converting the flood detection signal into river discharge values. The study uses data from 322 river measurement locations in Africa, Asia, Europe, North America and South America. Analysis of the potential factors affecting the satellite signal was based on a classification decision tree (random forest) and showed that mean discharge, climatic region, land cover and upstream catchment area are the dominant variables which determine good or poor performance of the measurement sites.

3 Methods

This section will discuss the detail of the process proposed in this study. Figure 1 shows the flowchart of the study.

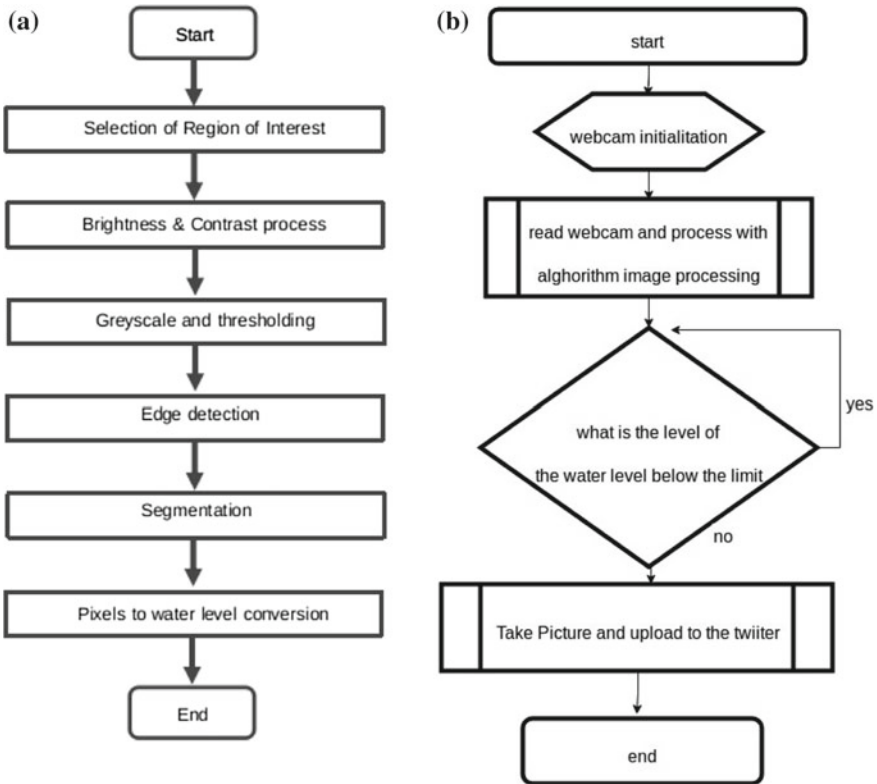


Fig. 1 Flowchart algorithm system image processing (a) and Flowchart algorithm system (b)

3.1 Region of Interest

Region of Interest (ROI) is basically samples within the data set identified for a particular purpose. The concept of ROI is to select a certain area in an image that will be used for the next operation such as filtering or performing some other operations on.

In this study, the complete image is captured from a camera that is placed in front of a water level measuring board. The water level measuring board is shown in Fig. 2. The measuring board contains regions which are represented in red, blue, yellow and green colours. Different observation places have their own representation colours for the water level measuring board.

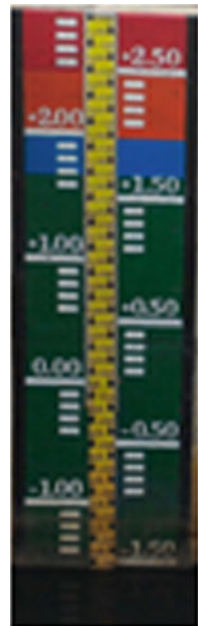
Figure 2a shows the area with normal condition, where the water current flow is low. Figure 2b shows the area with a high water current flow.

The ROI used in this study is the area of the water level measuring board. The selection is done by using template matching. The template used here is the water level measuring board. Figure 3 shows the template used in this study.



Fig. 2 Water level measuring board **a** during normal condition and **b** during high water flow

Fig. 3 Template of water level measuring board



3.2 *Brightness and Contrast Process*

Brightness and contrast is one of basic operation of image processing. Brightness is often used to get a brighter image [7]. Increasing brightness means increasing the value of a pixel in coordinate (x, y) with a constant α . If α is positive value, the brighter image will be generated otherwise the darker image will be generated.

$$g(x, y) = f(x, y) + \alpha \tag{1}$$

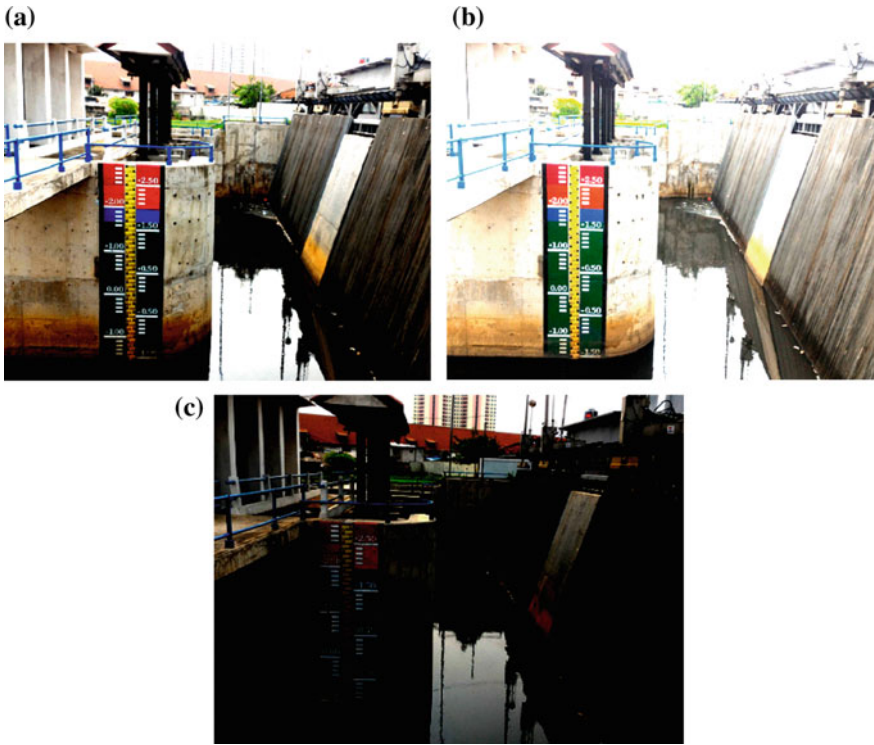


Fig. 4 Brightness and contrast image of Fig. 2a with contrast range **a** 0.3–0.7, **b** 0.1–0.5 and **c** 0.6–1

Figure 4 shows the result of brightness and contrast process from Fig. 2a. This brightness and contrast process is conducted to obtain a clearer image when the weather condition changes. During the cloudy day, Fig. 4a, b will be used. During the bright sunny day, Fig. 4c will be used for the next process.

3.3 *Grayscale and Threshold*

Grayscale is an image in which the value of each pixel is a single sample, that is, it carries only intensity information. Images of this sort, also known as black-and-white, are composed exclusively of shades of gray, varying from black at the weakest intensity to white at the strongest [8]. Threshold is a point which can be used to convert a grayscale image into a binary image. The intensity below this point will be converted into black and the other will be converted to white [9]. The grayscale image with its histogram is shown in Fig. 5 and binary image is shown in Fig. 6.

Fig. 5 a Grayscale image and b its histogram

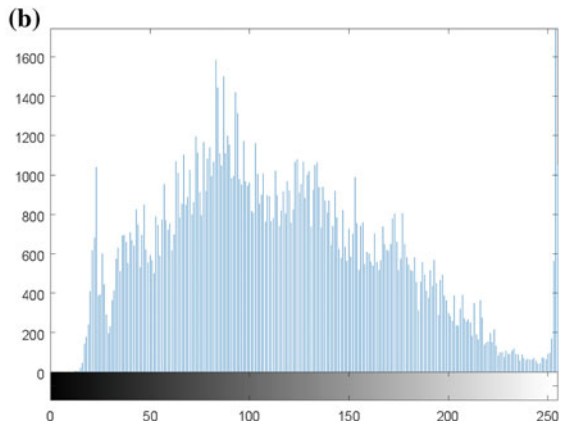
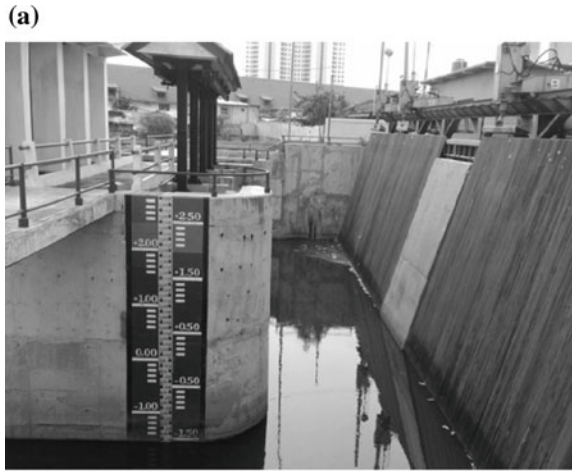


Fig. 6 Binary image from thresholding of Fig. 5



Table 1 Pixel to water surface level conversion

Pixel	Water surface level (cm)
160	200
150	250
140	300
130	350
120	400
110	450
100	500
90	550
80	600
70	650
60	700
50	750

3.4 Edge Detection

An edge detection algorithm is used to find edge points on a (relatively) horizontal water line and point of dam's height. This edge detection scheme was both effective and fast at finding the water edge. The result of edge detection is a segmented image, which separate water image and the others. The segmented image after edge detection is shown in Fig. 4. The red rectangle is Region of Interest area, the green rectangle is the edge detected and connected by lines.

A success edge-detection will generate a segmentation which separates the water image and the other. The system will compare the edge pixel coordinate (in this case y coordinate) to calculate the current water surface level. If the water surface level is increased, the value of y pixel will be decreased and the green rectangle will be shorter. The pixel to water surface level conversion used in this simulation is shown in Table 1. To get an accurate calculation, the system has to be calibrated first to get pixel/cm value.

4 Result and Discussion

The result after applying the proposed method is shown in Fig. 7. This figure shows the edge detection of Fig. 2a. The detected water level measurement board is highlighted with a green box after conducting the edge detection. Figure 8 shows the segmented image. The green box in Fig. 8 is the area of water level measurement board that is not contacted with the water. Then the total number of pixel on this area is calculated to get the real water level measurement.

The water level reading uses a program called checker. The result shows that the indicated water level is 473.115 cm. The real height of the water is 475 cm. This



Fig. 7 Detected water level measurement board



Fig. 8 Segmented image

shows that the difference in reading is 1.9 cm or about 0.4% of error. This means the accuracy of the high reading of water using this tool is around 99.6%.

Several experiments were conducted to find the relation between the detected pixel using the proposed image processing and the real water level measurement. Table 1 shows the result of the process.

5 Conclusion

This study proposed a system for flood detection using image processing. The proposed system is an embedded systems that were built using Raspberry-PI, webcam, and openCV for image processing. The result of the study by using the proposed prototype is that the system can read the water conditions with an increase in accuracy about 99.6%. Automatic thresholding method with triangle thresholding method and Otsu method helps to determine what threshold value is given. The subpixel method makes the reading more accurate.

References

1. Riyanto, I., Margatama, L.: Study of watershed segmentation for flood area mapping in Jakarta. In: International Conference on Information Technology and Electrical Engineering (ICITEE) Proceedings, pp. 52–55. Universitas Gadjah Mada, Yogyakarta (2014)
2. Pramusinto, W., Riyanto, I.: Mobile system to support flood area information distribution. Case study: central Jakarta area. In: The 5th Indonesia-Japan Joint Scientific Symposium Proceedings, pp. 301–306. Chiba University, Chiba, Japan (2012)
3. Akbar, Y.M., Musafa, A., Riyanto, I.: Image processing-based flood detection for online flood early warning system. In: The 6th Indonesia-Japan Joint Scientific Symposium Proceedings, Universitas Gadjah Mada, Yogyakarta (2014)
4. Isworo, H.: Sensor level air dan pengontrol pompa air otomatis berbasis Mikrokontroler Atmega8. *Jurnal Dinamika UMT* **1**(2), 84–97 (2016)
5. Ulinuha, B.D., Widjiantoro, B.L.: Rancang bangun sistem pengendalian level pada mini mikrohidro skala laboratorium di workshop instrumentasi. Institut Teknologi Sepuluh Nopember, Surabaya (2012)
6. Revilla-Romero, B., Thielen, J., Salamon, P., De Groeve, T., Brakenridge, G.R.: Evaluation of the satellite-based Global Flood Detection System for measuring river discharge: influence of local factors. *Hydrol. Earth. Syst. Sci.* **18**(11), 4467–4484 (2014)
7. Kadir, A.: *Pengolahan Citra Teori dan Aplikasi*. 1st edn. Andi, Indonesia (2018)
8. Otsu, N.: A threshold selection method from gray-level histograms. In: *IEEE Trans. Sys., Man., Cyber.* **9**(1), 62–66, IEEE (1979)
9. Abutaleb, A.S., Eloteifi, A.: Automatic thresholding of gray-level pictures using 2-D entropy. In: *Applications of Digital Image Processing X Proceedings, SPIE, USA* (1988)

Enhancement on Stain Detection for Automatic Handwashing Audit Vision System



Faradila Naim, Muhammad Aizat Romaino and Rosyati Hamid

Abstract Hand hygiene of the health care worker is critical to prevent infectious disease such as airborne diseases, nosocomial infections, and Hepatitis A among patients. Currently, the handwashing audit among hospital staffs are done manually by observation from an expert. There is a need for automation ease the process and accuracy in detection using vision system. This paper focus on the enhancement of the established prototype and the detection system by the additional third template. The prototype is enhanced by size reduction, sturdier material and hands placement base. The vision system uses a robust threshold to detect the discolored stain with an enhancement on stain templates. The detection and recognition of palm in images is a key research topic that has attracted attention owing to an unveiling human perception mechanism. The system accuracy has increased by 40% from previous work by the enhancement which for three cases the system accurately detects stains on washed hands with Glo Germ by 71% and unwashed hand with Glo Germ by 81%.

Keywords Handwashing · Hand detection · Image processing

1 Introduction

Hand hygiene is an important aspect of health control. A number of infectious diseases can be spread from one person to another by contaminated hands. These diseases include gastrointestinal infections, such as Salmonella, and respiratory infections, such as influenza. Washing hands properly can help to prevent the spread of the germs (like bacteria and viruses) that cause these diseases. To reduce the infection of the diseases, the hand-washing screening audit's method was done manually. Thus, this process can be automatically detecting the area of unclean hand without the help from the human expert. The goal is to accurately detect stain percentage that using technology likes computer to help this process. Hand washing using plain soap will

F. Naim (✉) · M. A. Romaino · R. Hamid
Univeristi Malaysia Pahang, 26600 Pekan, Pahang, Malaysia
e-mail: faradilan@ump.edu.my

© Springer Nature Singapore Pte Ltd. 2019
Z. Md Zain et al. (eds.), *Proceedings of the 10th National Technical Seminar on Underwater System Technology 2018*, Lecture Notes in Electrical Engineering 538,
https://doi.org/10.1007/978-981-13-3708-6_33

not remove pathogens from the hands of healthcare workers' (HCWs). Adoption of hand washing using alcohol-based hand rubs is considered for hand hygiene.

This issue is promoted by the CDC and WHO and embraced by many national hand hygiene guidelines which based on the evidence of better microbiology efficacy, less time required to achieved the desired effect, point of patient care accessibility and a better skin tolerance profile [1]. Rough eyes cannot detect the germ just by looking the hand. To tackle and overcome this problem, the modern technology or new machine is needed to improve the work style and lifestyle [2]. Therefore, the Hand wash screening vision system was done to reduce the infection of the diseases. On other hand, this process can be easily detected the area of unclean hand without help from the human. The aim is to accurately detect stain percentage that using technology like computer and selected software to generate the system [3].

David F Llorca et al. propose a vision system that detects the correctness of handwashing technique according to the six-steps handwashing technique to detect all six motions being done correctly by the user. In this study: hand segmentation was done by combining color and motion analysis, hand tracking was done using particle filter and k-means clustering, and classification of hand gestures using support vector machine ensemble. The result was shown to be accurate up to 97.81% as compared to human expert in one of six pose of the hands [4]. This system is designed to detect the correctness of handwashing techniques based on the motions and angles of the person when washing their hands. Meanwhile, this paper is to detect the amount of stained left on washed hands to indicate the correctness of handwashing.

Amiraj Dhawan et al. proposed a hand segmentation technique for Human Computer Interaction application that is based on Otsu's threshold to segment out the hand from the background. Fingers detection was done using convex hull method which also includes hand's orientation detection based on calculated object's mid-point and convexity defect's depth. This study is useful in hand gesture's controlling a computer graphics or robots amongst many HCI applications [5].

Ching-Liang Su have proposed a system that entitled of palm extraction and identification to determine the precise location of fingertips and finger to finger valleys on a hand. The robust method used to detect the hand and fingers images has the flexibility in hands positioning. In the extracting palm process, the finger-to-finger valleys are precisely located. The index, middle and ring fingers can be truncated after locating the valley positions. Author also give other extracting method for finger image with two additional pixels for further erosion and truncation of the small finger [6].

Navil Parveen et al. compared four template methods including Navie Template Matching(NTM), Image Correlation Matching(ICM), Pattern Correlation Image(PCI), Grayscale Based Matching(GBM), Edge Based Matching(EBM) which he concluded that for large image processing, these methods are lacking of these methods being highly computational although it is useful in many fields of applications such as biological science, image processing, computer vision and remote sensing [7].

Most of the previous work mentioned are related to hand detection techniques which is incomparable to this work. This work is focused on the handwashing audit

Table 1 The dimension of the prototype

Dimension measurement	Size (cm)
A—Length	19.7
B—Width	37.0
C—Height	27.5
D—(Hand insert window height)	6.5
E—(camera to side of the box)	11.0
F—(side of box to camera)	5.3
G—(camera to UV lamp)	4.0
H—(UV lamp to side of box)	6.0

done to the hospital staffs to measure their correctness of handwashing by calculating the amount of stained left on their washed hands. The work presented in this paper is focusing on the prototype and system enhancement of unclean handwashing vision machine.

2 Methodology

2.1 Enhanced Hardware Prototype

Previously, the first prototype was designed with darkened Perspex to ensure no light reflection from surrounding can interfere with image captured and has bigger square dimension [8]. The dimension followed by second generation prototype has reduced its dimension by 40% [9]. The third generation prototype in this paper has been reduced by 50% and the new dimension is stated in Table 1 and Fig. 1.

The prototype includes a UV lamp and a USB camera attached to the inside the top cover located at position described in Fig. 2 and Table 1. The camera is connected to the computer to capture the image of left hand palm from the prototype to be processed for stain detection. For hand placement under the UV light, fingers positioning is very critical since stain detection will be done using template matching techniques. This is to overcome the mismatched problems in previous work where fingers position did not match the templates used [9]. Hence, the finger skeleton pattern is introduced on the prototype base to guide the user in finger positioning to have accurate template matching for stain detections.

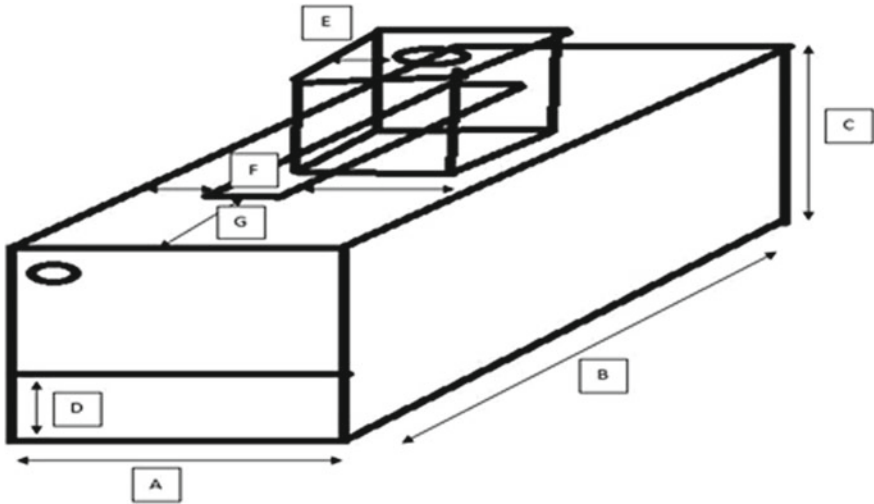


Fig. 1 Enhancement of the dimension of the prototype



Fig. 2 Guidelines for the stains area on hands to be detected [10]

2.2 Image Processing

In order to understand the image processing techniques to be used in this system, one needs to understand how the stain detection on unclean washed hands protocol is done using the third generation prototype. The first step is when the user rubs the GloGerm on their palm gently to imitate bacteria on hand. Then, they have to

wash their hands according to the six steps handwashing techniques promoted by the World Health Organization (WHO). The washed hand then will be inserted to the prototype to be audited. UV light is on in the prototype will highlight the traces of GloGerm on the palm signifying that the user was not properly washed their hands that left some stains on the palm. This is done by the camera capturing the palm image and processing it to only detect the highlighted are with GloGerm. The level of hand washing technique is determined by where the stained is detected on hands area given by three areas; never missed area, frequently missed area and sometimes missed area as shown in Fig. 2. These locations on hands indicate the areas which bacteria must not be present when the hand is properly washed in the six-steps guideline by WHO.

Image processing techniques to detect the stained was done using Matlab 2017b. Previously [9], template matching technique was used to identify the handwashing level based on 2 templates only. This paper improved this method by adding another template. The third additional template which is the never missed template is the most important template since any stained detected in this area means that the user has a poor handwashing techniques since in these spots if the user washes their hands properly according to the six steps handwashing techniques, all the stains must be cleared in the area. Previously, the work done focuses only in the frequently missed area and sometimes missed area to accurately calculate the percentage of the stains that a user might get even with a proper handwashing technique. These percentages will be useful in further study related to handwashing techniques or even the study of related infectious diseases caused by unhygienic hands.

The data involved in the study includes 20 individuals hand images giving in the total of 90 images grouped in three cases as mentioned in Sect. 3.

2.3 Handwashing Templates

The templates are generated from Fig. 3 are three templates: never missed template, frequently missed template and sometimes missed templates. The first template (never missed) signify the area of hand which must not be missed if the six-steps handwashing techniques is applied correctly. If any stain is detected in this area, the user has a very poor handwashing technique. The second template which is the sometimes missed area which indicate that if any stain is detected in this area, it is acceptable if only 30% or less area detected then user can pass the audit. The last template if stain is detected less than 50% in this area, then user will pass the audit. This is summarized in Table 2 and the templates generated in binary format is shown in Fig. 2.

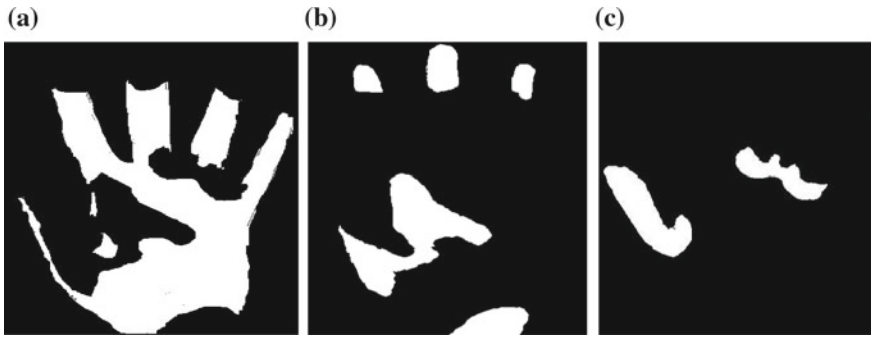


Fig. 3 **a** Never missed template, **b** sometimes missed template, **c** frequently missed template

Table 2 The percentage of area allowed for a successful hand wash audit

Type of Template	Area of Detected Stain (%)
Never missed	<0
Sometimes missed	<30
Frequently missed	<50

Table 3 Threshold values used in Hue for detection

Item	Minimum Value	Maximum Value
Separate palm and stain	30	45
Separate palm and background	18	28

2.4 Stain Detection

The input image captured resolution is 330×474 in RGB (red-green-blue) color space. Conversion to HSV (hue, saturation, value) space is done to threshold the palm color. Two sets of hue value ranges are used to separate out the: palm-background and palm-stain as stated in Table 3. The image then undergoes the morphology operations for a refined area of stains. The stained image will be matched to all three templates and the area of detected stains in each template will be calculated to decide the level of hand washing technique.

3 Results and Discussion

Three types of image sets were captured; unwashed hands without GloGerm, Wash Hands with GloGerm and unwashed hand without GloGerm. Figure 4a is the input image for Washed Hands with Glogerm. The orange area is the area of GloGerm stained left unwashed and Fig. 4b is the detected area of stains after hue threshold range is applied.

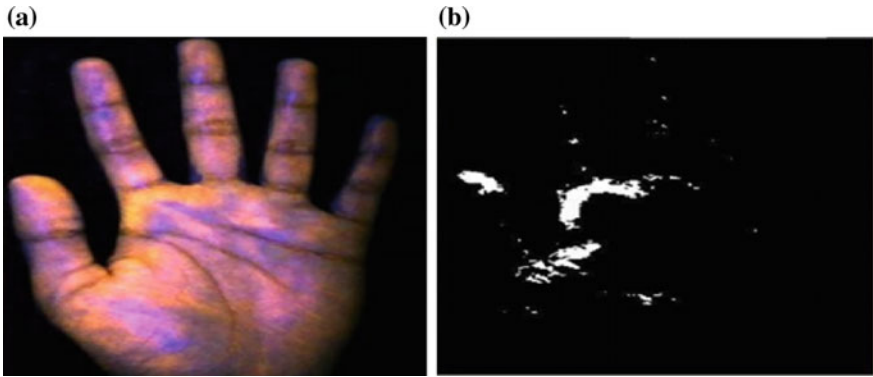


Fig. 4 a Input image, b stain detected

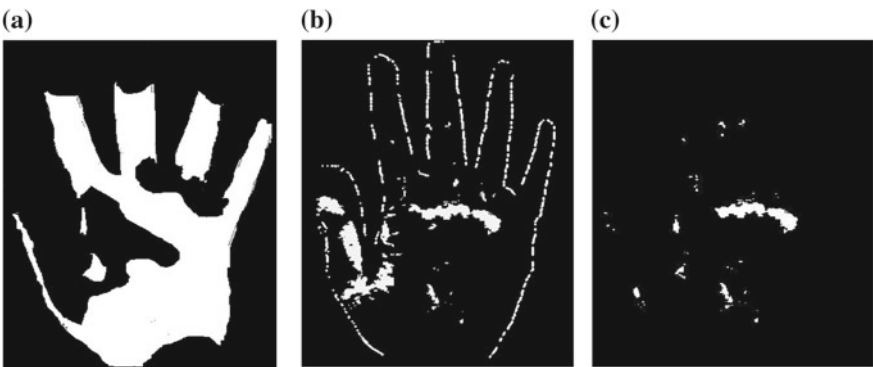


Fig. 5 a Template for never missed area, b detected stain from input image, c matched stains detected from the template

The detected stain image is then resized to the template image size of 303×247 pixels so that the template matching can be applied. The stain image will be matched to all three templates as shown in; Fig. 5 for the never missed area, Fig. 6 for the frequently missed area and Fig. 7 for the sometimes missed part. In all figures (a) are the templates extracted from [9] that highlights the area to locate the stains. These templates were matched to the detected stain image in (b) after image processing applied to the input image. The images in (c) is the final detected stains according to the designated area based on the template. Then the percentage area of stains in each category will be calculated to decide the level of handwashing technique based on Table 2.

A total of 90 images were collected with 20 individuals in three different cases as shown in Table 4. In the first case, palm without being stained with GloGerm is use an input image to verify that the system will not detect any stained on hand. The second set of images, the hand palm was applied and rubbed with GloGerm and not washed

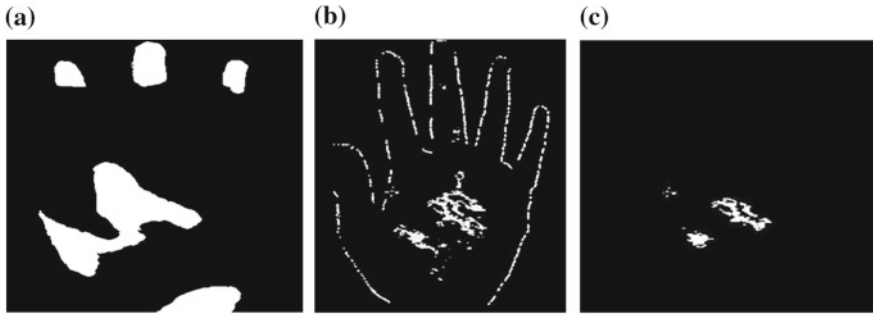


Fig. 6 a Template for sometimes missed area, b detected stain from input image, c matched stains detected from the template

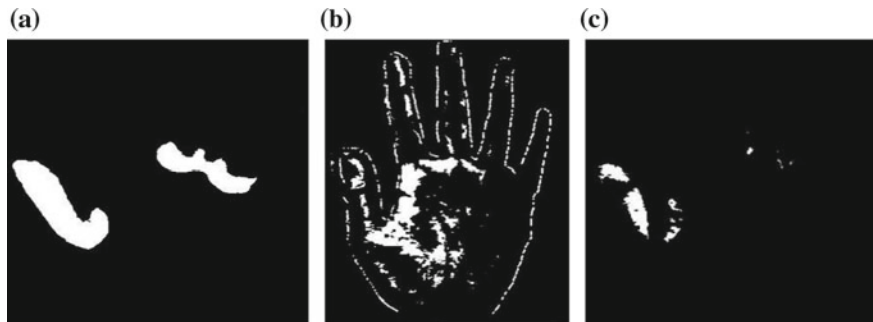


Fig. 7 a Template for frequently missed area, b detected stain from input image, c matched stains detected from the template

Table 4 The accuracy of the stain

Case	Samples for each case	Number of image samples with correct detection	Accuracy (%)
1. Plain Palm	20	20	100
2. GloGerm without Wash	32	26	81.25
3. GloGerm with wash	38	27	71.05

as the input image to the system will definitely detect the stained on hand since the Glogerm color is very bright and can be easily detected by the system. The third case sets of images were the real case inputs where the palm is applied with GloGerm and washed according to the six-steps handwashing techniques. These third case images will verify the accurateness of the system by detecting the stains left on hands which are missed by the user in the given areas by the templates.

It is concluded that the numbers of failed detection of total images is only 23 samples. This may be due to color variation of stains in the images. The system’s accuracy of the stain detected is given in the last column of the table. For plain palm

that did not apply the Glogerm liquid, no stain can be detected hence, output will tell the user that their left hand is clean and no germ detected. For unwashed palm with GloGerm, the system accurately detects the stains by 81%. This number is higher as compared to washed hands with GloGerm with percentage of 71%. This is due to the discoloration of GloGerm after washed that leads to missed pixels' detection of the stains. Previously in [9], for Case 2 accuracy of detection was 57% and Case 3 with 36% accuracy. With the implementation of the third template and new skin threshold value, the system has increased its accuracy by 40%.

4 Conclusion

The third template for never missed area applied in the system has increased the accuracy of handwashing level. The third generation prototype has significantly reduced its size compared to the first generation by 50% in length. The goal of increasing stain detection's accuracy has been successfully done by implementing the third template which has increased accuracy by 50% for Case 3 which involved the real case data.

Acknowledgements The work is done using UMP's research grant RDU170130 that promotes publications of the work and future verification with the collaborator from HUSM.

References

1. GOV.UK Homepage, <https://www.gov.uk/government/news/save-lives-clean-your-hands>. Last accessed 25 Nov 2017
2. Amal, K.H., Carole, T., Shamima, A., Abbas, B., Richard, J., Stephen, P.L.: Observed hand cleanliness and other measures of handwashing behavior in rural Bangladesh. *BMC Publ. Health* **10**, 545 (2010)
3. Allegranzi, B., Pittett, D.: Role of hand hygiene in healthcare-associated Infection prevention. *J. Hosp. Infect.* 305–315 (2009)
4. Llorea, D.F., Parra, I., Sotelo, M.A., Lacey, G.: A vision based system for automatic hand washing quality assessment. *Machine vision and application* (2011)
5. Dhawan, A., Honrao, V.: Implementation of hand detection based techniques for human computer interaction. *Int. J. Comput. Appl.* (0975–8887) **72**(17), 6–13 (2013)
6. Chin-liang su: Palm extraction and identification. *Expert system with applications, Expert Syst. Appl.* **36**, 1082–1091 (2009)
7. Perveen, N., Kumar, D., Bhardwaj, I.: An overview on template matching methodologies and its applications. *Int. J. Res. Comput. Commun. Technol.* **2**(10), 988–995 (2013)
8. Faradila, N., Rawaida J., Arshad, N.W., Rosyati, H., Razali, M.N.: Unclean hand detection machine using vision sensor. *Electronics, Communications and Photonics Conference (SIEPCP)*, pp. 1–4. Saudi International, IEEE (2013)
9. Faradila, N., et al.: Analysis of unclean hand system detection using template matching technique. *J. Telecomm. Electron Comput. Eng. (JTEC)* **10**(1–2), 143–146 (2018)
10. Best sanitizers inc.: hand hygiene, <http://gobrandstand.com/index.php?/hand-hygiene/>. Last accessed 20 Apr 2017 (2013)

Classification of Transient Facial Wrinkle



Rosdiyana Samad, Mohammad Zarif Rosli, Nor Rul Hasma Abdullah, Mahfuzah Mustafa, Dwi Pebrianti and Nurul Hazlina Noordin

Abstract Classification of transient wrinkle is an important application in research related to the skin aging, facial expression and skin analysis. Many researches have been done in the detection or classification of wrinkle, but it still needs some improvement in the algorithms, either in feature extraction part or classification. In this study, classification of transient wrinkle is proposed by using wrinkle features that extracted from the combination algorithms of Gabor wavelet and Canny operator. The facial wrinkle features are then classified by using artificial intelligent method which are Artificial Neural Network (ANN) and K-Nearest Neighbors (KNN). These two classifiers are trained and tested, and then the performance of each classifier is compared to getting the higher accuracy. 130 face images from various sources are used in the experiments, 65 of the total face images contains wrinkles on the forehead. The results show that ANN classifier only achieves 96.67% accuracy, while the KNN classifier obtained the highest accuracy with 100%. The comparison demonstrates that KNN works well in this classification. This result also proved that the extraction of facial wrinkle using a combination of Gabor and Canny detector is successful.

Keywords Facial wrinkle · Gabor wavelet · K-nearest neighbor · Classification

1 Introduction

Researchers have developed numerous algorithms for extracting the information from the human face to be used for the computer vision application. This is because the human face conveys considerable amount of non-verbal information such as gender, age, expression, etc. [1]. One of the representative feature of face that can be obtained from face image is a wrinkle features, which can be cooperated in image-

R. Samad (✉) · M. Z. Rosli · N. R. H. Abdullah · M. Mustafa · D. Pebrianti · N. H. Noordin
Faculty of Electrical and Electronics Engineering, Universiti Malaysia Pahang, 26600 Pekan,
Pahang, Malaysia
e-mail: rosdiyana@ump.edu.my

© Springer Nature Singapore Pte Ltd. 2019
Z. Md Zain et al. (eds.), *Proceedings of the 10th National Technical Seminar
on Underwater System Technology 2018*, Lecture Notes in Electrical Engineering 538,
https://doi.org/10.1007/978-981-13-3708-6_34

based applications related to face textural analysis, age range estimation, skin wrinkle analysis, expression simulation and animation.

The wrinkle is a small furrow or creases in the skin, especially of the face, caused by aging or expression. Wrinkles can be categorized into permanent and transient wrinkles, where the permanent wrinkle exists on aging skin, while the transient wrinkle only arise with movement of facial muscle or facial expression [2]. During a specific expression, sometime, the transient wrinkle arises on the forehead, corner of the eyes and corner of the mouth. The shape and intensity of transient wrinkle normally are unusual and appear differently for every person. In the research of computer vision, an application based on transient wrinkles is not easy to develop because the transient wrinkle has an inconsistent pattern and need a good feature extraction algorithm to extract wrinkle features [2]. Furthermore, choosing the best classification algorithm is quite tricky because there are lots of algorithms to choose from, and then to understand their strengths and weakness in an application.

The objective of this study is to develop a facial wrinkle classification. In this study, only transient wrinkle is chosen, instead of permanent wrinkle. This work focuses on the classification task, that involves two algorithms, which are Artificial Neural Network (ANN) and K-nearest neighbors (KNN). Each algorithm has their own unique parameters, thus by choosing the right parameters could produce a better classification result. The ANN and KNN classifiers are trained and tested with the facial wrinkle features and then, their performance is compared with each other to obtain high accuracy in the classification. The facial wrinkle features are extracted by using Gabor wavelet and Canny edge detector.

2 Related Works

Wrinkle detection had been a high-interest topic for the researcher to develop applications. Ng et al. [3], used Canny detector to extract wrinkle for age estimation, while Jane and Park [4] used wrinkle as facial marks to increase the accuracy of face recognition. There is a lot more research rely on wrinkle nowadays like face recognition [5], facial expression recognition [6, 7, 8], demographic (gender, race, age, etc.), classification [9, 10, 11, 12], facial digital beauty [13, 14] and etc. In age estimation analysis, wrinkle detection and wrinkle analysis are used for the age estimation. Khan et al. [11] focused on the wrinkle at the cheeks area for age estimation. In his study, the wrinkle increased in cheek region was also increased the age. The wrinkle energy was calculated by using Discrete Cosine Transform (DCT). The higher the energy, the higher the estimated ages. Soni et al. [10] were used geometric features to classify baby faces and used wrinkle features to classify young, middle aged, and old person. Facial wrinkle detection also has been applied in facial digital beauty and facial retouching work. Facial digital beauty aims to detect wrinkle before a facial treatment and detect wrinkle after the treatment for evaluating effectiveness of the treatment [15]. For facial retouching, Batool et al. [16] used Gaussian Mixture

Models and Markov random field to detect wrinkle skin. The detected the wrinkles was processed by *inpaint* algorithm to cover the wrinkle.

In recent years, Artificial Intelligence (AI) research has been on the pioneering end that was increasingly being used in computer sciences, social sciences, physical sciences, engineering and statistics and etc. There are numerous of artificial intelligence applications available now included robotic, indoor positioning scheme [17], directed graph [18], smart car, fraud detection, online customer support, security surveillance, music and movie recommendation services, smart home devices and etc. In wrinkle detection and classification applications, AI is used as intelligent classification, which can reduce a lot of human tasks in manual classification or recognition. The well-known algorithm for the classification or recognition is an Artificial Neural Network and K-Nearest Neighbors. The ANN has been used widely in many research areas, including computer vision and specifically in the wrinkle detection. Although ANN models may be computationally intensive, the evolution in high speed computer has promoted their application. The ANN can be used for predicting because of having the capability of examining and determining the historical data used for prediction [19]. The KNN classifier is conceptually and computationally quite simple because it is based on distances. Furthermore, it is non-parametric, which the distribution of the data does not need to be known [20]. Therefore, these two classifiers are selected for the transient wrinkle classification to classify the face images into wrinkle and non-wrinkle. In this study, the extraction of facial wrinkle was proposed earlier in [2], and these features are used in this work to get better accuracy in proposing a classification method.

3 Facial Wrinkle Features

Figure 1 shows facial wrinkle classification framework that consists of pre-processing, facial wrinkle feature extraction and wrinkle classification. This section describes pre-processing and feature extraction of facial wrinkle using image processing methods. This study utilizes 130 images of human faces. These images are collected from Cohn-Kanade Facial Expression Database [21], internet sources and our own database. In this study, 65 face images contain forehead wrinkles and 65 images without any wrinkle.

The original image is in RGB format and the size of images is 640×480 resolutions. In the pre-processing stage, the images are converted into a grayscale image. The processing of the whole face image is time consuming and not essential. There is a particular region of the face that shows perceptible skin textural changes, which is forehead. Therefore, only the forehead region is cropped and used for this study. The other region is not used in this study because the wrinkle features normally appear in the forehead region. By cropping the image into a small portion, the processing time also can be reduced. Later on these images are resized to a new width and height, which are 160 pixels width and 60 pixels height.

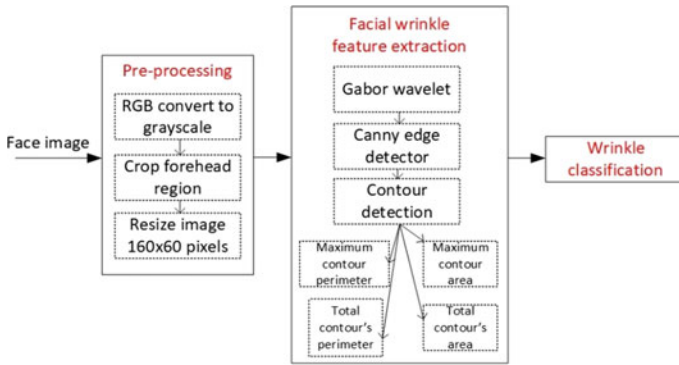


Fig. 1 Block diagram of facial wrinkle classification framework

The face image data is too large and it is suspected to be redundant, thus it can be reduced into a set of features. The next step is a wrinkle feature extraction that facilitates subsequent classification and maximizing the recognition rate with the least amount of unnecessary information. Gabor wavelet is used to extract the facial wrinkle and a few algorithms are implemented to get the final features.

The first Gabor features were in 1-dimensional and then upgraded in 2-dimensional by Daugman [1]. The Gabor features consist of a bank of Gabor filters with different scales and orientations generated from a mother Gabor kernel. In previous research, most of the researchers had used Gabor filter bank of 40 filters consisting of five different scales and 8 orientations. Some researchers had modified Gabor filter bank and selected a few scales and orientations as their preferred [22, 23]. A 2-dimensional Gabor kernel is given by Eqs. (1), (2) and (3) as follows:

$$g(x, y; \lambda, \theta, \psi, \sigma, ks) = \exp\left(\frac{-x'^2 + ks^2 y'^2}{2\sigma^2}\right) \cos\left(2\pi \frac{x'}{\pi \lambda}\right) + \psi \quad (1)$$

where,

$$x' = x \cos\theta + y \sin\theta \quad (2)$$

$$y' = x \sin\theta + y \cos\theta \quad (3)$$

where λ represents the wavelength of the wavelet, θ represents the orientation of the stripes wavelet, ψ represents the phase offset, σ represent the standard deviation of the Gaussian envelope, and ks represents the kernel size.

In this study, only 1 Gabor filter is used, instead of 40 filters. The Gabor parameters have been selected carefully by testing the Gabor filter on wrinkle image. Those parameters are $ks = 21$, $\sigma = 4$, $\theta = 90^\circ$, $\lambda = 60$ and $\psi = 92$. The θ value is set to 90° , so that the stripe of the wavelet has a similar orientation with the wrinkles in the forehead. Kernel size σ , control the size of the wavelets based on image region that

being analyzed. However, the phase offset ψ does not have much effect, compares to λ , and kernel size. It controls the position of the wavelet's stripe.

Later on this image is processed by an edge detector operator, Canny by applying the threshold range of 120–255 grayscale intensity. The function of the Canny edge detector is required to extract the wrinkle lines, where it shows white pixels on the image as a wrinkle. Then, the *findContours()* function from OpenCV library is applied to detect edges or wrinkles in the image. In this function, the contour approximation method is used, where it compresses the horizontal, vertical and diagonal segments and leaves only their endpoints [24]. This method retrieves only the extreme outer contours. After that, the detected output contours are listed in the Freeman chain code and stored as vector points. By using these vector points, the contour area and perimeter are calculated. In this study, to obtain the wrinkle features of the image, 4 types of calculation have been done which are maximum contour perimeter, total contour perimeter, maximum contour area and total contour area. The maximum contour perimeter shows the longest wrinkle line and total contour perimeter shows the summation of all perimeters in the image. The maximum area shows the biggest wrinkle found in the image and the total contour area is a value of the total area for all wrinkles in the image.

4 Facial Wrinkle Classifications

In this study, 2 types of classifier are used to classify the facial image that has a wrinkle or not, which are Artificial Neural Network and K-Nearest Neighbors (KNN). The performance of these classifiers is compared to get the better success rate or accuracy. The training and testing on the classifiers have been done by using Matlab with 130 feature datasets. 100 datasets are for training (50 face with wrinkle and 50 without wrinkle) and 30 datasets are for testing.

4.1 Artificial Neural Network (ANN)

The ANN classifier is designed by using multilayer feed forward backpropagation neural networks. This classifier mainly consists of an input layer, hidden layer and output layer. The input layer has 4 neurons equal to the number of wrinkle features and output layer have only one neuron that classifies the image into wrinkle class and non-wrinkle class as shown in Fig. 2. In this study, the number of hidden layer is 1. The number of neurons in the hidden layers is decided through experimentation. The ANN is trained by supervised learning approach, where the inputs with its target are known. The training and testing of classifier consist of two phases, feedforward recall phase and error backpropagation phase. In the first phase, neuron in each layer is connected to neurons in the next layer only in the forward direction. In the second phase, the error between the estimated output and the desired output is

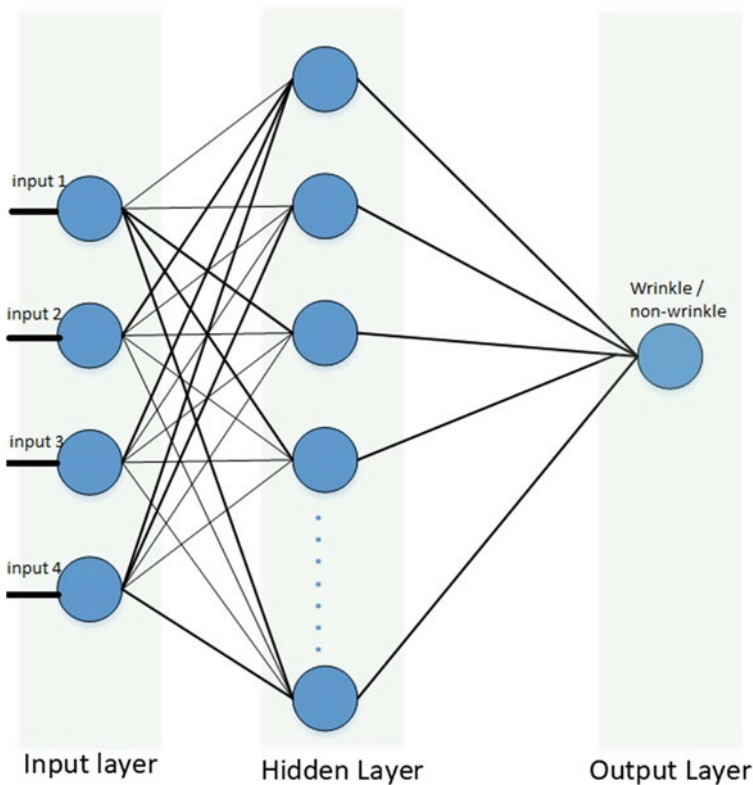


Fig. 2 Neural network configuration

back propagated from the output layer to the input layer. The error is minimized by adjusting the weights of neurons in the output layer first and then hidden layer [1].

Before the final network is obtained, the network is trained by varying 3 parameters which are learning rate, number of epochs and the minimum error gradient. Training algorithm that is used in this training is Levenberg-Marquardt. From the previous studies show that this algorithm is better than other training algorithms. Levenberg-Marquardt is highly recommended as a first choice manages algorithms because it does not require a lot of memory and it is fast. To get number of neurons in the hidden layer, a network is created with n neurons ($n = 5, 6, 7, 8, 9, 10$) and the simulation is running 10 times for each number of neurons. The best number of neurons is selected when the training achieves high success ratio. The second factor that is varied is a number of epochs used in the network. The network is simulated with 4 different epochs, 50, 60, 70, and 80 and then the number of epochs that achieves a high success ratio is chosen. Learning rate that is set for this study are 0.1, 0.01, and 0.001. Finally, the last parameter to determine for the network is the minimum error

Table 1 Training configuration parameters

Configuration Parameters	Values/Type
Number of epochs	50, 60, 70, 80
Number of hidden neurons	5, 6, 7, 8, 9, 10
Learning rate	0.1, 0.01, 0.001
Minimum error gradient	1e-010, 1e-0100, 1e-01000
Training algorithm	Levenberg-Marquadt
Transfer function (hidden layer)	Tan-Sigmoid
Transfer function (output layer)	Linear

gradient. 3 different values are chosen for this training, which are 1e-010, 1e-0100, and 1e-01000. All training configuration parameters are shown in Table 1.

After determining the optimal parameters for the network, then used these parameters and the network is trained again for 10 times by using the training data set. The average success rate for this simulation is calculated. Finally, test performance of the network by using a test data set and the success rate is recorded.

4.2 *K-Nearest Neighbors (KNN)*

K-nearest neighbour (KNN) is a simple algorithm, which stores all cases and classify new cases based on similarity measure. It is based on the idea that samples with similar parameter values should belong to similar classes. The classifier is trained simply by giving it access to a database containing pairs of parameter sets and classes, where each set of parameters belongs to the class it is paired with. When a new set of parameters is tested, the distance between the parameter set and all other set is measured and the k sets in the training database, which are closest, are looked at. The classifier then assigns the set the class of the majority of the k nearest.

In this algorithm, there are two important parameters have been tested which are distance and rules. The distance type that is used in the experiment are *Euclidean*, *Correlation*, *Cosine*, and *Cityblock*. Three rules are used, which are *nearest*, *random*, and *consensus*. The test set is classified with k varies from 1 to 12.

5 Results and Discussion

This section presents the experimental results of facial wrinkle classification. Facial features are extracted by using a combination of Gabor wavelet and Canny edge detector algorithm. The images of feature extraction result are shown in Fig. 3. The facial features are then input to the classifier, which are ANN and KNN. Later on,

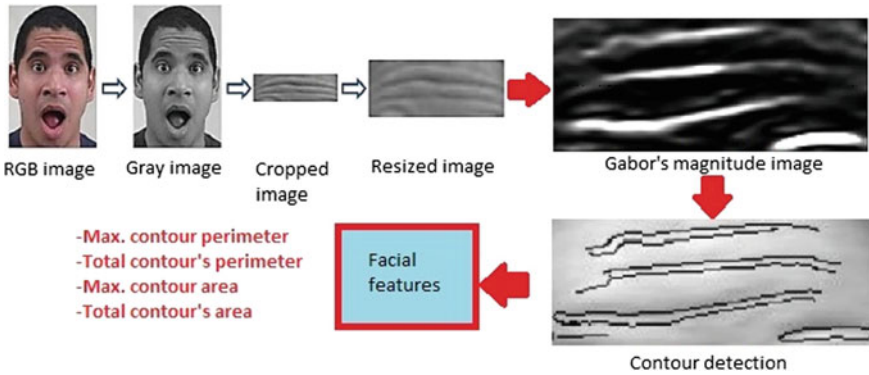


Fig. 3 Feature extraction results

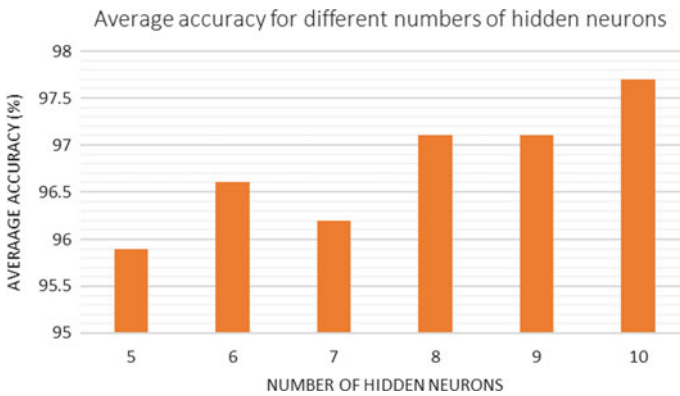


Fig. 4 Average accuracy for different numbers of hidden neurons

the results of each classifier are compared to find the best result for the wrinkle classification.

The ANN is designed by using a multilayer feedforward backpropagation network with Levenberg-Marquadt as training algorithm. The network is trained by varying the number of hidden neurons, learning rate, the minimum error gradient and number of epochs, and then the average accuracy is calculated. Figure 4 shows success rate for different numbers of hidden neurons. The training simulation has been done for 10 times for each selected neurons. The results show that the network achieves higher average accuracy with 10 hidden neurons. 10 neurons are used in the final network to get a better classification accuracy and reduces the total computation time in the tests.

During the training, the network shows better performance with learning rate 0.1, 0.01 and 0.001. Therefore, the network is trained again with these three values of learning rate and different the minimum error gradient. In each training, the number of epochs is varied from 50 to 80 epochs and the simulation is iterated for 10 times. The

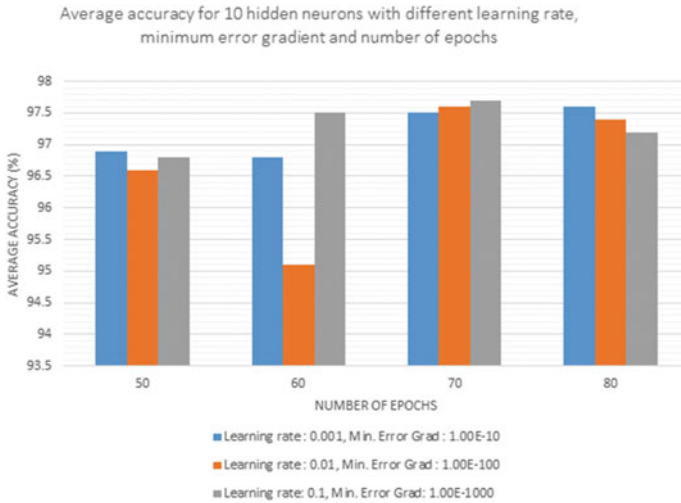


Fig. 5 Average accuracy for 10 hidden neurons with different learning rate, minimum error gradient and number of epochs

results are shown in Fig. 5. It can be seen that the higher average accuracy (97.7%) is when 70 epochs, learning rate is 0.1 and minimum error gradient is 1.0E-1000 are used in the network. The accuracy given by 70 epochs is enough in this case, therefore all successful parameters are used for the final neural network. After determining the optimal parameters for the neural network, the final network is created with the parameters obtained from the training and classify the 30 test datasets. The network testing achieves 96.67% accuracy.

For KNN classifier, there are three parameters have been tested, which are distance, rule and *k* value. The *k* value varies from 1 until 12. The results are shown in Figs. 6, 7 and 8. In Fig. 6, the type of distance is *Euclidean*, shows the rule that gives better result is *random* with *k* = 3. For the KNN with correlation distance as shown in Fig. 7, both rules, *nearest* and *random* give almost the similar higher accuracy values with *k* value within 1 and 5. The *cityblock* distance results in Fig. 8, shows all *k* values that are used in the classification give high accuracy (100%) for both rules, *nearest* and *random*. The final distance parameter, *cosine*, as shown in Fig. 9, shows the *nearest* and *random* rules give high accuracy compare to *consensus* and the suitable *k* value to be used is range from 3 to 12. In overall, the *cityblock* distance with rules either nearest or random can be used for final KNN classifier and it gives 100% accuracy.

In comparison KNN and ANN, the results show the highest accuracy is achieved by the KNN classifier with 100% accuracy, while ANN only achieves 96.67% accuracy. In the case of KNN performance, the 100% accuracy is possible in this study because it shows KNN performs much better when all data used in the training and testing have the same scale. KNN works well with a small number of input variables,

KNN CLASSIFICATION WITH 'EUCLIDEAN' DISTANCE

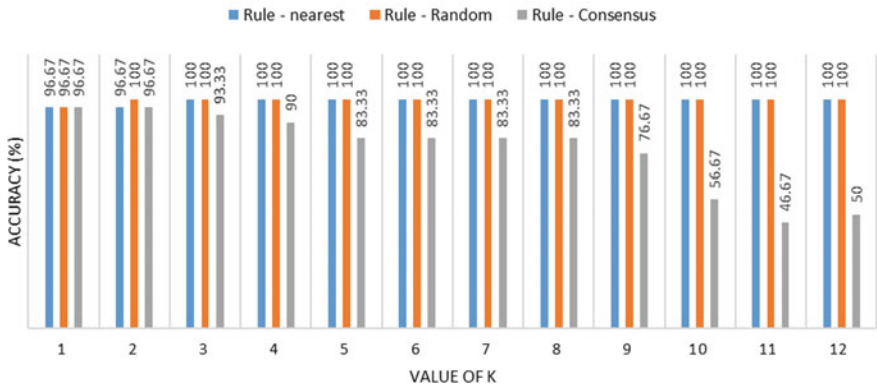


Fig. 6 KNN classification with *Euclidean* distance

KNN CLASSIFICATION WITH 'CORRELATION' DISTANCE

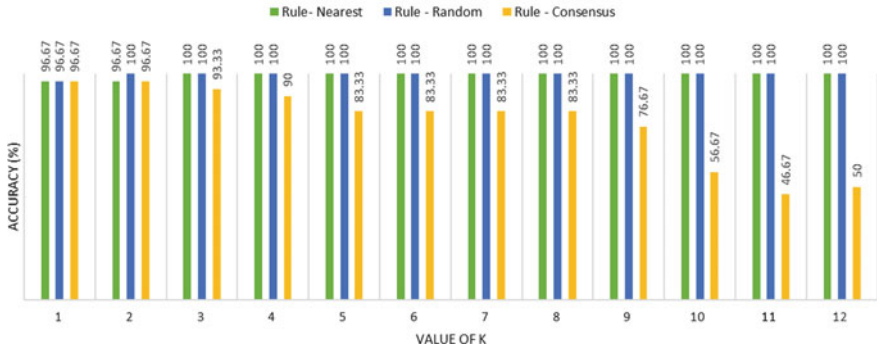


Fig. 7 KNN classification with *correlation* distance

but it may struggle when the number of inputs is very large. In this study, KNN performs well with the facial features and the time taken to train the classifier is shorter than ANN. This is because of the simplicity of the KNN algorithm and the number of datasets is not so huge. Maybe the performance of KNN has slightly different if a large number of datasets are used and the computational time can be slow for real-time prediction. In overall, the success of the classifier also depending on the quality of the facial features that generated from a combination of the Gabor wavelet and the Canny edge detector. From the results of classification accuracy, it shows that the wrinkle can be extracted well from the facial image, and KNN classifier is suitable to be used for the wrinkle classification.

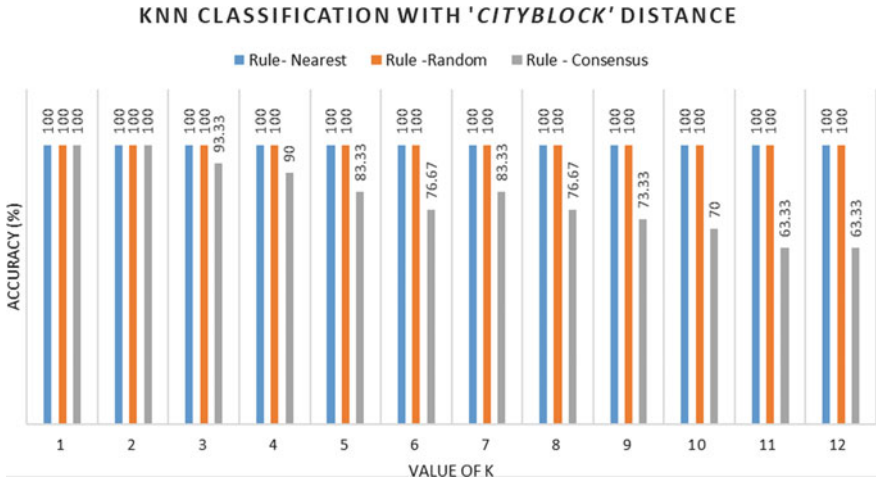


Fig. 8 KNN classification with *cityblock* distance

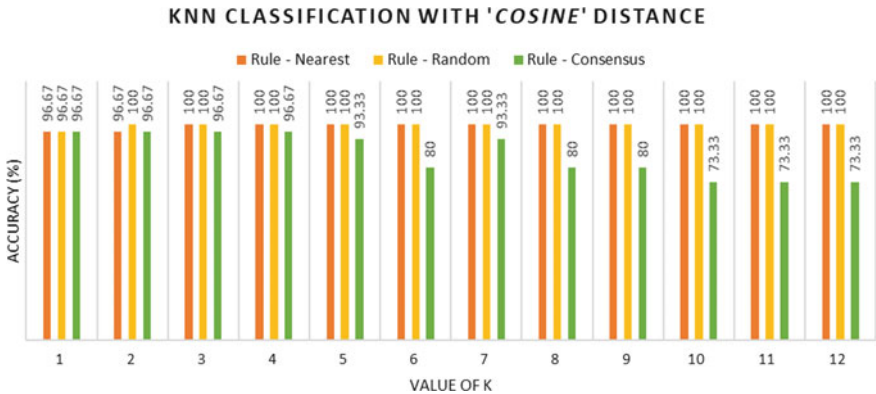


Fig. 9 KNN classification with *cosine* distance

6 Conclusion

A wrinkle classification framework is proposed to classify the face image into two classes (wrinkle or non-wrinkle) by using a combination of Gabor and Canny facial features. Two classifiers are trained and tested with the generated facial features and then, analysis on the classifier’s performance based on selected parameters is done. From the results show the classifier that suitable to be used in the wrinkle classification framework is KNN with 100% accuracy. The selected KNN’s parameters that contribute to KNN performance are distance type *cityblock* and rules, random and nearest. The *k* values from 1 to 12 are performed better in this configuration compare to other distance types such as *Euclidean*, *cosine* and *correlation*. In future,

this study will be continued and a lot of improvement will be made. The number of images can be increased to train and test KNN classifier, and also to test with other available classifiers. The classification also can be done more specifically, for example, classify the face image into three categories: no-wrinkle, strong wrinkle and weaker wrinkle.

Acknowledgements This work is supported by a Fundamental Research Grant Scheme (FRGS) (RDU160143) and Faculty of Electrical and Electronic Engineering, Universiti Malaysia Pahang (www.ump.edu.my).

References

1. Jagtap, J., Kokare, M.: Human age classification using facial skin aging features and artificial neural network. *Cogn. Syst. Res.* **40**, 116–128 (2016)
2. Samad, R., Hoe, P.J., Mustafa, M., Abdullah, N.R.H., Pebrianti, D., Noordin, N.H.: Comparison of filtering methods for extracting transient facial wrinkle features. *J. Telecomm. Electron. Comput. Eng.* **10**(1–2), 99–104 (2018)
3. Ng, C.C., Yap, M.H., Costen, N., Li, B.: An investigation on local wrinkle-based extractor of age estimation. In: *International Conference on Computer Vision Theory and Applications (VISAPP)*, pp. 675–681 (2014)
4. Jain, A. K. and Park, U.: Facial marks: soft biometric for face recognition. In: *16th IEEE International Conference on Image Processing (ICIP)*, pp. 37–40 (2009)
5. Batool, N., Taheri, S., and Chellappa, R.: Assessment of facial wrinkles as a soft biometrics. In: *10th IEEE International Conference and Workshops on Automatic Face and Gesture Recognition (FG)*, pp. 1–7 (2013)
6. Huang, Y., Li, Y., Fan, N.: Robust symbolic dual-view facial expression recognition with skin wrinkles: local versus global approach. *IEEE Trans. Multimedia* **12**, 536–543 (2010)
7. Xie, W., Shen, L., and Jiang, J.: A novel transient wrinkle detection algorithm and its application for expression synthesis. *IEEE Trans. Multimedia* (2016)
8. Xie, W., Shen, L., Yang, M., and Hou, Q.: Lighting difference based wrinkle mapping for expression synthesis. In: *8th International Congress on Image and Signal Processing (CISP)*, pp. 636–641 (2015)
9. Yang, Z. and Ai, H.: Demographic classification with local binary patterns. In: *International Conference on Biometrics*, pp. 464–473 (2007)
10. Soni, A.K., Kumar, R., Kishore, D.K.: Estimation of age groups based on facial features. In: *International Conference on Applied and Theoretical Computing and Communication Technology*, pp. 681–687 (2015)
11. Khan, S., Khan, T., Hussain, A., Siddique, A., and Ahmad, N.: Wrinkles energy based age estimation using discrete cosine transform. In: *International Conference on Emerging Technologies (ICET)*, pp. 1–4 (2015)
12. Hadchum, P., Wongthanavas, S.: Facial age estimation using a hybrid of SVM and Fuzzy Logic. In: *12th International Conference on Electrical Engineering/Electronics, Computer, Telecommunications and Information Technology (ECTI-CON)*, pp. 1–6 (2015)
13. Batool, N., Zerubia, J.: Image-based evaluation of treatment responses of facial wrinkles using LDDMM registration and Gabor features. In: *IEEE International Conference on Image Processing (ICIP)*, pp. 1747–1751 (2015)
14. Batool, N., Chellappa, R.: Detection and in-painting of facial wrinkles using texture orientation fields and Markov random field modeling. *IEEE Trans. Image Process.* **23**, 3773–3788 (2014)
15. Jiang, L.I., Stephens, T.J., Goodman, R.: SWIRL, a clinically validated, objective, and quantitative method for facial wrinkle assessment. *Skin Res. Technol.* **19**, 492–498 (2013)

16. Batool, N., Chellappa, R.: Modeling of facial wrinkles for applications in computer vision. *Advances in Face Detection and Facial Image Analysis*, pp. 299–332. Springer, New York (2009)
17. Islam, A., Hossan, M.T., Chowdhury M.Z, and Jang Y.M.: Design of an indoor positioning scheme using artificial intelligence algorithms. In: *International Conference on Information Networking (ICOIN)*, pp. 953–956 (2018)
18. Zhou, Y., Xu, F., Research on application of artificial intelligence algorithm in directed graph. In: *International Conference on Computing Intelligence and Information System (CIIS)*, pp. 116–120, (2017)
19. Keong, K.C., Mahfuzah, M., Mohammad, A.J., Sulaiman, M.H., Abdullah, N.R.H, Samad, R., Perbrianti, D.: Levenberg-Marquadt flood prediction for Sungai Isap Residence. In: *International Proceedings on IEEE Conference on System, Process and Control (ICSPC 2016)*, pp. 160–165, Melaka, Malaysia (2016)
20. Luis, J., Medina, V.: Reliability of classification and prediction in K-nearest neighbor, (2013)
21. Lucey, P., Cohn, J.F., Kanade, T., Saragih, J., Ambadar, Z., Matthews, I.: The extended Cohn-Kanade dataset: a complete dataset for action unit and emotion-specified expression. In: *Proceeding of IEEE Computer Society Conference on Computer Vision and Pattern Recognition Workshops (CVPRW)*, pp. 94–101, (2010)
22. Samad, R., Sawada, H.: Extraction of the minimum number of Gabor wavelet parameters for the recognition of natural facial expressions. *Artif. Life. Robot.* **16**, 21–31 (2011)
23. Samad, R., Sawada, H.: Edge-based facial feature extraction using Gabor wavelet and convolution filters. In: *IAPR Conference on Machine Vision Applications (MVA2011)*, 430–433, Japan (2011)
24. Bradski, G., Kaehler, A.: *Learning OpenCV: computer vision with the OpenCV library*, 1st edn. O'Reilly Sebastopol, California, USA (2008)

Electromyograph (EMG) Signal Analysis to Predict Muscle Fatigue During Driving



Muhammad Amzar Syazani Mohd Azli, Mahfuzah Mustafa,
Rafiuddin Abdubrani, Amran Abdul Hadi, Syarifah Nor Aqida Syed Ahmad
and Zarith Liyana Zahari

Abstract Electromyography (EMG) signal obtained from muscles need advance methods for detection, processing and classification. The purpose of this paper is to analyze muscle fatigue from EMG signals. At the beginning, 15 subjects will answer a set of questionnaires. The score of the questionnaires will be calculated and the score will determine if the driver is fatigued or mild fatigue or fatigue based on their driving habit. Next, EMG signals will be collected by placing two surface electrodes on the Brachioradialis muscle located at the forearm while driving Need For Speed (NFS) game. A simulation set of steering and pedals will be controlled during the driving game. The drivers drive for two hours and the EMG signal will be collected during they are driving. The output signals will be pre-processed to remove any noise in the signal. After that, the data is normalized between value 0 to 1 and the signal is analyzed using frequency analysis and time analysis. Mean and variance will be calculated for time domain analysis and graph of mean versus variance is plotted. In frequency domain analysis, Power Spectral Density (PSD) is extracted from the peak frequency of PSD in each signal is obtained. All results will be divided into three classes: non-fatigue, mild-fatigue and fatigue. Based on results obtained in time domain, average normalized mean (non-fatigue: 0.5004), (mild-fatigue: 0.497) and (fatigue: 0.494). While, for frequency domain analysis, average peak frequency (non-fatigue: 13.379 Hz), (mild-fatigue: 11.969 Hz) and (fatigue: 12.782 Hz).

Keywords EMG · Muscle fatigue · Driver fatigue · Time-domain
Frequency-domain

M. A. S. Mohd Azli · M. Mustafa (✉) · R. Abdubrani · A. Abdul Hadi · S. N. A. Syed Ahmad
Z. L. Zahari
Universiti Malaysia Pahang, Pekan, Pahang, Malaysia
e-mail: mahfuzah@ump.edu.my

Z. L. Zahari
Universiti Kuala Lumpur British Malaysian Institute, Gombak, Selangor, Malaysia

© Springer Nature Singapore Pte Ltd. 2019
Z. Md Zain et al. (eds.), *Proceedings of the 10th National Technical Seminar
on Underwater System Technology 2018*, Lecture Notes in Electrical Engineering 538,
https://doi.org/10.1007/978-981-13-3708-6_35

1 Introduction

Muscle fatigue is the decrease in the ability of a muscle to generate force. Muscle fatigue can cause to road accident Usually, muscle fatigue in driving will occur when the driver drives for a long period of time. According to statistic from Malaysia Institute of Road Safety Research (MIROS), in 2016, 521,466 total accidents were reported. These crashes resulted in 1.38% deaths [1]. Muscle fatigue is one of the factors contributes to the road accident. Muscle fatigue is a common problem faced by most of the drivers. Muscle fatigue can cause the driver to fall asleep or muscle cannot function well during driving, this can cause accidents to happen even though many claim they can drive for a long time without tired or feeling fatigue. In the biomedical study, Electromyograph (EMG) often used to measure muscle activity.

The EMG signal is a biomedical signal measures electrical currents generated in muscles throughout its contraction representing contractile organ activities [2]. This signal is a function of time and is can be described will be represented in terms of its amplitude, frequency and phase. In order to determine the features of EMG signal, it need to be analysed first.

This project is focused on time domain analysis and frequency domain analysis. Basically, EMG signal is a valuable signal contained a lot of information. A raw EMG signal contained a lot of artefact or noise. This noise can be remove by using Butterworth filter. The amplitude, frequency and phase can determine the muscle fatigue. Without analysing the signal, it is hard to determine when is the muscle start fatigue.

2 Methodology

Figure 1 shows the flowchart used in this experiment. At first, fifteen random people are chose to answer questionnaire related to driving habits. Each questionnaire provides a score that will class them into non-fatigue, mild-fatigue and fatigue. Data collection of EMG is collected while they are driving, using a simulation driving game for two hours. The first step of signal analysis is a signal pre-processing to remove any noise or artefacts. Then the signal is analyse using two methods, time domain and frequency domain. For the time domain, statistical analysis of mean and variance is performed. While frequency domain used PSD analysis to obtain the peak frequency of each graph. Both results of the analysis will be compared and validate with the questionnaire.

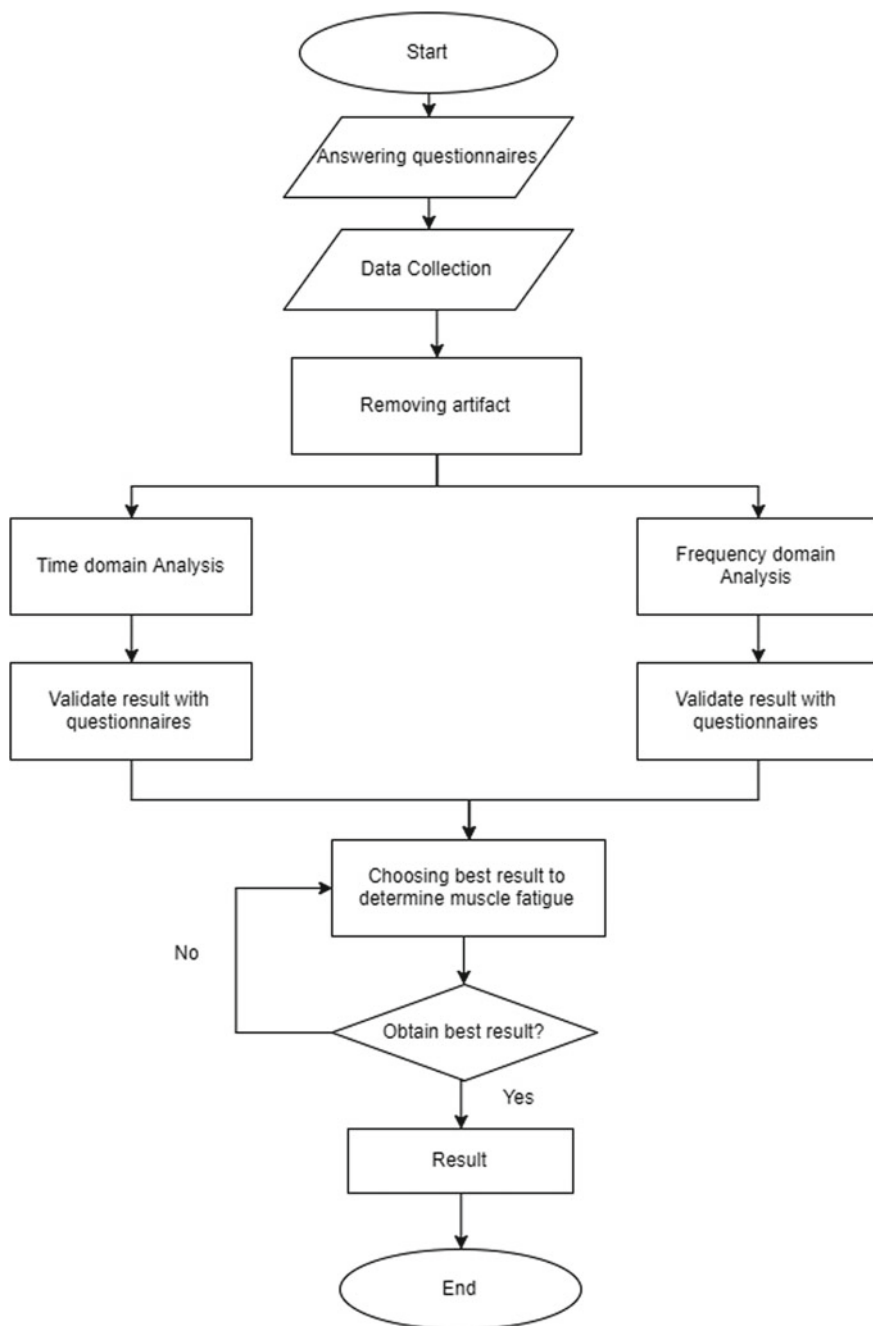


Fig. 1 Flow chart of methodology

2.1 Answering Questions

Fifteen students will be randomly selected in Universiti Malaysia Pahang, Pahang. The range of age suggested is 18–25 years old. Firstly, they need to answer a set of questionnaires, each question provided marks. Time given for them to answer the questionnaire is set to 10 min. They need to answer a set of question on driving assessment test. At the end, total score is calculated using given formula and the score will class them into three classes of driver, non-fatigue, mild-fatigue and fatigue. The total score for non-fatigue (0–15), mild-fatigue (16–34) and fatigue (35 and above).

2.2 Data Collection

After answering questionnaire, they will rest for 10 min before data EMG collection started. They need to make sure they take precaution before data collection. After that, they will perform a driving simulation in Need for Speed game for two hours. The data is collected all the time while they are driving. The simulator used is PXN-V3II Racing Wheel which contain pedal, steering and gear.

The surface electrode is placed on the dominant forearm. For examples, if someone is a left handed, so the electrode is placed on the left arm and vice versa. Brachioradialis or also known as Venke Muscle, is located at the forearms [3]. The brachioradialis muscles is uses to rotate our arm. Contraction of brachioradialis is take place when a person about to rotate steering. Every muscle within the body is connected to a nerve that provides the muscle with electrical impulses from the brain, and therefore the nerve that is connected to the brachioradialis is the radial nerve.

This electrical impulse is measured by the Shimmer EMG kit and the sampling frequency is set to 128 Hz. Time taken for data collection is set to two hours of driving. The EMG kit is connected through laptop using Bluetooth connection.

2.3 Removing Artefact

A raw EMG signal is a signal that originates in the muscle and various noise elements that unit endemic and inescapable [4]. These noises can cause associate incorrect interpretation of the signal. Hence, the artefact need to be removed first before start the signal analysis. A Butterworth bandpass filter with cornering frequency of 10–20 Hz [4].

2.4 Signal Analysis

Signal process issues the analysis, synthesis, and modification of signals. In this project, the process of analysis will be performed in MATLAB r2016 software. Two methods of signal analysis will be used in this project. The first method is time domain and the second method are frequency domain.

Time Domain Signal Analysis. The data will be plot in time domain using sampling frequency of 128 Hz. Next, the data is normalized (0 to 1). By using a function inside the MATLAB, mean and variance can be extracted for analysis purpose. Mean will determine the average amplitude of the signal while variance could indicate enlisting of motor units or firing rates of recruited motor units [5]. The formula of mean, variance can be obtained by these formulas [6, 7]:

Mean,

$$\bar{X} = \frac{\Sigma X}{N} \quad (1)$$

where ΣX is total score and N is the total number of scores.

Variance,

$$S^2 = \frac{\Sigma(X - \bar{X})^2}{N - 1} \quad (2)$$

where X represents score, \bar{X} is mean while N is the total number of scores.

After mean and variance is obtained, average of mean and variance for each muscle condition is calculated. In theory, low mean shows a sign of muscle fatigue because our brain wanted to limit our muscle to perform excessive work. While for variance, higher variance shows a sign of muscle fatigue since higher firing rates of recruited motor units performed. At the end, scatter graph of mean versus variance is plotted to see the pattern for muscle fatigue.

Frequency Domain Signal Analysis. Frequency spectrum can be produced by performing Fast Fourier Transform (FFT) from the time domain signal [8]. The PSD of an electrical signal is the distribution of the amplitudes and phases of each frequency component against frequency [9]. This frequency can indicate the muscle fatigue. Usually, when a muscle start to fatigue, most of the frequency will be shifted to the left of the graph (in lower frequency) [10]. Fourier discovered that such a complex signal could be decomposed into an infinite series made up of cosine and sine terms and a whole bunch of coefficients, which can (surprisingly) be readily determined. Here is the equation of FFT.

$$f(t) = \frac{1}{2}a_0 + \sum_{n=1}^{\infty} a_n \cos\left(\frac{2\pi nt}{T}\right) + \sum_{n=1}^{\infty} b_n \sin\left(\frac{2\pi nt}{T}\right) \quad (3)$$

The coefficients a_n and b_n can be found by the following formulas,

$$a_n = \frac{1}{L} \int_{-L}^L f(t) \cos \frac{n\pi t}{L} dt \quad (4)$$

$$b_n = \frac{1}{L} \int_{-L}^L f(t) \sin \frac{n\pi t}{L} dt \quad (5)$$

2.5 Validity of Questionnaire

The result of both methods of signal analysis, then will be validated the questionnaire. Each question provided marks for the driver. The marks will be recorded and will determine the muscle fatigue of the driver by comparing the questionnaire marks and the signal analysis results. Both results will be compared to determine which the best methods to determine muscle fatigue are. Both results will be compared to determine which the best method to determine muscle fatigue is.

3 Results and Discussion

3.1 Data Collection and Questionnaire

Fifteen students answered a set of questionnaires on simple driving assessment. Each questionnaire consisted of 15 total questions. Most of the questions related on the driving habits that will lead to fatigue during driving. Each objective question provided three answers with a score. At the end, the total score will be calculated and the score of the questionnaire will determine if the driver is fatigued or mild fatigue or fatigue.

From Table 1, the result shows four drivers are in non-fatigue state while three drivers are in mild fatigue state and the other three are in fatigue state. However, this result cannot be used to determine muscle fatigue. Hence, there will be several analyses performed to validate the questionnaire and the analysis result.

All of the respondents need to do driving simulation using driving simulator device on Need for Speed game. The sample for two hours and the data is taken while they are driving. The EMG data is saved in .txt file that will further import into MATLAB.

3.2 Remove Noise

A raw EMG data contain artefacts usually caused by human and device sensitivity that can cause misleading of data analysis. EMG signal has a frequency range of

Table 1 The score of questionnaire and the driving condition

Driver	Score	Condition
1	13	Non-fatigue
2	18	Mild-fatigue
3	36	Fatigue
4	30	Mild-fatigue
5	25	Mild-fatigue
6	15	Non-fatigue
7	38	Fatigue
8	35	Fatigue
9	10	Non-fatigue
10	8	Non-fatigue
11	12	Non-fatigue
12	35	Fatigue
13	36	Fatigue
14	8	Non-fatigue
15	10	Non-fatigue

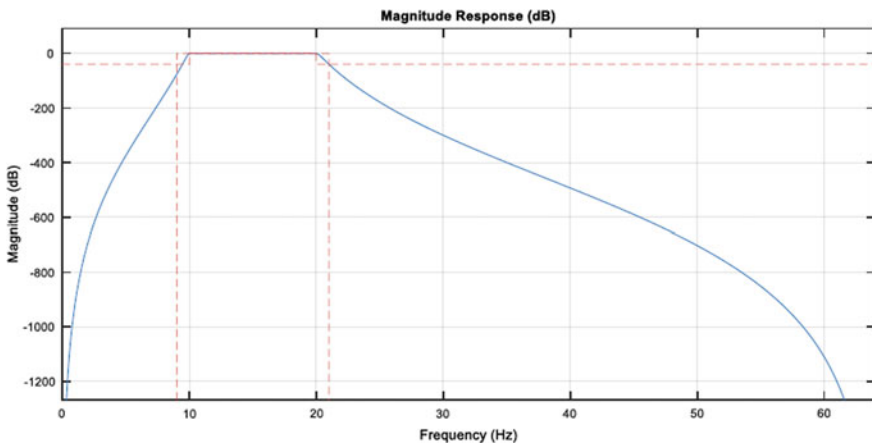


Fig. 2 Magnitude respond of Butterworth bandpass filter

10–20 Hz [11]. Hence, a bandpass filter of cornering frequency is the best filter to remove the noise. The Butterworth bandpass filter can be used. The Butterworth filter is a type of signal processing filter designed to have as flat frequency response as possible in the bandpass. Figure 2 shows the magnitude response of bandpass filter used in this project.

A Butterworth bandpass filter with cornering frequency 10–20 Hz is applied to a raw EMG signal to remove the artefact. The process of filtering is performed by

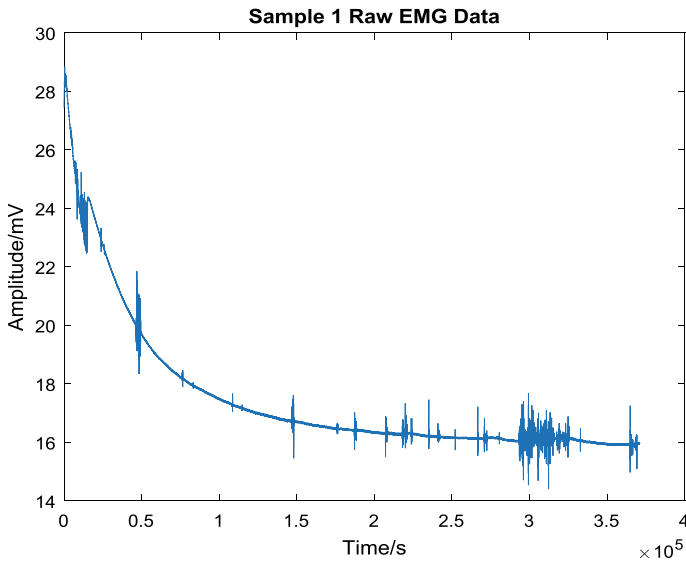


Fig. 3 Raw EMG data of sample 1

using MATLAB software. Figure 3 shows a sample of raw EMG data and Fig. 4 shows filtered EMG data using 10–20 Hz Butterworth bandpass filter. After filtering the raw data, the amplitude of the EMG signals dropped in the range of -5 to 5 mV, which is in the range of EMG data. After filtering process done, the signal is then normalized between 0 and 1.

3.3 Data Normalization

Normalization helped to reach a linear and more robust relationship. Since the device used to collect the data is very sensitive, that can collect up to twenty three decimal values. The data are needed to normalize between value 0 to 1. This process is crucial for the next process in time domain analysis during scatter graph plotting.

3.4 Time Domain Signal Analysis

For time domain analysis, firstly the normalized signal is plotted in time domain. The graph is plotted in time (second) versus amplitude (mV). Figure 5 shows non-fatigue signal, Fig. 6 shows mild-fatigue signal and Fig. 7 shows fatigue signal. As can be seen, all the signal is plotted in the time domain. All signals contain spike or

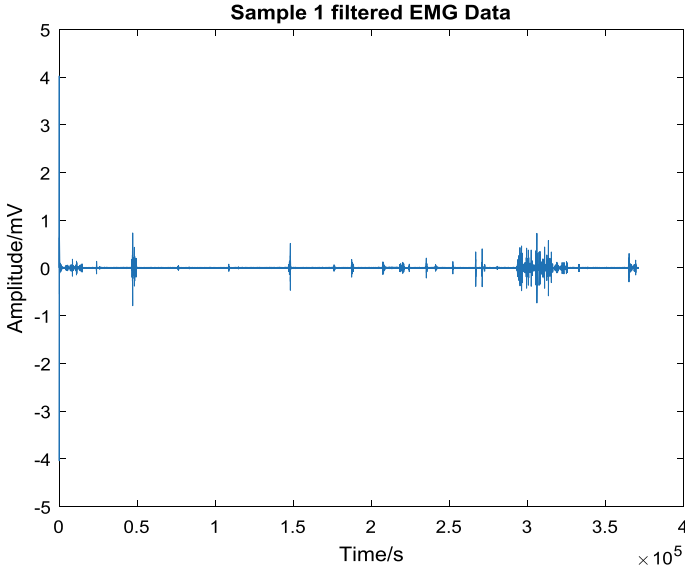


Fig. 4 Filtered EMG data of sample 1

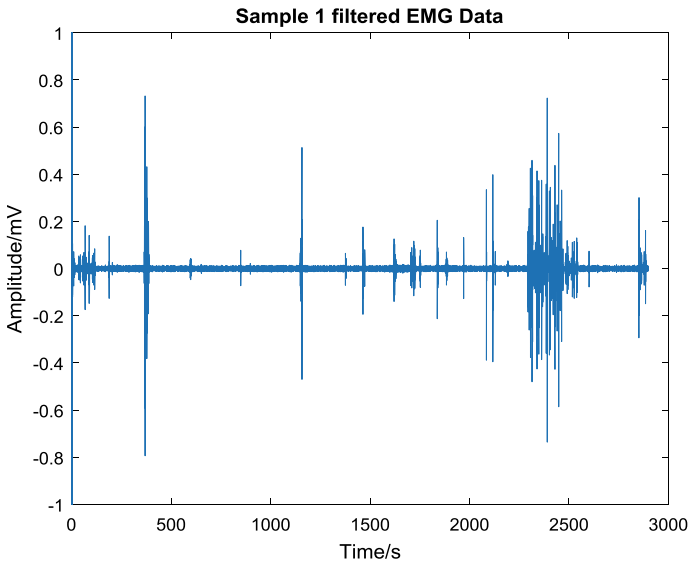


Fig. 5 Non-fatigue signal (Sample 1)

glitch even after it was filtered. It can be observed non-fatigue signal has the highest amplitude compared to mild-fatigue signal and fatigue signal.

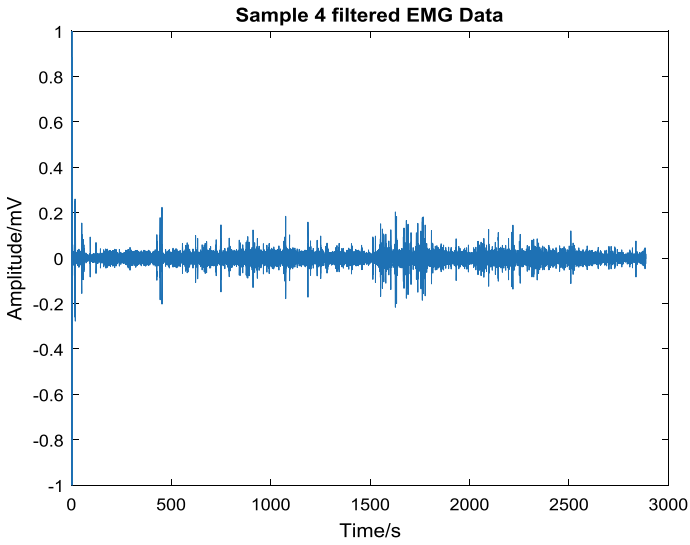


Fig. 6 Mild-fatigue signal (Sample 4)

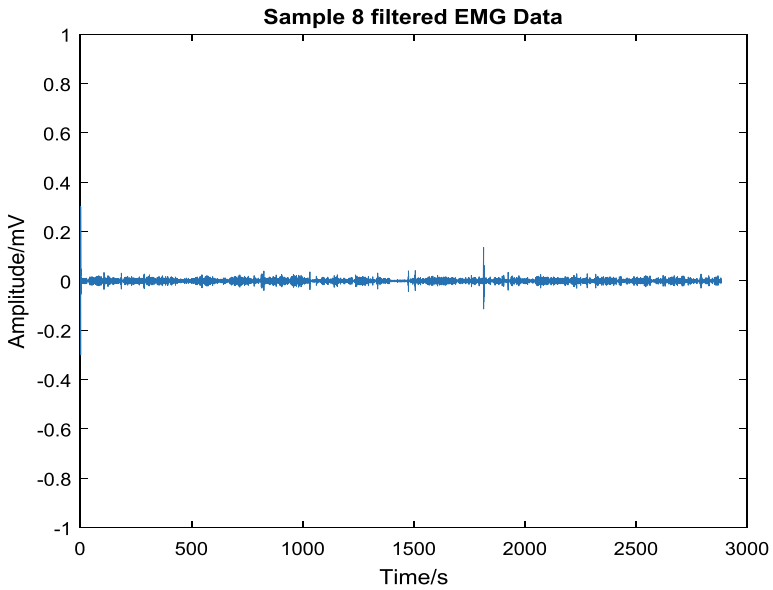


Fig. 7 Fatigue signal (Sample 8)

However, graphs cannot classify the characteristics of the EMG data. It needs to be analysed using statistical analysis. A statistic is a method of mathematics dealing with the collection, analysis, interpretation, presentation, and organization of data.

Table 2 Mean and variance for time domain analysis

Sample	Condition	Mean	Variance
1	Non-fatigue	0.501	1.73E-05
2	Mild	0.495	4.85E-05
3	Fatigue	0.498	2.25E-05
4	Mild	0.499	3.69E-05
5	Mild	0.498	2.41E-05
6	Non-fatigue	0.506	1.78E-04
7	Fatigue	0.499	5.06E-01
8	Fatigue	0.499	3.26E-05
9	Non-fatigue	0.515	3.26E-05
10	Non-fatigue	0.498	3.26E-05
11	Non-fatigue	0.502	3.669910624033691E-05
12	Fatigue	0.486	4.427226235418381E-05
13	Fatigue	0.489	0.006668588880724
14	Non-fatigue	0.481	0.006549874988565
15	Non-fatigue	0.502	0.002678505522447

Table 3 Mean range and variance range for frequency domain analysis

Condition	Mean range	Average of mean	Variance range	Average of variance
Non fatigue	0.481-0.514	0.5004	0.00001725-0.006667	0.0014000
Mild fatigue	0.492-0.49	0.497	0.00002415-0.00004851	0.0000365
Fatigue	0.486-0.49	0.494	0.00002251-0.5060	0.1026

Hence, mean and variance is obtained by using a function in MATLAB. The data for the mean and variance are as in Table 2.

By analysing this table, the range value of mean and variance for non-fatigue, mild fatigue and fatigue are obtained as in Table 3.

In theory, when a muscle started to be fatigue, the amplitude of the voltage will be decreased as a sign for our muscle to slow their work. This can be verified from reference [5]. From the average mean of normalized data, non-fatigue shows the highest value (0.5004), followed by mild-fatigue (0.497) and fatigue is the lowest (0.494). While in term of variance analysis, higher variance shows the muscle start to fatigue as it shows higher firing rates of recruited motor units performed. From the average variance of normalized data, fatigue shows the highest value (0.1026), followed by non-fatigue (0.0014) and mild is the lowest (0.0000365). These results proves that when a muscle start to fatigue, the amplitude will slowly decrease while variance will be increased. It can be observed non-fatigue signal has the highest mean (0.515) compare to mild fatigue signal and fatigue signal. Scatterplot is used

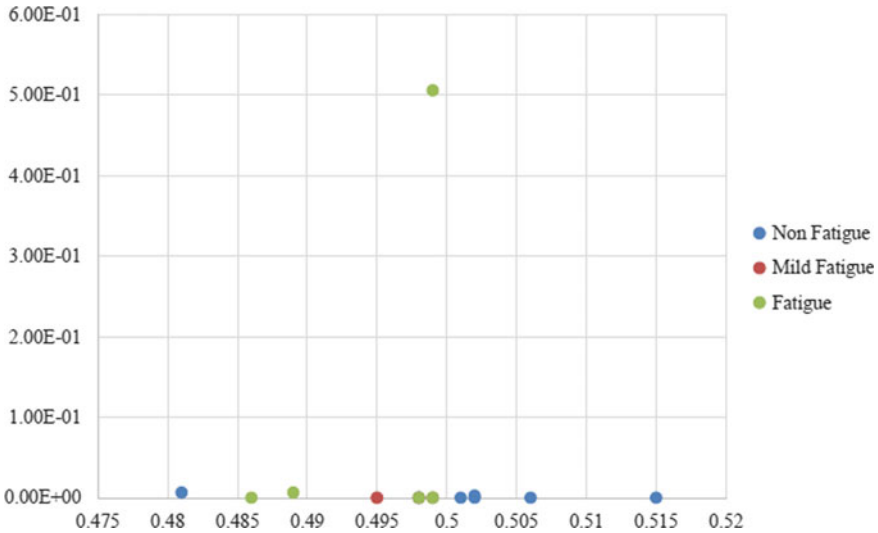


Fig. 8 Graph for mean versus variance

to analyse patterns in bivariate data. Next, a graph of mean versus variance is plotted to see a pattern. This pattern of graph is as follows (see Fig. 8).

3.5 Frequency Domain Signal Analysis

From the normalized time domain signal, it is then further transformed to Power Spectral Density (PSD) signal. PSD describes the power present in the signal as a function of frequency, per unit frequency. All signals are plotted in PSD and the peak frequency value of each graph is obtained (see Table 4).

From these three PSD graphs, Figs. 9, 10 and 11, the feature of muscle fatigue cannot be seen as the data are too crowded, overlapped. Suppose to be when a muscle starts to fatigue, the graph will be shifted to left, lower frequency. In this case, peak value of each data will be extracted to see its features.

From Table 5, non-fatigue shows highest mean frequency 11.379 Hz, followed by mild-fatigue 11.969 Hz and fatigue is least with 11.582 Hz. For frequency range there are frequency values overlapped for non-fatigue, mild-fatigue and fatigue. It is hard to know what is the exact frequency a muscle start to fatigue because every person have the different muscle fatigue condition. Hence, fatigue characteristics cannot be determined. This might be caused by oversampling of EMG data. Maybe, it needs to sample the data higher than 500 Hz and become more pronounced as sampling rate increases.

Table 4 The peak frequency for PSD

Sample	Peak frequency
1	12.17
2	12.796
3	10.027
4	12.7732
5	10.338
6	12.311
7	12.796
8	11.764
9	12.984
10	10.066
11	17.920
12	12.945
13	10.379
14	11.272
15	16.790

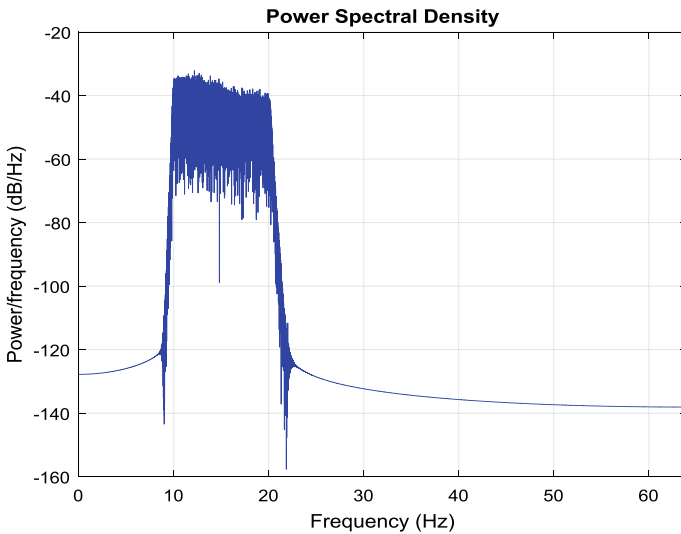


Fig. 9 PSD graph for non-fatigue (sample 1) with 12.17 Hz peak frequency

3.6 Analysis Comparison

The result of this project shows the time domain analysis method manage to validate the result with the questionnaire. These results prove that when a muscle starts to fatigue, the amplitude will slowly drop and the variance will be increase.

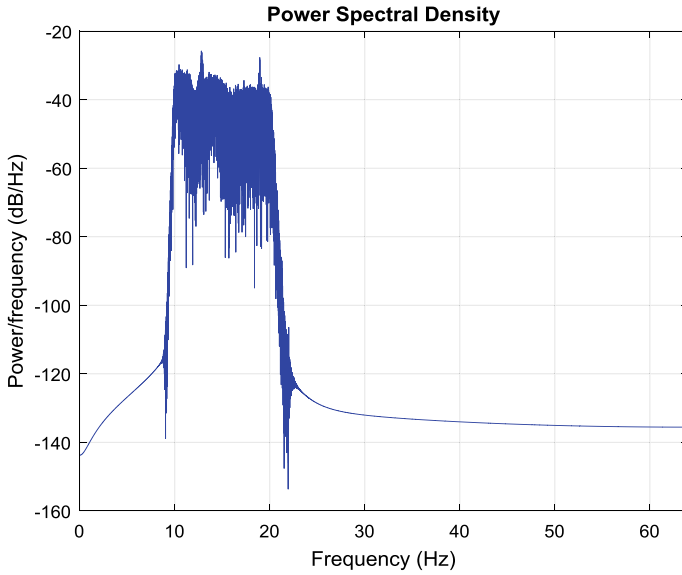


Fig. 10 PSD graph for mild-fatigue (sample 2) with 12.796 Hz peak frequency

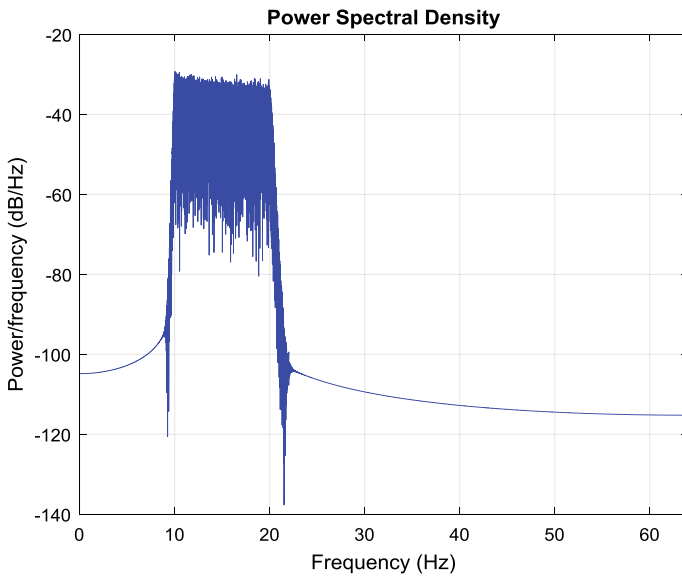


Fig. 11 PSD graph for fatigue (sample 3) with 10.027 Hz peak frequency

On the other hand, frequency domain could not clearly show the characteristic of muscle fatigue. Some data have overlapping value in frequency response that disturb the process of analysing. The mean of peak frequency in non-fatigue (13.379 Hz) fol-

Table 5 Frequency ranges for non-fatigue, mild-fatigue and non-fatigue

Condition	Mean frequency	Frequency range (Hz)
Non fatigue	13.379	10.066–16.79
Mild fatigue	11.969	10.338–12.796
Fatigue	11.582	10.027–12.945

lowed by fatigue (12.782 Hz) and mild-fatigue (11.969 Hz). This trend of frequency does not follow the theory of frequency analysis.

4 Conclusion

As a conclusion, time domain analysis is a better option to determine muscle fatigue compare frequency domain signal analysis in this experiment. Time domain analysis shows accurate result of muscle fatigue in term of mean and variance. In frequency domain, the characteristic cannot be clearly seen. Overlapping data could shadow the response. Therefore, an early precaution, especially during sampling the data need be taken into account when monitoring the onset and development of fatigue.

Acknowledgements This research was supported by a Grant at the Universiti Malaysia Pahang (RDU160391).

References

1. MIROS Homepage. <https://www.miros.gov.my/1/page.php?id=17>. Last accessed 24 May 2018
2. Raez, M.B.I., Hussain, M.S., Mohd-Yasin, F.: Techniques of EMG signal analysis: detection, processing, classification and applications. *Biol. Proced. Online* **8**, 11–35 (2006)
3. Khandey, S.: Morphology of brachialis muscle: variations and clinical significance. *Int. J. Anat. Res.* **2**(1), 184–186 (2014)
4. De Luca, C.J., Donald Gilmore, L., Kuznetsov, M., Roy, S.H.: Filtering the surface EMG signal: movement artifact and baseline noise contamination. *J. Biomech.* **43**, 1573–1579 (2010)
5. Broman, H., De Luca, C.J., Mambrito, B.: Motor unit recruitment and firing rates interaction in the control of human muscles. *Brain Res.* **337**(2), 311–319 (1985)
6. Mihai, M.: An integral mean value theorem concerning two continuous functions and its stability. *Int. J. Anal.* 1–4 (2015)
7. Wang, Z., Tian, F.: A note of the expected value and variance of fuzzy variables. *Int. J. Nonlinear Sci.* **9**, 486–492 (2010)

8. Haque, M.N., Uddin, M.S.: Accelerating fast fourier transformation for image processing using graphics processing unit. *J. Emerg. Trends Comput. Inf. Sci.* **2**(8), 367–375 (2011)
9. Karrenberg, U.: Signals in the time and frequency domain. *An Interactive Multimedia Introduction to Signal Processing*, pp. 22–63. Springer, Heidelberg (2007)
10. Siemiński, A., Keibel, A., Klajner, P.: Fatigue independent amplitude-frequency correlations in EMG signals. *Zeszyty Naukowe Katedry Mechaniki Stosowanej* **26**, 315–320 (2006)
11. Wang, J., Tang, L., Bronlund, J.E.: Surface EMG signal Amplification and filtering. *Int. J. Comput. App.* **82**(1), 15–22 (2013)

Time-Frequency Analysis from Earthing Application



Jun Hou Ting, Mahfuzah Mustafa, Zarith Liyana Zahari, Dwi Pebrianti, Zainah Md Zain, Nurul Hazlina Noordin and Rafiuddin Abdubrani

Abstract Body earthing or grounding means that connecting the body in direct and uninterrupted contact with the earth by touching the soil, sand, water, or a conductive surface that is in contact with the earth. By earthing the body, positive charge can be neutralized and return the body to a neutral state as the positive charge that builds up can lead to health problems. There are few types of time-frequency analysis method such as Gabor, Wavelet and Wigner. The experiment of body earthing is done by recording the EEG signal from human brainwave with the Emotive EPOC Headset. To remove the noise of the signals, in pre-processing stage is important to separate the signal into two band frequency band which are alpha band and beta band with the threshold of signal amplitude was set to -100 to $100 \mu\text{V}$. Then the peak points were plotted into a histogram to compare the changes of the Alpha and Beta band signals. Lastly, the results of before body earthed and after body earthed were compared through the histogram plotted. The result shows that, before the body earthed, the Alpha band signals are low, while the Beta band signals are high. Then after body earthed, the Alpha band increased, while the Beta band are decreased. From the result show that the body earthing reduced the stress of the student.

Keywords EEG signal · Time frequency · Gabor transform · Wavelet transform Wigner transform

J. H. Ting · M. Mustafa (✉) · Z. L. Zahari · D. Pebrianti · Z. Md Zain · N. H. Noordin
R. Abdubrani
Universiti Malaysia Pahang, Pekan, Pahang, Malaysia
e-mail: mahfuzah@ump.edu.my

Z. L. Zahari
Universiti Kuala Lumpur British Malaysian Institute, Gombak, Selangor, Malaysia

© Springer Nature Singapore Pte Ltd. 2019
Z. Md Zain et al. (eds.), *Proceedings of the 10th National Technical Seminar on Underwater System Technology 2018*, Lecture Notes in Electrical Engineering 538, https://doi.org/10.1007/978-981-13-3708-6_36

1 Introduction

Grounding or earthing can be known as placing naked or bare feet on the ground no matter it is sand, soil, grass, dirt or concrete. As the technology is advancing in modern lifestyle, humans are separated from having contact with the earth. When grounding feet to the earth with ample of electrons, large amounts of negative charge electrons are absorbed into the body through the soles of the feet. This can help to maintain the body at the same rate of negative charged electrical potential with the earth as positive charge can be neutralized and return the body to a neutral state which can benefit to the health of body [1]. Body earthing contributes many positive effects of the body as it can help decrease levels of inflammation and pain. Being grounded can help relieve inflammation. In a small study of 12 subjects, when grounding the body during sleep decreases night-time levels of cortisol and it causes the cortisol hormone secretion to occur more in alignment compare to the natural 24-h circadian rhythm profile [2]. Besides that, it also helps to improve circulation. When grounding the body to the ground, it helps in delivering of oxygen and nutrients to every part of the body. It also helps to improve better blood circulation to the face [3].

An electroencephalogram (EEG) is a method used to monitor the electrical activity in the brain or can be known as brain wave. EEG is a medical imaging analysis technique that translates all the signal and waveforms generated by the brain, which is also known as the brain electrical activity. The brain cells interact with each other by generating electrical impulses. EEG can be used to detect potential problems related to brain activity by tracking and recording the brain wave patterns. This signal will manipulate under different condition of the brain, such as pain, happy, relax, stress and sleep. Besides EEG, there are also Electrooptigraphy (EOG) for eye movements' measurements and Electrocardiography (ECG) for heartbeat measurement and which is similar to the EEG imaging techniques to the human body. In this era of globalization, electrobiological measurements are commonly in use in many research and medical fields [4, 5].

The EEG recording displays the continuous signal of brain activities. The amplitude and frequency is dependent on the activities of the brain stem. The EEG signals are classified into four frequency bands which displays different types of brain activities. For normal people that are in a calm and conscious state, it will have Alpha waves with amplitude that is less than $13 \mu\text{V}$. For people that are carrying out mental activities that is intense or required highly concentration, it will have Beta waves with frequency range from 13 to 30 Hz and maximum amplitude value of $20 \mu\text{V}$. For adults and young children, which are in a state of hypnotized, meditating or sleeping, but not into deepest stages of sleep, it will have Theta waves with frequency range from 4 to 7 Hz and amplitude less than $100 \mu\text{V}$. In sleeping there are four stages of sleep. During the stage three of sleep, part of Delta wave begins to appear, but during the stage four of sleep, mostly all brain activities are Delta wave. Delta wave has the frequency between 0.5 and 4 Hz and amplitude less than $100 \mu\text{V}$ [5]. Nonetheless, there are three parts in time-frequency analysis, which are time domain, frequency domain and time-frequency domain. From time-frequency domain, more feature and

information can be obtained. The one-dimensional signal consists of a complex or real value, function and some transform which their domain is the real line. It is acquired from the original signal from some transform. Instead of analyzing the one-dimensional signal, time-frequency can be study of two-dimensional signal where the function's domain is on a two-dimensional real plane. From a time-frequency transform, a signal in two-dimensional is acquired [2, 6].

Functions and their transforms representation normally are quite crowded and connected nearly. With time-frequency analysis, they can be clearer by analyzing them together instead of differently. As many signals change significantly over time and consist of short duration, the classical Fourier analysis considers signals are periodic or infinite in time. Short-time Fourier transform is one of the most basic time–frequency analysis (STFT) meth-od, but as time passed there are more advanced methods coming out such as Gabor, Wavelet and Wigner.

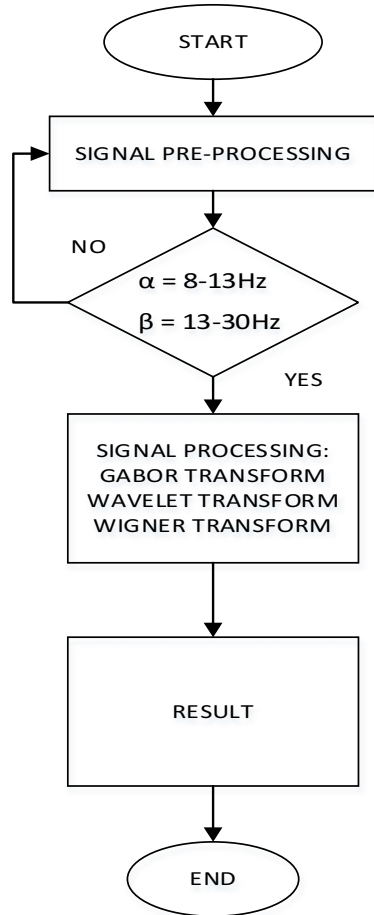
2 Methodology

Figure 1 shows a flowchart system. Firstly, the signal is processed in the signal pre-processing stage where the raw EEG data are filtered into a frequency range of 8–13 Hz for Alpha band signals and frequency range of 13–30 Hz for Beta band signals [7]. If the EEG data filtered is not Alpha or Beta band then loop back to signal pre-processing process. After the Alpha and Beta band signals are confirmed, signal processing methods which were Gabor, Wavelet and Wigner are applied to the signal. The experiment is focused at the anterior frontal EEG Cluster such as FP1 and FP2 channel.

2.1 Pre-processing Stage

The data acquired were stored in the form of .edf file format. Edfread function was used to read the edf file in MATLAB software. In pre-processing, all EEG data were pre-processed with MATLAB software. The Band-pass filter was used to filter and categorize the EEG data into the Alpha band and Beta band. Due to the passbands and stopbands that were maximally flat and absent of ripples the Band-pass filter. Butterworth is chosen as it can result in better output signal for different frequency bands [8]. The raw EEG data were filtered into a frequency range of 8–13 Hz for Alpha band signals and frequency range of 13–30 Hz for Beta band signals [5]. Frequency out of Alpha band and Beta band range will be filtered. After filtering, amplitude range of -100 to $100 \mu\text{V}$ was set to threshold the signal to eliminate unwanted artifacts and noises as they will affect the accuracy of the result.

Fig. 1 Flowchart system



2.2 Gabor Transform

In short-time Fourier transform the Gabor transform is a special case and being used in determining the phase and sinusoidal frequency information. This information is obtained from the local section of the signal as the signal varies over time. A Gaussian function is used to multiply with the function that is required to be transformed which can also know as the window function. Next, the Fourier transform is used to transform the function obtained to derive the time-frequency analysis. As the signal gets near the time being analyzed which is also the window function will be having a higher weight. The general form of Gabor transform (GT) can be expressed as Eqs. 1 and 2 below:

$$G_X(t, f) = \sqrt[4]{\sigma} \int_{-\infty}^{\infty} e^{-\sigma \Pi(\tau-t)^2} x(\tau) e^{-j2\pi f \tau} d\tau \quad (1)$$

$$= \sqrt[4]{\sigma} \int_{t-1.9143}^{t+1.9143} e^{-\sigma \pi(\tau-t)^2} x(\tau) e^{-j2\pi f \tau} d\tau \quad (2)$$

The width of Gaussian windowed function is determined by σ . To obtain a result with better resolution of time and degraded frequency σ chosen has to be larger and the width of the windowed function also becomes narrower. This may cause unclear information in the target position. By choosing quite large σ and increase the density of frequency points a more accurate and precise of target position within an interval of short time can be obtained successfully as higher density point will result in long computing time [9]. The energy extracted from the scalogram by using Eq. 3:

$$E = \iint_{-\infty}^{\infty} \left| \frac{G_X(t, f)}{N} \right|^2 \quad (3)$$

2.3 Wavelet Transform

Wavelets are being classified as the main family of functions established from dilations and conversions of one function, which is the mother wavelet by Morlet. The mother wavelet can be defined by Eq. 4.

$$\psi_{b,a} = \frac{1}{\sqrt{|a|}} \psi \left(\frac{t-b}{a} \right), a, b \in R, a \neq 0 \quad (4)$$

In the above equation, a is the scaling parameter where the amount of compression is measured. While for b , it is the parameter where the conversion that determines the wavelet position in time. If $|a|$ is less than 1, then the wavelet in Eq. 3 corresponds more to higher frequencies and is the smaller version mother wavelet in time-domain. Next, if $|a|$ is more than the wavelet in Eq. 3 corresponds more to lower frequencies and is the bigger version mother wavelet in time-domain. Hence, wavelets have frequencies that adjusted with time-widths and this is the reason for Morlet wavelets to be applied successfully in signal time-frequency analysis and signal processing [10]. The energy was extracted from the spectrogram by using Eq. 5:

$$E = \iint_{-\infty}^{\infty} \left| \frac{CWT(a, b)}{N} \right|^2 \quad (5)$$

2.4 Wigner Transform

The Wigner distribution, which are known as Wigner-Ville distribution. The Wigner-Ville distribution is known for its applying high clear quality but there are some drawbacks such as cross terms problems. The representation of windowed Wigner-Ville distribution function can be defined by Eq. 6:

$$W_x(t, f) = \int_{t-c}^{t+c} x\left(t + \frac{\tau}{2}\right)x^*\left(t - \frac{\tau}{2}\right)e^{-j2\pi f\tau} d\tau \quad (6)$$

If there is more than one or two components of signal with different frequencies exist at the same time cross terms will occur. To decrease the cross terms number by avoiding summing too many signal components, selecting a smaller C will be helpful in the implementation stage. Even though the signal is in complex-valued, the Wigner-Ville distribution will be always real-valued. The frequency domain is consistent for real-valued signals when comparing with the spectrum and a spectrogram definition for real-valued signals. The Wigner distribution also satisfies the marginals of time and frequency, defined as time marginal and a frequency marginal equation in 7 and 8:

$$\int_{-\infty}^{\infty} W_x(t, f)df = |x(t)|^2 \text{ (Time marginal)} \quad (7)$$

and

$$\int_{-\infty}^{\infty} W_x(t, f)dt = |x(f)|^2 \text{ (Frequency marginal)} \quad (8)$$

The energy was extracted from the spectrogram by using Eq. 9:

$$E = \iint_{-\infty}^{\infty} \left| \frac{W_x(t, f)}{N} \right|^2 \quad (9)$$

3 Results and Discussion

3.1 Gabor Transform

Figures 2 and 3 shows the image representation of Alpha band and Beta band for FP1 channel. Meanwhile, Figs. 4 and 5 are the image representation of FP2 channel.

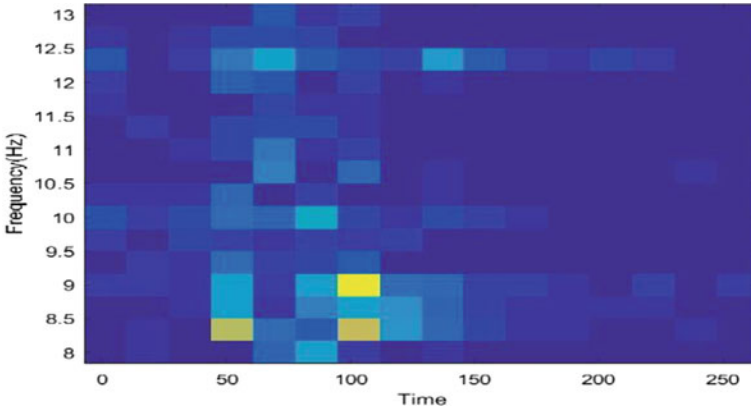


Fig. 2 GT image for alpha band FP1

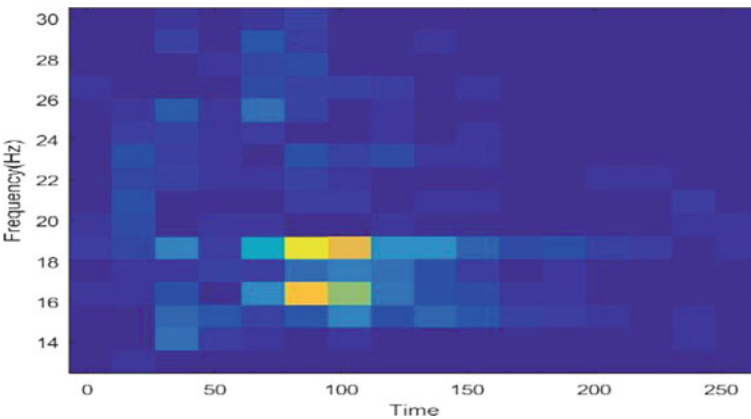


Fig. 3 GT image for Beta band FP1 (8–13 Hz)

Yellow colour which is the brightest colour, indicates the highest energy from Figs. 2 and 3. The highest energy lies in between the frequency bands where 8–13 Hz for Alpha band signals in and 13–30 Hz for Beta band signals.

The average of the energy for both channels is plotted in Figs. 6 and 7. From Figs. 6 and 7, the energy of Alpha band signal and Beta band signal both shows a slight decrement. Alpha band is high before body earthing and slightly decreased after body earthing. The decrement of the Alpha band might be caused by an error that occurred in the experiment. Meanwhile, the Beta band is high before body earthing and it slightly decreases after body earthing. The decreased of Beta band signal activities show that the subject is alert and focus. This is considered as a negative body earthing as only Beta shows the correct pattern of body earthing.

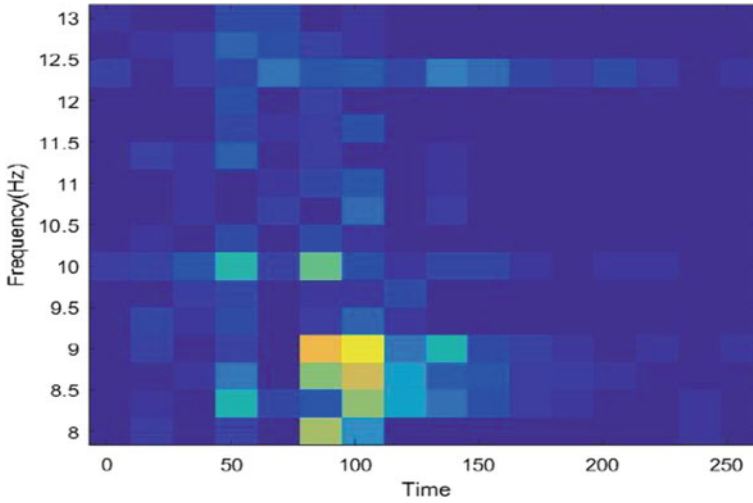


Fig. 4 GT image for alpha band FP2 (8–13 Hz)

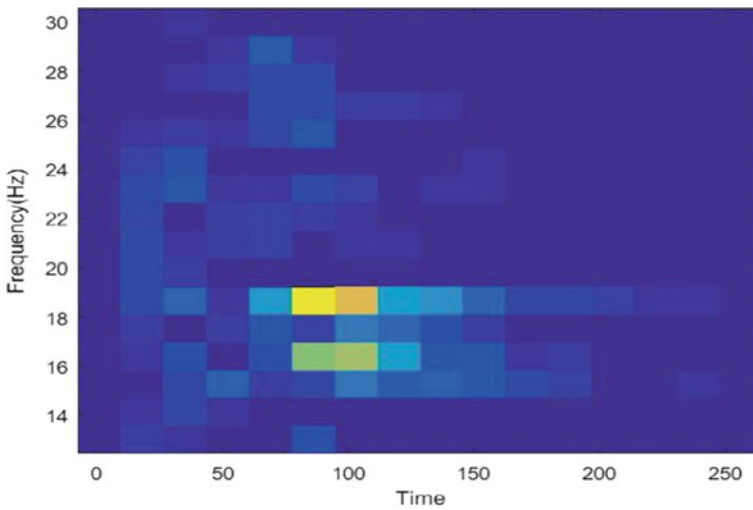


Fig. 5 GT image for alpha band FP2 (14–30 Hz)

3.2 Wavelet Transform

Figures 8 and 9 shows the scalogram image representation of Alpha band and Beta band for FP1 respectively. Meanwhile, Figs. 10 and 11 are the scalogram image representation for FP2 channel. Yellow colour, which is the brightest colour, indicates the highest energy from Figs. 9 and 10. The highest energy lies in between the frequency bands where 8–13 Hz for Alpha band signals and 13–30 Hz for Beta band

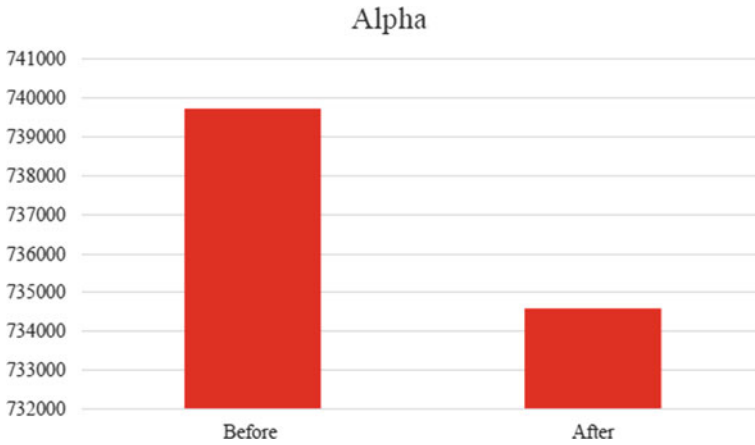


Fig. 6 Histogram of Alpha frequency band for FP1 and FP 2 channel before and after earthing

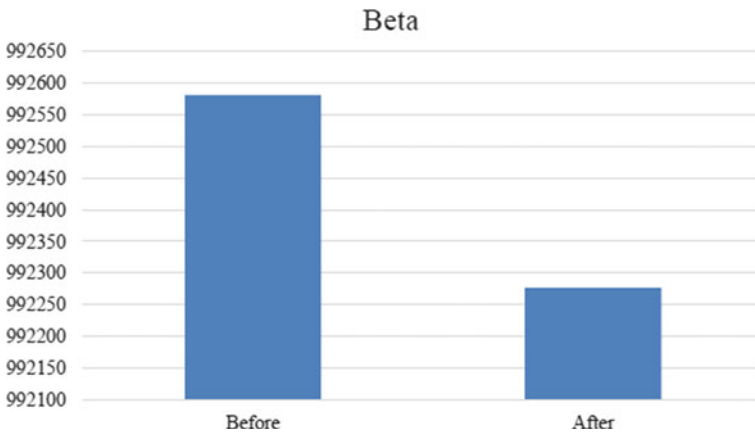


Fig. 7 Histogram of Beta frequency band for FP1 and FP 2 channel before and after earthing

signals from Figs. 11 and 12 is the scalogram image contour plot where Alpha and Beta band can be seen clearly by the distribution of wavelet coefficients.

The average of the energy for both channels is plotted in Figs. 12 and 13. From Figs. 12 and 13, the energy of the Alpha band signal and the Beta band signal both shows a slight increment. This can be concluded that, Alpha band is low before body earthing and slightly increased after body earthing. The increment of the Alpha band signal activities shows that subject is calm. Meanwhile, the Beta band is low before body earthing and it slightly increases after body earthing. The increment of the Beta band might be caused by an error that occurred in the experiment. This is considered as a negative body earthing as only Alpha shows the correct pattern of body earthing.

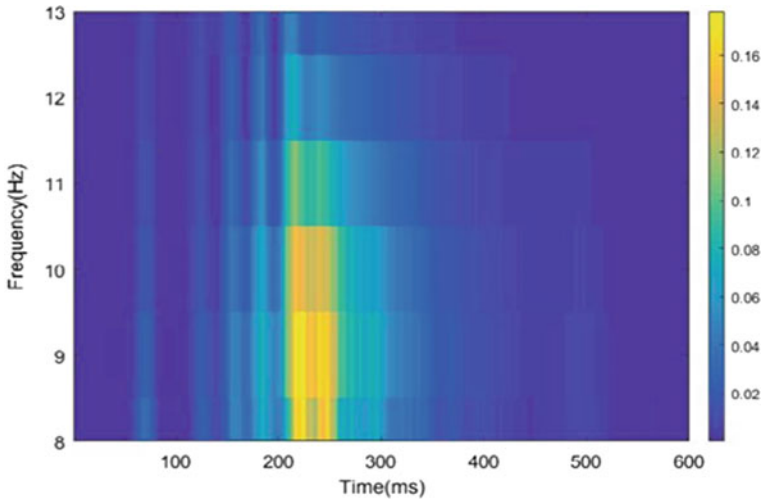


Fig. 8 WT scalogram image for Alpha band in FP 1

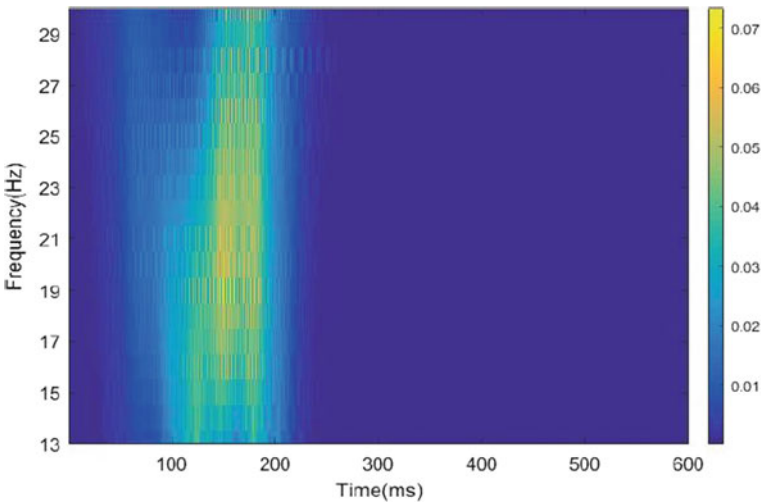


Fig. 9 WT scalogram image for Beta band in FP 1

3.3 Wigner Transform

Figures 14 and 15 shows the scalogram image representation of Alpha band and Beta band for FP1 respectively. Meanwhile, Figs. 16 and 17 are the scalogram image representation for FP2 channel. Yellow colour, which is the brightest colour, indicates the highest energy from Figs. 15 and 16. The highest energy lies in between the

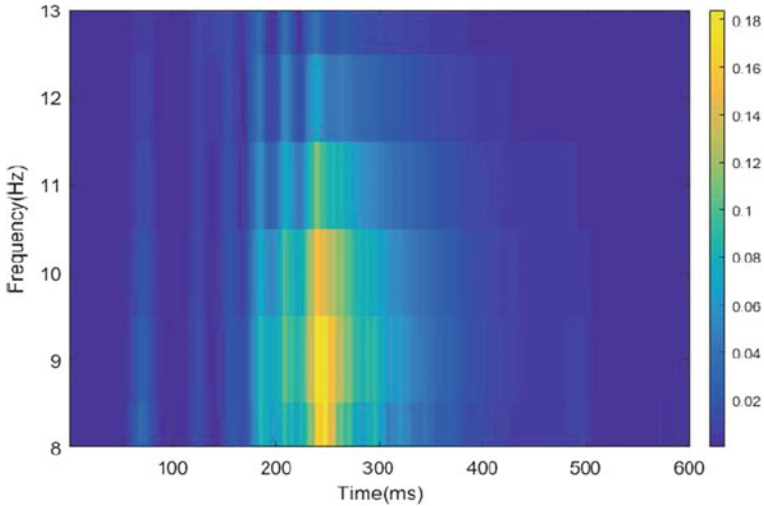


Fig. 10 WT scalogram image for Alpha band in FP 2

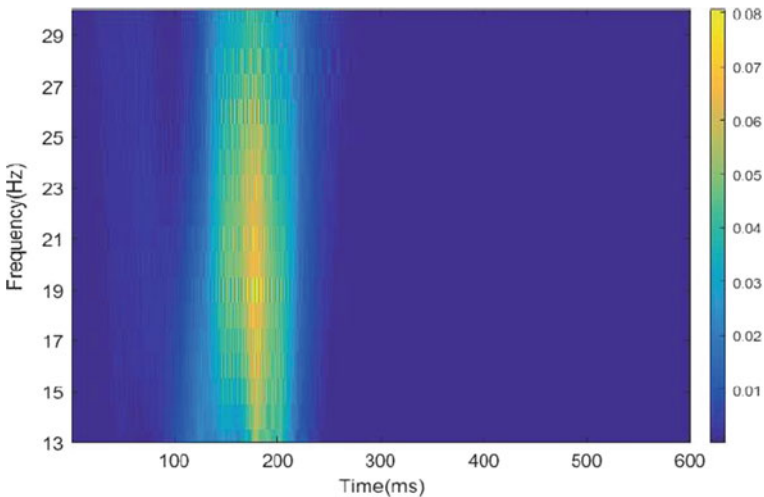


Fig. 11 WT scalogram image for Beta band in FP 2

frequency bands where 8–13 Hz for Alpha band signals and 13–30 Hz for Beta band signals.

Refer to Figs. 18 and 19, Alpha band is low before body earthing and slightly increased after body earthing. The increment of the Alpha band signal activities show that subject is calm. Meanwhile, the Beta band is low before body earthing and it slightly increases after body earthing. The increment of Beta band might be caused

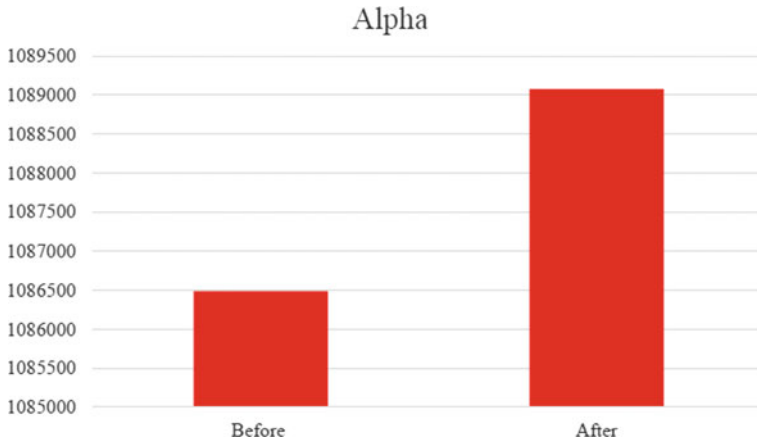


Fig. 12 Histogram of Alpha Frequency band from FP 1 and FP 2 channel before and after body earthing

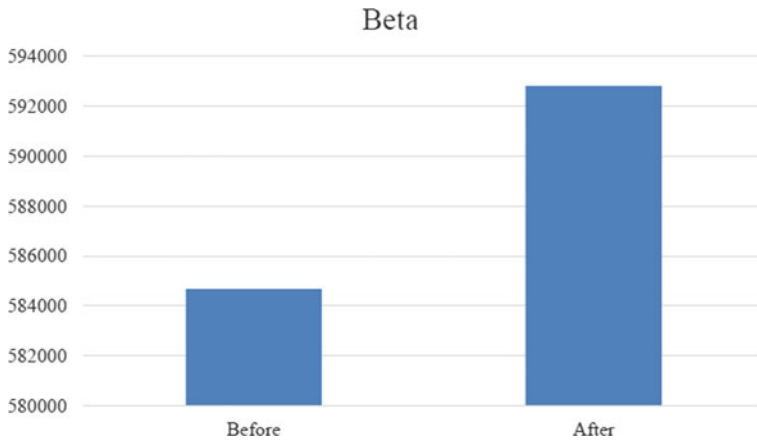


Fig. 13 Histogram of Beta Frequency band from FP 1 and FP 2 channel before and after body earthing

by an error that occurred in the experiment. This is considered as a negative body earthing as only Alpha shows the correct pattern of body earthing.

4 Conclusion

Electroencephalography (EEG) signals characteristics for body earthing application, to employ time-frequency analysis such as Gabor, Wavelet and Wigner and to obtain the best result of time-frequency analysis in terms of accuracy. The increment in

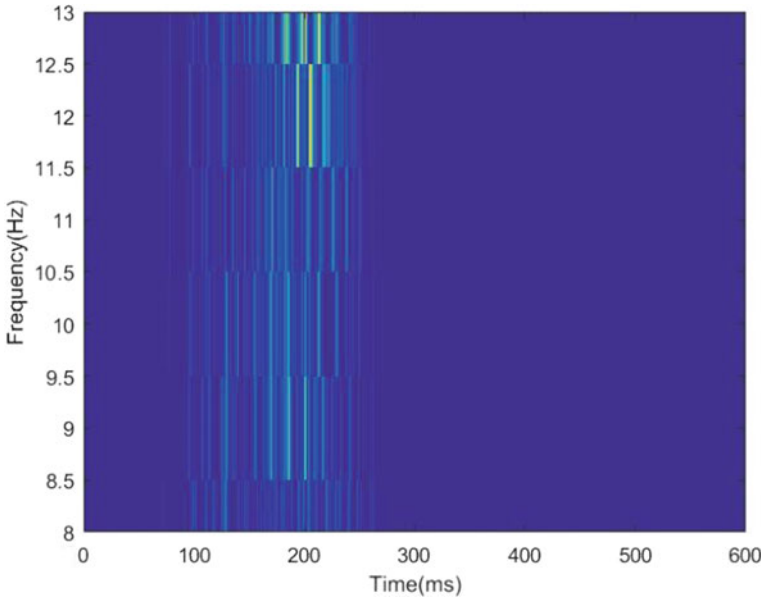


Fig. 14 WD scalogram image for Alpha band in FP 1

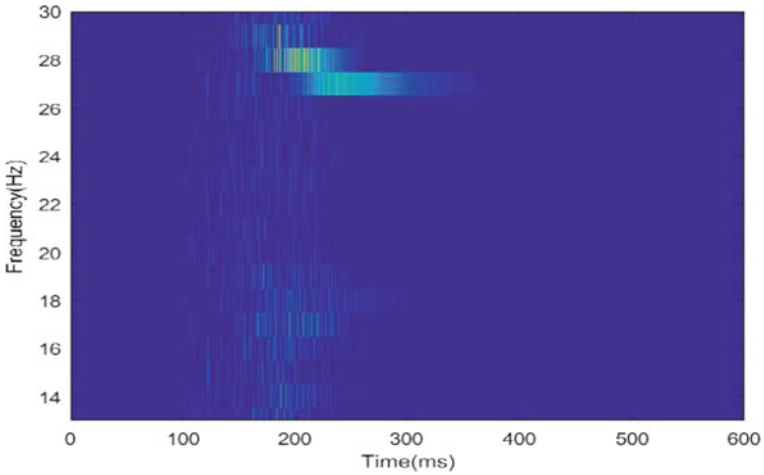


Fig. 15 WD scalogram image for Beta band in FP 1

Alpha band signal activities show that subjects tend to be more calm. Meanwhile, the decrement of Beta band signal activities show that subjects are tend to be more alert and focus [11]. According to the result, Alpha band decreased and Beta band decreased after body earthing for Gabor Transform. Gabor Transform displayed a negative body earthing as only Beta showed the correct pattern of body earth-

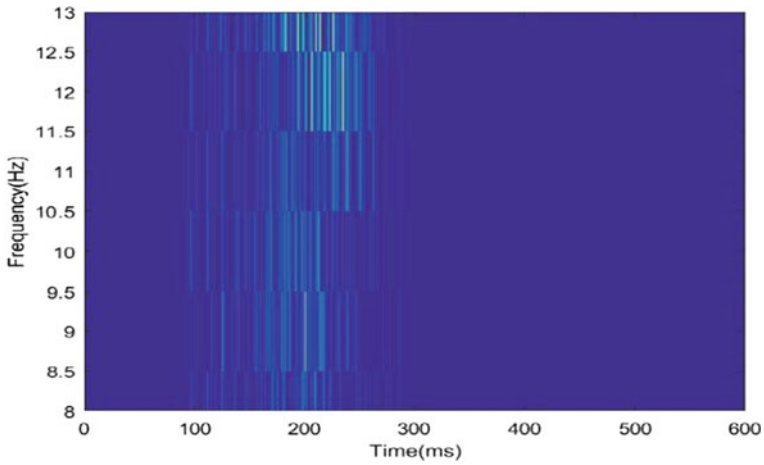


Fig. 16 WD scalogram image for Alpha band in FP 2

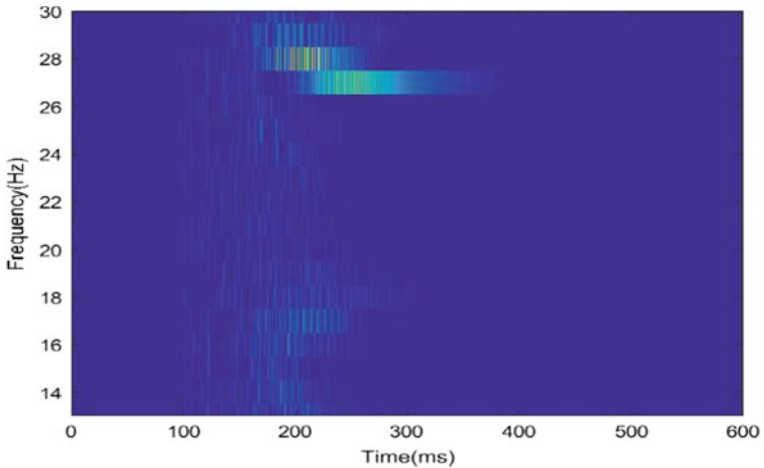


Fig. 17 WD scalogram image for Beta band in FP 2

ing. Next, Alpha band increased and Beta band increased after body earthing for Wavelet Transform. Wavelet Transform displayed a negative body earthing as only Alpha showed a correct pattern of body earthing. Alpha band increased and Beta band increased after body earthing for Wigner Distribution. Wigner Distribution displayed a negative body earthing as only Alpha showed correct pattern of body earthing. In suggestion, the EEG signal, there are various machine methods that can be implemented such as Support Vector Machine (SVM) and Fuzzy Logic Method. As for the data acquisition, the protocol for data acquisition of EEG signal must be obeyed in order to acquire accurate result.

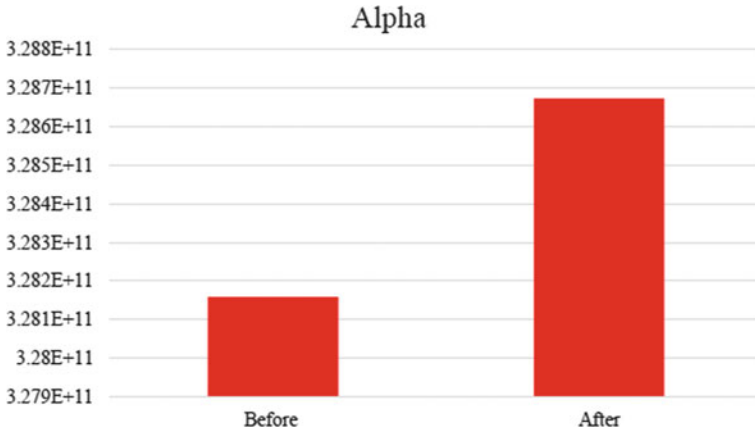


Fig. 18 Histogram of Alpha frequency band from FP1 and FP2 channel before and after earthing

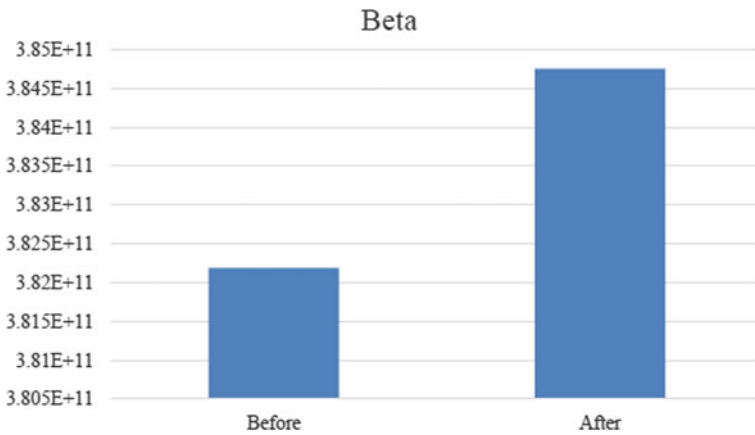


Fig. 19 Histogram of Beta frequency band from FP1 and FP2 channel before and after earthing

Acknowledgements This research was supported by a Grant at the Universiti Malaysia Pahang (RDU170365).

References

1. Chevalier, G., Sinatra, S., Oschman, J., Sokal, K., Sokal, P.: Earthing: health implications of reconnecting the human body to the earth’s surface electrons. *J. Environ. Public Health* **2012**, 1–8 (2012)
2. Cohen, L.: Time-frequency distributions—a review. In: *Proceedings of the IEEE*, pp. 941–981. IEEE (1989)

3. Ghaly, M., Teplitz, D.: The biologic effects of grounding the human body during sleep as measured by cortisol levels and subjective reporting of sleep, pain, and stress. *J. Altern. Complement. Med.* **10**(5), 767–776 (2004)
4. Alazrai, R., Alwanni, H., Baslan, Y., Alnuman, N., Daoud, M.I.: EEG-based brain-computer interface for decoding motor imagery tasks within the same hand using Choi-Williams time-frequency distribution. *Sensors* **17**(9), 1–27 (2017)
5. Teplan, M.: Fundamentals of EEG measurement. *Meas. Sci. Rev.* **2**(2), 1–11 (2002)
6. Sejdić, E., Djurović, I., Jiang, J.: Time–frequency feature representation using energy concentration: an overview of recent advances. *Digit. Signal Proc.* **19**(1), 153–183 (2009)
7. BrainClinicHomepage. <https://www.brainclinics.com/dynamic/media/1/document/Onderzoeksinstytut/FilteringinBioExplorer.pdf>. Last accessed 2018
8. Oschman, J.L., Chevalier, G., Brown, R.: The effects of grounding (earthing) on inflammation, the immune response, wound healing, and prevention and treatment of chronic inflammatory and autoimmune diseases. *J. Inflammation Res.* **8**, 83–96 (2015)
9. Su, L., Wu, H.S., Tzuang, C.C.: 2-D FFT and time-frequency analysis techniques for multi-target recognition of FMCW radar signal. In: *Proceedings of the Asia-Pacific Microwave Conference*, pp. 1390–1393. IEEE, USA (2011)
10. Sifuzzaman, M., Islam, M.R., Ali, M.Z.: Application of wavelet transform and its advantages compared to fourier transform. *J. Phys. Sci.* **13**, 121–134 (2009)
11. Chang, C.R.: EEG based pattern recognition method for classification of four mental tasking. In: *International Conference on Automation, Cognitive Science, Optics, Micro Electro-Mechanical, and Information technology*, pp. 0–5. Indonesia (2016)

Energy Spectral Density Analysis of Muscle Fatigue



Noor Aisyah Ab Rahman, Mahfuzah Mustafa, Rosdiyana Samad,
Nor Rul Hasma Abdullah and Norizam Sulaiman

Abstract Driver's vigilance level is easily distracted when in a state of fatigue and drowsiness. Most drivers' shows sign of visual fatigue and loss of vigilance during long and monotonous driving. Their ability to maintain adequate driving performance is affected by various factors. A Popular technique to estimate driver's vigilance level is physiological measure that uses electromyogram (EMG) signal in estimating driver muscle fatigue while driving. In this project, the EMG signal will be obtained by attaching the electrodes to the biceps brachii of each 15 subjects during playing Need for Speed (NFS) game for two hours. Be-fore that, subjects will answer a set of questionnaires and the scores obtained will be calculated. From the questionnaires, driver condition can be determined whether the driver is non-fatigue or mild fatigue or fatigue. Then signal preprocessing is applied to remove artifact in EMG signal. Next, the EMG signal is analyzed by using frequency domain analysis and Energy Spectral Density (ESD) extracted from the analysis. Mean, variance and peak energy of ESD is obtained from all the samples. Based on results obtained, the normalized mean (non-fatigue: 0.0514–0.1255), (mild fatigue: 0.0554–0.0802) and (fatigue: 0.0069–0.0188). For the variance range (non-fatigue: 0.0050–0.0311), (mild fatigue: 0.0054–0.0802) and (fatigue: 0.0006–0.0047). While for the peak energy of ESD (non-fatigue: 28,480–2,943,000 J/Hz), (mild fatigue: 99,440–120,500 J/Hz) and (fatigue: 537.7–11,440 J/Hz).

Keywords Fatigue · ESD · EMG

1 Introduction

Recently, the numbers of car crashes or road accidents are still increasing even though a lot of improvements in road and vehicle design for the driver safety. According to the statistics from the Malaysian Institute of Road Safety Research (MIROS)

N. A. A. Rahman (✉) · M. Mustafa · R. Samad · N. R. H. Abdullah · N. Sulaiman
Universiti Malaysia Pahang, Pekan, Pahang, Malaysia
e-mail: nooraisyahabraham@gmail.com

© Springer Nature Singapore Pte Ltd. 2019
Z. Md Zain et al. (eds.), *Proceedings of the 10th National Technical Seminar on Underwater System Technology 2018*, Lecture Notes in Electrical Engineering 538,
https://doi.org/10.1007/978-981-13-3708-6_37

489,606 road crashes with 6706 road deaths in the year 2015, and the number of crashes is two times higher than a year before. Scanning for the countermeasures to decrease the measure of car crashes and upgrade the public road safety has turned into an earnest issue for the governments and automakers. It is very important to create an automatic system that intelligently can recognize the driver's unfit status and makes warning to the drivers once necessary. There are many causes that can lead to the road accidents such as fatigue, sleepiness, stress and distraction. In addition, physical discomfort such as extreme ambient temperature, uncomfortable driving condition and muscle fatigue in the neck/shoulder/back area might impact driver behavior [1]. Great proportion of fatigue related accidents occurs between the hours of 2–6 a.m. and 2–4 p.m. approximately [2]. Amid these two periods, driver's body effortlessly gets into normal drowsiness, which increment the chance of accidents. Meanwhile, sleep quality plays a critical role in driver's behavior. Lack of sleep can cause basically degradation of all aspects of functions, including psychological procedures, consideration and focusing, vigilance, and numerous other parameters.

Selecting the effective measurements in developing the automatic system to measure drivers' status is very crucial. Usually the measures are classified into three categories which are vehicle behavior measures, video-based measures and physiological measures [1]. Vehicle behavior measure are includes acceleration, lane position deviation, vehicle speed, gear changes, braking and steering [3]. While, for the video-based measures the detectors used to detect the hand movements, interpret the eye gaze status and monitor the facial expression have been explored by the researches. Recently, features extracted from physiological signals such as galvanic skin response (GSR), electrocardiogram (ECG), electroencephalogram (EEG) and electromyogram (EMG) show relatively high identification in accuracy and get insight into drivers' states directly [1].

Electromyography (EMG) signal are used to detect the muscle fatigue. Muscle fatigue occurs when muscle experiences a reduction in its ability to produce force and accomplish the desired movement. Muscle fatigue can happen because bodies are too tired of overwork in a long time and can affect the daily routines. Muscles are a soft tissue found in most humans and animals, its cells contain protein filaments that slide past one another. Forty percent of body weight consists of muscle that composes the fibers, nerves, and connective tissues. Tension is produced by contraction of fibers that associated by tendons and tissues. Muscle tissue is surrounding in fascia, which is attached to other structures including ligament [4].

Muscle fatigue is when the muscle stops contracting efficiently and when lactic acid builds up in the muscles during anaerobic respiration after vigorous exercise. This causes oxygen debt, which is the amount of oxygen needed to oxidize lactic acid, when oxygen reacts with the lactic acid to break it down into water and carbon dioxide. Oxygen debt is why we take deep breaths for a while after exercise [5]. Hostens and Ramon mention on their paper muscle fatigue usually occurs in the neck, shoulder and back area can give impact to the driving behavior [6].

In this project, the signal which comes from active muscles is detected by sensors is placed on the skin directly above the muscles. The pattern of the signal is seen on a computer and is analyses by using MATLAB; a software programming. The

data then will be undergoing the pre-processing step in order to remove any noise or obstacles during the EMG process. Energy spectral density is the best techniques to identify muscle fatigue. Biceps brachii muscle is acceptable in exploring muscle fatigue while driving since it associated with the development of the elbow and shoulder.

2 Proposed Method

The EMG signal will be obtained by attaching the electrodes to the biceps brachii of each during playing Need for Speed (NFS) game for two hours. The raw EMG data will be collected by using SHIMMER TM Model. Before that, subjects will answer a set of questionnaires and the scores obtained will be calculated. From the questionnaires, driver condition can be determined whether the driver is non-fatigue or mild fatigue or fatigue. Then signal preprocessing is applied to remove artifact in EMG signal. Next, the EMG signal is analyzed by using frequency domain analysis and Energy Spectral Density (ESD) extracted from the analysis. Mean, variance and peak energy of ESD is obtained from all the samples.

2.1 Data Collection

Fifteen of subjects with valid driving license were randomly chosen from the students and staffs in Universiti Malaysia Pahang (UMP) which are age between 18 to 65 years old. They are consists of 10 males and 5 females [7, 8]. For the EMG signals recording for 2 h per subject [9], no nap authorized and free from sleep disorders. It's to make sure that the accuracy of data will not be affected.

The raw EMG data will be collected by using SHIMMER TM Model from the biceps brachii muscles [10, 11]. Before electrode is placed on the skin of subject, BD alcohol swab is used to clean the skin to remove any particles inhibitory particles and allow the alcohol to vaporize so that the skin will be dry. For best result, electrode gel is used to reduce the electrode-skin impedance and increase the conductivity of the muscle and the electrodes.

The driver will be using Logitech Driving Force GT as driving simulation in Need for Speed Game for two hours. Sampling frequency used to collect the data is 128 Hz. The output data collection will be saved in txt file. The txt file will be import into MATLAB R2013A software.

2.2 *EMG Signal Preprocessing*

A raw EMG signal is a signal that originates in the muscle and various noise components which are endemic and unavoidable. These noises will cause an erroneous interpretation of the signal. Hence, the artifacts need to be removed first before start the signal analysis. The Band-pass “Butterworth” filter was used to remove any artifacts as well as high frequency noises with cut-off frequency between 10 and 20 Hz [12]. The Band-pass filter “Butterworth” is chosen because it has the most flat and no ripple pass band. All EMG data were pre-processed by using MATLAB software.

2.3 *EMG Signal Analysis*

EMG signal is analyzed by using frequency domain analysis. Energy Spectral Density (ESD) extracted from the analysis. Energy spectral density in the analysis used to measure the signal energy over the frequency. Computation of ESD is done directly by the method called DFFT. PSD is commonly expressed in joules per hertz (J/Hz). The Fourier transform transforms a time domain signal into a frequency domain representation of that signal. This means that it generates a description of the distribution of the energy in the signal as a function of frequency. This is normally displayed as a plot of frequency (x -axis) against energy (y -axis) called an energy spectrum density. It explains detailed property of probability density function like moment, mean, mean square value, variance standard deviation and probability distribution function [13].

2.4 *Questionnaire*

The result of both methods of signal analysis will be validated by the questionnaire. Each question provided marks for the driver. The marks will be recorded and will determine the muscle fatigue of the driver by comparing the questionnaire marks and the signal analysis results. Both results will be compared to determine which the best method to determine muscle fatigue is.

3 *Result and Discussion*

Fifteen subjects answered set of questionnaires on driving habits that will lead to fatigue during driving. Each objective question provided three answers with three levels of score. The total score will be calculated to determine the condition of the driver whether in non-fatigue, mild fatigue or fatigue state.

Table 1 Scores and driver’s condition based on questionnaire

Driver	Score	Condition
1	10	Non-fatigue
2	16	Mild
3	35	Fatigue
4	30	Mild
5	32	Mild
6	10	Non-fatigue
7	35	Fatigue
8	38	Fatigue
9	12	Non-fatigue
10	15	Non-fatigue
11	10	Non-fatigue
12	35	Fatigue
13	38	Fatigue
14	14	Non-fatigue
15	15	Non-fatigue

Table 1 shows the scores and driver’s condition from the questionnaire. From the table, it shows that five drivers are in fatigue state and three drivers are in a mild fatigue state while the others are in non-fatigue state. However, this questionnaire result cannot prove that the muscle fatigue occurred. Hence, frequency domain analysis was performed to validate the questionnaire and analysis result.

Figure 1 show raw EMG for the subject’s no. 8 and Fig. 2 show the filtered EMG data using 10–20 Hz Butterworth bandpass filter. After filtering the raw data, the amplitude of the EMG signals dropped between -0.4 and 0.4 mV.

Figures 3, 4 and 5 shows the Energy Spectrum Density (ESD) of fatigue, mild-fatigue and non-fatigue respectively. Based on the ESD graph, the non-fatigue condition has higher peak than mild-fatigue and fatigue. From the ESD, the mean, variance and peak energy were obtained.

By analyzing Table 2, the range value of mean and variance for non-fatigue, mild fatigue and fatigue are obtained as Table 3.

Based on Table 4, the peak energy of ESD was extracted. From Table 4, non-fatigue shows highest energy 2,943,000 J/Hz, followed by mild-fatigue 120,500 J/Hz and fatigue is least with 11440 J/Hz. For the energy range based on Table 5, there are overlapped values for non-fatigue, mild-fatigue. So, both conditions can be grouped in the same level.

Table 2 Mean variance from ESD

Sample	Mean	Variance
1	0.0956	0.0150
2	0.0554	0.0054
3	0.0069	0.0006
4	0.0747	0.0097
5	0.0802	0.0113
6	0.0632	0.0091
7	0.0107	0.000773
8	0.0188	0.0047
9	0.1255	0.0311
10	0.0738	0.0112
11	0.0514	5.00E-03
12	0.0117	7.85E-04
13	0.0188	0.0047
14	0.0573	0.0122
15	0.0738	0.0112

Table 3 Mean and variance range for non-fatigue, mild-fatigue and fatigue

Condition	Mean range	Variance range
Non-fatigue	0.0514–0.1255	0.005–0.0311
Mild-fatigue	0.0554–0.802	0.0054–0.0802
Fatigue	0.0069–0.0188	0.0006–0.0047

Table 4 Peak energy from ESD

Sample	Peak energy (J/Hz)
1	28,480
2	120,500
3	11,440
4	110,100
5	99,440
6	721,000
7	667.3
8	537.7
9	381,000
10	2943,000
11	795,900
12	613.1
13	537.7
14	142,800
15	294,300

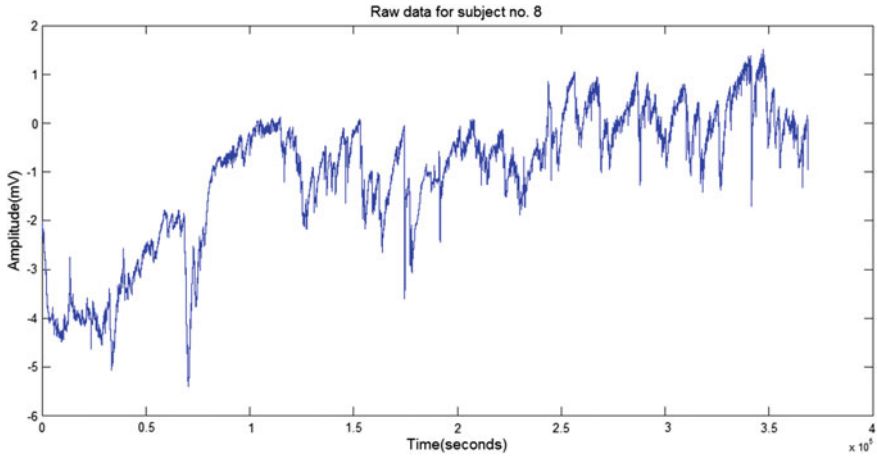


Fig. 1 Fatigue signal (Sample 8)

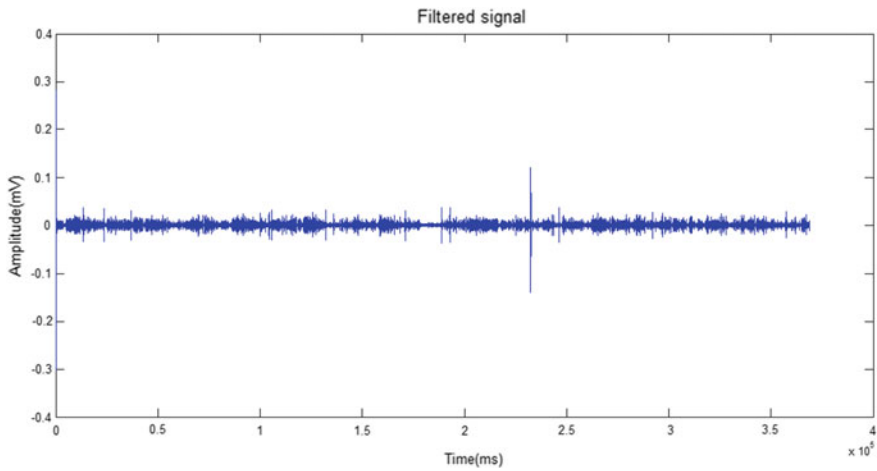


Fig. 2 Filtered fatigue signal (Sample 8)

Table 5 Energy range for non-fatigue, mild-fatigue and fatigue

Condition	Energy range (J/Hz)
Non-fatigue	28,480–2,943,000
Mild-fatigue	99,440–120,500
Fatigue	537.7–11,440

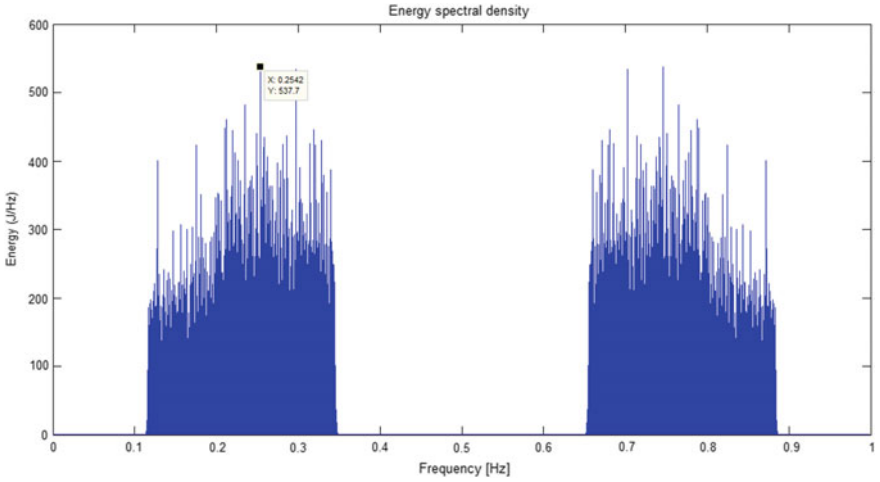


Fig. 3 ESD for fatigue signal (Sample 8)

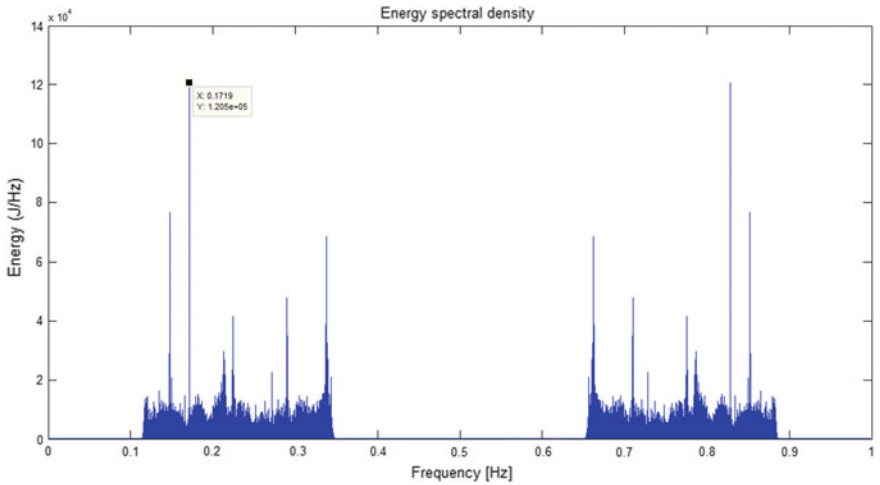


Fig. 4 ESD for mild fatigue signal (Sample 2)

4 Conclusion

All the objectives of this project are achieved. Frequency domain analysis, which is ESD can be used to analyses muscle fatigue. Next, the questionnaire used in this project is validated by the results obtained. The result of this project shows the Energy Spectrum Density method manage to validate the result with the questionnaire. This result proves that when a muscle starts to fatigue, the energy will slowly drop. Based

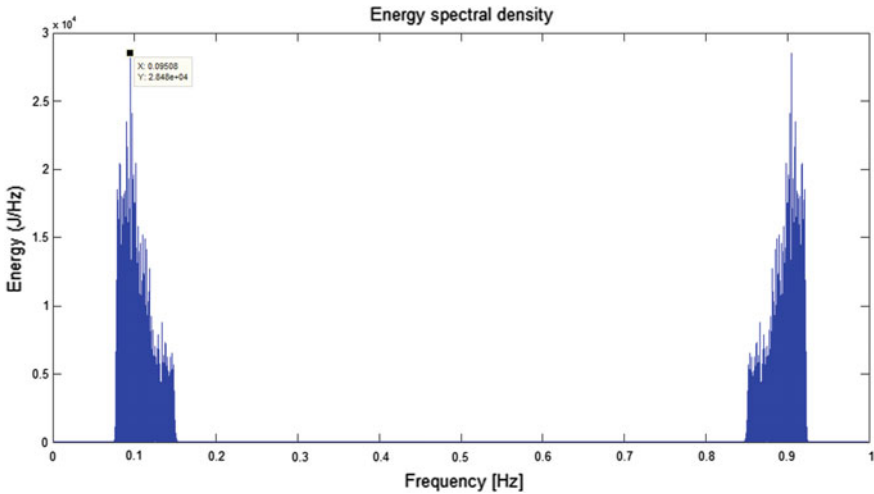


Fig. 5 ESD for non-fatigue signal (Sample 1)

on theory, muscle fatigue occurred when energy deficiency in the muscle. So, that's why when muscle fatigue occurs, the value of energy is low.

As recommendation, since the Shimmer Consensys EMG kit limits the data collection only for two hours, it needs to be improvised. For further analysis, the samples need to involve with three different age groups because time for muscle fatigue occurs is different between age groups. Besides that, for the games that have been used in this project, the types of road in the game such as winding road and straight road can be used to make comparisons which types of road can affect more to muscle fatigue.

Acknowledgements The research was supported by a Grant at the Universiti Malaysia Pahang (RDU160391).

References

1. Chen, L.L., Zhao, Y., Ye, P.F., Zhang, J., Zou, J.Z.: Detecting driving stress in physiological signals based on multimodal feature analysis and kernel classifiers. *Expert Syst. Appl.* **85**, 279–291 (2017)
2. Williamson, A., Friswell, R.: Investigating the relative effects of sleep deprivation and time of day on fatigue and performance. *Accid. Anal. Prev.* **43**(3), 690–697 (2011)
3. Horberry, T., Anderson, J., Regan, M.A., Triggs, T.J., Brown, J.: Driver distraction: the effects of concurrent in-vehicle tasks, road environment complexity and age on driving performance. *Accid. Anal. Prev.* **38**(1), 185–191 (2006)
4. Rahman, N.S.A. et al.: Initial experiment of muscle fatigue during driving game using electromyography. In: *Proceedings of 7th IEEE International Conference on System Engineering Technology ICSET 2017*, pp. 101–105. IEEE, Malaysia (2017)
5. Meiss, R.: Skeletal muscle and smooth muscle. In: *Structure*, pp. 152–176

6. Hostens, I., Ramon, H.: Assessment of muscle fatigue in low level monotonous task performance during car driving. *J. Electromyogr. Kinesiol.* **15**(3), 266–274 (2005)
7. Sahayadhas, A., Sundaraj, K., Murugappan, M.: Detecting driver drowsiness based on sensors: a review. *Sensors* **12**(12), 16937–16953 (2012)
8. Akin, M., Kurt, M.B., Sezgin, N., Bayram, M.: Estimating vigilance level by using EEG and EMG signals. *Neural Comput. Appl.* **17**(3), 227–236 (2008)
9. Sahayadhas, A., Sundaraj, K., Murugappan, M.: Drowsiness detection during different times of day using multiple features. *Australas. Phys. Eng. Sci. Med.* **36**(2), 243–250 (2013)
10. Abd Rahman, N.S.: Assessing muscle fatigue during driving game using EMG Signal. Bachelor Degree Thesis, Universiti Malaysia Pahang (UMP) (2016)
11. Mohd Azli, M.A.S.: Electromyograph (EMG) signal analysis to predict muscle fatigue. Bachelor Degree Thesis, Universiti Malaysia Pahang (UMP) (2017)
12. Phinyomark, A., Phukpattaranont, P., Limsakul, C.: Feature reduction and selection for EMG signal classification. *Expert Syst. Appl.* **39**(8), 7420–7431 (2012)
13. Kumar, A., Arya, N.: A study relation between energy spectral density and probability density function with impulse response first order control system. In: *International Conference on Electronics, Communication and Aerospace Technology*, pp. 152–154. IEEE, India (2017)

Modelling Automatic IoT Home Light System (SmartLi) by NODEMCU ESP8266



Muhammad Muttaqin A. Rahim, Nor Shazwanie Ramli,
Najwa Raihana Abdul Wahab and Rohana Abdul Karim

Abstract Most people always forgot to switch off the light when they go for a holiday and leave the light on as long as they are away. This could lead to the waste of electricity. If the lights are turned off, dark surroundings will make the house prone to burglary. Technology in network and communication system allows us to remotely control the lightings either off or on in order to pretend the house is occupied. The aim of this project is to develop an automatic home lighting system that can be controlled remotely using internet of things (IoT) technology. Mobile application (SmartLi) for home lightings was developed and integrated with intensity and motion sensor. The porch lamp will light up when it's dark and will also become brighter whenever any motion is detected nearby.

Keywords Arduino Uno · Automatic light · Home · IoT · NodeMcu ESP8266
Porch

1 Introduction

People always try to prevent their house from being targeted by burglars when they are away from home. One of the popular approaches is to switch ON the porch and home lightings for the whole holiday duration. However, it will lead to wastage of electrical energy, especially power on the lamp during the day. Since most of the energy use in residential buildings comes from lighting, its automation is one of the alternatives in reducing the electrical usage [1, 2].

Besides, it is also useful for the purpose of home security due to the ability to mimic the owner's presence, although the house is empty. Controlling the lighting system can therefore eliminate the risk of the house being targeted by burglars.

M. M. A. Rahim · N. S. Ramli · N. R. Abdul Wahab · R. Abdul Karim (✉)
Faculty of Electrical & Electronics Engineering, Universiti Malaysia Pahang, 26600 Pekan,
Pahang, Malaysia
e-mail: rohanaak@ump.edu.my

© Springer Nature Singapore Pte Ltd. 2019
Z. Md Zain et al. (eds.), *Proceedings of the 10th National Technical Seminar
on Underwater System Technology 2018*, Lecture Notes in Electrical Engineering 538,
https://doi.org/10.1007/978-981-13-3708-6_38

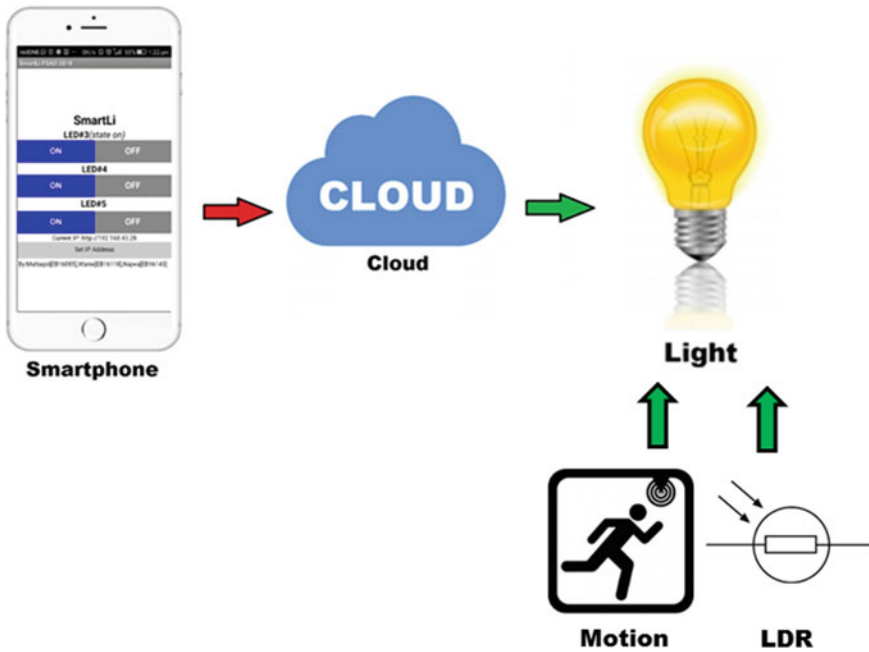


Fig. 1 Overview of the proposed system

There are two common approaches for automatic control of lighting system; (1) sensor and (2) intelligence based [3, 4]. Sensor based was widely used for control lighting system compared to the intelligence based. It is because, sensor based is easy to install and low cost. Meanwhile, intelligence based requires extra devices such as memory and Central Processing Unit (CPU) for processing the data. Due to that, the installation process becomes complicated.

Today, the advancement of technology in network and communication system allow user to control the lighting system from a long distance using IoT. The IoT will be more helpful when the owner goes out either for holiday or others. It also can help save the electricity. Integration of IoT and sensor based application such as motion sensor will help in saving energy since it will trigger the lighting system to take some necessary action. For example, the light becomes dim or turned off when there is no motion detected within the time limit. In addition, the variation of light intensity will provide an extra illusion for the existence of the owner.

Therefore, the aim of this paper is to introduce an application called “SmartLi” which is able to control the lights via smartphone and sensor based application. The system involves real time processing and detection of movement against the surrounding light intensity, and a signal from the smartphone. This motion-triggered light can be installed outside the house, preferably at the entryway. IoT system has also been implemented into the lighting system in the house, by connecting it through Wi-Fi network. Figures 1 and 2 show an overview of the proposed system.

Fig. 2 Overview of the model



2 Related Works

IoT is an interrelated computing device where digital objects are connected via network without human to computer interaction. It is a new trend for digital evolution, especially for Industry 4.0. Therefore, numerous studies have explored the implementation of IoT.

Research [5] explored the application of IoT for autonomous vehicles. The aim of the study was to track the state trajectory of nonlinear systems by remotely controlling the vehicles. Researcher also takes into consideration the suitable communication link system such as encoder and decoder for enhancing the efficiency of IoT.

Besides that, the usefulness of IoT has been discovered for businesses. Research from [6] used IoT for customer feedback data collection. The data were processed in order to find out the customer's demand. As a result, demand forecasting has improved the serviceability, increased the revenue and reduced the operation cost.

Another field that is significant for IoT application is agriculture. Research [7] attached four types of sensors for data collection. They were; (1) air temperature, (2) humidity, (3) leaf wetness and (4) soil moisture reading. Each sensor updates their reading value over time for the purpose of monitoring. Further actions from other devices are required if the reading value is less or greater than standard value. For example, if the soil moisture level less than the standard reading, the irrigation system will turn on the water pump to the field.

Previous researches have demonstrated that the controlled lighting system is a part of home automation. The work by Wang et al. [8] has demonstrated the success of IoT to turn on and off lights. Wireless sensor and actuator network (WSAN) has been used as a connecting module. However, the function to control lights was very limited to switch the light on or off.

Besides, the feasibility of the web application as a front end platform has been explored for controlling lights and home appliances [9]. In this work, motion sensor was used to automatically turn on lights whenever a motion is detected. However,

this study did not consider the light intensity for turning on or off the light as well as whether it is daytime or night.

A Similar approach was adopted by Asadullah et al. [10]. They used smartphone with Bluetooth as the connecting module to remotely control home automation system and plant irrigation. The dual system was integrated with Android Uno to control 18 home appliances and two sensors namely (1) ultrasonic and (2) soil moisture for water level detection and automatic plant irrigation respectively. However, the aim of this project was to provide control within short distance signal coverage. At the same time, using Bluetooth is advantageous since it consumes low energy [11].

From the literature reviews that have been conducted, it is proven that IoT is a very important system to enhance the efficiency of daily life activities. Despite the success of previous works, there are still opportunities for further enhancements to control lighting system, such as considering the light intensity towards the Green World goal.

3 Proposed Modelling

3.1 System Design

Block diagrams of the proposed system are illustrated in Figs. 3 and 4. This project consists of three main parts which is inputs, processor and output as shown in Fig. 3. The Light dependent resistor (LDR) and PIR motion sensor are the inputs and the LED 1 and LED 2 are the outputs. PIR motion sensors function as the motion detector to control the lamp brightness. The LDR works as the indicator to switch on/off the porch light (LED 1). It senses the light intensity from surroundings and decides whether it is day or night. In addition, it automatically turns on when the surrounding is dark and turns off when it receives light from surroundings. Arduino Uno is a processor that receives an input signal, processing the signal into meaningful information and delivers the output for smart light actions. While in Fig. 4, it shows that the application called SmartLi can directly control the NodeMcu ESP8266 remotely with the internet connection to give output readings for LED 3, LED 4 and LED 5. In this project, mobile hotspot is used as wireless internet connection. This system is developed in order to make it easier for users to remotely turn the lights on or off.

Fig. 3 Block diagram for Arduino system

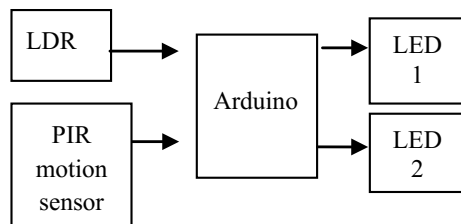
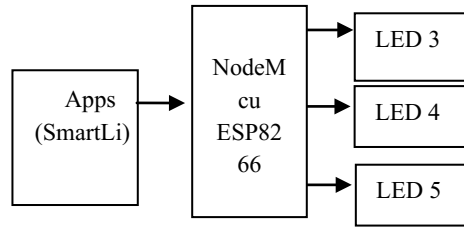


Fig. 4 Block diagram of the NodeMcu ESP8266 system



In Fig. 5 Arduino is powering on checking the photo resistor, if the measured value of the photo resistor (LDR) shows the value within the dark level, it will turn on the LED 1 at the porch. Next condition is checking the existence of movements by PIR motion sensor. In order to activate the PIR motion sensor, the LDR must be switched on first, then, the LED 2 will turn on. It indicates that LED 2 will only work when LDR is in the dark condition. To avoid waste of energy, the status of movement is repeatedly checked after LED 2 turn on for 5 s. If any motion is detected, LED 2 will continue to stay alight. Otherwise, it will turn off. The sensitivity of the motion sensor and the activation time is changeable, so as the motion module with dedicated potentiometer. While the flowchart in Fig. 6. shows that LED 3, LED 4 and LED 5 will only turn on when their buttons were pushed.

3.2 Hardware

The system basically consists of five components. They are: Arduino Uno, PIR motion sensor, Light dependent resistor (LDR), LED lights, NodeMcu ESP8266. The overview of the proposed model was shown in Fig. 2. The detailed function of each component is explained as follows:

Components used in this project are:

(1) **Arduino Uno**

- Acts as a microcontroller. It is used to perform various functions and operations throughout the system.

(2) **PIR motion sensor**

- Acts as a sensor. It is used to detect a movement.

(3) **Light dependent resistor (LDR)**

- Acts as a sensor. It is used to detect the surrounding intensity.

(4) **LED lights**

- Acts as an output device. It will produce light upon receiving voltage.

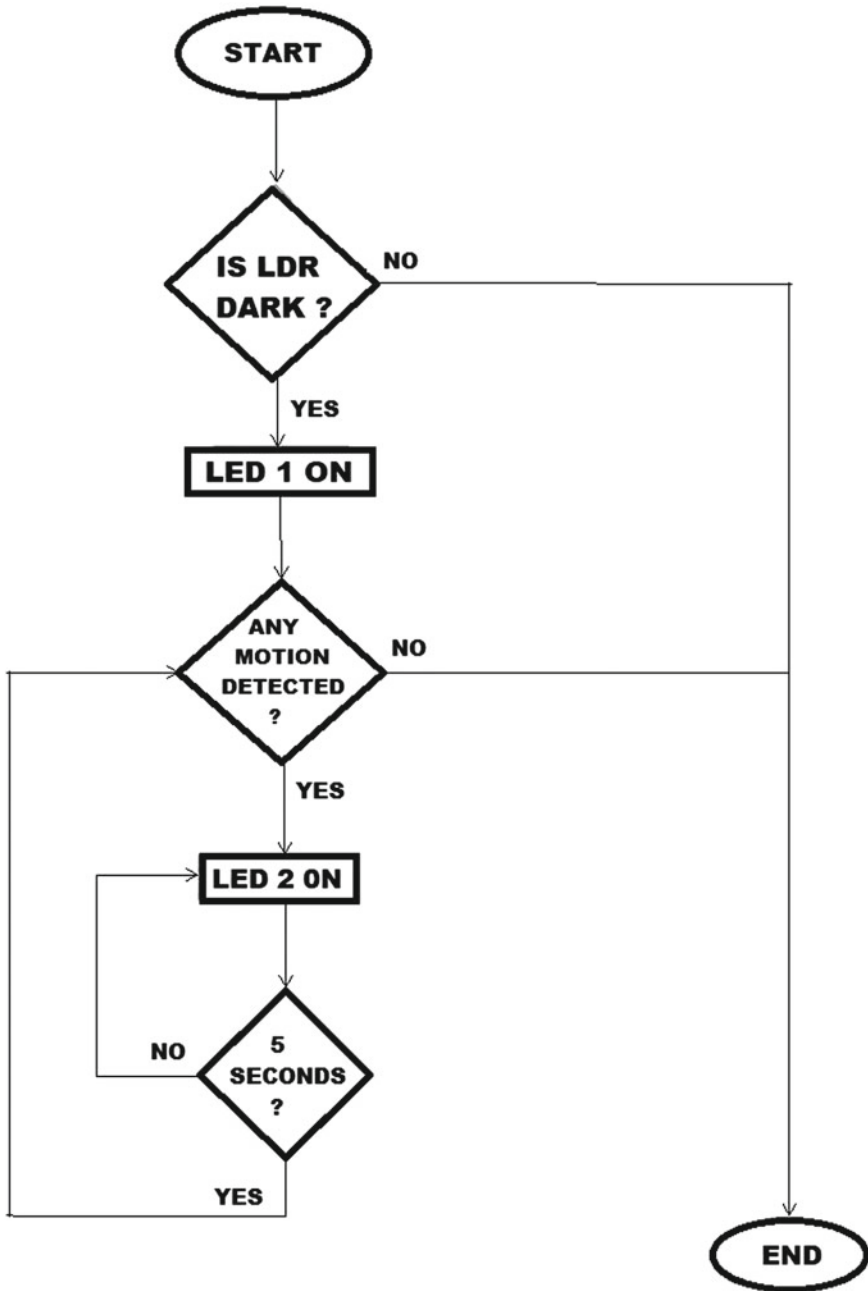


Fig. 5 Flowchart for Arduino system

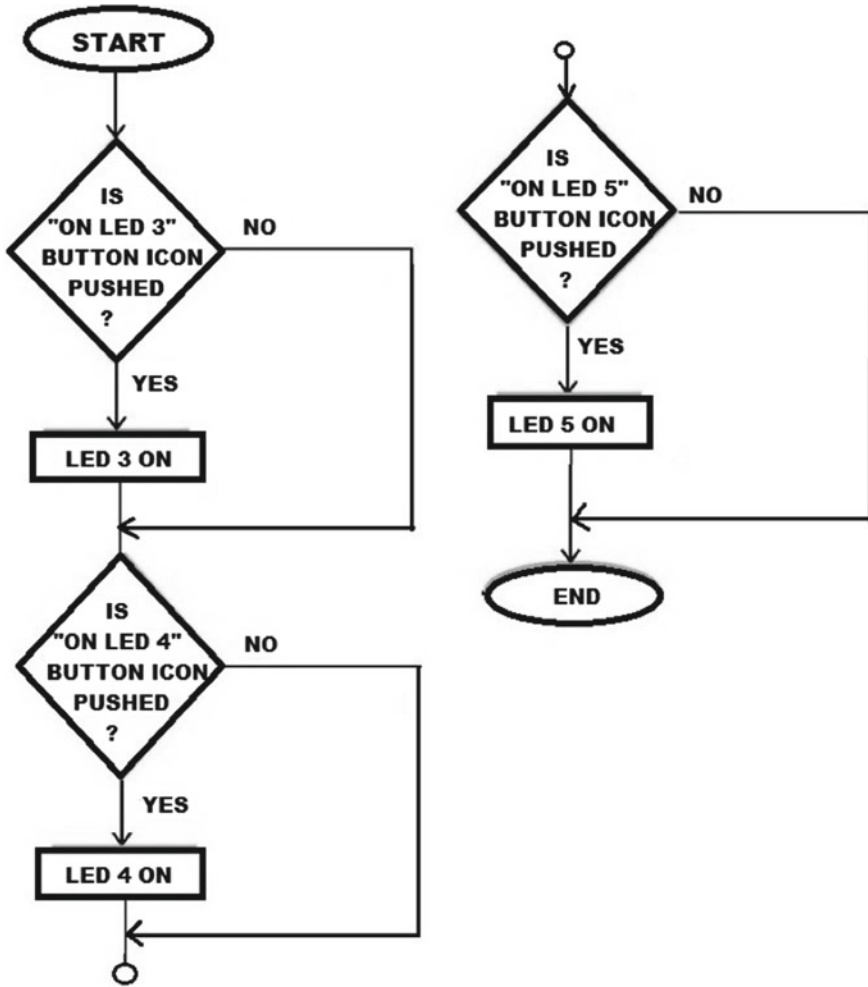


Fig. 6 Flowchart for IoT system

(5) NodeMcu ESP8266

- Acts as a microcontroller. It is used to perform various functions and operations throughout the system via Wi-Fi connection. NodeMcu ESP8266 was chosen because it consumes small power to switch on, able to connect with USB-Serial. Besides, it is very breadboard-friendly and its application is suitable for development beginner which does not require the Arduino Uno module.

Table 1 Limit of parameter

Sensor/Signal	Maximum value
Motion sensor	14 cm
LDR	100 lx
Wi-Fi	20 m

4 Results and Discussion

4.1 Final Output Results

Figure 7 shows the porch light (LED 1) will only turn on when the light intensity is very low. Therefore, the illusion of an occupied home at night is in place. Meanwhile, Fig. 8 demonstrates the motion light (LED 2) only will turn on when the sensor detect a movement. The intention is to pretend that the owner realized the existence of a burglar. Lastly, the room lights (LED 3, LED 4, LED 5) can be monitored and controlled remotely using a smartphone or computer with SmartLi app or any internet browser via an internet connection (Fig. 9).

4.2 Limit of Parameter

The limit parameter shown in Table 1 is the measurement of the default setting for the project. However, it can be changed or set to a higher or lower value. It also depends on the setting of each component involved.

**Fig. 7** Changes of the intensity

Fig. 8 Movement detection



Table 2 Signal strength for various distances

Distance (m)	Output (LED 3, 4, 5 ON)
5	ON
10	ON
15	ON
20	OFF

4.3 Mobile Hotspot Signal Strength

IoT Wi-Fi mobile hotspot connection is tested by varying the distance between the home model and the smartphone to verify the suitability Wi-Fi distance for our model. The type of propagation was a direct line of sight. Experiments showed that the output of LED 2, LED 3 and LED 4 have worked properly by turning on the selected LED in the range between 1 and 15 m. However, Wi-Fi signal was lost at 20 m from the home model without any obstacles. It was due to the existence of wireless interference from other users and the mobile data was not strong enough to reach the maximum distance as shown in Table 2.

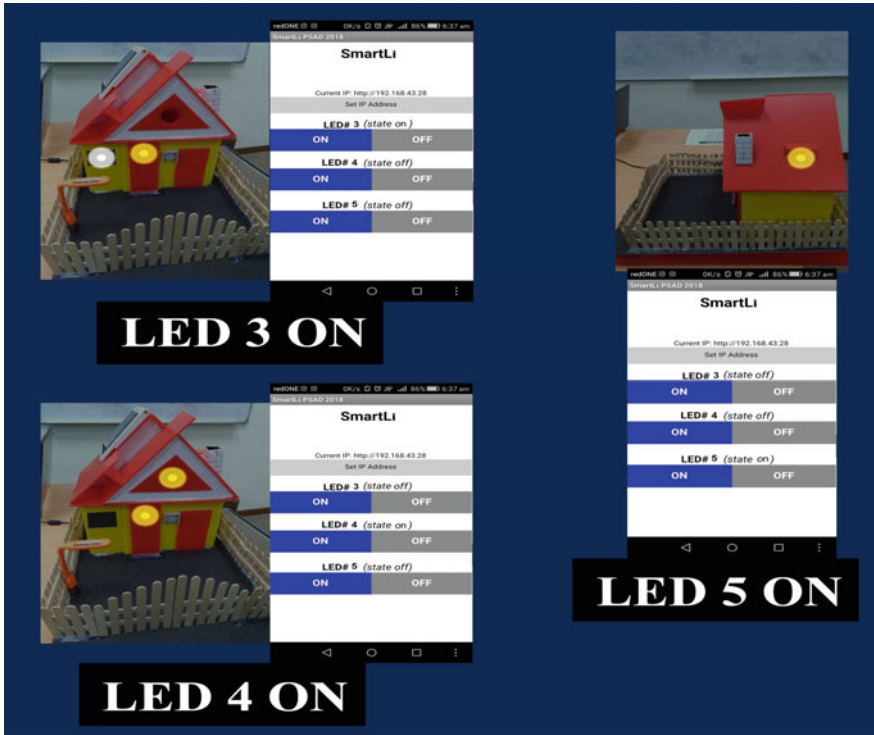


Fig. 9 Output for “SmartLi” application

4.4 Discussion

When LDR was in bright condition, no LED was activated. But when LDR was in dark condition, LED 1 will light up. Next, if motion is detected, LED 2 will also light up on conditions that the LDR was in the dark too. Besides that, the mobile application created was used to turn on/off the LED 3, LED 4 and LED 5.

The system used the dim color of LED 1 to light in a small amount of current to save energy. Whilst the brightest LED used was LED 2 because it serves to give a clear vision for porch area. For example, when someone either goes in or out of the house through the porch, the LED light helps to improve their sight at night. At the same time it also gives an alert to the homeowner of any possible break-in.

IoT connection is not established from 20 m to upwards due to the loss of signal. However, the strength of the signal can be established using Wi-Fi network and external signal boosters.

5 Conclusion

The IoT automatic solar light system (SmartLi) has been successfully built as we proposed. The LDR, Motion sensor and IoT system are able to work properly and we managed to analyze the surrounding intensity, movement, the signal from smartphone and embedded the information into the Arduino Uno and NodeMcu ESP8266 board. Besides that, we were also able to produce the output of the system in showing the Yellow/White LED as a signal when it detect dark surroundings, movement or receives information from smartphone and display the IoT light status to the user. In addition, we have also successfully implemented Internet of Things (IoT) by developing a lighting system controlled by smartphone and also built an apps for the system.

Acknowledgements We would like to acknowledge funding provided by Universiti Malaysia Pahang (RDU1703233).

References

1. Selvaraj, K., Chakrapani, A.: Smart office automation system for energy saving. *Int. J. Adv. Comput. Electron. Eng.* **2**(9), 8–12 (2017)
2. Raimondi, F.M., et al.: Energy savings for indoor lighting in a shopping mall: a case of study. In: 2018 Thirteenth International Conference on Ecological Vehicles and Renewable Energies (EVER). IEEE, Monaco (2018)
3. Tran, D., Yen, K.T.: Sensorless illumination control of a networked LED-lighting system using feedforward neural network. In: *IEEE Transactions on Industrial Electronics*, pp. 2113–2121. IEEE (2014)
4. Liao, H., Xihua, S., Dongsheng, Y.: Design of adaptive lighting system based on fuzzy PID. In: 2018 Chinese Control and Decision Conference (CCDC), pp. 1543–1547. IEEE, China (2018)
5. Parsa, A., Alireza, F.: Measurement and control of nonlinear dynamic systems over the internet (IoT): applications in remote control of autonomous vehicles. *Automatica* **95**, 93–103 (2018)
6. Yerpude, S., Tarun, K.S.: Impact of internet of things (IoT) data on demand forecasting. *Ind. J. Sci. Technol.* **10**(15), 1–5 (2017)
7. Davcev, D., et al.: IoT agriculture system based on LoRaWAN. In: 2018 14th IEEE International Workshop on Factory Communication Systems (WFCS). IEEE, Italy (2018)
8. Wang, M., et al.: An IoT-based appliance control system for smart homes. In: *International Conference on Intelligent Control and Information Processing (ICICIP)*, pp. 744–747. IEEE, China (2013)
9. Baby, C.J., et al.: Home automation using web application and speech recognition. In: *International conference on Microelectronic Devices, Circuits and Systems (ICMDCS)*. IEEE, India (2017)
10. Asadullah, M., Khalil, U.: Smart home automation system using Bluetooth technology. In: *International Conference on Innovations in Electrical Engineering and Computational Technologies (ICIEECT)*. IEEE, Pakistan (2017)
11. Terán, M., et al.: IoT-based system for indoor location using bluetooth low energy. In: 2017 IEEE Colombian Conference on Communications and Computing (COLCOM). IEEE, Colombia (2017)

Development of Automated Gate Using Automatic License Plate Recognition System



Luai Taha Ahmed Al-Mahbashi, Nurhafizah Abu Talip Yusof,
Syamimi Shaharum, Mohamad Shaiful Abdul Karim
and Ahmad Afif Mohd Faudzi

Abstract This paper presents a prototype of automated gate powered by automatic license plate recognition system. The prototype is an embedded system running a Raspbian operating system on the Raspberry Pi microcontroller. A USB camera, LCD, and a servo motor are attached to capture an image of a vehicle, to display information and to represent an automated gate respectively. OpenALPR library is used to perform the license plate recognition, while the complete automated gate system, which is used performing image capturing, license plate recognition, and authentication to gate operation is built using the Node-RED software. As a result, the system successfully recognizes the vehicle number plate and categorize them. All information about the vehicle are displayed on the LCD, and if the vehicle is authorized, the gate operated accordingly. The analysis results show that the system is able to achieve a recognition rate of 87.50–90.90% on images with a specified height and angle.

Keywords Image processing · OpenALPR · License plate recognition system
Automated gate system

1 Introduction

In the 2017 crime index by Numbeo, numbers have shown that Malaysia is ranked as top 5th in the world [1]. Crime rates, such as break-ins and thefts, have raised to a level where people in the street are afraid for their safety and well-being. Therefore, the market is now demanding for properties within a gated-and-guarded community [2].

L. T. A. Al-Mahbashi · N. Abu Talip Yusof · S. Shaharum · M. S. Abdul Karim
A. A. Mohd Faudzi (✉)
Faculty of Electrical and Electronics Engineering, Universiti Malaysia Pahang,
26600 Pekan, Pahang, Malaysia
e-mail: afif@ump.edu.my

© Springer Nature Singapore Pte Ltd. 2019
Z. Md Zain et al. (eds.), *Proceedings of the 10th National Technical Seminar
on Underwater System Technology 2018*, Lecture Notes in Electrical Engineering 538,
https://doi.org/10.1007/978-981-13-3708-6_39

Some gated communities are still using stickers to differentiate between residents and guest. However, this monitoring method is inadequate as the stickers can be easily tempered, duplicated, or even misused. The security guard might stop the guest and inquire where they are going. Some may or may not be required to register at the guard house and perhaps leave behind driver's license or some other form of identification. However, in some cases, the guest just needs to drive up to the gate and wave at the guard. The guard then waves back and promptly proceeds to open the gate, allowing the guest easy access to the housing area.

Due to these issues, the authors develop a prototype of the automated gate using Automatic License Plate Recognition (ALPR) system to monitor the authorized and unauthorized vehicles. Many researchers have been focusing on improving license plate recognition [3, 4]. Vahab and Wong proposed Skew Detection and Correction stage using Pearson Correlation to maintain the accuracy of the car plate at the high level [3]. Norizam et al. proposed the combination of image processing and OCR [4]. However, in this project, the authors focus on building a complete standalone system using the well-known OpenALPR library [5].

The prototype of this system is developed using a microcontroller called Raspberry Pi attached with a Logitech webcam, 5-inch touch LCD screen, and a servo motor. The software development is done using Node-RED software and open source library called OpenALPR [6]. Furthermore, this project is expected to enhance the efficiency and improve the security of any potential client; i.e., gated community, factory, and university.

The organization of this paper is described as follows: the introduction of OpenALPR and Node-RED are presented in Sect. 2. Section 3 clarifies the prototype development. The performance of the prototype is discussed in Sect. 4. Finally, Sect. 5 provides a conclusion and future works.

2 OpenALPR and Node-RED

2.1 OpenALPR

In this project, the authors use OpenALPR, an open source Automatic License Plate Recognition library. It is capable of analyses video streams and images to identify license plates. The execution of OpenALPR will output the text representation of any license plate. Currently, OpenALPR supports many countries including Indonesia. Even though Malaysia is not listed as countries supported by OpenALPR, by using training data for a country that has plates that are similar to the one in Malaysia, high accuracy rate is expected.

OpenALPR operates as a pipeline with seven different stages. Each stage plays an important role as described in Table 1, performing various processing from receiving an image as the input until it generates the possible plate numbers. Further detail can be accessed at [5].

Table 1 The pipeline stages [5]

Pipeline phase	Description
Detection	Finds potential license plate region
Binarization	Converts plate image into black and white
Char analysis	Finds character-sized “blobs” in the plate region
Plate edges	Finds the edges of the plate
Deskew	Transforms the perspective to a straight-on view based on the ideal license plate size
Character segmentation	Isolates and cleans up the characters so that they can be processed individually
OCR	Analyses each character image and provides multiple possible letters/confidences
Post processing	Creates a top n list of plate possibilities based on OCR confidences. Also performs a Regex match against region templates if requested

2.2 Node-RED

In this project, the software development is done using Node-RED [6]. Node-RED is a flow-based programming tool that has a network of nodes. Each node can be designed to receive some data, process the data, and pass on that data. The flow of the data between the nodes is controlled by the network.

Figure 1 shows the Node-RED flow editor that can be accessed using a web browser. Via the browser, the user can create an application by dragging nodes from

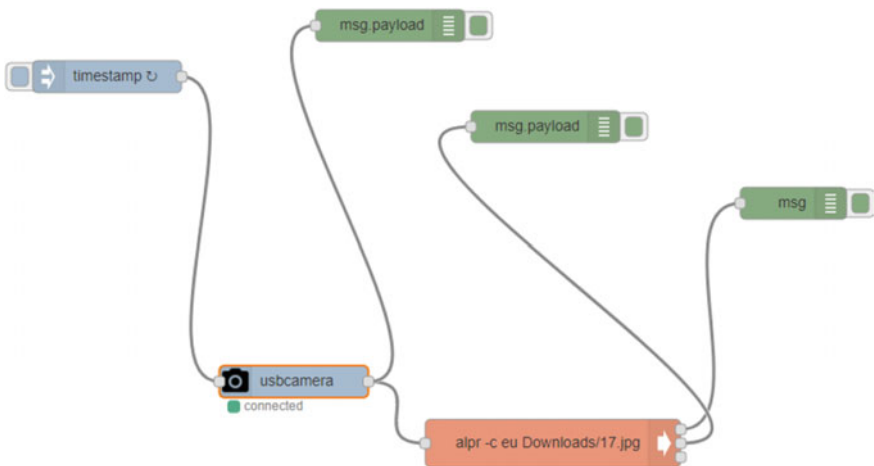


Fig. 1 A simple program build using Node-RED that was designed to capture an image using USB camera and then pass the image data to another node where the license number will be recognized

the provided palette into a workspace and start to wire them together. The Inject node, which is the blue node, can be used to manually trigger a flow by clicking the node's button within the editor. It can also be used to automatically trigger flows at regular intervals. Debug node, which is the green palette, can be used to display messages in the Debug sidebar within the editor. The webcam node is to take a photo in a given format directly from a USB camera on Raspberry Pi. The image of the photo is stored into the file-system, and `msg.payload` will provide you with the path and the filename including an extension to the photo or a Buffer object.

3 Prototype Development

The prototype of the automated gate is an embedded system. Raspberry Pi is used as the microcontroller attached to the Logitech C270 h USB camera for grabbing the images, the USB web camera has 3.0 megapixels, and it can take a clear image of the license plates of the cars. The image taken will be saved in a file inside the controller in JPEG format or any other format. An LCD is used to present information and a motor as an actuator to represent the gate barrier.

The Servo motor is employed as an output of the system. Its pin is connected to GPIO24 of the Raspberry Pi. Since the servo motor HB3001 plastic gear can be powered up using a 5 V voltage source, an additional voltage supply is not required.

At first, the system will capture an image continuously until a license plate is detected. The camera will send the captured image to the processing node. The image will be processed through the OpenALPR library in this node. The image will go through the image processing steps, which the image will be Binarized and follow the other steps of OpenALPR library processing to detect the license plate. If a license plate is recognized, the result will be generated and send the result to the database checking node. Here, the system will compare the result to the database that was prepared beforehand. After that, the system will display the information on the LCD and move the gate accordingly. The system will warn the security if the license plate is not recognized. The complete flow chart of the system is shown in Fig. 2.

3.1 Database

The database for this system has been developed using the Node-Red software. A node called 'switch' is used to store the related information; e.g., the name of the car owner, identification card number, and the number plate of the car.

Since the OpenALPR will generate a list of the possible recognition results, only license plate with the highest confidence level will be compared and authenticated. If the number plate is registered in the switch node, the system will display the related information on the display. There will be a LED indicator to show whether the authentication is passed or not. Green LED for the authorized number plate, and red LED for the unauthorized plate number.

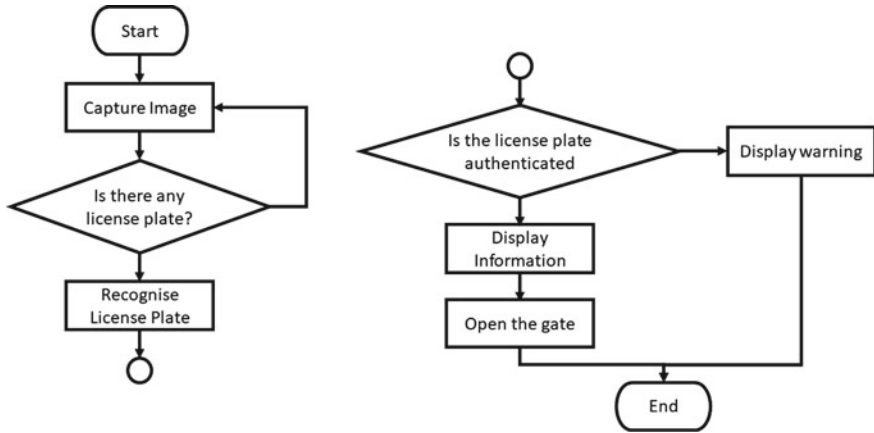


Fig. 2 Flow chart of the system

3.2 Graphical User Interface

Figure 3 shows the GUI for the automated gate prototype. The GUI is also developed using Node-RED application that is used in software development. There are four push buttons, which are ‘Start’, ‘Read No. Plate’, ‘Open the gate’ and Close the gate’.

‘Start’ button will reset and restart the system while ‘Read No. Plate’ button will capture and recognize the number plate on demand. The other two buttons are for the user to manually operate the gate. There are also indicators, such as LED for

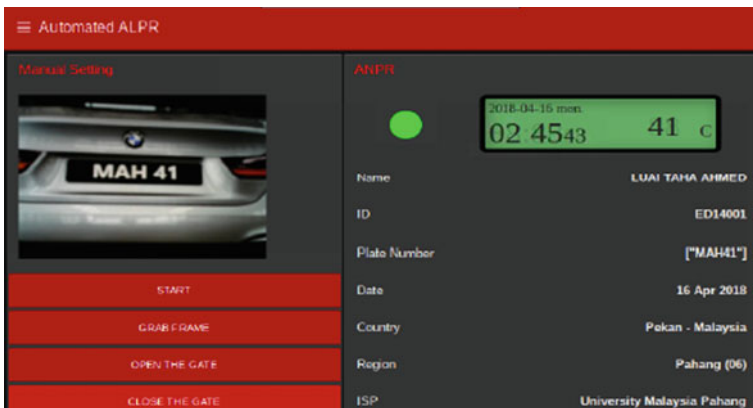


Fig. 3 GUI of automated gate build using Node-RED software

authorized and unauthorized vehicle notification, as well as the vehicle registered name and recognized number plate. When the system detected an unauthorized vehicle, the LED will turn red.

4 Result and Analysis

4.1 License Plate Recognition Result

The testing image data are collected manually using the USB camera and also collected from the web. The resolution of images is not fixed. When the webcam is grabbing images, the recognized number plate will show with different confidence level as shown in Fig. 4. The highest confidence level will be chosen and send to the database for comparison. The confidence level is based on a given list of all possible OCR characters and confidences, it is a function called post-processing which will determine the best possible plate letter combinations. It is organized as a top of the list after detecting the license plate.

As analyzed, the recognition rate achieved 87.50% correct recognition. Out of 80 testing samples, 70 license plates were successfully recognized. The analysis calibration result in cases where the camera is capturing from a fixed position, and all plates generally are seen at the same angle which is straight to point. This feature is best for short-angle cameras or cameras capturing at a close distance. There was false recognition due to some reason such as different size of the plate, character shape, distance and camera angle.

Another analysis has been conducted, the camera was set up with different height and angle which this analysis has been done to show how is the accuracy of recognizing the license plates when the height and angle will be changed. Based on the analysis, the height tested in two levels, which are 1.5 m and 2.0 m from the ground, angle analyzed based on straight and skewed coordination setup. As shown

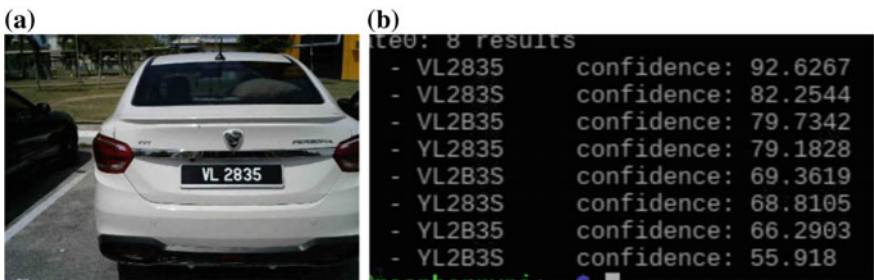


Fig. 4 a Image with license plate b The recognition result

Table 2 The comparison results for camera coordination in term of camera height and angle

Height from the ground (m)	Angle	No. of sample	No. of correct result	Success rate
1.5	Straight	11	10	90.90
1.5	Skewed	11	8	72.72
2.0	Straight	11	9	81.81
2.0	Skewed	11	9	81.81

in Table 2 the best recognition for setting up the camera to get the best result is when the height is 1.5 m and the angle is straight. The recognition rate achieved 90.90% correct recognition in this position.

5 Conclusion

This paper presents methods and developments to implement automated number plate recognition (ANPR) system. The automated number plate region detection algorithm works based on OpenALPR Library using the Raspberry Pi controller. Character recognition task is accomplished by Analyze each character image and provides multiple possible letters/confidences. The proposed method able to achieve a detection rate of 87.50% and recognition rate of 90.90% on images with specified height & angle, respectively. The system will automatically recognize the vehicle number plate and categorize them. All information about the vehicle will be displayed on LCD and if the vehicle authorized, the gate will be automatically open. The advantage of the proposed system is that it consumes considerably low computational time and it is feasible to be implemented in real time. Apart from this, we plan to utilize infrared camera in the near future to enhance our current system capability of operating in the different type of lightings such as daytime and night. Furthermore, this system is expected to integrate with the client database system to monitor the vehicle inside the determined area.

Acknowledgements The authors would like to thank Universiti Malaysia Pahang (UMP) for providing the facilities and fund to complete this project. This work is supported by UMP Internal Grant of RDU1703140.

References

1. Numbeo Homepage. <https://www.numbeo.com/crime/rankings.jsp?title=2017>. Last accessed 20 July 2018
2. Hanif, N.R., et al.: Gated and guarded communities in Malaysia: The new roles of the state and civil society. Planning Law and Property Rights (PLPR) Conference, UK (2012)

3. Keong, W.W., Iranmanesh, V.: Malaysian automatic number plate recognition system using Pearson correlation. In: 2016 IEEE Symposium on Computer Applications & Industrial Electronics (ISCAIE), pp. 40–45. Batu Feringghi, Malaysia (2016)
4. Sulaiman, N., et al.: Development of automatic vehicle plate detection system. 2013 IEEE 3rd International Conference on System Engineering and Technology (ICSET), pp. 130–135. Shah Alam, Malaysia (2013)
5. OpenALPR Homepage. <https://github.com/openalpr/openalpr>. Last accessed 20 July 2018
6. Node-RED Homepage. <https://nodered.org/>. Last accessed 20 July 2018

Design of T-Shaped UWB Antenna with Dual Band Rejection Using Inverted U- and C-Shaped Slots



Salwa Awang Akbar, Ahmad Syahiman Mohd Shah,
Ahmad Afif Mohd Faudzi, Sabira Khatun, Syamimi Mardiah Shaharum,
Nurhafizah Abu Talip @ Yusof and Mohamad Shaiful Abdul Karim

Abstract An ultra-wideband antenna design is proposed in this paper based on simple and easy-fabricated rectangular patch antenna. The proposed antenna is inserted with two slots; inverted U- and C-shaped to minimize interference in WiMax and WLAN band. The antenna can afford a good range of operating frequency from 2.852 to 12.176 GHz, which covers ultra-wideband frequency range set by Federal Communication Commission and in the same time be able to avoid undesired band.

Keywords U slot · C slot · UWB · Dual band · Notch frequency

1 Introduction

Ultra-wideband (UWB) antenna has been widely used in the field of military, remote sensing and radar technology [1] in these past years. UWB has a large operating bandwidth, good data transmission ratio, high resolution localization and ability to propagate through high permittivity medium even solid materials. These are the main factors lead to development UWB antenna for underwater communication. However, in this paper the design of compact antenna is proposed based on the modification of simple rectangular patch antenna to be used in free space. Different to free space, underwater environment needs consideration of conductivity, permittivity, propagation, wavelength and intrinsic impedance of water.

According to the Federal Communication Commission (FCC) on 2002, the UWB antenna frequency are covering from 3.1 to 10.6 GHz [2]. Therefore, the proposed antenna should be able to operate in these such wide frequency and in the same time, it is necessary to eliminate IEEE 802.16 WiMax and IEEE 802.11a WLAN band

S. Awang Akbar · A. S. Mohd Shah · A. A. Mohd Faudzi · S. Khatun · S. M. Shaharum
N. Abu Talip @ Yusof · M. S. Abdul Karim (✉)
Faculty of Electrical and Electronics Engineering, Universiti Malaysia Pahang,
26600 Pekan, Pahang, Malaysia
e-mail: mshaiful@ump.edu.my

© Springer Nature Singapore Pte Ltd. 2019
Z. Md Zain et al. (eds.), *Proceedings of the 10th National Technical Seminar on Underwater System Technology 2018*, Lecture Notes in Electrical Engineering 538,
https://doi.org/10.1007/978-981-13-3708-6_40

which are allocated from 3.4 to 3.69 GHz and from 5.15 to 5.825 GHz, respectively [3]. Many researchers have proposed different shaped slots to obtain band notched frequency such as L-shaped [4], Pi-shaped [5], U-shaped [6] and C-shaped [7] slots.

In this paper, we propose a modified rectangular UWB patch antenna with a partial ground plane. Two different slots are designed to achieve Wimax and WLAN band notch characteristics. The optimization of the design is done by using electromagnetic simulation software which is based on Finite Element Method (FEM).

2 Antenna Design

2.1 Antenna Design Without Slot

The fundamental design is based on microstrip rectangular patch antenna. The dimension of the rectangular patch is 19 mm \times 25 mm. Rectangular patch antenna is simple and easy to design as shown in Fig. 1a, but it cannot afford wide frequency range as mismatching impedance occurred especially at the bottom corner which leads to the power loss. Hence, in this work we utilized the step design at the edge of the rectangular to reduce the edge effect as shown Fig. 1b. Figure 1c shows the ground plane that placed at the back of the patch where only partially grounded plane is used. The antenna is designed on FR4 substrate with permittivity of 4.4. The dimension of the antenna is 25 mm \times 29 mm \times 1.6 mm and, the dimension of step is $W_s = 4.65$ mm and $L_s = 5.80$ mm.

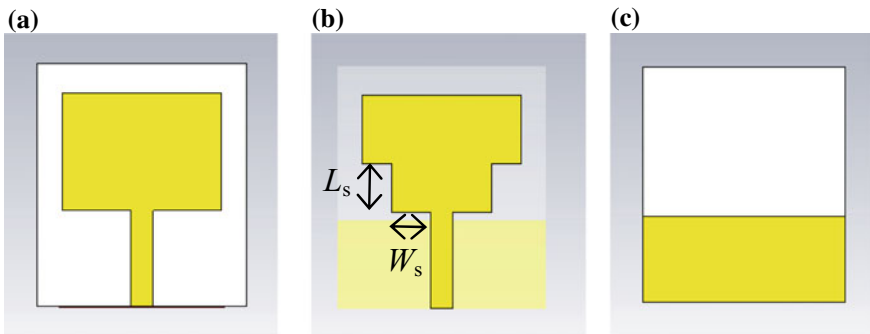


Fig. 1 Design of antenna without slot. **a** Rectangular patch antenna. **b** T-shaped patch antenna. **c** Partially ground plane

2.2 Antenna Design with Inverted U-Shaped Slot

An inverted U-shaped slot is introduced as shown in Fig. 2a to eliminate WiMax band from 3.4 to 3.69 GHz. The width and length of the slot are 0.6 and 27 mm, respectively. These dimensions are chosen mainly based on the level of difficulty during fabrication and the notched bandwidth, where the closest with WiMax band is preferable. The position of slot is very crucial as a small position error will cause the frequency shift. Therefore, in the next chapter the analysis of slot's position is presented. At first, the slot is positioned 1 mm from the top boundary between patch and substrate. Then, the distance is increased by 1 mm increment.

2.3 Antenna Design with C-Shaped Slot

While, C-shaped slot (Fig. 2b) is applied to the step design antenna in order to remove WLAN band that covers from 5.15 to 5.825 GHz. The width is fixed at 0.5 mm and length at 22 mm by considering the same aspects as explained before. Also, the position analysis of slot is conducted. The position is varied from the center of the patch until 2 mm lower than the center. The analysis starts from the center in order to avoid congestion or overlapping with the previous slot.

The analyses of inverted U- and C-shaped are conducted independently. Both slots are combined after we obtained the best dimensions and configurations, and the minor adjustment will be made.

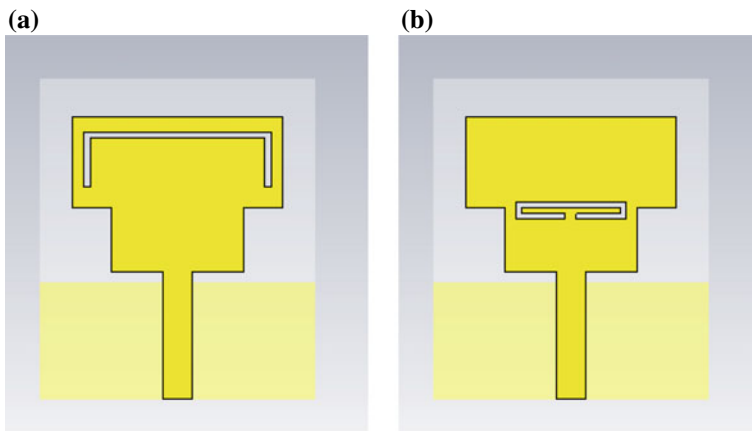


Fig. 2 An introduction of **a** inverted U-shaped slot, **b** C-shaped slot

3 Results and Discussion

3.1 Antenna Design Without Slot

Figure 3 shows the return loss of microstrip-fed T-shaped antenna. For comparison, the return loss of rectangular antenna is included. The blue region shows that the return loss is below than -10 dB and the power of antenna is radiated effectively. Because of the edge effect is reducing by introducing the step, the bandwidth is improved from only 1.668 GHz (frequency range: 3.440–5.108 GHz) to 9.372 GHz (frequency range: 3.068–12.440 GHz) which covers UWB range.

3.2 U-Shaped Slot Insertion

Figure 4 shows the comparison of return loss when the position of slot is varied. When the slot is placed near to the boundary between patch and substrate region (top), the notched frequency band is between 3.500 and 3.908 GHz, which is not removing the entire band of WiMax. For middle and bottom position, the notched band are 3.296–3.980 GHz and 2.720–4.064 GHz, respectively. Both positions are able to eliminate WiMax band but middle position is preferable since the notched band is narrower.

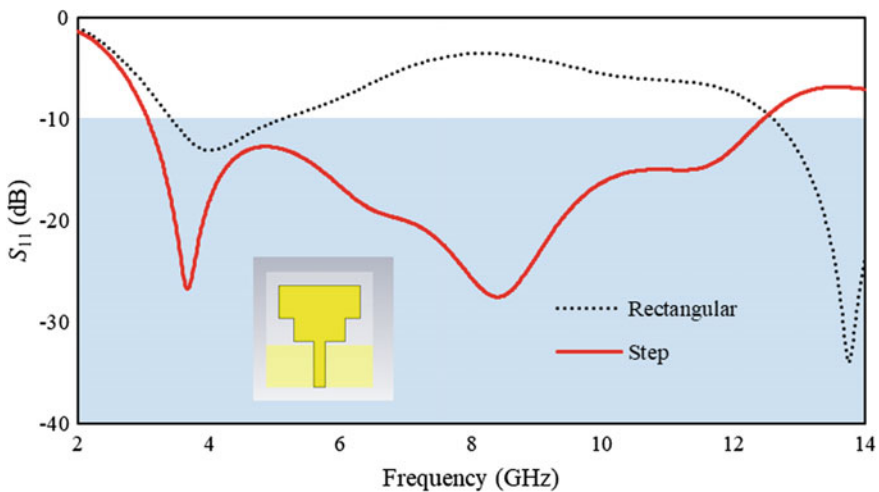


Fig. 3 Comparison of return loss for rectangular patch antenna and modified patch antenna

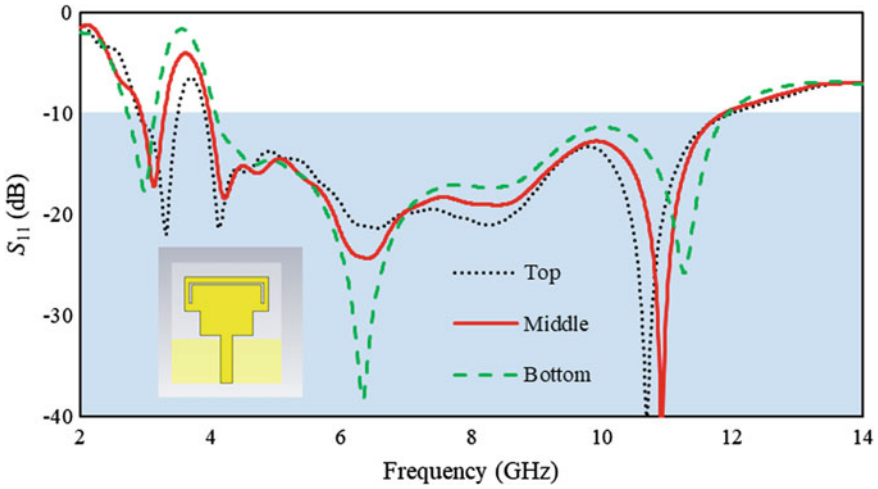


Fig. 4 Position analysis for inverted U-shaped slot

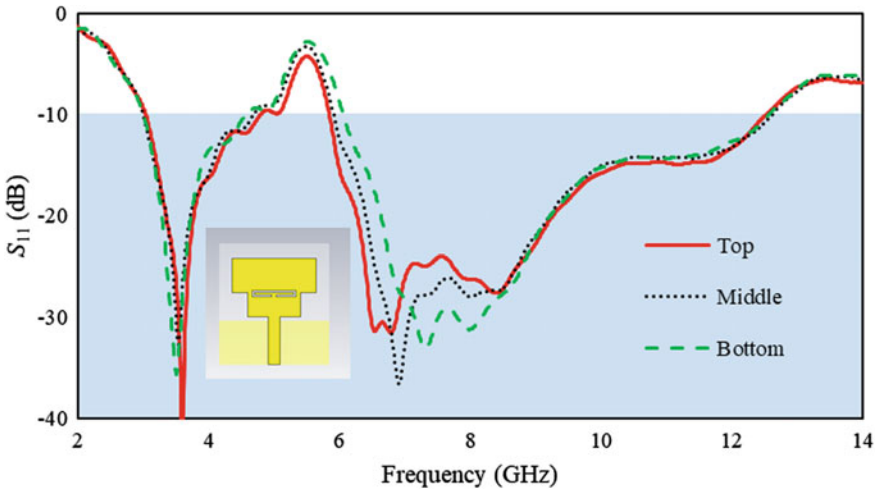


Fig. 5 Position analysis for C-shaped slot

3.3 C-Shaped Slot Insertion

Same as before, the analysis for the slot position is conducted for C-shaped slot and the result is shown in Fig. 5. The notch band is 4.808–5.840 GHz when the slot is inserted at the center of the patch (labeled as ‘Top’ in the graph). This position is preferable compared to lowered position where the notch band are 4.700–5.900 GHz and 4.580–6.056 GHz for middle and bottom position, respectively.

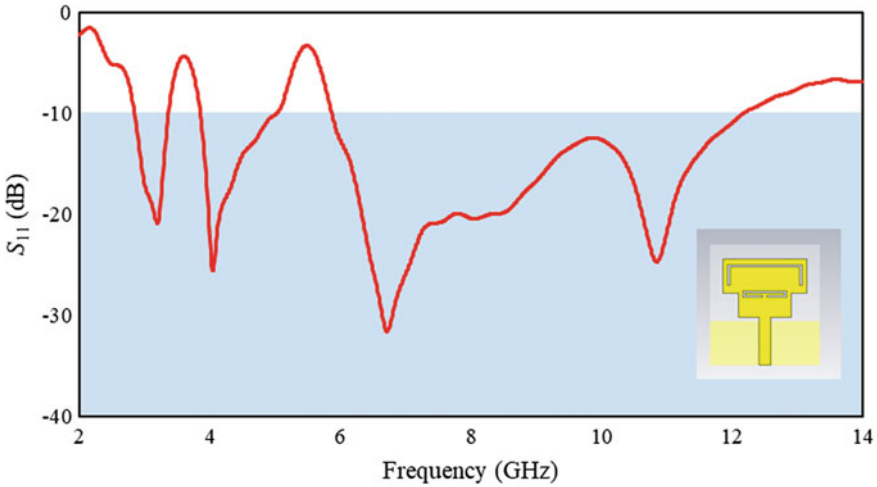


Fig. 6 Return loss of combined slots

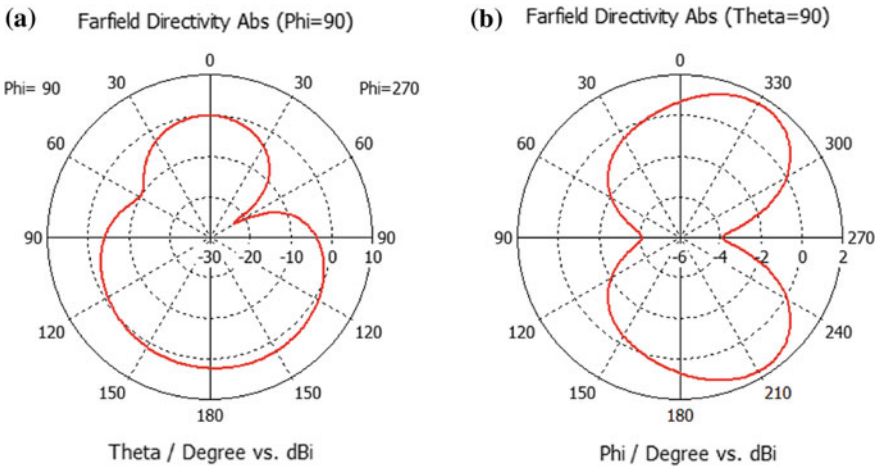


Fig. 7 Radiation pattern at 5.87 GHz in a E-plane and b H-plane

3.4 U- and C-Shaped Slot Insertion

The simulation return loss of combined slots is shown in Fig. 6. The notched frequency bands are 3.380–3.848 GHz and 5.036–5.864 GHz. In addition, the antenna can cover very wide frequency range which is between 2.852 GHz and 12.176 GHz (exceeds FCC regulations). We confirmed that the dual notch band, i.e., WiMax and WLAN can be achieved by the proposed design.

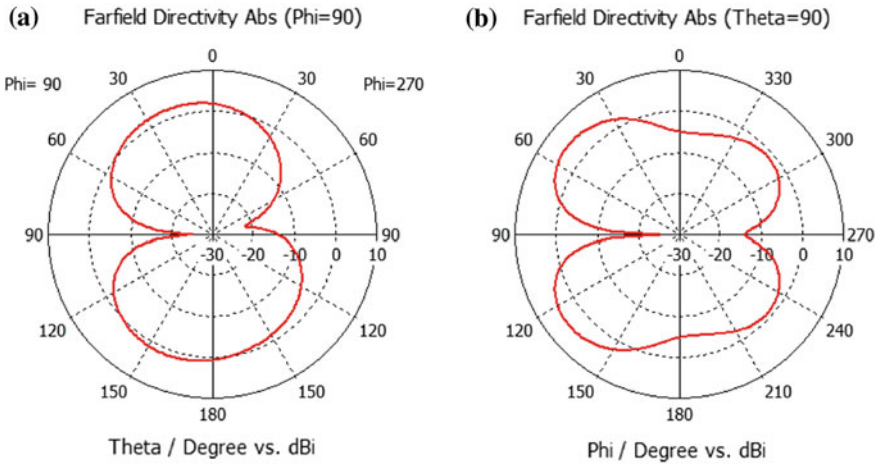


Fig. 8 Radiation pattern at 9.05 GHz in **a** E-plane and **b** H-plane

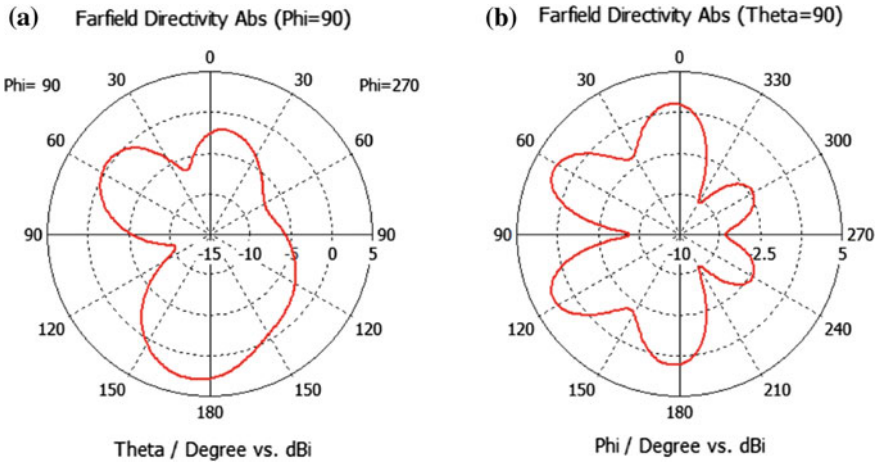


Fig. 9 Radiation pattern at 12.2 GHz in **a** E-plane and **b** H-plane

Radiation patterns for E- and H-plane at lower bound frequency 5.87 GHz, middle bound frequency 9.05 GHz and upper bound frequency 12.2 GHz are shown in Figs. 7, 8 and 9, respectively. It is observed that the radiation patterns in H-plane are in bi-directional pattern and in E-plane good radiation pattern can be obtained. Therefore, the coverage for the proposed antenna are suitable to be used in UWB application.

4 Conclusion

This work presents the design of UWB antenna using step technique for having good impedance matching. In order to avoid interference in WiMax and WLAN frequency bands, inverted U-shaped and C-shaped slots were introduced. The simulation results show that the proposed design is able to provide wide frequency range in supporting UWB systems and to eliminate the undesired bands.

Acknowledgements The work was partly supported by the Research and Innovation Department, Universiti Malaysia Pahang (grant number RDU170370). The authors would like to be grateful to the Faculty of Electrical and Electronics Engineering, Universiti Malaysia Pahang for providing financial support as well as research facilities.

References

1. Yadav, D., Tiwari, V.: UWB antenna designing: Challenges and solutions. *Int. J. Comput. Commun. Instrum. Eng.* **1**(1), 39–42 (2014)
2. FCC: Ultra-wideband Operation FCC Report and Order. In: Technical Report US 47 CFR Part 15 (2002)
3. Naharuddin, N.Z.A., Noordin, N.H.: Multiband UWB trapezoidal antenna using U and Pi-shaped slots. In: *Electromagnetics International Workshop on Applications and Student Innovation Competition (iWEM)*, pp. 1–2. Hsinchu, Taiwan (2015)
4. Sam, W.Y., Zakaria, Z.: Design of a dual-notched ultra-wideband (UWB) planar antenna using L-shaped bandstop resonator. In: *11th European Conference on Antennas and Propagation (EUCAP)*, pp. 2237–2241. Paris (2017)
5. Antenna, P., et al.: 5 GHz WLAN band-notched UWB symmetrical slotted PI-notched parasitic planar. In: *2013 International Conference on Advances in Computing, Communications and Informatics (ICACCI)*, pp. 338–342. Mysore, India (2013)
6. Sudhakar, A., et al.: Single band-notched UWB square monopole antenna with double U-slot and key shaped slot. In: *Fifth International Conference on Communication Systems and Network Technologies*, pp. 88–92. Gwalior, India (2015)
7. Yadav, A., et al.: CSRR and C-slot loaded triple band notched ultra wideband antenna. In: *International Conference on Information, Communication, Instrumentation and Control (ICICIC)*, pp. 1–4. Indore, India (2017)

Inter Vehicle Communication System for Collision Avoidance



Nurul H. Noordin, Althea C. Y. Hui, Nurulfadzilah Hassan
and Rosdiyana Samad

Abstract In inter vehicle communication, there are many aspects that must be taken into considerations. The utmost important aspect is the speed of sending data packet, which is the key factor in preventing emergency message delay in traffic network. Other than that, the accuracy in reading and processing sensors' data by microcontroller are essential in cases of collisions avoidance. The aim of this paper is to overcome the communication problems between vehicles located at intersection. In this paper, two conditions have been proposed: vehicle-to-vehicle (V2V) communication and vehicle-to-infrastructure (V2I) communication. Experiments have been conducted using prototype cars. The results show that the prototype cars are able to avoid collision through activation of communication system at certain section on the road.

Keywords Inter-vehicle communication system · Vehicle-to-vehicle (V2V) Vehicle-to-infrastructure

1 Introduction

Accident at intersections has been reported as one of the major cause of fatal accidents involving vehicles on the roads [1]. Most cases were caused by vehicle blind spots. Motorcyclists squeezing in between vehicles can be dangerous as they may be in blind spot area of other vehicles and ends up in an accident [2].

There are several accidents happened at the intersection University Malaysia Pahang (UMP), Gambang Campus, since 2010. Recently, there are few fatal accidents reported, involving UMP students at intersections in the campus. Accidents often occur at the intersection without traffic lights. However, accidents can be prevented, if there is some form of communication between vehicles, crossing inter-

N. H. Noordin (✉) · A. C. Y. Hui · N. Hassan · R. Samad
Fakulti Kejuruteraan Elektrik & Elektronik, Universiti Malaysia Pahang, Pekan, Pahang, Malaysia
e-mail: hazlina@ump.edu.my

sections. This project focused on the inter-vehicle communications at intersection at University Malaysia Pahang (UMP), Gambang Campus, which has no traffic lights.

Generally, inter vehicle communication covers the area of vehicle-to-vehicle communication (V2V) and vehicle-to-infrastructure communication (V2I). The difference between these two conditions is with whom the focused vehicle is communicating with, while crossing a junction. In the first condition, the focused vehicle communicates with another constantly moving vehicle. Whilst in the second condition, the focused vehicle is communicating with a static roadside infrastructure.

In this project, V2V communication between two moving prototype cars at an intersection is investigated. The prototype cars communicate with each other through radio frequency communication at certain section of the road where the communication is necessary to be performed. On the other hand, V2I communication investigated in this project focused on communication between the prototype car and the built roadside infrastructure. In this setting, the infrastructure communicates with the prototype car through radio frequency communication.

1.1 Collision Avoidance

Absence of traffic lights and lack of inter vehicle communication can cause accidents to happen at intersection. Thus, exchange of position information between vehicles at intersection is the key to avoid collision as it allows drivers to react before it is too late.

GPS can be one of the options for collision avoidance but it is affected by large buildings or structures. The accuracy of GPS depends on the received signal quality and the signal may get affected because of the atmosphere, multipath and electromagnetic interference [3]. Furthermore, the response from GPS has some delays which will impact on the drivers' responses. The proposed system in this project is equipped with sectional activation communication system for inter vehicle communication aimed to prevent collision.

2 Literature Review

2.1 Vehicle Navigation and Control

Wang et al. proposed an intelligent vehicle control system based on LabVIEW, to meet the needs of intelligent vehicles [4]. In the proposed system, camera is used as input for image acquisition. Then LabVIEW software was loaded on a computer. The system accepts, displays and sends intelligent vehicle information such as speed, angle, traffic information and other data, for real-time monitoring the movement of intelligent vehicle. Diane and Peters [5], introduces a means of modifying a com-

mercially available Radio Controlled car into an autonomous car by implementing a wireless Master-Slave scheme of architecture using a microcontroller and an NI myRIO FPGA device. NI myRIO is the master, while an on board microcontroller unit (MCU) is the slave. It describes the hardware and software modifications required to successfully carry out closed-loop control of the car. For wireless communications, Digi Xbee wireless module with frequency range of 2.4 GHz (802.15.4) is used. The first step is to initialize MCU before the MCU can take data of the prototype. After that, transmit sensor packet data to myRIO via Xbee. Control algorithm is implemented in LabVIEW and then the control signal packet data is transmitted to MCU via Xbee to control the motor driver and steering servo.

2.2 Collision Avoidance at Intersections

Azimi et al. proposed collision detection at intersections using Collision Detection Algorithm for Intersections (CDAI) [6]. The algorithm will analyze the direction of the vehicle heading to and calculate whether the lane will be occupied when the vehicle is about to reach the lane at the intersections. Besides, intersections protocols such as Stop-sign Protocol, Throughput Enhancement Protocol (TEP), and (TEPA) Throughput Enhancement Protocol with Agreement are proposed in controlling the vehicle movement at the intersections. GrooveNet, a hybrid vehicular network simulator is used in stimulating the situations of the vehicles at intersections and thus obtain the results. They further described and evaluate 4 based models, which are Stop-sign model, Traffic-light model, V2V Stop sign model, TEP model and TEPA model. However, this research did not deal with position inaccuracies and packet losses in wireless communications.

Prasad et al. [3], have proposed a method of using LabVIEW and myRIO in the situation for overtaking vehicle in front. Firstly, the data are acquired using GPS module. Then, myRIO calculates distance and speed by subtracting the values of longitude at different instant of time. If another car is travelling in the same lane in opposite direction with 50 m of range, then the system alerts the driver. If no obstruction is present the system just displays the speed and distance of the oncoming car [3]. This system is able to assist drivers when overtaking vehicle by estimating the speed of the oncoming cars. However, the authors mentioned that drivers cannot depend on the system solely without own judgement because the system may malfunction.

2.3 Communication Between Vehicles

Ghosal et al. [7], analyze technique for reliability/safety/integrity of wireless communication, also known as Dedicated Short Range Communication (DSRC). Analysis of a design is done based on formal models, simulation, emulation, and testing. This

research shows strong correlation between analytical model, Markov model and simulation data, Monte-Carlo mobility generator to create synthetic mobility traces. In intervehicle communication, communication technique is important in making sure there is no data loss during information transfer.

García [8] proposed delivery latency occurred due to high speed of vehicles. Besides the topology which is not purely linear since highway has more than one lane, congestion of Emergency Warning Message (EWM) will cause the delay in transferring the message, which consequently affects the response of the driver in emergency situations.

Vehicular Collision Warning Communication Protocol presented in this paper proposes an alternative to improve road safety. It manages to get a small EWM delivery delay and supports a large number of coexisting vehicles that send the EMW. It also included a system to discard redundant EWM, taking advantage of the natural chain effect of emergency events.

3 Methodology

There are two conditions being proposed in this project. The first condition is V2V communication, where communication is between two prototype robot cars. There is no roadside infrastructure communicating with any of the prototype cars. As for second condition, the V2I communication, the prototype car communicates with the roadside infrastructure. Based on the information exchanged, the prototype car will decide whether to cross the intersection or not. In this project, sectional activation communication is being proposed as the communication method, to prevent message data packet traffic congestion and also to ensure the message arrive at the correct destination.

3.1 Description of the System

The flow chart of the V2V and V2I systems are illustrated in Fig. 1.

The block diagram for condition 1, which is V2V communication is proposed in Fig. 2. The detailed components connection and interaction is also shown.

The block diagram for condition 2, which is V2I communication is showed in Fig. 3. The detailed components connection and interaction for Vehicle 2 and roadside infrastructure are also shown. There is communication between 2 nRF24L01 components. The roadside infrastructure will sense the location of Vehicle 1 and then pass the information to Vehicle 2. The roadside infrastructure will make decision whether Vehicle 2 should pass the junction or not. Vehicle 2 will react according to the message received from the road side infrastructure. Prototype of the model is shown in Fig. 4.

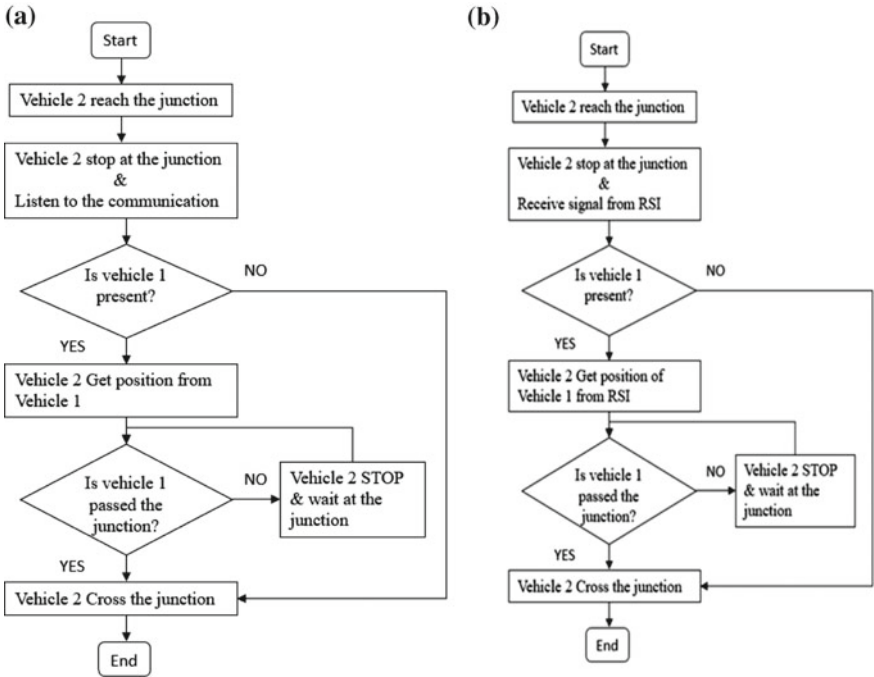


Fig. 1 Flow chart of the proposed system. a V2V communication. b V2I communication

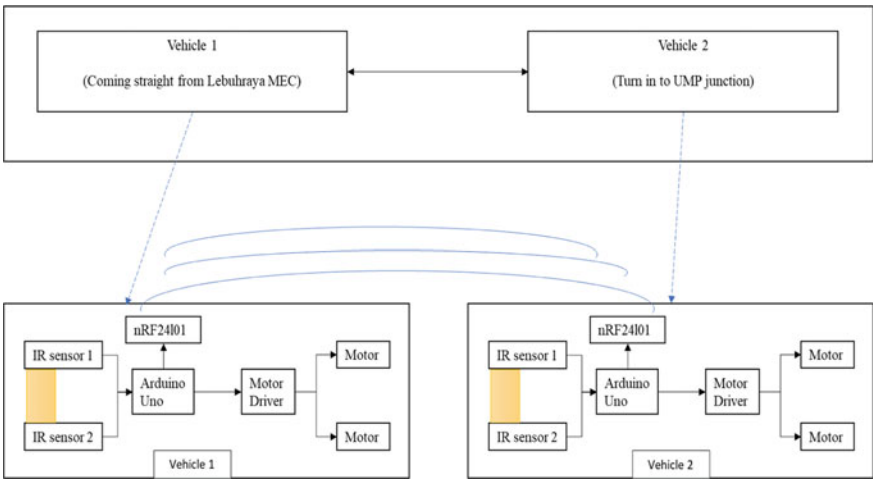


Fig. 2 Block diagram of V2V communication

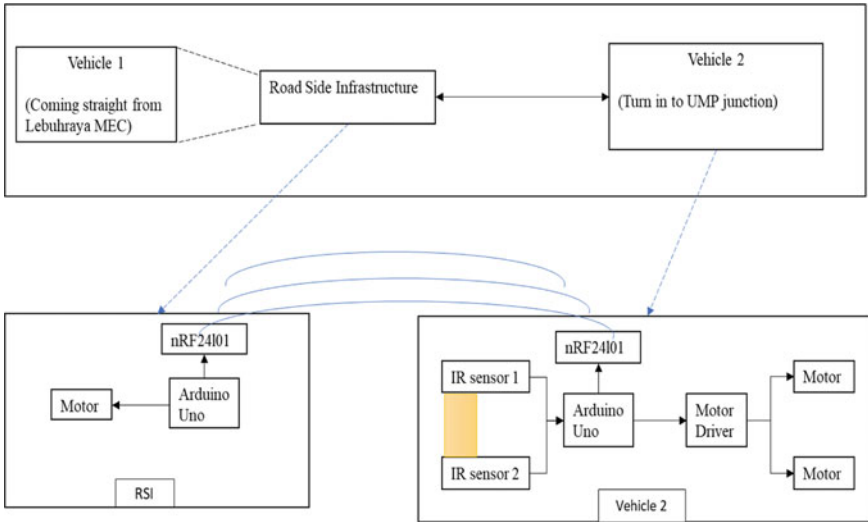


Fig. 3 Block diagram of V2I communication

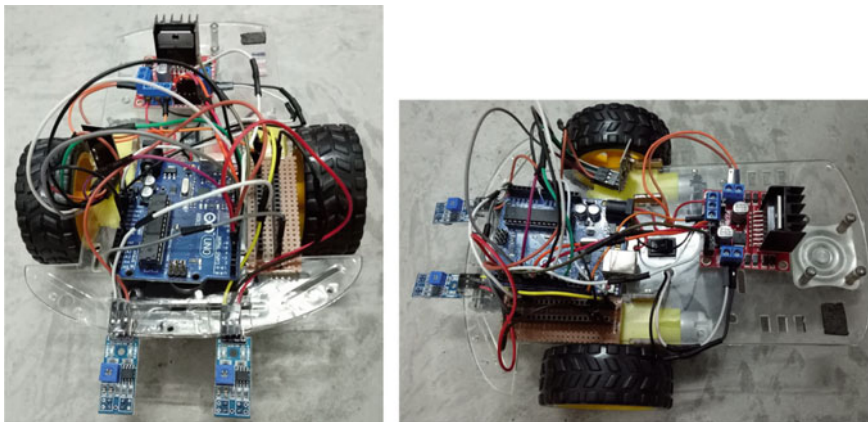


Fig. 4 Prototype robot car

3.2 Sectional Activation of Communication System

Sectional activation communication method operates only when the focused vehicle reaches certain region or area of the road where the communication is necessary to prevent collision. This is done through detection from the sensors attached on the vehicle. This is to ensure the vehicle communicating within only the assigned destination. One of the benefits of using this method is that traffic congestion of the communication system can be avoided. Besides that, this method can be used to

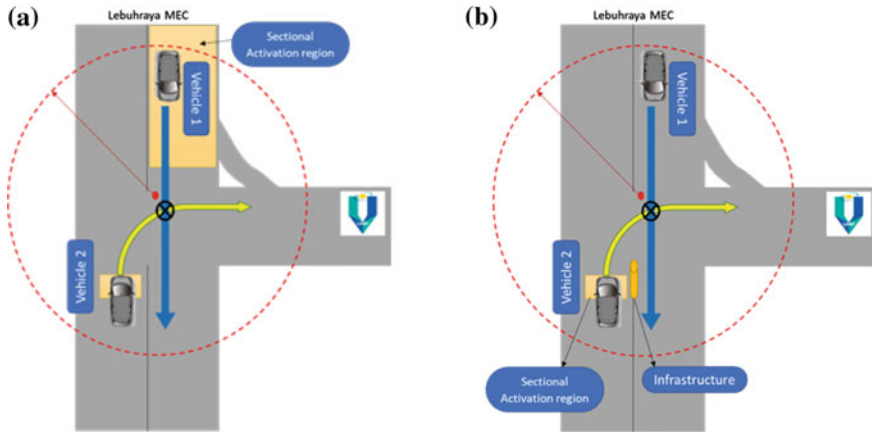


Fig. 5 Sectional activation communication system. **a** V2V communication. **b** V2I communication

replace the usage of GPS which has delay in detecting the changes of position of the vehicles.

Two conditions have been set for this project. In Condition I, there are two regions of sectional activation of the communication system. The first region is the region where the Vehicle 1 coming from Leburaya MEC, whereas the second region is at the junction where Vehicle 2 located.

In Condition II, there is only one region of sectional activation of the communication system. The region is located at the junction where Vehicle 2 located. When Vehicle 2 reaches this region, the communication system will be turned on for it to communicate with the roadside infrastructure (RSI). The roadside infrastructure will send the messages to the vehicles which are in that region to inform them whether it is safe to cross the intersection.

4 Results and Discussion

The prototype system is tested under both conditions. Then comparison is made between V2V and V2I communication system. For this paper, the results from condition II (V2I communication) was chosen because the communication established between the vehicle and RSI is more stable. Figure 5 shows the view for Sectional Activation Communication System for (a) V2V Communication and (b) V2I Communication. Then Table 1 compares the results between Condition I—V2V Communication and Condition II—V2I Communication.

The node reservation algorithm is not suitable in this case as hardware is implemented. Node reservation algorithm is used in software simulation through Dynamic Programming [9]. Each vehicle is treated as a computer server to generate the mes-

Table 1 Comparison between V2V and V2I system

Condition I—V2V communication	Condition II—V2I communication
Direct communication between vehicles	Communication between vehicle and RSI
Vehicles without the communication system cannot communicate	Vehicles with the communication system can communicate with the RSI
Installation of sectional activation sensors at region of vehicle 1 and vehicle 2	Installation of RSI and installation of sectional activation sensors at region of vehicle 2
Fluctuate communication network	More stable communication network

sages to send to the intersection manager over Wi-Fi, IP address. Another computer will be used as the intersection manager to simulate the crossing of vehicles. There is another computer function as a server for simulation of another vehicle. The simulation is run on a stand-alone computer. Thus, the algorithm is usable for software simulation in terms of messages transferring timing and distance, but not suitable for hardware implementation.

5 Conclusion

The prototype vehicles and design model have been implemented in modelling inter-vehicle communication to prevent collision. Furthermore, network simulation using software has been carried out. In conclusion, the outcomes of this project have been achieved. The prototype cars and model are constructed to demonstrate inter vehicle communication. The prototype cars are able to avoid collision through activation of communication system at certain section on the road. In the future, the system can be improved by using better sensors and implementing more hardware.

Acknowledgements This research is being sponsored by RDU1703222 Universiti Malaysia Pahang.

References

1. Smith, E.: Statistics on Intersection Accidents. <https://www.autoaccident.com/statistics-on-intersection-accidents.html>. Last Accessed 25 Sept 2018
2. Sin, A.L.Y.: Motorcyclists urged to be more vigilant on the roads. In: The Straits Times, Singapore (2016)
3. Prasad, S.V.S., Kumar, D.A., Niharika, B.: Smart car collision avoidance system. *IOSR J. Comput. Eng. (IOSR-JCE)* **18**, 01–03 (2016)
4. Wang, L., Liu, N., Wang, J., Hu, J., Liang, F.: Design of an intelligent vehicle control system based on LabVIEW. *Metall. Min. Ind. (7)*, 21–27 China (2015)
5. Diane, D.I., Peters, L.: Development of a miniaturized autonomous vehicle: modification of a 1:18 scale Rc car for autonomous operation. In: Proceedings of the ASME 2015 Dynamic Systems and Control Conference, Columbus, Ohio, USA (2015)

6. Azimi, S., Bhatia, G., Rajkumar, R., Mudalige, P.: Vehicular networks for collision avoidance at intersections. *SAE Int. J. Passeng. Cars Mech. Syst.* **4**(1), 406–416 (2011)
7. Ghosal, F.B.A., Debouk, R., Zeng, H.: Reliability and safety/integrity analysis for vehicle-to-vehicle wireless communications. *SAE Int. J. Passeng. Cars Electron. Electr. Syst.* **4**(1), 156–165 (2011)
8. García, D.L.: Inter-Vehicular Communication Systems. <http://www.mi.fu-berlin.de>. Last accessed 25 Sept 2018
9. Wuthishuwong, C., Traechtler, A.: Vehicle to infrastructure based safe trajectory planning for autonomous intersection management. 2013 13th International Conference on ITS Telecommunications (ITST), Tampere, 175–180 (2013)

IOT—Eye Drowsiness Detection System by Using Intel Edison with GPS Navigation



Auni Syahirah Abu Bakar, Goh Khai Shan, Gan Lai Ta
and Rohana Abdul Karim

Abstract The number of traffic accidents continues to increase due to the driver's fatigue has become a serious problem to the society especially for the driver who drove for long distance. Technology in digital computer system allows us to create a drowsiness detection system. Studies for drowsiness detector system have focused on development of computer vision algorithm and lack of Internet of Things (IoT) and notification system, either awake or sleep or might involve in accident, and current location. Thus, we decide to develop a drowsiness detection system with notification of accident and the location by using Global Positioning System (GPS) navigation. In this system, if the driver's eyes are closed about more than 4 s, the driver considers as drowsy and an alarm system will be activated to warn the driver and notify the status and location to relative for further action via message (SMS).

Keywords Eye drowsiness · Intel edison · GPS navigation · IoT
Smartphone setup

1 Introduction

Nowadays, a safe driving is a major concern of societies all over the world. The percentages of car accident also keep increasing year by year. Malaysia also has the highest road fatality risk (per 100,000 populations) among the ASEAN countries that cause by car accidents [1]. There are also some factors that contribute to the car accident which caused by the vehicle problem itself and human behavior. Drowsiness is one of the famous caused in Malaysia which the drivers falling asleep at the wheels.

Normally, after long hours of driving journeys or in absent of alert mental state, the eyelids of driver will become heavy due to fatigue. The attention of the driver starts to lose focus, and that creates risks for accidents. These are typical reactions

A. S. Abu Bakar · G. K. Shan · G. L. Ta · R. Abdul Karim (✉)
Faculty of Electrical & Electronics Engineering, Universiti Malaysia Pahang, 26600 Pekan,
Pahang, Malaysia
e-mail: rohanaak@ump.edu.my

© Springer Nature Singapore Pte Ltd. 2019

Z. Md Zain et al. (eds.), *Proceedings of the 10th National Technical Seminar
on Underwater System Technology 2018*, Lecture Notes in Electrical Engineering 538,
https://doi.org/10.1007/978-981-13-3708-6_42

485

of fatigue, which is very dangerous. Usually many exhausted drivers are not aware that they are falling asleep even for a moment (microsleep). Unfortunately, accident might happen anytime, less than one second. Besides, there are cases of death due to the absence of rescue. No report and emergency call to authorized person due to unknown occurrence and location of the accident by people around there [2, 3]. As a result, injuries become worse and the chances to death are increase.

Therefore, it is essential to develop a real-time safety system for drowsiness detection system which able to monitor eye condition and notify the responsible person (relatives/parent) by sending message and current location that the driver might get into accident. Fast action could be taken to save golden lives of the accident victims, even for a few seconds. By leverage the advancement of internet and communication technology, this project aim to propose a preliminary system of eye drowsiness detection with GPS navigation.

2 Related Works

A lot of studies for drowsiness were focused on development of robust features and algorithm for drowsiness detection such as bio-features [4], yawning [5], skin color [6] and etc. Besides, there also have several studies focused on integrated hardware and software for drowsiness system. Results proved the studies successfully integrated hardware and software elements, but lack of IoT implementation for automatic notification system [5, 7, 8]. As a result, rescue failed arrived as soon as possible.

In-vehicle webcam is commonly installed to realize the possible reasons of car accidents by detection of drowsiness [9] behavior. Recently, smartphone camera have been used widely to replace the webcam due to high-speed (3G, 4G) data transmission [10]. However, studies [5, 7, 8, 10] does not considered setting of smartphone for data acquisitions during the experimental design.

3 Proposed Modelling

3.1 System Design

The overview of the proposed system is illustrated on Figs. 1 and 2. The system involves real time processing and detection of drowsiness are processed by evaluate eye blinking using image processing analysis which is Open Source Computer Vision (OpenCV) [11]. The smartphone camera is attached on the windshield of the car and used as a sensor to capture video. The video are sent to cloud for analyze eye condition either sleep or awake. Synchronously, the GPS navigation module is activated to trace the current location data of the driver. All the captured data of eye analysis and

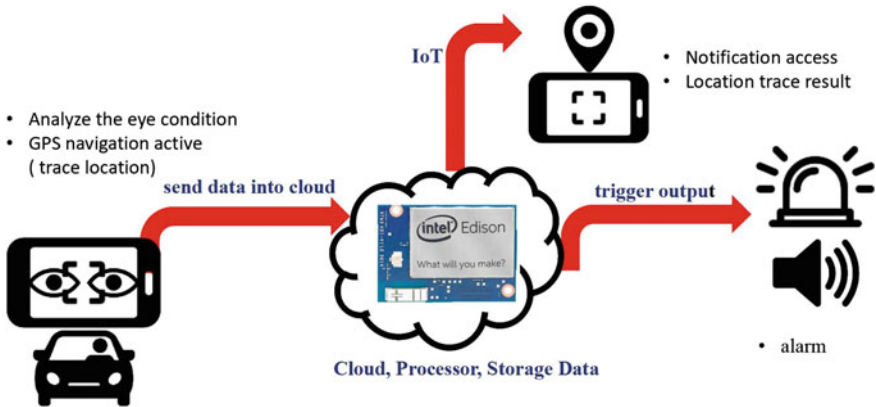


Fig. 1 Overview of the purposed system

location will be send to the cloud storage. Then, the information that has been stored into the cloud will be sent to Intel board for communicating with hardware. Intel processor will trigger the output system via LCD, LED, buzzer and Global System for Mobile (GSM) notification.

The Internet of Things (IoT) also has been implemented into the system, by connecting it using a network wireless connection (WiFi). This system will identify the eyes state of the driver and an alarm system will be activated to warn the driver whenever the driver’s eyes is closed more than 4 s [12] and it will send notification message to driver’s family members when eyes is closed for another 8 s for further action. According to [12], 4 and 12 s are a blink patterns and lid-contact times in dry-eye for normal subjects.

3.2 Hardware

The system basically consists of Smartphone Camera, Intel Edison board, GSM module, buzzer, LEDs and LCD. Circuit diagram of the proposed system is shown in Fig. 3. Details functions of hardware are explained in Table 1.

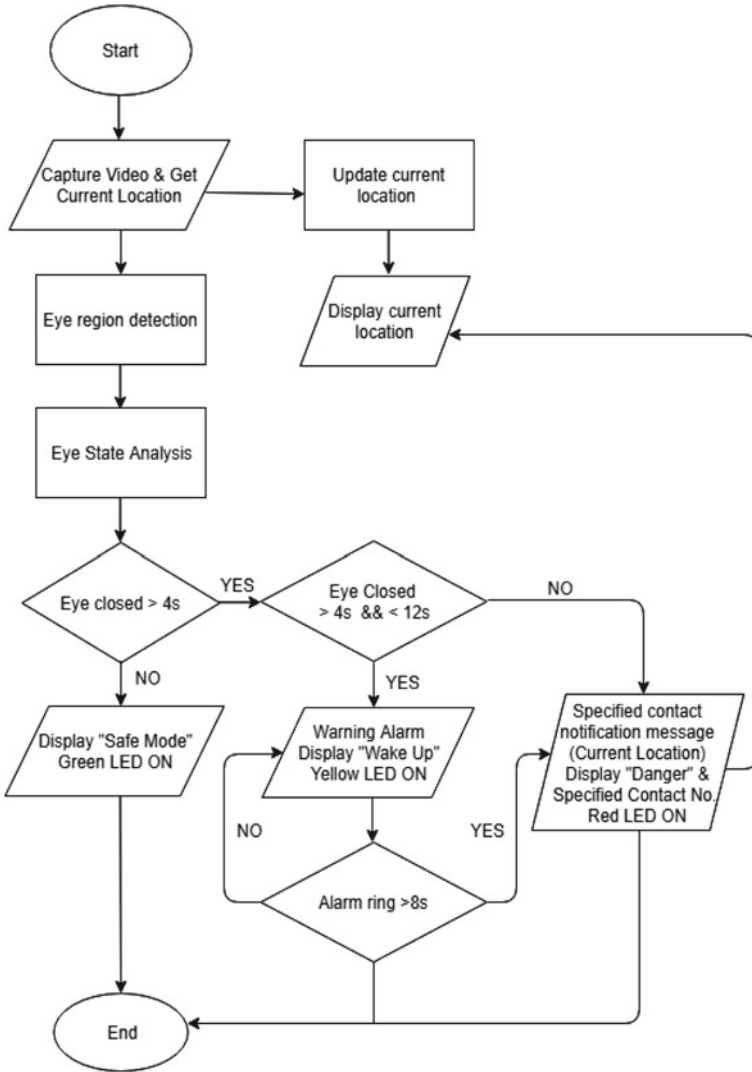


Fig. 2 Flowchart of the purposed system

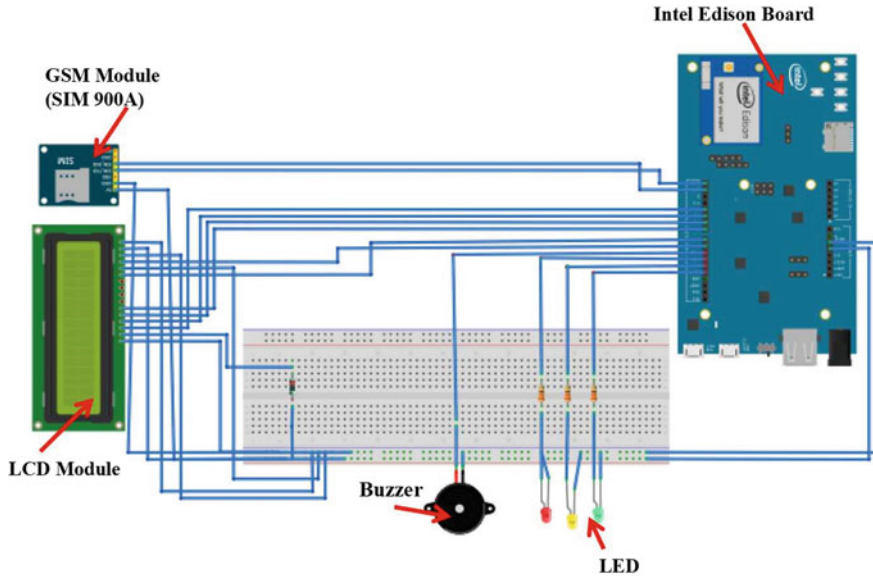


Fig. 3 Circuit diagram of the system

Table 1 Hardware functionality

Item	Function
Intel Edison Board	Intel Edison acts as a microcontroller. It is used to perform various functions and operations throughout the system
GSM module (SIM 900A)	GSM is used in this system for alerting and messaging system to notify the family members or emergency agency by sending message (current location) when the driver is suspected to involve in accident
LCD module	The I2C 1602 LCD module is a 2 line by 16 characters display interfaced to an I2C daughter board. LCD module is used to display the eyes condition of the driver
Buzzer	Buzzer acts as alarm to wake the driver up, three different led light (Green, Yellow and Red) which is the indicator to show the fatigue of the driver where green led indicates safe mode, yellow led means alarm is ringing due to eyes is closed more than 4 s and red led represents danger mode and message is ready to be sent
Smartphone Camera	A smartphone camera is a video camera that feeds its image in real time by install an IP camera which uses a direct connection using Ethernet or Wi-Fi. This camera will use to capture the eye condition of the driver

Table 2 Image resolution and processing delay measurement

Image resolution (pixel)	Delay (s)	Drowsiness detection
1920 × 1080	15	True
1440 × 1080	12	True
720 × 480	9	True
640 × 480	6	True
480 × 320	3	True
352 × 288	0	True

4 Results and Discussion

4.1 Experimental

4.1.1 Setup Image Resolution (Video)

Experiment to identify the best image resolution was conducted. Table 2 illustrated the experimental results. The lowest image resolution (352 × 288) performed accurate result with 0 s delay compared to the highest image resolution with 15 s delay. Internet image transmissions for high-resolution video were noisy and prevent the detection from working effectively. This indicates that the lower image resolution is best suited for the proposed system.

4.1.2 Smartphone Placement

The effectiveness of smartphone placement between windshield car and driver was evaluated by varying the distance of smartphone from driver as shown in Table 3. Experimental results found out that the suitable distance of a driver from smartphone camera was 25 cm to less than 100 cm. Distance 100 cm and above shows unstable results between sleeping and not sleeping. It is because when the eyes was located far away from a camera, the image of eye were getting smaller and opened eyes is seemed like closed eyes.

Table 3 Different distances between driver and phone

Distance (cm)	Drowsiness detection
25	True
50	True
70	True
100	True/false








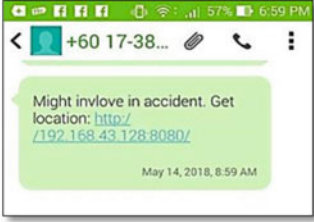
Condition	Result	
The eye is open		
The eye is close for ≥ 4 s and < 12 s		
The eye is close for ≥ 12 s microsleep		
	‘Danger’ on LCD display and Red LED is ON.	related/responsible person contact number on LCD display
		
	GPS navigation of driver location	Screenshot of messages sent

Fig. 4 Result hardware and software integration

4.2 Simulation Results

We have successfully detected the drowsy condition of the driver’s eye and alert the driver by giving alarm and send the notification to responsible or related person. During this process, when the eyes is not closed more than 4 s then Green LED is ON and LCD will display ‘Safe Mode’ while the eyes is closed more than 4 s then Yellow LED and Alarm are ON together with LCD display ‘Wake Up’. If the driver’s eyes are opened after the alarm is rung then the system will go back to the first stage

where Green LED is ON and ‘Safe Mode’ is displayed. When alarm is rung for more than 8 s, Red LED is ON indicated it is in ‘Danger Mode’ and at the same time the notification message in terms of current location of the driver will be sent out to the specified contact and emergency agencies. During this stage, the system will continue to display contact number of family members of the driver for the people around the accidents place to call the driver’s family members. Figure 4 illustrated visual results of hardware and software integration.

5 Conclusion

Eye Drowsiness Detection system was successfully built as proposed. The phone camera able to capture the eye of the driver and managed to analyze the eye condition i.e. open or close by embedded the information into the Intel Edison board. Besides, output integration of hardware successfully showing the Green/Yellow/Red LED, LCD and buzzer as a signal to indicate and display the condition of the driver as proposed design. The best setup for smartphone placement is between 25 and 99 cm. Meanwhile, for image resolution is 352×288 pixel. In addition, this study also successfully implemented Internet of Things (IoT) into our system by developed a sending notification system and GPS navigation access.

Acknowledgements We would like to acknowledge funding provided by Universiti Malaysia Pahang (RDU1703233).

References

1. Ruxyn, T.: *Says.com*. Retrieved from <http://says.com/my/news/malaysia-sroads-among-the-world-s-most-dangerous-and-deadliest>. Last accessed 01 Sept 2018
2. <https://www.hmetro.com.my/mutakhir/2018/03/324770/derita-kereta-terhumban-dalam-gaung>. Last accessed 01 Sept 2018
3. <http://www.sinarharian.com.my/mobile/semasa/dua-kanak-kanak-maut-dalam-kemalangan-di-lpt-1.406312>. Last Accessed 01 Sept 2018
4. Ghazali, K.H.B., Ma, J., Xiao, R.: Driver’s face tracking based on improved CAMSHIFT. *Int. J. Image Graph. Signal Process.* **5**(1), 1 (2013)
5. Omidyeganeh, M., Shirmohammadi, S., Abtahi, S.: Yawning detection using embedded smart cameras. *IEEE Trans. Instrum. Measur.* **65**(3), 570–582 (2016)
6. Ramzi, S.: Proactive driver alert system (PDAS) for drowsy drivers. *J. Soc. Sci. (COES&RJ-JSS)* **5**(1), 42–55 (2016)
7. Das, P., Pragadeesh, S.: A microcontroller based car-safety system: implementing drowsiness detection and vehicle-vehicle distance detection in parallel. *Int. J. Sci. Technol. Res.* **4**(2) (2015)
8. Kulkarni, A.S., Shinde, S.B.: A review paper on monitoring driver distraction in real time using computer vision system. *Int. J. Comput. Sci. Eng.* **5**(6) (2017)
9. Kulkarni, S.S., Harale, A.D., Thakur, A.V.: Image processing for driver’s safety and vehicle control using raspberry Pi and webcam. In: 2017 IEEE International Conference on Power, Control, Signals and Instrumentation Engineering (ICPCSI), pp. 1288–1291 (2017)

10. You, C.-W., et al.: CarSafe: a driver safety app that detects dangerous driving behavior using dual-cameras on smartphones. In: Proceedings of the 2012 ACM Conference on Ubiquitous Computing. ACM (2012)
11. <https://github.com/tahaemara/sleep-detection>. Last accessed 01 Sept 2018
12. Ousler 3rd, G.W., Abelson, M.B., Johnston, P.R., Rodriguez, J., Lane, K., Smith, L.M.: Blink patterns and lid-contact times in dry-eye and normal subjects. Clin. Ophthalmol. (Auckland, NZ) **8**, 869 (2014)

Automatic Detection of Diabetic Retinopathy Retinal Images Using Artificial Neural Network



Syamimi Mardiah Shaharum, Nurul Hajar Hashim,
Nurhafizah Abu Talip @ Yusof, Mohamad Shaiful Abdul Karim
and Ahmad Afif Mohd Faudzi

Abstract The Diabetic Retinopathy (DR) is a critical vascular disorder that can cause a permanent blindness. Thus, the early recognition and the treatment are required to avoid major vision loss. Nowadays manual screening is done however, they are very incompetent to large image database of patients and most importantly they are very time consuming. Besides, it required skilled professionals for the diagnosis. Automatic DR diagnosis systems can be as an optional method to the manual methods as they can significantly reduce the manual screening process labor. Screening conducted over a larger population can become effective if the system can distinguish between normal and abnormal cases, as a replacement for the manual examination of all images. Hence, the development of an Automated Diabetic Retinopathy detection systems has been recognized in the current times. This study has successfully developed an automated detection system for proliferative diabetic retinopathy symptoms using an artificial neural network with two types of feature used; mean of pixel and area of the pixel. The highest accuracy of this system is 90% with 30 hidden neurons in the neural network trained for all features. The results clearly show that the proposed method is effective for detection of Diabetic Retinopathy.

Keywords Diabetic retinopathy · Artificial neural network · Automated detection

1 Introduction

The Diabetic Retinopathy (DR) is a critical vascular disorder that might lead to complete blindness. Diabetic retinopathy is one of the devastating significances of diabetes that damage the blood vessels that supply and nourish the retina which leads

S. M. Shaharum (✉) · N. H. Hashim · N. Abu Talip @ Yusof · M. S. Abdul Karim
A. A. Mohd Faudzi

Faculty of Electrics and Electronics, Universiti Malaysia Pahang, 26600 Pekan, Pahang, Malaysia
e-mail: syamimimardiah@ump.edu.my

© Springer Nature Singapore Pte Ltd. 2019

495

Z. Md Zain et al. (eds.), *Proceedings of the 10th National Technical Seminar*

on Underwater System Technology 2018, Lecture Notes in Electrical Engineering 538,

https://doi.org/10.1007/978-981-13-3708-6_43



Fig. 1 Example of a scene viewed by a person with: **a** normal vision, **b** diabetic retinopathy [2]

to significant vision loss. Diabetic Retinopathy also is known as diabetic eye disease caused the formation of small veins in the retina of the human eye which can finally lead to blindness [1]. Thus, the early recognition and the treatment are required to avoid major vision loss.

The issue confronted in diabetic retinopathy is that the patient is not conscious of the disease until the changes in the retina have developed to a level that treatment will tend to be less effective. Observed in Fig. 1 of a vision of a normal person compared with a diabetic retinopathy patient.

A regular eye examination done by an expert ophthalmologist is a manual way in diagnosing and screening process need a lot of work, consume a lot of time and unproductive on a large image file of patients thus higher tendency of error in diagnosis and also late detection of diabetic retinopathy. The number of ophthalmologists is not sufficient to cope with a large number of patients particularly in rural areas or if the capacity of local ophthalmologists is substantial. The screening of diabetic patients can help to lower the risk of blindness at least by 50%. Therefore, automated detection for diabetic retinopathy has great significance in assisting ophthalmologists in detecting and treating the disease more efficiently, saving cost and time, reducing manual labor involved and also reducing the chances of complete blindness due to late detection.

Diabetic retinopathy is classified into two types which are known as Non-Proliferative Retinopathy (NPDR) and Proliferative Retinopathy. NPDR is an initial phase of diabetic retinopathy that causes changes in the eye, for example, microaneurysms, hemorrhages, hard exudates, and cotton wool. The appearance of red spots on the retina is called microaneurysms that happen due to dilatations of the blood capillaries. The occurrence of hemorrhages is due to burst of microaneurysms. Blood vessels become congested and are lack of blood supply as the disease progress. New irregular and fragile blood vessels are formed on the surface of the retina when trying to create new paths for blood supply. This is called neovascularization which occurs at the stage of Proliferative Diabetic Retinopathy [3].

Nowadays manual screening is done however, they are very incompetent to large image database of patients and most importantly they are very time consuming.

Besides, it required skilled professionals for the diagnosis. Automatic DR diagnosis systems can be an optional method to the manual methods as they can significantly reduce the manual screening process labor. Chaudhuri et al. [4] described that there are several methods to detect and classify diabetic retinopathy from the literature such as techniques that based on mathematical morphology, Gabor filter banks, pattern recognition, fuzzy C-means clustering and region growing techniques. By using the two-dimensional matched filter, blood vessels were detected.

Grisan et al. [5] proposed a new system to extract vascular Structure in retinal images automatically which is based on a sparse tracking method that involved pixels processing, tracking vessel cross sections and extracting the vessel center, calibrate and direction. Followed by work done by Tyler [6] developed a new method of retinal blood vessel segmentation for retinal images based on overlay and Isodata algorithm. Instead of using the green channel, RGB is converted to Gray using PCA through a process that was developed in the algorithm; "Hybrid Lesion Detection Algorithm Using Principle Component Analysis." The Isodata algorithm will calculate the global image threshold using an iterative isodata method which is used to convert an intensity image to a binary image. Moreover, Nafeela et al. [7] introduce a neural network scheme which is used to classify pixels and compute a 7 D vector, composed of gray level and moment invariant based features for pixel representation. The vessel extraction method does not involve user interference and has reliable performance in normal and abnormal images.

Screening conducted over a larger population can become effective if the system can distinguish between normal and abnormal cases, as a replacement for the manual examination of all images. Hence, the development of an automated diabetic retinopathy detection system has been recognized in the current times. Automatic diabetic retinopathy detection systems will employ computer vision techniques and image processing to detect anomalies related to retinopathy. This study will develop an automated detection system for diabetic retinopathy retinal images using the artificial neural network (ANN).

2 Methodology

The overall frameworks in developing the automated system is presented in Fig. 2. From Fig. 2, the following process stage represent the method approach on data collection, data preprocessing, feature extraction and data classification. It can be seen that initial phase is to take the input retinal images and apply image processing techniques which included image segmentation process. The process is executed to extract the features from it. Hence, the features will be classified in data classification stage using supervised classification method using Artificial Neural Network (ANN).

The first step in methodology is data collection. In this study, all retinal images were obtained from a publicly available database. The DRIVE (Digital Retinal Images for Vessel Extraction) was established to allow relative studies on segmentation of blood vessels in retinal images and consists of a total of 45 color fundus

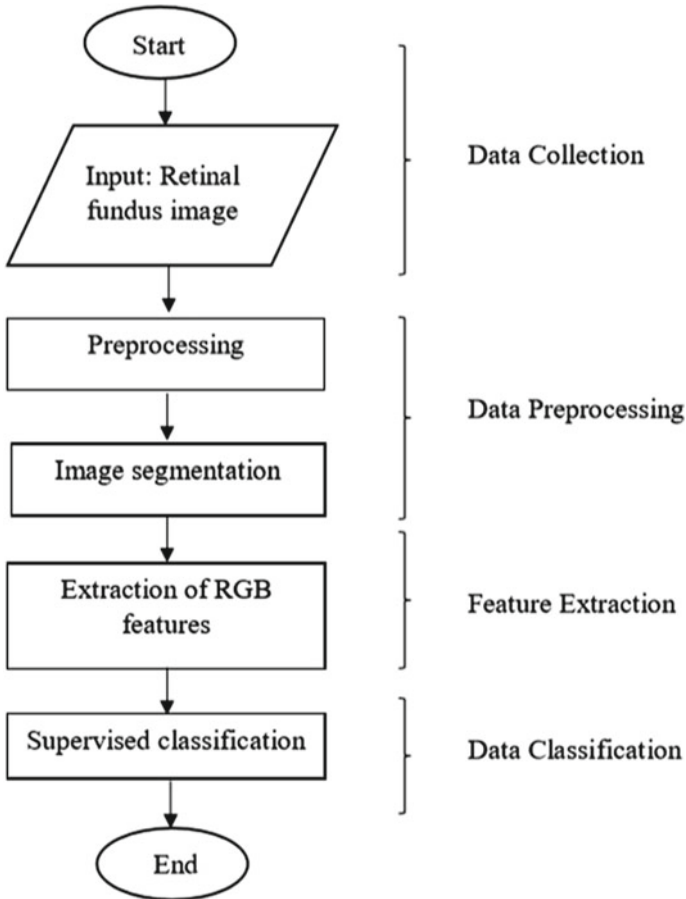


Fig. 2 Overall framework in developing the system

photographs. In this study, only a set of 30 images will be used which includes healthy and diabetic retinopathy patients [8]. The examples of retinal images from DRIVE are shown in Fig. 3.

The images were acquired via a Canon CR-1 fundus camera with a field of view of 45° and different acquisition setting [8]. The examination had to be repeated if the first image has poor quality. Approximately, both images will share the same field of view although there are small shifts that triggered by eye movements between the acquisitions. All of the images in the database were essentially used for the purpose of clinical diagnoses [9].

The original images contain non-uniform spatial variations across the image. To perform medical image processing and disease detection, some image processing operations are required to improve the quality of the obtained image and to perform detection. The various preprocessing steps include green channel extraction, contrast

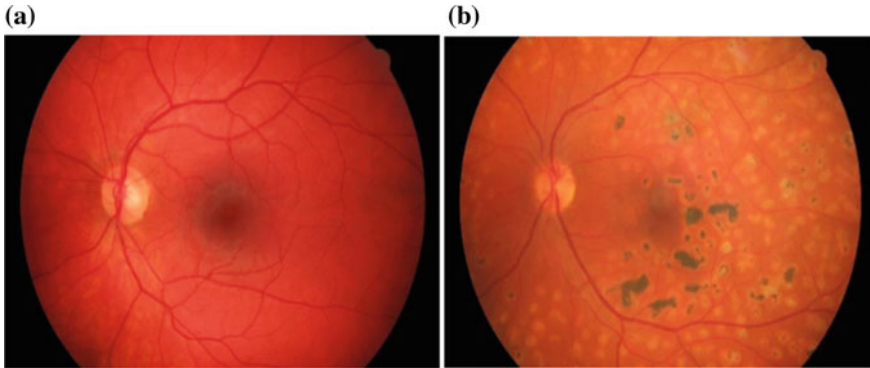


Fig. 3 Retinal images from DRIVE: **a** healthy retina, **b** diabetic retinopathy retina [9]

enhancement and gray level-based features. During the analysis, we restrict ourselves to the green channel due to that its properties contain the highest contrast between the vessels and the background, while it is not under illuminated or oversaturated like the other two channels [9]. All of the images are resized to 768 by 584 pixels. The field of view (FOV) of each image is circular with a diameter of approximately 540 pixels [8].

Image enhancement is done to improve image quality and increase the perception of data in images as medical images are often depreciated by noise due to interference and other phenomena that affect the imaging processes. Impulse noise is removed by the Median filter. Next, the edges are emphasized to enhance the sharpness to increase more visible details in an image. As for image normalization, it is achieved by decreasing the intensity variations in the input images in preprocessing methods.

The process of segmentation involved vessel extraction of the processed image. The extraction can be done by using green channel image for filtering and histogram equalization. Then, the elements are structured to identify bifurcation and cross-over of vessels. False detection of vessels is avoided by applying morphological operation. After the vessel has been successfully segmented, feature such as area of pixel and mean of pixel are extracted. The overall process involved in the pre-processing and image segmentation method can be observed in Fig. 4.

As for the classification process, supervised classification will be used. Supervised learning is the machine learning task of learning a function that plots an input to an output based on example input-output pairs [10]. It infers a function from labeled training data consists of a set of training examples [11]. Each sample is a pair containing an input object and the desired output value. The algorithm of supervised learning will analyze the training data and produces a function which can be used for mapping new examples. An optimal situation will allow the algorithm to correctly determine the class labels for hidden instances. Hence, the Artificial Neural Network (ANN) is proposed for this system with the use of Neural Network Toolbox in MATLAB software.

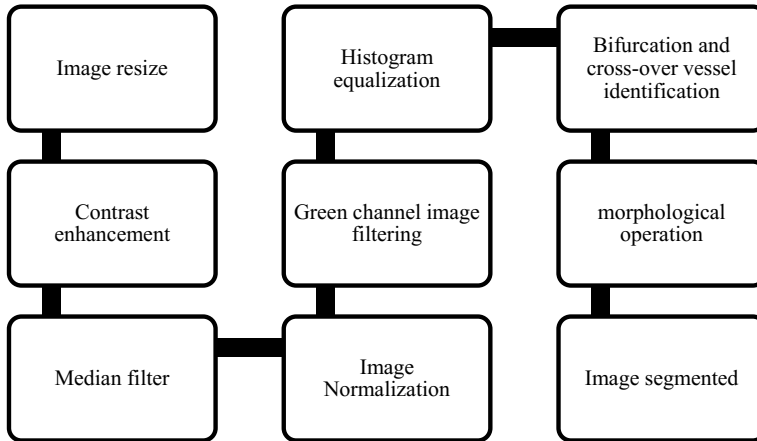


Fig. 4 Overall process involved in the pre-processing and image segmentation method

Neural network is a two-layer of feed-forward network with sigmoid hidden and softmax output neurons which can categorize vectors arbitrarily well that gives enough neurons in its hidden layer. The network will be trained with scaled conjugate gradient backpropagation. Input data will randomly divide up to 70% for training purpose, 15% for validation and the rest for testing.

3 Result and Discussions

The final goal of this system is to classify the retinal images which are normal or a retina with DR symptoms. In this proposed system, thirty images have been used to test the productivity of the system. All the images are successfully segmented. Therefore, the blood vessels segmentation step can be shown in Fig. 5.

From Fig. 5 can be observed that the retinal images which represent the diabetic retinopathy retinal image consist of larger volume in the vein produced which represent the neovascularization symptoms and also there are some dot-like images which represent the microaneurysms symptoms in DR. After all of the images have been successfully undergoes an image segmentation process, the feature will be extracted. Using the data obtained from the feature extraction of the images, the data are separated into two portions that is training and testing data. In this proposed method, the ratio of 70:30 data are used during the training and testing of the classifier with hidden nodes from 5 to 100. Overall classification result can be observed in Fig. 6.

From Fig. 6, can be observed that the highest accuracy has been obtained by combining all of the feature used adapting 30 hidden neurons with 90% average accuracy obtained. Moreover, a more stable average accuracy can be observed again

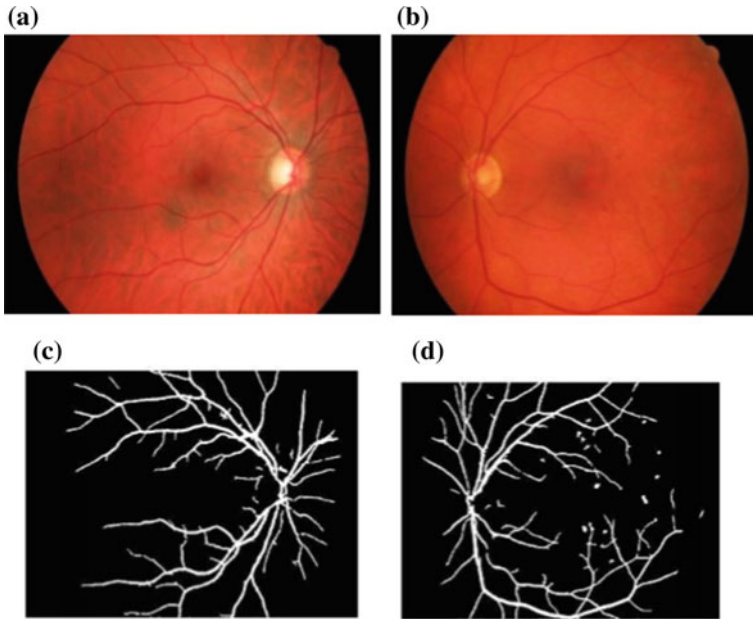


Fig. 5 The result of segmentation of blood vessels from the proposed method: **a** normal retinal image, **b** diabetic retinopathy retinal image, **c** segmented image of normal retinal image, **d** segmented image of diabetic retinopathy retinal image

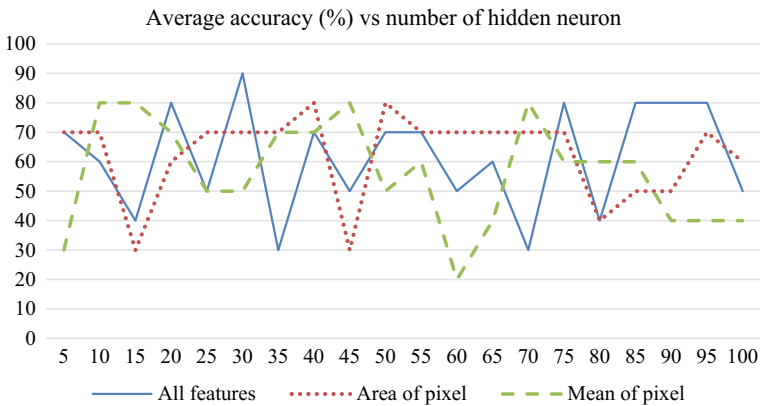


Fig. 6 Graph of average accuracy of network trained

by using the same feature combination with 80, 90 and 95 hidden neurons which obtain average accuracy of 80%. The lowest average accuracy is 20% which is obtained from using mean of pixel with 20 hidden neurons.

Table 1 Result comparison table among works done using DRIVE database

Author	Accuracy (%)
Proposed method	90.00
Chaudhuri et al. [4]	92.84
Staal et al. [8]	94.42
Dizdaroglu et al. [12]	94.10

From the overall result, can be summarized that it is better to combine both of the feature extracted which is mean and area of the pixel rather than utilizing them separately. This is due to that, the mean of the pixel which produces a lower performance compared to the area of the pixel may not significant in distinguishing between the normal and DR retinal images. Mean may adopt an averaging technique that may miss the existence of microaneurysms images that is represented by a small sparse dot.

In comparison with other related research that opted the use of the same DRIVE database, can be observed that result obtain in this work does perform as good as the other work done. The overall comparison can be observed in Table 1. However, the comparison cannot be made directly due to that each of the work done opted a different overall method including in the pre-processing, image segmentation, feature extraction and also in the classification method. Due to the difference of method used, the large variation of the method has been tested that can be used as a reference thus enables more room of improvement in developing a better method in the future work.

4 Conclusion

In this work, an automated detection of diabetic retinopathy retinal images using neural network has been proposed. The process involved in the image database, pre-processing, segmentation, and classification. The proposed method based on the morphological operation for image segmentation is successfully done. The ANNs with the highest average accuracy were used to define network architecture. The highest accuracy of this system is 90% with 30 hidden neurons in neural network trained for all features. The results clearly show that the proposed method is effective for detection of Diabetic Retinopathy. As for the future work, the detection of diabetic retinopathy can also be done by using other methods. Early diagnosis for detection of diabetic retinopathy is absolutely needed to prevent blindness due to late treatment. Lastly, this system can be improved for better detection of diabetic retinopathy in the future.

References

1. International Diabetes Federation and World Health Organization.: The Western Pacific Declaration on Diabetes, Kuala Lumpur, June 2000. WHO, Manila (2000)
2. Van Grinsven, M., van Ginneken, B., Sanchez, C.: Computer-Aided Diagnosis of Diabetic Retinopathy (CAD-DR). Diagnostic Image Analysis Group [Online] (2018). [Diagnijmegen.nl](http://diagnijmegen.nl). Available at: [http://diagnijmegen.nl/index.php/ComputerAided_Diagnosis_of_Diabetic_Retinopathy_\(CAD-DR\)](http://diagnijmegen.nl/index.php/ComputerAided_Diagnosis_of_Diabetic_Retinopathy_(CAD-DR)). Accessed 27 May 2018
3. Associates, A.: Diabetic Retinopathy. Arleo Eye Associates [online] (2018). Available at: <http://arleoeye.com/services/common-eyedisorders/diabetic-retinopathy/>. Accessed 24 May 2018
4. Chaudhuri, S., Chatterjee, S., Katz, N., Nelson, M., Goldbaum, M.: Detection of blood vessels in retinal images using two-dimensional matched filters. *IEEE Trans. Med. Imaging* **8**(3), 263–269 (1989)
5. Grisan, E., Pesce, A., Giani, A., Foracchia, M., Ruggeri, A.: A new tracking system for the robust extraction of retinal vessel structure. In: 26th Annual International Conference of the IEEE Engineering in Medicine and Biology Society, IEMBS'04, vol. 1, pp. 1620–1623 (2004)
6. Tyler, C.: A Novel Retinal Blood Vessel Segmentation Algorithm for Fundus Images. <http://www.mathworks.com/matlabcentral/fileexchange/50839>. MATLAB Central File Exchange. Last accessed 01 Sept 2018
7. Nafeela, J.N.: Detecting and segmenting digital retinal blood vessels using neural network. *Int. J. Eng. Res. Rev.* **2**(1), 36–43 (2014)
8. Staal, J., Abràmoff, M.D., Niemeijer, M., Viergever, M.A., Van Ginneken, B.: Ridge-based vessel segmentation in color images of the retina. *IEEE Trans. Med. Imaging* **23**(4), 501–509 (2004)
9. Budai, A., Bock, R., Maier, A., Hornegger, J., Michelson, G.: Robust vessel segmentation in fundus images. *Int. J. Biomed. Imaging* **2013** (2013)
10. Russell, S.J., Norvig, P.: *Artificial Intelligence: A Modern Approach*, 3rd edn. Prentice Hall (2010). ISBN 9780136042594
11. Mohri, M., Rostamizadeh, A., Talwalkar, A.: *Foundations of Machine Learning*. The MIT Press (2012). ISBN 9780262018258
12. Dizdaro, B., Ataer-Cansizoglu, E., Kalpathy-Cramer, J., Keck, K., Chiang, M.F., Erdogmus, D.: Level sets for retinal vasculature segmentation using seeds from ridges and edges from phase maps. In: 2012 IEEE International Workshop on Machine Learning for Signal Processing (MLSP), pp. 1–6 (2012)

Regional Assessment of Facial Nerve Paralysis Using Optical Flow Method



Wan Syahirah W. Samsudin, Rosdiyana Samad, Kenneth Sundaraj,
Mohd Zaki Ahmad and Dwi Pebrianti

Abstract The face composed of variation of facial muscles which are responsible to interact through the expressions. The facial nerve contains approximately 10,000 of fibers and any damage to these facial nerve will affects all of muscles associated with facial expressions. Thus, it is one of the most extensive destruction in peripheral nerve injuries which demanded for rapid and accurate commencement of assessment to a better treatment and rehabilitation. The traditional methods involved the subjective assessment of medical professionals which may lead to observer error and acquired different decisions on treatment method. However, an ideal and good objective assessment system is still have to rely on a standardized scale to make it more fits to clinicians' use for daily applications. In this study, a diagnosis system for the quantitative assessment of facial nerve paralysis has been proposed using optical flow method which provides the degree of precise movements based on House-Brackmann system on each regional parts of face. The system is not only provided the right-left ratio of facial movement to present the side of paralysis, but also offered the regional score for each movements which lead to total score and afforded the most important highlighted scores, which is the House-Brackmann score for each subjects. The regional scores by using the distance measurement has shown the most outstanding result, at about 98% in classifying the patients and may become a great aid to clinicians in determining the condition of patients from the offset of the paralysis.

Keywords Facial paralysis · Facial nerve assessment · Bell's palsy · Optical flow Kanade-Lucas-Tomasi (KLT) · House-Brackmann system

W. S. W. Samsudin (✉) · R. Samad · D. Pebrianti
Faculty of Electrical & Electronics Engineering, Universiti Malaysia Pahang, 26600 Pekan,
Pahang, Malaysia
e-mail: wansyahirahwsamsudin@yahoo.com

K. Sundaraj
Faculty of Electronics & Computer Engineering, Universiti Teknikal Malaysia Melaka, Hang
Tuah Jaya, 76100 Durian Tunggal, Melaka, Malaysia

M. Z. Ahmad
Department of Otorhinolaryngology, Hospital Tuanku Ampuan Afzan (HTAA), Jalan Tanah
Putih, 25100 Kuantan, Pahang, Malaysia

1 Introduction

Any impairments in along the pathway of facial nerve may results facial paralysis. Since this pathway is in a long distance, hence, the facial paralysis may resulted from many causes. As the facial nerve is responsible for motor supply to the muscles of facial expressions, the patients of this kind of paralysis will have difficulties in smiling, puckering, whistling and having severe implications for both social and physical well-being due to not able communicate well with others [1]. Unilateral facial paralysis, with an incidence of around 25 per 100,000 population, is a common neurologic disorder mimicking a stroke. It often leads to emergency department visits. Bell's palsy, also known as idiopathic facial paralysis, is the most common cause of unilateral facial paralysis, accounting 70% of these cases [2]. In other cases, bilateral facial paralysis is exceedingly rare, representing less than 2% of all the facial paralysis cases, and has an incidence of 1 per 5,000,000 population [3].

Precise characterization of facial paralysis must be accomplished to provide proper patient counselling regarding prognosis and treatment [1]. Deliberate assessment and documentation of facial nerve function should include a detailed description of the status of motion of the upper, middle and lower face. House-Brackmann [4] scale is the most commonly used standardized tool for assessing the degree of facial weakness due its simplicity, time saving, and require no special equipment [5, 6]. While the House-Brackmann scale is used widely, nevertheless the results are invariable and not reproducible since the scale is ensured by subjective assessment of human examiner [5]. Various objective and computerized grading systems have been proposed, to compensate for these problems [7, 8].

In this study, the methods used is the same as our previous work [9], but here the results presented have proved this proposed regional system is robust and reliable since the results are outstanding which is 98% of accuracy in classifying the patients using the distance measurement despite on different environment and lighting condition and also different types of data tested on this system.

2 Materials and Method

2.1 Ethical Statement

Procedures in this study were approved by the Medical Research and Ethics Committee (MREC), Ministry of Health, Malaysia (Ref No.: KKM/NIHSEC/800-2/2/2/P13-96) and was carried out in agreement with the Declaration of Helsinki due to human participation. The Patient Information Sheet and Patient Consent Form were given to the subjects before the data acquisition begun as expressing their assent to be involved in this study.

2.2 *Experimental Setup*

A video camera with a 640×480 resolution was placed in front of the subject who were seated upright on a chair at a distance of 1.0 m to capture the video of the frontal face view of subject's face at a rate of 30 frames per second. Sufficient lighting system was developed in order to ensure the video recordings were in a decent condition to be processed. The data for this analysis was acquired at Physiotherapy and Rehabilitation Department of Hospital Tengku Ampuan Afzan (HTAA), Pahang—Malaysia.

2.3 *Data Acquisition*

To date, there is no publicly available database for subjects with facial nerve paralysis which have satisfying the requirement of this study. Thus, a database was developed which comprised of the normal and patient subjects. For the data acquisition, the subject was first asked to familiarize themselves with the provided facial exercise lists and complied with the designed protocol. Three standard rehabilitation exercises were picked out—Rise Forehead, Close Eyes and Smile. Each exercise was repeated for three times for each subject and each trial composed of 100–300 frames depending on the durations taken for each movement. There are three phases for each video recordings which are started from expressionless face at rest in initial frame, then followed by the facial exercises at middle frames and then ended with expressionless face once again at end of the frames. The order in which the exercises were performed was randomized for each subject.

The study consisted of 25 normal subjects, 13 males and 12 females, with no history of facial nerve paralysis and have symmetrical facial function, which means that the left side of the face acted harmoniously with the right side of face. The age was ranged from 23 to 45 years old. The patients' subjects consisted of 19 patients, 11 males and 8 females with unilateral facial palsy, who ranged in age from 21 to 75 years old. The main etiology of the paralysis is Bell's palsy.

2.4 *Distance and Area Computation by Motion Algorithm*

As mentioned before, there are three facial exercises involved in this study and these exercise videos were analysed by using the Kanade-Lucas-Tomasi (KLT) algorithm [10, 11]. Due its simplicity and limited assumptions are made regarding the underlying image, the KLT method stays as the best video-feature tracking algorithm [12–14] as in offering a high level of computational efficiency, accuracy and robustness. The position of landmarks in the video clip as shown in Tables 2.1 and 2.2 were designated by manual clicking which is based on muscle movements and the selection

was agreed by clinicians from HTAA. The optical flow algorithm has automatically tracks for each point on the face within the Cartesian plane and with a designed and custom-written Matlab® application, the coordinates of the pixel of all the landmarks are obtained and recorded for further analysis. This study has investigated two parameters, Euclidean distance and Eclipse area, for all the exercises and can be measured by using these formula respectively:

$$D = \sqrt{(x_2 - x_1)^2 + (y_2 - y_1)^2} \quad (1)$$

$$A = \pi D_1 D_2 \quad (2)$$

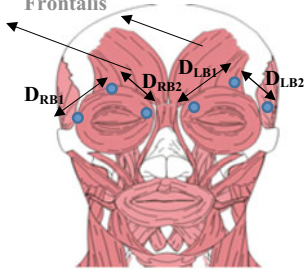
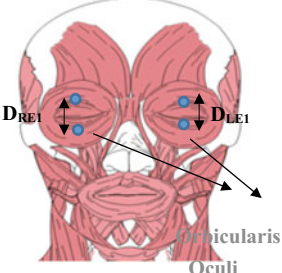
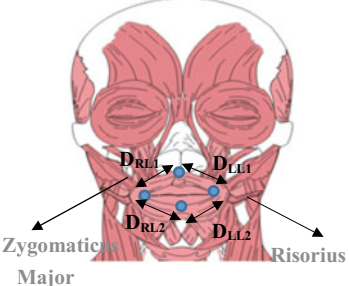
By referring to the Eqs. 1 and 2, x and y are the coordinates of pixel of the landmarks. The distance and area are measured based on these values. The selection of these landmarks are crucial procedure to evaluate the functionality of facial nerve accurately. Therefore, a set of facial exercises were designed and tested for this study to achieve the maximum performance in evaluation of each facial muscle. Finally, three exercises as shown in Tables 1 and 2 were picked out since those exercises are complied with House-Brackmann grading which essentially required in this study. Our selected landmarks are indicated in a blue circle shape to represent the facial muscular activities.

As presented in Table 3, the distance and area are quantified for both sides of face for a comparison since the most of facial paralysis cases only affected on one side of face. For example, in raising the eyebrows movement, the patient will have difficulties to elevate the affected eyebrow. This results in inadequate distance compared to the other healthy side. Besides that, the patient almost not able to close the affected eye in severe facial paralysis. Hence, the distance between the eyelids was measured to assess the functionality of the Orbicularis Oculi muscle in closing and opening the eyes. In addition, the maximum smile also will not be accomplished in patient with facial paralysis because of the droop mouth on the affected side. The region of the involved muscles for each exercise are considered and evaluated in area measurement. For area measurement, the ellipse equation was used by assuming all parts of the face involved in each exercise are shaped almost like an ellipse.

2.5 Distance and Area Computation by Motion Algorithm

For devising a quantitative tool for the assessment of facial paralysis, an individual score table as presented in Table 4 was proposed to evaluate the both sides of face on each regional parts. This individual score table was developed by performing a number of trials of experiment on normal subjects to obtain a more accurate range of scores for both normal and patient subjects. These scores are assigned based on the calculated difference value between initial and maximum movement of the landmarks as follow:

Table 1 Selected landmarks for distance measurement [9]

Facial exercise	Involved muscle	Selected landmarks
Rise forehead	Frontalis	 <p>Frontalis</p> <p>D_{RB1}, D_{RB2}, D_{LB1}, D_{LB2}</p>
Close eyes	Orbicularis oculi	 <p>D_{RE1}, D_{LE1}</p> <p>Orbicularis Oculi</p>
Smile	Risorius and zygomaticus major	 <p>D_{RL1}, D_{LL1}, D_{RL2}, D_{LL2}</p> <p>Zygomaticus Major, Risorius</p>

$$D_{diff} = D_{max} - D_0 \tag{3}$$

$$A_{diff} = A_{max} - A_0 \tag{4}$$

Then, the percentage value of difference of distance and area was calculated by using this equation:

$$\text{Percentage value, } D_{diff}(\%) = \frac{D_{diff}}{D_0} \times 100\% \tag{5}$$

$$\text{Percentage value, } A_{diff}(\%) = \frac{A_{diff}}{A_0} \times 100\% \tag{6}$$

Table 2 Selected landmarks for area measurement [9]

Facial exercise	Involved muscle	Selected landmarks
Rise forehead	Frontalis	<p>Frontalis</p>
Close eyes	Orbicularis oculi	<p>Orbicularis Oculi</p>
Smile	Risorius and zygomaticus major	<p>Zygomaticus Major</p> <p>Risorius</p>

Table 3 The characteristics of each measurement

Exercise	Distance measurement	Area measurement	Characteristics
Rise forehead	$D_{RB} = D_{RB1} + D_{RB2}$ $D_{LB} = D_{LB1} + D_{LB2}$	$A_{RB} = \pi \cdot (D_{RB3}/2) \cdot (D_{RB4}/2)$ $A_{LB} = \pi \cdot (D_{LB3}/2) \cdot (D_{LB4}/2)$	Right brow Left brow
Close eyes	$D_{RE} = D_{RE1}$ $D_{LE} = D_{LE1}$	$A_{RE} = \pi \cdot (D_{RE1}/2) \cdot (D_{RE2}/2)$ $A_{LE} = \pi \cdot (D_{LE1}/2) \cdot (D_{LE2}/2)$	Right eye Left eye
Smile	$D_{RL} = D_{RL1} + D_{RL2}$ $D_{LL} = D_{LL1} + D_{LL2}$	$A_L = \pi \cdot (D_{L1}/2) \cdot (D_{L2}/2)$	Right lip Left lip

Table 4 Individual score chart

$\% \Delta$	Score assigned
<1	0
1–5	1
6–10	2
11–15	3
16–20	4
21–25	5
26 and above	6

Table 5 Paralysis score chart

House-Brackmann grade	Descriptions	Total score
I	Normal	22–36
II	Slight dysfunction	11–21
III	Moderate dysfunction	7–10
IV	Moderate severe dysfunction	4–6
V	Severe dysfunction	1–3
VI	Total paralysis	0

Afterwards, a total score can be obtained after all the three exercises have been conducted by the subject. Again based on the repeated trials and also from the logical judgment of the circumstantial evidence from the previous records of patient, a paralysis score chart was designed with the agreement with medical professionals as presented in Table 5. The total scores can demonstrated the condition of subjects whether he/she is having a normal facial function or a patient with House-Brackmann level of paralysis. Based on this table, the ranges from 22 to 36 has indicated the lowest grade of House-Brackmann which is level I and the subjects classified as normal and having a normal facial function. If the subject was classified with above than level I of House-Brackmann, it can be determined that the subject is a patient and has abnormal facial function with different degrees of paralysis.

3 Results and Discussions

For the results analysis purposes, the reference data (ground truth) used is the assessment results acquired from a medical professional which consists of condition of subjects, paralyzed side and HB level of paralysis. The outcomes of the regional assessment for all the subjects were compared with the reference data by tested on different measurements, distance and area, to determine the most eligible parameter to be implemented in the final system.

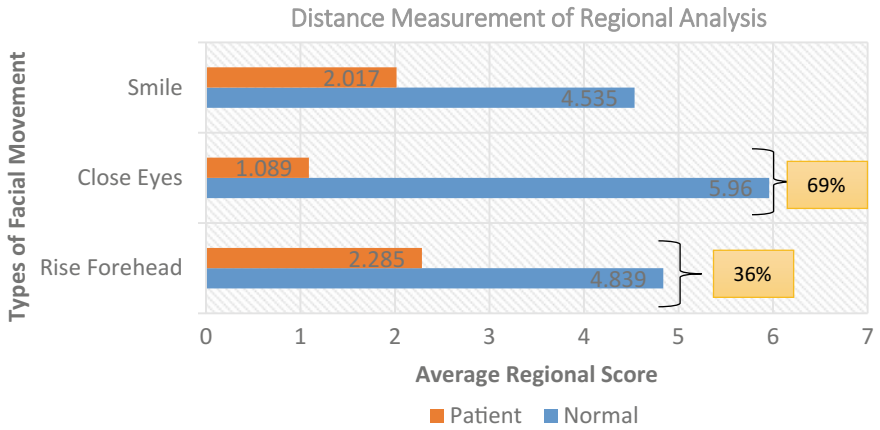


Fig. 1 Distance measurement of regional analysis

From Fig. 1, the results shows that the closing eyes movement in distance measurement present the highest percentage of differences of regional score between the normal and patient subjects. For the Bells' palsy patients, the affected eye is easily open since the muscle which opens the eye is activated by separate cranial nerve. However, the patients will have difficulties in closing their eyelids. As a consequence, most patient with Bell's palsy has suffered eye syndrome known as exposure keratitis. Besides that, the other types of movement, smiling and forehead rising, also gives good results for the distance measurement since the differences between normal and patients have been classified well.

For area measurement in this regional analysis, the results is shown in Fig. 2, the overall results are not desirable because the percentage differences of average regional score for all types of movement are lower than the percentage differences in distance measurement. Even though the closing eyes movement is still the highest percentage compared to the other types of movement, however, with the low percentage of differences, the normal and patients cannot be classified well since the average scores are close by each other.

By comparing the results of distance and area measurement in the accuracy table as shown in Table 6, there are about 98% of patients can be classified well in the test group of distance measurement even though the categorization of normal subjects is not appears so good. The faults are mainly presented due to the lower score of normal subjects in raising their forehead and smiling movement. It is because that the normal subject may have some difficulties in raising their forehead even though they have the normal facial nerve function. In addition, in smiling movement, there are three distinct types of smile which using the different facial muscle combinations to smile [15]. There are 'reward', 'affiliation' and 'dominance' smiles. So, the subjects may smile in various ways which consequently make the results becomes unstable and not accurate. These problems should be dealt properly by strictly asking the subjects

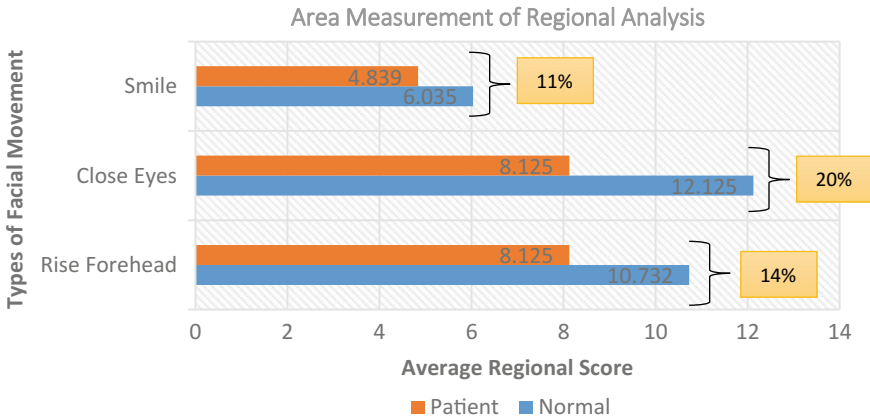


Fig. 2 Area measurement of regional analysis

Table 6 Accuracy table of distance and area measurement

Types of measurement	Subject type	Number of data	Number of correctly classified data	Overall accuracy (%)
Distance	Patient	56	55	98
Area	Patient	56	17	30

to do a precise movement in the next experiment. Then, higher accurate regional analysis of facial nerve paralysis by using distance measurement will be developed.

4 Conclusions

The important element in this study is the refinement of our previous regional system. It is proved based on the demonstration above, that the proposed system is robust and reliable to be implemented in the final assessment system of facial paralysis. By using the same method as our previous work, this regional system was tested with different group of subjects and also different location of experiment added with new lighting system. As a result, the patients were classified well at about 98% of accuracy using the distance measurement in spite of different environments, lighting condition and type of subjects. Furthermore, the proposed regional method was able to provide a quantitative measurements on each regional parts with individual scores. Clinicians can benefited from these attributes to find out which muscles of the patients are facing problems. In addition, the proposed approach can also facilitate the clinicians to systematically detect the improvements of a patient’s exercise through the level of House-Brackmann offered by this system. Moreover, even though with the different types of subjects, environments and light sources, the distance still shows the good

results in determining the regional condition of facial paralysis. Besides that, the closing eyes movement has affected the most of the results in classifying between the patients and normal subjects. The limitation in the smiling and raising forehead movement are mainly introduced by unintentional movement of the face and lead to incorrect estimation of the optical flow. Thus, encouraging the patient to execute the facial movements in an accurate manner should ameliorated the performance of the regional system.

Acknowledgements This research is funded by Fundamental Research Grant Scheme (RDU160143). Many thanks to Director General of Health Malaysia for giving the authorization to publish this paper. Finally, we thank the Medical Research and Ethics Committee (MREC) of Malaysia for providing the ethical approval to collect the data from Hospital Tuanku Fauziah (Ref. No.: NMRR-12-1195-14374). Finally, thanks also goes to the Ministry of Higher Education (MoHE) for the financial support.

References

1. Gordin, E., et al.: Facial nerve trauma: evaluation and considerations in management. *Cranioaxillofacial Trauma Reconstr.* **8**(1), 1 (2015)
2. Singhi, P., Jain, V.: Bell's palsy in children. *Semin. Pediatr. Neurol.* Elsevier (2003)
3. Keane, J.R.: Bilateral seventh nerve palsy analysis of 43 cases and review of the literature. *Neurology* **44**(7), 1198–1198 (1994)
4. House, J.W., Brackmann, D.E.: Facial nerve grading system. *Otolaryngol. Head Neck Surg.* **93**(2), 146–147 (1985)
5. Minamitani, H., et al.: Computerized diagnosis of facial nerve palsy based on optical flow analysis of facial expressions. In: *Engineering in Medicine and Biology Society, 2003. Proceedings of the 25th Annual International Conference of the IEEE*, pp. 663–666 (2003)
6. Samsudin, W.S.W., Sundaraj, K.: Evaluation and grading systems of facial paralysis for facial rehabilitation. *J. Phys. Ther. Sci.* **25**(4), 515–519 (2013)
7. Samsudin, W.S.W., Sundaraj, K.: Clinical and non-clinical initial assessment of facial nerve paralysis: a qualitative review. *Biocybern. Biomed. Eng.* **34**(2), 71–78 (2014)
8. Samsudin, W.S.W., Kenneth Sundaraj, R.S., Abdullah, N.R.H.: Correlation of objective assessment of facial paralysis with House-Brackmann score. *Telkomnika* **15**(2), 829–835 (2016)
9. Samsudin, W.S.W., et al.: Initial assessment of facial nerve paralysis based on motion analysis using an optical flow method. *Technol. Health Care* **24**(2), 287–294 (2016)
10. Lucas, B.D., Kanade, T.: An iterative image registration technique with an application to stereo vision. In: *International Joint Conference on Artificial Intelligence*, pp. 674–679 (1981)
11. Tomasi, C., Kanade, T.: Detection and tracking of point features, Technical report, CMU-CS-91-132 (1991)
12. Ali, S., Shah, M.: A Lagrangian particle dynamics approach for crowd flow segmentation and stability analysis. In: *2007 IEEE Conference on Computer Vision and Pattern Recognition*, pp. 1–6 (2007)
13. Fradet, M., Robert, P., Pérez, P.: Clustering point trajectories with various life-spans. In: *2009 Conference for Visual Media Production*, pp. 7–14 (2009)
14. Hu, M., Ali, S., Shah, M.: Detecting global motion patterns in complex videos. In: *19th International Conference on Pattern Recognition ICPR 2008. IEEE*, pp. 1–5 (2008)
15. Rychlowska, M., et al.: Functional smiles: tools for love, sympathy, and war. *Psychol. Sci.* **28**(9), 1259–1270 (2017)

Design of Ultra-Wideband (UWB) Horn Antenna for Non-destructive Fruit Quality Monitoring



Nurhafizah Abu Talip @ Yusof, Syamimi Mardiah Shaharum, Ahmad Afif Mohd Faudzi, Sabira Khatun, Mohamad Shaiful Abdul Karim and Siti Fatimah Hazali

Abstract This paper presents an ultra-wideband pyramidal horn antenna for non-destructive fruit quality monitoring system. The proposed design simulation operates in the frequency range of 3.1–10.6 GHz. The antenna is supported by the rectangular waveguide feeder. The design is chosen based on the ability of the antenna to transmit and receive signal with wide bandwidth, high directivity and gain, and low Voltage Standing Wave Ratio. The antenna is designed and simulated by using Computer Simulation Technology Microwave Studio. The simulation result also validated by the experimental result. The simulation result shows that the proposed UWB pyramidal horn antenna exhibits small return loss with low VSWR as well as good radiation pattern in the frequency range of 3.1–10.6 GHz.

Keywords Ultra-wideband antenna · Horn antenna · Fruit quality Non-destructive

1 Introduction

Local fruit industry has a potential to export the fruits globally to accommodate demands on the fresh tropical fruits, e.g., mangoes, bananas, papayas, etc. Hence, it is necessary to ensure the quality of the fruits prior to export. The main fruit quality characteristics include, the level of maturity, ripeness, and moisture content. Traditional local technique normally characterizes the fruit quality by their appearance, which based on human gut feeling and their experiences. The quality can be very subjective to harvesters' experience. Some works have been done and adopted to characterize fruit quality based on electrical properties, which include

N. Abu Talip @ Yusof (✉) · S. M. Shaharum · A. A. Mohd Faudzi · S. Khatun
M. S. Abdul Karim · S. F. Hazali
Faculty of Electrical and Electronics Engineering, Universiti Malaysia Pahang, 26600 Pekan,
Pahang, Malaysia
e-mail: hafizahs@ump.edu.my

© Springer Nature Singapore Pte Ltd. 2019
Z. Md Zain et al. (eds.), *Proceedings of the 10th National Technical Seminar on Underwater System Technology 2018*, Lecture Notes in Electrical Engineering 538,
https://doi.org/10.1007/978-981-13-3708-6_45

complex permittivity. Those works are based on either infrared or radio frequency (RF), but the used power level is high. As a result, ionization of fruit flesh is undetermined, although those are claimed as non-destructive. Hence, a non-destructive and non-ionizing automatic detection system is in demand. Ultra-Wideband (UWB) is a promising RF technique to overcome all the above problems (including ionizing) and is suitable to be used for any kind of living things. UWB-based works have been done for early cancer detection successfully without any negative impact on human health [1].

The quality of fruits is mainly affected by moisture content that can be closely related to electrical properties (dielectric properties) [2, 3] especially when water content is high. Some of characterization method of electrical properties utilized infrared spectroscopy (0.3–430 THz) [4]. However, penetration in fruit for infrared is shallower than microwave that might lead to inaccurate material characterization. In addition, at higher frequencies, i.e., infrared, ionization might happen and decrease water level in the fruit. At microwave frequency (0.3–300 GHz), most common characterization methods that have been used to assess electrical properties for fruit are open-ended coaxial cable [5, 6], transmission-line [7] and resonant method [2, 5]. These methods require sample to be processed and placed in a holder or container that can cause damage on the fruit. Meanwhile, transmission-line characterization method can afford wide frequency measurement. However, the sample under test has to be prepared precisely as it needs to fill the whole cross-section of waveguide. Resonant method promises a very accurate measurement but only limited for low-loss material which is not applicable for dielectric measurement of flesh fruits. In addition, same as transmission-line method, precise sample preparation is necessary. Hence, these three methods are not recommended for non-destructive and non-ionization dielectric measurement.

Presently, free space characterization method [8] is the easiest method to assess material property as no sample preparation needed. Furthermore, this method can be implemented on-site at plantation farm easily. In creating the free space characterization method, a high precision design of antenna is needed. Therefore, in this paper we proposed a design of UWB pyramidal horn antenna that can operate and has good radiation pattern over 3.1–10.6 GHz of frequency band for fruit quality monitoring.

2 Methodology

In this paper, the approximation value of gain 15 dB is utilized to design the pyramidal horn antenna as well as to indicate the overall size of the antenna. In designing the proposed antenna, the feeding waveguide of the antenna is selected based on the desired frequency range (Fig. 1).

The selected inner dimension is $47.55 \times 22.15 \text{ mm}^2$ which supports the frequency range of 3.95–5.85 GHz (G-Band) and it closer to WR-187. The calculation of the aperture dimension $W_2 \times H_2$ has been executed under the same length of E-plane and H-plane. It shows that E and H planes are under the equal beam width. The 15 dB

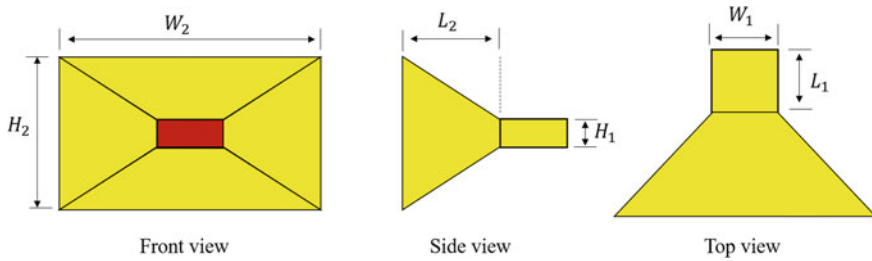


Fig. 1 Basic design of pyramidal horn antenna

Table 1 The parameter of UWB pyramidal horn antenna

Parameter	Dimension (mm)
Width of waveguide, W_1	47.55
Height of waveguide, H_1	22.15
Length of waveguide, L_1	47.75
Width of horn, W_2	139.18
Height of horn, H_2	113.65
Length of horn, L_2	113.87

gain is chosen due to design a small and compact UWB pyramidal horn antenna. Table 1 shows the parameter dimensions of the proposed antenna.

3 Result and Discussion

The completed design of UWB pyramidal horn antenna is simulated in Computer Simulation Technology (CST) software. The parameters that are obtained from the simulation result are the S11 (return loss), frequency, voltage wave standing ratio (VSWR), gain, directivity, radiation pattern, and bandwidth. Figure 2a shows the S11 parameter result that indicates to the amount value of return loss of the designed horn antenna.

The simulation results of reflection coefficient of S11 is less than -10 dB for frequency operated between 3 and 11 GHz. When the return loss is lower than -10 dB, it gives the signal radiated almost in equilibrium state. The signal transmitted and the signal received in the horn antenna are almost perfect with lower attenuation. This indicates that the strength of the signal received during transmission is stable enough to produce a precise picture of the data. The performance of the horn antenna is also validated by the simulation results of VSWR. Figure 2b shows the value calculated VSWR through simulation. The peak value of VSWR shown is 1.43 which is less than 2 and it is considered as fairly well produced transmission signal with lower attenuation result.

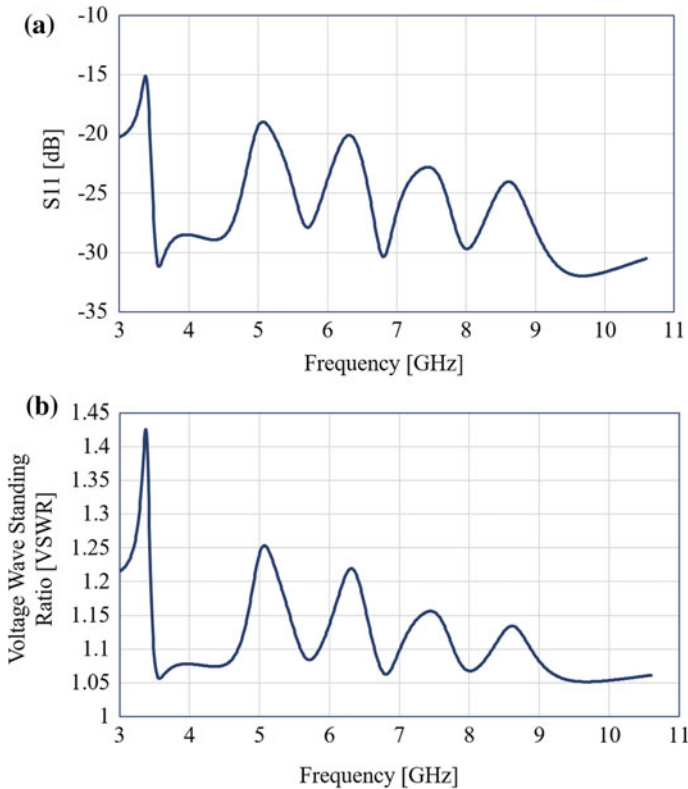


Fig. 2 Frequency characteristics of simulation result; **a** return loss, **b** VSWR

In the development of UWB pyramidal horn antenna, antenna gain is the most essential in the fundamental property of an antenna. In order to ensure the size of horn antenna small and to achieve the target of approximation, the gain produced must be around 15 dB. Figure 3a shows gain 15.21 dB of the horn antenna through simulation. It is increased by 0.21 dB from approximated gain with the efficiency of software simulation. The gain 15.21 dB is expected enough for the antenna to be used in non-destructive fruit quality monitoring system. The ability of the signal penetration into the flesh of the fruit is subjected to the power gain of the antenna.

As the gain increased, the directivity produced also increased. The region with maximum gain and strongest emission of the signal radiated is the reference of directivity. Stronger radiated signal through the aperture of the pyramidal horn antenna will lead to the higher directivity. As shown in Fig. 3b, the obtained directivity is 15.25 dBi at frequency 7 GHz as respected to isotropic antenna.

The radiation pattern of UWB pyramidal horn antenna basically consists of main lobe, side lobes and back lobe. The simulated magnitude of the main lobe obtained is 15.2 dBi while side lobe is -14.3 dB, as shown in Fig. 3c. This shows that more

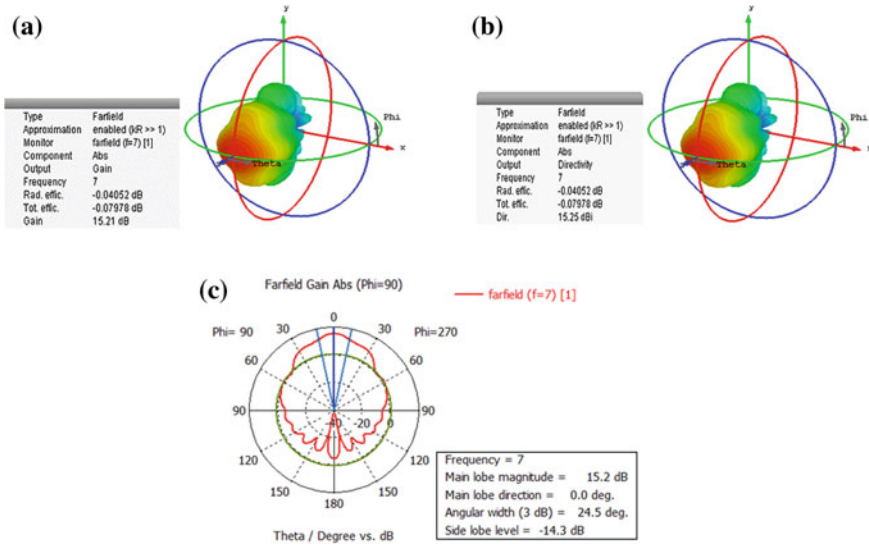


Fig. 3 a Gain 15.21 dB, b directivity 15.25 dBi, c radiation pattern at 7 GHz

power is radiating through main lobe compared to other directions which comes from side lobes and back lobes. A narrow main lobe leads to higher intensity of radiation. Radiation pattern is representative of the electromagnetic power distribution in the free space and relatively considered as the field strengths of the field radiated by the antenna [9].

Figure 4 shows the graph of S11 parameter from the fabricated UWB pyramidal horn antenna. The fabricated antenna is tested by utilizing Keysight (Agilent) E5072A 2-Port Network Analyzer, 30 kHz–4.5/8.5 GHz as shown in Fig. 5. An aluminium of 1 mm thickness with 3.5×10^7 S/m conductivity is used to fabricate the antenna. Due to the limitation of frequency range that can be covered with the available measurement devices, the return loss amount is recorded in between 3 and 8.5 GHz. The return loss is below than -10 dB starting from 3.5 GHz until 7.5 GHz, which is not cover the UWB frequency range and not in good agreement with simulation result. The main factor that leads to this error is imperfection during fabrication since there are outstanding air gap at the junction between top and side metal. Furthermore, dimension error of fabricated horn antenna may cause the error. The graph falls at frequency 3–4 GHz with -48 dB. The more the graph falls the better the performance of antenna for monitoring system, as the return loss is small. When the return loss is small the performance of antenna for non-destructive fruit quality monitoring is more effective.

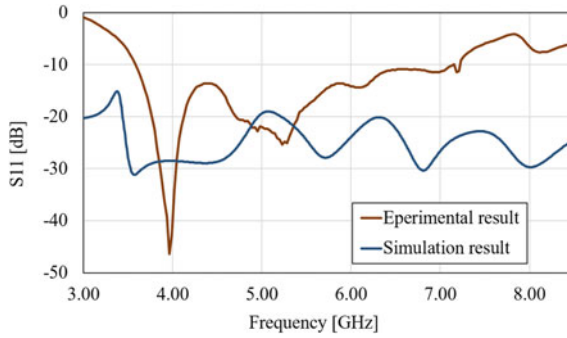


Fig. 4 Experimental and simulation result of return loss UWB pyramidal horn antenna

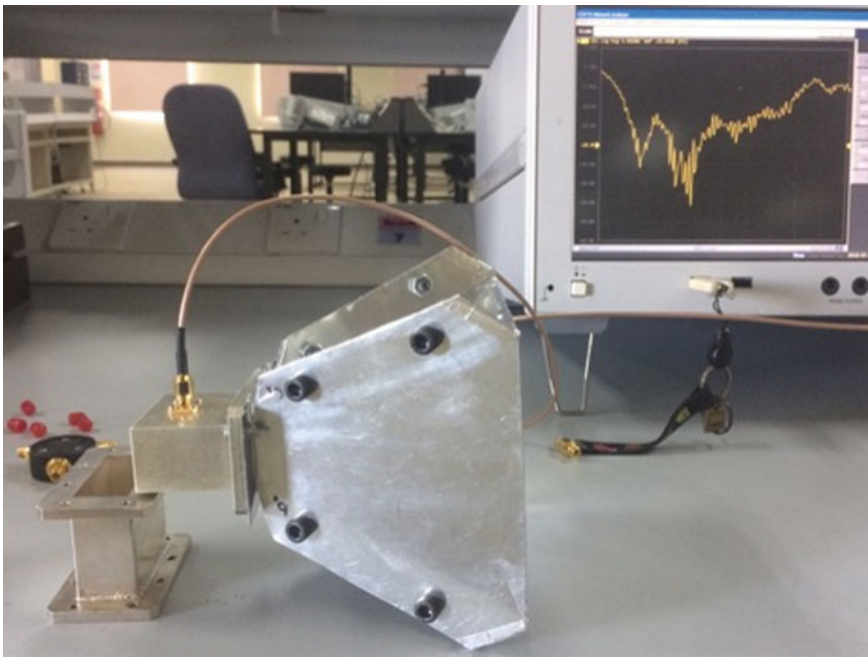


Fig. 5 Fabricated UWB pyramidal horn antenna connected to vector network analyzer

4 Conclusion

The proposed design simulation of UWB pyramidal horn antenna with rectangular waveguide feeders provides wide bandwidth, high directivity and gain, and low VSWR. The design simulation is validated by the return loss of fabricated horn antenna which gives less than -10 dB in the frequency range of 3.5–7.5 GHz. This indicates that the fabricated antenna can transmit and receive the signal effectively.

Hence, it is possible to be used in monitoring the quality of the fruit by creating the free space characterization method using the proposed antenna design.

For future improvement, the UWB pyramidal horn antenna can be improved in terms of its design. The design can be changed or improved in order to get better antenna performance. The aperture design of horn antenna can be added with tapered ridges to increase the gain and directivity. The amount value of VSWR also can be suppressed by adding the ridges inside the antenna. The added ridges inside the horn antenna will be designed on H-plane and E-plane, allowing the signal to propagate and focus to one direction with strong radiation. The radiation becomes narrower and stronger, and will contribute to higher accuracy of detection to apply in non-destructive fruit quality monitoring.

Acknowledgements This work is supported by Universiti Malaysia Pahang Internal Grant of RDU1703236.

References

1. Karli, R., Ammor, H., Shubair, R.M., AlHajri, M.I., Alkurd, R., Hakam, A.: Miniature planar ultra-wide-band microstrip antenna for breast cancer detection. In: Microwave Symposium (MMS), 2016 16th Mediterranean. IEEE, pp. 1–4 (2016)
2. Karim, M.S.B.A., Abu Talip Yusof, N., Kitazawa, T.: Scattering analysis of rectangular cavity with input and output waveguides and its application to material characterization. In: 2017 IEEE Asia Pacific Microwave Conference (APMC), Kuala Lumpur, pp. 588–591 (2017)
3. Karim, M.S.B.A., Konishi, Y., Kitazawa, T.: Robustness analysis of simultaneous determination method of complex permittivity and permeability. In: 2014 International Conference on Numerical Electromagnetic Modeling and Optimization for RF, Microwave, and Terahertz Applications (NEMO), Pavia, pp. 1–4 (2014)
4. Jha, S.N., et al.: Nondestructive prediction of maturity of mango using near infrared spectroscopy. *J. Food Eng.* **124**, 152–157 (2014)
5. Chen, J., et al.: Temperature-dependent dielectric and thermal properties of whey protein gel and mashed potato. *Trans. Am. Soc. Agric. Biol. Eng.* **56**(6), 1457–1467 (2013)
6. Nelson, S.O., Trabelsi, S.: Historical development of grain moisture measurement and other food quality sensing through electrical properties. *IEEE Instrum. Meas. Mag.* **19**(1), 16–23 (2016)
7. Karim, M.S.B.A., Konishi, Y., Harafuji, K., Kitazawa, T.: Determination of complex permittivities of layered materials using waveguide measurements. *IEEE Trans. Microw. Theory Tech.* **62**(9), 2140–2148 (2014)
8. Kim, S., Novotny, D., Gordon, J.A., Guerrieri, J.R.: A free-space measurement method for the low-loss dielectric characterization without prior need for sample thickness data. *IEEE Trans. Antennas Propag.* **64**(9), 3869–3879 (2016)
9. Othman, M.A., Aziz, M.Z.A.A., Saysoo, N., Othman, A.R.: Development of ultra-wideband (UWB) horn antenna using approximation method. In: IEEE Symposium on Wireless Technology and Applications (ISWTA), pp. 276–279 (2012)

Ionospheric Modeling and Precision Positioning Global Navigation Satellite System



Nurul Fazira Abd Rahman, Sabira Khatun, Kamarul Hawari Ghazali, Md. Moslemuddin Fakir, Mamunur Rashid and Bifta Sama Bari

Abstract In ionosphere, the total electron content (TEC) contributes a significant role in determining the scintillation. Ionospheric scintillation can affect severely in satellite-based navigation and communication systems. Thus, the study of TEC of ionosphere is very crucial. The correlation between TEC and temperature in different weather and time has been presented in this paper. The TEC data was taken from the global positioning system (GPS) receiver at University Malaysia Pahang, Malaysia (120° 24.7388'E and 36° 14.5310'N). These data were analyzed by the SPSS software using multiple regression and leveling process methods, then a model for TEC estimation has been proposed. The results show that during sunny weather, the TEC is highly correlated with temperature compared to the rainy weather. TEC is also correlated with time, the maximum correlation is found ~94% with corresponding TEC value ~35.24. The highest TEC can be obtained from 12 pm to 4 pm, which is around 35 in average. Besides, multiple regression method enhanced TEC estimation accuracy ~8.77% than leveling process method.

Keywords Total electron content (TEC) · Ionospheric scintillation · GNSS

1 Introduction

The portion of atmosphere that holds charged particles is known as ionosphere and this region lies 70–1000 km above the Earth. These ionized particles change their speed of propagation and trajectory when they react with a propagating electromagnetic wave [1]. There are some often occurred disturbances in the ionospheric

N. F. Abd Rahman · S. Khatun (✉) · K. H. Ghazali · M. Rashid · B. S. Bari
Faculty of Electrical and Electronics Engineering, Universiti Malaysia Pahang, Pekan, Pahang, Malaysia
e-mail: sabirakhatun@ump.edu.my

Md. M. Fakir
CARIFF, Faculty of Chemical & Natural Resources Engineering, Universiti Malaysia Pahang, Gambang, Pahang, Malaysia

© Springer Nature Singapore Pte Ltd. 2019

Z. Md Zain et al. (eds.), *Proceedings of the 10th National Technical Seminar on Underwater System Technology 2018*, Lecture Notes in Electrical Engineering 538, https://doi.org/10.1007/978-981-13-3708-6_46

523

region which are scintillation, travel ionosphere disturbance (TID), plasma bubble etc. [2]. Ionospheric scintillation is the prompt alteration of amplitude and/or phase of global navigation satellite system (GNSS) signal when the ionospheric abnormalities are appeared [3]. Because of amplitude scintillations, the positioning accuracy of GPS may degrade and this phenomenon also causes the data loss in GPS receiver while the phase scintillation causes the phase lock loss [4]. The scintillation varies on some factors which are the regional time, season, magnetic and solar activity and magnetic latitude. At low latitudes and at high latitudes, the scintillation happening is the most severe [5–8]. TEC is another important feature in the ionospheric research and it is the total amount of electrons exist along the signal path from the GPS satellite to the receiver. The proper ionospheric model contributes the largest role in navigation and communication systems based on satellite. If the ionospheric model is not sufficiently well, then it creates error in single frequency of GNSS receivers [9]. To mitigate the ionospheric disturbance, study of characteristics of ionospheric TEC is essential as it influences the propagation of the short waves. During storm, ionospheric scintillation and change in TEC have been studied in [10] and the results have shown that pronounced phase and amplitude scintillations and dramatic rise in TEC is clearly noticed during the storm. Zou et al. [11] have observed that amplitude scintillations of nighttime at Guilin, china always took place with TEC fluctuations and phase scintillations but TEC vacillations never occurred during scintillations of daytime. The morphologic features of ionospheric scintillations and TEC fluctuations and their impacts on the performance of GPS receiver have been absent in their findings. Ya'acob et al. [12] gave their focus on the observation of equatorial plasma bubbles (EPBs) due to solar flare event in Malaysia. The result shows that plasma bubbles commence three days after the solar flare event occurred and affect the ionosphere layer which can cause the ionospheric disturbance. The ionospheric scintillation is rarely noticed at daytime but seen frequently during nighttime reported in [13, 14]. Moreover, the highest TEC seasonal variation is found in the equinoxes whereas the lowest in the summer and winter. In reference [15], the highest GPS amplitude scintillation is seen in the months of equinoctial solar maximum. An analysis on the correlation of scintillation index S4 and TEC depletion index has been also done and the result shows a well consistency during post-sunset hours. In this paper, the correlation between TEC, temperature and time has been analyzed in different time and weather.

2 Methodology

An overall work procedure of this research is shown in Fig. 1. The data is received from the satellite through the receiver and then processed using a data transform software known as SPSS software. To find data trend, it is necessary to plot the data for every day (day basis) and observe whether there occurred any trend changing or not. With the satisfied trend identification, the subsequent step is to develop a model.

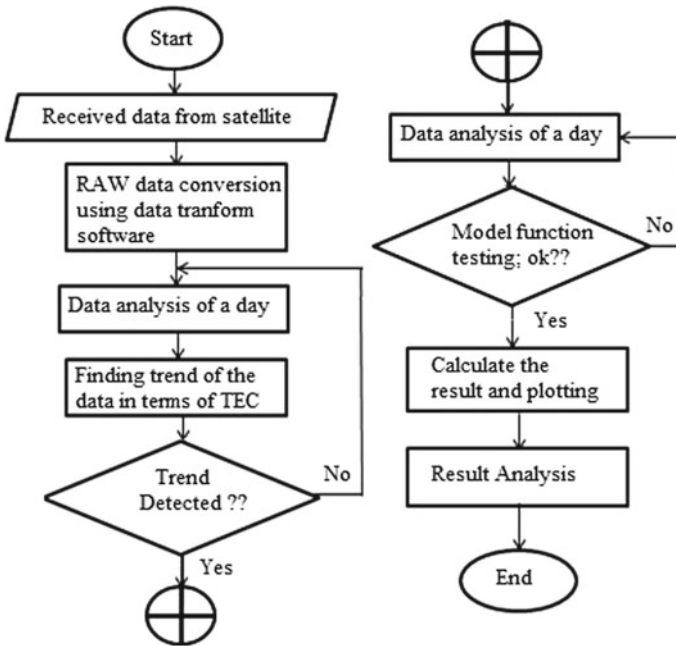


Fig. 1 Flow chart of the data analysis

2.1 TEC Calculation Using Multiple Regressions

The purpose of a model using multiple regressions is to learn the relationship between independent as X terms and dependent as Y terms. The dependent variable is something like a target or criterion variable. Multiple regressions are an extension equation from a simple linear regression. It is used to express an outcome in advance, for some values of a variable, which depends on the values of two or more variables. In this model, the parameter TEC, time and temperature are denoted as Y, X1 and X2. Then the average of each variable is calculated to include into multiple regressions.

$$\tilde{Y} = \frac{(Y_1 + \dots + Y_n)}{N} \tag{1}$$

$$\ddot{X}_1 = \frac{(X_1 + \dots + X_n)}{N} \tag{2}$$

$$\ddot{X}_2 = \frac{(X_1 + \dots + X_n)}{N} \tag{3}$$

where, Y is the TEC, X1 is the time, X2 is the temperature, and N is the total number of data. The parameter, $i = 1, 2, 3, \dots, n$. The value of β_0, β_1 and β_2 are calculated with Eqs. (4) and (5) as follows.

$$\beta_1 \text{ and } \beta_2 = \frac{\sum(\ddot{X}_i - \ddot{X})(\ddot{Y}_i - \ddot{Y})}{\sum(\ddot{X}_i - \ddot{X})} \quad (4)$$

$$\beta_0 = \ddot{Y} - \beta_1 \ddot{X}_1 - \beta_2 \ddot{X}_2 \quad (5)$$

Finally, the value of β_0 , β_1 and β_2 are need to substitute into the equation of multiple regression as in Eq. (6).

$$Y = \beta_0 + \beta_1 X_1 + \beta_2 X_2 + \dots + \beta_n X_n \quad (6)$$

2.2 TEC Calculation Using Leveling Process

Each GPS positioning satellite transmits two electromagnetic carrier waves which are denoted by L1 and L2. The frequency used for L1 and L2 are 1575.42 and 1227.60 MHz respectively. A fundamental frequency is marked as f_0 and the value is 10.23 MHz. The relations among f_1 , f_2 and f_0 are: $f_1 = 154 f_0$, whereas $f_2 = 120 f_0$. Since the carrier frequencies holds codes modulation, TEC study can be done with the help of both phase and code measurements of L1 and L2. The dissimilarity in ionospheric delay between L1 and L2 is measured by a GPS receiver of dual-frequency and the equation of group delay can be expressed as in Eq. (7).

$$P_2 - P_1 = 40.3 TEC \left(\frac{1}{f_2^2} - \frac{1}{f_1^2} \right) \quad (7)$$

where, P_1 , P_2 denote the group path lengths, f_1 and f_2 are the corresponding high and low GPS frequency respectively. Thus, the TEC is expressed from Eq. (7) as follows.

$$TEC = \frac{1}{40.3} \left[\frac{f_1^2 f_2^2}{f_1^2 - f_2^2} \right] (P_2 - P_1) \quad (8)$$

3 Results and Discussions

The data have been collected from 9 November 2017 until 11 May 2018. An excellent trend has been found based on the correlation between time and TEC. Five days for high correlation and another five days for low correlation have been taken as reference to see the factor of TEC changes as shown in Fig. 2. From the comparison between high and low correlations for TEC and time, it is seen that during the high correlation, the condition of weather was good and no rain was recorded during that time period. This happens due to the increased number of electron with increased radiation from the hot sun (resulting higher temperature) during sunny days in tropical weather in Malaysia. This indicates TEC is directly proportional to sun-activity (as more

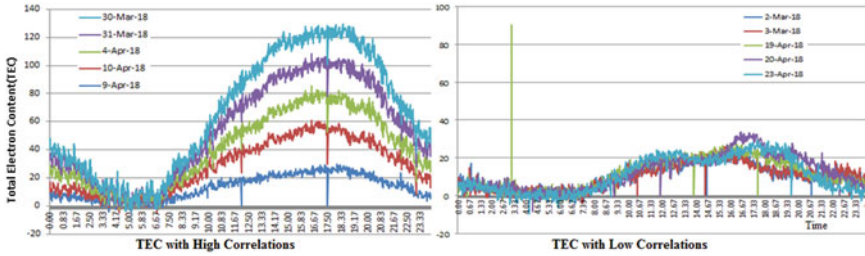


Fig. 2 Graph of TEC with high and low correlations

electron emitted at ionospheric layer due to more or strong sun-light and heat as usual). The average TEC was also in increasing trend on those days. The highest correlation has been observed about 94% with maximum TEC value ~35.24 on 10 April 2018 during good weather. Whereas the lowest correlation is about 74% with minimum TEC value of ~-3.27 on 2 March 2018 during rainy weather.

The correlation between TEC, temperature and time has been compared between good and rainy weather for 7 days shown in Fig. 3. Roughly, the minimum TEC was occurred during post-midnight until morning, whereas the maximum TEC was occurred around post noon until evening. As TEC varies with temperature (as seen from Fig. 2), this phenomenon is as expected, because, the Sun comes closest to earth atmosphere during mid-day and the atmosphere start to become hotter to hottest at some point during post afternoon. Followed by, as the Sun starts to move apart, the temperature gradually reduces and reach to lowest after mid-night until the Sun rises in the next morning. This TEC-cycle is co-related and consistent with day-night Sun-cycle (24 h) and related temperature. It is also true for both sunny and cloudy/rainy weather. In average, within day-night cycle, the lowest temperature can be observed at around 5–6 am (~25 °C) with lowest TEC value (~0). Similarly, the highest temperature can be observed at around 2–3 pm (~31 °C) with high TEC value (~32) as shown in Fig. 4. Average is used to make the equation more precise and it reduces the error due to sufficient data. As we can see from Fig. 4, the average value for 30 days able to produce the TEC estimation closer to the actual TEC value.

The accuracy of TEC calculation with different methods is shown in Fig. 5. The accuracy of TEC calculation with multiple regression is 95.81% whereas for leveling process method it becomes 87.04%. It shows, multiple regression method is able to enhance the accuracy ~8.77% by demonstrating its efficiency. This happens because multiple regression method calculates the TEC values using adaptive weighting average by taking into account temperature and time (Eq. 6), as a result, the TEC values are very close approximation of actual compared to other method.

On the other hand, levelling process, there are some discrepancy because of assumption as: frequency L1 1575.42 MHz, L2 1227.60 MHz, and multiply by $(P_2 - P_1)$, pseudorange (distance between satellite and receiver based on speed of light), which is not realistic as shown in Eq. (8).

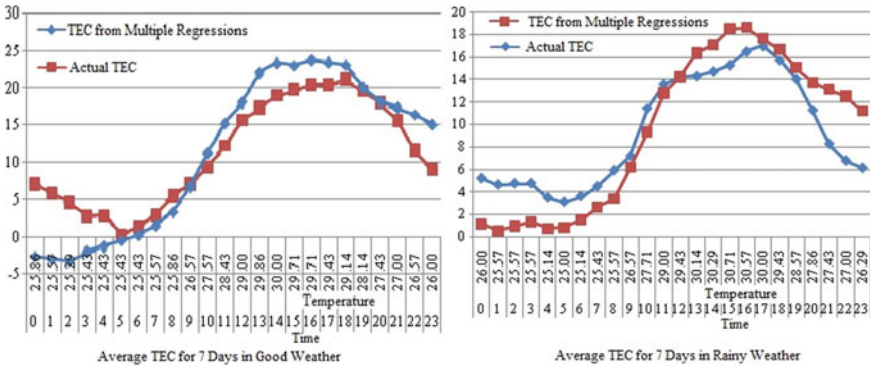


Fig. 3 Average TEC in good and rainy weather for 7 days

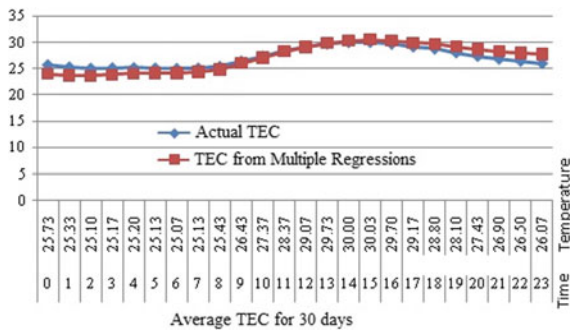


Fig. 4 Average TEC for 30 days

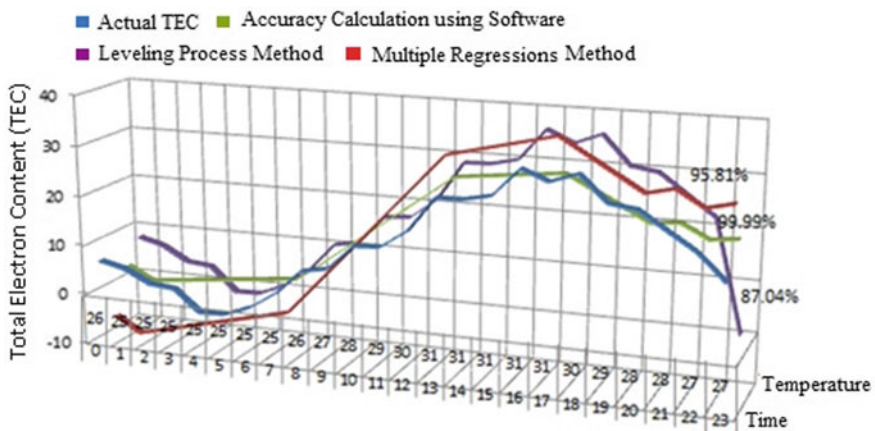


Fig. 5 Accuracy comparison of TEC calculation

4 Conclusion

The trend of TEC correlation with time and temperature in various weather conditions is observed and a model is proposed using multiple regression method. Several data have been used with multiple regression and leveling process methods for TEC calculation. During a good weather, the TEC is highly correlated with temperature compared to the rainy weather. TEC is also in good correlation with time, the highest correlation is around 94% (with corresponding TEC value ~ 35.24 for sunny weather); whereas, the lowest correlation is $\sim 74\%$ (with minimum TEC value of ~ -3.27 for rainy weather). The highest TEC and temperature can be found from 12 pm to 4 pm in tropical climate of Malaysia, which are in average approximately 30°C to 35°C respectively. However, sometime it may vary due to the local time, season and location. The multiple regression method is able to enhance TEC calculation accuracy $\sim 8.77\%$ more than leveling process method, by demonstrating its superiority.

Acknowledgements The authors would also like to thank the Faculty of Electrical & Electronics Engineering, University Malaysia Pahang for providing the facilities to complete this work. This work is supported by Internal Grant (with grant number RDU1703125) of University Malaysia Pahang (www.ump.edu.my).

References

1. Barclay, L.: Propagation of Radiowaves, 2nd edn. The Institution of Engineering and Technology, London (2003)
2. Ya'acob, N., Azmin, A., Yusof, A.L., Ali, M.T., Idris, A., Ali, D.M.: Mitigate the GPS ionospheric scintillation during solar flare. In: 2012 IEEE Control and System Graduate Research Colloquium. Shah Alam, Selangor, pp. 333–337 (2012)
3. Kintner, P.M., Ledvina, B.M., De Paula, E.R.: GPS and ionospheric scintillations. *Space Weather* **5**(9) (2007)
4. Bhattacharya, S., Purohit, P.K., Tiwari, R., Gwal, A.K.: Study of GPS based ionospheric scintillation and its effects on dual frequency receiver. *J. Eng. Sci. Manag. Educ.* **1**, 55–61 (2010)
5. Aarons, J.: Global morphology of ionospheric scintillations **70**(4), 360–378 (1982). (IEEE)
6. Basu, S., Basu, S.: Equatorial scintillations: advances since ISEA-6. *J. Atmos. Terres. Phys.* **47**, 753–768 (1985)
7. Alfonsi, L., Spogli, L., De Franceschi, G., Romano, V., Aquino, M., Dodson, A., Mitchell, C.N.: Bipolar climatology of GPS ionospheric scintillation at solar minimum. *Radio Sci.* **46**, RS0D05 (2011)
8. Sparks, L., Komjathy, A., Mannucci, A., Altshuler, E., Walter, T., Blanch, J., Bakry, M., Lejeune, R.: Extreme Ionospheric Storms and Their Impact on WAAS (2005)
9. Shanmugam, S., Jones, J., MacAulay, A., Van Dierendonck, A.J.: Evolution to modernized GNSS ionospheric scintillation and TEC monitoring. In: Proceedings of the 2012 IEEE/ION Position, Location and Navigation Symposium, Myrtle Beach, SC, pp. 265–273 (2012)
10. Hasbi, A.M., Ali, M.A.M., Misran, N.: Ionospheric TEC and scintillation during the 15–16 May 2005 major storm over equatorial anomaly region at ARAU. In: 2007 Asia-Pacific Conference on Applied Electromagnetics, Melaka, pp. 1–5 (2007)
11. Zou, Y., Wang, D., Shen, Q.: GPS scintillations and TEC monitoring at Guilin, China. In: 2008 International Workshop on Education Technology and Training & 2008 International Workshop on Geoscience and Remote Sensing, Shanghai, pp 429–433 (2008)

12. Ya'acob, N., Binti Suhaimy, S.N., Yusof, A.L., Hashim, M.S., Abd Razak, N.I.: Observation of GPS TEC depletions due to equatorial plasma bubbles during solar flare. In: 2013 IEEE International Conference on Space Science and Communication (IconSpace), Melaka, pp. 128–133 (2013)
13. Seif, A., Abdullah, M., Hasbi, A.M., Zou, Y.: Observation of GPS ionospheric scintillation at UKM, Malaysia. In: Proceeding of the 2011 IEEE International Conference on Space Science and Communication (IconSpace), Penang, pp. 45–50 (2011)
14. Tam Dao, N.H., Vinh Duong, V.: TEC and scintillation observed over Ho Chi Minh, Vietnam during 2009–2012. In: 2013 IEEE International Conference on Space Science and Communication (IconSpace), Melaka, pp. 434–439 (2013)
15. Ning, B., Li, G., Liu, K.: Characteristics of GPS ionospheric scintillation and TEC depletion in the Chinese low latitude region. In: 2016 URSI Asia-Pacific Radio Science Conference (URSI AP-RASC), Seoul, pp. 90–92 (2016)

Enhancing the Integrated Vaccine System (IVS) Using *MyKidVAX* Mobile Application



Mohd Azrul Hisham Mohd Adib, Nur Hazreen Mohd Hasni,
Nor Fazlin Zabudin and Muhammad Shahminan Lukman

Abstract The conventional manual method of recording vaccination information is less organized and difficult to be retrieved back. IVS is an integrated information technology system that tries to address the weaknesses in the conventional method by providing storage for child's vaccination data and the use of *MyKidVAX* grant parents as a reminder for the next vaccination date. A software editor called Dreamweaver is used in creating the IVS form. IVS showed more benefit with the use of this latest mobile application and positively progressed.

Keywords Integrated vaccine system · *MyKidVAX* · Mobile application
Cloud system · Database

1 Introduction

Development of integrated information technology system called Integrated Vaccine System (IVS) [1] incorporates the Hospital/Healthcare Information System (HIS) and Telemedicine aspirations. HIS is an integrated computer system installed throughout the hospital [2]. The objectives of HIS implementation are to ease data reporting and retrieval, reduce errors, increase efficiency, improves healthcare quality as well as better communication between healthcare providers [3]. Telemedicine was meant to provide healthcare and health-related services by using telecommunications, information and multimedia technologies to link the consumers, healthcare providers, suppliers, consumer and other agencies [4].

M. A. H. Mohd Adib (✉) · N. F. Zabudin · M. S. Lukman
Medical Engineering & Health Intervention Team (MedEHiT), Human Engineering Group,
Faculty of Mechanical Engineering, Universiti Malaysia
Pahang, 26600 Pekan, Pahang, Malaysia
e-mail: azrul@ump.edu.my

N. H. Mohd Hasni
Klinik Kesihatan Kurnia, Ministry of Health Malaysia (MOH), Batu 3,
25150 Kuantan, Pahang, Malaysia

© Springer Nature Singapore Pte Ltd. 2019
Z. Md Zain et al. (eds.), *Proceedings of the 10th National Technical Seminar
on Underwater System Technology 2018*, Lecture Notes in Electrical Engineering 538,
https://doi.org/10.1007/978-981-13-3708-6_47

The IVS system is about storing vaccine intake information in a database by the healthcare organization and retrieving the data as a reviewed schedule regarding vaccination dates and information by the parents on an application. The parents would also be notified for the next vaccination date through the application. The objective is to have a proper and organized information storage regarding vaccine intake information and also to alert the parents of the vaccination date which is not able to be fulfilled by the conventional manual method.

Albania, Vietnam, Guatemala, Senegal and South Sudan are among the countries that have implemented this integrated information technology system on vaccination. Immunization Information system (IIS) was developed by Albania to support birth and vaccination registration, vaccine stock management, cold chain management and hostile events management following vaccination [5]. More on IIS, it is a confidential computerized database that is population-based, recording all immunization doses residing in certain geopolitical areas. The advantages of IIS include providing the immunization histories that are consolidated to determine appropriate vaccination and also aggregate vaccination data for surveillance and program operations to improve vaccination rates and reduce diseases that can be prevented by vaccine. By having consolidated record, it can provide official immunization records for school, camping and other activities entry requirements. IIS also able to remind immunization due date, ensuring the children to only take the needed vaccination [6].

In Malaysia, this kind of vaccination integrated system has not been developed yet. For this time being, our Malaysia's experts under the programme of Immunise4life have developed an application called *MYVaksinBaby*. The application can provide information about vaccines and vaccines-preventable diseases. It provides a list of recommended vaccines under Malaysia's National Immunization Programme and also additional optional vaccines that can be obtained in private hospitals and clinics. Issues or questions such as the safety of vaccines and vaccination status in Islam are also addressed by the *MYVaksinBaby* application. Other than that, this app is also able to send auto-reminder for the next vaccination date [7].

In this paper, the integrated vaccine system for vaccination database is developed for address the weaknesses in the conventional method by preparing storage for vaccination information. Therefore, *MyKidVAX* enhanced the efficiency of the IVS system.

2 Methodology

2.1 Development Phase of IVS

The registration form is created using Bracket software. The script from the registration form is sent into phpMyAdmin database using php and SQLi coding. The "phpMyAdmin" is used to store the information such as background information of

the parents and babies, vaccination schedule (appointment date, type of vaccine and baby weight) and others. A software editor called Dreamweaver is used in creating the form. For the vaccine database consists of two separate tables: patient information table and vaccine schedule table. Patient information table is to store all data in the registration form while vaccine schedule table is to record vaccination information of the babies.

2.2 Implementation Phase of IVS

Person in-charge (PIC) has been trained by the researcher to help in data collection and registration process. PIC could be nurses or research assistant. They were registered and owned personal 'Username' and 'Password' to ensure data safety and confidentiality' (refer Figs. 1 and 2).

Registration process is the first step in data collection. Person in-charges will help to key-in the data (i.e.: demographic, birth details, vaccination status) into the IVS (refer Fig. 3). Once completed, parents will be given a unique ID.

Several features in IVS enables an efficient performance of medical personnel daily job. For examples, the whole list of patients registered in IVS can be view as below in Fig. 4. Therefore, it make easier for the medical personnel (i.e., nurses, or doctors) in detecting the patients status of vaccination). Moreover, the upcoming appointment of patient can be searched by date of appointment, as seen below in Fig. 5. The personal care concept which has been practicing among the nurses with their patients could promote a better health delivery and improves quality of care.

A simple data analysis (ready to be present) could be retrieve from the IVS. As shown below in Fig. 6, the demographic statistic of parents received vaccination at outpatient clinic. Not only for data storage, IVS could be simple analyzing tools and provides a virtual real time data which can benefit not only doctors, but also researcher.

Later, parents were asked to install *MyKidVAX* mobile apps (refer Figs. 7 and 8) through Google Play Store. Unique ID will be require at the main page to provide safety in archiving the data specifically the vaccination schedule and the next vaccination appointment date. Extra features available for parents; an automated notification alarm will appear one week and one day before the appointed vaccination date. The process will be repeats until the child reached age 2 years old; except for registration and application installation session.



Fig. 1 Top: safety login with ID and password and; bottom: main page appearance of the IVS

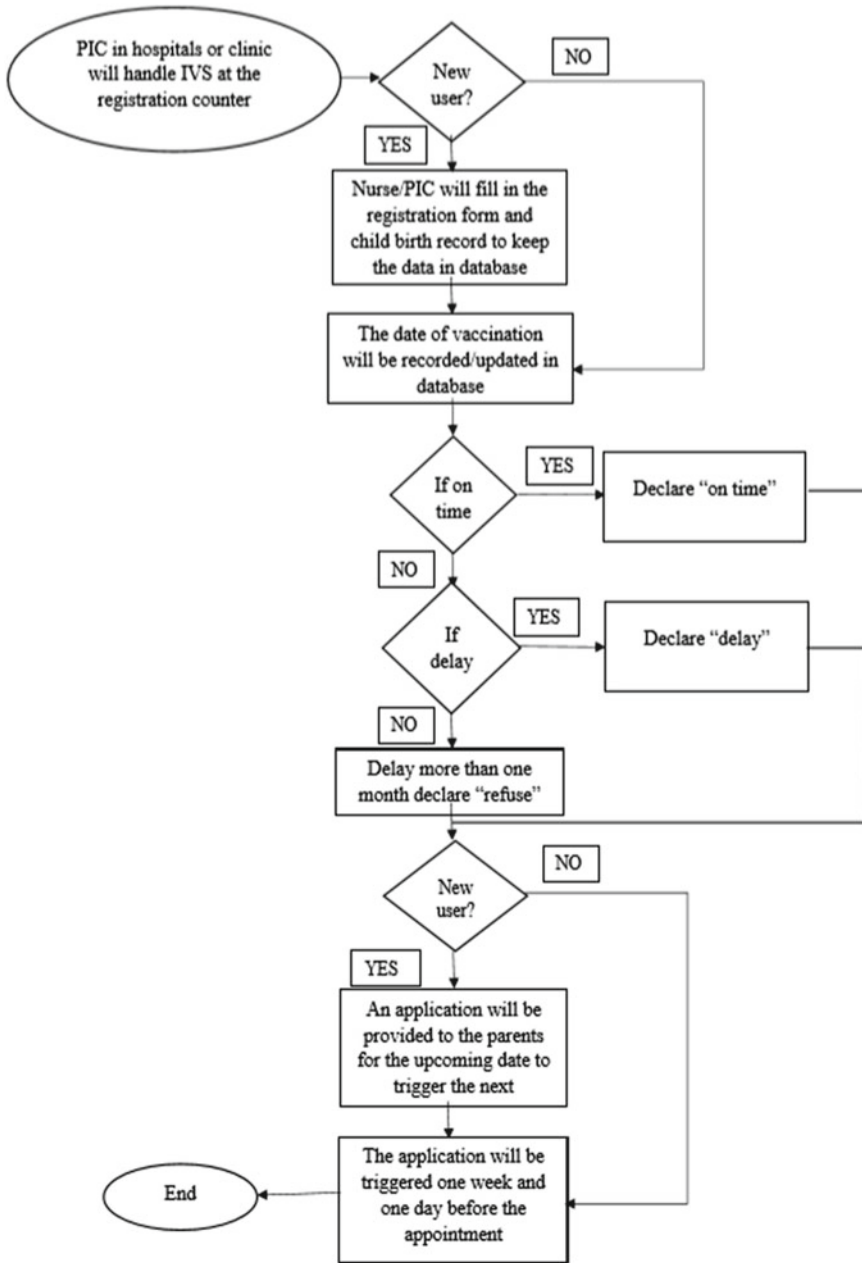


Fig. 2 Flowchart of IVS implementation

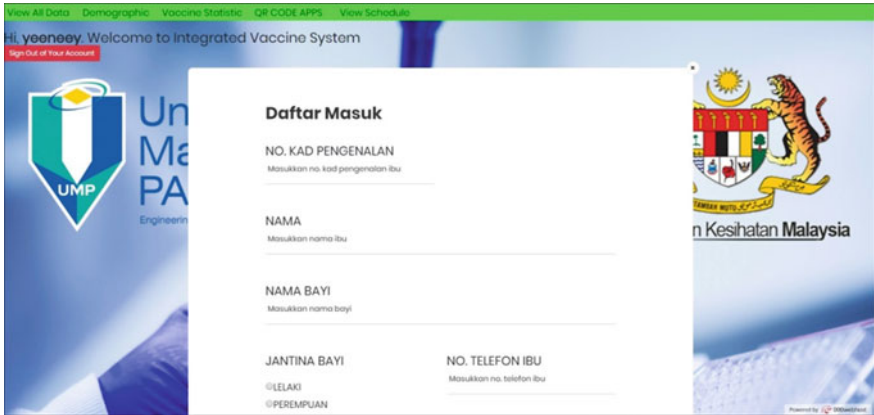


Fig. 3 IVS registration form

Home

NAME OF PATIENTS

ID NO.	INFANT'S NAME	MY KID NO.	MOTHER'S NAME	PHONE NO.	ACTION
18000002	B/O MASNIAH BINTI MOHAMMAD	KIV	MASNIAH BINTI MOHAMMAD	0199515377	Update Details Schedule
18000003	B/O ZULAIKA BINTI MOHD RAZALI	KIV	ZULAIKA BINTI MOHD RAZALI	0187865678	Update Details Schedule
18000004	NUR FATHIAH HILMAIRA BINTI MOHD FAIZAL	180521060756	ROSHAYU BINTI ZAKARIA	0129872950	Update Details Schedule
18000005	AMALIN NUR AISYAH BINTI MOHD FAKIRUL AKIMAL	180430060734	NOR HAFIZAH MOHD NAZARI	0179542495	Update Details Schedule

Fig. 4 List of patients during registration process in IVS

3 Conclusion

IVS operation has been enhanced by the use *MyKidVAX* mobile application based on the positive feedback during the implementation phase of the whole system. By showing a great progress, the vaccine database will be updated and more organized. Moreover, a novel reminder application will be improvised with more information about vaccine and many more features.

Home

UPCOMING APPOINTMENTS

dd/mm/yyyy Filter by Date

ID NO.	INFANT'S NAME	MOTHER'S NAME	PHONE NO.	ACTION
18000002	B/O MASNAH BINTI MOHAMMAD	MASNAH BINTI MOHAMMAD	0199515377	Schedule
18000003	B/O ZULAIKA BINTI MOHD RAZALI	ZULAIKA BINTI MOHD RAZALI	0187865678	Schedule
18000004	NUR FATHIAH HJUMAIRA BINTI MOHD. FAIZAL	ROSHAYU BINTI ZAKARIA	0129872950	Schedule
18000005	AMALIN NUR AISYAH BINTI MOHD FAKHRUL AKIMMAL	NOR HAFIZAH MOHD NAZARI	0179542495	Schedule

Fig. 5 List of upcoming patients can be search according to appointment date

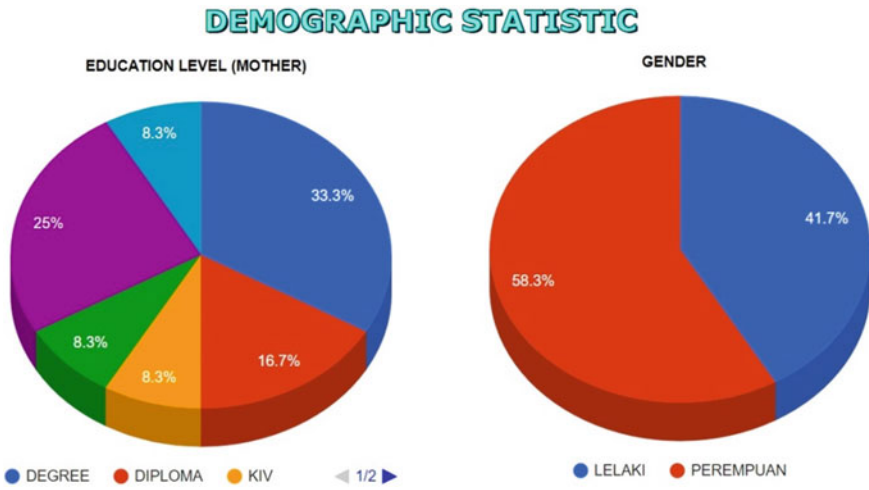


Fig. 6 Data analysis can be retrieve using IVS

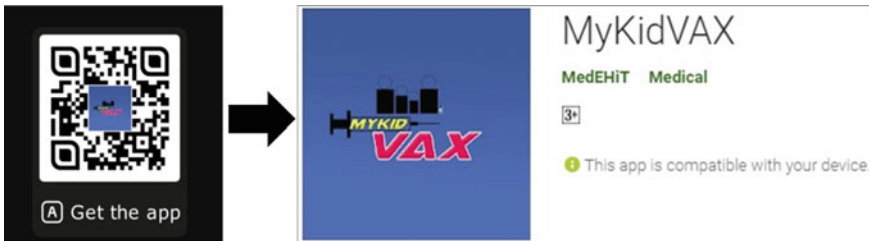


Fig. 7 Left: barcode of MyKidVAX apps for installation; right: appearance of MyKidVAX apps which now available at Google Play Store

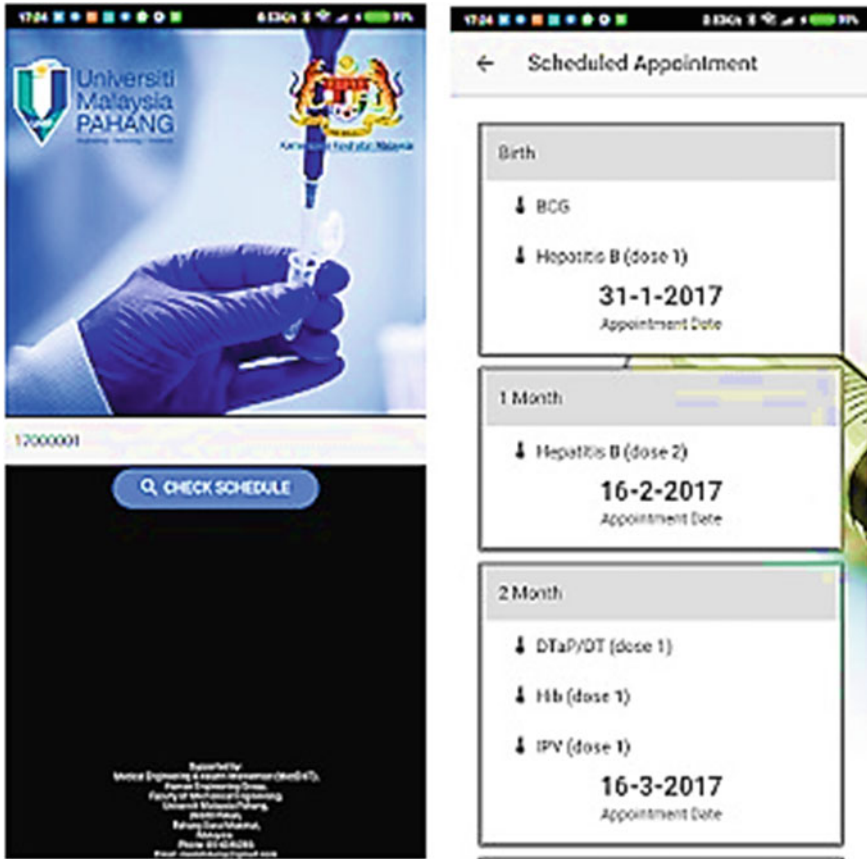


Fig. 8 Left: appearance of *MyKidVAX* main page showing a safety unique ID required during login; right: *MyKidVAX* showing details of next vaccination scheduled sync with IVS appointed date

Acknowledgements A big thank you dedicated to University Malaysia Pahang (UMP) for providing us with a good environment, facilities and funding under research grant in order to complete this research. By this opportunity, we would like to thank Dr. Siti Suhaila Binti Suradi, MD. for sharing valuable information and giving us an approval for conducted the pilot study at Klinik Kesihatan Kurnia, Kuantan and accordance to our research interest. We would face many difficulties without her assistance.

References

1. Adib, M.A.H.M., Zabudin, N.F., Lukman, M.S., Hasni, N.H.M.: Development of Integrated Vaccine System (IVS) for Vaccination Database. IRID (2018)
2. Kim, C., Lee, J., Kim, Y.: Early stage evolution of a hospital information system in a middle income country: a case study of Korea. *Int J Healthc Technol Manage* **4**, 514–524 (2002)
3. Zakaria, N., Mohd Yusof, S.A.: Understanding technology and people issues in hospital information system (HIS) adoption: case study of a tertiary hospital in Malaysia. *J Infect Public Health* **9**(6), 774–780 (2016)
4. Multimedia Super Corridor, Ministry of Health Malaysia (1997)
5. World Health Organization (WHO) and PATH, OPTIMIZE (2013)
6. Centres for Disease Control and Prevention (CDC), U.S. Department of Health & Human Services (2016)
7. Immunise4life, Ministry of Health Malaysia(2016)

Microwave-Assisted Synthesis for Environmentally ZnO Nanoparticle Synthesis



Norlin Pauzi, Norashikin Mat Zain and Nurul Amira Ahmad Yusof

Abstract Zinc oxide (ZnO) nanoparticles are versatile materials in many applications due to their unique chemical and physical properties. Recently, researchers tend to find the fast, simple, cost effective and eco-friendly method to synthesis ZnO nanoparticles. Microwave heating method has special heating capabilities have produced desirable products of ZnO nanoparticles. In this study, ZnO nanoparticles were synthesized by a precipitating method assisted with microwave heating method. Zinc nitrate had been used as zinc salt, sodium hydroxide as reducing agent and gum arabic as stabilizing agent. The objective of this paper was to determine the optimum microwave heating power to obtain small size of ZnO nanoparticles. The powers for microwave heating were selected at 250–850 W with 4 min synthesis time. All the synthesized microwave conditions gave single phase of ZnO with wurtzite structure. Dynamic Light Scattering (DLS) was employed to measure the size of ZnO nanoparticles. The size of ZnO nanoparticles increased with increasing microwave power from 250–850 W. At 350 W, smaller size of ZnO nanoparticles obtained. The Ultraviolet–visible spectroscopy (UV–vis) absorption spectra were found in the range of 340 nm. The Fourier-transform infrared spectroscopy (FTIR) spectra showed peaks range from 424 to 475 cm^{-1} which indicating standard of Zn–O stretching.

Keywords Microwave heating · ZnO nanoparticle · Gum arabic

1 Introduction

Zinc oxide (ZnO) has received much attention due to its unique physical, chemical, effective biological properties and wide applications in various fields [1]. The conventional synthetic methods of nanoparticle synthesis often depend on the energy

N. Pauzi · N. Mat Zain (✉) · N. A. Ahmad Yusof
Faculty Chemical and Natural Resources Engineering, Universiti Malaysia Pahang, Lebuhraya
Tun Razak, 26300 Gambang, Kuantan, Pahang, Malaysia
e-mail: shikin@ump.edu.my

© Springer Nature Singapore Pte Ltd. 2019
Z. Md Zain et al. (eds.), *Proceedings of the 10th National Technical Seminar
on Underwater System Technology 2018*, Lecture Notes in Electrical Engineering 538,
https://doi.org/10.1007/978-981-13-3708-6_48

541

inputs from external heat sources such as water/oil bath, furnace and heating mantle [2]. From the environment viewpoint, problems associated with such heating methods resulted intensive energy consumption and low reaction efficiencies in term of reaction time and reaction rate [3]. These limit their industrial applications.

Therefore, as an environmentally benign technology with wide applications, microwave synthesis has the advantages of homogeneous volumetric heating, and high reaction rate compared with other physical and chemical methods. Microwave heating methods can address the problem of heating inhomogeneity, while providing a scalable platform for industrial applications. In fact, microwave heating has been demonstrated to enhance reaction rates, selectivity and product yields in organic chemistry [4].

Microwave provides an adjustable heating manner to manipulate the formation of nanoparticles. Specifically, the wavelength of microwaves has a strong impact on the penetration depths in the reaction mixtures, and thus largely determines the heating rate. Therefore, the nucleation as well as the subsequent growth in the formation of nanoparticles are controllable [5]. Besides that, this method shows yield improvement, small particle size, narrow particle size distribution, high purity materials and enhanced physicochemical properties.

Different power of microwave heating will synthesize different ZnO nanoparticles size and shape. A few researchers focused on the effect of microwave power from lower range of 50 W [6] to higher range 850 W [7]. There reported that average particle size decrease with decreasing microwave power [8]. However, some researchers found out that at higher microwave power of 710 W the smaller crystalline size of ZnO was achieved [7]. The objective of this paper was to determine the optimum microwave heating power to obtain smaller size of ZnO nanoparticles using gum arabic as stabilizing agent. It should be noted that controlled synthesis of nanoparticles using microwave irradiation is still in its beginning and its full potential is yet to be realized, in term of understanding of reaction mechanism and the optimization of reaction parameters.

2 Methodology

2.1 Method of ZnO Nanoparticles Synthesis

Firstly, 1% of gum arabic was dissolved in 100 ml of distilled water and heated for 2 min (in 450 W microwave) to fully dissolve the gum arabic. 2.974 g of solid $\text{Zn}(\text{NO}_3)_2 \cdot 6\text{H}_2\text{O}$ zinc nitrate was added into 1% of gum arabic solution subjected to continuous stirring. Then the obtained solution was heated for 2 min in the microwave running at 450 W. 1 M NaOH solution was dripped into the zinc nitrate and gum arabic solution undergoing vigorous stirring until pH 10 achieved. Again, the mixture solution was exposed to microwave heating at microwave power, varied from 250 to

850 W for 4 min. The white precipitate was cleaned using distilled water before the precipitate was dried in an oven at 80 °C.

2.2 Characterization

Dynamic Light Scattering (DLS). Here, 30 μL of ZnO solution was diluted in 2 mL of de-ionized water. The nanoparticle size in liquid suspension at 25 °C were measured using Zetasizer Nano ZS (Malvern Instruments). A 633 nm, He–Ne laser was used as the light source and the avalanche photodiode was employed as the detector. The dynamic light scattering method was used to measure the particle size. Here, the scattered light was collected at 173°. The value of parameter Z-Ave was treated as the mean diameter of nanoparticles. The cumulant method was adopted for data analysis. Both hydrodynamic diameter and polydispersity index were measured. All particles in the liquid underwent the Brownian motion, whereby the motion speed was inversely proportional to the particle size.

UV–vis Spectrophotometer. The optical properties of ZnO nanoparticles was analysed using the UV–vis spectrophotometer (U-1800 spectrophotometer Hitachi). The maximum absorption spectra of all samples were measured in the range of 250–800 nm, with a slit width of 2 nm and a scanning rate of 100 nm/min.

Fourier Transforms Infrared Spectroscopy (FTIR) Analysis. The chemical composition of the synthesized nanoparticles was studied using the FTIR spectrometer (Perkin-Elmer brand, spectrum 100 model). The quality and the composition of ZnO nanoparticles were analyzed using the Fourier transform infrared (FTIR) spectroscopy in the range of 400–4000 cm^{-1} .

3 Result and Discussion

As shown in Fig. 1, the calculated average hydrodynamic diameter based on DLS analysis shows increased from 350 to 850 W. However at lower microwave heating (250 W), the hydrodynamic size was bigger compared to hydrodynamic size at microwave power 350 W.

Moreover, it was also identified that the nanoparticle size are directly proportional to microwave power. By applying microwave power at higher rate, the nanoparticle grows bigger due to Ostwald ripening. Similar results were obtained by Promnopasa et al. [9]. They observed an effect of the microwave power rise on the increase in the size of the obtained ZnO. Particle coarsening is another important phenomenon contributes to larger particle size when high power was apply to ZnO nanoparticles synthesis. When a large particle meets a smaller one, classical sintering theory predicts that the grain boundary migrates towards the small particle and the size of large particle increases [10].

Fig. 1 ZnO nanoparticles hydrodynamic size at different microwave heating (watt) based on DLS analysis

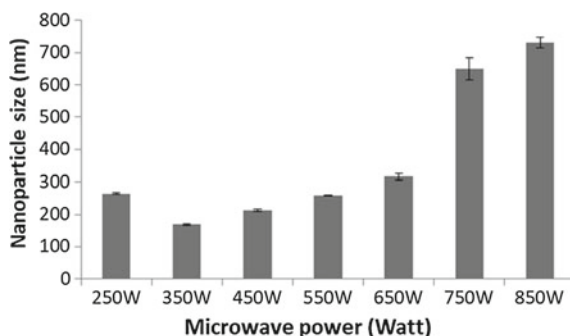
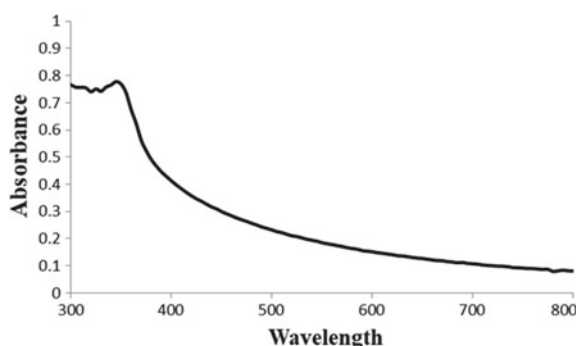


Fig. 2 UV-vis spectra of ZnO nanoparticles synthesis at microwave heating 350 W



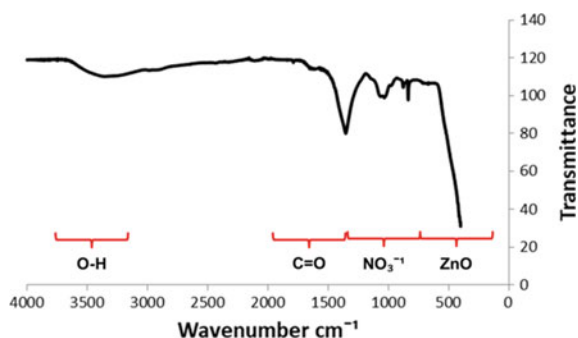
At microwave power of 750 W and above the sample simply burn off and the particles will go through all sorts of changes that directly increased sharply the nanoparticle size. In addition, higher microwave power will directly increased the heating rate that will effected the gum arabic coating to stabilized the nanoparticle resulted increase in the nanoparticles agglomerated size.

The correlation between the size of ZnO nanoparticles aggregates and the microwave heating power, which we observed, can be explained by the mechanism of solvothermal synthesis of ZnO nanoparticles. The DLS results revealed the possibility to control the size of ZnO nanoparticles by changing the used of microwave power. Microwave power at 350 W was selected for the best microwave power of heating in order to obtain small size of ZnO nanoparticles in just within 4 min.

Figure 2 shows the optical properties of ZnO nanoparticles synthesized at 350 W microwave heating. A sharp peak was formed at 355 nm, representing the hexagonal phase of ZnO nanoparticle [7].

In order to understand the mechanism of the formation of ZnO nanoparticles, the FTIR measurement was conducted at room temperature for wavenumber ranging from 4000 to 400 cm^{-1} . Figure 3 shows the compositional analysis of ZnO nanoparticles synthesized at 350 W. The broad band at 3447 cm^{-1} corresponded to the O–H mode of vibration within the hydroxyl groups. A peak at 1352 cm^{-1} might be due to carboxylic acid. A peak near 1033–835 cm^{-1} is due to NO_3 bonding which might be

Fig. 3 FTIR spectra of ZnO nanoparticle synthesis at microwave heating 350 W



due to the absorption of nitric acid group on the ZnO surface. The peak in the region between 424 and 475 cm^{-1} is allotted to Zn–O stretching [11].

4 Conclusion

In summary, microwave heating is a fast, simple and inexpensive way for obtaining small particles in short times of heating. ZnO nanoparticles size increase with the increase of microwave power of heating. 350 W is the best microwave power of heating in order to obtain small size of ZnO nanoparticles in just within 4 min.

Acknowledgements We acknowledge the financial support from a research university Grant number RDU 150333 of Universiti Malaysia Pahang (UMP) and Mybrain15 scholarship under Ministry of Higher Education Malaysia. Thanks for providing all facilities to carry out this research work and for awarding financial support through Doctoral Scholarship Scheme.

References

1. Pauzi, N., Zain, N.M., Yusof, N.A.A.: The potential of gallic acid and ascorbic acid as green reducing agent in ZnO nanoparticle synthesis. *Malays. J. Catal.* **3**(1), 13–16 (2018)
2. Mishra, R.R., Sharma, A.K.: Microwave-material interaction phenomena: heating mechanisms, challenges and opportunities in material processing. *Compos. Part A Appl. Sci. Manuf.* **81**, 78–97 (2016)
3. Bilecka, I., Niederberger, M.: Microwave chemistry for inorganic nanomaterials synthesis. *Nanoscale* **2**(8), 1358–1374 (2010)
4. Meng, L.Y., Wang, B., Ma, M.G., Lin, K.L.: The progress of microwave-assisted hydrothermal method in the synthesis of functional nanomaterials. *Mater. Today Chem.* **1–2**, 63–83 (2016)
5. Breitwieser, D. et al.: In situ preparation of silver nanocomposites on cellulosic fibers-microwave vs. conventional heating. *Carbohydr. Polym.* **94**(1), 677–686 (2013)
6. Cho, S., Jung, S.H., Lee, K.H.: Morphology-controlled growth of ZnO nanostructures using microwave irradiation: from basic to complex structures. *J. Phys. Chem. C* **112**(33), 12769–12776 (2008)

7. Papadaki, D., et al.: Life cycle assessment of facile microwave-assisted zinc oxide (ZnO) nanostructures. *Sci. Total Environ.* **586**, 566–575 (2017)
8. Barreto, G.P., Morales, G., Quintanilla, M.L.L.: Microwave assisted synthesis of ZnO nanoparticles: effect of precursor reagents, temperature, irradiation time, and additives on Nano-ZnO morphology development. *J. Mater* **2013**(1), 1–12 (2013)
9. Promnopas, W., Thongtem, T., Thongtem, S.: Superlattices and microstructures effect of microwave power on energy gap of ZnO nanoparticles synthesized by microwaving through aqueous solutions. *Superlattices Microstruct.* **8**, 71–78 (2015)
10. Li, F., Pan, J.: Modelling “nano-effects” in sintering. In: Castro, R.H.R., van Benthem, K. (eds.). *Engineering Material*, vol. 35, pp. 17–34. Springer, Heidelberg (2013)
11. Manoj, V., et al.: Synthesis of ZnO nanoparticles using carboxymethyl cellulose hydrogel. *Asian J. Appl. Sci.* **7**(8), 798–803 (2014)

Part IV
Power Systems and Sustainable Energy

Micro-Hydro Energy Estimation for Hydrokinetic Energy Harnessing at Sungai Lembing



W. I. Ibrahim, R. M. T. R. Ismail and M. R. Mohamed

Abstract The hydrokinetic system is an electromechanical device that has been used to harness the electricity in river stream or marine environment. The system is considered as a promising renewable energy resources especially at the remote areas near to the river. This paper presents the results of site investigation on the hydrokinetic potential at Pasir Kubur River, Sungai Lembing Kuantan. From the analysis, it is shown that from the sampling measurement, the average water velocity is 1.1 m/s while the depth at the Station 2 is ranging between 0.55 and 5.0 m. The estimated output power is between 200 and 500 W depending on water velocity (V) and the swept area (A) of the turbines. Consequently, based on these results, the total annual energy yield can be achieved between 1.8 up to 4 MWh at the average water velocity of 1.1 m/s with 1.0 and 1.5 m² turbines swept area respectively.

Keywords Hydrokinetic · Hydrology · Micro-hydro · Energy harnessing

1 Introduction

The increase of awareness to reduce the CO₂ emission, greenhouse effect and environmental pollution is the main factor to improve the research in renewable energy [1]. Developing country such as Malaysia is still depending on fossil fuels which are rapidly being depleted to generate the electricity. Besides, the price of fossil fuel will continue to rise and subsequently increase the cost of energy productions. Therefore, the requirements of renewable energy are significant to supply and sustain the electricity with less impact to the environment.

W. I. Ibrahim (✉) · M. R. Mohamed

Sustainable Energy & Power Electronics Research Group, Faculty of Electrical & Electronics Engineering, Universiti Malaysia Pahang, 26600 Pekan Pahang, Malaysia
e-mail: wismail.ibrahim@gmail.com

R. M. T. R. Ismail

Instrumentation & Control Engineering, Faculty of Electrical & Electronics Engineering, Universiti Malaysia Pahang, 26600 Pekan Pahang, Malaysia

© Springer Nature Singapore Pte Ltd. 2019

Z. Md Zain et al. (eds.), *Proceedings of the 10th National Technical Seminar on Underwater System Technology 2018*, Lecture Notes in Electrical Engineering 538, https://doi.org/10.1007/978-981-13-3708-6_49

549

Table 1 Small scale hydropower classification by power generation [5]

Classification	Size in kW
Small hydro	1000–30,000
Mini hydro	100–1000
Micro hydro	<100

Renewable energy resources from wind, sun, ocean, biomass and geothermal can produce the green and clean energy to sustain the electricity without being depleted [2]. Currently, micro-hydro system is the most reliable option to generate the electricity for the remote areas nearest to water flowing source [3]. The hydrokinetic system is a new category of hydropower by extracting kinetic energy based on free-flowing water, instead of potential energy of falling water. The hydrokinetic system has been classified under micro-hydro categories that able to generate below than 100 kW capacity as shown in Table 1.

The hydrokinetic system has a similarity with a wind turbine especially on electrical hardware, turbine dynamic and the principles of operation. The advantage of this system is on its installation which only involves a minimum civil work as it does not require a dam or a water storage system. In addition, the system also gives a minimal impact to the environment and predictable especially for river stream and tidal current. Even though the output power is small, the amount of energy can be increased by installing multiple arrays system like a wind turbine farm [4].

The assessment and feasibility studies regarding the potentials of hydrokinetic energy have been conducted in several countries to estimate the capacity of resources. For example, the assessment at small and medium river in Lithuania able to generate 79.4 GWh of electrical energy per year [6].

Malaysia has a potential to harness the electricity from the hydrokinetic energy due to the combination of highland area and hilly topography along the entire length and width of the country. In addition, Malaysia is blessed with the abundant water resources almost 150 rivers in peninsular and 50 rivers in Sabah and Sarawak [7]. However, up to this date, there is a lack of research regarding the assessment and estimation of hydrokinetic power potentials in Malaysian rivers.

Therefore, the evaluation of river for hydrokinetic energy deployment is essential to see the potential for electricity production. In this paper, the investigation of the hydrokinetic energy harnessing at the Sungai Lembing has been carried out to determine the energy harnessing potential. Three checkpoint stations has been created along 250 m of Pasir Kubur river to measure and collect the data of water velocity, width and river depth. The sampling data is required to determine the energy capacity, annual energy production and finally the suitable design for turbine placement in the river.

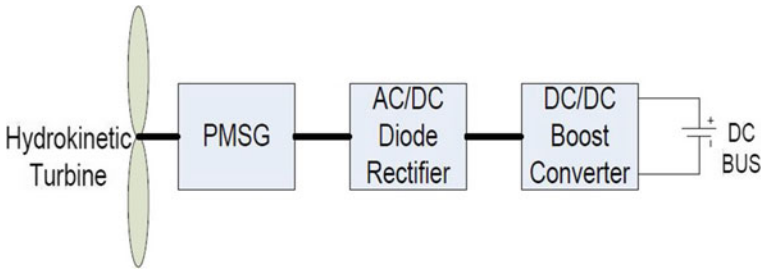


Fig. 1 The stand-alone hydrokinetic system

1.1 Hydrokinetic System

The energy conversion in hydrokinetic system is similar to the wind turbine technology. The system consists of turbine, permanent magnet synchronous generator (PMSG), rectifier, DC converter, controller unit and inverter for grid connected [8]. The hydrodynamic power is converted into electrical power through turbine and PMSG. Then, the variable AC (three-phase) output of the PMSG is converted into variable DC voltage through three-phase passive rectifier. Finally, the variable DC output voltage of the diode bridge is connected to a DC-DC boost converter. The output of the DC-DC boost converter is a constant DC bus. Figure 1 shows the hydrokinetic configuration for stand-alone system. Battery banks are usually used to store the extracted energy as well as to provide a constant dc bus voltage on the load side for the stand-alone system.

1.2 Principle and Operation

The volume and velocity of the water will determine the amount of energy that can be generated from the hydrokinetic system. This type of energy is most suitable to be installed at the velocity ranging from 0.5 m/s and above. However, if the water velocity is more than 4.0 m/s the system will automatically shutdown to protect the turbine and generator from the damaged. The total output power (P_o) of hydrokinetic system are determined by the water density, swept area of turbine, water velocity, turbine coefficient and the converter efficiency [5].

$$P_o = \frac{1}{2} \rho A V^3 C_p C_n \tag{1}$$

where, A is the turbine swept area (m^2), ρ is the water density (1000 kg/m^3), V is the water current velocity (m/s), C_p is the turbine power and C_n is the converter efficiency.

The swept area represents the area of the turbine rotor in square meters. For the horizontal axis turbine, the swept area can be calculated by;

$$A = \pi r^2 \quad (2)$$

where π is 3.142 and r is the turbine radius.

Meanwhile, for the vertical axis turbine, the swept area is calculated by the equation below.

$$A = h \cdot d \quad (3)$$

where, h is the height and d is the diameter of the turbine.

The power coefficient, (C_p) is the percentage of power that the turbine can extract from the water flowing through the turbine. According to the studies carried out by Betz [5], the theoretical maximum amount of power that can be extracted from a fluid flow is about 59%, which is referred as the Betz limit. The C_p is also having a non-linear function to the Tip Speed Ratio (TSR) and pitch angle (β). In hydrokinetic system, the pitch angle is considered as zero, so the C_p is only determined by the TSR. The expression for TSR is shown below.

$$\lambda = \frac{\omega R}{V} \quad (4)$$

where, λ is the *TSR*, ω is angular velocity of turbine, R is the turbine radius and V is the water velocity.

1.3 Turbine Classification

The turbines can be classified into horizontal and vertical axis turbine based on the alignment of the rotor with respect to the water flow [8]. The horizontal axis turbine having the rotational axis parallel to the water flow. As can be seen on Fig. 2a the rotor axis is inclined with the direction of water flow. Meanwhile, for vertical axis turbine, the direction of rotor axis is perpendicular with the direction of the water flow as shown in Fig. 2b.

Horizontal axis turbines are commonly used for marine hydrokinetic and tidal energy system. On the other hand, vertical axis turbines are familiarly seen in river current energy harnessing [1]. Darrieus (curved blades), H-Darrieus, Gorlov (helical blades) and Savonius are among the examples of vertical axis turbines. The advantages and disadvantages of both horizontal and vertical axis turbines are further discussed in details in some papers for references [1, 5].

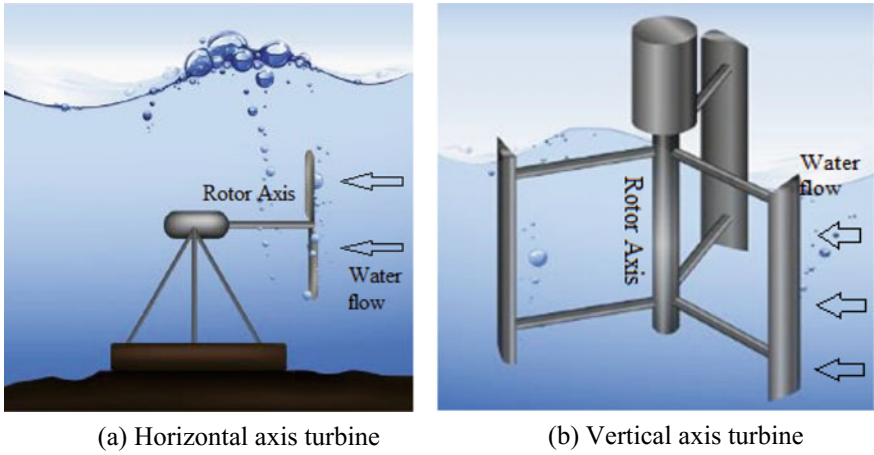


Fig. 2 Turbine classification. Taken from [1]

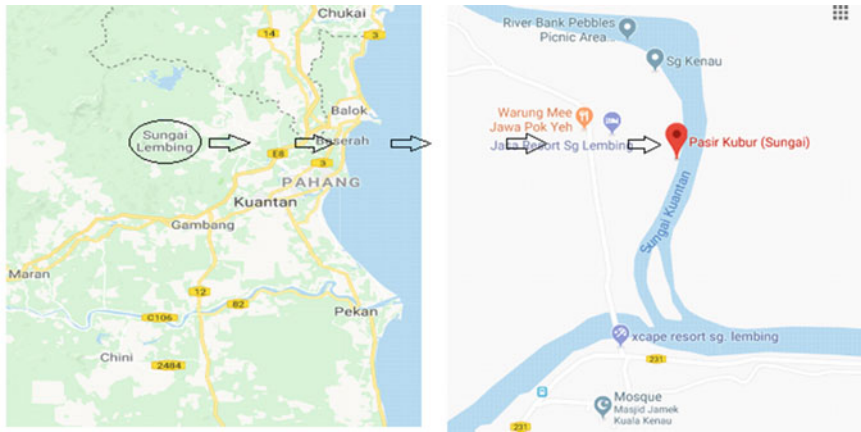


Fig. 3 The location of Pasir Kubur river, Sungai Lembing. Source Google image

2 The Study Area

Sungai Lembing is located in the district of Kuantan, Pahang, East Coast of Peninsular Malaysia, almost 35 km from Kuantan town. Figure 3 shows the location of the study area which located at the Kampung Seberang Kuala Kenau which is about 4 km from the main town of Sungai Lembing. The exact location of Sungai Pasir Kubur is between latitude $3^{\circ} 56' 24.4''N$ and longitude $103^{\circ} 3' 3.1''E$. This area is selected due to easy access and study due to the river conditions such as suitable depth, width and water velocity.

Pasir Kubur River is well-known as the recreation area among Kuantan's people especially during the weekend. While keeping the places as a recreation area, the function of the river can be expanded as one of the renewable energy sources. Half of the river cross-section can be used to produce the electricity by installing hydrokinetic energy harnessing. However, several factors are needed to be considered when selecting the resources area such as the channel geometrics, slope and roughness and the climate condition [9].

3 Methodology

The investigation on the potential of hydrokinetic energy harnessing at Sg. Lembing required evaluation method, simulation and flow velocity measurement. The evaluation method has been developed for river assessment to determine the energy capacity and to locate the most potential resources sites. The method covers several steps including the flow measurement and data validation.

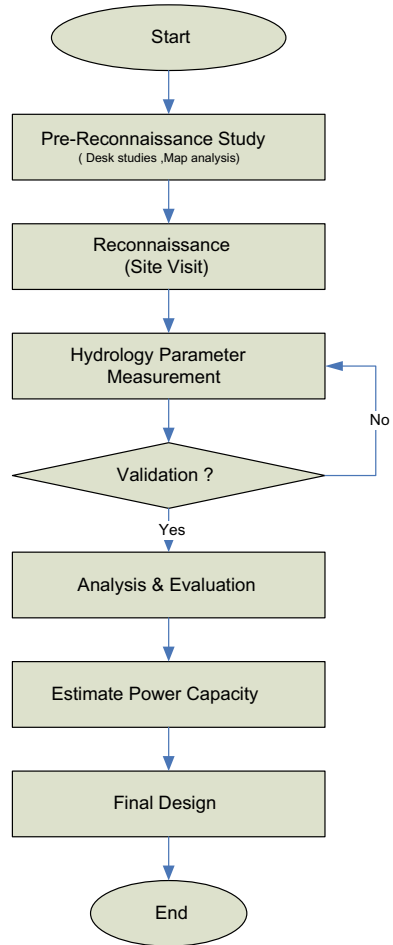
3.1 Evaluation Method

The evaluation method for hydrokinetic energy harnessing can be applied to any river to investigate the resources potential. Figure 4 shows the flow chart of evaluation method before the installation of hydrokinetic turbines. The first step is the pre-reconnaissance study which involves the desk studies and maps analysis to determine and narrow-down the suitable locations. The second step is the reconnaissance study. This step required the site visits to observe the physical location of resources area. The proper observation at the sites will influence the operation for optimal performance and cost viability of the project.

The third step is the hydrology studies which requires the sampling measurement activities. The river velocity, depth, cross sectional area and discharges rate needs to be measured to investigate the potential of resources area. Nevertheless, the primary requirement for hydrokinetic energy harnessing in the river is sufficient water velocity with suitable depth [6]. The validation data could be fulfilled if the river basin near to the gauging station. In Malaysia, the Department of Irrigation & Drainage (DID) have a responsibility to manage the river basin, water resources, hydrology, flood and coastal zone [10]. The data regarding the water discharge, water level, rainfall, flood, water quality can be taken freely or either buying the information at DID Ampang.

Analysis and evaluation steps are required in order to locate the river segments with the greatest potential either for single turbine placement or array turbines arrangement. The average bed depth and cross-section width with the suitable flow velocity could be considered. Thus, the turbines placements can be configured in the river segment for establishment in operation.

Fig. 4 The evaluation step for river energy potential



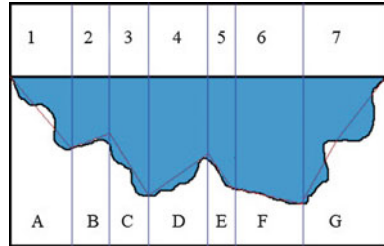
The next step is to calculate the amount of power that can be harnessed in the river. The annual energy yield can be estimated by equation below [11, 12],

$$E = T \int_0^{\infty} f(v) \frac{1}{2} \rho A V^3 C_p dv = T \cdot \bar{P}_W \tag{5}$$

where, T is the integral time interval (8760 h for time period of 1 year), ρ is the water density, A is the turbine swept area, $f(v)$ is the function of mean water speed, C_p is the turbine power coefficient, \bar{P}_W is the average output power over the interval T .

The final design is the last steps in evaluation method. At this level, the hydrokinetic system is suitable for ultimate deployment in the river after a very high con-

Fig. 5 Schematic of cross river section



fidence analysis. This stage requires a much greater effort and time commitment especially in simulation and test rig hardware.

3.2 Velocity Measurement

The water velocity has been measured using the Current Meter (FP211) produced by the Global Water. The probe is a rugged and highly accurate water velocity instrument and ideal for measuring flows in rivers and streams [13]. Three methods can be used to determine the average of water velocity in the river using the FP211. The first method is suitable for small streams. The probe can be placed in the flow then moved slowly and smoothly from top to bottom of the flow during average velocity measurement. Keep moving the probe for 20–40 s to obtain the accurate average value.

The second method is well-known as velocity-area method and suitable for larger streams and rivers. The measurement has been collected by subdividing a stream cross section into segments as shown in Fig. 5. The flow velocity and depth for each segment (A–G) has been measured to obtain the average velocity in cross-section. The probe needs to move vertically from top to bottom smoothly for 20–40 s to obtain good average. The total discharge can be calculated by the summation of all the segment and expressed by the equation below.

$$Q = \sum_{i=1}^n a_i v_i \tag{6}$$

where Q is the total discharge in cubic m^3/s , a_i is the area of cross section at i th segment (m^2) and v_i is velocity at i th segment (m^2/s).

The third method is by applying the U.S. Geological Survey (USGS) Six-Tenth Depth Method. Based on the theory, an observation of velocity is made at 0.6 of the depth below the water surface as a mean velocity for the vertical segment [14]. The Flow Probe is placed at the center of the subsection at a depth from the surface of 0.6 of the total depth. The Flow Probe is held in place and the average velocity is obtained over a period of 40 s.

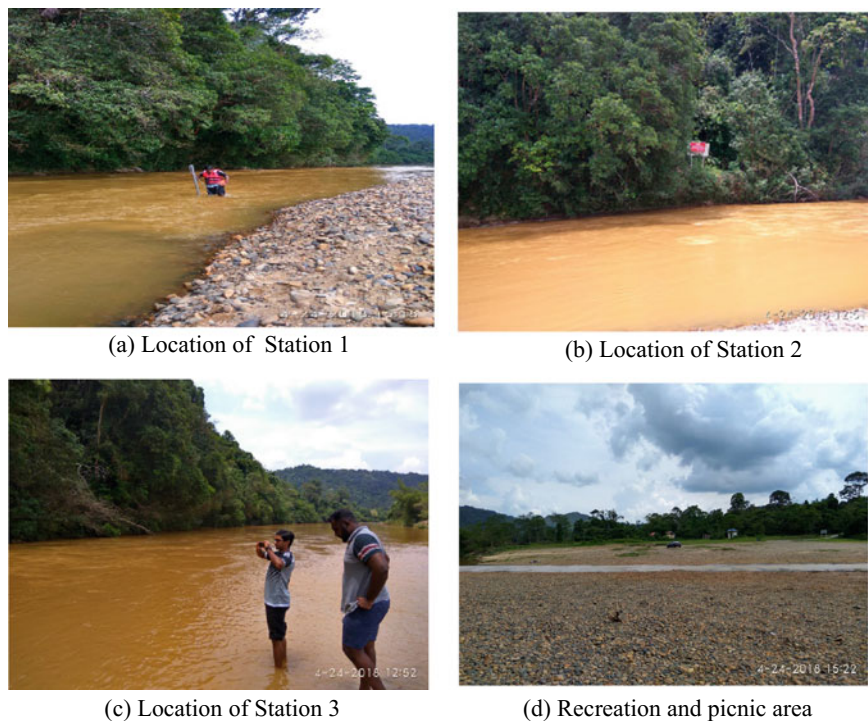


Fig. 6 The location of the sampling station

The sampling measurement were carried out at three stations along the Pasir Kubur River as shown in Fig. 6a–c. All of the measurements were recorded using the USGS Six-Tenth Depth Method because of the measurement accuracy. The distance between sampling station to another is around 70 m with total length of measurements is almost 250 m. Based on observation and measurement the depth of the stream at Station 1 is ranging between 0.4 and 0.7 m with the width around 30 m. Station 2 is quite narrow with the highest velocity among the stations. However, several areas at Station 2 have a turbulent flow and a restricted area for swimming due to several drown cases [15, 16]. Station 3 can be classified as a shallow stream with the depth around 0.2–0.45 m. Figure 6d shows the river bank pebbles which is suitable for recreation and picnic area.

4 Result and Discussion

The reconnaissance study and hydrological sampling were carried out on April 2018 which represented data for the dry season. Another hydrological sampling data will

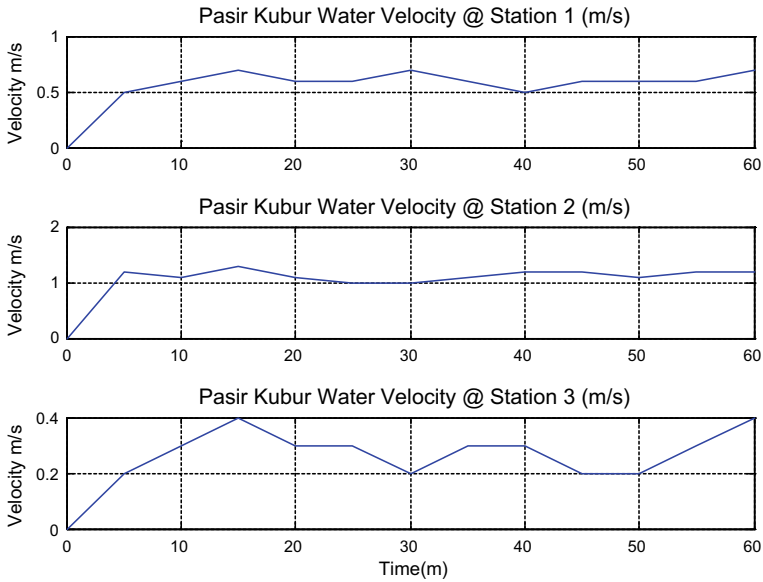


Fig. 7 The water velocity at the three sampling station

be conducted at the end of this year to represent the raining season. Based on the investigation, the river velocity at Pasir Kubur Sungai Lembing is ranging from 0.4 to 1.3 m/s as shown in Fig. 7. The trend of velocity from Station 1 to Station 2 is slightly increased but gradually decrease at Station 3.

Twelve sampling measurement data has been recorded during one-hour session at each station. Based on the study, Station 2 has a potential for hydrokinetic turbine placement due to high water velocity with average 1.1 m/s. The velocity at Station 2 also can achieve 1.3 m/s maximum with 1 m/s minimum water speed. The depth at the Station 2 also ranged between 0.55 and 5 m which is suitable for horizontal and vertical axis hydrokinetic turbine. Whereas, the Station 1 and Station 3 are not suitable for hydrokinetic deployment due to shallow water depth even the water velocity at Station 1 is in the acceptable range.

Figure 8 shows the water velocity at Station 2 in 60 min. The MATLAB fitting tool has been used to generate the curve of the 4th polynomial equation. As can be seen, the graph shows the variation of water velocity which can be the challenged for the amount of energy extraction. The maximum power point tracking (MPPT) algorithm commonly has been used with the addition of the PI controller for optimal energy extraction in the hydrokinetic system [17].

As mentioned previously, the output power of the hydrokinetic system can be calculated using Eq. (1). The water density (ρ) was assumed as 1000 kg/m^3 whereas the power coefficient (C_p) is 0.46 for H-Darrieus turbine. The simulation of four H-Darrieus turbines with different swept area (A) have been used to estimate the output power. As can be seen, the output power will be increased as the water velocity

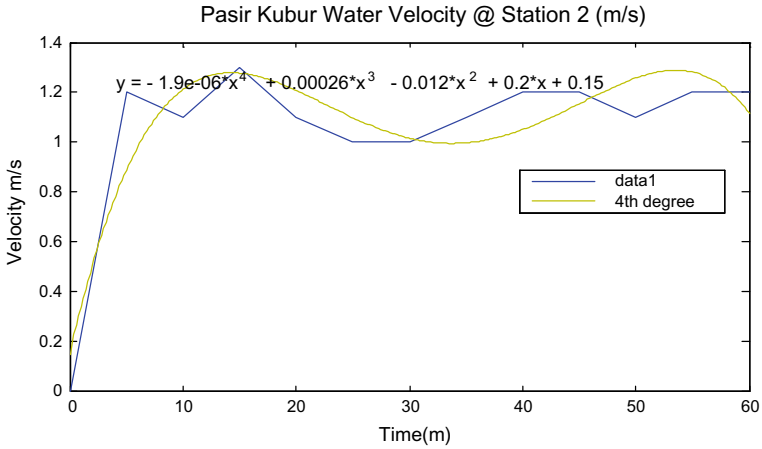


Fig. 8 The water variation at Station 2

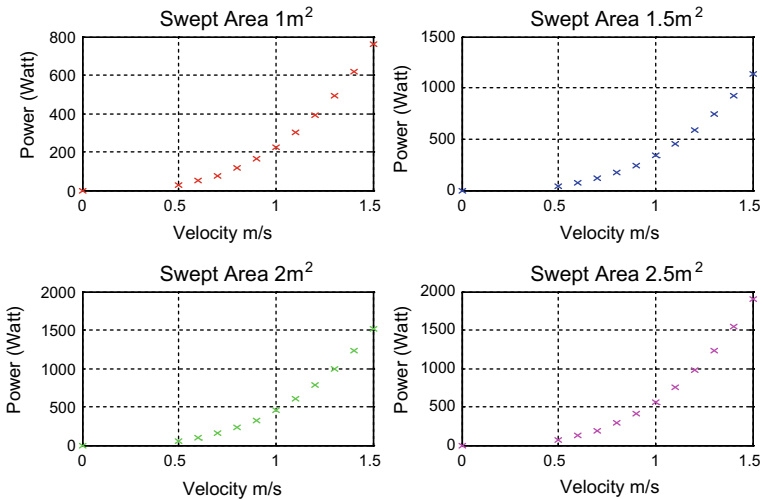


Fig. 9 Power Versus velocity at different size of turbine

(V) and swept area (A) is increased as shown in Fig. 9. The output power is ranged between 200 and 500 W at average 1.1 m/s water velocity with different size of turbines.

By considering the mean annual velocity as 1.1 m/s, the annual energy yield can be estimated using the Eq. (5) to determine the capacity of hydrokinetic potential. The value is quite reasonable because the sampling data was taken during the Southwest Monsoon or well known as the dry season. It is expected that the value could be more than 1.1 m/s during the Northeast Monsoon due to the high quantity of rainfalls. The sampling data can be verified by the data from DID Telemetry Station (Sg. Kuantan

Table 2 The turbines specification

Name	H-Darrieus	Darrieus	Gorlov (helical)
Type of turbine	Vertical axis	Vertical axis	Vertical axis
Tip speed ratio (TSR)	2.7	3	2.5
Power coefficient (C_p)	0.46	0.45	0.32
Lift coefficient	1.353	1.353	1.353
Drag coefficient	0.086	0.027	0.086
Number of blades	3	3	3

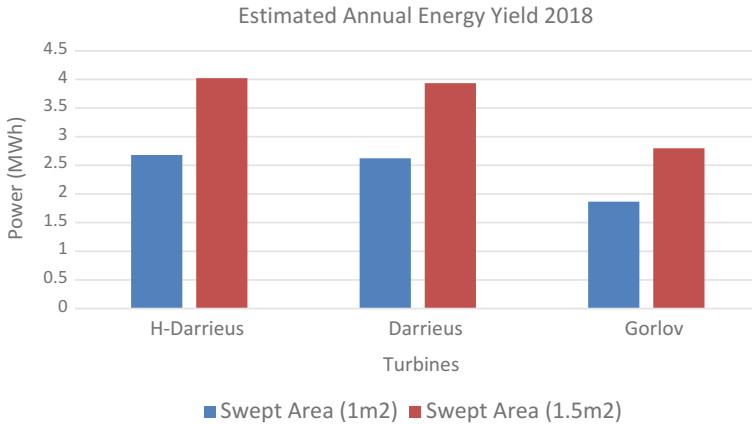


Fig. 10 Estimation of annual energy production at different swept area of turbine

at Bukit Kenau) because the station is almost 1000 m from the studies area. However, the data from DID are not ready due to several technical problems.

The simulation by three different turbines with different size of the swept area (A) and power coefficient (C_p) have been used to estimate the energy capacity. The specification of the H-Darrieus, Darrieus and Gorlov turbines is shown in Table 2. The simulation by QBlades software has been used to determine the turbines parameter and it characteristic for all turbines.

Figure 10 shows the estimation of annual energy yield for three different type of turbines at the Station 2 based on turbines simulation. As can be seen, the energy capacity is ranged between 1.8 and 4 MWh with 1.1 m/s mean water velocity. Based on H-Darrieus, it shows a better performance compared to Darrieus and Gorlov turbines due to high power coefficient with 2.68 and 4.02 MWh on 1.0 and 1.5 m² swept area respectively. The energy capacity is also depending on the type of turbines, power coefficient (C_p) and swept area (A) of the turbines. H-Darrieus turbine is more preferred in this case due to high power capacity, simple construction and high-power coefficient compared to other turbines. The turbines swept area of 1.0 and 1.5 m² seen reasonable with the river depth and the condition of the riverbed at Sg. Pasir Kubur Sg Lembing.

5 Conclusion

Pasir Kubur river at Sungai Lembing, Kuantan, Pahang has a potential to harness the energy by hydrokinetic system based on the sampling study. The hydrological indicator such as water flow, river depth and width are the important factor in determining the total energy that can be extracted from the site area. Station 2 is the best potential site with the average water velocity at 1.1 m/s. The depth is ranged between 0.55 and 5 m able to produce more than 4 MWh annually with 1.5 m² swept area of H-Darrieus turbine.

References

1. Behrouzi, F., Nakisa, M., Maimun, A., Ahmed, Y.M.: Global renewable energy and its potential in Malaysia: a review of hydrokinetic turbine technology. *Renew. Sustain. Energy Rev.* **62**, 1270–1281 (2016)
2. Yah, N.F., Oumer, A.N., Idris, M.S.: Small scale hydro-power as a source of renewable energy in Malaysia: a review. *Renew. Sustain. Energy Rev.* **72**, 228–239 (2016)
3. Izadyar, N., Ong, H.C., Chong, W.T., Mojumder, J.C., Leong, K.Y.: Investigation of potential hybrid renewable energy at various rural areas in Malaysia. *J. Clean. Prod.* **139**, 61–73 (2016)
4. Ibrahim, W.I., Ismail, R.M.T.R., Mohamed, M.R.: Hydrokinetic energy harnessing for river application. *J. Telecommun. Electron. Comput. Eng.* **10**(1), 133–138 (2018)
5. Vermaak, H.J., Kusakana, K., Koko, S.P.: Status of micro-hydrokinetic river technology in rural applications: a review of literature. *Renew. Sustain. Energy Rev.* **29**, 625–633 (2014)
6. Sarauskienė, D.: Assessment of hydrokinetic resources of small and medium-size rivers: the Lithuanian case. *Baltica* **30**(1), 23–30 (2017)
7. Hussein, I., Raman, N.: Reconnaissance studies of micro hydro potential in Malaysia. In: *Proceedings of the International Conference on Energy and Sustainable Development: Issues and Strategies (ESD)*, pp. 1–10 (2010)
8. Khan, M.J., Bhuyan, G., Iqbal, M.T., Quaiocoe, J.E.: Hydrokinetic energy conversion systems and assessment of horizontal and vertical axis turbines for river and tidal applications: a technology status review. *Appl. Energy* **86**(10), 1823–1835 (2009)
9. Canadian Hydraulics Centre (National Research Council of Canada): *Assessment of Canada's Hydrokinetic Power Potential (Phase I Report, Methodology and Data Review)*, Natural Resources Canada, pp. 1–63 (2010)
10. Official Page: Department of Irrigation & Drainage, Ministry of Water, Land and Natural Resources, 2018. [Online]. Available: <https://www.water.gov.my/index.php/pages/view/349?mid=220>. Accessed: 20 Aug-18
11. Ani, S.O., Polinder, H., Ferreira, J.A.: Comparison of energy yield of small wind turbines in low wind speed areas. *IEEE Trans. Sustain. Energy* **4**(1), 42–49 (2013)
12. Papathanassiou, S.A., Boulaxis, N.G.: Power limitations and energy yield evaluation for wind farms operating in island systems. *Renew. Energy* **31**(4), 457–479 (2006)
13. Global Water: FP111-FP211-FP311 Global Water Flow Probe User's Manual, no. 38330112. Global Water Instrumentation Inc., (2009)
14. Turnipseed, D.P., Saue, V.B.: *Discharge Measurements at Gaging Stations*, in *Discharge Measurements at Gaging Stations*, pp. 1–106. U.S. Geological Survey, Virginia (2010)

15. Drowned student's body found in river, The Sunday Daily, 2014. [Online]. Available: <http://www.thesundaily.my/news/1071984>. Accessed 19 Aug 2018
16. Kamsani, N.: Dua lelaki dikhuatiri lemas di kawasan perkelahan Sungai Lembing, Astro Awani, 2018. [Online]. Available: <http://www.astroawani.com/berita-malaysia/dua-lelaki-dikhuatiri-lemas-di-kawasan-perkelahan-sungai-lembing-171868>. Accessed 19 Aug 2018
17. Ginter, V.J., Pieper, J.K.: Robust gain scheduled control of a hydrokinetic turbine. *IEEE Trans. Control Syst. Technol.* **19**(4), 805–817 (2011)

Investigation of Binary Search Algorithm as Maximum Power Point Tracking Technique in Solar PV System



Meng Chung Tiong, Hamdan Daniyal, Mohd Herwan Sulaiman
and Mohd Shafie Bakar

Abstract This paper describes a study in maximum power point tracking (MPPT) technique for photovoltaic (PV) system using binary search algorithm (BSA). The aim of this study is to identify the effectiveness of BSA in performing MPPT under constant irradiance and rapid change irradiance conditions. The BSA MPPT model, together with a well-established particle swarm optimization (PSO) algorithm were developed and implemented with a DC-DC boost converter in MATLAB Simulink. Direct control strategy was implemented to simplify the development of the controller which generates the switching duty cycle of the power converter. In order to examine the performance of both algorithms, five different constant irradiance test cases and four rapid changing irradiance test cases were imposed to the PV system to examine the capability of the both algorithms. BSA exhibits a faster convergence speed with zero steady state oscillation. Both of the algorithms have shown the capability to adapt the rapid change irradiance condition effectively with tracking efficiency up to 99%.

Keywords Maximum power point tracking · Particle swarm optimization
Binary search algorithm

1 Introduction

Solar photovoltaic (PV) is no longer a new topic as a renewable energy source for power generation. Solar PV has become a popular choice of renewable energy due to its inexhaustible source from the sun, environmental friendly as well as the application is almost maintenance free. However, due to the relative high installation cost and low power conversion efficiency, it is necessary to maximize the power extraction from the installed system [1]. One of the most economical way is to

M. C. Tiong · H. Daniyal (✉) · M. H. Sulaiman · M. S. Bakar
Faculty of Electrical and Electronics Engineering, Universiti Malaysia Pahang,
26600 Pekan, Pahang, Malaysia
e-mail: hamdan@ump.edu.my

© Springer Nature Singapore Pte Ltd. 2019
Z. Md Zain et al. (eds.), *Proceedings of the 10th National Technical Seminar on Underwater System Technology 2018*, Lecture Notes in Electrical Engineering 538,
https://doi.org/10.1007/978-981-13-3708-6_50

ensure the PV system is always operating at its maximum power point (MPP). One of the easiest way to achieve this is to implement maximum power point tracker into the PV system.

Due to the nonlinear characteristic of the current and voltage ($I-V$) of PV curve, the MPP tracking remains challenge where it requires the MPPT algorithm to react instantly under rapid changing irradiance. Although the aim for MPPT algorithms are to track for maximum power operating point, the performance of different MPPT algorithms are differ by the convergence speed, steady state oscillation and cost effectiveness. In this study, the performance of binary search algorithm MPPT technique was compared with a well-established particle swarm optimization algorithm. The performance of both algorithm was evaluated and examined under constant irradiance and step changing irradiance conditions.

2 Maximum Power Point Tracking Algorithm

2.1 Particle Swarm Optimization

Particle swarm optimization (PSO) is a stochastic, population based search algorithm which is modelled after the behavior of bird flocks [2, 3]. The algorithm utilizes a swarm of individuals (also known as particles), where each of the individual represents a candidate solutions. The search particles move around in the search space to improve their search position which follows a simple behavior where it emulate the success of the surrounding particles and its own achieved successes. The movements of the particles follow the equation below:

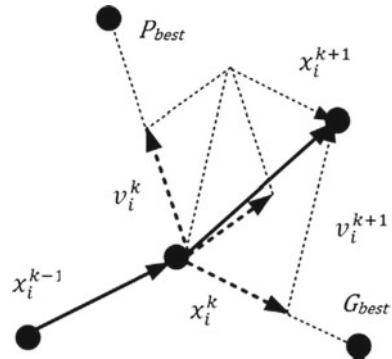
$$x_i(k+1) = x_i(k) + v_i(k+1) \quad (1)$$

where x is the position of the particle while the velocity vector v_i can be calculated by:

$$v_i(k+1) = \omega v_i(k) + c_1 r_1 \{P_{best_i} - x_i(k)\} + c_2 r_2 \{G_{best} - x_i(k)\} \quad (2)$$

where ω is the inertia weight, c_1 and c_2 are the acceleration constants, $r_1, r_2 \in U(0, 1)$, P_{best_i} is the personal best position of particle i and G_{best} is the best known position achieved by the entire population. The typical movement of the particles in optimization process is shown in Fig. 1. In MPPT application, the position of the particles can be represented by the duty cycle of the power converter while the velocity component, v , can be represented by the change of duty cycle for the subsequence iterations.

Fig. 1 Movement of search particle in particle swarm optimization process



2.2 Binary Search Algorithm

Binary search algorithm (BSA) also known as half interval search or logarithmic search, which it is a search algorithm that is used in computer science application to search for a specific target in a sorted set [4, 5]. In each iteration, the algorithm will compare the targeted value with the middle element of the dataset. If the two values were equal, the search operation will be terminated, else, the algorithm will eliminate the half set of the element in the array which the target cannot lie on. The search will then continue with the comparison of the targeted value with the remaining dataset until the target is found or the whole dataset has been processed. Throughout the process, the elements in the dataset will be reduced by half for each iteration, hence it is effective in processing a large dataset.

For MPPT application, the targeted value in the search will be the output power from the PV system while PV operating voltage is the position in the array [4]. Unlike the computer science application where the targeted value was predefined, the targeted value in MPPT application was not predefined due to the maximum power point of the system is unknown. Therefore, the targeted value will be updated in every iteration to which it will be the next higher value that the search can achieve. In order to eliminate the steady state oscillation at MPP, a predetermined constant, th_{osc} , was introduced in the algorithm to terminate the search process when the change of power tracked is sufficiently small. In addition, another predetermine threshold value, th , was included so that the algorithm will expands its search boundaries accordingly whenever the system experienced a large power changes due to weather conditions. The flowchart of the operation of binary search algorithm is shown in Fig. 2.

3 Simulation Model Development

A simulation model comprises of a PV string connected to a DC/DC boost converter together with a MPPT controller was developed in Matlab Simulink. The PV string

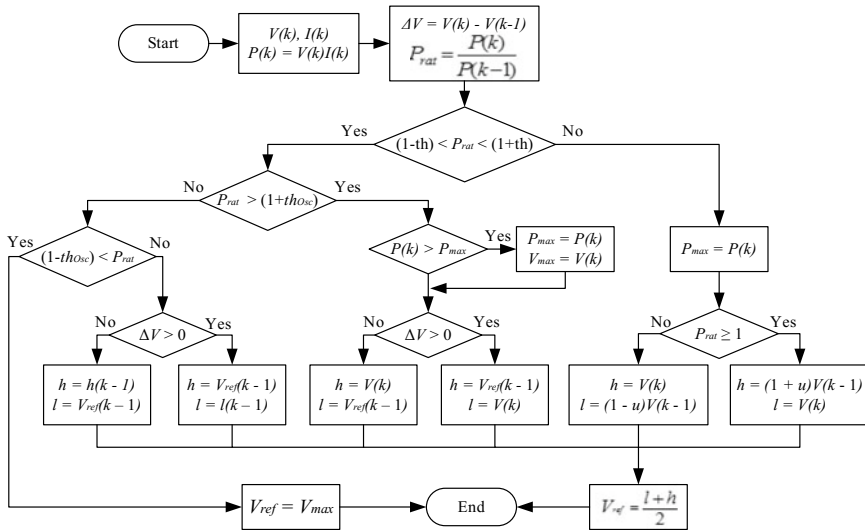


Fig. 2 Operation flowchart of flowchart of the operating flow of binary search MPPT technique

was made up of three series connected 245 W multicrystalline PV modules manufactured by Malaysia Solar Resources (MSR), model MYS-60P/B3/CF-245. The PV module was mathematically modelled with the reference of the technique introduced in [6]. The mathematical model of the PV module was examined so that it will have the same characteristics as stated in manufacturer datasheet.

The MPPT algorithms in study were implemented in the MPPT controller which it controls the operating point of the PV system by adjusting the duty cycle of the DC/DC boost converter. Both the algorithms in study were developed and simulated with the PV system in Matlab Simulink. In order to ensure the search agents had obtained their steady state during sampling process, the sampling interval for both methods was chosen at 0.05 s [3, 7]. The switching duty cycle of the power converter was also computed directly by the MPPT algorithms through direct control strategy which it simplifies the design of the system while maintaining the optimal tracking results [3, 8].

In PSO MPPT algorithm, three search particles were implemented in this study while the other parameters were chosen as $c_1 = 1.2$, $c_2 = 1.6$ and $\omega = 0.4$. These parameters were adapted from the study which has been done in [9, 10], where the same parameters were also implemented in similar case study as in [11, 12]. For BSA, the search boundaries were initiated to include a large search region so that the maximum power operating point can be located effectively. In addition, the two predetermined threshold, which is to eliminate the steady state oscillation at MPP (th_{osc}) and to enable the algorithm to expand the search boundaries during drastic weather change (th) were chosen at 0.003 and 0.05 respectively. For boundaries expanding as described in Fig. 2, the constant was chosen at $u = 0.05$.

To examine the performance of both algorithms, both techniques were simulated and examined under 5 constant irradiance conditions and 4 rapid changes irradiance conditions. For comparison, the MPP tracked by both algorithms were compared to the theoretical value which is obtained through sweeping the operating point of the PV string from zero operating voltage (short circuit current) to open circuit voltage.

4 Results and Discussions

The simulation of two MPPT algorithms in study were carried out in Matlab Simulink. The MPP tracked by both algorithms in study under different test cases of constant irradiance conditions and rapid changed irradiance conditions are shown in Tables 1 and 2 respectively. It can be seen clearly from the results that both algorithms were able to perform MPP tracking up to 99% efficiency. However, for the case under 200 W/m² irradiance condition, both the algorithms were not perform well as in high irradiance condition. This is because under low irradiance tracking condition, the output current from the PV module was very low. This caused the system to experience significant variation in the current when the large changes of searching duty cycle during the tracking process, which in term also caused severe oscillation in system voltage. Due to this, it increases the tracking difficulty of the algorithms.

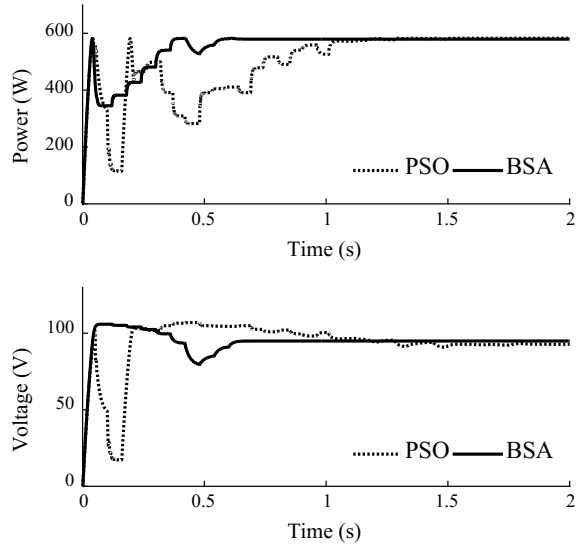
Table 1 Simulation results of PSO and BSA tracking under constant irradiance condition

Irradiance (W/m ²)	Output power (W)			Efficiency (%)	
	Theoretical	PSO	BSA	PSO	BSA
1000	735.0	734.8	734.8	99.97	99.97
800	582.6	582.5	581.4	99.98	99.79
600	430.3	430.0	429.2	99.93	99.74
400	280.3	278.0	278.4	99.18	99.32
200	134.5	125.7	127.1	93.46	94.50

Table 2 MPP tracked by PSO and BSA under rapid changed irradiance condition

Irradiance changes (W/m ²)	Output power (W)			Output power (W)		
	(before irradiance changes)			(after irradiance changes)		
	Theoretical	PSO	BSA	Theoretical	PSO	BSA
800–1000	582.6	579.5	582.4	735.0	734.9	734.6
600–1000	430.3	430.4	429.2	735.0	734.7	734.9
1000–800	735.0	734.8	734.8	582.6	582.5	581.9
1000–500	735.0	734.8	734.8	355.3	355.1	354.7

Fig. 3 Tracking performance of PSO and BSA under constant irradiance at 800 W/m^2

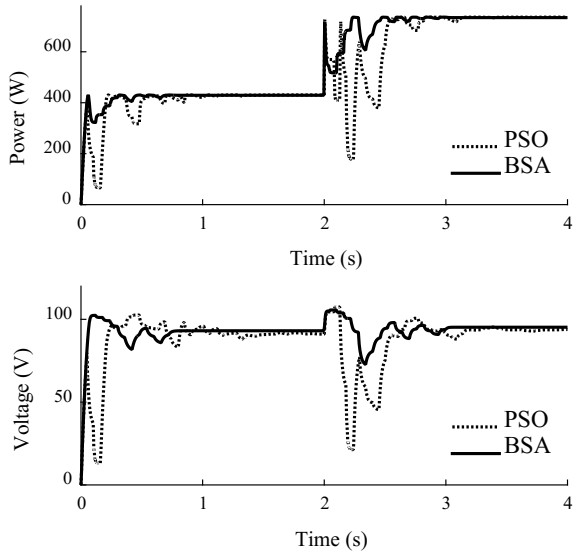


From the study, it can also realized that the tracking speed of the both algorithms varies with the tracking condition. Unlike conventional hill climbing MPPT methods, the soft computing methods perform random searched from the search space and the outcome from the search will directly affect the tracking speed and efficiency. However, in this study it can be found that the BSA was able to perform faster tracking than PSO under most situation. As can be seen from the results shown in Fig. 3, under 800 W/m^2 irradiance condition, the time taken for the BSA to reach MPP was approximately 0.56 s while the time taken for PSO to reach MPP was 1.05 s. However, it can be seen that under 800 and 600 W/m^2 irradiance condition, BSA shows slightly lower efficiency than PSO. This is because whenever the change of system power is within the predetermined steady state oscillation threshold (th_{osc}), the algorithm will assume the MPP has been achieved and the search process was terminated.

One of the key components for a MPPT algorithm is to react promptly and effectively towards the sudden change in system power. Such condition is very common especially in tropical country where cloud often covers the sun and cause the sudden drop in irradiance level. The ability of the MPPT algorithm to cater this situation effectively is extremely important to ensure that the PV system can always operate at its optimal operating point to extract maximum power. In this study, both MPPT algorithms were examined under rapid increasing (positive rapid changing) and rapid decreasing (negative step changing) irradiance environment to examine the tracking ability. As can be seen from the results in Table 2, it can be observed in this study that both algorithms were able to cater the rapid change irradiance condition effectively.

From the results shown in Table 2, both algorithms were able to alter the operating point of the PV system in order to ensure that the system was still operate at its MPP

Fig. 4 Tracking performance of PSO and BSA under rapid change irradiance condition from 600 to 1000 W/m²



after the change of irradiance. Besides that, the prompt response of the algorithms during the change of irradiance was also crucial to ensure that the system power loss was minimized. As observed in Fig. 4, it was found that both algorithms were able to respond immediately at the instance of irradiance changing. However, it can also be seen that the BSA was able to converge towards the MPP faster than PSO. This is due to the relative simpler of the nature of the algorithm where it only requires the change of search boundaries with the comparison of the tracked power with its achieved MPP.

5 Conclusion

In this study, the performance of both binary search algorithm and particle swarm optimization MPPT method were implemented and evaluated successfully in Matlab Simulink. From the study, BSA has shown the capability to adapt to the rapid change of irradiance effectively together with PSO. In addition, with the less tuning parameters and fast convergence of BSA, it also brought to the potential of the implementation of the algorithm in PV system.

Acknowledgements The authors would like to thank Faculty of Electrical and Electronics Engineering, Universiti Malaysia Pahang for supporting this work under research grant RDU160151 and PGRS170351.

References

1. Heydari-doostabad, H., Keypour, R., Khalghani, M.R., Khooban, M.H.: A new approach in MPPT for photovoltaic array based on extremum seeking control under uniform and non-uniform irradiances. *Sol. Energy* **94**, 28–36 (2013)
2. Eberhart, R., Kennedy, J.: A new optimizer using particle swarm theory. In: Proceedings of the Sixth International Symposium on Micro Machine and Human Science, vol. 1, pp. 39–43. IEEE, Japan (1995)
3. Ishaque, K., Salam, Z., Shamsudin, A., Amjad, M.: A direct control based maximum power point tracking method for photovoltaic system under partial shading conditions using particle swarm optimization algorithm. *Appl. Energy* **99**, 414–422 (2012)
4. Marquez, A., Leon, J.I., Vazquez, S., Franquelo, L.G., Carrasco, J.M., Galvan, E.: Binary search based MPPT algorithm for high-power PV systems. In: 10th International Conference on Compatibility, Power Electronics and Power Engineering (CPE-POWERENG), 168–173. IEEE, Poland (2016)
5. Arazi, B.: A circular binary search. *IEEE Trans. Comput.* **41**(1), 109–112 (1992)
6. Walker, G.: Evaluating MPPT converter topologies using a MATLAB PV model. *J. Electr. Electron. Eng. Aust.* **21**(1), 49 (2001)
7. Soufyane Benyoucef, A., Chouder, A., Kara, K., Silvestre, S.: Artificial bee colony based algorithm for maximum power point tracking (MPPT) for PV systems operating under partial shaded conditions. *Appl. Soft Comput.* **32**, 38–48 (2015)
8. George, K.J.: Direct control method applied for improved incremental conductance mppt using SEPIC converter. In: Proceeding IEEE International Conference on Green Computing Communication and Electrical Engineering (ICGCCEE). IEEE, India (2014)
9. Miyatake, M., Toriumi, F., Endo, T., Fujii, N.: A novel maximum power point tracker controlling several converters connected to photovoltaic arrays with particle swarm optimization technique. In: European Conference on Power Electronics and Applications, EPE, Aalborg, Denmark (2007)
10. Miyatake, M., Veerachary, M., Toriumi, F., Fujii, N., Ko, H.: Maximum power point tracking of multiple photovoltaic arrays: a PSO approach. *IEEE Trans. Aerosp. Electron. Syst.* **47**(1), 367–380 (2011)
11. Sundareswaran, K., Palani, S.: Application of a combined particle swarm optimization and perturb and observe method for MPPT in PV systems under partial shading conditions. *Renew. Energy* **75**, 308–317 (2015)
12. Ishaque, K., Salam, Z., Amjad, M., Mekhilef, S.: An improved particle swarm optimization (PSO)-based MPPT for PV with reduced steady-state oscillation. *IEEE Trans. Power Electron.* **27**(8), 3627–3638 (2012)

Filter Design for a Nine Level Voltage Source Inverter for Renewable Energy Applications



Ibrahim Haruna Shanono, Nor Rul Hasma Abdullah and Aisha Muhammad

Abstract The rapid deflation of fossil reserves coupled with environmental pollution and degradation caused by direct and indirect crude oil-related activities has resulted in the need for a sustainable alternative and environmentally friendly means of energy generation. The quest triggers the upsurge of research in the field of Renewable energy sources and its conversion. Multilevel voltage converters serve as the main interface between the renewable energy source (solar, wind etc.) and the utility grid. The converter nonlinear nature results in the need for special modulation techniques and output filters that will minimise or eliminates the output harmonics to comply with the IEEE 519 standards. Therefore, this paper aims at assessing and comparing the harmonic content of a nine-level voltage source converter using four passive filters i.e. LC, LCL, LCL with series and parallel resistance. The output voltage and current waveforms, frequency spectrum and total harmonic distortion (THD) of all the filters are compared and analysed. It is found that all the filters have THD less than 5% with LCL with parallel resistor having the least THD content of 1.82%. The investigation is carried out via simulation using PSIM and Matlab software.

Keywords Multilevel converters · Harmonic distortion · Passive filter
Voltage source inverters (VSI)

I. H. Shanono (✉) · N. R. H. Abdullah
Faculty of Electrical and Electronics Engineering, Universiti Malaysia Pahang, 26600 Pekan,
Pahang, Malaysia
e-mail: snnibrahim01@gmail.com

N. R. H. Abdullah
e-mail: hasma@ump.edu.my

I. H. Shanono
Department of Electrical, Faculty of the Engineering, Bayero University, Kano, Nigeria

A. Muhammad
Department of Mechatronics, Faculty of the Engineering, Bayero University, Kano, Nigeria

1 Introduction

Multilevel inverter (MLI) prominence in Renewable energy conversion has exceeded that of its conventional two-level counterpart. This is attributable to the vast limitations of the latter it has overcome and the inherent advantages it possesses. The converter modular nature makes it possible to integrate smaller rated power electronic switches to achieve high power capability [1]. It also eases maintenance and allows the possibility of incorporating redundancy. MLI increased output step level minimises the output harmonics, and this translates to smaller output filter size, smaller cooling system due to reduced system losses which consequently improved the overall system efficiency.

Several new MLI topologies were recently developed, most of which are modifications or hybrid of the famous three conventional topologies namely Diode Clamp (DC), Flying Capacitor (FC) and Cascaded H-bridge configurations [2–4]. Depending on the inverter topology and its control strategy; a suitable output power filter is designed and then interfaced between the inverter circuit and the grid as depicted in Fig. 1.

From Fig. 1, it can be seen that the filter forms an integral part of the Renewable Energy System (RES). As the name implies, its main function is to remove or mitigate unwanted signals in the output of any system [5]. In the field of power systems and power electronics, non-linear loads tend to inject unwanted signals called harmonics into the system, which are said to be integer multiples of the fundamental frequency (2nd, 3rd, 4th, ... etc.). These harmonics are harmful pollutants to the entire system in that it results in overheating of devices and pulsating torque in motors. Hence, it affects both system performance and efficiency. Harmonics are generated due to the non-linear characteristic properties of some electronic equipment involved. Due to the quarter wave symmetry theorem of AC signals, even harmonics (2nd, 4th, 6th, ... etc.) cancel each other in the output, leaving behind the odd harmonics [6, 7].

Filters are broadly classified into active and passive based on the type of component (active or passive) used in constructing it. The most commonly used is the passive filter, due to its availability and cheapness of components, less design complexity and its ability to effectively perform its desired task [8, 9]. There are quite a

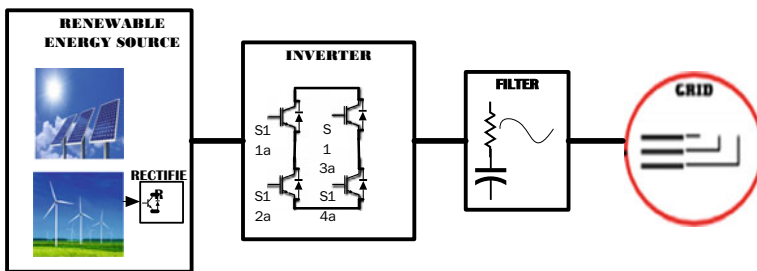


Fig. 1 System block diagram

number of filter design procedures the likes of ripple calculation, iterative algorithms and power losses optimisation [10–12].

The objective of this paper is to design and compare the THD elimination capability of four sets of passive filters on the output of a Cascaded H-bridge Nine-level voltage source inverter presented in [1]. The filters considered in this work are LC, LCL and LCL with series and parallel damping. Their stability characteristics are analysed using frequency response obtained through bode plot. The manuscripts equally justify the efficacy of selective harmonic elimination (SHE) technique in eliminating selected lower order harmonics. Therefore, aiding in achieving smaller size filter inductors by pushing up the filter cut off frequency (f_c).

2 Materials and Methods

This section explains the inverter topology principles of operation, how the switching angles are obtained, and the switching function used to generate the required nine level voltage waveform.

2.1 Inverter Circuit Description

The circuit shown in Fig. 2 is the inverter topology used in generating the nine-level output waveform. The circuit comprises of two Cascaded H-bridge topology modules that shared the same input source with their output connected to a transformer having two independent primary and series connected secondary windings with 1:1, and 1:3 turns ratio respectively. The single DC input source could be either Photovoltaic, lithium ion batteries or fuel cells. IGBT modules (S_1 to S_8) are used as the power switches. Each of the gating terminal is controlled using pre-calculated switching angles stored in a pulse generator (G_1 to G_8). With an appropriate control signal, each of the H- module is capable of generating three voltage steps ($-V_{DC}$, 0, and V_{DC}). Table 1 gives the state of each switch and the corresponding terminal voltages. The transformer turns ratio gives the opportunity of increasing the number of steps from the usual five level in conventional topology to nine level, which is one of the novelties of the proposed circuit [1].

However, the circuit configuration did not depict the filter in the output, but each designed filter is connected between the inverter output and the load.

Figure 3 is the sketch of the nine level voltage waveform to be generated by the converter topology. The first module is used for level generation as it adds more notches to the waveform while the majority of the power is transferred through the second module. Note that the research is not intended to address switching and power balancing among the electronic switches and transformers; it is a separate study on its own.

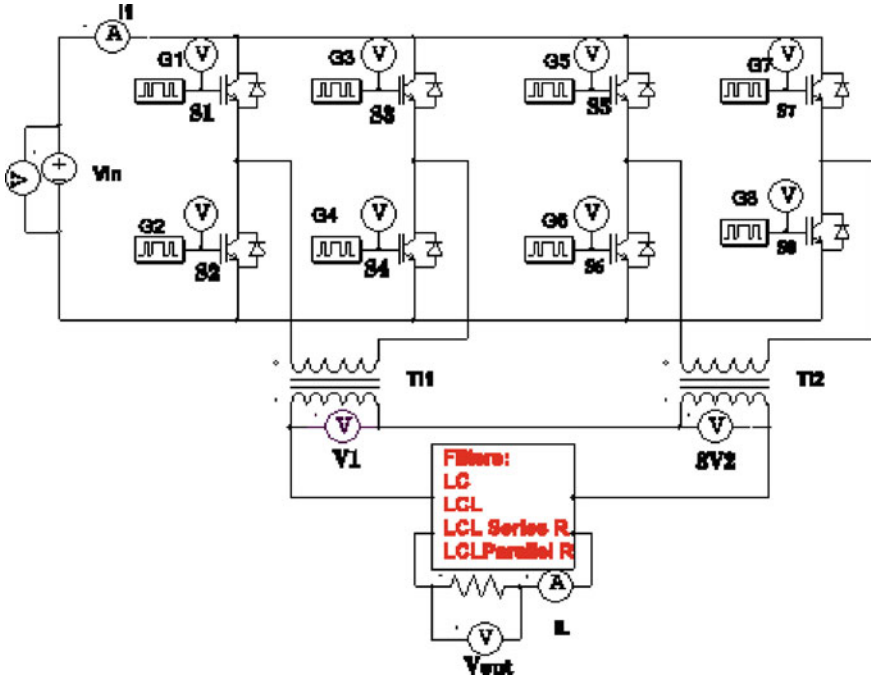


Fig. 2 Converter circuit topology

Table 1 Switching combinations

Voltage	Switching states							
	S ₁	S ₂	S ₃	S ₄	S ₅	S ₆	S ₇	S ₈
0	1	0	1	0	1	0	1	0
+E	1	0	0	1	1	0	1	0
+E	1	0	1	0	1	0	0	1
0	0	1	0	1	0	1	0	1
-E	0	1	1	0	1	0	1	0
-E	1	0	1	0	0	1	1	0

2.2 Switching Angles

The multilevel inverter is controlled using Selective harmonic elimination (SHE) pulse width modulation (PWM) technique. Therefore, the switching angles are obtained by optimally solving the generated non-linear transcendental equations using a Genetic Algorithms optimisation technique. Equation (1) shows the generalised output waveform equation. There are twelve angles with each representing a single notch (N) added per-quarter waveform at predetermined points. The equation representing the fundamental component ($n = 1$) is equated to a specific value,

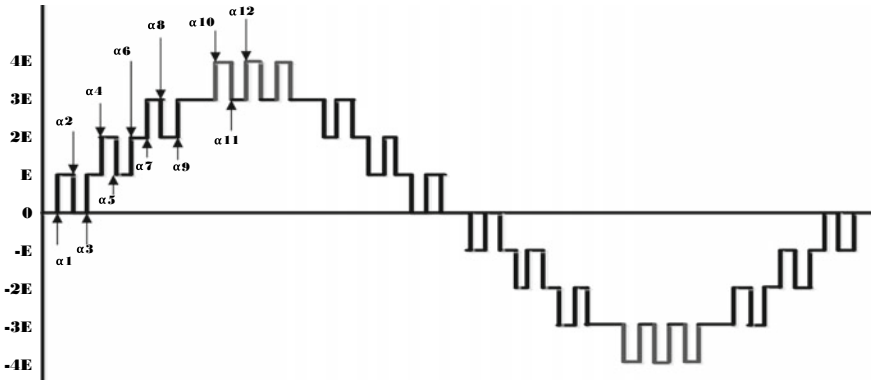


Fig. 3 Nine level waveform with 3/3/3 distribution ratio

Table 2 The optimised switching angles

s/n a_n	0–90	90–180	180–270	270–360
1	5.9272	174.0728	185.9272	354.0728
2	9.3878	170.6122	189.3878	350.6122
3	12.3888	167.6112	192.3888	347.6112
4	22.1571	157.8429	202.1571	337.8429
5	24.6285	155.3715	204.6285	335.3715
6	29.2705	150.7295	209.2705	330.7295
7	45.9568	134.0432	225.9568	314.0432
8	51.0958	128.9042	231.0958	308.9042
9	55.1359	124.8641	235.1359	304.8641
10	75.9694	104.0306	255.9694	284.0306
11	78.7371	101.2629	258.7371	281.2629
12	88.0822	91.9178	268.0822	271.9178
13	90	180	270	360

whereas all other equations are equated to zero meaning all harmonic amplitudes are zeros. Based on selective harmonic elimination theory, the converter eliminates $(N - 1)$ harmonics, which means that all the 11 lower order odd harmonics(3rd, 5th, 7th, 9th, 11th, 13th, 15th, 17th, 19th, 21st, 23rd) are eliminated in the output [1].

$$h_1 = \frac{4 * E}{n\pi} \{ \cos(n\alpha_1) - \cos(n\alpha_2) + \dots \pm \cos(n\alpha_{12}) \} \tag{1}$$

Table 2 shows the twelve switching angles in degrees. The remaining angles were calculated based on quarter wave symmetry theorem.

3 Filter Design

This section discusses the four types of filters used in this research, their circuits configuration and the design steps.

3.1 LC Filter

An LC filter is classified as a second order filter in that it has two energy storage components. Unlike its first order counterpart (L), it has an additional capacitor connected in parallel to the grid. This makes it have a better attenuation factor of 40 dB per decade. It attenuates higher frequencies above the filter cutoff frequency (f_c), whereas the lower frequency harmonics were selectively eliminated using the SHE modulation technique. The optimum goal is to realise a THD of less than 5% hence, satisfying the IEEE. 519 standard. The switching method used is capable of eliminating the first 11 lower order odd harmonics. Consequently, the most dominant harmonic in the output is the 25th order. As such, the filter cut off frequency (f_c) is chosen to be 1250 Hz. The filter inductance L is selected such that the voltage drop across it is less than 3% of the inverter output voltage. Figure 4 is the circuit arrangement for the LC filter. Equations (2) and (3) are the expressions used in selecting the inductor and capacitor values.

$$I_{Lmax} * X_L = I_{Lmax} * (2\pi Lf) < 0.03 * V_{in} \tag{2}$$

$$C = \frac{1}{L * (2\pi f_c)^2} \tag{3}$$

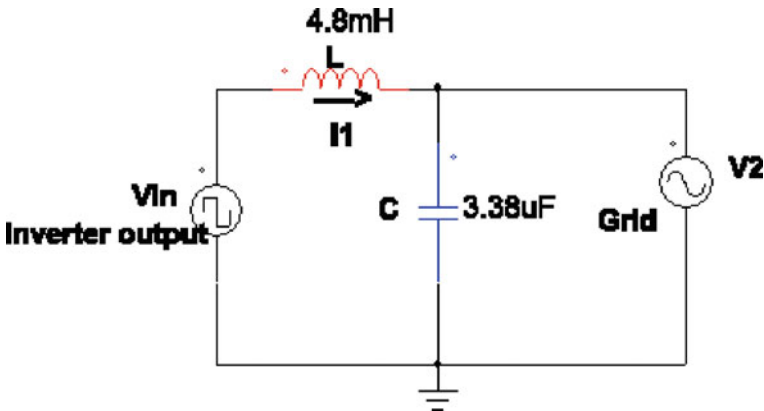


Fig. 4 LC filter

I_{Lmax} is the current through the inductor and f is the fundamental frequency (50 Hz), while V_{in} is the RMS value of the inverter output voltage.

Base on the circuit configuration, the filter input-output relation is given by the transfer function below. The values of the L and C are substituted in the transfer function which will be used to obtain the filter frequency response.

$$G_{(s)} = \frac{V_g}{V_{in}} = \frac{1}{1 + LCS^2} = \frac{1}{1.622e - 8 S^2 + 1} \tag{4}$$

3.2 LCL Filter

Due to the large inductor size, time delay and resonance issues associated with the LC filter, LCL filter was introduced to address the said problems [13]. It is a third order filter because it has three energy storage components with an attenuation factor of 60 dB per decades. Its circuit is distinct from LC filter in that it has an additional series connected inductance between the capacitor and the grid. This filter effectively addresses the problem of size and time delay but still has resonance issues, which if not addressed can cause instability in the voltage and current at the resonance frequency. Figure 5 shows the LCL filter circuit arrangement.

The below expression gives the above circuit transfer function. It is used to analyse the filter stability margin using a bode plot.

$$G_{(s)} = \frac{I_2}{V_{in}} = \frac{1}{(L_1 + L_2)S + L_1L_2CS^3} = \frac{1}{1.035e - 11S^3 + 0.00064S} \tag{5}$$

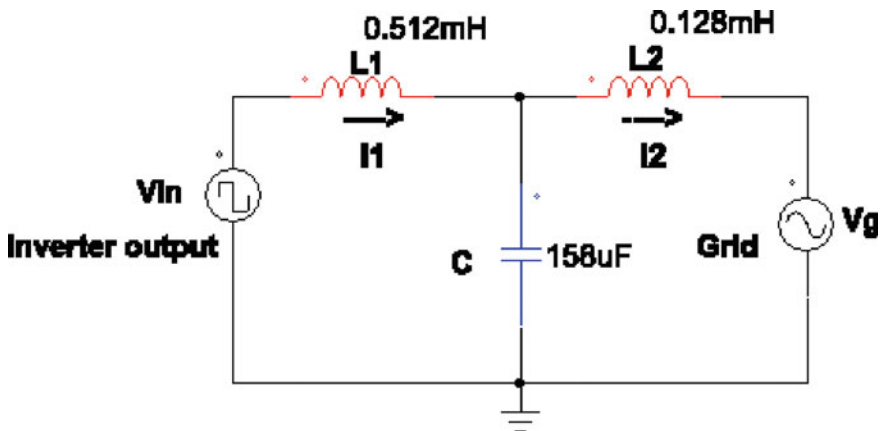


Fig. 5 LCL filter

The resonance issue is addressed by damping the system. The damping is achieved by connecting a resistor either in series or parallel to the filter capacitor. Figure 6, b represents the two filter circuit arrangements respectively. The circuits transfer function for both the two circuits are given in Eqs. (4) and (5). The resistance value needs to be carefully selected to minimise losses due to I^2R .

The transfer function for series damping configuration.

$$G_{(s)} = \frac{I_2}{V_{in}} = \frac{1 + RCS}{(L1 + L2)S + (L1 + L2)RCS^2 + L1L2CS^3}$$

$$= \frac{3.16e - 6S + 1}{1.035e - 11S^3 + 2.022e - 9S^2 + 0.00064S} \tag{6}$$

While the parallel connection transfer function is given by:

$$G_{(s)} = \frac{I_2}{V_{in}} = \frac{R}{(L1 + L2)RS + (L1L2)S^2 + L1L2RCS^3}$$

$$= \frac{2}{2.071e - 11S^3 + 6.55e - 8S^2 + 0.00128S} \tag{7}$$

Some rules and approximations need to be followed when designing an LCL filter. One of which is that the inductor voltage drop should not exceed 5–10% of the network root mean square of the rated voltage [14]. Whereas the current ripples, should not be more than 25% of the rated current. In most cases, it lies within the range of 15–25% [15]. Lastly, the reactive power absorbed by the capacitor (Q_c) should be less than the generated active power (P_g). With the help of the above assumptions, the below expressions are derived.

$$I_{Lmax} * X_L = I_{Lmax} * (2\pi Lf) < 0.05 * V_{in} \tag{8}$$

$$Q_c = \frac{V_g^2}{X_c} = V_{in} * (2\pi Cf) = 0.05 * P_g \tag{9}$$

$$L_1 = 4L_2 \tag{10}$$

$$W_{res} = \sqrt{\frac{(L1 + L2)}{L1 * L2 * C}} \tag{11}$$

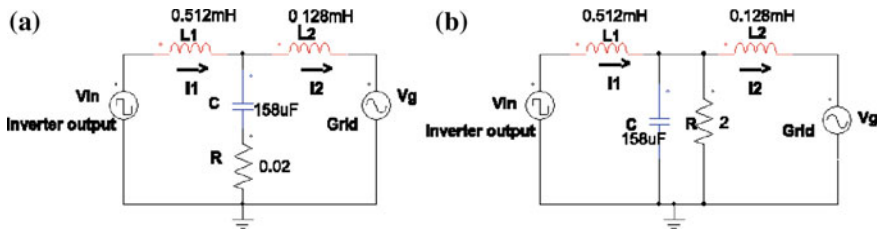


Fig. 6 a Series damped filter, b parallel damped filter

Table 3 List of filter components

Filter type	L1 (mH)	L2 (mH)	C (μF)	R (Ω)
LC	4.8	–	3.38	–
LCL	0.512	0.128	158	
LCL series damped	0.512	0.128	158	0.02
LCL parallel damped	0.512	0.128	158	2.00

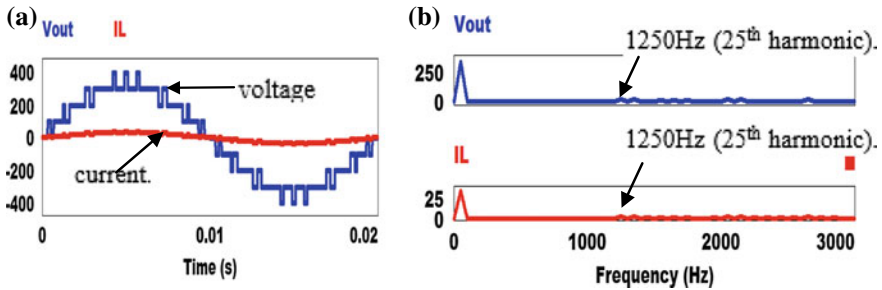


Fig. 7 a Unfiltered inverter output voltage and current waveform, b unfiltered voltage and current FFT

$$R = \frac{1}{3W_{res} C} \tag{12}$$

The passive components of all the four set of filters are calculated using Eqs. (2) and (3), (8–12). The parameters obtained are presented in Table 3.

4 Simulation Results and Discussion

This section presents the inverter output current and voltage waveforms along with their respective FFT. Based on the inverter output, three sets of filters were design and analysed. The stability margin for all the filters is ascertain using bode plot.

4.1 Inverter Output Without a Filter

The proposed inverter topology is simulated in PSIM software controlled using the obtained switching angles to generate the nine-level output voltage. Figure 7a shows the current and voltage waveforms across a resistive load. The benefit of SHE-PWM technique is it reduces the inverter output harmonic contents by eliminating lower

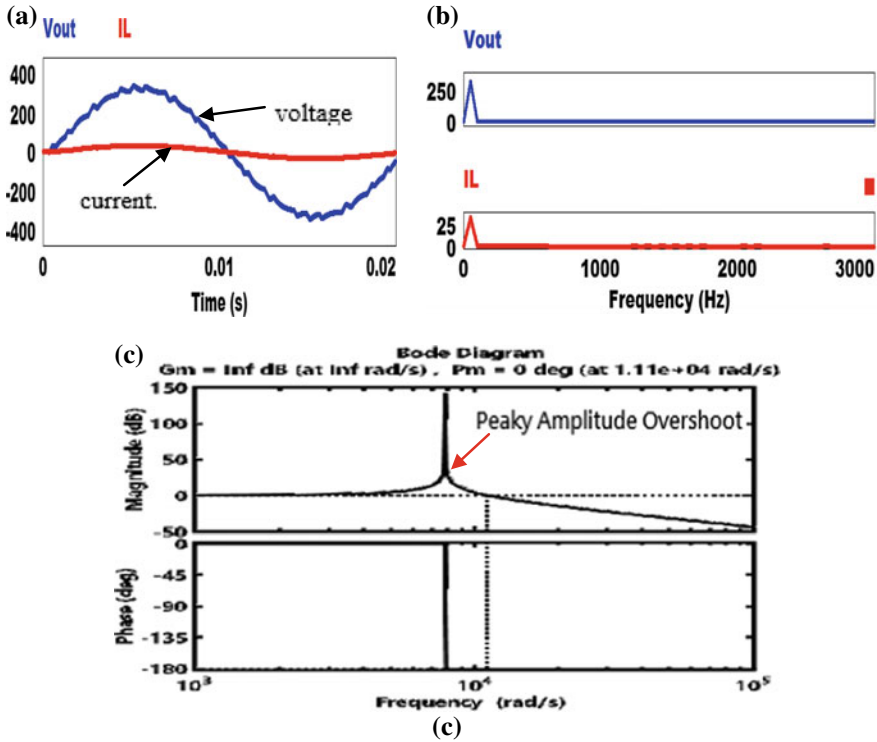


Fig. 8 a LC filtered inverter output voltage and current waveform, b LC filtered voltage and current FFT, c LC filter bode plot

order harmonics. Figure 7b shows the Fast Fourier Transform (FFT) for both the output voltage and current. As seen, all the lower harmonics are eliminated in both waveforms. Harmonics become visible at the 25th order, which is not within the SHE-PWM elimination range. Hence, this results in the need for a smaller size filter with cutoff frequency 1250 Hz. The Inverter Total Harmonic Distortion (THD) is 16.1%, which is higher than the acceptable 5%.

4.2 Inverter Output with LC Filter

To make the inverter output closer to a sinusoid, an LC filter is designed and integrated into the system. Figure 8a shows the filtered output current and voltage waveforms. The filter eliminates all the remaining higher order harmonics above the 1250 Hz in the output, as seen in the output FFT plot in Fig. 8b. This results in the THD decline from 16.1% to 2.70%. Therefore, the inverter satisfies the IEEE.519 standard requirement. The drawback with this filter is its sizeable passive component size, time

delay, poor stability margin and resonance issue. The bode plot in Fig. 8c depicts the filter frequency response with peaky amplitude overshoot occurring at the resonance frequency.

4.3 Inverter Output with LCL Filter

To address the LC filter drawbacks, an LCL filter is designed. Figure 9a shows the inverter output current and voltage waveforms. The waveform appears to be smoother than that of LC filter. LCL is capable of solving the inductor size problem and as well reduces the total harmonic distortion (THD) to 2.06%. Figure 9b, c represents the output FFT and the filter bode plot respectively. Even though the filter is not able to address resonance effects, but there is a significant improvement in the filter frequency response due to an increase in the filter phase margin and reduction in the resonance overshoot period.

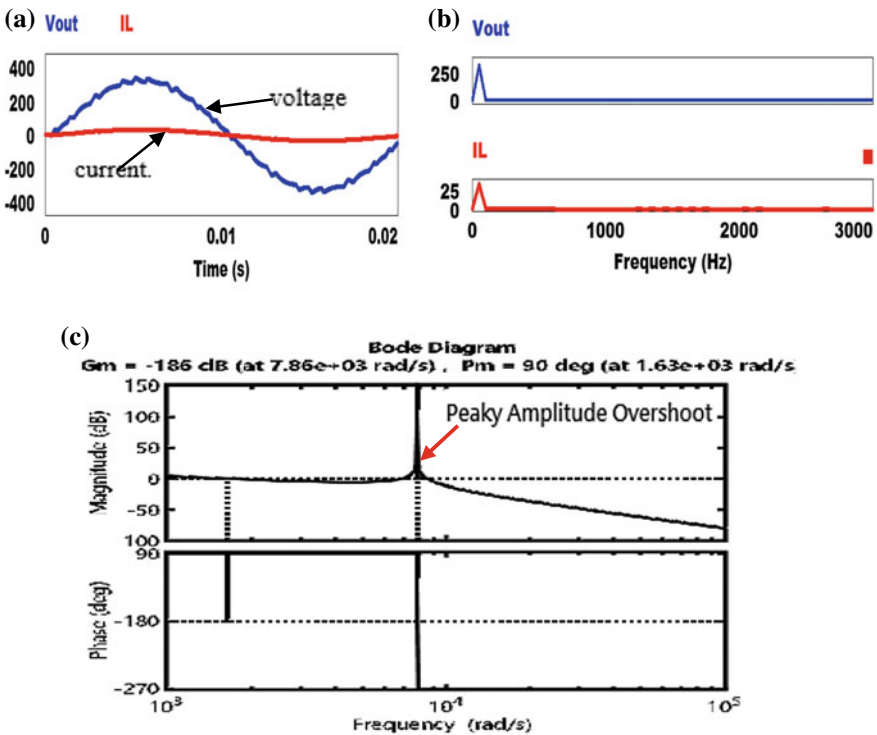


Fig. 9 a LCL filtered inverter output voltage and current waveform, b LCL filtered voltage and current FFT, c LCL filter bode plot

4.4 LCL Filter with Series Damping

To solve the resonance problem associated with the LCL filter, damping resistance is connected in series with the filter capacitor. Figure 10a shows the output waveform with slightly reduced ripples, which results in a harmonic reduction to 2.05%. Figure 10b shows its FFT plot, which has no visible physical changes from that of LCL. This is because only slight THD improvement occurs (down by 0.01%). It can be seen from Fig. 10c that the filter was able to suppress the resonance effect by damping the overshoot. This results in better stable frequency response and smooth phase transition at the resonance frequency. The drawback of this filter arrangement is high losses due to I_c^2R , as such the resistance value needs to be carefully selected.

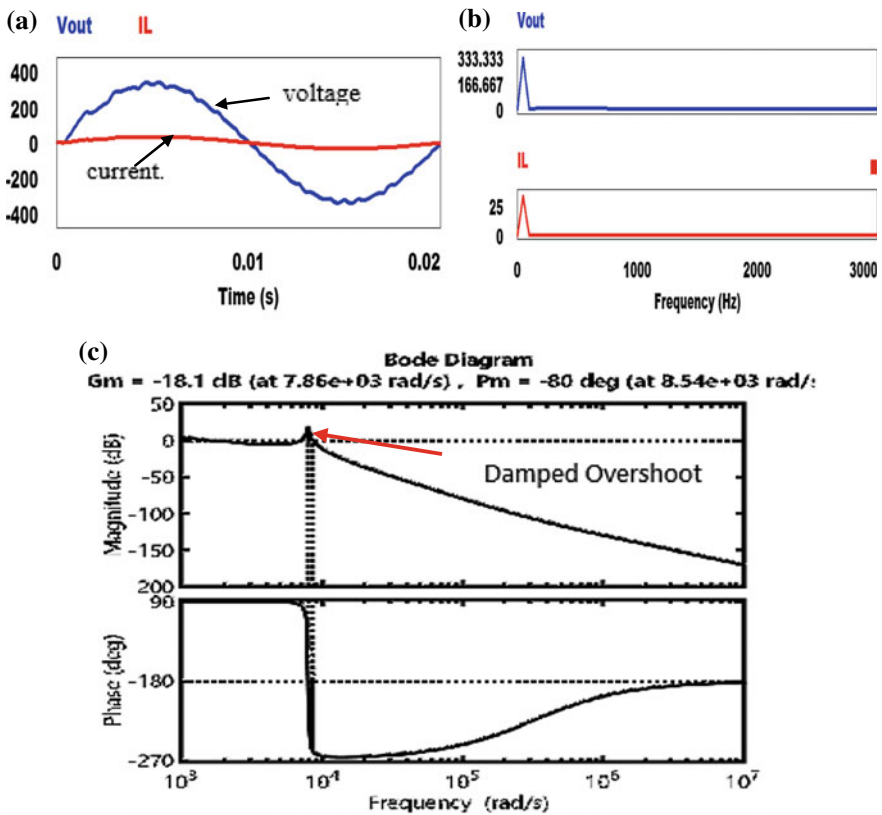


Fig. 10 a LCL series resistance filtered Inverter output voltage and current waveform, b LCL series resistance filtered voltage and current FFT, c LCL series resistance filter bode plot

4.5 LCL Filter with Parallel Damping

The filter-damping factor can as well be improved by connecting a resistor in parallel with the capacitor. This arrangement appears to have the least amount of THD value standing at 1.82%. Figure 11a, b shows the smooth inverter output waveforms and harmonic free FFT plot. The filter frequency response in Fig. 10c has significantly improve with almost zero overshoot at the resonance frequency and has better phase and gain margins.

Table 4 present the THD summary obtained for the four filters along with the one obtained without filter.

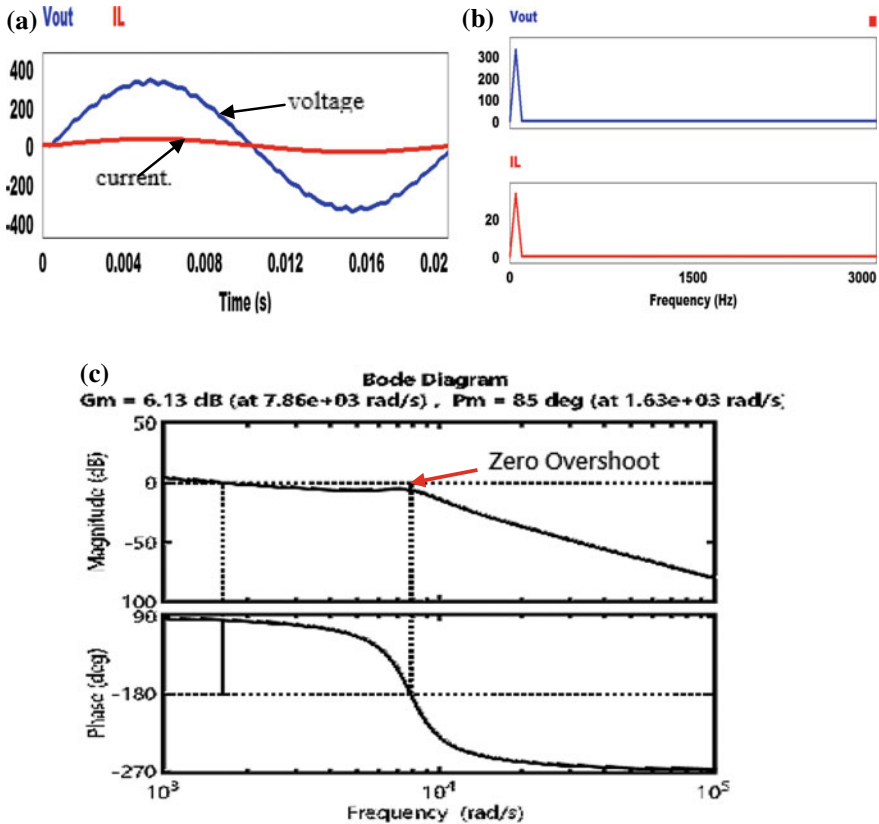
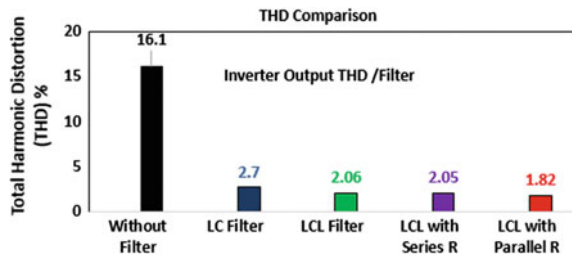


Fig. 11 a LCL parallel resistance filtered Inverter output voltage and current waveform, b LCL parallel resistance filtered voltage and current FFT, c LCL parallel resistance filter bode plot

Table 4 Filters THD comparison

Filter type	THD (%)
No filter	16.1
LC	2.70
LCL	2.06
LCL series damped	2.05
LCL parallel damped	1.82

Fig. 12 THD comparison histogram



5 Conclusion

In this paper, four sets of filters were designed for a 9-level cascaded H-bridge inverter with a cascaded transformer. The inverter is controlled using an optimised SHE-PWM modulation technique, which successfully eliminates the dominant lower order odd harmonics in the output. The output THD of the inverter is very high above the IEEE acceptable standard, therefore requires a filter to eliminate the remaining higher harmonics. The filters harmonic elimination capability was evaluated by measuring the THD values obtained in both the voltage and current output waveforms across a resistive load. Figure 12 presents the THD comparison chart of the inverter output without a filter and with the four filters.

All the filters THD value falls below 5%, therefore satisfying the IEEE 0.519 standard. In addition to that, the filters frequency response, phase and gain margins were obtained using a bode plot. Even though both LC and LCL filters satisfy the IEEE requirements, they still have poor stability margin due to resonance effect. This problem was addressed by connecting an appropriate resistance value in either series or parallel to the filter capacitance. This helps in damping the sudden overshoot that occurs at the filter resonance frequency. Out of all the four filters, LCL with parallel-connected resistance has the least THD value and better stability margin. Hence, making it more compatible with our inverter topology and control strategy.

Acknowledgements The authors gratefully acknowledge the financial supports from Universiti Malaysia Pahang Grant, with number RDU1703226.

References

1. Shanono, I.H., Nor Rul, H., Abdullah, A.M.: 9-level voltage source inverter controlled using selective harmonic elimination. *Int. J. Pow. Elec. Dri. Syst.* **9**(3), 1251–1262 (2018)
2. Venkataramanaiah, J., Suresh, Y., Panda, A.K.: A review on symmetric, asymmetric, hybrid and single dc sources based multilevel inverter topologies. *Renew. Sust. Energy Rev.* **76**(1), 788–812 (2017)
3. Shanono, I.H., Nor Rul, H., Abdullah, A.M.: A survey of multilevel voltage source inverter topologies, controls, and applications. *Int. J. Pow. Elec. Dri. Syst.* **9**(3), 1186–1201 (2018)
4. Yuan, X.: Derivation of voltage source multilevel converter topologies. *IEEE T. Ind. Electron.* **64**(2), 966–976 (2017)
5. Beres, R.N., Wang, X., Liserre, M., Blaabjerg, F., Bak, L.C.: A review of passive power filters for three-phase. *IEEE J. Em. Sel. Top. P. Electron.* **4**(1), 54–68 (2016)
6. Shehu, G.S., Kunya, A.B., Shanono, I.H., Yalcinoz, T.: A review of multilevel inverter topology and control techniques. *Int. J. Autom. Control* **4**(3), 233–241 (2016)
7. Shanono, I.H., Abdullah, N.R.H., Muhammad, A.: Five-level single source voltage converter controlled using selective harmonic elimination. *Indonesian J. Elec. Eng. Comp. Scia.* **12**(3), 924–932 (2018)
8. Cheepati, K.R., Prasad, T.N.: Importance of passive harmonic filters over active harmonic filters in power quality improvement under constant loading conditions. *IOSR J. Electr. Electron. Eng.* 21–27 (2016)
9. Kumar, D., Zare, F.: Analysis of harmonic mitigations using hybrid passive filters. In: 16th International Power Electronics and Motion Control Conference and Exposition, pp. 945–951. IEEE, Antalya, Turkey (2014)
10. Liserre, M., Blaabjerg, F., Hansen, S.: Design and control of an LCL-filter-based three-phase active rectifier. *IEEE T. Ind. Appl.* **41**(5), 1281–1291 (2005)
11. Reznik, A., Simoes, M., Al-Durra, A., Muyeen, S.: LCL filter design and performance analysis for grid-interconnected systems. *IEEE T. Ind. Appl.* **50**(2), 1225–1232 (2014)
12. Elsharty, M.: Passive L and LCL filter design method for grid-connected inverter. In: IEEE Innovative Smart Grid Technologies - Asia (ISGT ASIA), pp. 13–18. IEEE, Kuala Lumpur (2014)
13. Lahlou, T., Abdelrahem, M., Valdes, S., Herzog, H.G.: Filter design for grid-connected multi-level CHB inverter for battery energy storage systems. In: International Symposium on Power Electronics, pp. 831–836. IEEE, Anacapri, Italy (2016)
14. Renzhong, X., Lie, X., Junjun, Z., Jie, D.: Design and research on the LCL filter in three-phase PV. *Int. J. Comput. Electr Eng* **5**(3), 322–325 (2013)
15. Wang, T.C.Y., Ye, Z., Sinha, G., Yuan, X.: Output filter design for a grid-interconnected three-phase inverter. In: Power Electronics Specialist Conference, PESC '03. 2003 IEEE 34th Annual, pp. 779–784. IEEE, Acapulco, Mexico (2003)

Effects of Transformer's Turn Ratio Mismatch Towards the Performance of Dual Active Bridge Converter



Suliana Ab Ghani, Hamdan Daniyal, Nur Huda Ramlan
and Meng Chung Tiong

Abstract This paper presents the study of the effect of transformer's turn ratio mismatch on the performance of dual active bridge (DAB) converter. DAB converter was part of the components of a solid state transformer (SST) where it provides galvanic isolation as well as interface systems with different voltage level. In this study, a DAB circuit was developed and the performance was examined in both MATLAB Simulation and hardware-in-the-loop (HIL) simulation. The DAB system was examined under five different transformer ratio. The behavior of the DAB shows a comparable results under both test platform. The real-time performance of DAB converter has shown an efficiency up to 95.91%.

Keywords Dual active bridge converter · Transformer ratio
Hardware-in-the-loop · MATLAB simulink

1 Introduction

Recent years, the global growth of economy has led to the growing demand for energy in developing and emerging economies. This has brought to the needs of higher power capacity, efficient generation, transmission and utilization of electrical energy. With this, power electronics technology has been widely implemented in different parts of electrical system ranging from power generation to power utilization by end consumers.

The power electronics technology plays an important role in power system to control parameters such as frequency, voltage, active and reactive power as well as harmonics [1]. Therefore, the development of new, innovative and low-cost power converter has become the interest of various researchers. However, the complex hardware and software components often requires the time-consuming construction

S. Ab Ghani · H. Daniyal (✉) · N. H. Ramlan · M. C. Tiong
Faculty of Electrical and Electronics Engineering, Universiti Malaysia Pahang,
26600 Pekan, Pahang, Malaysia
e-mail: hamdan@ump.edu.my

© Springer Nature Singapore Pte Ltd. 2019

Z. Md Zain et al. (eds.), *Proceedings of the 10th National Technical Seminar on Underwater System Technology 2018*, Lecture Notes in Electrical Engineering 538,
https://doi.org/10.1007/978-981-13-3708-6_52

587

of the prototypes as well as poses the challenge of testing the system behaviour under various operating conditions. With the available of hardware-in-the-loop (HIL) platform, the development and validation of power converter as well as power grid can be easily carried out.

HIL is a simulation technique used in the development and testing of complex real-time embedded system [2–4]. HIL simulation provides a platform where the complexity of the simulated components can be incorporated as the controlled plant to the test platform. In addition, the sensors and actuators of the controlled plant can be electrically emulated and interfaced directly with the real control components (controllers). HIL simulation is a real-time simulation platform where the output and input relations of the signal in a particular system is maintained same as that of real process. This simulation technique presents the benefits of eliminating the costly and dangerous failure during the development of a newly proposed system. Apart from that, it also reduces the cost and brought to the ease of study for the large system such as smart grid study.

This paper addresses the performance study of a dual-active-bridge (DAB) DC-DC converter with the comparison between software simulation in MATLAB Simulink and real-time results from HIL simulator. With the same DAB system embedded in HIL, a digital signal processor (DSP) was implemented as controller to interface with the HIL simulator to examine the performance of the system. The performance and behaviour of the DAB system under both evaluation method was discussed.

2 Dual Active Bridge DC/DC Converter

2.1 Dual Active Bridge Application

Solid state transformer (SST) has been proposed as an emerging technology in smart grid application by National Science Foundation (NSF) Generation-III Engineering Research Centre (ERC) “Future Electric Energy Delivery and Management (FREEDM) Systems” in 2008 [5, 6]. SST has been discussed in 1970 [7] as an element that comprises of multistage power electronics converter isolated with high frequency (HF) transformer. SST is also known as power electronic transformer to interface the medium voltage (MV) system with low voltage (LV) system through dual active bridge converter. In SST, it can be represented with three stage system which consist of AC-DC converter, DC-DC converter and DC-AC converter as depicted in Fig. 1.

Besides the advantages of having smaller volume and reducing weight due to the application of HF transformer [8], the overall losses in the distribution system can also be reduced because the harmonics and poor power factor at the load side was isolated from the grid side [9]. The DAB DC-DC converter is one of the main element in the modular cascaded of the SST which it performs galvanic isolation between the AC to DC and DC to AC conversion. It presents the benefits of high efficiency, soft switching control, high reliability and allow the bidirectional power flow [10, 11].

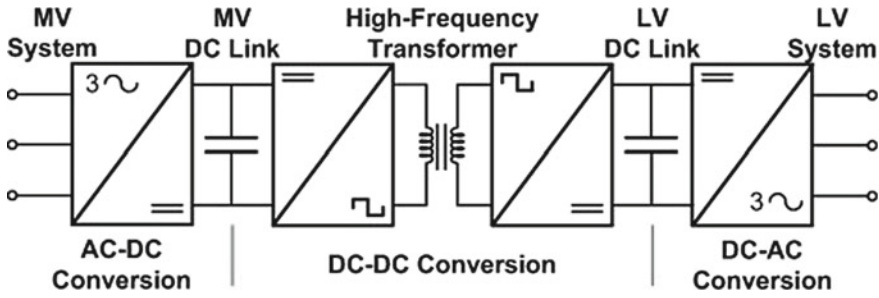


Fig. 1 Basic diagram of solid state transformer [12]

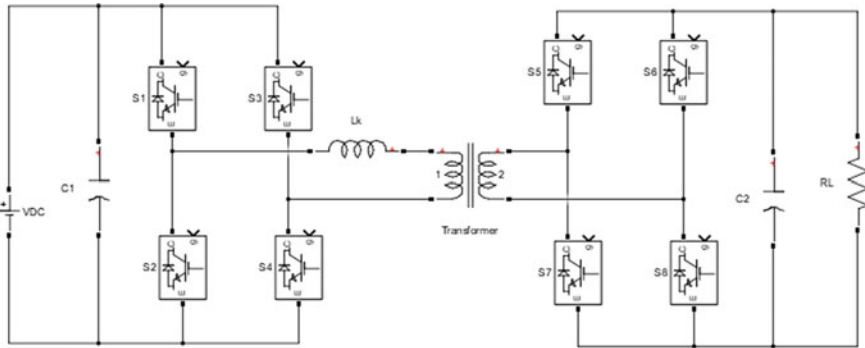


Fig. 2 Schematic of DAB

2.2 Circuit Description

The schematic diagram of the DAB converter illustrated in Fig. 2 consist of two full bridge converter circuits at both MV and LV side, isolated by a HF transformer. In DAB, it allows energy to transfer from MV side to LV side or vice versa, with a fixed frequency. According to energy conservation law, the power supplied must be equal to the power consumed, and without considering the power losses during energy transferring, it can be assumed that;

$$P_{in} = P_{out} \tag{1}$$

The isolated DAB converter is chosen due to high conversion ratio that is usually applicable when the input value is different with the output value [11]. On other hand, the leakage inductance (L_k) of the transformer plays an important role in DAB acting as an energy transfer element. With the additional coupling inductor added in series with the existing L_k , the overall inductance of the system can be increased according to the needs. In the operation of DAB, before the load side receive the

energy from the supply side, a small fraction of energy in every cycle will be stored in L_k temporarily [13].

3 Methodology

The comparison study of the performance of the DAB converter was carried out in both simulation and real-time study. In general, the control variables for control variable for the power flow of DAB are the phase shift and duty cycle [14]. In this paper, the focus of the study is to compare the performance of DAB in software simulation platform with the real-time simulation platform. In this study, the switches at inverter side were operated at a fixed 20 kHz pulse width modulation (PWM) switching signal of 50% duty cycle, while the load side was acting as passive rectifier. The switching signal for S1 and S4 were identical while S2 and S3 were fired by the complementary signal as S1 and S4 as depicted in Fig. 3. The 50% duty cycle was chosen in this study so as to produce a symmetrical square wave, however, for the asymmetrical square wave cases, it can be generated by varying the duty cycle [15].

In this study, the behavior of the DAB converter was examined by implementing different transformer ratio to the converter to perform voltage transformation in the system. The turn ratio of the HF transformer is 1:N, where the different voltage level of the two buses is possible to be matched by choosing appropriate number of turns. The design parameters for DAB converter for both software and real-time simulation is shown in Table 1. The converter was designed to operate in open loop system where there is no feedback control. The input voltage as well as the load of the converter remained unchanged throughout the study. With the implementation of different transformer ratio, the input and output of the converter was examined.

In software simulation study, the DAB converter as shown in schematic diagram in Fig. 2 was developed in MATLAB Simulink, with the design parameters described as in Table 1. Whereas for real-time study, the same system were developed and embedded in Typhoon HIL-402. The switching signals of the power switch were

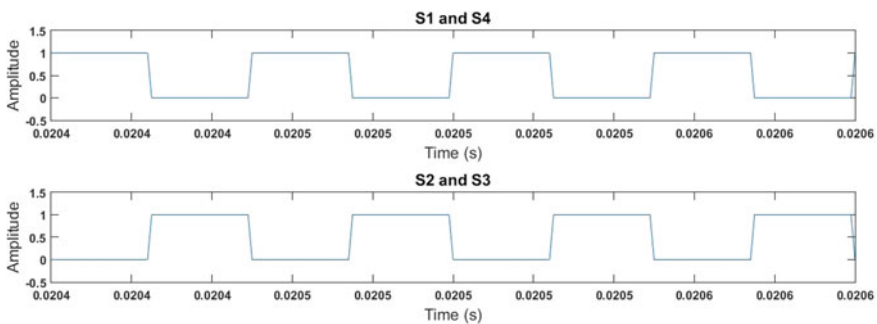
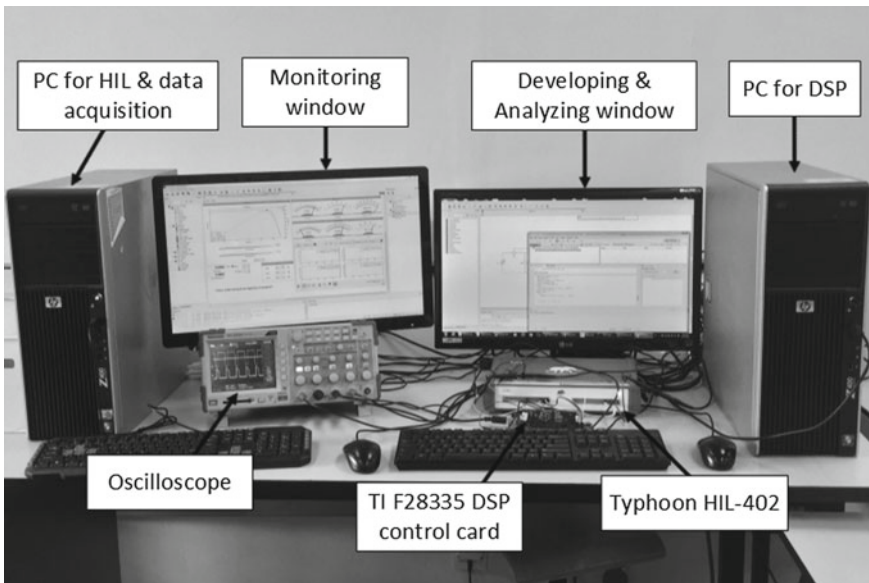


Fig. 3 Gate signal of the inverter

Table 1 Design parameters of DAB

Parameter	Value
Switching frequency	20 kHz
Leakage Inductance	1 μ H
Capacitor	4.7 μ F
Input voltage	300 V
Maximum power	3 kW

**Fig. 4** Experimental setup to study the real-time response of DAB converter

generated by using Texas Instrument F28335 DSP control card while the output response of the HIL and DSP were examined by using oscilloscope. Besides using the oscilloscope, the output of the HIL can also be monitored using the supervisory control and data acquisition (SCADA) function of the HIL. The experimental setup of the real-time study is shown in Fig. 4.

4 Results and Discussions

In the operation of the DAB converter, each power switch at the input side was controlled by constant duty cycle (50%) to generate a HF square wave voltage at its transformer terminals. By referring to the waveform shown in Fig. 5, the input voltage of the DAB is supplied by 300 V. As the turn ratio of transformer is set to 1:1, hence the secondary output yield of the transformer for MATLAB simulation

and HIL simulation were 298.4 and 287.79 V respectively. Tables 2 and 3 illustrate the MATLAB simulation results and HIL simulation results of the DAB converter with varying transformer ratio of 0.2, 0.4, 0.6, 0.8 and unity.

For the MATLAB simulation results, the output power that was produced in the unity transformer ratio was around 2968 W, which approximate to the rated system of 3 kW. In addition, this system was having highest efficiency than others due to the lowest power losses. By changing the winding ratio of transformer to 5:4, the output voltage drops to approximately 80% and the input and output power of the system decreased to 1977 and 1894 W correspondingly. Furthermore, the power of the system remained at 113 W for the 1:0.2 ratio as well as the efficiency decreased to 91.92%.

The performance results of real-time HIL simulation presented in Table 3 shows that the performance of the system under HIL simulation was comparable with MATLAB simulation result. The same trend occurred as in software simulation where unity transformer ratio configuration was operating with highest system efficiency. The relationship of the secondary output voltage of the transformer correspond to the turn ratio of the transformer was relatively accurate in HIL simulation than MATLAB simulation. Nevertheless, the output efficiency of the turn ratio 5:1 shown a rough different from that with MATLAB simulation result, which it shown 91.92%

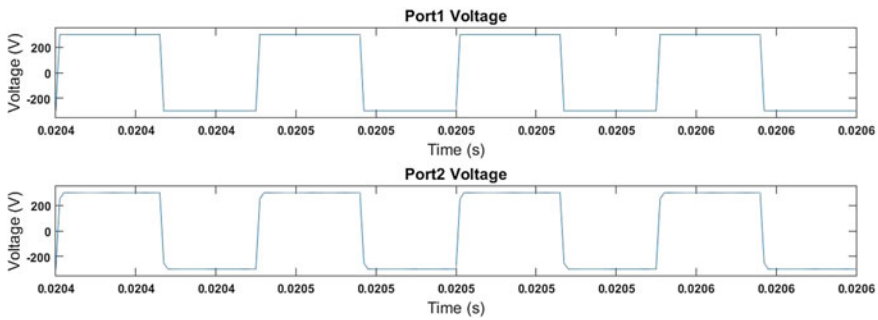


Fig. 5 Voltage waveform at transformer

Table 2 Performance of DAB converter in MATLAB simulation

Transformer ratio	Input			Simulation output			Efficiency (%)
	Voltage (V)	Current (A)	Power (W)	Voltage (V)	Current (A)	Power (W)	
5:1	300	0.41	123.7	58.4	1.95	113.7	91.92
5:2	300	1.64	493.1	118.4	3.95	467.3	94.77
5:3	300	3.70	1111	178.4	5.95	1061	95.50
5:4	300	6.59	1977	238.4	7.94	1894	95.80
1:1	300	10.31	3092	298.4	9.95	2968	95.99

Table 3 Performance of DAB converter in HIL real-time simulation

Transformer ratio	Input			HIL output			Efficiency (%)
	Voltage (V)	Current (A)	Power (W)	Voltage (V)	Current (A)	Power (W)	
5:1	300	0.41	122	57.58	2.01	116	95.08
5:2	300	1.62	486	115.15	4.04	465	95.68
5:3	300	3.64	1092	172.71	6.06	1047	95.88
5:4	300	6.47	1940	230.27	8.08	1860	95.88
1:1	300	10.10	3030	287.79	10.10	2906	95.91

for MATLAB simulation results whereas 95.08% for HIL simulation. Despite all this, the efficiency of the DAB system was still achieved with more than 90%.

5 Conclusion

In this study, the effect of transformer's turn ratio mismatch of DAB converter was examined under MATLAB simulation platform as well as by using HIL platform as real-time simulation. The performance parameters of both simulation results indicate that the response of DAB converter was comparable. The efficiency of DAB converter from MATLAB simulation are approximate to the HIL simulator results. Then, it revealed that the DAB converter has the high conversion ratio and simultaneously producing small losses. As conclusion, it shown that HIL simulation platform are credible, relatively simple and cost effective test platform.

Acknowledgements This work is supported by Faculty of Electrical and Electronics Engineering, University Malaysia Pahang, under research grant RDU1703129.

References

1. Kashani, M.G., Mobarrez, M., Bhattacharya, S.: Variable interleaving technique for photo-voltaic cascaded DC-DC converters. In: IECON Proceedings of Industrial Electronics Conference, pp. 5612–5617. Dallas, USA (2014)
2. Montazeri-Gh, M., Nasiri, M., Jafari, S.: Real-time multi-rate HIL simulation platform for evaluation of a jet engine fuel controller. *Simul. Model. Pract. Theory* **19**(3), 996–1006 (2011)
3. Gambino, G., Siano, G., Palmieri, G., Mauro, W., Vanoli, G., Criscuolo, F., Del Cogliano, D., De Rossi, F., Glielmo, L.: A low-cost HIL platform for testing professional refrigerators controllers. In: IFAC Proceedings, vol. 19, no. 3 (2014)
4. Ben Said, S., Ben Saad, K., Benrejeb, M.: HIL simulation approach for a multicellular converter controlled by sliding mode. *Int. J. Hydrogen Energy* **42**(17), 12790–12796 (2017)
5. Ye, Qing, Mo, Ran, Li, Hui: Multiple resonances mitigation of paralleled inverters in a solid-state transformer (SST) enabled AC microgrid. *IEEE Trans. Smart Grid* **3053**, 1 (2017)

6. Ashok, S.: Solid state transformer (SST) concepts, modeling, applications, advantages & challenges. In: *Power Electronics for Grid Connected Renewable Energy System (PEGCREs)*, pp. 1–137. Virginia, USA (2015)
7. McMurray, W.: Power converter circuits having a high-frequency link. U.S. Patent 3517300, June 23 (1970)
8. Zhao, T., Yang, L., Wang, J., Huang, A.Q.: 270 kVA solid state transformer based on 10 kV SiC power devices. In: *IEEE Electric Ship Technologies Symposium, ESTS 2007*, pp. 145–49 (2007)
9. Falcones, S., Ayyanar, R., Mao, X.: A DC—DC multiport-converter-based solid-state transformer integrating distributed generation and storage. *IEEE Trans Power Electron* **28.5**, 2192–2203 (May, 2013)
10. Shi, J., Gou, W., Yuan, H., Zhao, T., Huang, A.Q.: Research on voltage and power balance control for cascaded modular solid-state transformer. *IEEE Trans. Power Electron.* **26**(4), 1154–1166 (2011)
11. Rodriguez, A., Vazquez, A., Lamar, D.G., Hernando, M.M., Sebastian, J.: Different purpose design strategies and techniques to improve the performance of a dual active bridge with phase-shift control. *IEEE Trans. Power Electron.* **30**(2), 1–10 (2015)
12. Guerra, G., Martinez Velasco, J.A.: A solid state transformer model for power flow calculations. *Electr Power Energy Syst*, **89**, 40–51 (2017)
13. Chou, H.M.: Multiport DC-DC power converter for renewable energy application. Master Thesis. Texas A&M University (2009)
14. Tao, H., Kotsopoulos, A., Duarte, J.L., Hendrix, M.A.M.: Family of multiport bidirectional DC-DC converters. *IEEE Proc. Electr. Power Appl.* **153**(3), 451–458 (2006)
15. Tao, H., Kotsopoulos, A., Duarte, J.L., Hendrix, M.A.M: Triple- Half -Bridge Bidirectional Converter Controlled by Phase Shift and PWM. *Proc. IEEE Applied Power Electronics Conference and Exposition (APEC)*, pp. 1256–12637. Dallas, USA (2006)

Impact of Overcurrent Protection Coordination on the Location of the Distributed Generation Sources



Noor Zaihah Jamal, Mohd Herwan Sulaiman and Omar Aliman

Abstract In presence of the Distributed Generation (DG) brought new challenges to the protection engineers since novel coordination scheme is no longer appropriate with the penetration of the DG. The extreme case is violation to the primary and backup relay selectivity constraint. This violation will have resulted to the degradation of the relay performance. Therefore, this paper proposes the best location of the DG penetration to decrease the effect of the DG presentation to the relay performance using the grey wolf optimization (GWO) algorithm. The impacts of the DG prior to the location of the insertion are implemented to the radial 7 bus test system. As a consequence, the best location of the DG penetration is then identified.

Keywords Grey wolf optimization · Distributed generation
Protection coordination

1 Introduction

Distributed generation (DG) are becoming an important backup source to the electrical distribution system due to reasons such as increasing power demand, environmental factor and advances in technology. On the other side of advantages of DG, it has opposing effect to the distribution system, as the value of short circuit current increases depending upon its size, location and level of DG [1–3]. The type of DG insertion also has significant effect on the protection coordination problem.

Protective devices are to detect fault occurrences and remove the faulty section to ensure the reliability of the system is remaining as normal operation. Relay is widely used in power system protection at distribution and sub-transmission level.

N. Z. Jamal (✉)

Faculty of Engineering Technology, Univesiti Malaysia Pahang, 26300 Gambang, Malaysia
e-mail: zaihah@ump.edu.my

M. H. Sulaiman · O. Aliman

Faculty of Electrical & Electronics Engineering, Univesiti Malaysia Pahang, 26600 Pekan, Malaysia

© Springer Nature Singapore Pte Ltd. 2019

Z. Md Zain et al. (eds.), *Proceedings of the 10th National Technical Seminar*

on Underwater System Technology 2018, Lecture Notes in Electrical Engineering 538,

https://doi.org/10.1007/978-981-13-3708-6_53

Coordination among relays in a distribution network is a complicated problem. The overall protection scheme should be smart enough to ensure that a large part of the network gets un-interrupted power supply. In a case of fault at any feeder, the primary relay should be the first to react, whereas if it fails, the backup relay should play role to replace the operation. During this process, the selectivity constraint known as coordination time interval (CTI) should be in consideration to ensure no redundancy of operation is occurring. If any of the CTI are violated, the coordination among the relay pairs are considered fail.

Grey Wolf Optimization (GWO) algorithm was selected to be implemented for the coordination study. GWO was inspired from hunting mechanism and sership hierarchy of grey wolves in nature. The GWO had been first introduced by Mirjalili [4]. In the grey wolves' hierarchy, the first tier is nominated as a leader which known as alpha (α), next tier is beta (β), delta (δ) and followed by Omega (ω). The grey wolves' hunting activity is dedicated into three phases known as tracking, encircling and attacking the prey. The GWO has been reported to be very flexible and efficient in various areas [5–7]. The GWO algorithm is implemented to the original power distribution system (without presence of DG) to optimized the selection of the parameter of the time multiplier setting (TMS) and plug setting (PS). This selection with regards to the several constraints as mention in Sect. 3 will be the system's novel coordination scheme. The scheme will be verified with the DG penetration to several locations to test the constraints violation of CTI value. The less violation to the constraint of DG location will be testified as the best results.

2 DG Integration Problem

The integration of the DG to the conventional system will no longer maintain the existing configuration such as fault current value. The problem arises from the fault current value is depends on location, size and type of the DG integrated to the system [8]. The additional voltage sources can cause higher value of the fault current which leads to the changes of the protection scheme. This modification will initiate sympathy trip and fuse blowing which leads to huge impact to the system reliability, damages to the components and decrease the productivity of the users [9]. The increasing short circuit value will also have affected the sizing of the cable, circuit breaker, relay, transformer size and etc.

Basically, the protection scheme is accommodating with primary and secondary relay in order to response during fault occurrences to ensure the safety of the equipment and users. The requirement of the coordination time interval (CTI) in between primary and secondary relay should be followed to ensure no redundancy of the response relay had happened. The violation to the CTI value is known as coordination loss [10]. During the integration of the DG, the relay will sense the different value of the short circuit current and as a result, the circuit breaker will trip either faster or slower from the predetermined value in original scheme. As example, fault has occurred at bus E (see Fig. 1), from the existing coordination scheme R9-R5

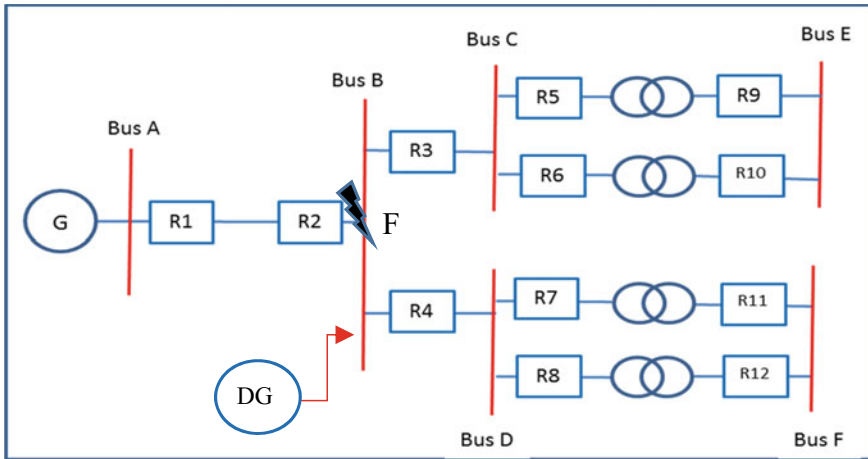


Fig. 1 Radial distribution system

(primary-backup) and R10-R6 (primary-backup). Due to the DG integration, the short circuit current is increased, R9 and R10 will respond to the fault faster than the existing predetermined value. This leads to CTI violation for which the original scheme without DG is used. This modification will be affected protection coordination scheme in whole.

During the fault occurrence, the relay will sense and initiate the circuit breaker to break the line and isolate the faulty area from the system. When the fault is cleared, the system will automatically reconnect to the main line. However, with the DG integration, the faulty portion of the system will be isolated from the main network due to natural condition. As an example, when a fault occurs at point F (see Fig. 1), relay R2 will respond and isolate the remaining line of bus B, D and F from the network and form a micro grid fed by the DG (with assumption that the capacity of DG is sufficient for a stable operation for the new grid). If a fault re-occurs during the isolation period at any point on bus B, D and F; short circuit current value sensed by the relay R4, R7, R8, R11 and R12 is low and suffers time delay in clearing the fault. The delaying in response time can cause a huge problem to the equipment, end user and protection device itself.

3 Problem Formulation

The objective of the optimization problem is to optimize the parameter of the time multiplier setting (TMS) and plug setting (PS) in order to minimize the total operating time of the primary relay while maintaining the selectivity (coordination time interval

(CTI) value in between primary and backup relays with regards the location of the DG integration.

3.1 Objective Function

The objective function of the problem is expressed as below:

$$\min z = \sum_{i=1}^m T_i \quad (1)$$

where m is the number of relays inside the system that need to be coordinated. T_i is the operating time of near end fault relay.

3.2 Characteristic Curve

In this paper, normal inverse definite minimum time (IDMT) characteristic will be used according to IEC standard where $k=0.14$ and $\alpha=0.02$. The relay time operating formulae is simplified as

$$T_i = \frac{k * TMS_i}{(I_f / PS_i)^\alpha - 1} \quad (2)$$

where PS_i is the plug setting, TMS_i is the time multiplier setting, I_f is the fault current which may be seen by the respective relay.

3.3 Inequality Constraints

The time delay for all relays are determined by the TMS value where TMS_{min} is minimum limit and TMS_{max} is maximum limit value of TMS. The bounds of TMS is varies from 0.1 to 1.1.

The current delay for all relays are determined by the PS value which given as: where PS_{min} and PS_{max} are the minimum and maximum value of PS for respective relay. The boundary limit is 1.5–5.

$$TMS_{min} \leq TMS \leq TMS_{max} \quad (3)$$

$$PS_{min} \leq PS \leq PS_{max} \quad (4)$$

Table 1 DG capacity for different distribution network [11]

Network location	Maximum capacity of DG
≤400 V network	50 kVA
400 V busbar	200–250 kVA
11–11.5 kV network	2–3 MVA
11.5 kV busbar	8 MVA
15–20 kV network and busbar	6.5–10 MVA
63–90 kV network	10–40 MVA

The Coordination time interval (CTI) value in between primary and back up relay must be fulfilled to ensure that relays are operating in sequence.

$$T_{i_{bc}} \geq T_{i_{pr}} + CTI \quad (5)$$

where $T_{i_{bc}}$ is the back-up relay time operating, $T_{i_{pr}}$ is primary relay time operating and CTI varies between 0.2 and 0.5 s.

4 Simulation Results

The 11 kV radial distribution system has been selected as the test system to study the impact of the location of the DG integration to the overcurrent coordination scheme. The size of the DG that was integrated to the system was chosen as referred to [11] (see Table 1). The short circuit current has been calculated. The GWO algorithm was implemented to the chosen test system with maximum no. of iteration is 1000 with 30 agents. The 0.3 s CTI value is considered. All simulations are using MATLAB and executed on 2.3 GHz with 8 GB RAM and an intel core i5-6200U CPU.

4.1 Radial 7 Bus Test System

The 11 kV system consists of 7 bus with 8 lines and 8 overcurrent relays (see Fig. 2). Two cases of DG penetration were considered when the DG of 2 MVA is penetrated to the bus A and bus C (nearer to the load). Value of the voltage drop due to the installation (such as material and length of the cable) of the DG will not be considered in this study. From this simulation, the best location (with less number of constraint's violation) during the DG penetration is then analyzed. The $CTI < 0.3$ s in between primary and back-up relay pair is considered as constraint's violation.

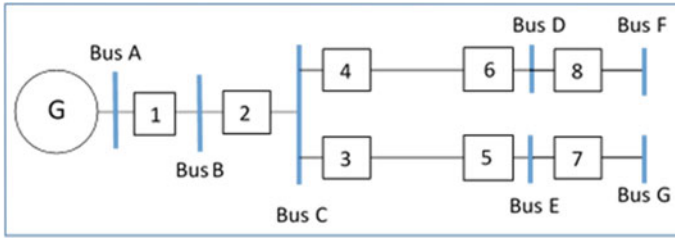


Fig. 2 Schematic of the 7 bus test system

Table 2 CTI value for system without DG, with DG at bus A and bus C

Relay no.	TMS	PS	CTI		
			Without DG	With DG at bus A	With DG at bus C
1	0.6383	0.5263	0.3000	0.2800	0.3000
2	0.4990	0.5181	0.3031	0.2999	0.3040
3	0.3508	0.7189	0.3037	0.3008	0.2995
4	0.3911	0.5139	0.3011	0.2973	0.2955
5	0.2009	0.5467	0.3021	0.4978	0.3009
6	0.1934	0.6190	0.3014	0.5046	0.3008
7	0.1002	0.5913	0.301	0.1523	0.1346
8	0.1006	0.6349	0.3005	0.1474	0.1254

Table 2 gives the optimize parameter of TMS and PS value which have been implemented with GWO algorithm for the original system (without DG integration). From the stated CTI value, it can be seen that without DG insertion, there were no CTI violation and it had fulfilled the selectivity constraint. However, the CTI value have been violated during DG presentation inside the system (see Fig. 3).

During the DG integration at bus A, the violation of the CTI value can be clearly seen at relay no. 1 with the decreasing value of 0.02 s. The decreasing value of CTI were worsen at relay no. 7 and 8. However, for DG integration at bus C, the CTI violations only started at relay no. 3 without interfering the upstream relay. The CTI value were worsen at the relay no. 7 and 8.

It can be concluded that, the best location of the DG penetration is at bus C since less number of relays are disturbed with less violation to the CTI value.

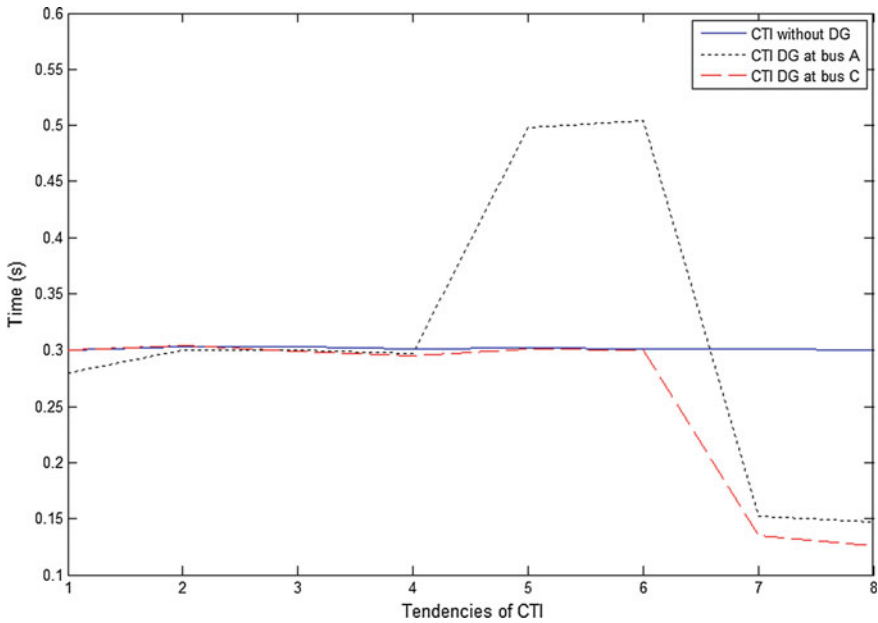


Fig. 3 Tendencies of CTI

5 Conclusion

The DG integration to the distribution network surely has numerous benefits but on the adverse side it also degraded the existing protection scheme and affected the sensitivity and selectivity sequence in between primary and backup relay during fault occurrences. The degradation varies depends on the location of the DG penetration. Therefore, studying the location of the DG integration using GWO algorithm manage to reduce the impact to the CTI violations and lessen the numbers of relays affected by the increasing short circuit value. The scheme is robust and appropriate to be implemented for future system operational and topology revolutions.

Acknowledgements This work was supported by Universiti Malaysia Pahang under grant no. RDU1803101.

References

1. Zhan, H., et al.: Relay protection coordination integrated optimal placement and sizing of distributed generation sources in distribution networks. *IEEE Trans. Smart Grid.* 7(1), 5–65 (2016)
2. Bastiao, F., Cruz, P., Fiteiro, R.: Impact of distributed generation on distribution networks. In: 2008 5th International Conference on the European Electricity Market. pp. 128–132 (2008)

3. Britto, T.M.D., et al.: Distributed generation impacts on the coordination of protection systems in distribution networks. In: 2004 IEEE/PES Transmission and Distribution Conference and Exposition: Latin America (IEEE Cat. No. 04EX956), pp. 623–628 (2004)
4. Mirjalili, S., Mirjalili, S.M., Lewis, A.: Grey wolf optimizer. *Adv. Eng. Softw.* **69**, 46–61 (2014)
5. Sulaiman, M.H., et al.: Using the gray wolf optimizer for solving optimal reactive power dispatch problem. *Appl. Soft Comput.* **32**, 286–292 (2015)
6. Panagant, N., Bureerat, S.: Truss topology, shape and sizing optimization by fully stressed design based on hybrid grey wolf optimization and adaptive differential evolution. *Eng. Optim.* 1–17, (2018)
7. Moazami Goodarzi, H., Kazemi, M.H.: An optimal autonomous microgrid cluster based on distributed generation droop parameter optimization and renewable energy sources using an improved grey wolf optimizer. *Eng. Optim.* pp. 1–21 (2017)
8. Chaitusaney, S., Yokoyama, A.: Impact of protection coordination on sizes of several distributed generation sources. In: 2005 International Power Engineering Conference, pp. 669–674 (2005)
9. Shih, M.Y., et al.: Mitigating the impact of distributed generation on directional overcurrent relay coordination by adaptive protection scheme. In: 2016 IEEE 16th International Conference on Environment and Electrical Engineering (EEEIC), pp. 1–6 (2016)
10. Shih, M.Y., et al.: An Adaptive overcurrent coordination scheme to improve relay sensitivity and overcome drawbacks due to distributed generation in smart grids. *IEEE Trans. Ind. Appl.* (99), 5217–5228 (2017)
11. Jenkins, N.: *Embedded generation*. Energy engineering series. 2000: Institution of Engineering and Technology (2010)

Investigation of Power Transfer in QAB Converter Via Phase Shift Modulation



Suliana Ab Ghani, Hamdan Daniyal, Nur Huda Ramlan
and Meng Chung Tiong

Abstract In line with high demand of renewable energy as well as the energy storage, the multiport DC–DC converters topology have recently received a lot of attention due to its own advantages. In this paper, a bidirectional quad active bridge (QAB) DC–DC converter with high frequency transformer is presented. Full bridge power converter is employed and the phase shift modulation is used in investigating the power transfer of QAB converter. In applying this proposed modulation, the changing or amount of delivering and receiving power in the QAB converter are influenced by the phase shift. Multiple cases of QAB configuration have been evaluated by (1) Multi-input single-output (balanced voltage source); (2) Multi-input single output (unbalanced voltage source); (3) Multi-input multi-output (balanced voltage source); and (4) Single-input multi-output (unbalanced load). The simulation results of a 2.5 kW system is analyzed through MATLAB/Simulink. Also, the power efficiency is discussed through this simulation. It is found out that maximum power can be achieved at 90° phase shift.

Keywords Quad active bridge · Bidirectional power flow · Phase shift modulation

1 Introduction

Nowadays, the attention towards the assimilation of renewable energy (RE) such as photovoltaic (PV) and wind turbine with the energy storage have become increasing. Due to the high needed of the interfacing of various energy sources and load either with multi input or multi output, the multiport converter have been applied by interconnection through a common DC bus [1]. This conventional method consume more conversion stages due to separate converter for individual sources or load and the limited of voltage range [1, 2]. Besides, as reported in [1], the other methods for

S. Ab Ghani · H. Daniyal (✉) · N. H. Ramlan · M. C. Tiong
Faculty of Electrical & Electronics, Universiti Malaysia Pahang, 26600 Pekan, Pahang, Malaysia
e-mail: hamdan@ump.edu.my

© Springer Nature Singapore Pte Ltd. 2019
Z. Md Zain et al. (eds.), *Proceedings of the 10th National Technical Seminar on Underwater System Technology 2018*, Lecture Notes in Electrical Engineering 538,
https://doi.org/10.1007/978-981-13-3708-6_54

603

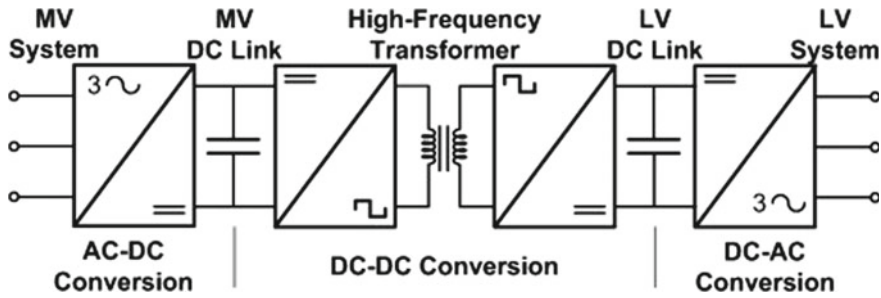


Fig. 1 Basic diagram of SST [6]

instance the time sharing concept only applicable for low power and unidirectional power flow.

An advancements in power electronics elements have bring out the design several smart grid technologies. A Solid State Transformer (SST) is one of those technologies [3] that promising technology in smart grid applications [4, 5] with the features of providing ports for integrating RE and energy storage,. Basically, the SST is a converter which contain three stages, interfacing a medium voltage (MV) system and low voltage (LV) system through high frequency (HF) transformer, as depicted in Fig. 1.

As the development of multiport DC–DC converters have gaining consideration from the researchers and the multi-active bridge (MAB) converters becomes an alternative solution [1]. The MAB is the extended version of dual active bridge (DAB) which the DC–DC converter stage in SST. With preserving the same advantages of the DAB converter such as bidirectional power flow and galvanic isolation, the QAB configuration was introduced in [7, 8]. This paper will investigate the power transfer characteristics among the ports in QAB converter and losses at the transformer by using phase shift modulation.

2 Theory of QAB

The QAB converter that have four active bridges at each ports have the possibility to exchange power among the ports, minimum conversion stages that harvest high power density, high efficiency and provides decoupling of RE and storage through a single four winding HF transformer with central controller of the whole system [9, 10]. Besides of protection side, this isolated topology can integrate different voltage levels with the turn ratio of transformer. As shown in Fig. 2, the leakage inductor at transformer will role as energy transfer element.

In QAB converter, each ports have three possibility of power flow directional that was controlled by the phase shift. Generally, the RE sources or energy storage are capable to have bidirectional power flow either delivering or receiving mode. For

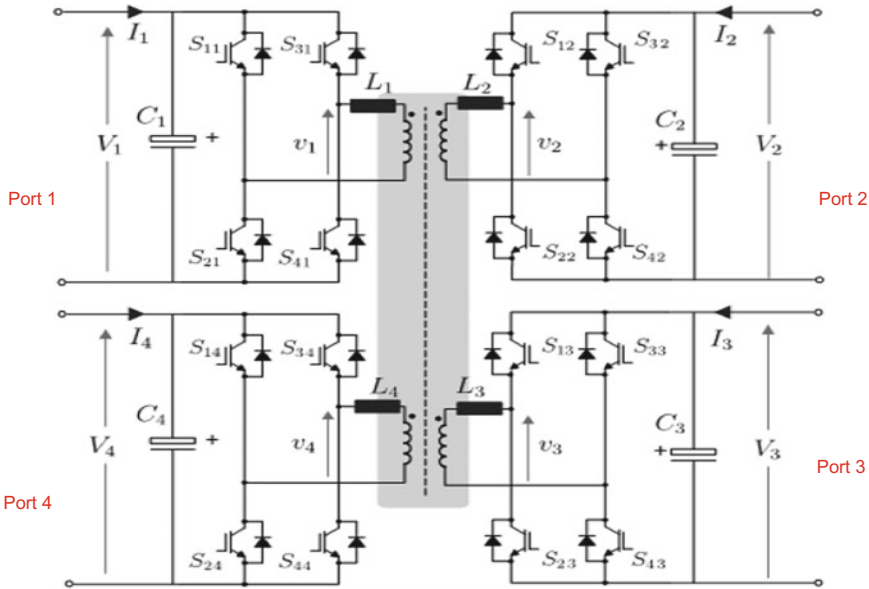


Fig. 2 Basic schematic of QAB [11]

the passive load, it just only operates in unidirectional power flow. The variation of power flow in the QAB converter have details elaboration in [7]. As example, if V_1, V_2, V_3 and V_4 are representing PV, wind turbine, fuel cell and battery respectively, the power can be transferred to the port 4 from the other three ports, which the battery acting as a load. Besides, during the charging mode of battery and fuel cell, it can receive the power from V_1 and V_2 . As referring to the energy conservation law, the total power generated in QAB must be same to the total power consumed regardless the losses as in (1).

$$\sum_{i=1}^{m+n} P_i = 0 \tag{1}$$

3 Phase Shift Modulation

There are few basic controller in DAB or multiport DC-DC converter; Single Phase Shift (SPS), Extended Phase Shift (EPS), Dual Phase Shift (DPS) and Triple Phase Shift (TPS) as reported in [12]. This paper used the SPS controller that will operates the QAB converter at fixed duty cycle with constant switching frequency. The SPS controller is simple controller compared to others, only varying the phase shift between the ports in order to control the power transferred [13]. Figure 3 illustrates

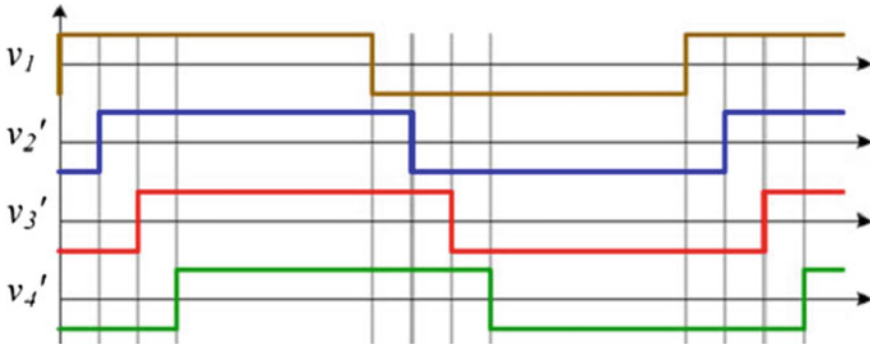


Fig. 3 Ideal waveform of phase shift modulation in QAB [15]

the ideal waveform of phase shift modulation in QAB. An amendment in the phase shift of any port will affect the power transfer in all ports. The power is flowing from the leading side to the lagging side that shows the phase is positive or negative correspondingly [10, 14]. The power transferred between four ports are the same derivation from the two ports converter. It can be expressed as:

$$P_{12} = \frac{V_1 V_2 \theta_{12}}{2\pi f_s L_{k12}} \left(1 - \frac{|\theta_{12}|}{\pi} \right), \theta_{12} = \theta_1 - \theta_2 \quad (2)$$

where θ_{12} is the phase angle between 2 ports, L_{k12} is the leakage inductance between port 1 and 2, V_1 and V_2 are the magnitudes of transformer winding voltages.

4 QAB Converter Design

The simulation of QAB converter are carried out as structured in Fig. 2 by using MATLAB/Simulink. Each full-bridge in QAB configuration is driven with a 50% duty cycle where the top switch is complemented with a bottom switch. It operates at a switching frequency of $f_s = 20$ kHz with considering all the leakage inductance, L_k have same values. All voltage applied at each port are equal with $V_n = 28$ V by assuming all ports have bidirectional way of power flow (Table 1).

The QAB is designed with multi input—multi output (MIMO) configuration and the circuit is applied with the SPS controller. In this paper, four cases of power transfer characteristics have been evaluated and investigated by varying the phase shift without change the QAB configuration. All analysis is done in open loop structure for:

(1) Case I: Multi-input single output (balanced voltage source);

All ports are 28 V with phase shift at load port (port 4 as P_{out}) is varied to 30° , 60° , 90° and 100° . Port 1, port 2 and port 3 are represented as P_{in1} , P_{in2} and P_{in3} .

Table 1 Simulation parameters [11]

Component	Value
Switching frequency (f_s)	20 kHz
Capacitor (C_1, C_2, C_3, C_4)	0.5 mF
Leakage inductance (L_1, L_2, L_3, L_4)	1 μ H
Voltage (V_1, V_2, V_3, V_4)	28 V
Power	2.5 kW
Rated current	90 A

(2) Case II: Multi-input single-output (unbalanced voltage source);

Input ports (port 1 as Pin1, port 2 as Pin2 and port 3 as Pin3) are applied to 28, 10 and 5 V and output port (port 4 as Pout) is 28 V with 30°, 60°, 90° and 100° of phase angle.

(3) Case III: Multi-input multi-output (balanced voltage source);

All ports are 28 V with phase shift at both load ports (port 3 as Po3 and port 4 as Po4) is varied to 30°, 90° (port 3) and 60° (port 4), 90° and 30° (port 3) and 90° (port 4).

(4) Case IV: Single-input multi-output (unbalanced load);

Output ports (port 2 as Po2, port 3 as Po3 and port 4 as Po4) are applied to 28, 10 and 5 V and input port (port 1 as Pin1) is 28 V. The phase shift is varied to 30°, 60°, 90° and 100° of phase angle to all loads.

5 Results and Discussions

The QAB converter was simulated using the MATLAB/Simulink and all the simulation results were presented in Fig. 4 according to the cases that was mentioned in previous topic. In Case I, three ports acting as input and one port as a load with same voltage. The port 4 as load part is varied by the phase shift of 30°, 60° and 90°. It can be seen that the maximum power in this case are received during 90° of phase angle. For the unbalanced voltage source, the source is applied to 28, 10 and 5 V for each port while the load side is 28 V with various phase shift as tested in Case I. The power transferred for each input side is difference according to their capacities. For instance, the port 1 with 28 V will transfer more power to the load and the port 3 which has 5 V of input voltage will produce less power compared to others. Then, the load received all the total power from the input ports with small losses. As well in Case I, the load side consumed the maximum power at a phase angle of 90°.

In multi-input multi-output case, the same voltage are applied at all ports and it shows that the power transferred between input ports is identical and the total power

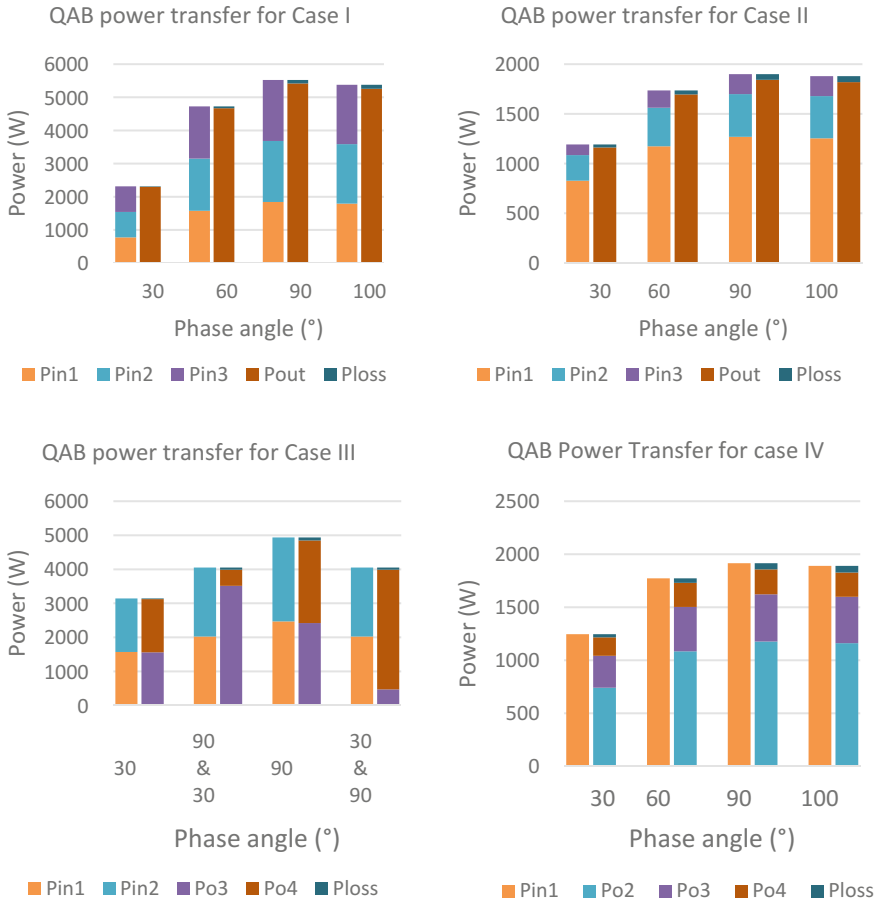


Fig. 4 Simulation results of QAB converter

to the output ports are quite balanced for the same phase shift applied at the both load ports. However, in difference phase shift, the power demand from each load is not same and the power will transferred accordingly. By referring to the Case III in Fig. 4, the port 3 that was shifted by 90° consumed almost 3500 W of power compared to the port 4 that have been shifted by 30° of phase angle just received only around 480 W.

Lastly, in Case IV, the various phase shift and voltage is applied to the output side with 28, 10 and 5 V to each port. The input voltage of 28 V will transfer all the power to the loads as per their request. For instance, the port 2, port 3 and port 4 at 60° phase angle received the power of 1 kW, 400 W and 200 W based on their voltage value, which the small voltage will demand for the low power and vice versa.

In all cases, it seems that the power source is balanced with the output power where it just yields less than 5% of transformer losses which the system produces up to 95% of efficiency. Also, the maximum power transferred occurred at 90° of phase angle.

6 Conclusion

It has been demonstrated that the QAB converter can manage the power exchange among the ports directly through the single multi-winding high frequency transformer. The input power is balanced with the output power in the QAB converter and it depicted that all ports can flow in bidirectional ways. The SPS technique that was carried out in the simulation are achieving the optimal efficiency with more than 95% of efficiency. As the conclusion, the power transfer characteristics in QAB have been investigated by harvesting less than 5% losses during the transferring power through the transformer.

Acknowledgements This work is supported by Faculty of Electrical and Electronics Engineering, Universiti Malaysia Pahang, under research grant RDU1703129.

References

1. Tao, M.A.M.H.H., Kotsopoulos, A., Duarte, J.L.: Family of multiport bidirectional DC–DC converters. *IEE Proc.-Electri. Power Appl.* **153**(3), 451–458 (2006)
2. Tran, Y.K., Dujic, D.: A multiport isolated DC–DC converter. In: *Applied Power Electronics Conference and Exposition (APEC)*, 2016 IEEE, pp. 156–162. IEEE (2016)
3. She, X., Yu, X., Wang, F., Huang, A.Q.: Design and demonstration of a 3.6-kV–120-V/10-kVA solid-state transformer for smart grid application. *IEEE Trans. Power Electron.* **29**(8), 3982–3996 (2014)
4. Ye, Q., Mo, R., Li, H.: Multiple resonances mitigation of paralleled inverters in a solid-state transformer (SST) enabled AC microgrid. *IEEE Trans. Smart Grid* **30****53**(c), 1 (2017)
5. Huber, J.E., Kolar, J.W.: Solid-state transformers: on the origins and evolution of key concepts. *IEEE Ind. Electron. Mag.* **3**, 19–28 (2016)
6. Guerra, G., Martinez-Velasco, J.A.: A Solid state transformer model for power flow calculations. *Int. J. Electr. Power Energy Syst.* **89**, 40–51 (2017)
7. Qiang, M.E.I., Wei-yang, W.U., Zhen-lin, X.U.: A Multi-directional power converter for a hybrid renewable energy distributed generation system with battery storage. pp. 1–5 (2006)
8. Falcones, S., Ayyanar, R., Member, S., Mao, X.: A DC–DC multiport-converter-based solid-State. *IEEE Trans. Power Electron.* **28**(5), 2192–2203 (2013)
9. Costa, L.F., Buticchi, G., Liserre, M.: Quad-active-bridge DC-DC converter as cross-link for medium-voltage modular inverters. *IEEE Trans. Ind. Appl.* **53**(2), 1243–1253 (2017)
10. Costa, L., Liserre, M.: Improving system efficiency for the more electric aircraft. *IEEE Ind. Electron. Mag.*, pp. 26–36 (2017)
11. Buticchi, G., Costa, L.F., Barater, D., Liserre, M., Amarillo, E.D.: A quadruple active bridge converter for the storage integration on the more electric aircraft. *IEEE Trans. Power Electron.* **33**(9), 8174–8186 (2018)

12. Tong, A., Hang, L., Li, G., Jiang, X., Gao, S.: Modeling and analysis of a dual-active-bridge-isolated bidirectional DC/DC converter to minimize RMS current with whole operating range. *IEEE Trans. Power Electron.* **33**(6), 5302–5316 (2018)
13. Zhao, B., Song, Q., Liu, W., Sun, Y.: Overview of dual-active-bridge isolated bidirectional DC-DC converter for high-frequency-link power-conversion system. *IEEE Trans. Power Electron.* **29**(8), 4091–4106 (2014)
14. Chou, H.M.: Multi-port DC-DC power converter for renewable energy application (2009)
15. Falcones, S., Ayyanar, R., Mao, X.: A DC–DC multiport-converter-based solid-state transformer integrating distributed generation and storage. *IEEE Trans. Power Electron.* **28**(5), 2192–2203 (2013)

Current Measurement of Engine Oils Under Various Voltage Application



Benedick Conolius, Norlin Pauzi, Mohd Herwan Sulaiman,
Mohd Razali Daud, Kadowaki Kazunori and Amir Izzani Mohamed

Abstract This paper presents the conduction current measurement of engine oil of a vehicle during engine oil usage. A motorcycle and car engine oil is the sample in this study. For motorcycle engine oil, sample was taken between 0 and 1500 km while for car engine oil, it was taken between 0 and 9000 km. The electrode was printed to PCB board and the oil was placed between electrode with 1 mm gap. The current was measured by a microammeter under voltage applied from 0.2 to 1.0 kV. From the result it is understood that the current decreases with the increase in travelling distance of each vehicle. Motorcycle engine oil shows a higher current decreasing rate as compares to car engine oil.

Keywords Engine oil · Current · High voltage

1 Introduction

Generally, condition monitoring increases the performance of an engine and its lifetime, lowers the operating costs, reduces the downtime cost and prevents failures [1]. This play an important role in engine-based technologies and maximizes engine reliability and maintainability. An engine's performance can be seen from three points of view; the condition of the lubricant, the presence of contaminants and engine wear and tear [2].

Engine oil is very important since its function is to reduce the wear and tear of engine. Primary function of the oil is to lubricate the moving parts and also to clean, prevent rust formation, improve the sealing and cooling the aggregate by

B. Conolius · M. H. Sulaiman · M. R. Daud · A. I. Mohamed (✉)
FKKE, Universiti Malaysia Pahang, 26600 Pekan, Pahang, Malaysia
e-mail: amirizzani@ump.edu.my

N. Pauzi
FKKSA, Universiti Malaysia Pahang, 26300 Gambang, Pahang, Malaysia

K. Kazunori
Electrical and Electronic Engineering, Ehime University, 790-8577 Matsuyama, Ehime, Japan

© Springer Nature Singapore Pte Ltd. 2019
Z. Md Zain et al. (eds.), *Proceedings of the 10th National Technical Seminar on Underwater System Technology 2018*, Lecture Notes in Electrical Engineering 538,
https://doi.org/10.1007/978-981-13-3708-6_55

transportation of heat from engine [3]. It is known that the engine part is moving against each other thus resulting to the friction and power loss through conversion into heat. Besides that, the process of oil degradation due to the high temperature in the engine will continue and consequently leads to a system malfunctions. So, engine oil needs to be changed regularly as a precaution [4].

Apart from that, it is known that there are a number of studies of degradation parameters in engine oil that have been done by so many researchers to ensure that the user can use their engine oil for maximum utilization. This is to prevent the user to bluntly follow the recommendation given by a mechanic and not knowing why the oil should be changed at a certain mileage. The contamination during oil use is the chemical by product of additives and the subsequent interaction among the resultant components to produce corrosive acids and other undesired substances [5].

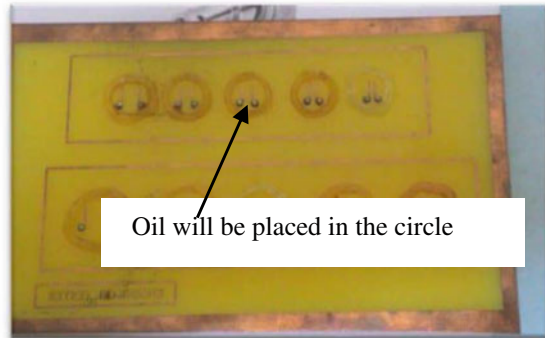
Engine condition monitoring techniques through engine oil analysis are widely used and are an effective way to diagnose abnormal wear and engine malfunctioning [2]. Therefore, the interest in developing a more sophisticated method in determining the condition of the lubricant (for oil changes) has grown amid automotive, industrial and lubricant companies. The changes in physical and chemical of engine oil proved that it is the main caused of finite life time engine oil that will degrade according to time and usage [6]. The easiest way to know the condition of oil is by measuring the change of viscosity of engine oil through spectroscopy technique [5, 6]. However, this technique requires one to bring the sample to a lab and is time-consuming. In this paper, current measurement was carried out on vehicle's engine oil during service. The value of current is expected to decrease with the increase of vehicle's mileage. This is based on the understanding that the byproduct of the oil during service is a form of oxide's particles; where the resistance is high due to non-conductive character of an oxide's particle, thus reducing the flow of current through the oil. The obtained result can be used as a benchmark to evaluate the quality of the oil later.

2 Methodology

2.1 Test Board

In this project, engine oil from vehicle's engine will be taken and tested. One to three drops of oil will fill the space between the electrodes as shown in Fig. 1. Various gap lengths between both electrodes were prepared on a PCB board and the current reading will be recorded manually. However, in this paper only result for 1 mm gap length will be discussed due to similar pattern observed in other gap length cases. Each electrode has thickness of 1 and 5 mm in length. The space to place the engine oil sample under test have a diameter of 5 mm, the gap length of 1 mm. A 1 mm radius of hole was drilled at the end of the copper from the PCB that represents the electrode.

Fig. 1 Electrodes with different gap length are printed on PCB



Then, a pin header is being soldered through the holes between the PCB copper as shown in Fig. 2. The function of the pin header is to connect the electrode to a multimeter (microammeter mode) and a high voltage dc (HVDC) power supply. Figure 3 shows the connection diagram of the measurement setup.

2.2 Sample

In this experiment, there are two types of oil that are being tested which are motorcycle and car engine oil as shown in Table 1. The motorcycle engine oil (CP1) was sampled at 0 km (new), 300, 500, 700, 1200 and 1500 km while for car engine oil (BDL), was taken for 0 km (new), 4000, 5000 and 9000 km. The vehicles usage in term of driver's driving attitude of speed or the use of air-conditioning and radio are not controlled.

3 Results

From the result obtained for both motorcycle (Fig. 4) and car (Fig. 5) engine oil, generally shows that the value of current decreases with the increase in voltage applied. For new oil at 0 km, the current reaches as high as 110 and 130 μA for motorcycle and car oil respectively, under 1 kV of applied voltage. As the mileage of both vehicles increases, the current decreases significantly to 50 μA for motorcycle oil, where the mileage reaches 1500 km. This value is approximately 54.5% reduction from its original values at 0 km. As a comparison, for car oil, the current does not decrease as much as that in motorcycle case, where it only decreases to 110 μA when the mileage reaches 1000 km. The higher rate of decreasing in motorcycle oil suggested that for motorcycle oil, it is necessary to change the oil even at a low mileage. The oil must have been heavily contaminated as compares to its new condition. Moreover, at 5000 km, the car oil finally decreases to 60 μA which is 53.8%

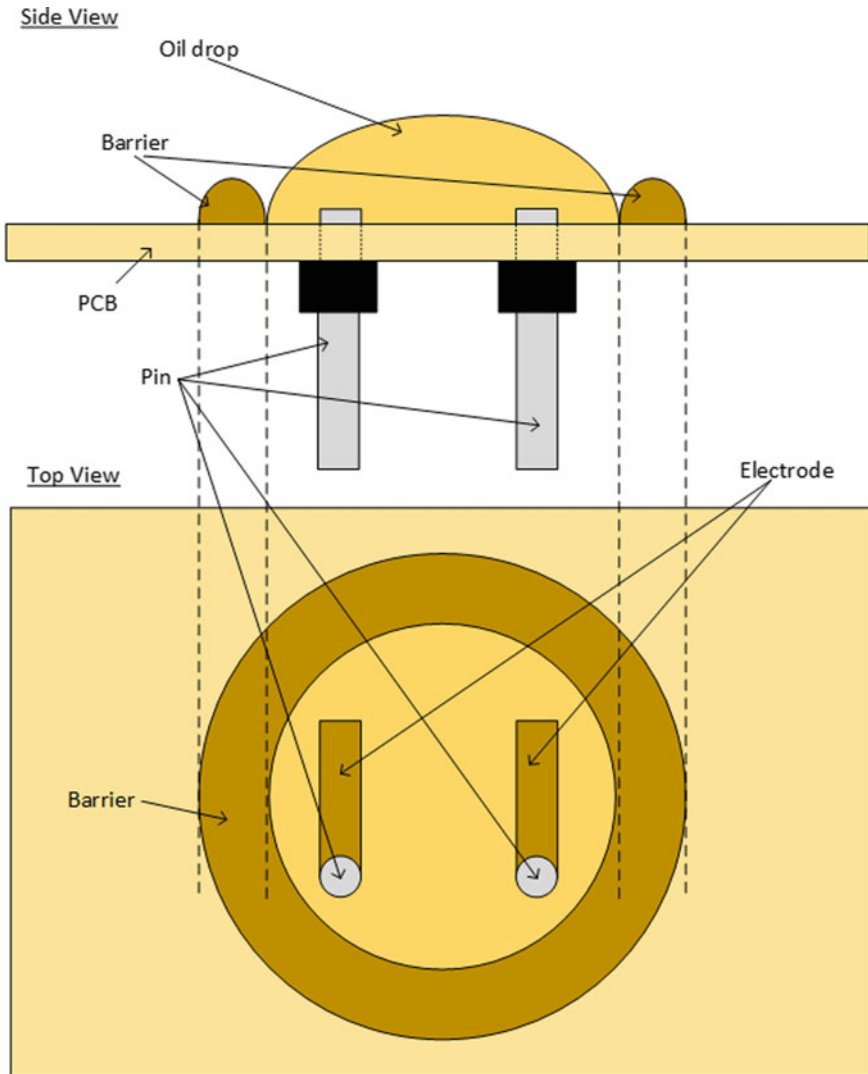


Fig. 2 Test board side view and top view

from original condition. In fact, at 9000 km, the measured current is very identical to that at 5000 km. Therefore, it can be assumed that the amount of contamination in the oil is at the same level, thus no change in current. For most cars, when semi-synthetic oil is used, it is suggested that to change oil between 5000 and 10,000 km. This value seems in agreement to the current values obtained from this study if the suggestion by the car maker is based on that contaminant level in the oil itself. Even though the current value obtained was different from the others [7–9], as a conclusion this study shows that the current value is influenced by the vehicle mileage.

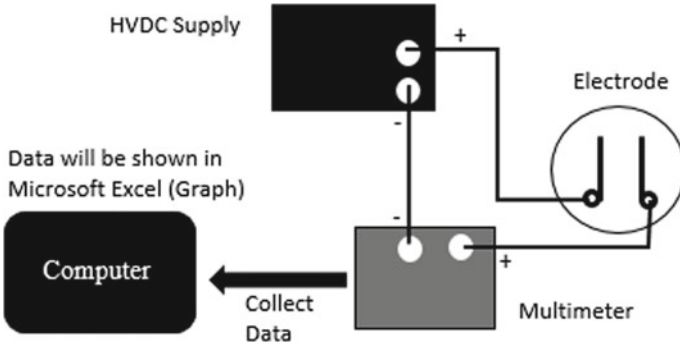


Fig. 3 Connection diagram the measurement setup

Table 1 Sample rating and sampling

Vehicle type	Brand	Rating (W)	Sampling (km)
Motorcycle 4 strokes	CP1	10–40	0, 300, 600, 900, 1200, 1500
Car	BDL	5–40	0, 4000, 5000, 9000

The two samples of motorcycle engine oil showed a slightly different of current because it depends on the purity of the liquid and the condition of the engines. Besides that, it also depends on the production of engine oil based on their base oil. Both

Fig. 4 Voltage-current characteristic of motorcycle oil under different voltage

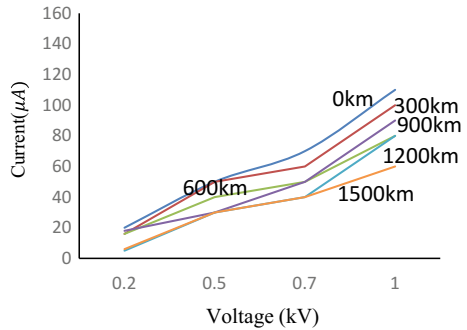
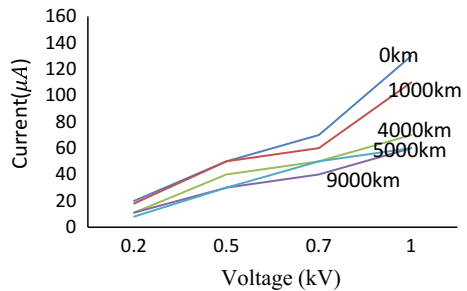


Fig. 5 Voltage-current characteristic of car oil under different voltage



types of engine oil showed much lower currents obtained after their utilization in transport system.

According to Ohm's Law ($V = IR$) the resistance value can be calculated by using that formulae directly. The decreases in current with the increase of vehicle's mileage shows that the resistance of the oil has increased and the contaminant is the resistive element which contributes to the decrease. Oxides is one form of resistive element that can be produced as a by-product from the engine activity. For further understanding of the by-product, a chemical analysis must be conducted in later stage of this study.

4 Conclusion

This experiment shows that the current for engine oil decreases after their utilization in a vehicle. Besides that, the value of current obtained for both sample of motorcycle oil was slightly different due to condition of the engine and the purity of engine oil. Apart from that, each type of engine oil has their own base oil and this may affect the result obtained. The result can be used as a benchmark or indicator later in order to evaluate the quality of engine oil, definitely after chemical analysis of the oil is carried out. It can be a reference for user to identify the engine oil condition.

References

1. Soleimani, M.: Thick film sensors for engine oil acidity detection. University of Southampton, Faculty of Engineering and the Environment, Doctoral Thesis (2014)
2. Thom, A.C.G.: Diesel engines diagnosis through analysis of lubricating oil. In: International Conference on Systems, Man, and Cybernetics (SMC), pp. 2751–2756. IEEE (2014)
3. Kardoš, S., Pietriková, A., Tóthová, J.: Possibilities of motor oil continuous diagnostics. In: 38th International on Spring Seminar on Electronics Technology, pp. 277–282. IEEE (2015)
4. Idros, M.F.M., Ali, S., Islam, M.S.: Quantitative analysis of spectroscopy's study for engine oil degradation monitoring due to temperature effect. In: Third International Conference on Intelligent Systems Modelling and Simulation, pp. 278–282. IEEE (2012)
5. Al-ghouti, M.A., Al-atoum, L.: Virgin and recycled engine oil differentiation: a spectroscopic study. *J. Environ. Manage.* **90**(1), 187–195 (2009)
6. Idros, M.F.M., Ali, S., Islam, M.S.: Optical behavior of transmission oil lubricant for degradation monitoring. In: IEEE Student Conference on Research and Development, pp. 225–228 (2011)
7. Dikarev, B.N., Ostaperiko, A.A., Karasev, G.G.: Viscosity dependence of dielectric liquids on electric field. In: 11th International Conference on Conduction and Breakdown in Dielectric Liquids (ICDL), pp. 1–5 (1993)
8. Romanets, R., Dikarev, B.N., Ostaperiko, A.A., Karasev, G.G.: Relaxation currents in dielectric liquids. In: 10th International Conference on Conduction and Breakdown in Dielectric Liquids, pp. 196–200 (1990)
9. Jwo, C., Jeng, L., Chang, H., Teng, T.: Experiment study on thermal conductivity of lubricant containing nanoparticles. *Rev. Adv. Mater. Sci.* **18**(7), 660–666 (2008)

Parameter (Voltage, Current) Study of Thermoelectric Cooler (TEC) for Automobile Air-Conditioner



Siti Nor Aisyah Burhanudin, Mohd Shawal Jadin
and Amir Izzani Mohamed

Abstract To overcome the weaknesses of the existing HVAC system, the use of newly emerging thermoelectric cooler which works on Peltier and Seebeck effect can be a solution. Thermoelectric cooling can be considered as one of the major applications of thermoelectric modules (TEM) or thermoelectric coolers (TEC). The aim of this project is to design a cooling system that will be mounted on a car AC conventional blower. Peltier effect is the main idea of this cooling system as it functions when a DC current flow through TE modules generating heat transfer and temperature difference across the ceramic substrates causing one side of the modules becomes cold and the other side to be hot. This project objective is to make use of the cold side of the modules to cool the ambient air to a lower temperature, so that it can be used as a personal cooler. Cooling system interfaces with a simple temperature controller is included. TEC air cooling for the sizing and design of the cooling system on the basis of analysis that can be deduced is indeed possible. Developed electronics is evaluated with simulated load. With hardware test results, the lowest cooling temperature can be achieved is 16.7 °C with power drawn by Peltier element is measured nearly 15.6 W.

Keywords Thermoelectric cooler · Peltier effect · Seebeck effect

1 Introduction

When a DC supply is applied to the TEC module, heat will be absorbed at one junction and release at the other junction. The direction of heat flow is regulated based on the direction of the supply DC power source, one surface of TEC absorbs heat making surface cold and the opposites sides gets heated [1]. This phenomenon can be described using Peltier effect. The minimum temperature that can

S. N. A. Burhanudin · M. S. Jadin · A. I. Mohamed (✉)
Faculty of Electrical and Electronics Engineering, Universiti Malaysia Pahang,
26600 Pekan, Pahang, Malaysia
e-mail: amirizzani@ump.edu.my

© Springer Nature Singapore Pte Ltd. 2019
Z. Md Zain et al. (eds.), *Proceedings of the 10th National Technical Seminar on Underwater System Technology 2018*, Lecture Notes in Electrical Engineering 538,
https://doi.org/10.1007/978-981-13-3708-6_56

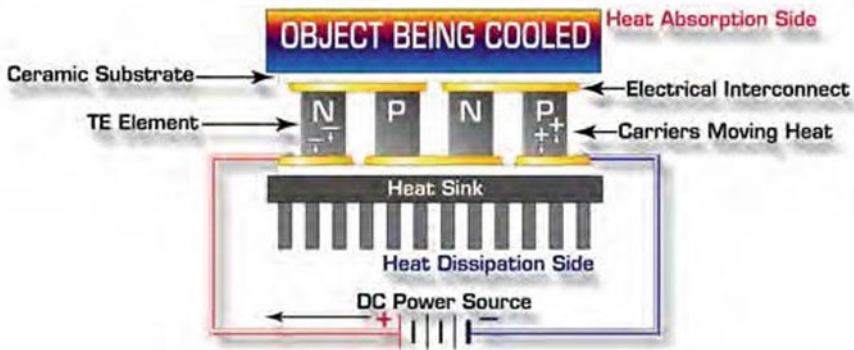


Fig. 1 TE module assembly [3]

be obtained through the cold surface depends upon certain factors including ambient temperature, voltage supplied, cooling mechanisms used in surfaces and quality of the TEC module [2].

A TEC module contains two plates made of ceramic. An array of p-type and n-type semiconductor couple is placed in between the two ceramic plates. These elements are arranged electrically series and thermal parallel. When a positive DC voltage is supplied to n-type semiconductor, electrons will pass from p-type element to n-type element causing heat reduction in cold surface and increased heat in hot surface. The rate of heat absorption is proportional to number of thermoelectric couples and amount of current applied as shown in Fig. 1 [3].

In this experiment, a pair of Peltier elements of TEM (Laird XA19) of size 4.5 cm × 4.5 cm is selected. The nominal characteristics of this Peltier element are given in Table 1 [4]. The research carried out was to implement the controller system for the thermoelectric cooling with intention to apply the system to automotive. Generally, it is understood that an automotive air conditioning system is powered by the internal combustion engine (ICE) itself, consequently reducing the effective output of the engine to the wheel. Therefore, by applying TEC in the automotive, the output of the ICE will not be compromised consequently lead to the improvement of fuel efficiency.

2 Methodology

2.1 Experimental Setup

A number of experiments were conducted to identify practical behavior of the TEC. All the experiments were done with samples of TEC (Laird XA19 series) at an ambient temperature of 22 °C. DC voltage application was varied from 5 to 24 V due

Table 1 Characteristics of Peltier element TEC Laird XA19 [4]

Characteristics	Value
Length (cm)	4.5
Width (cm)	4.5
Height (cm)	0.5
Wire length (cm)	12.0
I_{max} (A)	9.0
U_{max} (V)	30.0
Q_{cmax} (W)	24.0
T_{max} (°C)	-10.0 to 54.0

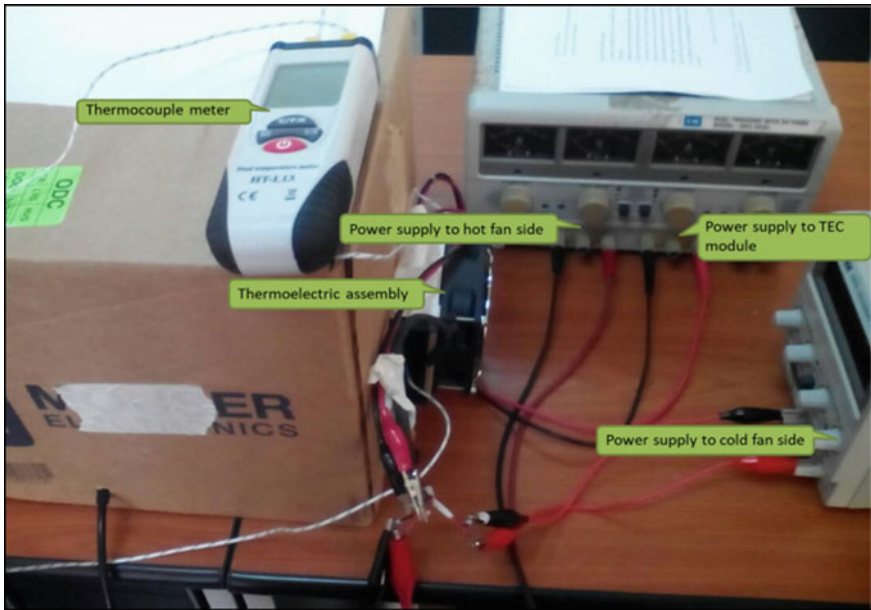


Fig. 2 Project connection diagram

to the limitation the power supply (Gw Instek Gps-3030d) and the maximum voltage specified for the module is 30 V. The temperature was measured with temperature sensor LM35Z for the ambient temperature of the cold side and thermocouple meter was used to measure the cold and hot side of TEC every 2 min. The TEC was assembled using aluminum heat sink and 10 V DC fans at both of hot and cool surfaces. An ambient temperature was created using a box as shown in Fig. 2. The inside of the box was covered with a sticker to reduce the heat loss due to radiation.

2.2 Experiment with ON-OFF Controller

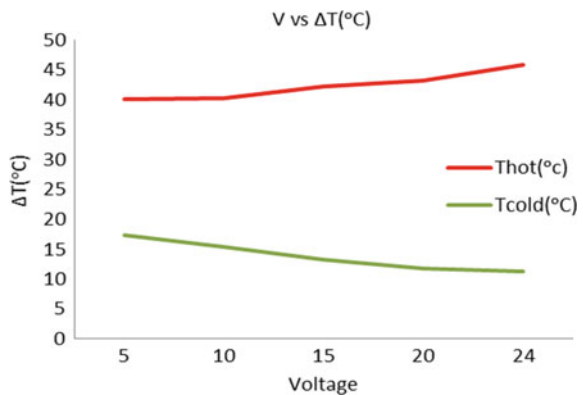
The code for the controller mode is uploaded to the Arduino board and is placed inside the box. The Arduino reads the temperature of the sample using the LM35Z temperature sensor which is connected to the Arduino. The TECs working as loads for the power drive to receive the necessary PWM signals and able to cool the attached sample to maintain the set-point temperature in a later stage of this project.

3 Results

3.1 Relationship Between Voltage and Current to the Temperatures of the Cold and Hot Surface of Thermoelectric Cooler

Users should be aware of the surface temperatures of TEC with various voltage values to use it in an application. Many of the manufacturer specifications provide the relationship between voltage and temperature gradient at specified hot or cold side temperatures. This test was done to verify the relationship between input voltage and surface temperature of both TEC side. The variation of temperature of both surface with the varying input voltage from 5 to 24 V is illustrated in Fig. 3. From the results it is clear that with the increment of voltage from 5 to 24 V, the cold side temperature reduces and increases temperatures of the hot side. The sample TECs had the lowest temperature for cool side of 11.3 °C at 24 V input. Therefore, if TECs are to be used in a refrigerating application, the relationship between voltage and the decrement of cold side temperature should be verified. Different maker of TEC may result in different temperature value corresponding to a certain voltage application.

Fig. 3 Temperature variation of cold surface (green) and hot surface (red) with the varying input from 5 to 24 V



3.2 Relationship Between Voltage and Current of Thermoelectric Cooler Using ON-OFF Controller

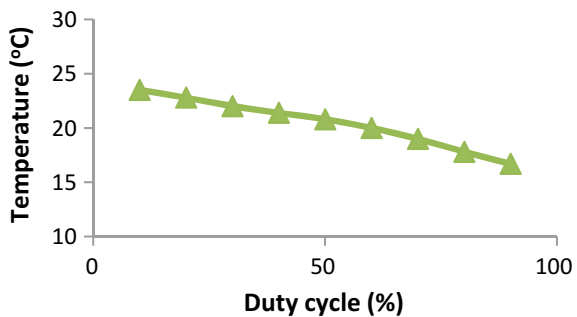
The relationship between the voltage and current is important in order to calculate power consumption and internal resistance of TEC. Table 2 shows the relationship duty cycle and output voltage of DC–DC converter, current and temperature of cold side. The increases in duty cycle causing the reduction of cold side temperature where the lowest value is 16.7 °C when duty cycle is at 90% and the calculated power of 15.6 W. By obtaining these values, temperature can be controlled through varying the duty cycle values. For example, if user wants to set the temperature to 20 °C, duty cycle of 50% must be selected. This type of controller keeps the TECs either completely turned on or completely turned off. The observed temperature and corresponding duty cycle of PWM are plotted in Fig. 4. One surface of the TEC starts absorbing heat and one surface starts releasing heat when a voltage is supplied. This is done in order to maintain the temperature gradient between two surfaces.

From the results summarized in Fig. 3 and 4, it can be observed that the cool surface of TEC had reduced its temperature between 17 and 14 °C within 2 min. When the voltage is gradually increased, the temperature of hot surface will keep increasing while the temperature of the cold surface will reduce. The temperature gradient will

Table 2 Characteristics of Peltier element in On-Off controller

Duty cycle (%)	Voltage output (V)	Current (A)	Power (W)	Temperature (°C)
10	1.36	0.14	0.19	23.5
20	2.24	0.26	0.58	22.8
30	2.76	0.44	1.21	22
40	3.35	0.67	2.24	21.4
50	3.67	0.93	3.41	20.8
60	4.32	1.26	5.44	20
70	5.19	1.62	8.41	19
80	5.8	2.06	11.95	17.8
90	6.32	2.47	15.61	16.7

Fig. 4 Relationship between duty cycle and temperature by using On-Off controller



increase gradually and come to a stable value. The temperature gradient will increase gradually and come to a stable value. The reduction of temperature shows a stepped nature. This could be the time taken by internal fans to achieve equilibrium inside the box. A better controller that can increase DC-DC converter voltage higher than this On-Off controller is needed in order to reduce the cold side temperature further.

4 Conclusion

The purpose of this study which is to implement the On-Off controller for TECs has been achieved. TECs show promising performance with varying voltage and duty cycle. When the voltage is gradually increased, the temperature of hot surface will keep increasing while the temperature of the cold surface will reduce. The temperature gradient will increase gradually and come to a stable value. There is a linear relationship between input voltage and current of TEC. The reduction of temperature shows a stepped nature. This could be the time taken by internal fans to make the equilibrium inside. The observed controller's response parameters demonstrated that the on-off controller responds faster but the maximum voltage supply to the TECs only can achieved 6.32 V output while the maximum voltage the TECs can hold is 24 V. However, since the output temperature produce is below the set point, which is quiet acceptable regarding the purpose of the experiment.

Acknowledgements This experiment was made possible by the support from Universiti Malaysia Pahang research grant RDU170375. Authors are very grateful for the support.

References

1. Nikam, A.N., Hole, J.A.: A Review on use of peltier effects, *2*(2), 6–12 (2014)
2. Alaoui, C.: Peltier thermoelectric modules modeling and evaluation. *Int. J. Eng. (IJE)* **5**, 114–121 (2011)
3. Patil, P.J., Patil, P.A.M.: Review on thermoelectric devices. *Int. J. Emerg. Technol. Adv. Eng.* **3**(10), 681–688 (2013)
4. Laird technology, thermoelectric modules. Retrieved from <https://www.lairdtech.com/product-categories/thermal-management/thermoelectric-modules>

Optimal Placement of TCSC for Reactive Power Planning Using Grasshopper Optimization Algorithm Considering Line Outage (N-M)



Muhamad Amirul Asyraf Juhari, Nor Rul Hasma Abdullah, Ibrahim Haruna Shanono, Mahfuzah Mustafa, Rosdiyana Samad and Dwi Pebrianti

Abstract Increment of power demand in power system can cause a rapid reduction in voltage profile that can disrupt the system stability thus make an entire system failure as the system has to work under contingencies and stress conditions. In this paper, Grasshopper Optimization Algorithm (GOA) has been applied for solving the reactive power planning, considering a line outage occurs in the system with Thyristor Controlled Series Compensator (TCSC) which minimizes transmission power loss. Standard IEEE-30 bus test system has been applied to the test system. Optimal setting of all control variables, namely locations and the sizes of the TCSC has been determined by GOA and power flow analysis method. The investigation is carried out via simulation using MATPOWER and MATLAB software.

Keywords TCSC · Optimization · Transmission loss · Line outage · GOA

1 Introduction

Nowadays, the power transmission systems have been changed a lot. The reactive power unbalanced effected the power transfer limitation has drawn attention to better utilize of the existing transmission line. One of the reasons to cause blackout or collapse in the transmission system can be the shortage of the reactive power thus the transmission line is overloading [1]. How to prevent and corrects it, become the main issues proposed in a power system planning. The placement of FACTS controllers is suggested as an effective method to prevent against the voltage collapse

M. A. A. Juhari · N. R. H. Abdullah (✉) · I. H. Shanono · M. Mustafa · R. Samad · D. Pebrianti
Faculty of Electrical & Electronics Engineering, Universiti Malaysia Pahang,
Pekan, Pahang, Malaysia
e-mail: hasma@ump.edu.my

I. H. Shanono
Department of Electrical, Faculty of the Engineering, Bayero University, Kano, Nigeria

© Springer Nature Singapore Pte Ltd. 2019

Z. Md Zain et al. (eds.), *Proceedings of the 10th National Technical Seminar*

on Underwater System Technology 2018, Lecture Notes in Electrical Engineering 538,

https://doi.org/10.1007/978-981-13-3708-6_57

by installation of Thyristor Controlled Series Capacitor (TCSC). It shows fast-acting reactive power compensation with a much faster response on high-voltage electricity transmission networks compared to traditional control devices [2]. However, due to the high cost of FACTS device, it is important to optimally place these controllers in the system.

The static and dynamic performances are mainly being used to determine the setting of FACTS devices in power system. Significantly, there are several ways to find the best optimal locations of FACTS devices in the power system network. The series controllers such as TCSC can be used to reduce the line loading by controlling power flow in the power system network [1]. One of the most challenging problems in the field of operation research is solving optimization problems. The placement and determining the sizes of FACTS devices can be described as an optimization problem. The aim is to reduce the power loss, maximize the voltage stability margin and minimize the voltage magnitude deviation [3]. Different steps need to be taken in order to solve an optimization problem. Optimal location of FACTS devices for controlling the reactive power in power system was proposed by [4]. The main point is to obtain the bus voltages of the system within good limits. By using genetic algorithm (GA) the locations of FACTS devices and their rated values are optimized simultaneously. Kaur and Khela have developed the optimal locations if multi type of FACTS devices for voltage profile improvement and minimize or reduces power system losses [5].

Demanding of high performance, low cost and losses in the power system are the example where the optimization approach is required. There are a lot of techniques and approaches allowing a more suitable optimization tool for power system [6] develops optimal location and parameter setting of TCSC for loss minimization based on Differential Evolution (DE) and Genetic Algorithm (GA). The objective is to increase the transfer capability and enhancing the stability of the transmission system. In addition, Differential Evolution (DE) [7] and the Firefly Algorithm (FA) [8] has been successfully applied for finding the optimal parameter setting of the TCSC considering loss minimization as the objective function in a power system. Grasshopper Optimization Algorithm (GOA) is another technique successfully applied for solving the optimization problems [9].

This paper focused on the steady-state modeling of a TCSC with GOA method applied in determining the optimal locations and sizes of TCSCs in the system. The objective is to minimize the transmission losses considered the equality and inequality constraint in power system. The simulation is tested on IEEE 30-bus RTS considering the system under stress and contingency namely line outage occurs in the system. The analyses carried out with and without outages for performance analyses.

2 Problem Formulation

In this paper, the GOA technique is implemented to determine the control setting variable of TCSC i.e., location of the installation and sizes of TCSCs for minimizing

the transmission losses in the system at a same time, satisfying all equality and inequality constraints. Ten initial variables (parent) i.e., $x_1, x_2, x_3, x_4 \dots$ and x_{10} are generated randomly where these values are the locations and sizes of TCSCs to be installed in the system. The values are transferred into the load flow program (MATPOWER) for determining the total transmission losses of the test system.

2.1 Objective Function

The expression of the objective function can be represented in Eq. (1) [1].

$$\text{Min } F_1 = P_{Loss}(x, u) = \sum_{L=1}^{NI} P_L \tag{1}$$

$$P_L = \sum_{K=1}^{NL} G_k(V_i^2 + V_j^2 - 2 * V_i * V_j * \cos \delta_{ij})$$

where

- x is the vector of dependent variables,
- u is the vector of control variables,
- P_L is the real power losses at line- L ,
- NI is the number of transmission lines,
- P_L is losses prevailing in the system,
- G_{ij} is the conductance of the line joining bus- i and bus- j ,
- δ_{ij} is the phase difference between the buses,
- V_i and V_j are the absolute value of voltages the buses i and j

2.2 Equality Constraints

Equality constraint includes the total system generation, namely the load demand of the system and the transmission losses. The equations for power balance constraints are shown below;

$$P_{Gi} - P_{Di} - V_i \sum_{j=1}^{NB} V_j (G_{ij} \cos \delta_{ij} + B_{ij} \sin \delta_{ij}) = 0 \tag{2}$$

$$Q_{Gi} - Q_{Di} - V \sum_{j=1}^{NB} V_j (G_{ij} \sin \delta_{ij} + B_{ij} \cos \delta_{ij}) = 0 \tag{3}$$

for $j = 1, 2, \dots N_B$ where

- N_B is the bus number
- P_{Gi} and P_{Di} are the active power of i th generator and load bus
- Q_{Gi} , Q_{Di} are the reactive power of i th generator and load bus
- G_{ij} and B_{ij} are the conductance, admittance between bus- i and bus- j
- δ_{ij} is the phase difference between bus- i and bus- j

2.3 Inequality Constraints

The inequality constraints are mathematically expressed as follow:

$$Q_{Gi}^{min} \leq Q_{Gi} \leq Q_{Gi}^{max} \tag{4}$$

$$tap_i^{min} \leq tap_i \leq tap_i^{max} \tag{5}$$

$$X_{TCSC}^{min} \leq X_{TCSC} \leq X_{TCSC}^{max} \tag{6}$$

where

Q_{Gi}^{min} Q_{Gi}^{max} are the reactive power output limit of generator- i , tap_i^{min} and tap_i^{max} are the tap-limits of tap-changing transformers, and X_{TCSC}^{min} and X_{TCSC}^{max} are the operating limits of TCSC

3 Thyristor-Controlled Series Compensation (TCSC)

Figure 1 shows the static model of TCSC. By inserting a variable reactance either inductive or capacitive in series with the transmission line, the power flow in the transmission line can be manipulated [2].

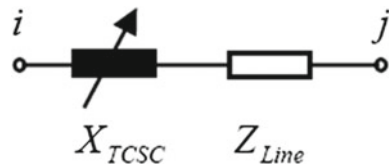
$$Z_{ij} = Z_{line} + jx_{TCSC} \tag{7}$$

$$x_{TCSC} = \gamma_{TCSC}x_{line} \tag{8}$$

where

- Z_{line} is the impedance of the transmission line,
- x_{TCSC} is the reactance of the line where TCSC is located,
- x_{line} is the reactance of TCSC, and

Fig. 1 Static model of TCSC



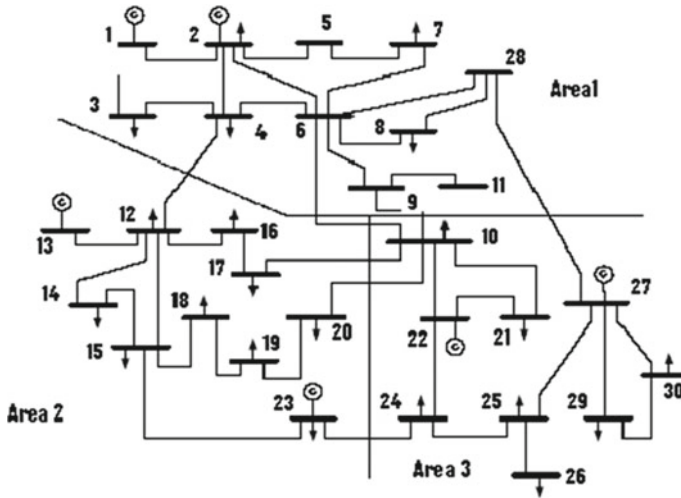


Fig. 2 Configuration of IEEE 30-bus System

γ_{TCSC} is the coefficient which represents the compensation degree of TCSC

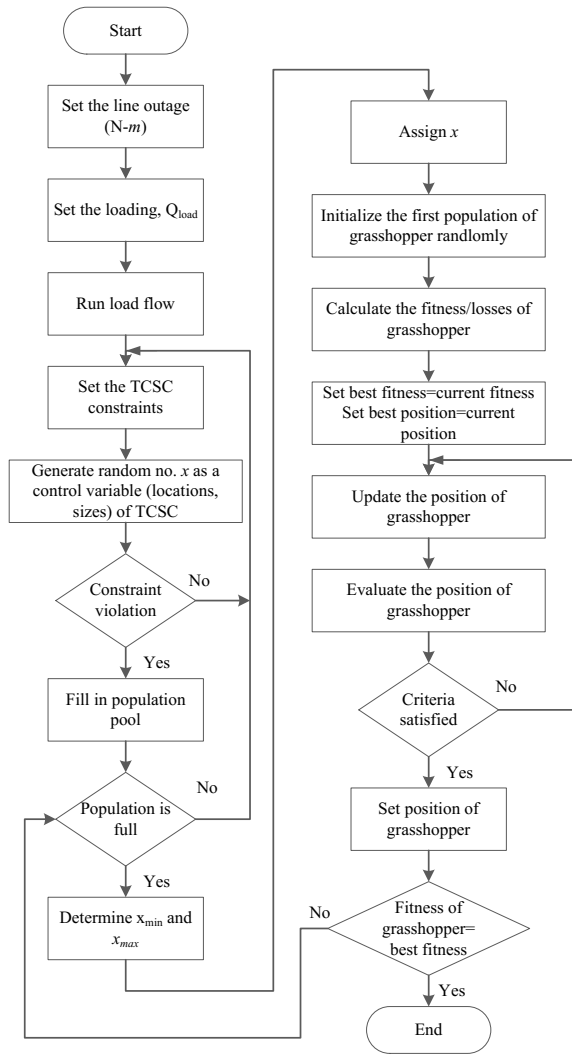
4 IEEE 30-Bus RTS System

The GOA technique has been tested on the IEEE 30-bus system. The bus system consists of five voltage control buses, twenty-four load buses, one slack bus, forty-one interconnected lines and four transformers tap changers. The base power is 100 MVA. The load bus 25 was selected to perform the test. Several outages are selected to be in the analysis. The configuration of the bus system is shown in Fig. 2.

5 Grasshopper Optimization Algorithm

The GOA is a nature-inspired optimization which mimicking the natural behavior of the grasshoppers in seeking the source of food in the shortest distance [9]. The search processes are divided into exploration and exploitation. In exploration, the search agents are moving abruptly while in exploitation, then tent to move locally. The life cycle of the grasshopper is starting from the egg, nymph and end with the adult phase. These insects are considered as a pest and in a large group it will damage the production of crops in a farm. In larval phase, the movement is slow and small step. While, in adult stage the movement is in contrast which long range and abrupt movement. The technique was implemented in the flowchart as shown in Fig. 3 and

Fig. 3 Flowchart of application of GOA in TCSC



the process of the implementation of GOA technique are described in the following section.

5.1 Swarming Behavior

The mathematical model for the swarming behavior is shown below [9];

$$x_i = S_i + G_i + A_i \tag{9}$$

where

- x_i is the position of the i th grasshopper,
- S_i the is social interaction of the i -th grasshopper,
- G_i is the gravity of the i th grasshopper,
- A_i is the wind advection of the i -th grasshopper

The equation can be written as $x_i = r_1S_i + r_2G_i + r_3A_i$, where r_1, r_2 and r_3 are random number.

5.2 Social Interaction, S

The S component in Eq. (9) is calculated as follows [9];

$$S_i = \sum_{\substack{j = 1 \\ j \neq i}}^N s(d_{ij})\widehat{d}_{ij} \tag{10}$$

where d_{ij} is the distance between the j th grasshopper, calculated as $d_{ij} = |x_i - x_j|$, s is a function to define the strength of social forces and $\widehat{d}_{ij} = \frac{x_j - x_i}{d_{ij}}$ is a unit vector from the i th grasshopper to the j th grasshopper.

The s function in Eq. (10) which defines the social forces is calculated as

$$s(r) = fe^{\frac{r}{l}} - e^{-r} \tag{11}$$

where

- f is the intensity of attraction and
- l is the attractive length scale

5.3 Gravity Force, G

The G component in Eq. (9) is calculated as follows [9];

$$G_i = -g\widehat{e}_g \tag{12}$$

where

- g is gravitational constant and

\widehat{e}_g is unity vector towards the centre of earth

5.4 Wind Advection, A

The A component in Eq. (9) is calculated as follows [9];

$$A_i = u\widehat{e}_w \tag{13}$$

where u is constant drift and \widehat{e}_w is unity vector in the direction of wind. Nymph grasshoppers don't have a wing therefore their movements are highly correlated with wind direction.

By substituting Eqs. (11) and (12) and Eq. (13) into Eq. (9), the equation becomes:

$$X_i = \sum_{\substack{j=1 \\ j \neq i}}^N s(|x_j - x_i|) \frac{x_j - x_i}{d_{ij}} - g\widehat{e}_g + u\widehat{e}_w \tag{14}$$

where

N is the number of grasshoppers

A modified version of this equation is proposed as the previous mathematical model cannot be used directly to solve optimization problems, [9]:

$$x_i^d = c \left(\sum_{j=1}^N c \frac{ub_d - lb_d}{2} s(|x_j^d - x_i^d|) \frac{x_j - x_i}{d_{ij}} \right) + \widehat{T}_d \tag{15}$$

where

ub_d is upper bound in the d th dimension, lb_d is lower bound in the d th dimension, \widehat{T}_d is value of d th dimension in the target and c is decreasing coefficient to shrink the comfort zone, repulsion zone and attraction zone.

6 Simulation Results and Discussion

This section discussed the analysis of data obtained for 50 iterations. The size and the location of TCSCs can determine by using GOA. Ten initial variables (parent) i.e., $x_1, x_2, x_3, x_4 \dots$ and x_{10} are generated randomly. These values will be the location and size of TCSCs to be installed and transferred into the load flow programme for evaluating the total losses. The highest iteration gives the best value of the unknowns of 'x' which indicates the sizes and locations of TCSCs to be installed. After several

Table 1 Boundaries setting for control variables for IEEE 30-bus system

Control variables	Lower bound	Upper bound
TCSC location	1	41
TCSC sizing (p.u)	-0.8	0.2

tests, the results after the 50 iterations give the same value of 'x'. The comparison data are made by adding gradually the reactive load to the bus 25, which is one of the most critical buses [2]. In addition, the contingency analysis, which is N-m, line outage is also considered to be applied at two weak lines. The selection for line outage was based on the most severe line in the system [2]. The line outage (N-m) is implemented for the contingency analysis in order to analyze the performance of the TCSC toward the effect of the outage occurs in the system. The results are divided into two cases; Case 1 consider for bus 25 being stressed from 0 until 40MVar and Case 2, with line outage occurs at line 1 or line 9 in the system. Table 1 tabulates the boundary setting control for the TCSCs.

6.1 Case 1: Solution for 50 Population Size (IEEE 30-Bus RTS) Without Line Outage

Results for total loss minimization are tabulated in Table 2. Loading in bus 25 is increasing gradually in order to observe the effect of total losses with the installation of TCSCs to the system. The load was increased until 40 MVar. The five locations and sizes of TCSCs installed in the network are also identified by using GOA. As shown in the table and Fig. 4, the GOA technique successfully reducing the total losses by determining the optimal setting variable of TCSCs. At loading condition $Q_L = 40$ MVar, the total losses are reduced to 7.8123 from 10.1585 MW with the optimal location at line number 33, 27, 17, 9 and 35. The values of TCSC are -0.5536, -0.1519, 0.1538, -0.4227 and -0.4913 p.u.

6.2 Case 2: Solution for 50 Population Size (IEEE 30-Bus RTS) with Line Outage

Result in total loss minimization considering (N-1) contingency in a transmission line is tabulated in Table 3 in line outage number 1 and Table 4 for line outage number 9. From the tables, bus 25 was subjected to variation of loading conditions. Loading in MVAR is increased gradually in order to observe the effect of total losses with the installation of TCSCs to the system. The load was increased up to 40 MVar. The five locations of TCSCs installation in the network and the sizes are identified by using GOA technique and shown in the table. Different loading condition shows a

Table 2 Transmission Losses with manipulated loading condition

Q _L (MVar)	Pre optimization (MW)	Post optimization (MW)	Location line no.	Sizing (MVar)
0	5.7635	5.5053	4	-0.4778
			1	0.0565
			2	0.1882
			40	-0.6466
			10	0.1329
10	6.3703	5.9422	1	0.1169
			25	-0.6912
			3	0.4913
			1	-0.7005
			35	-0.6098
20	6.8491	6.1736	40	-0.0752
			40	-0.7387
			4	-0.6468
			29	-0.7668
			35	-0.5759
30	8.1321	6.8421	15	-0.2237
			35	-0.7831
			14	0.1997
			41	-0.8000
			35	-0.5205
40	10.1585	7.8123	33	-0.5536
			27	-0.1519
			17	0.1538
			9	-0.4227
			35	-0.4913

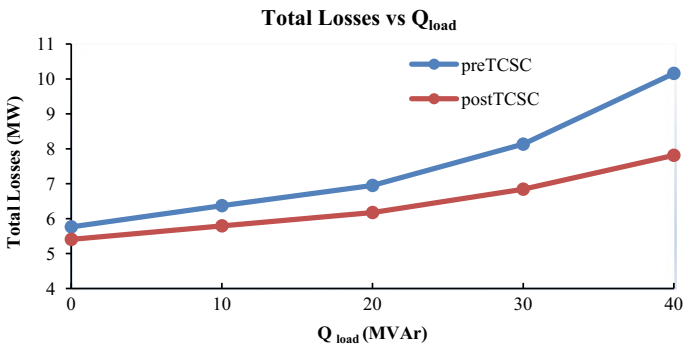


Fig. 4 Graph of comparison with manipulating loading condition

Table 3 Transmission Losses with manipulated loading condition with line outage 1

Q_L (MVar)	Pre optimization (MW)	Post optimization (MW)	Location line no.	Sizing (MVar)
0	8.7550	8.6044	14	-0.5582
			1	-0.3323
			40	-0.0519
			9	-0.6871
			2	-0.8000
10	9.1019	8.8303	7	-0.6528
			10	-0.2726
			40	0.5017
			19	0.0635
			34	-0.6432
20	9.9514	9.2162	2	0.1625
			1	-0.4198
			13	-0.6908
			5	-0.3674
			34	-0.5821
30	11.3487	9.9596	17	-0.7056
			2	-0.0091
			8	0.1497
			15	-0.8000
			34	-0.5208
40	13.5580	11.0259	20	-0.2550
			17	-0.0201
			33	-0.0468
			39	0.0755
			34	-0.4904

different location for TCSCs placement in the system as it were optimized by the GOA subjected to loading factor variation.

From Table 3 and Fig. 5, it is observed that the total losses value of the post-TCSC decreased with the increment in the loading factor. For instance, at loading condition of 40 MVar the losses have been reduced from 13.5580 to 11.0259 MW with the 18.7% lower than before the installment of TCSCs. In order to achieve this reduction, the values of TCSC are -0.2550, -0.0201, -0.0468, 0.0755 and -0.4904 p.u. which should be installed on line number 20, 17, 33, 39 and 34 respectively. The results for other loading factor are indicated in the same table.

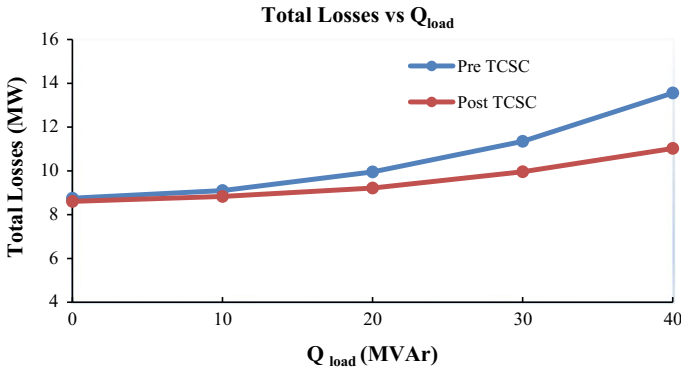


Fig. 5 Graph of comparison with manipulating loading condition (Line Outage No. 1)

7 Conclusion

This paper presented the application of Thyristor Controlled Series Compensator (TCSC) planning using a Grasshopper Optimization Algorithm (GOA) technique for transmission loss minimization for system under stress and contingency. In this study GOA is applied at bus 25 for the minimization of real power loss as the objective function. Simulation was carried out on IEEE 30-bus system. The GOA techniques performed well in most cases. Simulation results show that the GOA is practical for the transmission loss minimization. For future work, other FACTS devices such as UPFC, SVC, STATCOM and TCPAR can be incorporated together to achieve similar task.

Acknowledgements This work is supported by the Faculty of Electrical and Electronic Engineering, Universiti Malaysia Pahang Internal Grant (RDU1703226)

References

1. Abdullah, N.R.H., Musirin, I., Murthada, M.: Constrained reactive power control using evolutionary computation technique for static security enhancement. In: 2009 Second International Conference on Computer and Electrical Engineering, pp. 612–616 (2009)
2. Abdullah, N.R.H., Musirin, I., Othman, M.M.: Thyristor controlled series compensator planning using evolutionary programming for transmission loss minimization for system under contingencies. In: 2010 IEEE International Conference on Power and Energy (PECON2010), pp. 18–23 (2010)
3. Jiang, X., Chow, J.H., Edris, A.A., Fardanesh, B., Uzunovic, E.: Transfer path stability enhancement by voltage-sourced converter based FACTS controllers. *IEEE Trans. Power Delivery* **25**(2), 1019–1025 (2010)
4. Bansal, H.O., Agrawal, H.P., Tiwana, S., Singal, A.R., Shrivastave, L.: Optimal location of FACTS devices to control reactive power. *Int. J. Eng. Sci. Technol.* **2**(6), 1556–1560 (2010)

5. Kaur, S., Khela, R.S.: Review on the optimization of power system stability and analysis using FACTS controller. *9*(16), 8109–8114 (2016)
6. Rashed, G.I., Sun, Y., Shaheen, H.I.: Optimal location and parameter setting of TCSC for loss minimization based on differential evolution and genetic algorithm In: 2012 International Conference on Medical Physics and Biomedical Engineering Optimal, vol. 33, pp. 1864–1878 (2012)
7. Rashed, G.I., Sun, Y., Shaheen, H.I.: Optimal TCSC placement in a power system by means of differential evolution algorithm considering loss minimization. In: Proceedings of the 2011 6th IEEE Conference on Industrial Electronics and Applications (ICIEA2011), pp. 2209–2215 (2011)
8. Ritthipakdee, A., Thammano, A., Premasathian, N., Uyyanonvara, B.: An improved firefly algorithm for optimization problems. In: 5th International Symposium on Advanced Control of Industrial Processes, Hiroshima, pp. 159–164 (2014)
9. Saremi, S., Mirjalili, S., Lewis, A.: Grasshopper optimisation algorithm: theory and application. *Adv. Eng. Softw.* **105**, 30–47 (2017)